Title

HYDROCARBON CATALYSIS OVER PLATINUM SINGLE CRYSTAL SURFACES: THE ROLE OF ADSORBED CARBON DEPOSITS AND OTHER CHEMICAL ADDITIVES

Author

Davis, S.M.

Publication Date

1981-10-01

Lawrence Berkeley Laboratory
UNIVERSITY OF CALIFORNIA

Materials & Molecular Research Division

HYDROCARBON CATALYSIS OVER PLATINUM SINGLE CRYSTAL SURFACES: THE ROLE OF ADSORBED CARBON DEPOSITS AND OTHER CHEMICAL ADDITIVES

Stephen Mark Davis
(Ph.D. thesis)

October 1981

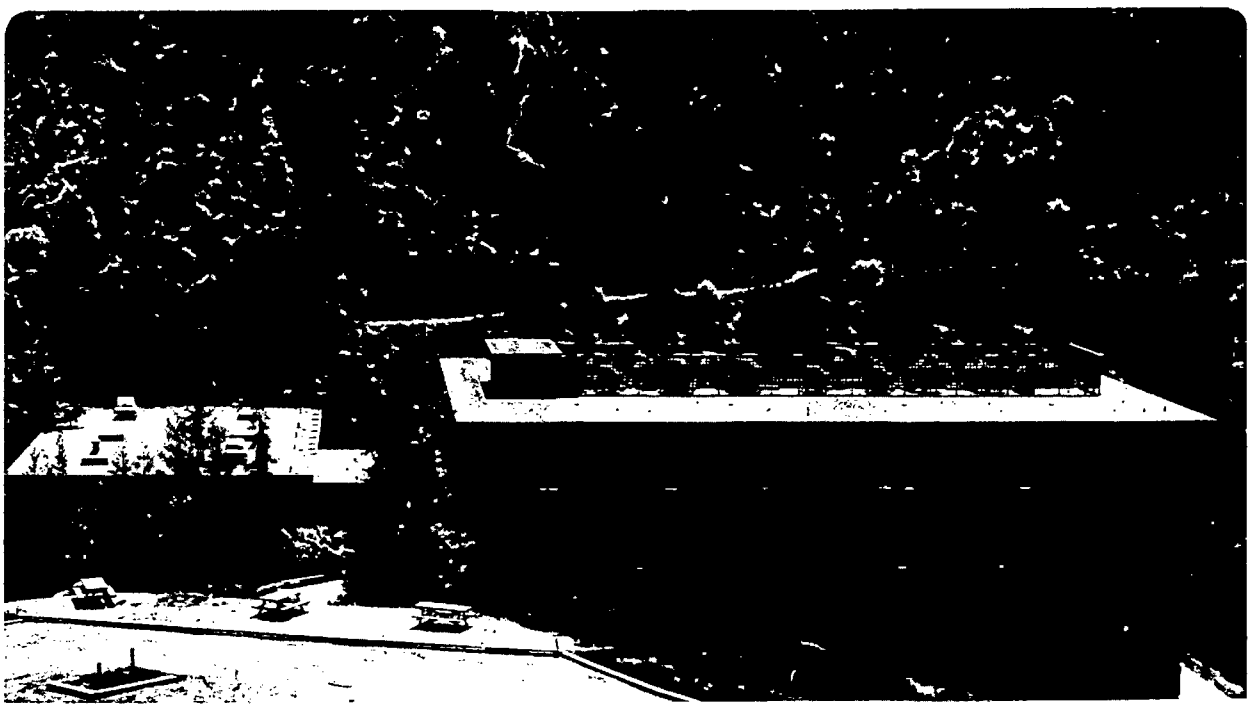

Prepared for the U.S. Department of Energy under Contract W-7405-ENG-48

DISCLAIMER

LBL-13051

HYDROCARBON CATALYSIS OVER PLATINUM SINGLE CRYSTAL SURFACES: THE ROLE OF ADSORBED CARBON DEPOSITS AND OTHER CHEMICAL ADDITIVES

Stephen Mark Davis

Ph.D. Thesis

October 1981

Materials and Molecular Research Division
Lawrence Berkeley Laboratory
University of California
Berkeley, CA 94720

This work was supported by the Director, Office of Energy Research, Office of Basic Energy Sciences, Material Sciences Division of the U.S. Department of Energy under Contract Number W-7405-ENG-48.

HYDROCARBON CATALYSIS OVER PLATINUM SINGLE CRYSTAL SURFACES:
THE ROLE OF ADSORBED CARBON DEPOSITS AND OTHER CHEMICAL ADDITIVES

Contents

HYDROCARBON CATALYSIS OVER PLATINUM SINGLE CRYSTAL SURFACES: THE ROLE OF ADSORBED CARBON DEPOSITS AND OTHER CHEMICAL ADDITIVES

Stephen Mark Davis

Materials and Molecular Research Division
Lawrence Berkeley Laboratory
and Department of Chemistry
University of California
Berkeley, CA 94720

ABSTRACT

The role of strongly adsorbed hydrocarbon deposits in reforming catalysis over platinum single crystal surfaces at atmospheric pressure and temperatures between 300 and 700 K has been established and a model developed for the working structure and composition of the active catalyst surface. For this purpose a sensitive counting system for carbon-14 radiotracer studies was developed and utilized to investigate the kinetics of hydrocarbon rehydrogenation and intermolecular hydrogen transfer reactions. Quantitative hydrogen thermal desorption methods were developed to determine the composition of adsorbed hydrocarbon species and the energetics of elementary, sequential C-H bond breaking processes. Carbon-monoxide adsorption-thermal desorption studies were used to titrate uncovered platinum surface sites before and after reaction rate studies. The dynamics of the metal-hydrocarbon interaction, including minimum surface residence times for dissociatively chemisorbed intermediates (10^{-2} - 10^{-1} sec) were revealed from simultaneous studies of the reaction kinetics for hydrocarbon-deuterium exchange and skeletal rearrangement. Restart reaction studies were used to investigate the catalytic activity and selectivity of carbon covered platinum. These studies together with deactivation kinetics

derived from reaction rate studies over initially clean platinum surfaces have clearly demonstrated that the primary role of the disordered, polymeric carbonaceous deposit is very simply that of a non-selective poison.

The structure sensitivity of n-butane, isobutane, neopentane, and n-hexane skeletal rearrangement catalyzed at atmospheric pressure and 530-700 K was investigated on a series of platinum single crystal surfaces with variable terrace, step, and kink structure. Only aromatization and bond-shift isomerization displayed structure sensitive reaction kinetics. High aromatization specificity was achieved on surfaces containing high concentrations of contiguous (111) microfacets. Butane isomerization activity and selectivity were maximized on platinum surfaces with high concentrations of (100) microfacets. Hydrogenolysis product distributions varied markedly with surface structure. Alkane hydrogenolysis, isomerization, and c_5-cyclization reactions all displayed inverse deuterium isotope effects (R_D/R_H = 1.3-3) that arise from a combination of kinetic and thermodynamic isotope effects. The influence of sulfur, strongly bound oxygen, and calcium oxide surface impurities on the hydrocarbon reaction kinetics has also been explored. Whenever possible, detailed comparisons have been made between the catalytic behavior of the single crystal surfaces and practical platinum catalysts.

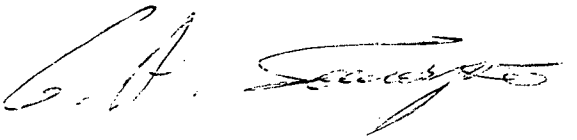

ACKNOWLEDGEMENTS

This thesis is the culmination of more hard work and sacrifice than I presently care to remember. Needless to say, the efforts of many exceptionally talented people were essential for bringing this work to fruition. I am most grateful to Professor Gabor Somorjai for providing me the opportunity to carry out exciting research with great freedom. His excellence, enthusiasm, and creativity as a scientist will always be a source of inspiration to me. I have learned immensely from his guidance, understanding and friendship.

The continuous collaboration and encouragement provided by a long list of former and present Somorjai group members was very important to the completion of this research. While everybody contributed to this, I am especially thankful to the Hemmingers, F. Wagner, B. Guthrie, T. Lin, J. P. Biberian, R. Carr, N. Spencer, M. Salmeron, S. Ferrer, F. Zaera, A. Sachtler, and B. Gillespie for providing technical knowledge, good ideas, and moral support. Gillespie even offered his apparatus when everything was going bad.

The excellent support staff of LBL contributed at least as much as I did to the preparation of this thesis and to the design, construction and maintenance of several pieces of apparatus. In this respect I am most grateful to J. Severns, M. Press, B. Gordon, W. Heppler, W. Wong, G. Baum, J. Wolslegel, G. Pelatowski, and B. McAllister.

Immeasurable thanks go to my parents for their continuous love and support and also to Professor Jack Lunsford (Texas A&M) who first introduced me to surface chemistry and catalysis science. Steve, Trues, and Don have been the best possible friends and housemates throughout the past four years in Berkeley, which, to say the least, were almost always exceedingly enjoyable.

This work was supported by the Director, Office of Energy Research, Office of Basic Energy Sciences, Material Sciences Division of the U. S. Department of Energy under contract number W-7405-ENG-48.

CHAPTER 1. INTRODUCTION AND OVERVIEW

The chemisorption and surface reactions of hydrocarbons on metal surfaces have been investigated intensively from the viewpoint of heterogeneous catalysis (1-3). Skeletal rearrangement reactions that encompass dehydrogenation, isomerization, cyclization, and aromatization of paraffinic hydrocarbons in the c_5-c_{10} gasoline range are of paramount importance in the catalytic reforming of about 4 billion barrels of petroleum feedstocks annually (4,5). The most important types of metal catalyzed hydrocarbon reactions are summarized in Scheme 1 along with pertinent thermochemical information for each reaction type (6). Several reaction pathways usually operate simultaneously to produce a wide distribution of reaction products. The enthalpies of these reactions vary predictably with the differences between average C = C (147 kcal/mole), C-C (83 kcal/mole), C-H (99 kcal/mole), and H-H (104 kcal/mole) bond energies. Hydrogenolysis and hydrogenation reactions that involve rupture of carbon-carbon bonds and formation of two carbon-hydrogen bonds are invariably exothermic. By contrast, dissociative dehydrogenation and aromatization reactions are highly endothermic and, as such, become thermodynamically feasible only under conditions of high temperatures or low hydrogen pressure. Aromatic compounds and branched isomers are desireable products of the catalytic reforming process which includes the reactions B-F and leads to blended fuels with superior octane (antiknock) characteristics.

The most important skeletal reforming reactions such as dehydrogenation and aromatization are catalyzed selectively by only a

Scheme 1. Important Types of Metal-Catalyzed Hydrocarbon Reactions

A. Double-bond isomerization of olefins,

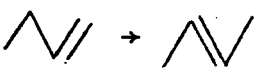

$\Delta H_{300} = -2.6$ kcal/mole

B. Hydrogenation of olefins and other unsaturated hydrocarbons,

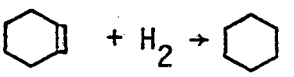

$\Delta H_{300} = -28.2$ kcal/mole

C. Dehydrogenation of cyclohexanes to aromatic hydrocarbons,

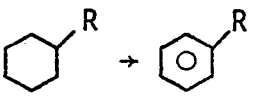

$\Delta H_{600} = 52.4$ kcal/mole

D. Dehydroisomerization of alkylcyclopentanes to aromatic hydrocarbons,

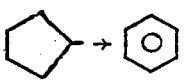

$\Delta H_{600} = 48.3$ kcal/mole

E. Isomerization of alkanes,

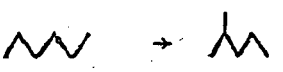

$\Delta H_{600} = -1.9$ kcal/mole

F. Dehydrocyclization of alkanes to cycloalkanes and aromatic hydrocarbons,

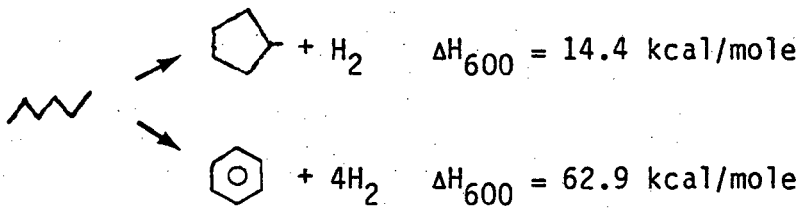

G. Hydrogenolysis and ring opening,

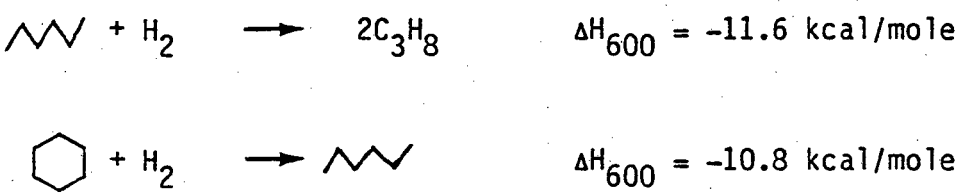

* * *

small group of transition metals and alloys, most notably platinum and bimetallic alloys including Pt-Au, Pt-Re, Ir-Au, and Pd-Au (1,7). Catalysts based on these noble metals display a unique combination of high catalytic activity with minimal tendency for the undesireable c-c bond breaking (hydrogenolysis) reactions that always accompany skeletal rearrangement (1). The selective skeletal rearrangement of c_4-c_6 alkanes on platinum catalysts forms the main subject of this thesis.

Commercial reforming processes are always carried out at high temperatures (670-820 K) and pressures (H_2/HC = 5-10, P_{tot} = 10-50 atm) in order to obtain maximum reaction rates and high equilibrium conversions. To achieve efficient utilization of the rare and expensive

metal component, commercial catalysts are utilized in a highly dispersed form in which small metal crystallites that average about 20-50Å in diameter are supported on high surface area oxides ($\gtrsim$200 m^2/g) such as alumina, silica-alumina, and zeolites. Both components, the support and the dispersed metal, play important catalytic roles that are characterized by a synergistic relationship known as bifunctional catalysis (4,5). In this case, olefins and other unsaturated molecules that are produced by the metal component readily undergo secondary isomerization and cyclization (but not aromatization) reactions on the acid-sites of the support (5). The metal alone catalyzes the same skeletal rearrangement reactions but at a much reduced rate as compared to dehydrogenation. Consequently, the activity and selectivity of bifunctional catalysts are usually far superior to that for the sum of the individual components considered separately.

One of the most important goals of modern catalysis science is to achieve the predictive ability to tailor-make new reforming catalysts which will display improved catalytic performance that is represented by any useful combination of superior activity, selectivity, and longer catalyst lifetime. For this purpose, it is essential to gain a detailed knowledge of how and why both components of good reforming catalysts work. Once the essential ingredients of high specifity are established, it may become feasible to incorporate this knowledge into the development of efficient, inexpensive substitutes for platinum, iridium, and related precious metals that are always employed as reforming catalysts. Alternatively, the discovery of improved support materials or more

efficient impregnation methods that deposit metal clusters with specific surface structure could substantially reduce the amount of Group VIII metal required in the conventional catalysts.

For these reasons, the catalytic behavior of platinum has been studied extensively along two diverse directions in an effort to elucidate the working atomic structure and composition of the active catalyst surface. The first approach involves the study of hydrocarbon-reactions catalyzed on high surface area practical catalysts as a function of catalyst pretreatment and average metal particle size. These catalysts include polycrystalline powders, evaporated films, and silica supported platinum. A comprehensive review of these studies including a unique and complete compilation of reaction kinetics published prior to 1980 was recently reported by this author (1). Traditionally, it has been difficult to draw detailed conclusions from these studies because the surface structure is always heterogeneous and the surface composition is rarely if ever well-defined. Despite recent advances in nuclear magnetic resonance (8), Mossbauer spectroscopy (8,9), EXANES (10), and EXAFS (10,11), it is still very difficult to accurately characterize practical catalysts on an atomic scale. Perhaps the most important concepts to emerge from these studies are the ideas of primary (12) and secondary (13) structure sensitivity. Primary structure sensitivity reflects a marked dependence of the reaction rates, mechanisms, or selectivities on the atomic arrangement and average coordination number of the exposed metal atoms. These structural properties vary most markedly as the average metal crystallite size is varied between about 10 and 60Å (14).

Secondary structure sensitivity, by contrast, reflects particle size dependent changes in catalytic behavior that originate exclusively from the presence of additives or impurities on the catalyst surface. Viewed in this context, alkane hydrogenolysis, isomerization, and aromatization reactions all appear to be structure sensitive reactions (1). Other reactions including olefin hydrogenation and ring opening generally appear to be structure insensitive (1). The structure insensitive reactions may proceed through a series of structure sensitive reaction steps that are not rate-limiting under the conditions of the experiment. An especially important attribute of practical catalyst studies is the fact that catalyst improvements can easily be translated into new petroleum technology.

A second major approach to the study of hydrocarbon catalysis was initiated in this laboratory about a decade ago after surface science provided techniques to characterize the influence of surface structure and composition on the reaction kinetics. This approach involves the study of hydrocarbon reactions catalyzed on small area (~1 cm^2) model catalysts including single crystal surfaces and polycrystalline foils. These catalyst systems can be easily characterized directly before and after reaction rate studies using low energy electron diffraction, Auger electron spectroscopy, and a wide variety of complementary surface analysis methods. In order to closely simulate the small metal particles of dispersed metal catalysts, ordered surface irregularities (steps and kinks) with fewer nearest neighbors can be introduced and their

concentrations systematically varied. This approach forms the basis for the research described throughout the remainder of this thesis.

Previous model catalytic studies at low (10^{-7} Torr) and high (1 atm) reactant pressures by Blakely (15), Herz (16), Smith (17), and Gillespie (18) revealed the special importance of surface structure and chemical additives in controlling the activity and selectivity of platinum in several important types of catalyzed hydrocarbon reactions. The presence of steps and kinks was essential for high catalytic activity in cyclohexane dehydrogenation and n-heptane aromatization (16,18). the specific combination of strongly bound oxygen with surface kink sites produced even greater changes in catalytic behavior (17,18); i.e., much enhanced hydrogenolysis rates at atmospheric pressure and enhanced dehydrogenation rates at low pressures. Perhaps the most general feature of these reaction rate studies was the unavoidable build-up of about one monolayer of strongly bound carbonaceous deposit on the catalyst surfaces. This carbon deposit represents an important example of a chemical additive which is deposited directly by the reaction mixture. In most cases the formation of this deposit was considered as a curiosity that aroused little if any active research interest. Gillespie (18) reported that these strongly bound, partially dehydrogenated surface species resulted in catalyst deactivation with only small changes in reaction selectivity. However, the composition of the carbonaceous deposit was not carefully defined, and its reactivity was not investigated. In earlier low pressure studies (15), Blakely reported drastic changes in catalytic behavior that could be correlated with whether or not the

carbonaceous deposit was ordered or disordered. Stepped platinum surfaces with ordered carbon overlayers displayed unique high activity for n-heptane aromatization (template effect), whereas platinum surfaces covered with disordered carbon were inactive. In view of this remarkable discovery, further catalytic studies on carbon covered platinum surfaces are clearly warranted.

The formation of surface carbon deposits on high area practical platinum catalysts has also been demonstrated (19). Commercial catalysts that operate selectively for thousands of hours before requiring regeneration appear to become covered by this carbonaceous deposit almost instantly as the reactions commence. The formation of this deposit, its rehydrogenation tendencies, and its interactions with other adsorbates is thus an essential feature of the catalytic chemistry. Expensive regeneration is required only after these surface species are transformed into irreversibly adsorbed "coke" deposits which plug the porous support and render the catalyst inactive. With the exception of largely unsupported speculation (20) with respect to the ability of the carbonaceous deposit to undergo hydrogen transfer with reacting surface species, no conclusive evidence exists to accurately describe the nature of the participation of these mysterious carbon deposits in hydrocarbon catalysis.

The theis research presented here was specifically designed to provide a detailed understanding of the role of strongly bound carbonaceous deposits in reforming catalysis by platinum. The two most important questions that may be asked are (1) how does the deposit participate in the catalytic cycle; i.e., does catalysis take place on top

of or in exchange with the deposit, or does the deposit simply block sites and render the catalyst inactive; and (2) if the carbon deposit does participate, is it possible to control the structure and composition of the metal-organic layer to provide high selectivities for specific reactions such as aromatization. In order to address these questions, detailed kinetic information was required for several competing chemical processes. Specifically, the relative rates of direct hydrogenation and hydrogen transfer reactions between strongly bound surface species must be separated and established. A sensitive counting system for carbon-14 radiotracer studies was developed and utilized for this purpose. Complementary studies of hydrocarbon-deuterium exchange reactions were carried out as a function of temperature, pressure, and surface structure to determine the kinetics of elementary hydrogen addition and elimination reaction steps. Thermal desorption methods were used to elucidate the energetics of C-H bond bond breaking. The kinetics of alkane skeletal rearrangement reactions were investigated simultaneously with deuterium exchange. It was discovered that deuterium exchange always occurs more rapidly than hydrocarbon conversion and that deuterium exchange takes place on uncovered platinum surface sites. The deuterium exchange kinetics provided minimum surface residence times for dissociatively adsorbed intermediates that were on the order of 10^{-2}-10^{-1} sec. Hydrogen and CO thermal desorption methods were developed to determine the (H/C) composition of the carbon deposits and the concentrations of uncovered platinum surface sites that are present before and after reaction rate studies. The uncovered site concentrations were

correlated with the catalytic activity and selectivity of carbon covered platinum and also with deactivation kinetics that were derived from reaction rate studies over initially clean platinum surfaces. These studies have produced a model for the working structure and composition of the active catalyst surface that is presented in Chapter 4. Stated simply, the general role of the carbonaceous deposit is that of a non-selective poison which blocks platinum surface sites from incident reactant molecules.

In addition to the role of the adsorbed carbon deposit, the structure sensitivity of alkane skeletal rearrangement reactions was investigated at atmospheric pressure and 530-700 K on a series of platinum surfaces with variable terrace, step, and kink structure. Of the many reactions investigated, only n-hexane aromatization and butane isomerization reactions displayed appreciable structure sensitivity. Aromatization selectivity was maximized on platinum surfaces with high concentrations of contiguous (111) microfacets; isomerization was favored on surfaces with high concentrations of (100) microfacets. Steps and kinks generally had only a small effect on reaction rates and selectivities. The natural (thermodynamic) influence of temperature and hydrogen pressure had a far more decisive effect on reaction selectivity. These studies are reported in Chapter 3 along with deuterium isotope effects for the skeletal rearrangement reactions. The role of other chemical additives (calcium oxide, sulfur, strongly

bound surface oxygen) in effecting the catalytic behavior of platinum is considered briefly in Chapter 5. Whenever possible, detailed comparisons have been made between the catalytic behavior of the single crystal surfaces and practical platinum catalysts.

REFERENCES

1. S. M. Davis and G. A. Somorjai, Hydrocarbon Conversion Over Metal Catalysts, in The Chemical Physics of Solid Surfaces and Heterogeneous Catalysis, Vol. IV, Elsevier, Amsterdam, 1981.
2. J. K. A. Clarke and J. J. Rooney, Adv. Catal. 25, 125 (1976).
3. J. R. Anderson, Adv. Catal. 23, 1 (1973).
4. B. C. Gates, J. R. Katzer, and G. C. A. Schuit, Chemistry of Catalytic Processes, McGraw-Hill, New York, 1979.
5. F. G. Ciapetta and D. N. Wallace, Catal. Rev. 5, 67 (1972).
6. D. R. Stull, E. F. Westrum, and G. C. Sinke, The Chemical Thermodynamics of Organic Compounds, Wiley, New York, 1969.
7. W. M. H. Sachtler and R. A. Van Santen, Adv. Catal. 26, 69 (1977); V. Ponec, Exchange and Reforming Reactions on Metals and Alloys, in The Chemical Physics of Solid Surfaces and Heterogeneous Catalysis, Vol. IV, Elsevier, Amsterdam, 1981.
8. W. N. Delgass, G. L. Haller, R. Kellerman, and J. H. Lunsford, Spectroscopy in Heterogeneous Catalysis, Academic Press, New York, 1979.
9. J. A. Dumesic and H. Topsoe, Adv. Catal. 26, 121 (1977).
10. See, for example, F. W. Lytle, P. S. P. Wei, R. B. Greegor, G. H. Via, and J. H. Sinfelt, J. Chem. Phys. 70, 4849 (1979).
11. P. Eisenberger, P. Citrin, R. Hewitt, and R. Kincaid, CRC Crit. Rev. Solid State and Mater. Sci. 10, 191 (1981).
12. M. Boudart, Adv. Catal. 21, 153 (1969).
13. W. H. Monogue and J. R. Katzer, J. Catal. 32, 166 (1974).

14. R. Van Hardeveld and F. Hartog, Surf. Sci. 15, 189 (1969).

15. D. W. Blakely, Ph. D. Thesis, University of California, Berkeley, 1976.

16. R. Herz, Ph. D. Thesis, University of California, Berkeley, 1977.

17. C. E. Smith, Ph. D. Thesis, University of California, Berkeley, 1978.

18. W. D. Gillespie, Ph. D. Thesis, University of California, Berkeley, 1980.

19. For recent reviews see Catalyst Deactivation (B. Delmon and G. F. Frement, eds.), Elsevier, Amsterdam, 1980.

20. S. J. Thomson and G. Webb, J. C. S. Chem. Comm. 526 (1976).

CHAPTER 2: EXPERIMENTAL METHODS

2.1. Apparatus

The research described in this thesis was carried out using two very similar low pressure-high pressure systems (1,2) that were designed for combined surface analysis and catalysis studies using small area (~1 cm^2) single crystal samples. A schematic diagram of the primary apparatus is shown in Fig. 2.1. Using this system, the single crystal samples were cleaned in ultra high vacuum (UHV) and characterized by low energy electron diffraction and Auger electron spectroscopy. An internal isolation cell could be closed around the samples and pressurized to several atmospheres to function as a high pressure microcatalytic reactor. Reaction rate studies were carried out by resistively heating the sample in a reactant gas mixture that was supplied to the isolation cell by an external gas recirculation system. Reaction products were analyzed in situ using a mass spectrometer and a gas chromatograph equipped with a flame ionizer detector. Following each reaction study, the isolation cell was evacuated and lowered in minutes which enabled the surface structure and composition to be recharacterized in UHV by low energy electron diffraction, Auger electron spectroscopy, and thermal desorption spectroscopy. In this manner the kinetics of hydrocarbon reactions catalyzed over single crystal surfaces at high and low pressures were correlated with the chemisorption properties of the reactants and the structure and composition of the active catalyst surface.

The main vacuum system consisted of a stainless steel belljar (~50L) that was pumped by a high speed oil diffusion pump (Varian VHS-6) and a water cooled titanium sublimation pump. A liquid nitrogen cold trap (Varian 362-6) separated the diffusion pump from the main chamber. Base pressures in the 10^{-10} Torr range were achieved after 24 hr baking at 425 K. During periods of continual experimentation the base pressure rose to 1-3 x 10^{-9} Torr (mostly H_2O, CO, H_2). These pressures were adequate to routinely prepare clean well annealed surfaces. Auxillary ports were equipped with

(1) an ion sputter gun (PHI 4-161) for crystal cleaning;

(2) a quadrupole mass spectrometer (UTI 100C) for residual gas analysis, thermal desorption studies, and analysis of deuterium exchange products;

(3) a nude ion gauge (Varian 971-5008) for pressure measurement;

(4) a glancing incidence CRT-electron gun for Auger excitation;

(5) a four grid electron optics-energy analyzer (Varian 981-0127) for LEED and AES;

(6) two variable leak valves (Varian 951-5106) for introducing gases at low pressures; and

(7) a surface barrier detector (Section 2.3) for ^{14}C-radiotracer analysis.

The single crystal samples were mounted on a rotable manipulator according to the sample mounting detail shown in Fig. 2.1. As discussed by Gillespie (2), this is the only acceptable mounting scheme which permits the samples to be heated to the high temperatures that

are required for cleaning and annealing ($\geq$1300 K) without introducing serious problems due to background catalytic activity. The 20 mil platinum mounting wires were kept very short ($\leq$4-5 mm) so that the exposed wire area represented only ~5-10 percent of the total platinum surface area. The wires were spot welded such that they were always cooler than the sample except at the small points of contact which represented only 1-3 percent of the total platinum surface area. The gold and copper rods acted as an effective heat sink for the platinum wires. The samples were repeatedly mounted and remounted until the heating was uniform and the contact points appeared to be no hotter than the sample itself.

A chromel-alumel thermocouple (5 mil wires) spot welded tightly to an edge or one of the faces of the crystal was used for temperature measurement. Since conductive heat losses from the thermocouple leads or poor thermal or electrical contact between the tc-junction and the crystal would cause the crystal temperature to be underestimated, it was of paramount importance to establish the accuracy of the temperature measurements. Two tests were used for this purpose. The first test was a simple visual check described in detail by Gillespie (2). When the thermocouple was properly attached to the crystal, the threshold temperature for observing optical emission in a dark laboratory was 785 $\pm$ 10 K. Studies of isobutane dehydrogenation reactions catalyzed on the platinum single crystals provided a more reliable method for determining the absolute temperature of the samples under reaction conditions. As discussed in Section 3.2, the dehydrogenation

reaction yielded equilibrium concentrations of isobutene under all reaction conditions. In Fig. 2.2 the equilibrium isobutene to isobutane yields determined in reaction rate experiments are compared as a function of 1/T with the theoretical yields that were calculated from published thermodynamic data (3). The theoretical yields correspond to an ethalpy of reaction of 29.1 kcal/mole whereas the experimental points correspond to ΔH = 28.7 kcal/mole. In general, the agreement between temperature scales was unexpectedly excellent. Near 573 K there was a systematic tendency for the experimental isobutene yields to exceed the theoretical yield by 5-18 percent. This difference corresponds to an error in the temperature measurement of 2-5 K. Such an error would be expected if (1) conductive heat losses take place at the crystal-thermocouple junction, or (2) the temperature of the crystal-support contacts was slightly higher than that for the sample itself. In any event, this method provided an important check to insure that the crystal temperature was closely standardized from one sample to the next.

A schematic diagram for the reactor and external gas handling system is shown in Fig. 2.3. A metal bellows pump provided continuous gas circulation, and a Wallace-Tiernan gauge was used for measuring the pressure of gaseous reactants. During reaction studies V_{11}, V_{13}, and V_{15} were always closed. The gas line from V_{15} to the main vacuum manifold was made from 3/4 in. tubing so that the isolation cell could be evacuated as rapidly as possible following all reaction studies. Evacuation was carried out using a mechanical pump and two

liquid nitrogen cooled sorption pumps. The bypass valve V_{12} was used to increase the conductance of the recirculation loop which was otherwise controlled by the small 1/16 in. internal tubing of the gas chromatograph sampling valve. The total volume of the reactor was varied from 236 to 744 cm^3 depending upon the type of reaction studied.

The gas chromatograph used in this work (HP-5830A) was equipped with a microprocessor that determined all peak areas. The sensitivity of the instrument was calibrated regularly using a primary standard gas mixture (Matheson) that contained 100 ppm (mole basis) methane in nitrogen. The sensitivity changed by less than 3 percent over the period of one year. All hydrocarbon products were calibrated relative to methane using published sensitivity factors (4). All reaction products were separated using 1/8 in. packed columns which contained either 0.19 percent picric acid on 80/100 carbopack or 10 percent squalene or 60/80 chromosorb W.

Because the gas sampling valve was not designed for vacuum applications, there was always a very small leak into the reactor of approximately 10^{-8} L/sec. Mass spectral analysis of this leak by Gillespie (2) indicated that it was about 95 percent nitrogen and 5 percent oxygen. Thus, the major portion of the leak appeared to result from the diffusion of nitrogen carrier gas within the valve rather than an external air leak. The maximum oxygen leak rate into the reactor is estimated to be 10^{-9} L/sec.

FIGURE CAPTIONS

Fig. 2.1. Schematic diagram of the low pressure-high apparatus for combined surface analysis and catalysis studies.

Fig. 2.2. Temperature dependence of the equilibrium ratio of isobutene to isobutane showing the excellent agreement between experimental data and thermodynamic predictions (3). This comparison provides a simple method to determine the absolute sample temperature under reaction conditions (H_2/HC = 10, p_{tot} = 220 Torr).

Fig. 2.3. Schematic diagram of the microbatch reactor and external gas handling system. The dashed lines represent the actual gas recirculation loop.

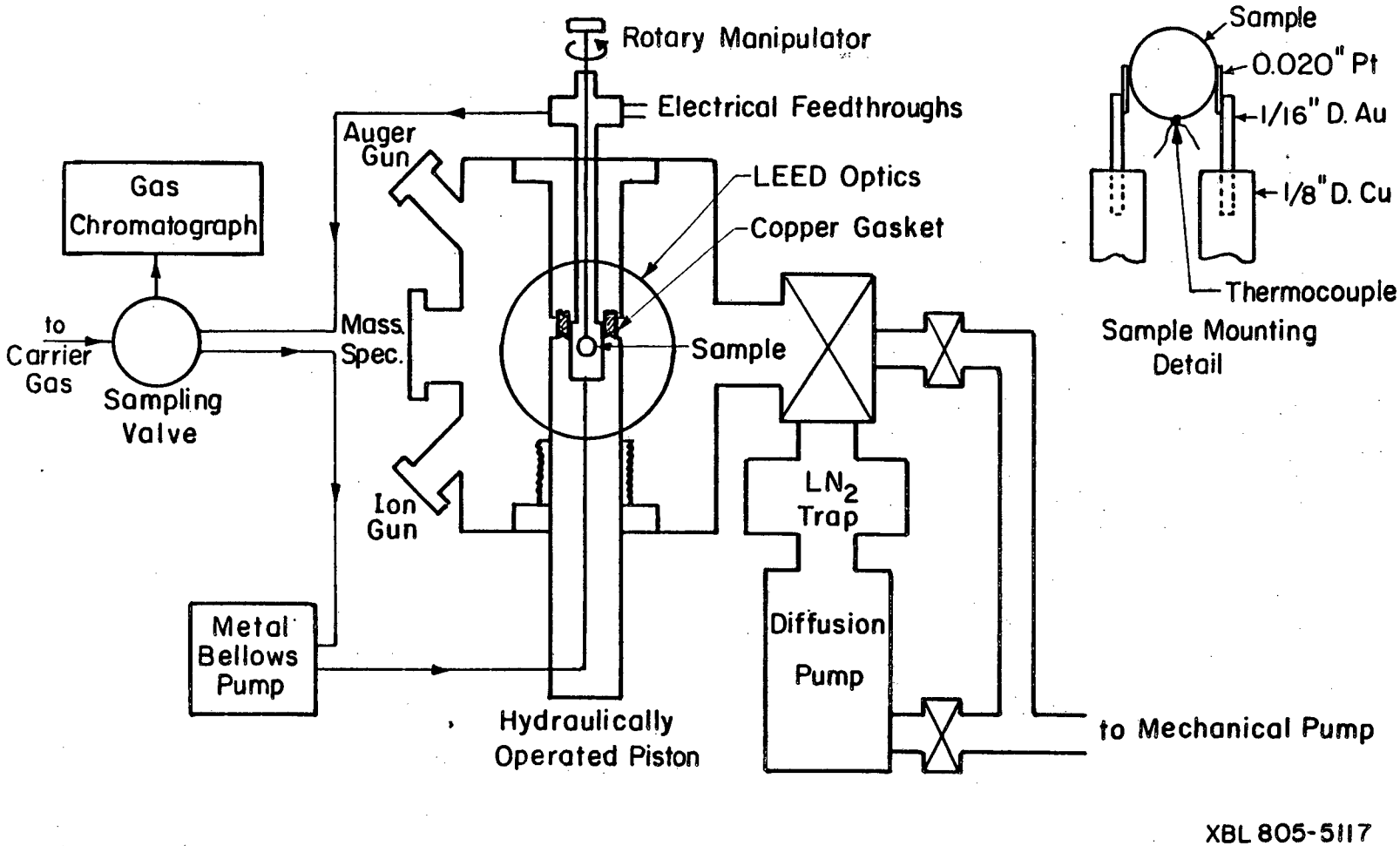
Rotary Manipulator
Electrical Feedthroughs
Auger Gun
LEED Optics
Copper Gasket
Gas Chromatograph
to Carrier Gas
Sampling Valve
Mass Spec.
Sample
Ion Gun
LN2 Trap
Diffusion Pump
Metal Bellows Pump
Hydraulically Operated Piston
to Mechanical Pump
Sample
0.020" Pt
1/16" D. Au
1/8" D. Cu
Thermocouple
Sample Mounting Detail
XBL 805-5117

Fig. 2.1

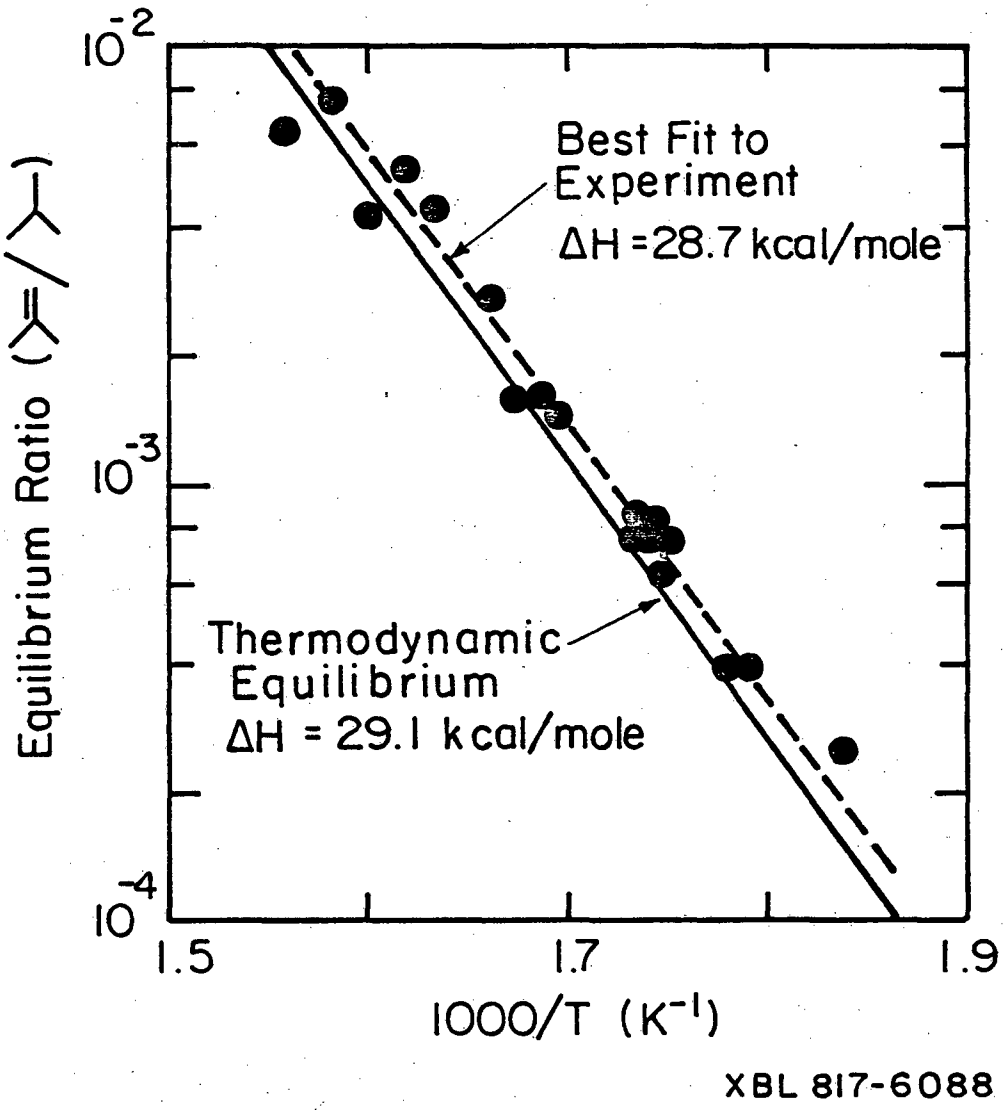
Equilibrium Ratio (⟩=/⟩—⟨)
10^-2
10^-3
10^-4
Best Fit to
Experiment
ΔH =28.7 kcal/mole
Thermodynamic
Equilibrium
ΔH = 29.1 kcal/mole
1.5
1.7
1.9
1000/T (K^-1)
XBL 817-6088

Fig. 2.2

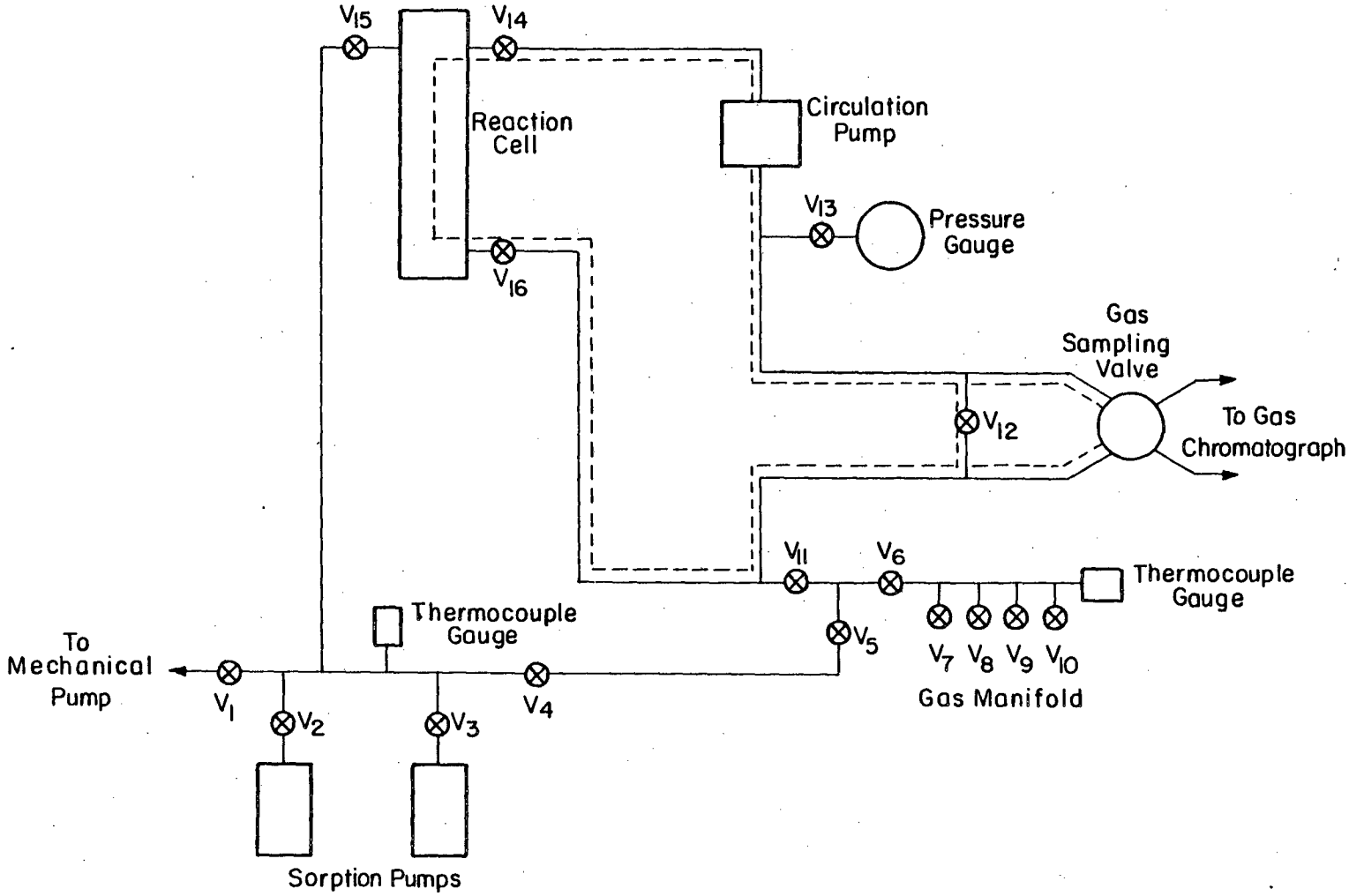
V15
V14
Reaction Cell
Circulation Pump
V13
Pressure Gauge
V16
Gas Sampling Valve
V12
To Gas Chromatograph
V11
V6
Thermocouple Gauge
Thermocouple Gauge
V5
V7 V8 V9 V10
Gas Manifold
To Mechanical Pump
V1
V2
V3
V4
Sorption Pumps
XBL 807-5523

Fig. 2.3

2.2. Surface Analysis Methods

Low energy electron diffraction (LEED), Auger electron spectroscopy (AES), and thermal desorption spectroscopy (TDS) were the primary surface analysis techniques used in this research to characterize the structure and composition of the platinum single crystal surfaces. Since the theory and applications of these techniques in surface science have been reviewed extensively elsewhere (viz., LEED (5,6), AES (7,8), and TDS(9,10)) only a brief discussion of each method is included here.

2.2.1. Low Energy Electron Diffraction

Low energy electron diffraction has emerged as perhaps the most powerful experimental technique available to investigate the atomic structure of the gas-solid interface. Electrons with energies in the LEED range of ~15-400 eV display deBroglie wavelengths of ~4 to 0.5Å which makes them ideally suited for diffraction from ordered ensembles of atoms or molecules. The great surface sensitivity of LEED originates from the large scattering cross sections for low energy electrons in condensed phases. All such phases display a similar dependence of the electron inelastic mean free path or kinetic energy. This dependence is represented by a "universal curve" like that shown in Fig. 2.4. Because electrons in the LEED energy range almost always have mean free paths shorter than about 10Å, diffraction represented by purely elastic backscattering can originate only with the topmost 1-4 atomic layers.

An idealized schematic diagram for the LEED experiment is shown in Fig. 2.5. Diffraction results from elastic backscattering of a monoenergetic primary electron beam which is produced by a cold cathode electron gun. Elastically scattered beams are filtered from the inelastically scattered electrons by a retarding potential that is applied to the second grid of the LEED optics. The elastically scattered beams continue their original trajectories and are post accelerated into a phosphorescent screen for viewing the diffraction pattern. The diffraction beams appear only at certain well-defined angles that are determined by the momentum conservation relation,

$$\vec{k}'_{\parallel} = \vec{k}_{\parallel} + \vec{g}_{\parallel} \tag{1}$$

and the energy conservation condition,

$$k'_{\perp} = \left[\frac{2mE}{\hbar^2} - k'^{2}_{\parallel}\right]^{1/2} \tag{2}$$

where $\vec{k}_{\parallel}$, $k_{\perp}$ and $\vec{k}'_{\parallel}$, $k'_{\perp}$ are the incident and scattered components of electron momentum parallel and perpendicular to the surface, E is the kinetic energy of the outgoing electron, and $\vec{g}_{\parallel}$ is a surface reciprocal lattice vector. The intensities and sharpness of the diffraction beams are primarily determined by the degree of long range microscopic ordering within the surface layers. In general, the diffraction beams can have significant intensities only if the 2D-ordering length is

comparable to the coherence width of the incident electron beam (ca. 100Å) (11,12).

In principle, LEED is capable of revealing all the information about surface structure that X-ray crystallography provides for bulk solid structure (i.e., bond lengths and bond angles). The symmetry and positions of LEED beams considered alone defines the size, shape, and rotational orientation of the 2D-surface unit mesh (6). The displacement of atoms normal to the surface phase and location of atoms within the unit mesh can be derived from the intensities of the diffracted beams as a function of energy (I-V profile) (5,6). In practice, interference between the backscattered waves (multiple scattering) must be considered for a precise 3-D structure determination. Extensive dynamical calculations that are required for this purpose can be reliably carried out only for the simpler systems where the unit mesh contains fewer than about ten atoms (13). In this thesis, only the obvious symmetries and positions of the diffraction beams that define the 2-D surface structure will be considered. These structures are presented using the Wood and matrix notation schemes (6).

2.2.2. Auger Electron Spectroscopy

Auger electron spectroscopy (AES) was used throughout this research to monitor the elemental composition of platinum single crystal surfaces directly before and after all chemisorption and catalysis studies. The great usefulness of AES as a routine surface analysis technique results from the facts that (1) every element has a

unique Auger spectrum that can be used as a fingerprint to identify the presence of adsorbates on solid surfaces (14); (2) AES is highly surface sensitive for the same reasons as described for LEED; and (3) good quality spectra can be obtained very rapidly (2-5 min) using relatively simple electron optics. Figure 2.6 shows typical Auger spectra for (a) a clean platinum surface and (b) a new platinum surface that was initially contaminated with several surface impurities (S, Ca, O). The spectra were obtained with the 4-grid LEED optics operating as a retarding field electron energy analyzer (RFA). In this case the first and third grids were grounded, a retarding DC ramp voltage was applied to the second grid, and a 300 V post accelerating positive bias was applied to the screen. The spectra were recorded in the first derivative mode in order to enhance the Auger signal intensity relative to the slowly varying secondary electron background. Differentiation of the spectra was carried out electronically by superimposing a small AC modulation voltage (2-7 V peak to peak) on the DC ramp voltage. The second harmonic of the modulation voltage was detected as a function of the ramp voltage using a phase-sensitive lock-in amplifier (PAR HR-8). The second harmonic corresponds closely to the first derivative Auger spectrum (15).

Auger transitions are autoionization processes that arise from electrostatic interaction between two electrons in an atom that is initially ionized in an inner shell. These excited ionic states can be created by photoionization, ion impact, or electron scattering (16). In this research 2.5 keV electrons from a cathode ray tube electron

gun were used as the primary excitation source. In this case, the most accurate ionization cross sections, σ, are reportedly those based on Gryzinski's classical calculations for inelastic electron scattering (17).

$$\sigma_i = \left(\frac{\pi e^4}{E_i}\right)^2 \frac{1}{\mu}\left(\frac{\mu - 1}{\mu + 1}\right)^{3/2} \left\{1 + \frac{2}{3}\left(1 - \frac{1}{2\mu}\right) \ln\left(2.7 + (\mu - 1)^{1/2}\right)\right\} \qquad (3)$$

where E_i is the binding energy of core level electrons in subshell i, E_o is the energy of the primary electron beam, and $\mu = E_o/E_i$. According to these calculations σ is maximized when μ = 3-5.

Once created the excited ionic states rapidly ($\bar{\tau} \sim 10^{-15}$ sec) undergo deexcitation by X-ray fluorescence, Auger electron emission, or a sequence of both these processes that are compared schematically in Fig. 2.7. In the Auger process an outer shell electron relaxes to the inner shell vacancy transferring energy to a second outer shell electron that is consequently ejected. The golden rule expression for the Auger transition probability per unit time is (16)

$$\omega_{fi} = \sum_{\substack{\text{final} \\ \text{states}}} \frac{2\pi}{\hbar} |D - E|^2 \rho(E_f) \qquad (4)$$

where D and E are the direct and exchange matrix elements of the electrostatic interaction Hamiltonian ($V_{int} = \sum_{i \neq j} e^2/|r_i - r_j|$), $\rho(E_f)$ is the density of final two-hole plus one free electron final states, and the difference D-E is taken to preserve the antisymmetry

of the initial and final states. The ejected Auger electron has an energy

$$E_{ijk} = E_i - E_j - E_k(z-\Delta) - \phi_e \qquad (5)$$

where E_j and E_k are the energies of the appropriate outer shell electrons, z is the atomic number of the atom, Δ is the effective charge (0.5–0.8) due to the initial ionization, and ϕ_e is the work function of the sample referred to the vacuum level of the spectrometer. In comparison, when deexcitation occurs by X-ray fluorescence, an outer shell electron relaxes to an inner shell vacancy with the emission of a photon. Auger emission is generally favored over X-ray fluorescence with low Z elements or when initial ionization occurs in the L, M, N, ... subshells (16).

The surface sensitivity of AES is determined by the energies of the scattered Auger and/or incident primary electrons. Maximum penetration depths of approximately 8–20Å normal to the surface are expected when 2.5 keV primary electrons are incident at a glancing angle of about 70° to the surface normal (Fig. 2.4). While Auger electrons can be created anywhere between the solid–vacuum interface and this maximum penetration depth, whether or not they have sufficient energy to escape the solid and be detected is largely determined by the energy of the Auger electrons. For energies between 50 and 150 eV it is apparent from Fig. 2.4 that most of the intensity arises from the topmost 2 or 3 atomic layers independent of the primary beam

energy. With increasing energy a significant fraction of the intensity originates from deeper within the solid thereby providing more information about the composition of the near surface region. With the exception of oxygen (510 eV), all Auger transitions of interest to this research have energies below 300 eV where the surface sensitivity is very high.

Several useful models have been developed to predict the distribution of Auger peak intensities for adsorbate covered surfaces depending upon the nature of the adsorbate film growth mechanism, viz. layer-by-layer (18), monolayer followed by 3D crystallites (19), or 3D crystallites (19). In the simplest case of layer-by-layer growth with homogeneous attenuation, the adsorbate and substrate peak intensities are expressed by

$$I_a = I_a^o(1-\exp(-Z/\lambda_a)) \tag{6}$$

and

$$I_s = I_s^o\exp(-Z/\lambda_s) \tag{7}$$

respectively, where I_a^o is the adsorbate intensity in the limit of infinite film thickness, I_s^o is the peak intensity for the clean substrate, Z is the overlayer thickness, and λ_a and λ_s are the inelastic mean free paths of the adsorbate and substrate Auger electrons, respectively.

2.2.3. Thermal Desorption Spectroscopy

Thermal desorption spectroscopy (TDS) was used extensively in this research to investigate the energetics of hydrocarbon chemisorption and to characterize the composition of adsorbed carbonaceous species as a function of their preparation conditions. When desorption of intact molecules takes place TDS can reveal (1) the multiplicity of adsorbate binding states and the relative concentrations of adsorbed species in each state; (2) the kinetic orders of the desorption process; and (3) the activation energies and pre-exponential factors for the desorption rate constants (10). On the other hand, when decomposition of the adsorbed species prevails, TDS can reveal (1) the temperature range and activation energy for the decomposition reaction; (2) the decomposition products, and (3) the composition of the decomposing species.

In all TDS experiments described here the single crystal samples were heated at linear (or nearly linear) rates (10-98 K/sec), and the desorption or decomposition of the adsorbed species was detected as a change in pressure with time using the UTI 100C quadrupole mass spectrometer. In about one half of the experiments the mass spectrometer ionizer was located in direct line of sight to the sample at a distance of about 10 cm. In the remaining experiments the ionizer was about 15° off normal at a distance of ~20 cm.

Kinetic analysis of TDS results invariably begins with the Wigner-Polanyi model to describe the desorption of species in a particular binding state. The rate of desorption is given by

$$R_d = -\frac{d\theta}{dt} = v_n \theta^n \exp(-E_d/RT) \qquad (8)$$

where θ is the surface coverage, n is the order of desorption, v_n is the desorption pre-exponential factor, and E_d is the desorption activation energy. Provided that adsorption is not activated E_d equals the enthalpy of adsorption. In this research the pumping speed ($300-10^3$ liter/sec) was always much greater than the desorption rate, and the samples were carefully mounted to provide uniform and linear heating rates (unless noted otherwise). Assuming that under these conditions E_d is independent of time and temperature, Redhead has shown that (20)

$$E_d/RT_p^2 = (v_1/\beta) \exp(-E_d/RT_p) \qquad \text{(1st order)} \qquad (9)$$

and

$$E_d/RT_p^2 = (v_2\theta_o/\beta) \exp(-E_d/RT_p) \quad \text{(2nd order)} \qquad (10)$$

where β is the sample heating rate, θ_o is the initial coverage, and T_p is the temperature of the maximum desorption rate (i.e., the temperature of the desorption peak maximum). According to this model, T_p should be independent of θ_o for first order desorption, and T_p should decrease with increasing θ_o for second order desorption. Thus it is often possible to determine the molecularity of a desorption reaction by simply monitoring T_p as a function of θ_o. Order plots

of $\ln R_d$ as a function of $\ln \theta_o$ can be constructed easily to determine the kinetic order of more complicated desorption processes; viz., zero, third, or fractional order reactions. Self-consistent determination of E_d and ν from Eqs. (9) and (10) requires that θ_o and β be varied independently. Experimentally this is difficult to achieve, and therefore, E_d is most often estimated by assuming that $\nu_1 = 10^{13}$ sec^{-1} and $\nu_2 = 10^{-2}$ $cm^2 sec^{-1}$. It has been noted (21) that this assumption is often unreliable because ν can differ by up to 3-orders of magnitude from the assumed values that are based on simple statistical considerations. These differences in ν can translate into a considerable error in the determination of E_d. For this reason two nearly equivalent methods have been devised by Edwards (22) and Chan et al. (12) that permit calculation of E_d from T_p and the desorption peak full width at half maximum, Δw, without a priori assumption of the pre-exponential factor. The original derivation of Edwards (22) produces the equations

$$E_d/RT_p = \frac{2.4464}{\Delta w/T_p}\left(1 - 0.5725\left(\frac{\Delta w}{T_p}\right) + 0.2625\left(\frac{\Delta w}{T_p}\right)^2 + \ldots\right) \qquad (11)$$

and

$$E_d/RT_p = \frac{3.5255}{\Delta w/T_p}\left(1 - 0.5673\left(\frac{\Delta w}{T_p}\right) + 0.2366\left(\frac{\Delta w}{T_p}\right)^2 + \ldots\right) \qquad (12)$$

for first and second order desorption, respectively. Whenever possible, desorption activation energies reported in this work have been calculated using both methods outlined above; i.e., the Redhead formulas (Eqs. (9) and (10)) and Edward's expansions (Eqs. (11) and (12)). Provided that the heating rates were less than about 25 K/sec good agreement (±10 percent) was obtained between these values. When higher heating rates were employed the desorption peaks were broadened appreciably resulting in unrealistically low values of E_d calculated by the Edwards method. Under these conditions ($\beta \geq 25$ k/sec) the Redhead formulas were used exclusively with the usual assumption that $\nu_1 = 10^{13}$ sec^{-1}.

Activation energies for the sequential dehydrogenation and skeletal rearrangement of chemisorbed hydrocarbons were estimated in an analogous manner by assuming that all such processes were unimolecular decomposition reactions. In this case, the rate of the decomposition reaction

$$C_nH_x(ads) \rightarrow C_nH_{x-a}(ads) + \left(\frac{a}{2}\right) H_2$$

is given by

$$-\frac{d\theta_{C_nH_x}}{dt} = \nu_d \theta_{C_nH_x} \exp(-E_a/RT) \qquad (13)$$

where v_d and E_a are the pre-exponential factor and activation energy for decomposition, respectively. Since hydrogen recombination and desorption are very fast at the temperatures ($\geq$425 K) where hydrocarbon rearrangement takes place (23), hydrogen thermal desorption spectra representing the sequential dehydrogenation of chemisorbed hydrocarbons can be used as a direct fingerprint of the decomposition rates. Kinetic analysis of the rearrangement process using Eq. (9) then becomes identical to that for first order molecular desorption. Baetzold (24), Benson (25), and others (26) have tabulated pre-exponential factors for unimolecular surface and gas phase reactions that are always in the range 10^{12} - 10^{15} sec^{-1}. An average value of $v = 10^{13}$ sec^{-1} was used in this work. While this assumption is not readily justified, it has been used here so that trends in the decomposition behavior of different hydrocarbons could be investigated.

2.2.4. Composition of Carbonaceous Species from AES and Hydrogen TDS

A simple experimental procedure was devised to determine the absolute (H/C) stoichiometry of hydrocarbon species irreversibly chemisorbed on platinum single crystal surfaces. Several applications of this method are discussed in Sections 4.3, 4.4 and 4.5. For the determination of (H/C) ratios, hydrogen thermal desorption spectra representing the sequential dehydrogenation and decomposition of chemisorbed hydrocarbon molecules were recorded using linear heating rates in the range 69 to 98 K/sec. Total areas under the H_2 desorption peaks were determined by weighing the spectra on an

analytical balance. For a given heating rate and crystal sample the measured area was assumed to be directly proportional to the total amount of hydrogen originally contained within the adsorbed layer. Comparison of this desorption peak area, A, with the C_{273}/Pt_{237} AES peak to peak height ratio, I, provided a relative measure of the initial (H/C) composition, i.e., $(H/C) = \alpha(A/I)$. The proportionality constant α was determined before and/or after each series of experiments by chemisorbing benzene or clean platinum at 300–315 K and executing the same hydrogen thermal desorption experiment. A standard ratio (H/C) = 1.0 was assumed under these conditions yielding $\alpha = (I/A)_{B_Z}$. This assumption is easily justified because it is well documented that benzene chemisorbs on platinum in a molecular form provided that the temperature is less than 340–370 K (27,28). Since heating rates, desorption peak areas, and AES peak height ratios were all reproducible to about ±5 percent, the uncertainty of the (H/C) determinations is estimated to be no more than ±20 percent.

FIGURE CAPTIONS

Fig. 2.4. Universal curve for condensed phases showing the dependence of the inelastic electron mean free path (attenuation length) on kinetic energy. Small mean free paths in the LEED energy range result in high sensitivity to the outermost surface layers.

Fig. 2.5. Schematic representation of the LEED experiment showing the backscattering of an incident electron beam into a series of well defined diffraction beams.

Fig. 2.6. Auger electron spectra for (a) a clean platinum single crystal surface, and (b) a platinum surface that was initially contaminated with several surface impurities.

Fig. 2.7. Energy level diagrams comparing the Auger emission and X-ray fluorescence mechanisms for deexcitation of an excited ionic state.

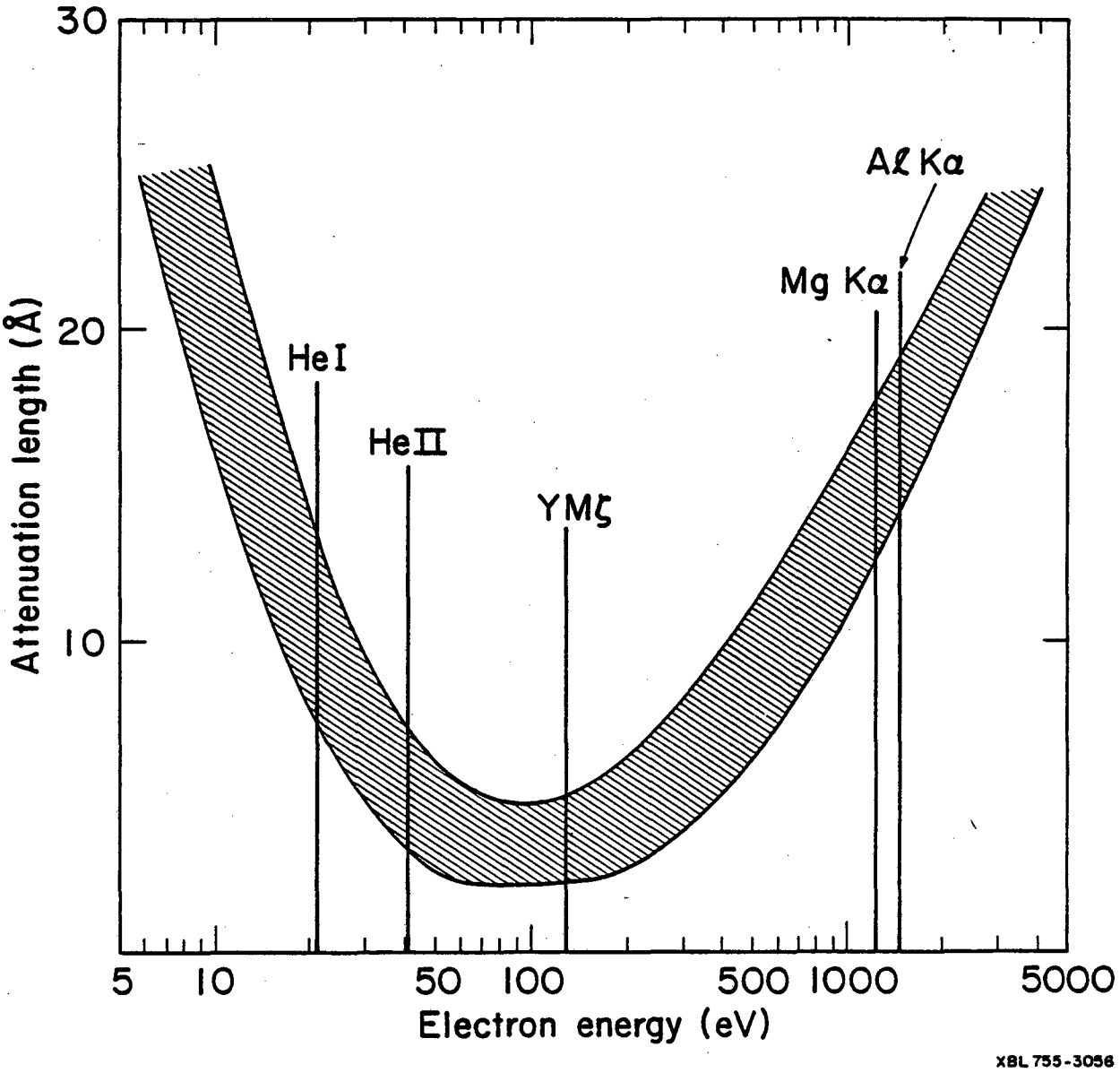
30
20
10
Attenuation length (Å)
HeI
HeII
YMζ
Mg Kα
Aℓ Kα
5
10
50
100
500
1000
5000
Electron energy (eV)
XBL 755-3056

Fig. 2.4

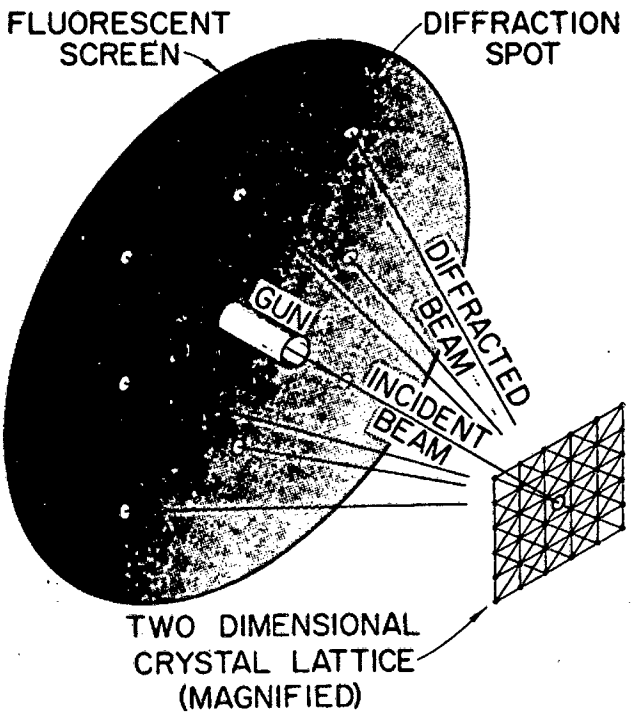

$$\underset{\sim}{k}' = \underset{\sim}{k} + \underset{\sim}{G}$$

XBB 708-3583

Fig. 2.5

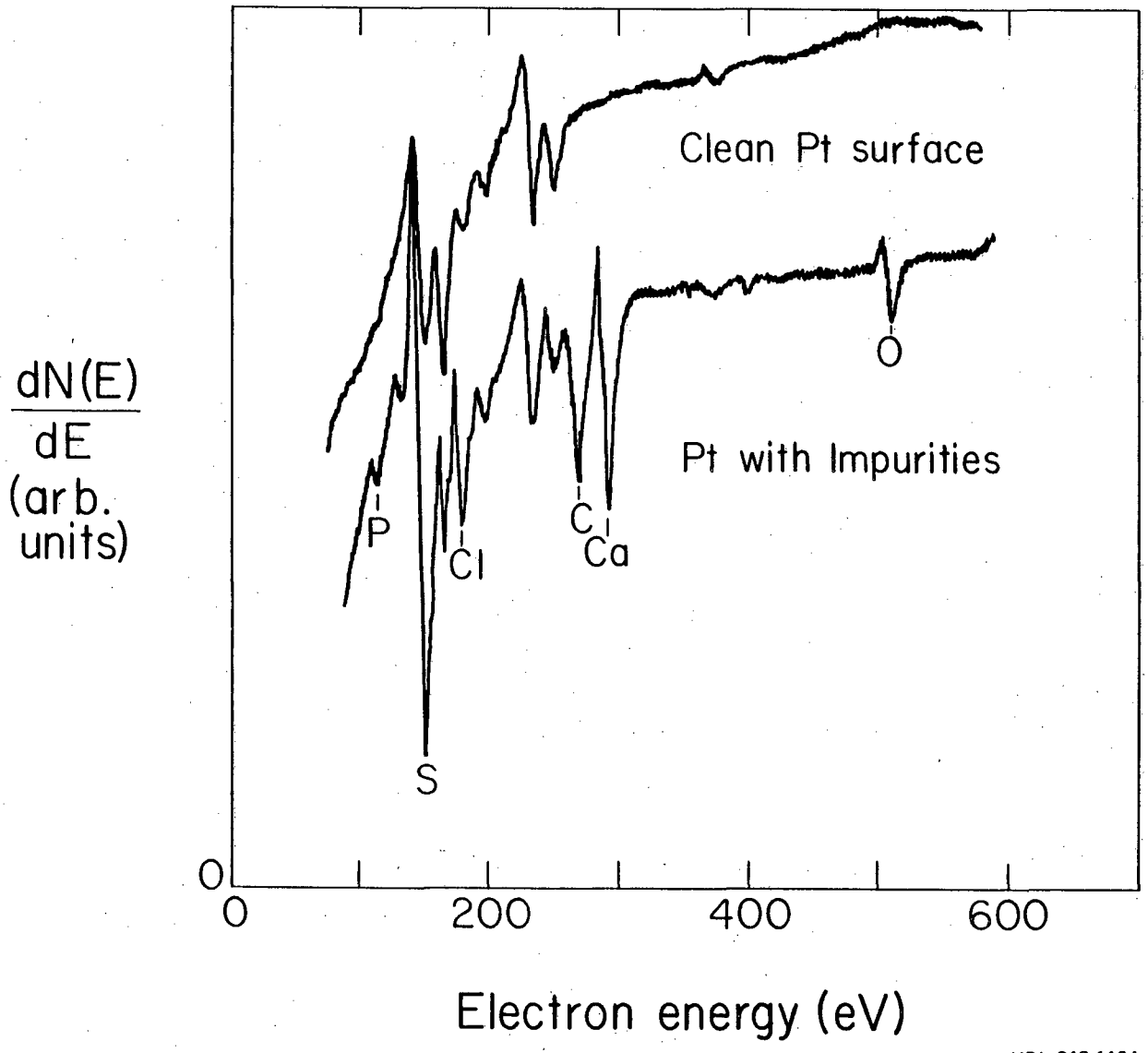
dN(E)
dE
(arb.
units)
Clean Pt surface
Pt with Impurities
O
P
Cl
S
C
Ca
0
0
200
400
600
Electron energy (eV)
XBL 818-1104

Fig. 2.6

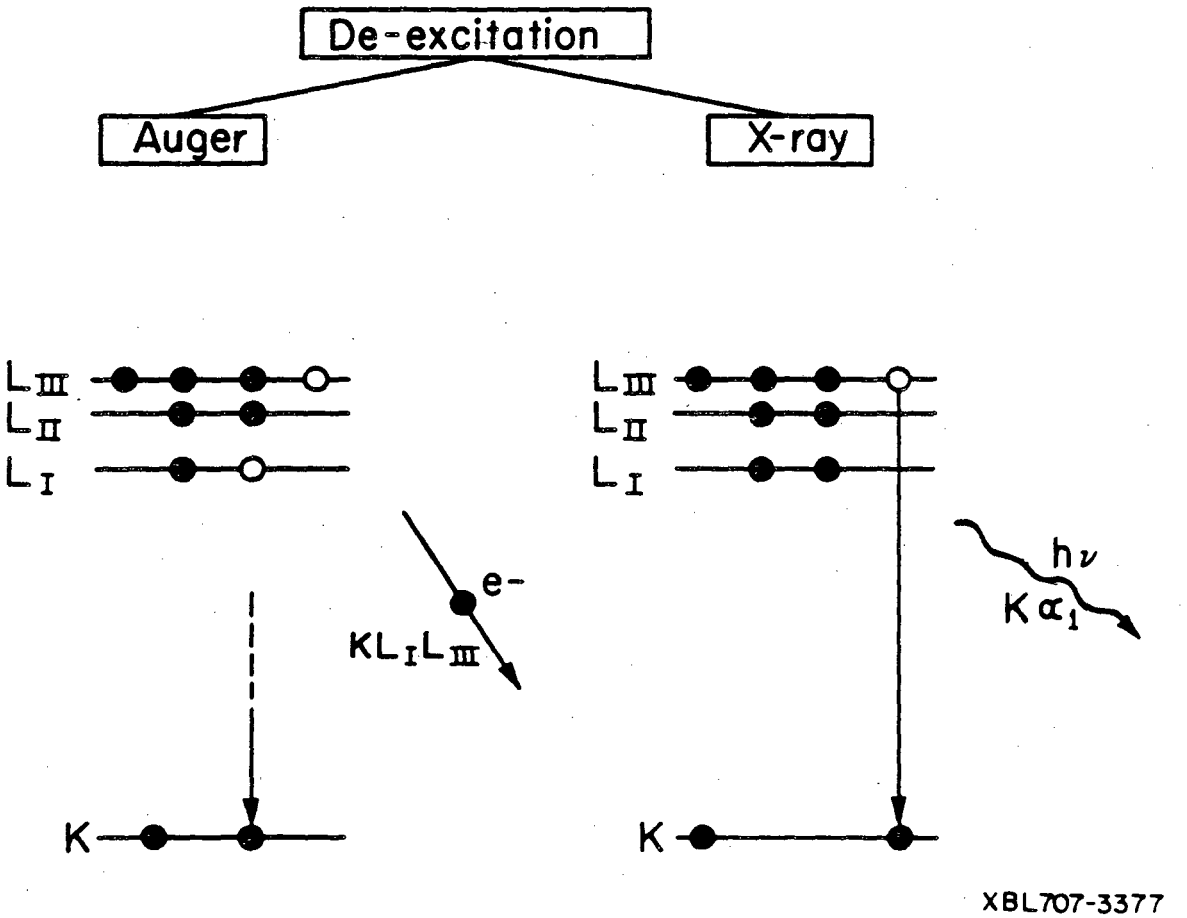
De-excitation
Auger
X-ray
L III
L II
L I
e-
KL I L III
K
L III
L II
L I
hν
K α1
K
XBL707-3377

Fig. 2.7

2.3. A Radiotracer Technique for Chemisorption and Catalysis Studies Using Single Crystal Surfaces in UHV

A radiotracer counting system was developed for adsorption and catalysis studies in ultrahigh vacuum using small area, single crystal surfaces. The counting system utilizes a rugged, compact, and rotatable surface barrier detector with a sensitivity sufficient to detect about 1×10^{12} molecules containing carbon-14. The counting system and its operating characteristics are described in this section. Applications of this technique to studies of ^{14}C-benzene and ^{14}C-ethylene chemisorption, hydrogenation, and hydrogen transfer reactions are presented in Chapter 4.

2.3.1. The Counting System

A block diagram showing the experimental arrangement and counting electronics for radiotracer studies is shown together with a cross section of a surface barrier detector in Fig. 2.8. The surface barrier detector (Ortec TA-23-25-300) is a large area diode consisting of a partially depleted slice of ultrapure n-type silicon mounted in an insulating ring, the front and back surfaces of which are metallized. The entrance contact-surface barrier (gold window, 40 $\mu g\ cm^{-2}$) and depth of the depletion region (300 μm) are chosen to optimize the detector efficiency for low energy beta radiation (^{14}C-E_{max} = 158 keV, range in Si $\simeq$ 150 μm). The front surface of the insulating ring is grounded to the metal case and to the shield side of a standard Microdot connector. The back surface of the ring contacts the center electrode of the connector which functions as a signal output and bias voltage connection. Free charge carriers created during operation by

ionizing radiation are separated by an electric field that is produced by an externally applied reverse bias (50 V). Integration of the current induced on the detector contacts yields an output pulse that is proportional to the energy of the ionizing radiation (29). Output pulses are amplified and shaped by a charge sensitive preamplifier (Ortec 142) and linear amplifier (Ortec 575). For point-by-point measurements, N(E) beta spectra are collected and stored in a pulse height analyzer (Tracor TN 1705). Energy scale is calibrated using the signal from a tail pulse generator (BNC RP2) applied to the preamplifier test input. Integration of the timed spectra yields a count rate that is proportional to the radioactivity present in the source. Alternatively, a ratemeter or multichannel scaler can be used for continuous measurements using an appropriately wide window (~35-158 keV).

A more detailed diagram of the detector mounting assembly is shown in Fig. 2.9. The entire assembly, including the detector, an electrical connection, and provisions for water or nitrogen cooling, are easily accommodated on a single 6 in. (152 mm) conflat flange. The detector (case diameter ~20 mm) is recessed into a copper jacket fixed to an L-shaped rotatable feedthru offset about 40 mm from the center of the 152 mm flange. The rotation mechanism allows the detector to be reproducibly aligned 5-10 mm directly in front of the crystal for counting adsorbed species or quickly rotated 90-180° for background corrections, high pressure reaction rate studies, or rapid interchange between other surface analysis methods. The output/bias connection from the detector to an external feedthru is made using a flexible 93

shielded cable. When bias is applied, the detector must be maintained at temperatures between -30 and 30°C. In practice, the background noise level can be minimized by operating the detector at about 15°C or less. Slight cooling of the detector is easily accomplished using two strips of flexible copper braid that are connected from the back-side of the copper jacket to an adjacent copper block that is cooled by circulating water or nitrogen.

Solid state detectors always display an appreciable level of low energy noise resulting from leakage current and random fluctuations in charge carrier density. This noise ordinarily amounts to 8-10 keV and must be discriminated against in order for quantitative analysis to be carried out. In practice, because of peak broadening in the pre-amplifier and amplifier, the lower discriminator level must be set at 2-3 times the detector noise level in order to eliminate all noise. This is illustrated in Fig. 2.10, where N(E) beta spectra are compared at two lower discriminator energies for a 1 cm^2 sheet of ^{14}C-polymethylmethacrylate suspended in the vacuum chamber at the same position as the platinum single crystal. The left hand spectrum obtained with the discriminator set to about 10 keV displays a sharp low energy peak due to detector noise superimposed on a slowly decreasing background which represents the actual ^{14}C-beta emission. The right hand spectrum obtained with the discriminator set to about 35 keV displays the ^{14}C-beta spectrum with no contribution by detector noise. To determine the optimum operating conditions for the surface barrier detector in UHV, the count rates for background, and the

^{14}C-polymethylmethacrylate sheet were monitored as a function of the lower discriminator energy. The results are shown in Fig. 2.11 where the ^{14}C-count rate (cpm) has been squared, divided by the background count rate (Bkg), and plotted as a function of the lower discriminator energy. For a source with low specific radioactivity, the maximum in cpm^2/Bkg (32 keV) defines the operating conditions with maximum signal to noise. To provide an additional measure of noise rejection, all measurements described hereafter were carried out with the lower discriminator set to 35 keV. To determine how much of the ^{14}C-beta emission would be rejected by 35 keV, we used a liquid scintillation counter to plot an unquenched ^{14}C-beta spectrum and calculated from this that about 40 percent of the activity would be rejected.

2.3.2. Calibration of the Detection Efficiency

As indicated in Fig. 2.9, the active area of the surface barrier detector is comparable to the crystal face surface area for a typical single crystal sample. The counting geometry defined as the solid angle subtended by the detector at a point source located 10 mm from this active surface is 0.34 π. Fortunately, the detector efficiency can be calibrated in a manner which corrects for the discriminator level, the counting geometry with a single crystal source, and the surface area of the crystal surface. In the efficiency measurements the single crystal samples were coated with several microliters of a solution (1.1 $\mu g/\mu l$; specific activity 4.56 $dpm/\mu l$; dpm = absolute disentegrations per minute) containing ^{14}C-polymethylmethacrylate dissolved in ethyl acetate. Evaporation of the solvent yielded thin films (ca. 1.1-6.7 μm) of

^{14}C-polymethylmethacrylate coated onto the single crystal surfaces. The film thickness was estimated from the amount deposited assuming a film density of 0.86 g/cm^3. The count rate for the polymer films was monitored as a function of the amount deposited to obtain a calibration curve like that shown in Fig. 2.12, where the observed efficiency (cpm/dpm) is plotted as a function of the estimated film thickness. For this (111) platinum crystal (area 0.22 ± 0.2 cm^2) and the limited range of film thickness investigated the counting efficiency was 2.9 ± 0.3 percent.

2.3.3. Sensitivity and Capability of the Radiotracer Technique

The absolute sensitivity of this radiotracer technique and the uncertainty of the counting statistics are derived from the total counts for adsorbed species and background. The total counts depend on several factors including the crystal surface area, the detector efficiency, the counting time, and the specific radioactivity of the adsorbed species. While many hydrocarbons and other molecules that contain carbon-14 are commercially available with specific activities ranging up to about 64 mc mmole^{-1} (carrier free), a nominal value of 10 mc mmole^{-1} is more common. Assuming this level of radioactivity, a crystal surface area of 25 mm^2, a background of 3 cpm, and a detection efficiency of 3 percent, a series of simple calculations reveals that surface concentrations of 1×10^{13}, 5×10^{13}, and 1×10^{14} molec cm^{-2} can be determined in a 20 min count with standard deviations of 23, 10 and 4 percent, respectively. Alternatively, 1×10^{14} molec cm^{-1} can be detected in only 4 min with a standard deviation of 10 percent. These

statistics can be improved by using longer counting times, a higher specific radioactivity, or a larger area detector. It is, therefore, clear that the radiotracer technique is a very sensitive method for general surface analysis studies. Surface coverages at 1 percent of the monolayer can be determined non-destructively with a high level of accuracy.

In UHV applications, surface barrier detectors offer several notable advantages over thin window Geiger counters described previously by Klier et al. (30,31). For low energy betas, surface barrier detectors are generally superior to gas counters because the window thickness is smaller, the detector is more compact, and the problems of window rupture or gas stability with time due to decomposition or diffusion through the window are absent (29). Because it is compact and rotatable, the solid state device can also be used easily in conjunction with other surface analysis methods. The primary disadvantage of the surface barrier detector is its lower efficiency (arising from the counting geometry and the need to eliminate noise pulses) which may necessitate longer counting times.

While the present discussion has been restricted to ^{14}C-radiotracers, it is important to note that any other elements possess radioisotopes that are suitable for surface studies using the same counting system. Table 2.1 lists several of these isotopes along with their half-lives and the maximum energy for their beta emission. Several notable applications for this radiotracer technique include

(1) determination of equilibrium adsorption isotherms in terms of absolute surface concentrations,

(2) studies of surface and bulk diffusion kinetics,

(3) studies of isothermal desorption kinetics,

(4) determination of absolute Auger calibrations for surface carbon coverage (Section 2.6),

(5) transient response studies of hydrocarbon hydrogenation and hydrogen transfer reactions,

(6) studies of the fate of sulfur in hydrodesulfurization catalysis, and

(7) studies of the fate of surface carbon in Fischer-Tropsch synthesis.

Table 2.1. Partial listing of radioisotopes suitable for surface studies using a surface barrier detector.

Isotope	E_{max} (keV)	Half-life (yr)
^{14}C	158	5720
^{22}Na	544	2.6
^{26}Al	1160	7.4×10^5
^{32}Si	210	710
^{35}S	167	0.24
^{36}Cl	714	3.0×10^5
^{137}Cs	510	30

FIGURE CAPTIONS

Fig. 2.8. Block diagram showing the experimental arrangement and counting electronics for radiotracer studies using a surface barrier detector in an ultrahigh vacuum chamber. An expanded cross-section of the surface barrier detector is also shown (29).

Fig. 2.9. Schematic diagram of the detector mounting assembly showing the detector offset along with the output/bias connection and provisions for cooling the detector with circulating water or nitrogen.

Fig. 2.10. Carbon-14 beta spectra measured with a surface barrier detector at two lower discriminator energies (ca. 10 and 35 keV).

Fig. 2.11. Plot of cpm^2/Bkg as a function of the lower discriminator energy obtained for the surface barrier detector using a ^{14}C-polymethylmethacrylate source.

Fig. 2.12. Efficiency calibration (cpm/dpm) for the surface barrier detector obtained by depositing thin films of ^{14}C-polymethylmethacrylate onto a platinum single crystal surface. Self-adsorption by the polymer is negligible for the range of film thickness investigated.

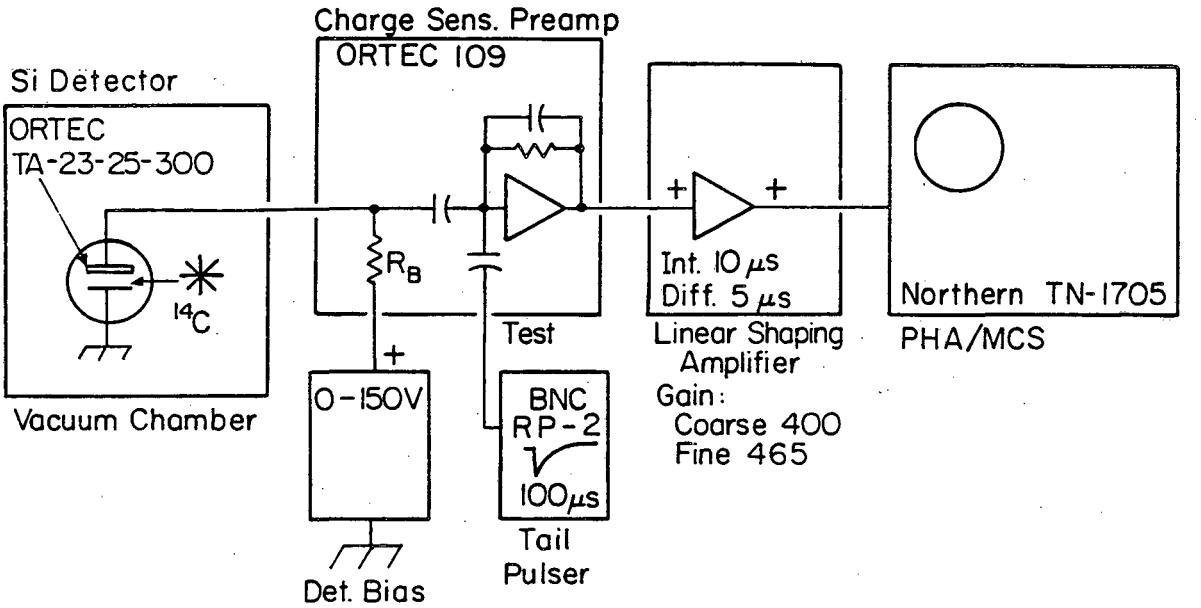

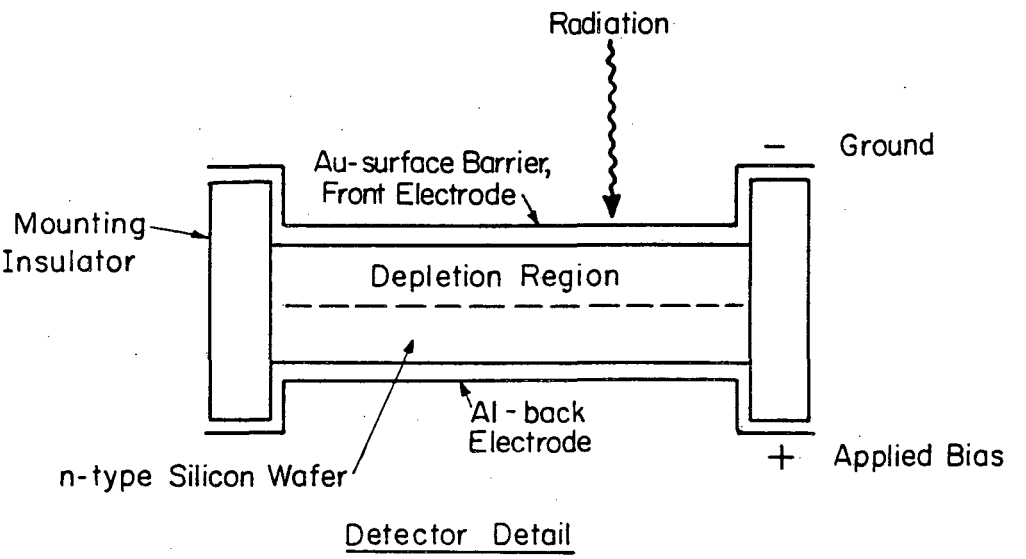

Detector Detail

XBL811-5007

Fig. 2.8

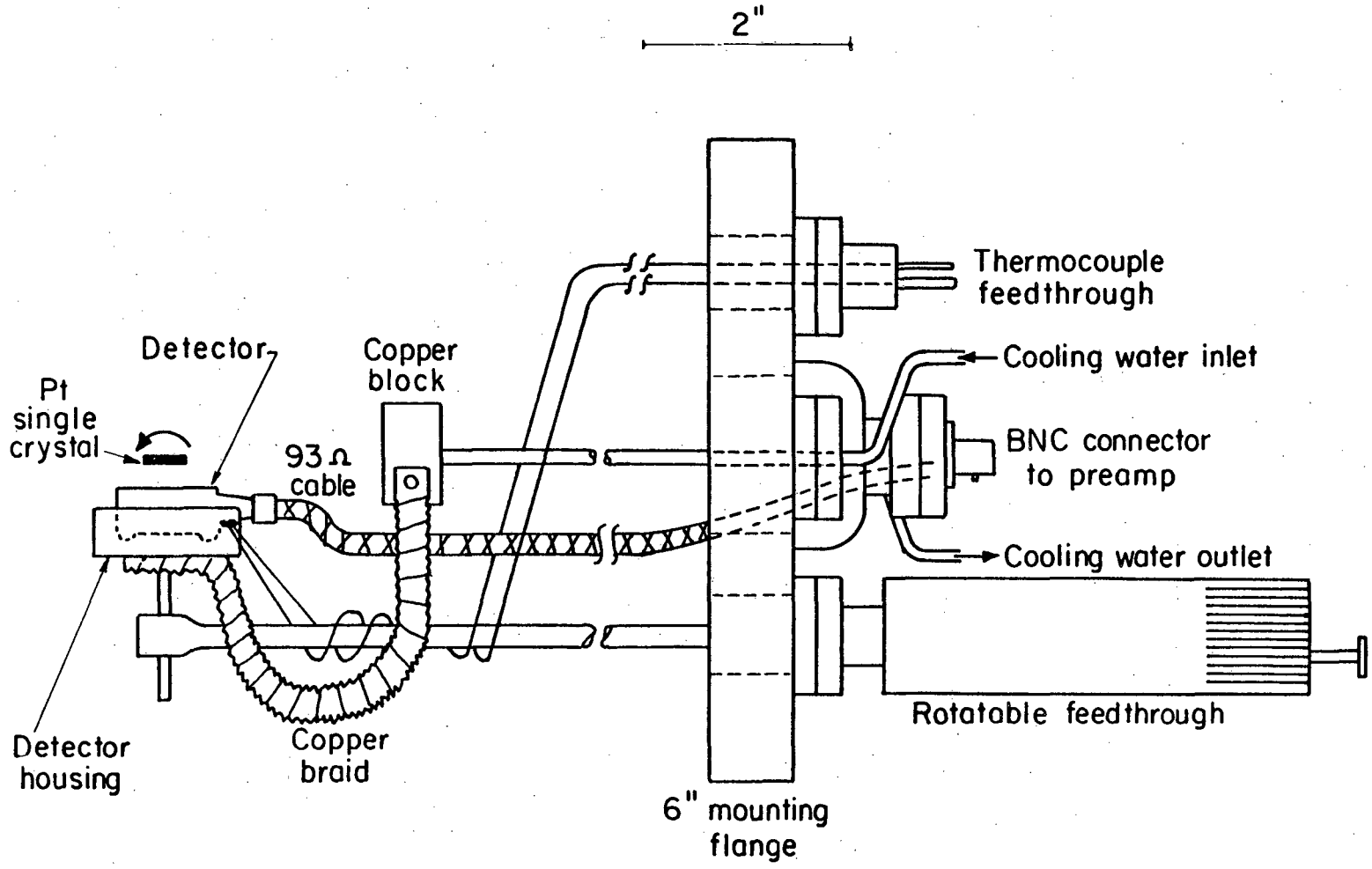
2"
Thermocouple feedthrough
Cooling water inlet
BNC connector to preamp
Cooling water outlet
Rotatable feedthrough
Detector
Pt single crystal
93 Ω cable
Copper block
Detector housing
Copper braid
6" mounting flange
XBL 811-5001

Fig. 2.9

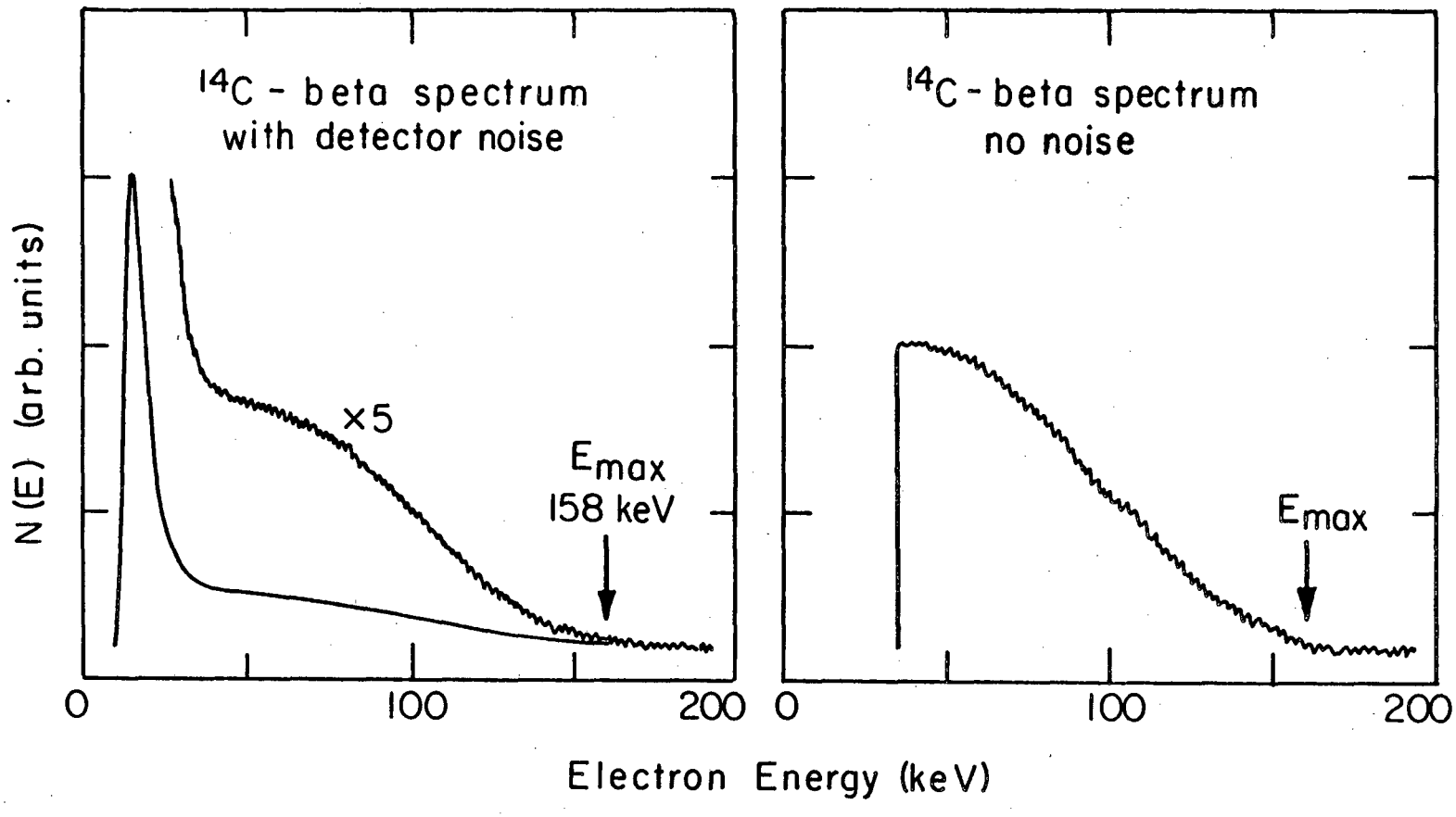

XBL811-5002

Fig. 2.10

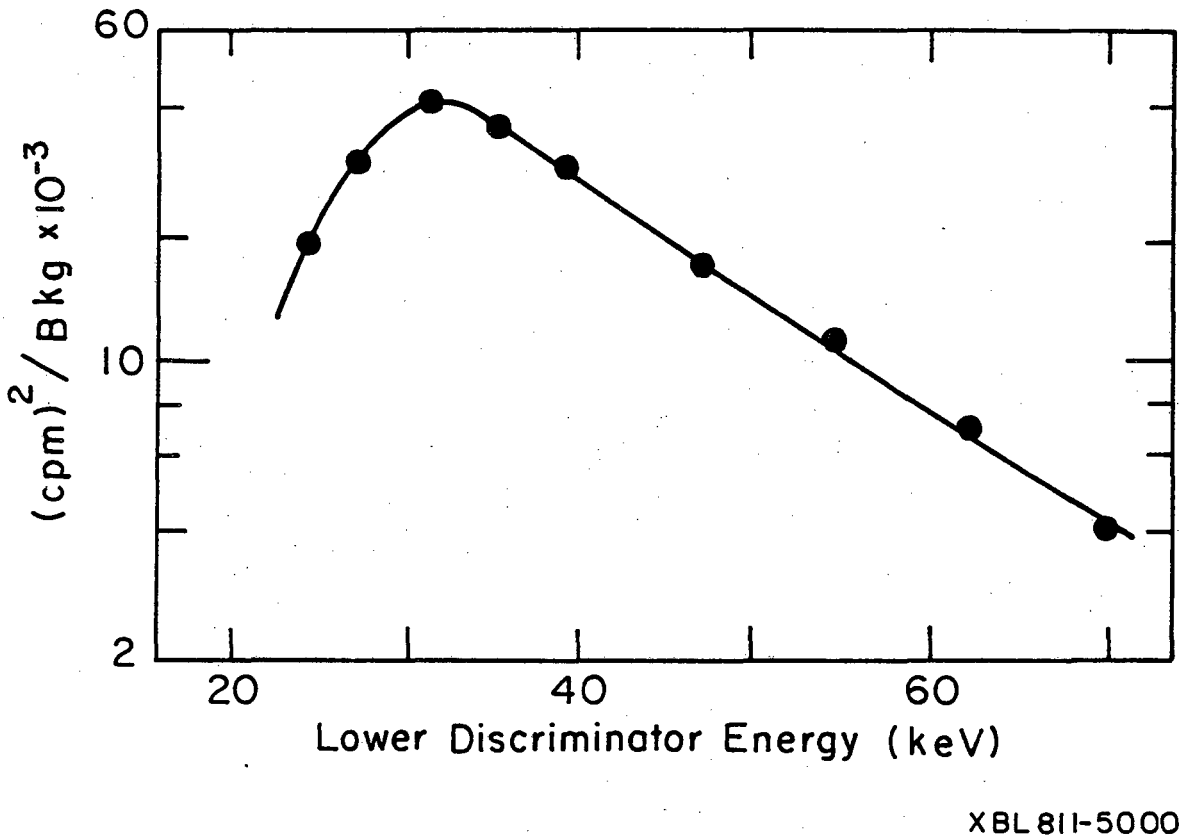
60
10
2
$(cpm)^2 / B kg \times 10^{-3}$
20
40
60
Lower Discriminator Energy (keV)
XBL 811-5000

Fig. 2.11

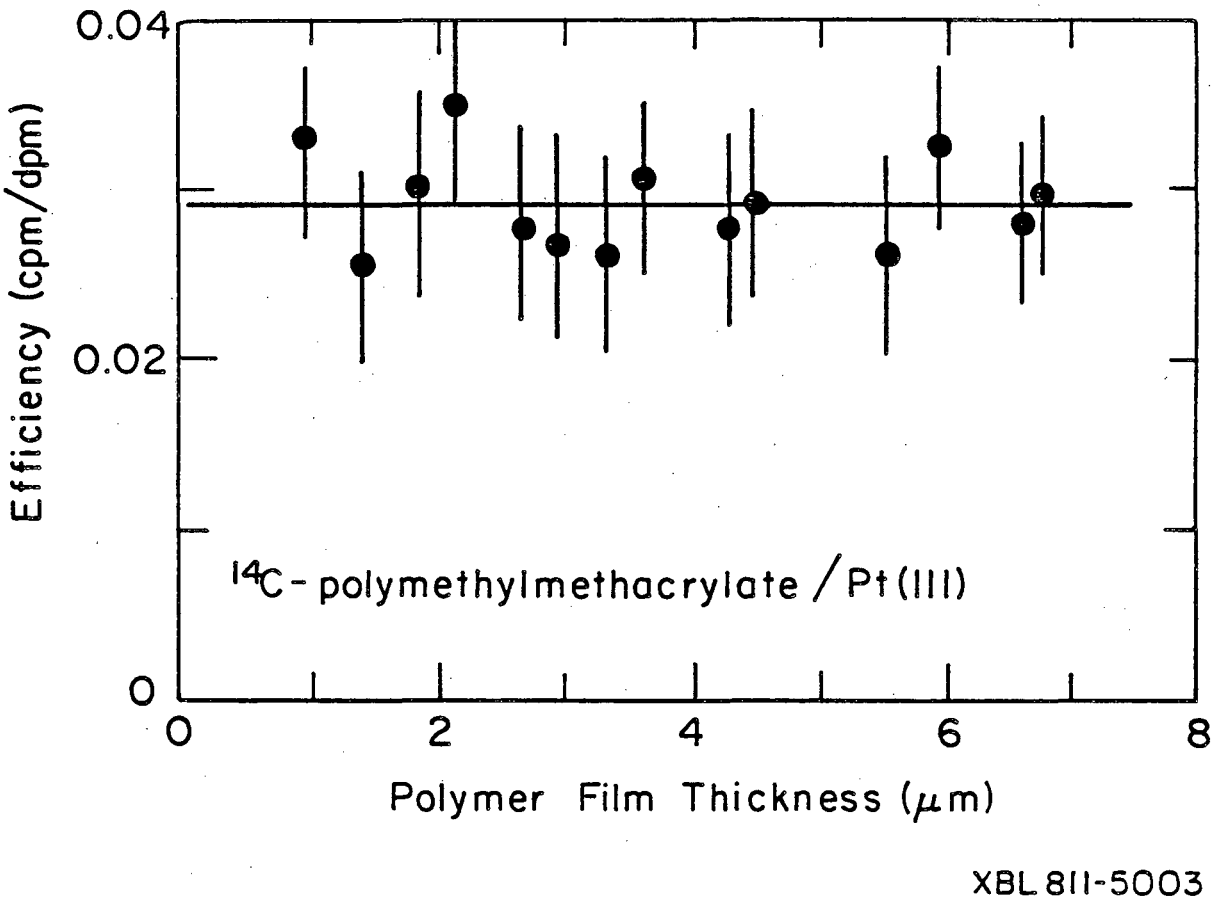
0.04
0.02
0
Efficiency (cpm/dpm)
^{14}C - polymethylmethacrylate / Pt(111)
0
2
4
6
8
Polymer Film Thickness (μm)
XBL 811-5003

Fig. 2.12

2.4. Materials

2.4.1. Reagents

Hydrogen and hydrocarbon reagents used in this research were of the highest obtainable research purity. A listing of reagents is supplied in Table 2.2 with sources, purities, and major detectable impurities. Liquid hydrocarbons were stored in pyrex vacuum flasks fitted with O-ring sealed teflon stopcocks. The liquids were outgassed by repeated freeze-pumping cycles at 77 K prior to initial use. Thereafter, this degassing procedure was repeated regularly at 1 to 2 week intervals. Hydrogen, deuterium, and gaseous hydrocarbons were used as supplied.

Carbon-14 labelled ethylene (Amersham; specific activity 128.5 mc/mmol) and benzene (New England Nuclear; specific activity 16 mc/mmol) were supplied in breakseal tubes adapted with vacuum stopcocks and were outgassed by repeated freeze pumping cycles prior to use. Radiochemical purities for these hydrocarbons were stated to be in excess of 99 percent.

Surface contamination by reactant impurities such as sulfur, chlorine, and oxygen is always an important consideration in reaction rate studies using small area single crystal catalysts. With a reactant pressure of 1 Torr and impurities present at concentrations of 1 ppm, in principle, it might take only 1 sec to deposit one complete monolayer of surface contamination. Auger electron spectroscopy was used throughout this work to monitor the elemental composition of the platinum surfaces following all reaction rate studies. Fortunately,

Table 2.2. Listing of reagents with sources, purities, and major detectable impurities.

Reagent	Source	Purity (a) (wt%)	Gas Phase (a) Impurities	Surface (b) Contaminants
O_2	LBL	≳99.9	CO	None
H_2	LBL-Matheson	≳99.99	-	None
D_2	LBL-Matheson	≳99.5 D_2 ≳99.95 D_2,HD,H_2	HD,H_2	None
CO	LBL-Matheson	≳99.5	-	None
Ethylene	Matheson	≳99.9	-	None
Isobutane	Matheson	≳99.995	C_2H_6, iso-C_4H_8	None

Table 2.2. Continued.

Reagent	Source	Purity (a) (wt%)	Gas Phase (a) Impurities	Surface (b) Contaminants
n-Butane	Matheson	≳99.92	C_3H_8, iso-C_4H_{10} n-C_4H_8	None
Neopentane	Matheson	≳99.92	n-C_4H_{10}, n-C_4H_8	Sulfur 1-5% monolayer
n-Hexane	Phillips	≳99.95	methylcyclopentane 3-methylpentane benzene	None
Cyclohexane	Matheson	≳99.8	-	None
Cyclohexene	Phillips Matheson	≳99.85 ≳99.6	Cyclohexane benzene methylcyclopentane	Sulfur 2-4% monolayer
Benzene	Matheson	≳99.8	-	-
n-Heptane	Phillips	≳99.93	Isohexanes Benzene	None

(a) Determined gas chromatographically.

(b) Determined by AES following high pressure reaction rate studies.

surface contamination never appeared to be a serious problem. Sulfur contamination was detected only after neopentane and cyclohexene reactions, and then the maximum sulfur coverage never exceeded ~7-9 x 10^{13} S/cm^2 based on the calibration presented in Section 2.6. The sulfur concentration at a given temperature was usually reproducible (±25 percent), and most often it was in the range 2-4 x 10^{13} S/cm^2. This sulfur appeared to be deposited rapidly within ~5 min as the reactions commenced. Low levels of surface and/or subsurface oxygen were observed irregularly following about 20 percent of the experiments ($O_{510}/Pt_{237} \leq 0.1$-$0.15$). This oxygen produced no detectable changes in reaction rates, selectivities or poisoning behavior. The most important surface species deposited by the reaction mixtures were the unavoidable carbonaceous deposits that form the main subject of this thesis. The behavior of the carbon deposit as a function of temperature, pressure, and reactant hydrocarbon clearly indicated that it was a genuine feature of the reaction chemistry.

2.4.2. Single Crystal Samples: Preparation, Characterization, Structure, and Cleaning Procedures

A variety of flat, stepped, and kinked platinum single crystal samples have been utilized in this research. Table 2.3 provides a listing of the crystallographic orientations expressed in Miller index form and in terms of microfacet indeces (32). Average terrace widths (Å) and kink densities (kinks/cm^2) are included where appropriate. The clean stepped surfaces appeared to be stable in atomic arrangements characterized by monatomic height steps (Section 2.4.3). Figures 2.13

Table 2.3. Miller indeces, microfacet indeces, average terrace widths, and average kink concentrations for platinum single crystal surfaces.

Miller Index	Microfacet Index	Average Terrace Width (Å)	Kink Concentration (Kinks/cm^2)
Pt(100)	Pt(100)	----	---
Pt(111)	Pt(111)	----	---
Pt(322)	Pt(s) - $[2_4(111) + 1_1(100)]$	11.2	---
Pt(321)	Pt(s) - $\left[\frac{3}{2}_3(111) + 1_1(100) + 1_1(11\bar{1})\right]$	5.5	3.7×10^{14}
Pt(654)	Pt(s) - $\left[\frac{9}{2}_9(111) + 1_1(100) + 1_1(11\bar{1})\right]$	13.9	1.5×10^{14}
Pt(13,1,1)	Pt(s) - $[12_6(100) + 1_1(111)]$	18.0	---
Pt(10,8,7)	Pt(s) - $\left[\frac{15}{2}_{15}(111) + 2_2(100) + 1_1(11\bar{1})\right]$	15.1	1.0×10^{14}
Pt(12,9,8)	Pt(s) - $\left[\frac{17}{2}_{17}(111) + 3_3(100) + \frac{1}{2}_1(11\bar{1})\right]$	12.9	7.7×10^{13}

and 2.14 show idealized atomic surface structures for the samples based on this conclusion. The flat (111) and (100) surfaces contain hexagonal and square close packed arrays of platinum atoms with coordination numbers 9 and 8, respectively. The other surfaces consist of extended arrays of (100) or (111) terraces which average 2-6 atoms in width that are periodically displaced by atomic steps and kinks. These coordinatively unsaturated surface irregularities have coordination numbers 7 and 6, respectively. The clean (100) and (13,1,1) platinum surfaces display surface reconstructions in which the topmost layer of platinum atoms is hexagonally packed and rotated slightly with respect to the underlying substrate (0.7° for Pt(100) (33)). Dynamical LEED intensity calculations for Pt(100) (33) indicate that the hexagonal layer is buckled and contracted 0.1-0.3Å perpendicular to the surface corresponding to a 6.3 percent average reduction in the d-spacing of the topmost layer. However, upon exposure to hydrocarbons (34) or other gases (35), the surface reconstructions dissappear and (1 x 1) diffraction patterns that correspond to the unreconstructed surfaces are obtained. Hydrocarbon catalysis appears to occur on these unreconstructed surfaces. For this reason, the (1 x 1) structures have been illustrated in Fig. 2.13, and will be referred to in all later discussions.

The single crystal samples used in this research either existed upon on my arrival or were prepared by Wini Heppler of the LBL support staff. Spark erosion was used to slice thin oriented discs (0.3-0.9 mm thick) from 0.48 or 0.63 cm diameter platinum single crystal rods that were obtained from Materials Research Corporation (MRC). Laue back

X-ray diffraction was used to insure that both crystal faces were within 1° of the specified orientation. Figure 2.15 shows Laue diffraction patterns for several of the samples. The crystals were polished to a mirror finish using standard metallographic procedures with the final step utilizing an aqueous slurry of 0.05 μm alumina powder on an ultrasonic vibrator. After etching for 15–30 sec in concentrated aqua regia, the samples were rinsed in water and acetone and then mounted in the vacuum chamber. Following the cleaning procedure described below, LEED diffraction patterns were photographed for each sample to make sure that the expected crystallographic orientation was preserved. Figures 2.14 and 2.16 show clean surface LEED patterns for the various samples. Average terrace widths, step orientations, and step heights were derived from the splitting and orientation of the diffraction beam doublets as described in the next section.

The platinum rods were reported by MRC to be at least 99.996 percent pure with carbon, oxygen, calcium, iron, silicon, and palladium as major impurities at maximum concentrations of 8, 9, 2, 5, 17, and 23 ppm, respectively. Auger spectra recorded for new samples invariably revealed surface contamination by sulfur (154 eV), carbon (273 eV), calcium (294 eV), and oxygen (510 eV); occasionally silicon (80 eV), phosphorous (119 eV), and chlorine (118 eV) were also detected. These impurities were removed to AES detection limits by repeated cycles of argon ion sputtering (0.5–1.5 keV) at 1100–1300 K, annealing at 1100–1480 K, and pretreatment with 1–10 x 10^{-7} Torr of oxygen at 1100–1300 K. The high temperature oxygen treatments induced

surface segregation of calcium and silicon as non-volatile oxides which facilitated their permanent removal by argon ion sputtering. As many as ten 1-3 hr sputter-anneal cycles were usually required to obtain a reproducibly clean surface. Following this initial cleaning procedure, Ca and/or Si impurities would sometimes reappear after a series of experiments or upon exposure of the sample to the atmosphere. For this reason it was necessary to repeat the sputter-anneal-oxygen treatment cycles at regular intervals not exceeding about 1 week. A Ca_{294}/Pt_{237} AES peak-to-peak height ratio <0.02 was arbitrarily chosen as the maximum level of calcium contamination that could be tolerated before reaction rate studies were carried out. This peak height ratio corresponds to a near surface region calcium concentration below 5×10^{12} Ca/cm^2 (14). Surface carbon and sulfur impurities could be easily removed by short (<1 min) oxygen treatments at 1050-1300 K without recourse to argon ion sputtering. However, ion sputtering followed by annealing to >1300 K was usually preferred in order to preclude any accumulation of strongly bound subsurface oxygen (2). During long periods of continual experimentation, a gradually increasing level of residual hydrocarbons in the vacuum chamber made it impossible to clean the samples by sputtering alone. Under these conditions, short pretreatments with oxygen at 1100-1300 K followed by flashing to >1300 K were used to completely clean the samples. Provided that the samples were clean and well annealed, reproducible results were obtained in reaction rate studies independent of the method of surface preparation.

All reaction rates reported in this thesis have been calculated on the basis of the total (edge + 2 faces) geometric surface areas of the single crystal samples. Table 2.4 summarizes the edge, face, and total areas for the various samples. The (100), (111), (322), (13,1,1), and (10,8,7) samples used for most of the reaction rate studies were deliberately cut very thin (~0.3-0.55 mm) so that the edge contribution would be minimized. Nevertheless, the polycrystalline edges still contribute a significant fraction of the total platinum surface area (ca. 10-18 percent). As pointed out by Gillespie (2), the presence of this unoriented area tends to make differences in reaction rates measured for surfaces with different atomic structure appear smaller than they would be if the entire surface was of the specified orientation.

2.4.3. Structure and Stability of Stepped Single Crystal Surfaces: Important General Considerations

While single crystal surfaces invariably display polishing abrasions and other macroscopic irregularities when viewed by optical or electron microscopy (36), LEED studies clearly indicate that the annealed surfaces are very regular on the atomic scale, and that most of the atoms occupy large ordered domains with uniform structure. The terrace width, step density, and kink concentration can be varied independently by changing the angles of cut and crystallographic orientation. Figure 2.14 showed surface structures and LEED patterns for a series of platinum surfaces in which the kink concentration was

Table 2.4. Surface areas of single crystal catalysts.

Crystal	Total Face Area (cm^2)	Total Edge Area (cm^2)	Total Area[a] (cm^2)	Total Pt Sites[a] x 10^{-15}
(100)	0.57	0.08	0.65	0.86
$(111)_1$	0.48	0.14	0.62	0.93
$(111)_2$	0.64	0.18	0.82	1.2
(321)	0.86	0.24	1.10	1.65
(322)	0.45	0.11	0.56	0.84
(654)	0.84	0.20	1.04	1.56
(13,1,1)	0.65	0.08	0.81[b]	1.09
(10,8,7)	0.66	0.12	0.78	1.18
(12,9,8)	0.53	0.22	0.75	1.13

(a) ±10 percent.

(b) Contains abnormally large contribution due to support wires (~0.08 cm^2).

varied from 8 x 10^{13} to 4 x 10^{14} kinks/cm^2 (4-20 percent kinks). If one assumes that step and kink atoms correlate in their chemical reactivity with the edge and corner atoms of small, dispersed metal crystallites, it can be shown (37) that the number distributions of surface atoms with different coordination numbers for these kinked crystal surfaces closely resembles that for octahedral fcc clusters containing about 20-2000 atoms ($\bar{d}$ ~ 10-40Å). Presently this assumption can be justified only for platinum and then only qualitatively because sufficient data for other metals are not yet available. It is nevertheless an interesting comparison because it emphasizes two unique and important features of stepped single crystal surfaces. These model catalysts can be prepared to expose virtually any type of surface site. The average concentration of these sites can be easily varied in a systematic and well controlled manner.

A large number of high Miller index copper (38), cobalt (39), nickel (40), rhodium (41), tungsten (42), rhenium (43), iridium (44), and platinum (45) surfaces have now been investigated by LEED. The diffraction patterns (cf. Figs. 2.14 and 2.16) display diffraction beam doublets that appear at well defined primary beam energies. The doublet pattern is produced by the constructive interference of beams diffracted from the terrace and macroscopic planes. To illustrate this phenomenon, Fig. 2.17 shows a schematic superposition of the reciprocal lattices expected for the terrace and macroscopic planes of a kinked (10,8,7) surface. Diffraction beams for the (111) terraces and (10,8,7) macroscopic plane are denoted by x's and o's, respectively.

The orientation of the doublets in reciprocal space defines the structure of the step in real space since the direction of the doublet splitting is the direction in the surface plane normal to the step edge. The doublet splitting $|\underset{\sim}{b}^*|$, is inversely proportional to the terrace width as this distance in the reciprocal lattice is fixed by the distance between step edges in real space. Average terrace widths in units of d, the nearest neighbor interatomic spacing, can be determined simply as a ratio $|\underset{\sim}{B}^*|/|\underset{\sim}{b}^*|$ of magnitudes of the reciprocal lattice vectors. Only those diffraction spots which are included within the circles are observed in the LEED pattern for the kinked (10,8,7) surface (cf. Fig. 2.14). The remaining diffraction beams for the (10,8,7) plane are not detected as a result of destructive interference (surface umklapp process) with the modes of the (111) diffraction. Within a kinematic approximation considering only scattering from the top layer atoms, Henzler has shown (46) that the scattered intensity at angle ϕ can be written in the form

$$I(\phi) = \alpha \frac{\sin^2\left[\frac{1}{2} ka(N+1) \sin\phi\right]}{\sin^2\left[\frac{1}{2} ka \sin\phi\right]} \times \sum_{i=-\infty}^{\infty} \delta\left[\frac{1}{2} k(Na + g) \sin\phi + \frac{1}{2} kd(1 + \cos\phi) - i\pi\right]$$

where α is an instrumental constant, $k = 2\pi/\lambda$, λ is the wavelength of the primary electrons, $N + 1$ is the average number of atomic rows with spacing a in one terrace, d is the step height, and g is the horizontal displacement of step edge atoms with respect to the underlying terrace

atoms. The first term of Eq. (13) arises from the finite number of atoms in a single terrace and corresponds to the intensity distribution for a grating with N + 1 slits. Maxima at angles ϕ such that $\frac{1}{2}$ ka $\sin\phi = n\pi$ are the "normal" spots expected for diffraction from a flat surface. The second term in Eq. (13) is a sum of delta functions in the limit of an infinite number of steps. This term depends only upon the step width (Na + g) and step height d. The separation between two adjacent delta functions corresponds to the doublet splitting that is closely approximated in the vicinity of the (0,0) beam ($\phi \approx 0$) by (46)

$$\Delta\phi_{(0,0)} \approx \lambda/(Na + g) \tag{14}$$

Thus, the average terrace width (Na + g) can also be determined simply from the splitting of the (0,0) doublet. The terrace width determined either in this manner or from a reciprocal lattice construction like that shown in Fig. 2.17 is a statistical average of the terrace width distribution (47).

Upon varying the primary beam energy, the delta functions of Eq. (13) continuously pass through the Bragg reflections of the terrace planes and coverage toward the specular reflection of the high index plane so that at certain energies no splitting is detected. This occurs for the (0,0) beam when (46)

$$V_{00}(\text{singlet}) = \frac{150}{4d^2}\, s^2 \tag{15}$$

where V_{00} are the primary beam energies in volts for observing a singlet (0,0) beam of maximum intensity, d is the step height in angstroms, and S is an integer. Equation 15 was used to confirm that the (321) and (654) platinum crystals used in this research were stable in structures characterized by monatomic height steps.

Wagner and co-workers have reported interesting work function measurements for a series of stepped gold, tungsten, and platinum single crystal surfaces (48). The work functions decrease linearly with increasing step density, and different step orientations give rise to slightly different work function reductions. These changes result from a charge in the surface dipole part of the work function due to the presence of steps. The surface dipole part of the work function arises from a change in the electrostatic potential in the surface region that can be interpreted in terms of dipole moments that are associated with each surface atom. The linear decrease in work function with increasing step density may be accounted for by attributing an additional dipole moment of 0.3 to 0.6 Debeye to each atom along the step edge. The attractive interaction of these dipoles with polarizable adsorbates may be partially responsible for the exceptional bond breaking abilities of step and kink atoms.

Calculations for platinum and other metals with large densities of states at the Fermi level indicate that large variations in charge density should exist at surface irregularities. The amplitude of s-electron charge density fluctuations (Friedal oscillations) was predicted to be enhanced at steps and kinks on platinum surfaces

(49). Consistent with this prediction, a recent platinum-NMR study revealed that these fluctuations are particularly striking for very small supported platinum clusters ($\bar{d}$ ~ 10-40Å) (50). The d-band electronic structures of the flat (111) and stepped (557) platinum surfaces have been compared within the tight binding approximation (51). A sharp surface bound state was predicted in the local density of states at the protruding edge of the stepped surface. The LDOS along the middle of the terraces was similar to that for Pt(111), while at the bottom of the step the LDOS appeared bulk-like. More recent ab initio calculations by Smith et al. (52). For the (100) surfaces of several Group VIII metals (viz., Ni, Pd, and Rh) suggest that surface states should be considered as a general feature of the surface chemistry of d-band metals. Angle resolved photoemission (ARUPS) studies have revealed surface states with sp-like character for normal emission from Cu(111) (53), Cu(211) (normal to the (111) terraces) (54), Ir(111) (55), Ni(111) (56), and Co(0001) (57). For a while it appeared that such a state was displayed 0.25 eV below E_f in the angle integrated photoemission spectrum of the unreconstructed Pt(100) - (1 x 1) surface (58). However, recent ARUPS studies for Ir(100) - (5 x 1) and Ir(100) - (1 x 1) have lead to the conclusion that this peak probably arises from a direct interband transition (59). This transition is obscured on the reconstructed surface due to surface Umklapp scattering (55).

Van Hove and Somorjai (32) have recently proposed a new microfacet rotation which simplifies visualization of high Miller index surfaces

in terms of the step structure and unit cell contents. This decomposition procedure supersedes the older step surface rotation, $M(s) - [N(h_t k_t l_t) \times M(h_s k_s l_s)]$ (60), which was often misleading when applied to kinked surfaces. The new notation was used in Table 2.3 and it is based on the fact that any set of Miller indeces can be decomposed uniquely in terms of linearly independent vectors that represent low index microfacets. The general formula is

$$(hkl) = M(S) - [a^1_{n_1}(h_1k_1l_1) + a^2_{n_2}(h_2k_2l_2) + a^3_{n_3}(h_3k_3l_3)] \qquad (16)$$

where M is the chemical element, S denotes a stepped or kinked surface, the $(h_ik_il_i)$ with i = 1,2,3 are appropriate low Miller index microfacets, the a^i's are the decomposed vector coefficients of (hkl) in terms of three sets of microfacet indices, and the n_i's are the numbers of unit cells of each microfacet contained in the unit cell of the surface. One or two terms may be omitted from this formula if the coefficients a_i vanish. As a consequence, flat, stepped, and kinked surfaces are conveniently represented by one, two, and three terms, respectively. The first term describes the number and type of terrace microfacets, the second denotes the step microfacets, and the third indicates the kink microfacet. With fcc materials it is convenient to use (100), (110) and (111) microfacets or (111), (11$\bar{1}$), and (100) microfacets as linearly independent bases. The latter basis set is preferable because each microfacet is close-packed. For fcc materials it is then easy to show that (32)

$$(hkl) = \frac{k + l}{2}(111) + \frac{k - l}{2}(11\bar{1}) + (h - k)(100) \qquad (17)$$

and

$$n_{hkl}:n_{111}:n_{11\bar{1}}:n_{100} = p_{hkl}:2(k + l):2(k - l):2(h - k)$$

where $p_{hkl} = 2$ if h, k, or l is even and $p = 4$ if h, k, and l are all odd. As examples, we now decompose stepped (322) and kinked (12,9,8) fcc surfaces into microfacet indices. Using Eq. (8),

$$fcc(322) = 2(111) + 1(100)$$

$$n_{322}:n_{111}:n_{111}:n_{100}: = 2:8:0:2 = 1:4:0:1$$

Thus

$$fcc(322) = M(S) - [2_4(111) + 1_1(100)]$$

Only two terms appear indicating that this surface is stepped. The unit cell contains 4(111) terrace microfacets and a single (100) step microfacet. For (12,9,8) the microfacet notation yields

$$fcc(12,9,8) = \frac{17}{2}(111) + 1(11\bar{1}) + 3(100)$$

$$n_{12,9,8}:n_{111}:n_{11\bar{1}}:n_{100} = 2:34:2:6 = 1:17:1:3$$

Thus

$$fcc(12,9,8) = M(S) - \left[\frac{17}{2}_{17}(111) + 3_3(100) + \frac{1}{2}_1(11\bar{1})\right]$$

Comparison with Fig. 2.14 confirms that the unit cell of this kinked surface contains 17(11$\bar{1}$) terrace microfacets, 3(100) step microfacets, and a single (111) kink microfacet.

The thermal stability of clean and adsorbate covered stepped surfaces is an important consideration in hydrocarbon catalysis over metals. Surface restructuring may occur at elevated temperatures in the presence of hydrogen and hydrocarbons or upon surface pretreatment in oxygen or other gases. These changes in surface morphology are closely related to sintering, redispersion, and poisoning of dispersed practical catalysts. Low energy electron diffraction was used to investigate the thermal stability of 25 different platinum surfaces (45) and several rhodium (41) and iridium (44) stepped crystal faces. While these surfaces possess higher surface free energies than low index crystal faces, the clean stepped surfaces are usually stable from room temperature to near the melting point of the metal in periodic arrays that are characterized by monatomic height steps. Exceptions for platinum occur along the ⟨100⟩ zone between the [110] and [100] low index poles. These surfaces reconstruct at temperatures below 1100 K yielding structures with multiple height steps or large low index facet planes. These changes in surface structure are exemplified schematically in Fig. 2.18. Blakely (45) has shown that the thermal

stability of the stepped platinum surfaces decreases abruptly in the presence of impurities such as graphitic carbon and strongly bound surface oxygen. In the presence of these additives, restructuring to low index facet planes (hill and valley structures) or multiple height steps is the rule rather than the exception. Surfaces which are stable in vacuum and in the presence of oxygen may restructure in the presence of carbon, while other surfaces may restructure only in the presence of oxygen. Figure 2.18 summarizes the various regions of stability for platinum surfaces that are clean, pretreated in oxygen at 1120 K, and covered with a monolayer of graphitic carbon. In the presence of oxygen stepped surfaces restructure more easily than kinked surfaces. This tendency is reserved on the graphite covered surfaces. Interestingly, the impurity-induced restructuring processes are all apparently reversible since the contaminated surfaces return to their original structures following the removal of oxygen or carbon.

There are several stable platinum surfaces which never restructure under the conditions of these experiments: the (111), (210), (211), (221), (321), and (331) crystal faces. These planes are commonly characterized by a very high density of periodic steps or no steps at all. Because of their exceptional structural stability, it is expected that these surface structures may play important roles in catalysis over platinum.

FIGURE CAPTIONS

Fig. 2.13. Idealized atomic surface structures for Pt(100), Pt(111), Pt(13,1,1), and Pt(322).

Fig. 2.14. Idealized atomic surface structures and LEED patterns for a series of platinum single crystal surfaces with variable kink concentrations.

Fig. 2.15. Laue back X-ray diffraction patterns for a series of platinum single crystals: (A) Pt(100); (B) Pt(13,1,1); (C) Pt(111), (D) Pt(12,9,8); (E) Pt(654); (F) Pt(321).

Fig. 2.16. LEED patterns for the (A) (100), (B) (223), (C) (111), and (D) (13,1,1) platinum single crystal surfaces. The diffraction pattern for Pt(13,1,1) has been taken from Ref. 34.

Fig. 2.17. Superposition of the reciprocal lattices expected for electron diffraction from the (111) terrace plane (X's) and (10,8,7) macroscopic plane (O's) of a kinked (10,8,7) platinum surface. Rotated doublets which are observed in the LEED pattern are indicated by the ellipsoids. The average terrace width is closely approximated by $|\underset{\sim}{B}^*|/|\underset{\sim}{b}^*|$.

Fig. 2.18. Schematic representations of surfaces exhibiting a multiple height step structure or hill-and-valley configuration consisting of large facet planes (upper half). Stereographic triangles indicating regions of stability in monatomic height steps, regions where multiple height steps are stable, and regions where steps are unstable for clean platinum surfaces, platinum surfaces heated in oxygen at 1100 K, and platinum surfaces covered with a monolayer of graphitic carbon, after Blakely (45), (lower half).

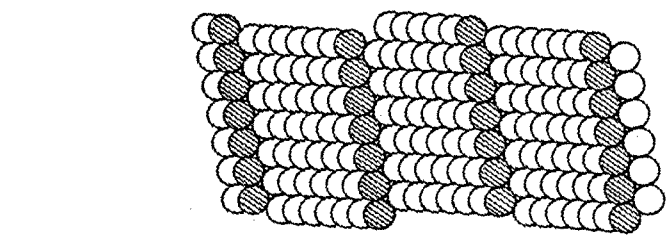

fcc (110)

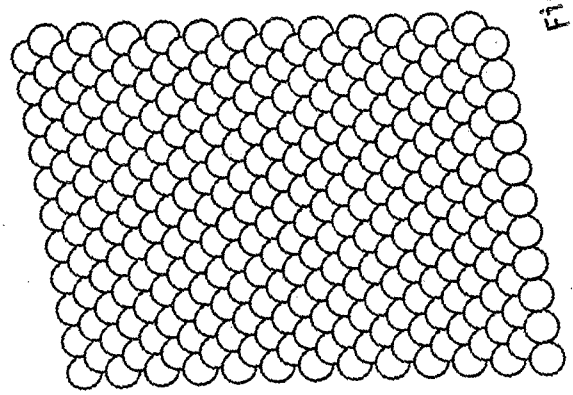

fcc (111)

Fig. 2.13

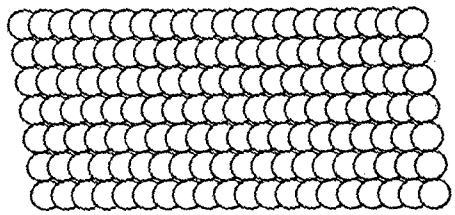

fcc (100)

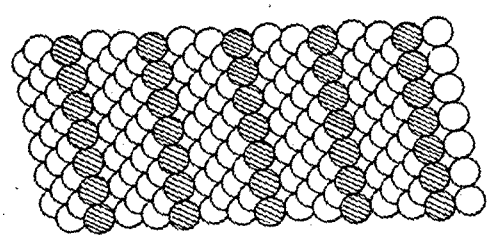

fcc (322)

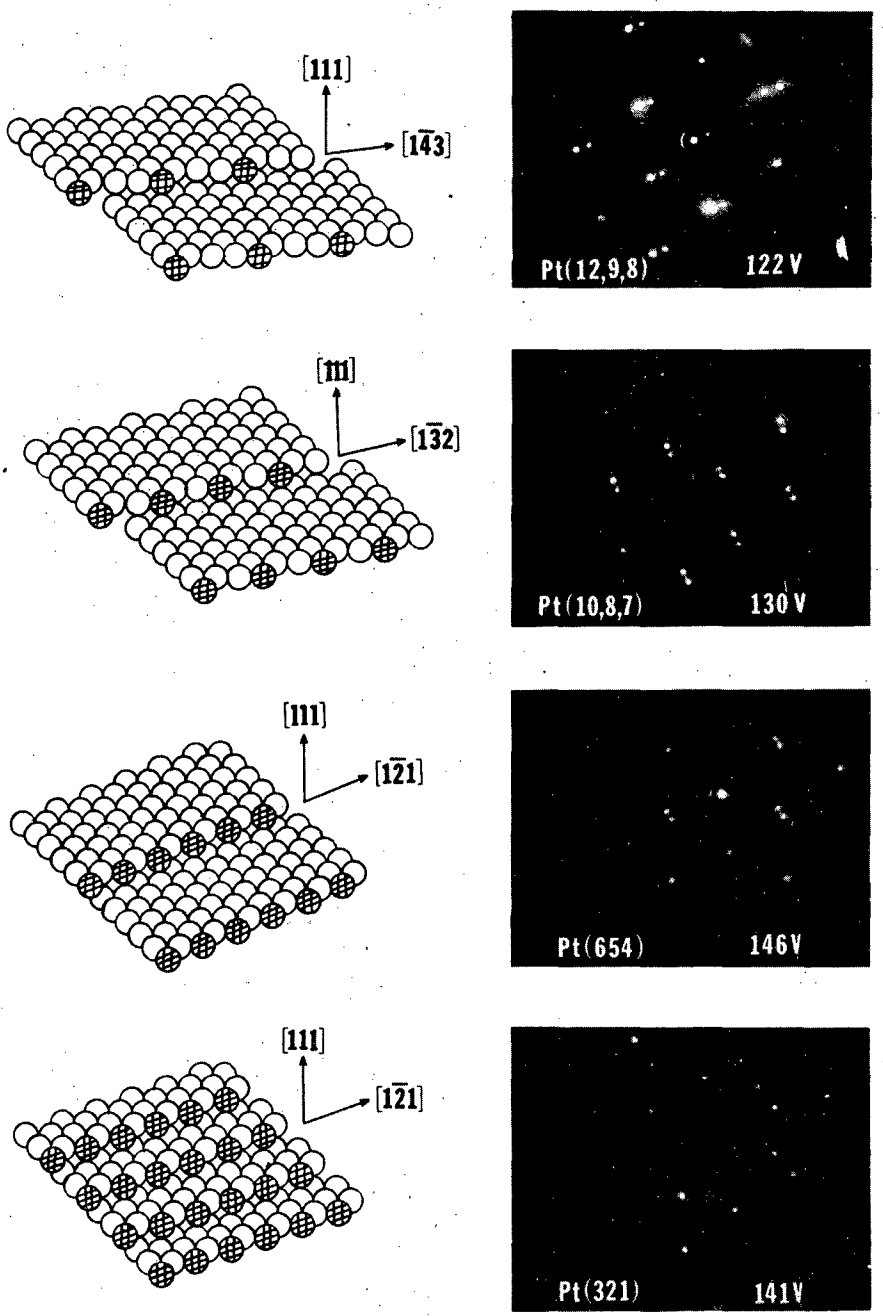

XBB 793-2960

Fig. 2.14

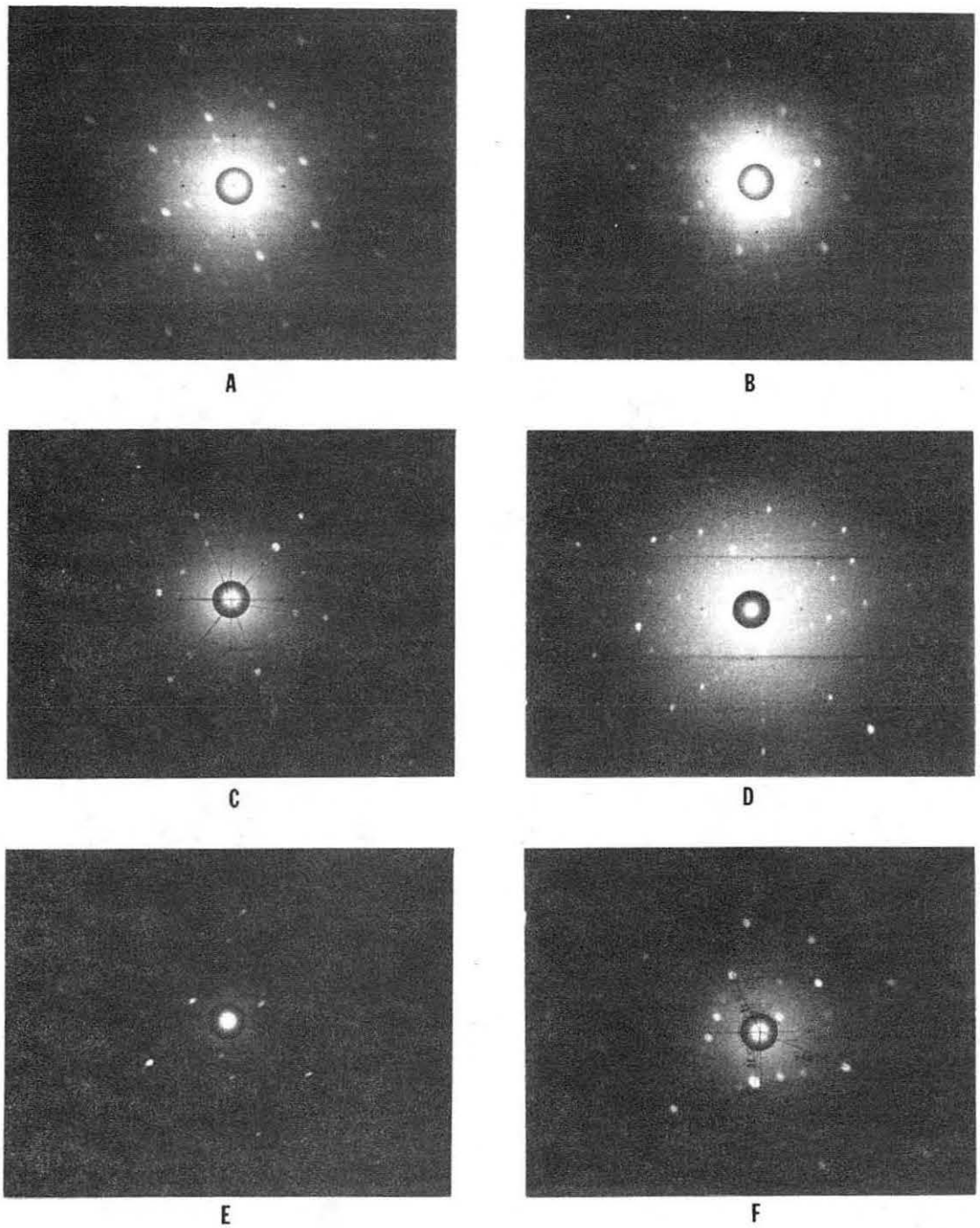

Fig. 2.15 XBB 815-4536

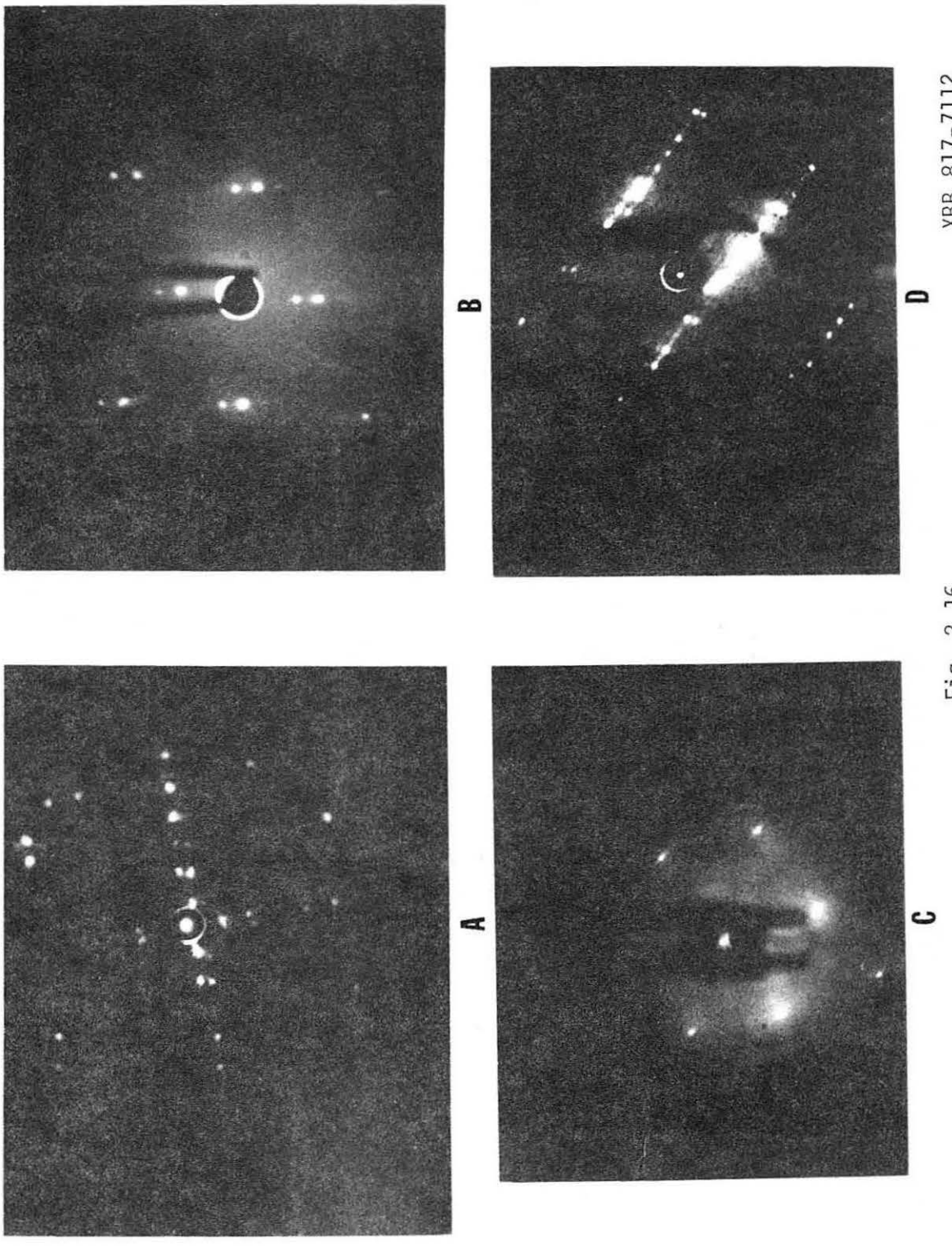

XBB 817-7112

Fig. 2.16

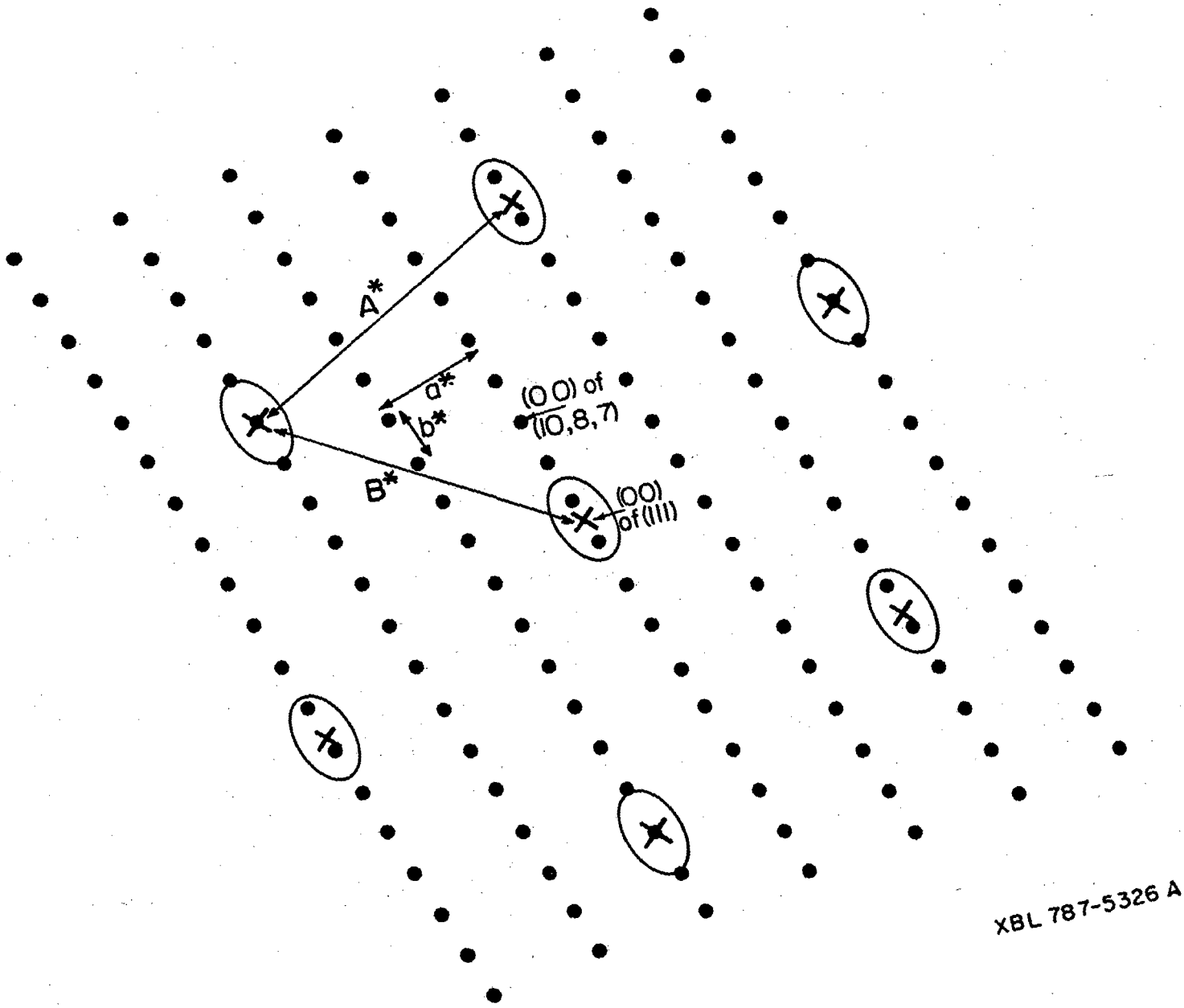

Fig. 2.17

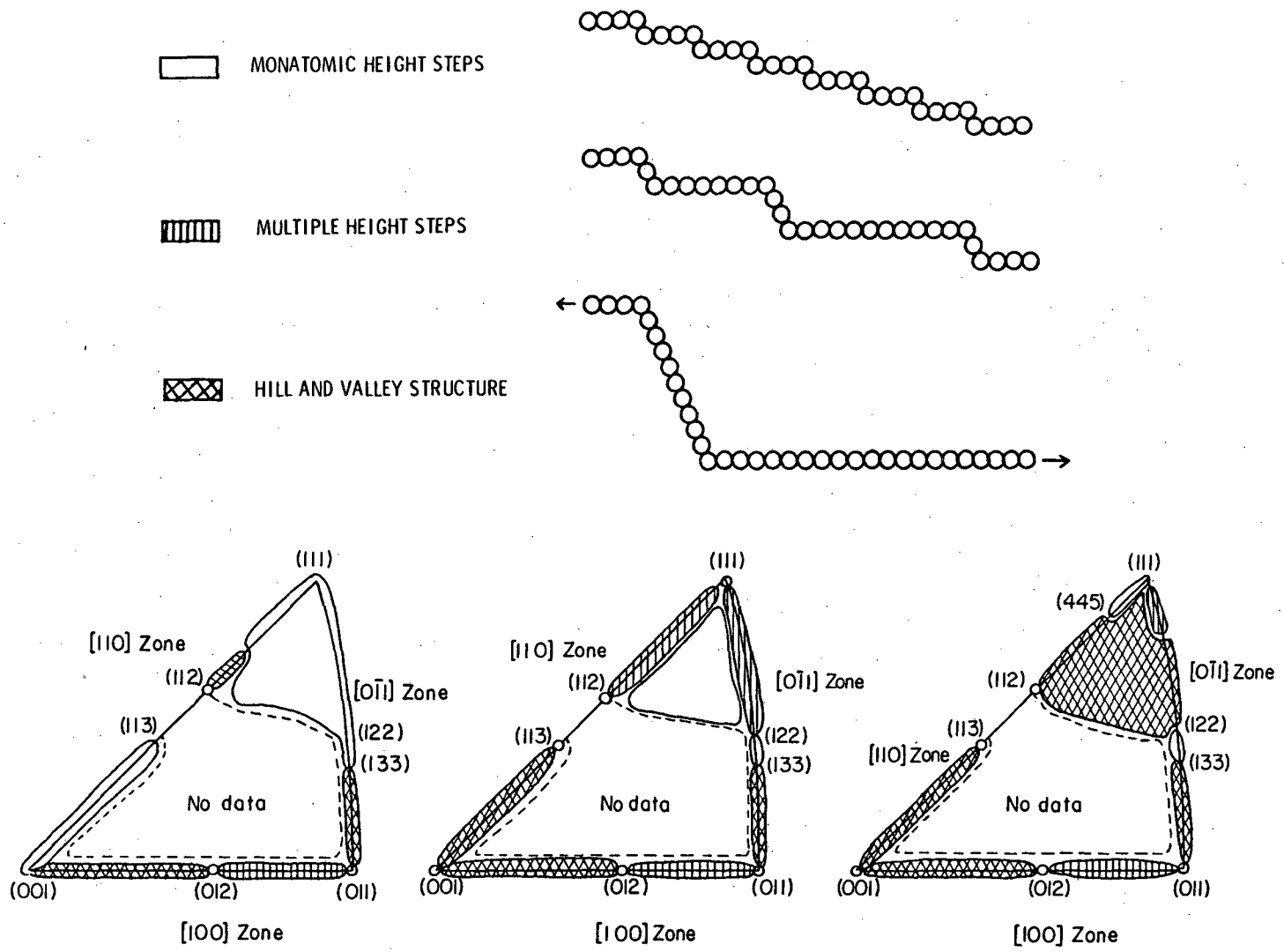

Fig. 2.18

XBL 763-6633A

2.5. Procedures for Reaction Rate Experiments

2.5.1. Reaction Studies on Clean Surfaces at Atmospheric Pressure

Prior to each reaction rate experiment, the single crystal samples were cleared in UHV as described earlier using a combination of argon ion sputtering, oxygen pretreatment, and annealing cycles at 1050-1400 K. After the surface composition was characterized by AES, the samples were briefly flashed to 1250-1400 K to remove any residual background gases. As the sample cooled below 425 K the isolation cell was quickly closed and pressurized to about 1 atm with H_2 or D_2 to cool the sample and supports below 320 K. After about 1 min the hydrogen was removed, hydrocarbon vapor and hydrogen (or D_2) were introduced to the desired total pressure, circulation was commenced for 3-8 min to provide complete mixing of the gases, and then the sample was heated to the reaction temperature over a period of about 1 min. For total reactant pressures below 200 Torr nitrogen was added as an inert diluent so that the metal bellows recirculation pump would operate effectively without overheating. A gas chromatogram was always obtained before the sample was heated to insure that the reactant mixture was pure and well mixed. Zero reaction time was taken as the time at which the crystal reached reaction temperature. The reaction temperature was continuously regulated to ±3K using a precision temperature controller with a DVM display referenced to the chromel-alumel thermocouple. Gas chromatograph samples were subsequently taken at periodic intervals of 7-14 min depending on the reaction studied. The reactions were usually allowed to proceed for 90-200 min after

which the sample was rapidly (~1 min) cooled in the reaction mixture to below 320 K, and then the gas mixture was pumped out. The evacuation procedure consisted of rough pumping to 10^{-1} Torr with a mechanical pump followed by an additional 3-20 min pumping to 10^{-3}-10^{-4} Torr with a sorption pump cooled by liquid nitrogen. Upon opening the isolation cell the pressure in the main chamber rose to 10^{-8}-4 x 10^{-7} Torr and then decayed rapidly (1 min) to 2 x 10^{-8} Torr. Subsequently Auger spectra were recorded for both crystal faces to provide an estimate of the total surface carbon deposited by the reaction mixture. The bonding and composition of the carbonaceous deposit was then characterized further by one of the following series of experiments, (a) CO chemisorption (36 L exposure) and quantitative CO thermal desorption were used to determine the concentration of uncovered platinum surface sites; or (b) quantitative hydrogen thermal desorption was carried out as described in Section 2.2.4 to determine the hydrogen content of the adsorbed carbonaceous species.

2.5.2. Reaction Studies at Low Pressures (10^{-5} Torr)

For the low pressure reaction rate studies described in Section 5.3, the original high pressure-low pressure apparatus was modified to operate as a continuous flow reactor. To begin a reaction, two leak valves were used to introduce hydrogen followed by hydrocarbon into the chamber at total pressures ranging from 10^{-4}-10^{-6} Torr. The single crystal samples were brought to the reaction temperature before admitting the hydrocarbon. The temperature was monitored continuously

with a Pt-Pt/10 percent Rh thermocouple spot welded to the crystal edge. Reaction rates were calculated using

$$TN_i = \frac{1}{A} \frac{dn_i}{dt} = P_i S_i / RT_g N_s \qquad (18)$$

where TN_i was the turnover frequency for the formation of product i in molecules per surface Pt atom per second; P_i was the corrected partial pressure of species, i; S_i was the pumping speed; T_g was 300 K; and N_s was the number of surface Pt atoms. Partial pressures were measured with the quadrupole mass spectrometer calibrated against the nude ion gauge for the gases of interest. Conductance limited pumping speeds with an isolable liquid nitrogen trapped 2 in. diffusion pump were 11 ± 3 liter/sec for H_2, 0.8 ± 0.2 liter/sec for C_6H_{12}, and 0.5 ± 0.2 liter/sec for C_6H_{10} and C_6H_6. Reaction rates were corrected for background reactivity by running blank reactions with the crystals contaminated by unreactive graphitic overlayers. The graphitic deposits formed with the crystals were heated in hydrocarbon at 900 ± 100 K. Other details concerning these low pressure experiments have been described in detail by Smith (61).

2.6. Auger Calibrations for Sulfur and Carbon Coverage on Platinum

Absolute Auger calibrations for surface sulfur and carbon coverage on platinum were determined so that changes in reaction kinetics due to these surface additives could be investigated in a quantitative manner. A simple and convenient calibration for carbon coverage on Pt(111) was obtained using the ^{14}C-radiotracer technique described in Section 2.3. Figure 2.19 shows the C_{273}/Pt_{237} AES peak-to-peak height ratio plotted as a function of C/Pt, the absolute number of carbon atoms per surface platinum determined by radiotracer analysis following the chemisorption of ^{14}C-benzene at 500-620 K. The Auger spectra were recorded at 7.0 V peak-to-peak (ptp) modulation and at constant angle of incidence (~70° to normal). For the range of coverage investigated the number of carbon atoms per surface platinum atom is given empirically by C/Pt = 0.62 (±15 percent)$[C_{273}/Pt_{237}]$. A similar calibration carried out for the (100) surface yielded C/Pt = 0.74 (±25 percent)$[C_{273}/Pt_{237}]$. The AES calibration for Pt(111) has been used throughout this research to estimate carbon coverages on stepped platinum surfaces with (111) terraces. The calibration for Pt(100) was used to estimate carbon coverages on Pt(13,1,1).

It is useful to compare this method of calibration for carbon coverage on platinum with that described previously by Biberian (18). In the Biberian calibration CO was decomposed on Pt(557) at 573 K, and the C_{273} ptp intensity was plotted as a function the Pt_{237} ptp intensity. With increasing coverage a "break" or discontinuity in the

graph was observed at C_{273}/Pt_{237} = 3.4 that was believed to represent the completion of one "monolayer." According to the radiotracer calibration this monolayer would contain 1.9 ± 0.4 carbon atoms per platinum atom which is much too high for a carbidic monolayer (C/Pt ≃ 1.0) and too low for a close packed graphitic overlayer (C/Pt = 2.57). It is notable that the maximum coverage achieved in the Biberian calibration (C_{273}/Pt_{237} ≃ 4.3) is very close to that expected for a graphitic overlayer (i.e., C_{273}/Pt_{237} = 4.1). Both methods indicate that at low pressures no three dimensional island growth occurs and little or no carbon is dissolved into the near surface region. However, results reported in later sections indicates that at high pressures and temperatures above about 600 K, 3D-island growth definitely takes place and carbon dissolution may as well. Under these conditions, the accuracy of both AES calibrations may become limited. Nevertheless, they have been used in this research to provide a convenient estimate of total surface carbon.

An approximate AES calibration for surface sulfur coverage on Pt(111) was derived from that for carbon coverage by chemisorbing thiophene (C_4H_4S) at low coverage and 573 K. It was determined that the S_{152} and C_{273} Auger cross sections were in the ratio 35 ± 3:1. From the carbon calibration presented above it follows that $S/Pt = 0.020[S_{152}/Pt_{237}] = 0.020(\pm 25 \text{ percent})[(S_{152} + Pt_{158})/Pt_{237} - 1.2]$. The factor 1.2 in the last expression corrects for the overlap of the S_{152} and Pt_{158} Auger peaks whose sum intensity is measured directly from the Auger spectrum. This calibration has been used to estimate

sulfur coverage on clean platinum surfaces with the assumption that the sulfur cross-section does not vary markedly with chemical state (i.e., heterocyclic or atomic sulfur). When sulfur was coadsorbed with carbon deposits an effort was made to correct the Pt_{237} ptp intensity for attenuation by surface carbon using an attenuation coefficient of 50 ± 5 percent for C/Pt = 2.57. Under these conditions sulfur coverage was estimated using S/Pt = 0.020(±40 percent)$[(Pt_{158} + S_{152})/(Pt_{237} + 0.12\ C_{273}) - 1.2]$.

FIGURE CAPTIONS

Fig. 2.19. Absolute Auger calibration for surface carbon coverage on platinum obtained by the radiotracer method using ^{14}C-benzene chemisorbed on Pt(111) at 510-620 K.

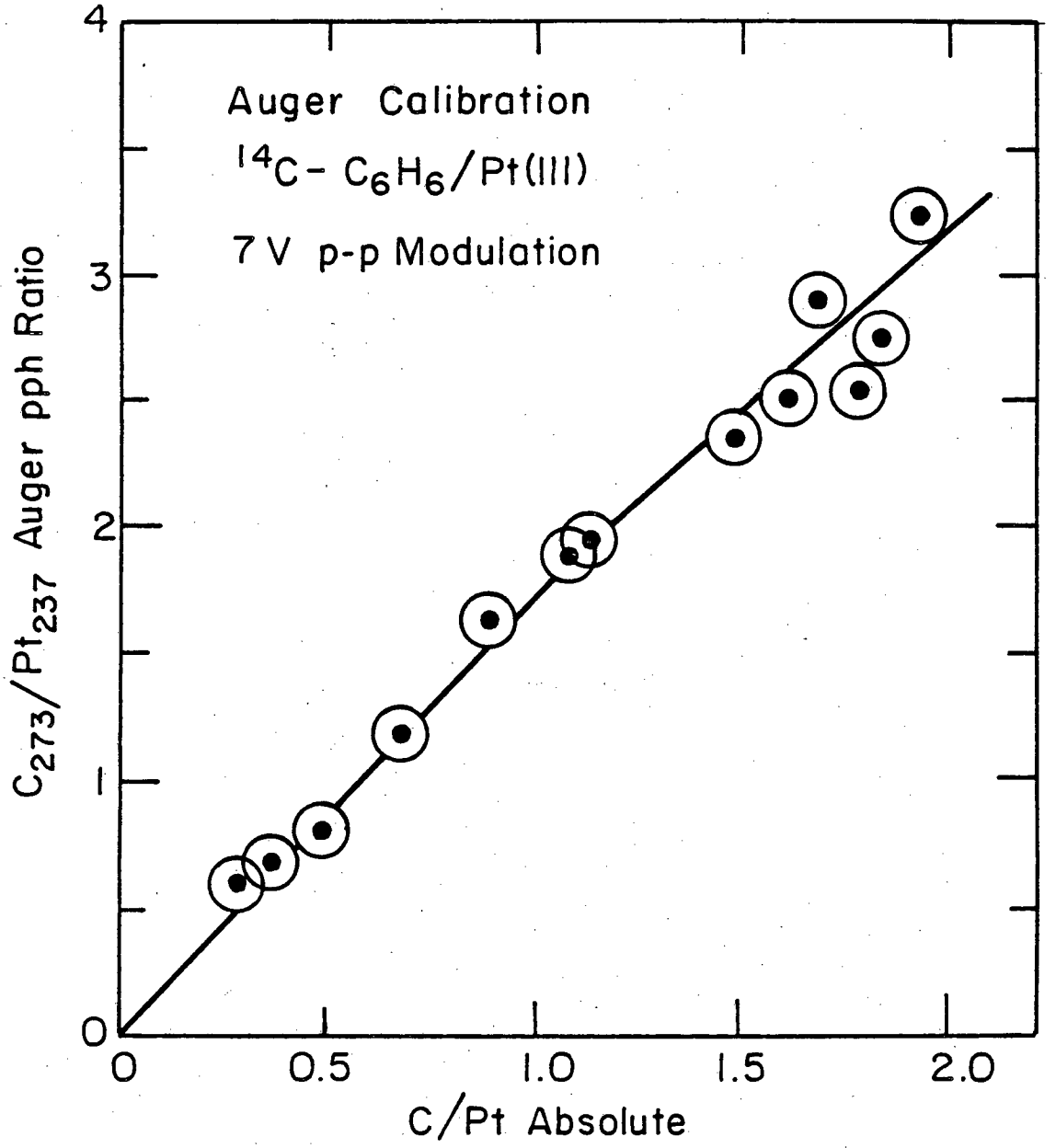
Auger Calibration
$^{14}C - C_6H_6/Pt(111)$
7 V p-p Modulation
C_{273}/Pt_{237} Auger pph Ratio
C/Pt Absolute
0
0.5
1.0
1.5
2.0
1
2
3
4

XBL 808-5689

2.7. Determination of Initial Reaction Rates, Reproducibility, and Blank Reaction Studies

The isolation cell and external recirculation system used for the high pressure reaction studies can be regarded as a well mixed micro-batch reactor (2). Reaction rates and product distributions were determined from the peak areas of gas chromatograms that were obtained at 5-15 min intervals. Initial reaction rates were deduced graphically from the initial slopes of the product accumulation curves determined as a function of time. For reaction temperatures below about 590 K, this procedure was accurate and straightforward as the first two or three (or more) sample points almost always fell on a straight line. Under these conditions the uncertainty of the initial rate determinations is estimated to be no more than ±10-15 percent. At higher reaction temperatures (>600 K) deactivation occurred more rapidly, and therefore it was more difficult to determine the initial rates. Under these conditions, the first one or two gas chromatograms were used for the initial rate determination. Since there was always a detectable amount of scatter in these gc-data, the uncertainty of these initial rate determinations was higher than that for reaction studies at lower temperatures. Because of the more rapid deactivation, it is expected that the initial rates which are reported at high temperatures may be slightly underestimated. However, based on the shapes of the product curves and the reasonable results that were obtained for the deactivation kinetics (Chapter 3), it is believed that the initial rates were underestimated by no more than 20-40 percent, even at the highest reaction temperatures (>650 K) studied.

While no attempt was made to reproduce every experiment described in this thesis, considerable effort was expended to insure that the experiments were reproducible, especially reaction rate studies over initially clean platinum surfaces. Table 2.5 summarizes reproducibilities that vary from best to worst case conditions for n-hexane and isobutane reactions catalyzed over the different platinum surfaces. The experimental reproducibility was usually in the range of ±10-20 percent, although in a couple of cases it was as poor as ±40-50 percent. Reaction selectivities were usually more reproducible than absolute reaction rates.

A series of blank reaction studies was carried out to determine if significant background catalytic activity originated from the sample mounting supports. For the blank reactions, the single crystal samples were heated to 750-800 K for 1-5 min in the presence of 5-30 Torr hydrocarbon. This pretreatment produced carbonaceous multilayers ($C_{273}/Pt_{237} \gtrsim 5$) on the single crystals that could be detected by AES. Subsequently, reaction rate studies were carried out in the usual manner in the presence of excess hydrogen. Figure 2.20 shows typical product accumulation curves for blank n-hexane reactions catalyzed over Pt(100) and Pt(10,8,7). Additional results for several blank reactions are summarized in Table 2.6. It can be seen that the background catalytic activity never represented more than 10 percent of the initial activity measured for clean platinum. Most often it was 2-3 percent. This activity is thought to originate mostly from the crystal edges and crystal supports. The background catalytic activity was usually more stable than that for the initially clean surfaces (Chapter 3).

Table 2.5. Initial reaction rates for hydrocarbon reactions catalyzed over platinum single crystal surfaces showing the reproducibility of the experiments (a).

Reaction	Catalyst	T(K)	Run No.	Initial Rate (molec/Pt atoms sec) Hydrogenolysis	Isomerization	Cyclization
Isobutane	Pt(10,8,7)	573 (b)	1	0.016	0.035	
			2	0.014	0.060	
n-Hexane	Pt(10,8,7)	573 (b)	1	0.0063	-	0.0063
			2	0.0067	-	0.0067
			3	0.0061	-	0.0050
n-Hexane	Pt(10,8,7)	623 (b)	1	0.021	-	0.019
			2	0.026	-	0.024
n-Hexane	Pt(10,8,7)	573 (c)	1	0.011	-	0.0035
			2	0.013		0.0041
n-Hexane	Pt(10,8,7)	673 (c)	1	0.088	-	0.056
			2	0.093	-	0.062
			3	0.098	-	0.081
n-Hexane	Pt(111)	602 (c)	1	0.032	0.046	0.046
			2	0.038	0.046	0.046
n-Hexane	Pt(111)	623±3 (c)	1	0.048	0.038	0.051
			2	0.060	0.030	0.053
n-Hexane	Pt(100)	556 (b)	1	0.0034	0.0018	
			2	0.0030	0.0020	
n-Hexane	Pt(100)	573 (b)	1	0.0055	0.0025	
			2	0.0060	0.0022	
n-Hexane	Pt(100)	592 (b)	1	0.0083		
			2	0.0090		

(a) Not all the columns used separated all products.

(b) $H_2/HC = 10$, $P_{tot} = 220$ Torr.

(c) $H_2/HC = 30$, $P_{tot} = 620$ Torr.

Table 2.6. Background catalytic activities measured in blank reactions and comparisons with clean platinum.

Reaction	Catalyst	T(K)	Blank Reaction Rates (molec/Pt atoms sec) Hydrogenolysis	Isomerization	Cyclization	R_B/R_{Pt}
n-Hexane	Pt(100)	573 (a)	2.5×10^{-4}	$\lesssim 1\times10^{-4}$	$\lesssim 1\times10^{-4}$	$\lesssim 0.05$
	Pt(111)	573 (a)	3.4×10^{-4}	$\lesssim 1\times10^{-4}$	$\lesssim 1\times10^{-4}$	$\lesssim 0.04$
	Pt(13,1,1)	573 (a)	$\sim 2\times10^{-4}$	$\lesssim 1\times10^{-4}$	$\lesssim 1\times10^{-4}$	$\lesssim 0.03$
	Pt(10,8,7)	573 (a)	5×10^{-4}	-	$<2\times10^{-4}$	$\lesssim 0.08$
	Pt(100)	673 (b)	2.5×10^{-3}	$<2\times10^{-4}$	1.2×10^{-3}	$\lesssim 0.04$-0.07
	Pt(10,8,7)	673 (b)	1.3×10^{-3}	-	$\sim 9\times10^{-4}$	$\lesssim 0.02$
	Pt(111)	623 (b)	2.2×10^{-4}	$<2\times10^{-4}$	-	$\lesssim 0.01$
Neopentane	Pt(10,8,7)	573 (a)	1.4×10^{-3}	1.7×10^{-3}	-	0.01-0.05
Isobutane	Pt(100)	573 (a)	$\sim 4\times10^{-4}$	-	-	$\lesssim 0.08$
	Pt(10,8,7)	573 (a)	$\sim 3\times10^{-4}$	$\sim 1.2\times10^{-3}$	-	0.02-0.03

(a) $H_2/HC = 10$, $p_{tot} = 220$ Torr.

(b) $H_2/HC = 30$, $p_{tot} = 620$ Torr.

(c) Ratio of blank and clean platinum reaction rates.

FIGURE CAPTION

Fig. 2.20. Product accumulation curves determined as a function of reaction time for blank reactions catalyzed at 573-673 K over the (100) and (10,8,7) platinum surfaces.

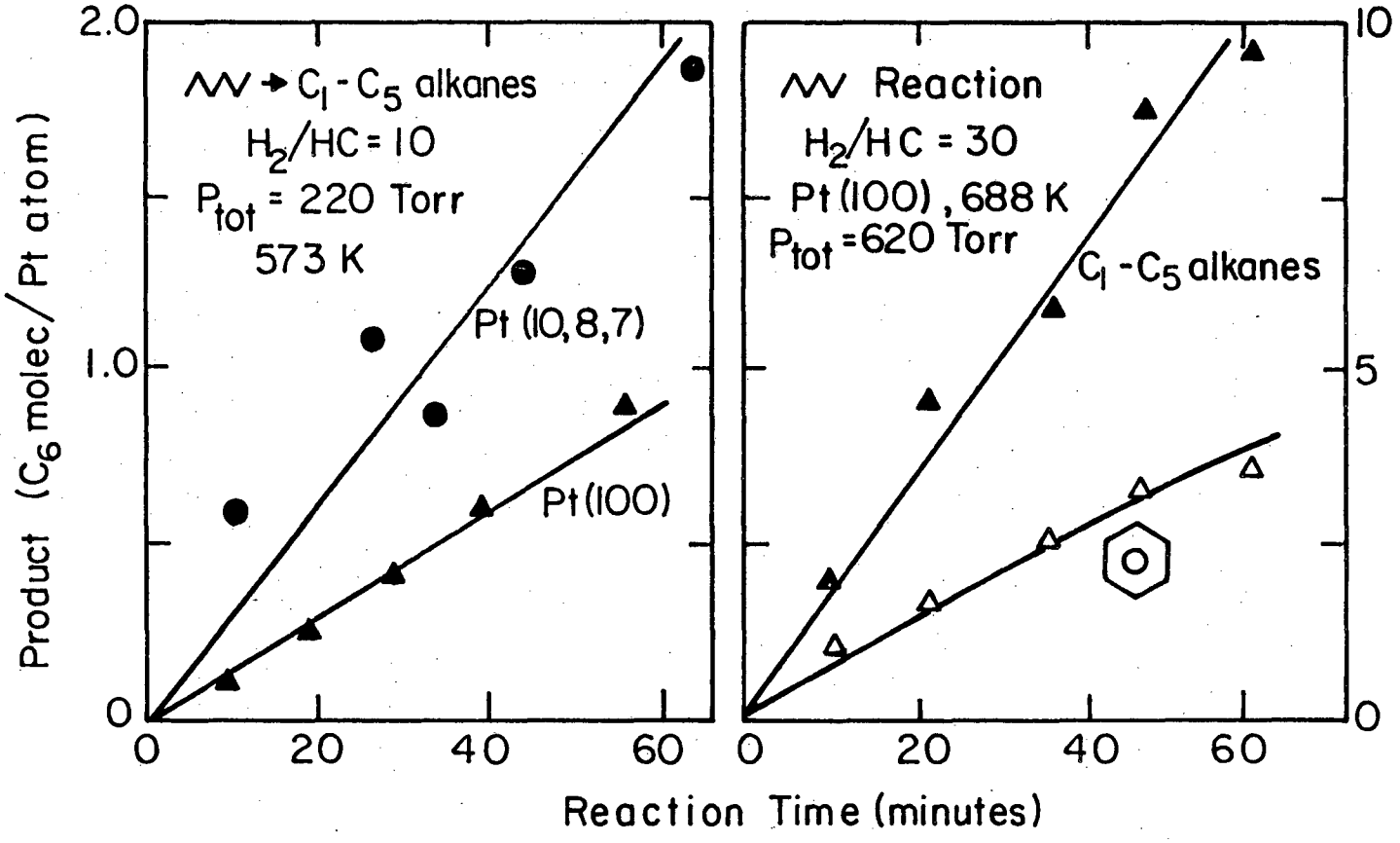

Fig. 2.20

XBL 817-6079

2.8. Reaction Studies in Deuterium: Isotope Effects and the Evaluation of Hydrocarbon-Deuterium Exchange Data

A series of reaction studies was carried out in the presence deuterium gas to determine if deuterium isotope effects could be detected for hydrocarbon conversion reactions (Section 3.5) and to investigate the kinetics of several hydrocarbon-deuterium exchange reactions (Section 3.4). For these studies, the external gas recirculation system was interfaced to a small dead volume which allowed 3-5 cm^3 samples of the reaction mixture to be withdrawn at 10-15 min intervals and introduced into the main vacuum chamber for mass spectral analysis. Each sample withdrawn represented less than 0.7 percent of the total reaction mixture. Deuterium exchange rates and product distributions for isobutane, n-hexane, and n-heptane were calculated from mass spectra that were recorded over the parent ion regions. Hydrocarbon conversion rates in the presence of deuterium were determined in the usual manner by gas chromatography. As flame ionization detector sensitivities for C_6H_6 and C_6D_6 were identical within 3 percent, no sensitivity corrections were made for reaction products with variable deuterium content. Using this system it was possible to measure hydrocarbon conversion rates, deuterium exchange rates, and deuterium exchange product distributions all simultaneously.

Isothermal retention times measured on a 0.19 percent picric acid on 80/100 carbopack column were used to estimate the average deuterium content of the hydrogenolysis, isomerization, and cyclization products that were produced in the hydrocarbon conversion reactions. In the presence of deuterium, the gas chromatograph signals were always

shifted 4–6 percent towards shorter retention times as compared to the retention times that were measured in hydrogen. These shifts (due mainly to rotational entropy effects (62)) indicate that the reaction products were always extensively deuterated, most probably perdeuterated (63). The exchange distributions within the reaction products were necessarily narrow because the gas chromatogram peaks for each reaction product were always sharp, never broadened detectably, and always shifted by the same length of time independent of the reaction temperature and deuterium pressure. Figure 2.21 compares gas chromatograms that were recorded during n-hexane reactions that were catalyzed in hydrogen and in deuterium over the (111) platinum surface.

The deuterium exchange reactions were always investigated at low total conversions (2–30 percent maximum in 3 hr). Mass spectra used for the exchange analysis were obtained using 70 eV ionization energy to minimize differences in sensitivity for parent ions with different deuterium content (64). Rates and product distributions determined at 573 K using 70 eV were reproduced well (±~15 percent) when one experiment was carried out using a much lower ionization energy of ≈20 eV. Most spectra were averaged over two consecutive scans with scan times of 20–30 sec for each spectrum. Parent peak heights were corrected for carbon-13 and statistical cracking to alkyl cations as described below. At the highest reaction temperatures studied (≥600 K) deuterated hexenes and heptenes made substantial contributions to the initial distributions of parent peak heights.

These contributions were eliminated using a series of calculations that are exemplified below.

Exchange rates in units of hydrocarbon molecules converted per surface platinum atom per second (molec $site^{-1}sec^{-1}$) were determined graphically from plots of the total product accumulation measured as a function of reaction time. Since the mass spectrometer sensitivities for deuterated compounds are lower than those for pure hydrocarbons (64), the absolute exchange rates determined in this manner are probably underestimated by 10-30 percent. The exchange rates were reproducible to ±15 percent and were corrected for background activity by running blank reactions over crystals that were covered with graphitic multilayer deposits (Section 2.7). The blank reactions revealed a very low level of background exchange activity corresponding to 2-8 percent of the initial activity measured for clean platinum.

Initial exchange product distributions were calculated from data that were always collected 12-40 min after the start of each reaction. The longer times were required at the higher reaction temperatures in order to obtain an accurate correction for olefin production. For each calculation, the relative concentrations of different isomers, d_i percent, were determined from corrected parent peak heights where d_i percent was the percentage of the total hexanes (or heptanes) with i deuterium atoms. The initial product distributions (α = mole percent)

were then computed where $\alpha_i = 10^2\, d_i / \sum_{j=1}^{n} d_j$, and n = 14 or 16 for n-hexane and n-heptane, respectively. From these initial distributions, the mean content of deuterium atoms per exchanged molecule $\bar{M} = (\sum_{j=1}^{n} j\alpha_j)/100$ was evaluated.

Two levels of calculations were carried out to correct parent peak heights, ϕ_i, measured directly from the mass spectra for (1) olefin production and (2) carbon-13 and statistical cracking to alkyl cations. While the latter corrections were always small, the olefin corrections became very important for reaction temperatures above about 550 K. Over the temperature range 550-650 K olefins accounted for 4-34 percent of the total uncorrected peak heights initially measured for deuterium containing products.

The total conversion to olefins, γ, was measured as a function of reaction time using the gas chromatograph. With n-hexane (n-heptane), it was assumed that the only olefins produced were $C_6H_2D_{10}$, C_6HD_{11}, and C_6D_{12} ($C_7H_2D_{12}$, C_7HD_{13}, and C_7D_{14}). This assumption was consistent with the retention time shifts in the gas chromatograms noted earlier and the isotopic dilution pattern that was displayed at 94-96 amu (110-112 amu). Hexane parent peaks heights at 94-96 amu were corrected for hexenes using

$$(\phi'_{94} + \phi'_{95} + \phi'_{96})/\phi_{86} = (\phi_{94} + \phi_{95} + \phi_{96})/\phi_{86} - n\gamma \qquad (19)$$

where the primes indicate corrected peak heights and n was the relative mass spectrometer sensitivity for detecting hexenes and n-hexane. A weighted average for this parameter, $n = 2.45$ was calculated for the

temperature range 550-650 K by using API sensitivities tabulated in Table 2.7 and assuming that hexenes were produced in the equilibrium ratios trans-2-hex/cis-2-hex/trans-3-hex/cis-3-hex/1-hex = 9.3/7.0/4.1/1.6/1.0 (3). The isotopic dilution patterns displayed at 98-100 amu were than employed to estimate the relative heights of the corrected peaks at 94-96 amu using

$$\frac{\phi_{94} - \phi'_{94}}{\phi_{96} - \phi'_{96}} \simeq \frac{10}{14} \frac{\phi_{98}}{\phi_{100}} \tag{20}$$

and

$$\frac{\phi_{95} - \phi'_{95}}{\phi_{96} - \phi'_{96}} \simeq \frac{10}{14} \frac{\phi_{99}}{\phi_{100}} \tag{21}$$

These corrections yielded reasonable (low) values for ϕ'_{94}, ϕ'_{95}, and ϕ'_{96} under all reaction conditions. At 593-623 K the values tended to become slightly negative as would be expected if small concentrations of olefins with lower deuterium content were produced. Under these conditions it was assumed that $\phi'_{94} = \phi'_{95} = \phi'_{96} = \phi_{min}$ where ϕ_{min} was the smallest peak height measured for a deuterium containing hexane (usually $C_6H_{10}D_4$). Application of this assumption never introduced more than a 2-8 percent error in the initial exchange rate determination.

Table 2.7. Relative mass spectrometer sensitivities for hydrocarbon molecular ions calculated from API Tables (a).

C_6-Hydrocarbon	Parent Ion Sensitivity	C_7-Hydrocarbon	Parent Ion Sensitivity
n-Hexane	1.0	n-Heptane	1.0
1-Hexene	1.62	1-Heptene	1.29
cis-2-Hexene	2.25	cis-2-Heptene	1.83
trans-2-Hexene	2.68	trans-2-Heptene	1.89
cis-3-Hexene	2.30	cis-3-Heptene	1.69
trans-3-Hexene	2.64		

(a) 70 eV ionization energy.

A series of linear equations was derived for each reactant hydrocarbon in order to correct the alkane peak heights for carbon-13 and statistical cracking to alkyl cations ($i\text{-}C_4H_9^+/i\text{-}C_4H_{10} = 0.89 = \alpha_4$; $n\text{-}C_6H_{13}^+/n\text{-}C_6H_{14} = 0.055 = \alpha_6$; $n\text{-}C_7H_{15}^+/n\text{-}C_7H_{16} = 0.026 = \alpha_7$). For n-hexane, the corrected parent peak heights, θ_i (for $n\text{-}C_6H_{14-i}D_i$), were given by

$$\theta_{14} = \phi_{14} - \phi_{13}\beta$$

$$\theta_{13} = \phi_{13} - \phi_{12}\beta$$

$$\theta_{12} = \phi_{12} - \phi_{11}\beta - \theta_{14}\alpha_6 - \frac{1}{14}\theta_{13}\alpha_6$$

$$\theta_{11} = \phi_{11} - \phi_{10}\beta - \frac{13}{14}\theta_{13}\alpha_6 - \frac{2}{14}\theta_{12}\alpha_6 \qquad (22)$$

$$\theta_j = \phi_j - \phi_{j-1}\beta - \frac{(j+2)}{14}\theta_{j+2}\alpha_6 - \frac{(13-j)}{14}\theta_{j+1}\alpha_6 \quad (j=3\text{-}12)$$

$$\vdots$$

$$\theta_2 = \phi_2 - (\phi_1 - \phi_0\beta)\beta - \frac{4}{14}\theta_4\alpha_6 - \frac{11}{14}\theta_3\alpha_6 - \phi_0\beta'$$

$$\theta_1 = \phi_1 - \phi_0\beta - \frac{3}{14}\theta_3\alpha_6 - \frac{12}{14}\theta_2\alpha_6$$

where $\beta = 0.0645$ was the experimentally determined correction factor for ^{13}C, $\alpha_6 = 0.055$ was the $n\text{-}C_6H_{13}^+/n\text{-}C_6H_{14}$ peak height ratio, and $\beta' = 0.00162$ was the correction factor for two ^{13}C atoms in unreacted n-hexane. A similar series of equations can be easily derived for n-heptane ($\beta = 0.0762$, $\alpha_7 = 0.026$, $\beta' = 0.0022$) and isobutane ($\beta = 0.042$, $\alpha_4 = 0.89$, $\beta' = 0.001$).

To illustrate the use of these correction procedures Table 2.8 summarizes a series of example calculations for n-hexane-D_2 exchange catalyzed at 553 K on the (111) platinum surface. The first row lists uncorrected mass spectrometer peak heights, ϕ_i, that were measured at 86-100 amu following 29 min reaction time. In the second row the 94, 95, and 96 amu peaks have been corrected for the production of deuterated hexenes using $\gamma = 1.22 \times 10^{-3}$. The third row summarizes θ_i values that were corrected for carbon-13 and statistical cracking to alkyl cations using Eq. (22). The fourth row lists d_i values, and the fifth row summarizes the initial exchange product distribution (mole percent).

Table 2.8. Example calculation of an n-hexane-deuterium exchange product distribution (D_2/HC = 10, P_{tot} = 220 Torr, 553 K, Pt(111).

Mass Number (amu)	86	87	88	89	90	91	92	93	94	95	96	97	98	99	100
ϕ (arb units)	251	17.5	0.71	0.17	0.14	0.15	0.15	0.15	0.17	0.34	0.77	0.21	0.39	0.99	2.60
ϕ'(arb units)	251	17.5	0.71	0.17	0.14	0.15	0.15	0.15	0.11	0.19	0.22	0.21	0.39	0.99	2.69
θ (arb units)	251	1.4	0.21	0.12	0.13	0.14	0.14	0.14	0.10	0.17	0.20	0.15	0.23	0.97	2.54
d (mole percent)	97.4	0.54	0.081	0.047	0.050	0.054	0.054	0.054	0.039	0.066	0.078	0.058	0.089	0.38	0.99
α (mole percent)	-	21	3.1	1.8	2.0	2.1	2.1	2.1	1.5	2.6	3.0	2.2	3.5	15	38

$$\bar{M} = 100^{-1} \sum_{j=87}^{100} (j - 86)\, \alpha_j = 9.4.$$

FIGURE CAPTION

Fig. 2.21. Gas chromatograms showing the shorter retention times that were detected for reaction products that were produced in the presence of deuterium gas.

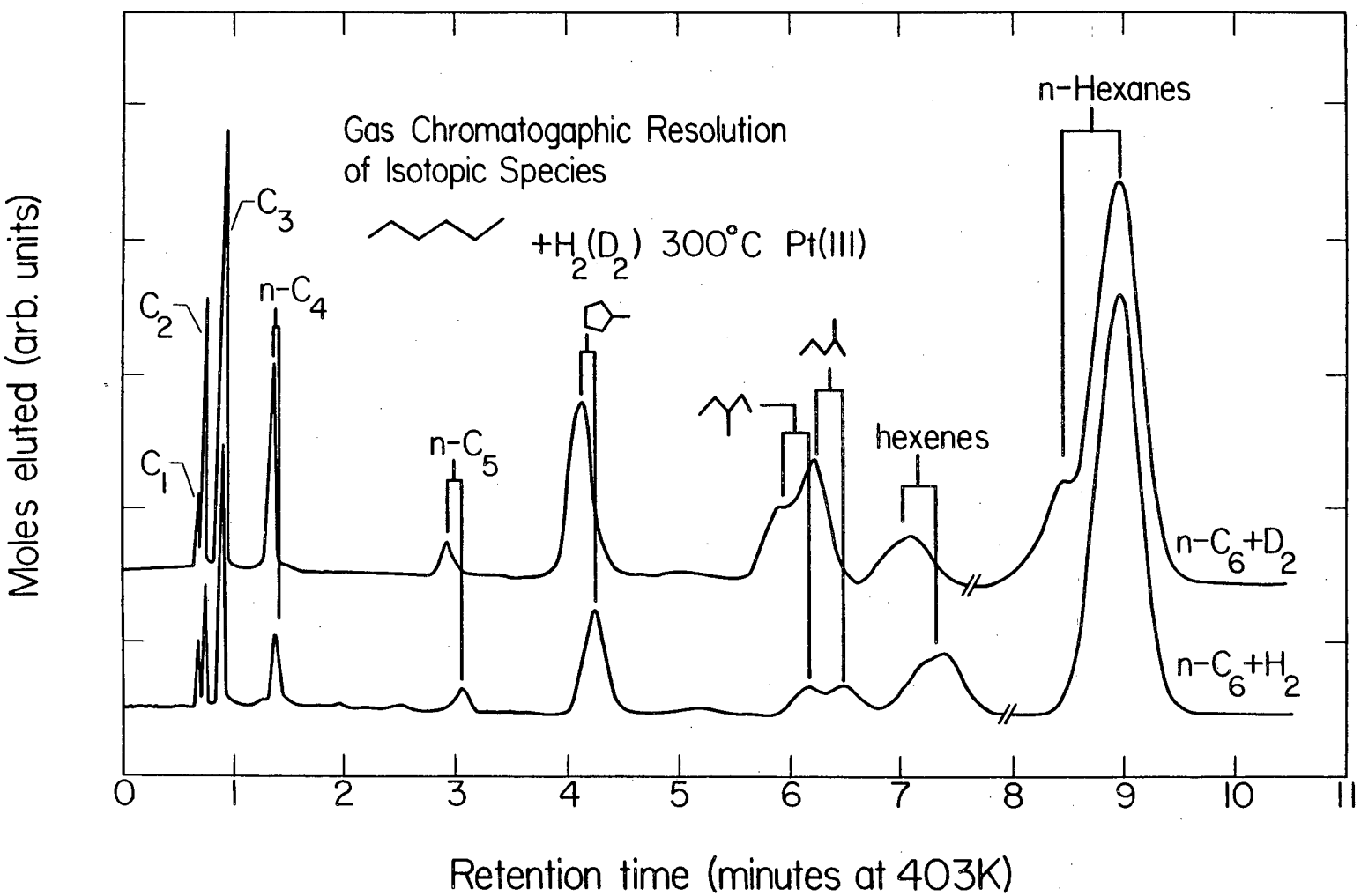

Fig. 2.21

XBL 818-1107

2.9. Low Pressure-High Pressure Apparatus as a Reactant Pulse Microcatalytic Reactor

An effort was made to modify the low pressure-high pressure apparatus to function as a reactant-pulse microcatalytic reactor. In principle that reactant pulse technique would be a very valuable method for investigating the reactivities of carbonaceous species chemisorbed on metal surfaces (65). In practice the usefulness of this technique was severely limited by the fact that the crystal surface area was very small as compared with the surface area of the reactor walls. As a consequence it was not possible to distinguish product molecules originating at the single crystal from those which desorbed from the reactor walls. While no meaningful results could be obtained by this method, it is appropriate to summarize the essential features of this experiment with the intention that future work may be able to eliminate the problems associated with desorption from the reactor walls.

A schematic diagram for the reactant pulse experiment is shown in Fig. 2.22. A metering valve introduces a slow continuous flow of inert carrier gas through the reaction cell and directly into the flame ionization detector of the gas chromatograph. A switching valve that is located before the reaction cell and connected to the external gas manifold can be used to introduce more-or-less rectangular pulses of hydrogen and/or hydrocarbon into the carrier gas stream. These pulses are directed past the crystal surface and into the gas chromatograph. The basic sensitivity of the FID is sufficient to detect about 4 percent of a monolayer of CH_4 (i.e., ~6×10^{13}) molec) desorbing from a platinum surface with an area of 1 cm^2.

Kinetic analysis of pulse reactor data is feasible (in the absence of well effects) only if the crystal diameter is much shorter than the pulse width so that gas phase concentrations depend only on time and remain essentially constant over the length of the crystal. The rate of reaction for a single component pulse is expressed by

$$R = kC_r^m(t) = kC_{r_o}^m \gamma^m(t) \tag{23}$$

where k is a rate constant, $C_r(t)$ is the reactant concentration, $\gamma(t)$ is the pulse shape (Gaussian, triangular, reactangular, etc.), and m is the reaction order. Similarly, for a binary pulse mixture the rate expression becomes

$$R = kC_a^m(t)C_b^n(t) = k \frac{\lambda^m}{(1 + \lambda)^{m+n}} C(t)^{m+n} \tag{24}$$

where $C(t) = (C_{ao} + C_{bo})\ \gamma(t)$ and $\lambda = C_{ao}/C_{bo}$. Rates are independent of pulse shape only for first order reactions. Selectivity is therefore a more meaningful observable of pulse reaction studies. The fractional selectivity for a particular reaction, S_j, is easily derived from a sum over fractional conversions to various products, X_i; that is $S_j = X_j / \sum_i X_i$. For a single component pulse under conditions of differential conversion X_i is given by

$$X_i = k_i C_{ro}^{m-1} \int_0^\infty \gamma^m(t)\ dt \Big/ \int_0^\infty \gamma(t)\ dt \tag{25}$$

FIGURE CAPTION

Fig. 2.22. Schematic diagram for the reactant pulse microcatalytic reactor.

Scheme for Pulse Reaction Studies

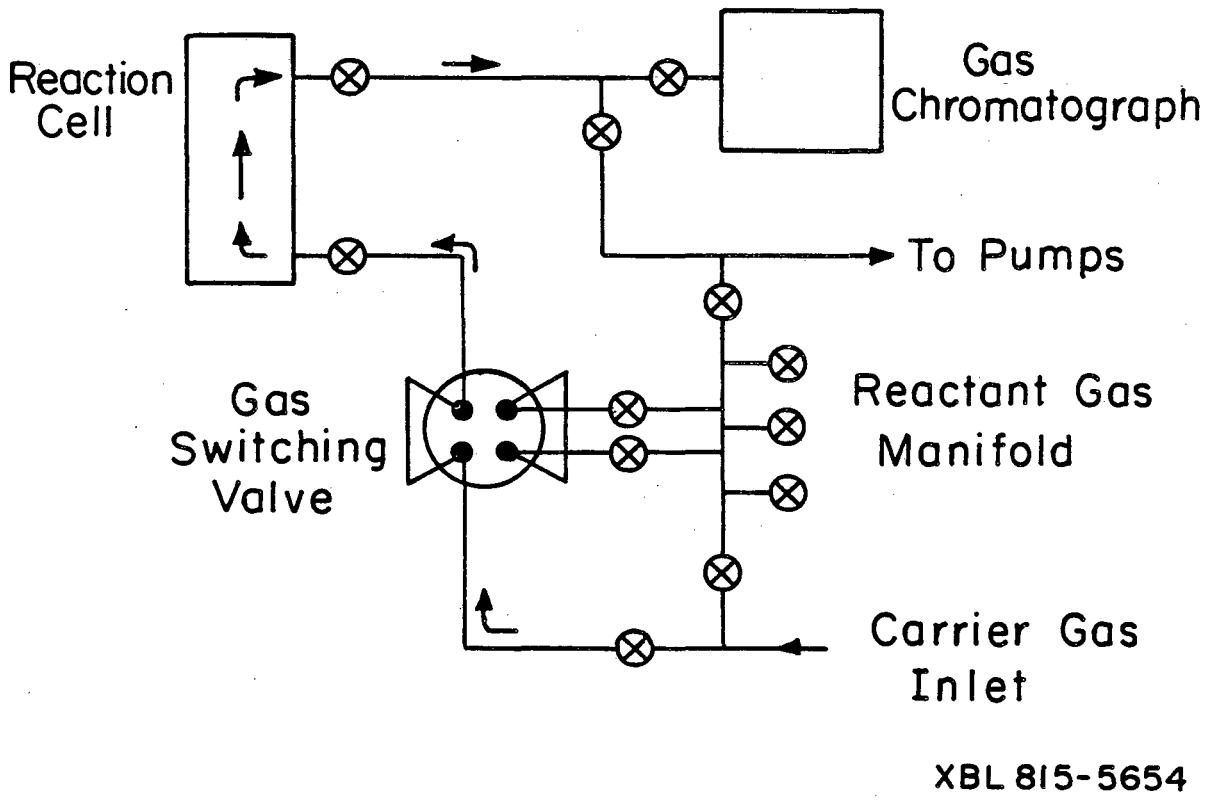

Fig. 2.22

REFERENCES

1. D. W. Blakely, E. Kozak, B. A. Sexton, and G. A. Somorjai, J. Vac. Sci. Technol. 13, 1091 (1976).

2. W. D. Gillespie, Ph. D. Thesis, University of California, Berkeley, 1980.

3. D. R. Stull, E. F. Westrum, and G. C. Sinke, The Chemical Thermodynamics of Organic Compounds, Wiley, New York, 1969.

4. W. A. Dietz, J. Gas Chromatography 68 (1967).

5. S. Y. Tong, Progress Surface Sci. 7, 1 (1975).

6. G. A. Somorjai and M. A. Van Hove, Adsorbed Monolayers on Solid Surfaces, in Structure and Bonding, Vol. 36, Springer Verlag, Heidelberg, 1980.

7. G. A. Somorjai and F. J. Szalkowski, Adv. High Temp. Chem. 4, 137 (1971).

8. G. A. Somorjai, Proc. Exxon Conf. Surface Sci., Linden N. J., 1980, and references therein.

9. L. D. Schmidt, Catal. Rev. 9, 115 (1974).

10. C. M. Chan, R. Aris, and W. H. Weinberg, Appl. Surface Sci. 1, 360 (1978), C. M. Chan and W. H. Weinberg, Appl. Surface Sci. 1, 377 (1978).

11. J. Pendry, Low Energy Electron Diffraction, Academic Press, NY, 1974.

12. G. Comsa, Surface Sci. 81, 57 (1979); R. L. Park, J. E. Houston, and D. G. Schreiner, Rev. Sci. Instr. 42, 60 (1971).

13. M. A. Van Hove and S. Y. Tong, Surface Crystallography by LEED, Springer Verlag, Heidelberg, 1979.

14. Physical Electronics Auger Handbook.

15. G. Ertl and K. Kuppers, Low Energy Electrons and Surface Chemistry, Verlag Chemie, Weinheim, 1974.

16. W. Bambynek, Rev. Mod. Phys. 44, 716 (1972); M. A. Listengarten, Bull. Acad. Sci. USSR Phys. Sci. USA 26, 182 (1962).

17. M. Gryzinski, Phys. Rev. 138, A336 (1966).

18. J. P. Biberian and G. A. Somorjai, Appl. Surf. Sci. 2, 352 (1979).

19. J. W. A. Sachtler and G. A. Somorjai, Surf. Sci. in press.

20. P. A. Redhead, Vacuum 12, 203 (1962).

21. I. Ibach, W. Erley, and H. Wagner, Surf. Sci. 92, 29 (1980).

22. D. Edwards, Jr., Surf. Sci. 54, 1 (1976).

23. M. Salmeron, R. J. Gale, and G. A. Somorjai, J. Chem. Phys. 70, 2807 (1979) and references therein.

24. R. C. Baetzold and G. A. Somorjai, J. Catl. 45, 94 (1976).

25. S. W. Benson, The Foundations of Chemical Kinetics, McGraw-Hill, New York, 1960.

26. See for example H. S. Johnston, Gas Phase Reaction Rate Theory, Ronald Press, New York, 1966).

27. M. C. Tsai and E. L. Meutterties, to be published.

28. S. Lehwald, H. Ibach, and J. E. Demuth, Surf. Sci. 78, 577 (1978).

29. Surface Barrier Detector Operating Manual and Technical Bulletin, E. G. and G. Ortec Corp., and references therein.

30. K. Klier, A. C. Zettlemoyer, and H. Leidheiser, J. Chem. Phys. 52, 589 (1970), and references therein.

31. A. D. Crowell and L. D. Matthews, Surf. Sci. 7, 79 (1967).

32. M. A. Van Hove and G. A. Somorjai, Surf. Sci. 92, 489 (1980).

33. M. A. Van Hove, R. J. Koestner, P. C. Stair, J. P. Biberian, L. L. Kesomedel, I. Bartos, and G. A. Somorjai, Surf. Sci. 103, 189 (1981); Surf. Sci. 103, 218 (1981).

34. D. W. Blakely, Ph. D. Thesis, University of California, Berkeley, 1976.

35. C. R. Helms, H. P. Bonzel, and S. Kelemen, J. Chem. Phys. 65, 1773 (1976).

36. P. N. Ross, Jr., private communication.

37. S. M. Davis and G. A. Somorjai, Hydrocarbon Conversion Over Metal Catalysts, in The Chemical Physics of Solid Surfaces and Heterogeneous Catalysis, Vol. 4,, Elsevier, Amsterdam, 1981.

38. J. Perdereau and G. E. Rhead, Surf. Sci. 24, 555 (1971).

39. K. A. Prior, K. Schwaha, and R. M. Lambert, Surf. Sci. 77, 193 (1978).

40. C. M. Friend, Ph. D. Thesis, University of California, Berkeley, 1981.

41. D. G. Castner, Ph. D. Thesis, University of California, Berkeley, 1979.

42. B. Krahl-Urban, E. A. Niekisch, and H. Wagner, Surf. Sci. 64, 52 (1977).

43. M. Housley, R. Ducros, G. Piquard and A. Cassuto, Surf. Sci. 58, 277 (1977).

44. B. E. Nieuwenhuys, D. I. Hagen, G. Rovida, and G. A. Somorjai, Surf. Sci. 59, 155 (1976).

45. D. W. Blakely and G. A. Somorjai, Surf. Sci. 65, 419 (1977).

46. M. Henzler, Appl. Phys. 9, 11 (1976).

47. J. E. Houston and R. L. Park,, Surf. Sci. 26, 269 (1971).

48. K. Besocke, B. Krahl-Urban, and H. Wagner, Surf. Sci. 68, 39 (1977).

49. L. L. Kesmodel and L. M. Falicov, Solid State Comm. 16, 1201 (1975).

50. I. Yu, A. A. V. Gibson, E. R. Hunt, and W. P. Halperin, Phys. Rev. Lett. 44, 348 (1980).

51. M. C. Desjonqueres and F. Cyrot-Lackmann, Solid State Comm. 18, 1127 (1976).

52. F. J. Arlinghaus, J. G. Gay, and J. R. Smith, Phys. Rev. B. 23, 5152 (1981).

53. P. O. Gartland and B. J. Slagsvold, Phys. Rev. B 12, 4047 (1975).

54. R. S. Williams, P. S. Wehner, S. D. Kevan, R. F. Davis, and D. A. Shirley, Phys. Rev. Lett. 41, 323 (1978).

55. J. F. van der Veen, F. J. Himpsel and D. E. Eastman, Solid State Comm. 34, 33 (1980).

56. F. J. Himpsel and D. E. Eastman, Phys. Rev. Lett. 41, 507 (1978).

57. F. J. Himpsel and D. E. Eastman, Phys. Rev., in press.

CHAPTER 3. STRUCTURE AND TEMPERATURE DEPENDENCE OF HYDROCARBON REACTIONS CATALYZED OVER INITIALLY CLEAN PLATINUM CRYSTAL SURFACES

3.1. Structure and Temperature Dependence of n-Hexane Skeletal Rearrangement Reactions Catalyzed on Platinum

3.1.1. Background

The catalyzed hydrogenolysis and skeletal rearrangement reactions of n-hexane have been investigated over many types of platinum catalysts including powders (1,2), evaporated films (3), silica (4) and alumina (5-7) supported catalysts, supported alloys such as Pt-Cu (8), Pt-Pd (9), Pt-Re (10), Pt-Sn (11), and Pt-Au (12-14), and also over other Group VIII metal catalysts such as Ni and Ni-Cu powders (15), Ir and Ir-Au films (16), and supported Pd, Pd-Au, Rh, and Rh-Cu catalysts (14,17). The great interest in n-hexane has mainly arisen from the fact that this is the simplest hydrocarbon molecule which is large enough to undergo a full spectrum of hydrocarbon conversion reactions including hydrogenolysis, isomerization, dehydrogenation, C_5-cyclization, and, most importantly, aromatization. As a result of this research a fairly detailed but sometimes conflicting picture has emerged with respect to the structure sensitivities and mechanisms of n-hexane conversion reactions. Dautzenberg and Platteeuw (6,7), and Ponec and co-workers (4) found no significant structure sensitivity for n-hexane reactions catalyzed at 1-10 atmospheres and 530-760 K over silica and alumina supported platinum. This conclusion resulted from studies of the isomerization and cyclization rates as a function of the average platinum particle size which was varied between about 15 and 80Å. Santacessaria (5) and Anderson (3), by contrast, reported

significant variations in catalytic activity for ultra thin films and Pt/SiO_2 catalysts for which the average metal particle size was varied between 10 and about 100Å (or more). in these studies very small 10Å platinum particles appeared to be at least four times more active than larger particles for n-hexane isomerization (3) and/or hydrogenolysis and c_5-cyclization (3,4). These differences were discussed in terms of different reaction mechanisms which prevail on the very small and larger platinum particles, namely, the cyclic (18-20) and bond shift (20-22) mechanisms, respectively.

Creative studies of the reaction mechanism by Gault, Maire, and co-workers (18,19,23-26) using ^{13}C-labelled molecules have permitted a distinction between these mechanisms and a detailed evaluation of their relative importance. In the c_5-cyclic mechanism, isomerization results from the ring opening of 5-membered cyclic intermediates, i.e.,

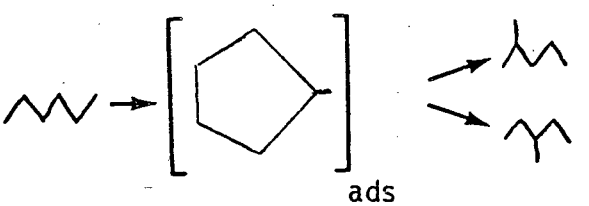

(1)

Very highly dispersed platinum catalysts always displayed a remarkable specificity for this reaction pathway which most often accounted for 85-95 percent of the total skeletal rearrangement (23,26). On the other hand, hexane isomerization over platinum catalysts with low and

medium dispersion appeared to occur mainly by the bond shift mechanism. The exact nature of this process is still unclear, but the bond shift pathway is undoubtedly intramolecular (21,23,16), and α,γ-adsorbed species of the type

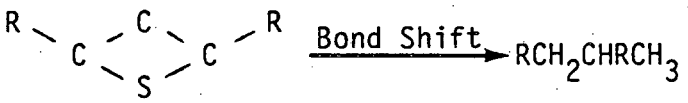

(2)

have been widely accepted as reaction intermediates (20,21,26,27). In this representation S is a surface site composed of one or more platinum atoms.

Unfortunately, the complex structure and undefined composition of very small platinum particles introduces a high level of uncertainty into the interpretation of structure sensitivity studies using these types of catalyst systems. In order to obtain more definitive information about the structure sensitivities of alkane skeletal rearrangement reactions, model catalytic studies have been carried out in this laboratory using platinum single crystal catalysts with well defined surface structure and composition (28-30). These studies have revealed the special importance of surface structure and chemical additives in controlling the rates and selectivities of many important types of catalyzed hydrocarbon reactions. Recent studies by Gillespie (28), for example, of n-heptane aromatization and hydrogenolysis catalyzed near atmospheric pressure showed that the rates and selectivities of these reactions are influenced markedly by the presence of surface irregularities (steps and kinks) on the platinum single

crystals. Aromatization activities and selectivities were maximized on stepped and kinked platinum surfaces with (111) terraces that were wide enough (4-5 atoms) to accommodate chemisorbed reactants and products. Hydrogenolysis displayed a much different dependence upon surface structure in which the flat (111) and very highly stepped-kinked (25,10,7) surfaces were most active for this undesireable C-C bond breaking reaction. Hydrogenolysis activity increased markedly over all the platinum surfaces in the presence of strongly bound subsurface oxygen. Studies of hydrogenolysis reactions over practical catalysts have lead to the general conclusion (27,31-33) that edge and kink defect sites are probably required for high hydrogenolysis activity. While surfaces with (100) terraces were not investigated in Gillespie's research (28), the results clearly indicated that surface irregularities were <u>not</u> required for high C-C bond breaking activity. In view of the marked oxygen effect, it was suggested (33) that metal-oxide support interactions might be responsible for the hydrogenolysis structure sensitivity that is often displayed by supported platinum catalysts (3,34,35).

In order to investigate the generality of these conclusions, the present research has extended the structure sensitivity studies to include reactions of n-hexane, n-butane, isobutane, and neopentane on platinum single crystal surfaces. Because an extensive data base already exists for comparison with practical catalysts (1-17), and because the reaction chemistry is very important from the viewpoint of petroleum reforming, n-hexane conversion was chosen as the primary

hydrocarbon reaction system investigated throughout this research. This section describes the structure and temperature dependence of n-hexane skeletal rearrangement reactions catalyzed on the initially clean flat (100) and (111), stepped (13,1,1) and kinked (10,8,7) platinum single crystal surfaces. The kinetics and selectivities of n-hexane deuterium exchange reactions that do not involve skeletal rearrangement are considered separately in Section 3.4. The effect of surface additives such as sulfur, calcium oxide, and carbonaceous deposits on the n-hexane reaction kinetics are discussed in Chapters 4 and 5.

The n-hexane reaction studies have revealed that aromatization is highly structure sensitive as previously reported by Gillespie (28). However, the rates of all other competing reactions displayed little dependence on surface structure. Temperature and hydrogen pressure played a more decisive role in controlling the rates and selectivities of skeletal rearrangement.

3.1.2. Results

Reaction studies were carried out over the flat (100) and (111), stepped (13,1,1), and kinked (10,8,7) platinum surfaces at temperatures between 520 and 750 K and at total pressures between 100 and 620 Torr (H_2/HC = 4-30). The rates of formation of benzene (Bz), methylcyclopentane (MCP), 2- and 3-methylpentanes (2MP, 3MP), and C_1-C_5 alkanes ($\Sigma < C_6$), have been monitored under virtually all conditions.

Structure Sensitivity of Catalyzed n-Hexane Reactions. Product accumulation curves determined as a function of reaction time at 573 K

(H_2/HC = 10) for n-hexane reactions catalyzed on the (100) platinum surface are shown in Fig. 3.1. Product accumulation curves determined at 573 K (H_2/HC = 10) for aromatization catalyzed over all four platinum surfaces are compared in Fig. 3.2. Figures 3.3 and 3.4 show typical product accumulation curves at several temperatures for aromatization, hydrogenolysis, and C_5-cyclization catalyzed on the (13,1,1) and (111) platinum surfaces (H_2/HC = 10-30). The rate of reaction at any time is given by the slope of the product accumulation curve at that time. Table 3.1 summarizes initial reaction rates and selectivities at 573 K for the different reaction pathways together with surface carbon coverages that were determined by AES following 110-170 min reaction time. The order of activities at 573 K for the parallel reactions followed the sequences:

Aromatization: $(10,8,7) \approx (111) > (13,1,1) \approx (100)$

Hydrogenolysis: $(111) \approx (13,1,1) \approx (10,8,7) \approx (100)$

C_5-cyclization: $(10,8,7) \approx (100) \approx (13,1,1) \approx (111)$

Isomerization: $(111) \gtrsim (10,8,7) \approx (100) \approx (13,1,1)$

Only the aromatization reaction displayed significant structure sensitivity that was characterized by a factor of 4 difference in initial rates between the most active (10,8,7) and least active (100) platinum surfaces. All other reactions displayed initial rates that differed by less than a factor of two on all four platinum surfaces.

Temperature Dependence of the Initial Reaction Rates. Arrhenius plots for n-hexane hydrogenolysis, isomerization, C_5-cyclization, and aromatization catalyzed over the four platinum surfaces at a total

Table 3.1. Initial reaction rates, selectivities, and surface carbon coverages determined for n-hexane reactions catalyzed at 573 K over platinum single crystal surfaces (a).

Catalyst	Reaction Rates (molec/Pt atom sec) x 10^3 (b)					Selectivities (mole percent) (c)		Surface (d) Carbon
	$\Sigma < C_6$	2MP	3MP	MCP	Bz	$S_{isom.}$	$S_{cyc.}$	
Pt(100)	5.7	2.4	3.4	9.8	1.4	0.26	0.49	2.3
Pt(111)	8.7	2.2	6.3	7.8	5.0	0.29	0.43	2.2
Pt(13,1,1)	6.8	1.7	2.6	9.5	1.6	0.20	0.50	2.5
Pt(10,8,7)	6.4	2.3	3.7	11.6	6.0	0.20	0.58	2.0
Activation Energies (kcal/mole) (e)								
P_{H_2} = 200 Torr	19-25	--16-22---		12-20	22-29			
P_{H_2} = 600 Torr	21-26	---~25----		18-26	25-33			

(a) $H_2/HC = 10$, $P_{tot} = 220$ Torr.
(b) (±20 percent).
(c) Fractional selectivities; iso = 2MP + 3MP; cyc = MCP + Bz.
(d) Carbon atoms per surface platinum atom at 100-150 min.
(e) Energies represents the spread in values for different surfaces.

pressure of 220 Torr are shown in Figs. 3.5-3.8. It is clear that the order of initial catalytic activities presented above displayed little dependence on reaction temperature. The (10,8,7) and (111) platinum surfaces were always more active in aromatization as compared to the (13,1,1) and (100) surfaces. All other reactions displayed little structure sensitivity at all reaction temperatures.

Hydrogenolysis and aromatization were the only reactions that displayed "normal" Arrhenius behavior over a wide range of temperature. Even for these reactions the apparent activation energies appeared to decrease with increasing reaction temperature. The isomerization and C_5-cyclization reactions displayed rate maxima at temperatures that varied from about 570 K for 2MP formation to 600-620 K for 3MP and MCP production. Figure 3.9 shows Arrhenius curves plotted together for all the parallel reactions catalyzed on the (13,1,1) platinum surface at a total pressure of 220 Torr. Similar data obtained with the (111) and (10,8,7) platinum surfaces at a total pressure of 620 Torr are shown in Figs. 3.10 and 3.11. Over these surfaces the rate maxima appeared to shift to higher temperatures with increasing hydrogen pressure.

The unusual temperature dependencies observed for the n-hexane reactions (coupled with rapid deactivation at high temperatures) prevented a reliable determination of activation energies for temperatures higher than about 600 K. Table 3.1 includes apparent activation energies at two total pressures that were estimated from the Arrhenius plots for reaction temperatures of 560-590 K. Based on the limited

data at these lower temperatures, these activation energies are believed to be accurate to no more than ±5 kcal/mole. Nevertheless, a tendency existed for the apparent activation energies to increase with increasing hydrogen pressure. All the activation energies decreased continuously and approached zero at the highest temperatures studied ($\gtrsim$650 K).

Dependence of the Initial Reaction Rates on Hydrogen Pressure. The dependence of the initial reaction rates on hydrogen pressure was investigated only for the (10,8,7) platinum surface. Figure 3.12 shows order plots at several temperatures for n-hexane hydrogenolysis and aromatization catalyzed over Pt(10,8,7). The order of the hydrogenolysis reaction with respect to hydrogen pressure increased from about 0.4 at 573 K to 0.9 at 640 K. Isomerization and C_5-cyclization displayed similar behavior (at 573 K). The order of the aromatization reaction with respect to hydrogen pressure was slightly negative at low temperatures (<590 K) but became positive at higher temperatures (>590 K).

Selectivities and Product Distributions. Because parallel reactions always displayed different catalytic behavior as a function of temperature and hydrogen pressure, the selectivities for n-hexane conversion over the single crystal catalysts varied markedly with reaction conditions. Fractional selectivities for n-hexane hydrogenolysis, dehydrocyclization (MCP + Bz), and isomerization (2MP + 3MP) catalyzed on Pt(111) at a total pressure of 620 Torr are shown as a function of reaction temperature in the upper half of Fig. 3.13.

Kinetic selectivities for the production of 2MP over 3MP and Bz over MCP are shown as a function of temperature in the lower half of Fig. 3.13. Figure 3.14 illustrates the same kinetic selectivity functions for n-hexane reactions catalyzed over all four platinum surfaces at a total pressure of 220 Torr. The 2MP/3MP ratios always decreased and the Bz/MCP ratios always increased with increasing reaction temperature. The temperature ranges where these kinetic selectivities changed most rapidly shifted towards higher temperatures with increasing hydrogen pressure.

Initial product distributions for n-hexane reactions catalyzed at 573 K (H_2/HC = 10) and 673 K (H_2/HC = 30) are compared in Figs. 3.15 and 3.16. The changes in product distributions with surface structure and reaction conditions are consistent with the observations detailed above. As compared to the flat (100) and (111) platinum surfaces, the initial selectivity for methylcyclopentane formation maintained a notably higher value to higher temperatures on the kinked Pt(10,8,7) surface.

Hydrogenolysis Selectivities. Whereas the catalytic activity for n-hexane hydrogenolysis displayed little dependence on platinum surface structure, the selectivity within hydrogenolysis varied markedly with surface structure and, to a lesser extent, with hydrogen pressure. Product distributions for n-hexane hydrogenolysis catalyzed over the four platinum surfaces are summarized for a variety of reaction conditions in Table 3.2. The (100) and (13,1,1) platinum surfaces displayed a clear preference for scission of internal C-C bonds leading

Table 3.2. Initial product distributions for n-hexane hydrogenolysis catalyzed over platinum single crystal surfaces (a).

Catalyst	T(K)	P_{H_2} (Torr)	Initial Hydrogenolysis Distributions (moles)				
			C_1	C_2	C_3	C_4	C_5
Pt(100)	556	220	13	20	42	18	7
	573	200	16	19	39	19	7
	592	200	18	20	38	16	8
Pt(111)	573	200	31	11	32	8	18
	593	200	36	10	30	5	19
	638	200	43	16	24	4	13
Pt(13,1,1)	573	200	15	22	39	17	7
	595	200	15	23	40	16	6
	623	200	16	22	43	13	6
Pt(10,8,7)	573	200	36	13	27	12	12
	599	200	30	10	37	10	13
	623	200	33	12	36	9	10
	658	200	36	14	31	10	9
Pt(111)	573	600	23	14	35	12	16
	623	600	28	15	33	8	16
	673	600	40	15	24	6	15
	753	600	64	13	14	2	7
Pt(10,8,7)	573	80	37	14	28	11	10
	573	600	31	17	24	14	14
	673	600	38	16	33	7	6

(a) Product distributions were calculated at 15-30 min reaction time, P_{HC} = 20 Torr.

primarily to the formation of ethane, propane, and butane. By contrast the (111) and (10,8,7) platinum surfaces displayed high selectivities for cleavage of the terminal and central C-C bonds. Low levels of hydrocracking activity, $n\text{-}C_6H_{14} \rightarrow CH_4 + C_2H_6$, that represented about 3-8 percent of the total n-hexane consumed by hydrogenolysis at 573 K, were detected over all four platinum surfaces. Hydrocracking was favored by high reaction temperatures and appeared to occur most easily on the (111) and (10,8,7) platinum surfaces.

The fission parameter, M_f, defined by (15)

$$M_f = [C_1]^{-1} \sum_{i=2}^{5} (6 - i)[C_i] \qquad (1)$$

was used to classify the hydrogenolysis selectivities that were exhibited by the different platinum surfaces. The concentrations of hydrogenolysis products with i carbon atoms are denoted by $[C_i]$. Selective hydrogenolysis of the terminal C-C bond produces $M_f = 1$, whereas purely statistical hydrogenolysis yields $M_f = 10$. When multiple hydrogenolysis (hydrocracking) is important $M_f << 1$. Fission parameters for n-hexane hydrogenolysis catalyzed at a total pressure of 220 Torr are shown as a function of reaction temperature in Fig. 3.17. The (111) and (10,8,7) platinum surfaces displayed values of M_f that were between 3 and 7 for all temperatures between 530 and 660 K. Fission parameters for the (100) and (13,1,1) surfaces were always much higher, i.e., 13-21. The fission parameters displayed a small dependence on hydrogen pressure, as shown for the (111)

platinum surface in Fig. 3.18. High hydrogen partial pressures and low temperatures favored statistical hydrogenolysis, whereas low hydrogen pressures and high temperatures favored terminal C-C bond splitting.

Deactivation Kinetics and Formation of Surface Carbon Deposits. Continuous deactivation was detected during all the n-hexane reaction rates studies. Hydrogenolysis, isomerization, C_5-cyclization, and aromatization displayed similar deactivation rates under each set of reaction conditions (Figs. 3.1-3.4). However, within isomerization, the deactivation behavior 2- and 3-methylpentane formation was clearly different. This is shown in Fig. 3.19 for n-hexane isomerization catalyzed over Pt(100) at 556 and 573 K. The selectivity for 2-methylpentane production relative to 3-methylpentane formation increased with increasing reaction time. This effect was most pronounced for the (100) and (13,1,1) platinum surfaces.

Deactivation rates at any given temperature were similar for all four platinum surfaces (Section 4.6). The deactivation rates always increased with increasing reaction temperature (Figs. 3.3 and 3.4). Deactivation appeared to result entirely from the formation of strongly adsorbed, partially dehydrogenated, carbonaceous deposits that covered a significant fraction of the platinum surface. The surface coverage by this carbonaceous deposit increased with increasing reaction temperature. Figure 3.20 summarizes C_{273}/Pt_{237} AES peak-to-peak height ratios measured following n-hexane reactions that were carried out between 525 and 678 K. These peak height ratios can be converted

into atomic ratios expressed as carbon atom equivalents per surface platinum atom by multiplying by 0.62 for Pt(111) and Pt(10,8,7) and 0.74 for Pt(100) and Pt(13,1,1), respectively (Section 2.6). Using these conversions, it follows that the apparent coverage by irreversibly adsorbed species was equivalent to 1-6 carbon atoms per surface platinum atom.

Several different kinetic models were investigated to describe the deactivation kinetics which assumed that the deactivation was half, first, or second order with respect to time. At the lowest temperatures investigated (560 K), the deactivation was well described by the first order model, $R_t = R_o \exp(-\alpha t)$, whereas at higher temperatures the deactivation displayed a fractional order time dependence; viz., $R_t = R_o \exp(-\alpha t^n)$, $0 < n \leq 1$. The second order model never provided satisfactory agreement with experiment. Figure 3.21 compares results obtained for n-hexane hydrogenolysis and aromatization catalyzed on Pt(10,8,7) at several temperatures using the first- and half-order deactivation models. Best fit orders for the deactivation process were determined from order plots (not shown) of $\ln(\ln(R(t)/R_o))$ as a function of $\ln t$. Deactivation orders determined in this manner decreased continuously with increasing reaction temperature from 1.0 ± 0.2 at 520-570 K to 0.5 ± 0.2 at 640-660 K. The apparent activation energy for deactivation was estimated from the initial slopes of deactivation plots like those shown in Fig. 3.21. Arrhenius plots for the deactivation rate constants yielded activation energies

that were always in the range 11-18 kcal/mole independent of the deactivation model.

n-Hexane Dehydrogenation Activity. The dehydrogenation of n-hexane yielded or unresolved mixture of 1-, cis- and trans-2-, and cis- and trans-3-hexenes under all reaction conditions. For reaction temperatures below about 590 K, the dehydrogenation reactions were very rapid and approached equilibrium over the first 20-30 min reaction time. At higher reaction temperatures the olefins achieved a more-or-less steady state concentration after about 1 hr which was much lower than that expected for thermodynamic equilibrium (15-40 percent) (36). Hexenes detected in the first gas chromatogram of each experiment were used to establish a lower limit for the initial dehydrogenation rates. These "lower limit" dehydrogenation rates are shown as a function of 1/T in Fig. 3.22. The dehydrogenation rates estimated in this manner were in the range 0.1-1 molec/Pt atom sec. In general, these dehydrogenation rates were at least 10 times faster the sum rates of all skeletal rearrangement reactions. The dehydrogenation activity displayed a maximum at temperatures of 600-640 K.

3.1.3. Discussion

Structure Sensitivities of Initial n-Hexane Reaction Rates. Important new information about the structure sensitivities of alkane reforming reactions have been derived from studies of n-hexane reactions catalyzed over platinum single crystal surfaces. Near atmospheric pressure and temperatures between 550 and 620 K, the (111) and (10,8,7) platinum surfaces were several times more active than the

(100) and (13,1,1) surfaces for the dehydrocyclization of n-hexane to benzene. Hexagonal (111) microfacets that were present in highest concentrations on the (111) and (10,8,7) surfaces displayed a unique ability to catalyze the complex skeletal rearrangements required for aromatization. The atomic structure of the terraces was the decisive source of structure sensitivity for this important reaction pathway. Steps and kinks that were present in high concentrations on the (13,1,1) and (10,8,7) surfaces increased the rate of dehydrocyclization only slightly (10–40 percent) as compared to the flat low index surfaces. It is important to remember that unoriented crystal edges that represented ~8–15 percent of the total platinum surface area tend to make the structure sensitivities appear smaller than they would be if the entire platinum surface area was of the specified orientation.

The only previous study that explicitly considered the structure sensitivity of n-hexane armoatization was the work of Dautzenberg and Platteeuw (6,7). At 10 atm and 760 K no significant structure sensitivity was detected for a series of non-acidic alumina supported platinum catalysts with dispersions between 0.2 and 0.65. Since the structure and composition of the supported catalysts was not known and the reaction conditions were far more severe, direct comparison of these results with those determined for the single crystals is not feasible.

The structure sensitivity of n-hexane aromatization might at first seem to suggest that Balandin's once popular "sextet-theory" (37,38) for cyclohexane dehydrogenation may have some validity. Since no

cyclohexane was detected in the present research, all ring closure pathways that produce C_6-rings must also be accompanied by dehydrogenation. If dehydrogenation was the slow reaction step then the structure sensitivities would certainly be consistent with the sextet-theory. However, recent studies by Gillespie (28) of cyclohexane dehydrogenation catalyzed over platinum single crystal surfaces clearly indicate that this is not the case. Under identical reaction conditions cyclohexane dehydrogenation was 10 - 10^4 times faster than n-hexane aromatization. Based on these results and other data presented below it appears clear that the rate determining step of n-hexane aromatization is a reaction step involving skeletal rearrangement. This reaction step occurs most easily over surfaces with contiguous (111) microfacets, not necessarily sextet sites.

In marked contrast to aromatization, the rates of n-hexane hydrogenolysis, isomerization, and C_5-cyclization displayed little dependence on platinum surface structure. The absence of significant structure sensitivity for these reactions is consistent with the studies of Ponec et al. (4) (Pt/SiO_2, $H_2/HC = 16$, $P_{tot} = 1$ atm, $T = 520$–570 K) and Dautzenberg and Platteeuw (6,7) (Pt/Al_2O_3, $H_2/HC = 4$, $P_{tot} = 9.5$ atm, 760 K). An important result of our studies is that C_5-cyclization occurred very easily on all the platinum surfaces, even the flat (111) and (100) surfaces with very low concentrations of step and kink defect sites. At the lower temperatures (530–570 K), methylcyclopentane was the dominant reaction product produced over every surface. It has often been suggested that isolated edge and

corner atoms are the preferred sites for this C_5-cyclization reaction (5,26,39). While are results do not support this conclusion, the possibility can not be ruled out, especially since the (13,1,1) and (10,8,7) platinum surfaces appeared to be about 20-50 percent more active than Pt(111). It appears likely that corner atoms with very few (3 or 4) nearest neighbors and/or metal support interactions may be responsible for the unique C_5-cyclization structure sensitivity that is often displayed by supported platinum catalysts with very high dispersion (5,23,26).

In Fig. 3.23, the initial rates of aromatization and C_5-cyclization at 573 K are compared as the function of surface structure. Our results clearly indicate that surface irregularities in low concentrations have only a small effect on the rates of n-hexane aromatization and C_5-cyclization. Aromatization was influenced strongly by the terrace structure, whereas C_5-cyclization was not. Terraces with (111) orientation led to a higher aromatization specificity. Further studies using more highly stepped and kinked surfaces would be worthwhile to further confirm these observations.

Isomerization of n-hexane to 2- and 3-methylpentanes displayed a similar lack of structure sensitivity in which all types of platinum sites were more-or-less equally active in effecting the skeletal rearrangement process. The flat (111) surface appeared to be slightly more active than the other platinum surfaces, especially for the production of 3-methylpentane.

The structure sensitivities of n-hexane reactions reported here compare favorably with results recently obtained by Gillespie for n-heptane hydrogenolysis and aromatization catalyzed over flat (111), stepped (557), and kinked (25,10,7) and (10,8,7) platinum surfaces (28). As compared to the flat (111) surface, n-heptane aromatization was faster and hydrogenolysis was slower by about a factor of two on the kinked (10,8,7) surface. The same trend was detected for n-hexane reactions, although the differences in rates due to surface irregularities were less pronounced.

The general conclusion arises that steps and kinks on platinum surfaces are not exceptionally effective for catalyzing low rate skeletal rearrangement reactions, at least in the vicinity of atmospheric pressure. This conclusion contrasts markedly with earlier results reported by Blakely et al. (30) for n-heptane and cyclohexane reactions catalyzed at very low pressures ($\sim 10^{-7}$ Torr). At low pressures steps and kinks appeared to be uniquely active for hydrogenolysis and aromatization. The different structure sensitivity at high and low pressures could result from a change in mechanism with increasing pressure (28,33), or it could also result from a change in the structure and growth mechanism of the carbonaceous deposit. Since the carbonaceous deposit formed within minutes at high pressures (Chapter 4), it is probable that this deposit may block or cover many of the surface irregularities that would otherwise possess different bond breaking abilities. A more detailed assessment of this possibility is considered in the next chapter.

Finally, it should be noted the overall n-hexane skeletal rearrangement rates determined for single crystal surfaces were always much higher than the rates of the same reactions catalyzed over practical platinum catalysts. Table 3.3 provides a comparison of initial rates for Pt(111) with those reported for other types of platinum catalysts, e.g., film, powders, and Pt/SiO_2. All the rates were determined under similar reaction conditions. With the exception of ultra thin platinum films that were prepared in UHV (3), the initial rates for Pt(111) were always 1-2 orders of magnitude higher than rates reported for practical catalysts. As noted by Gillespie (28) these differences undoubtedly arise from a combination of (a) surface contamination on the practical catalysts and (b) inaccuracies in the surface area determinations for the practical catalysts.

n-Hexane Reaction Selectivity. Product distributions for n-hexane skeletal rearrangement over the single crystal catalysts displayed striking variations as a function of temperature and hydrogen pressure. For any given set of reaction conditions the product distributions for all surfaces were rather similar (Figs. 3.15 and 3.16) except for the differences in aromatization selectivity that are expected from the structure sensitivity of this reaction detailed above. Isomerization, C_5-cyclization, and hydrogenolysis were always the main reactions at lower temperatures (570 K) and higher hydrogen pressures (200 Torr). Hydrogenolysis and aromatization selectivities increased with increasing temperature. At the highest temperatures studied (620 K)

Table 3.3. Comparison of initial n-hexane reaction rates on Pt(111) and practical platinum catalysts.

Catalyst	T(K)	H_2/HC	P_{tot}(Torr)	Initial Rate (a) (molec/Pt atom sec)	Ref.
Pt(111)	573	10	220	0.03	-
Pt-powder	573	6	760	$3x10^{-3}$	1
Pt/SiO_2 ($\bar{d}$=30Å)	573	11.2	180	$4x10^{-4}$	9
Pt(111)	553	10	220	0.02	-
Pt-film ($\bar{d}$-15-58Å)	546	10	110	0.02-0.03	3
Pt(111)	573	30	620	0.07	-
Pt/SiO_2 ($\bar{d}$=40-80Å)	573	16	750	$3-4x10^{-3}$	4

(a) Total rate of skeletal rearrangement.

hydrogenolysis and aromatization represented 65–90 percent of the total skeletal rearrangement.

Product distributions determined at the lower reaction temperatures (530–590 K) were generally very similar to those reported previously for practical platinum catalysts. This is shown in Fig. 3.24 for n-hexane reactions catalyzed over Pt(111), 0.22 percent Pt/SiO_2 (D = 1.0) (5), and 16 percent Pt/SiO_2 (D = 0.1–0.2) (12). A more complete comparison with other types of platinum catalysts is provided in Table 3.4. In nearly all cases the single crystal surfaces displayed higher selectivities for aromatization and C_5-cyclization and lower selectivities for isomerization as compared to the practical catalysts. From the perspective of petroleum reforming, the initially clean single crystal surfaces displayed superior selectivities than supported catalysts. However, these selectivity differences were usually small enough that the agreement must be considered reasonably good.

One would hope to be able to decompose the selectivities displayed by practical catalysts as a linear combination of selectivities for (100) and (111) microfacets. Unfortunately this is not possible because the cyclization selectivities displayed by single crystal surfaces are always too high.

Kinetic selectivities for 3MP over 2MP and Bz over MCP (Figs. 3.13 and 3.14) increased markedly with increasing temperature and decreasing hydrogen pressure. These changes in selectivity were quite dramatic indicating that major changes occurred in the reaction mechanism as a function of reaction conditions. The 2MP/3MP and Bz/MCP selectivities

Table 3.4. Comparison of n-hexane reaction selectivities for single crystal surfaces and practical platinum catalysts.

Catalyst	T(K)	H_2/HC	P_{tot}(Torr)	Fractional Selectivities (mole %) 2MP+3MP	MCP	Bz	$\Sigma<C_6$	$\frac{2MP}{3MP}$	$\frac{Bz}{MCP}$	Ref.
Pt/Al_2O_3	573	190	760	58	7.5	2	32.5	1.5	0.27	14
16% Pt/SiO_2	567	17	760	48	7	2	43	1.7	0.29	12
0.22% Pt/SiO_2 ($\bar{d}$=10Å)	573	~11	760	29	35	-	36	2.8	-	5
9.5% Pt/SiO_2 ($\bar{d}$=55Å)	573	~11	760	53	7	-	40	2.6	-	5
Pt-black	573	6	760	49	10	1-3	38	-	$\leq$0.3	1
Pt(111)	573	30	620	42	26	7	25	1.5	0.27	-
1% Pt/SiO_2 (d=30Å)	573	13.5	190	71	2.5	0.5	26	-	0.2	9
Pt(111)	573	10	220	29	26	17	28	0.4	0.6	-
Pt(100)	573	10	220	26	43	6	25	0.65	0.14	-
1% Pt/SiO_2 (d=30Å)	635	13.5	190	56	18	4	22	-	0.22	9
Pt(111)	638	10	220	14	13	33	40	$\leq$0.15	2.6	-
Pt-black	693	$\geq$20	760	5	4	18	73	-	5.0	2
Pt(111)	693	30	620	14	11	32	43	$\leq$0.2	2.8	-

determined at lower temperatures (<570 K) and higher hydrogen pressures (H_2/HC $\geq$ 30) were quite similar to these noted previously for practical catalysts (Table 3.4). However, the very low 2MP/3MP ratios ($\leq$0.2) and very high Bz/MCP ratios ($\geq$2-3) determined at higher temperatures and lower hydrogen pressures appear to be unique to single crystal surfaces and perhaps other forms of bulk platinum. In studies of n-hexane reactions catalyzed over Pt/SiO_2 catalysts, Van Schaik et al. (12) and Karpinski and Koscielski (9) failed to observe significant changes in the same kinetic selectivities over the temperature ranges 550-585 and 573-635 K, respectively. At high space velocities, 9.5 atm (H_2/HC = 4), and 710-760 K, 2MP/3MP and Bz/MCP ratios of about 2 and 0.1-0.5, respectively, were reported for monofunctional Pt/Al_2O_3 catalysts (6,7). Paal has reported Bz/MCP ratios as large as 5 for n-hexane reactions catalyzed over Pt-black at 690 K (2).

Maire and co-workers (40) recently investigated the isomerization of 2-methylpentane-2-^{13}C on several platinum single crystal surfaces and on a series of alumina supported platinum catalysts. The isotopic distribution of ^{13}C in the product hexanes was used to determine the proportion of the isomerization reaction which proceeded by the C_5-cyclic mechanism. At 620-720 K, the (111), (911), and (557) single crystal catalysts displayed cyclic percentages which were in the range 14-70 percent, although most often they were 50-70 percent. Since these cyclic percentages were the same as those displayed by supported catalysts with low and medium dispersion (<0.7), the Strasbourg group concluded that the single crystal surfaces are excellent models of

practical catalysts with low dispersion. While labelling studies were not carried out in the present work, two key observations from our research certainly tend to confirm that the cyclic mechanism is very important on the single crystal surfaces. Isomerization and C_5-cyclization displayed identical catalytic behavior as a function of temperature and hydrogen pressure; both reactions displayed maximum rates at 600-630 K, and both reactions displayed similar absolute rates over all surfaces under all conditions investigated. More importantly, whereas n-hexane isomerization exhibited no significant structure sensitivity, isobutane and n-butane isomerization were exceedingly structure sensitive over the same platinum surfaces under exactly the same reaction conditions used for the n-hexane reaction studies (Section 3.2). These light alkanes are restricted to isomerization by the bond shift mechanism. It is difficult to rationalize a process by which bond shift isomerization would be structure sensitive for isobutane and n-butane but not n-hexane, unless, of course, the bond shift mechanism is of minimal importance for n-hexane. In this context, it is important to note that the ^{13}C-labelling method can be used only to determine the minimum fraction of reaction which occurs by the cyclic mechanism. This fact has not been emphasized previously. Gault (41,42) has noted that consecutive rearrangements during a single residence on the surface must be invoked to explain the product distributions observed for reactions of ^{13}C-labelled 2,3-dimethylbutanes

and n-heptane, although this possibility appears to have been neglected in the case of hexane isomerization. Consecutive rearrangements provide a rational explanation for "internal bond shift" that is always observed for C^{13}-hexane isomerization (23-26). Results reported in the next section indicate that these consecutive rearrangements take place readily on the (100) and (13,1,1) platinum surfaces. The minimum surface residence times of dissociatively adsorbed hexane intermediates that are on the order of 10^{-1} sec (Section 3.4) are certainly long enough for many rearrangements to take place. Multiple rearrangements will generally make the cyclic percentages of ^{13}C-containing products appear too low. The important point is that all existing evidence indicates that the cyclic mechanism is very significant on the platinum single crystal surfaces.

If it is accepted that n-hexane isomerization is mostly cyclic, then the changes in 2MP/3MP selectivity with temperature, hydrogen pressure, and reaction time mainly result from changes in the positional selectivity for ring opening of the C_5-cyclic intermediates. Isomerization to 3-methylpentane was favored on initially clean platinum at high temperatures and low hydrogen pressures. Isomerization to 2-methylpentane was favored at longer reaction times after the surfaces had become extensively covered by strongly adsorbed carbonaceous species. A similar change in isomerization selectivity with reaction time was noted by Carra et al. (1) for n-hexane conversion at 573 K over platinum black. It appears likely that this change in selectivity as carbon is deposited on the surface may arise from a

change in the steady state surface concentration of chemisorbed hydrogen (Section 4.6).

It is widely accepted (20,27,33) that n-hexane aromatization can occur by a combination of direct 1,6-ring closure and parallel 1,5-cyclization followed by dehydroisomerization, i.e.,

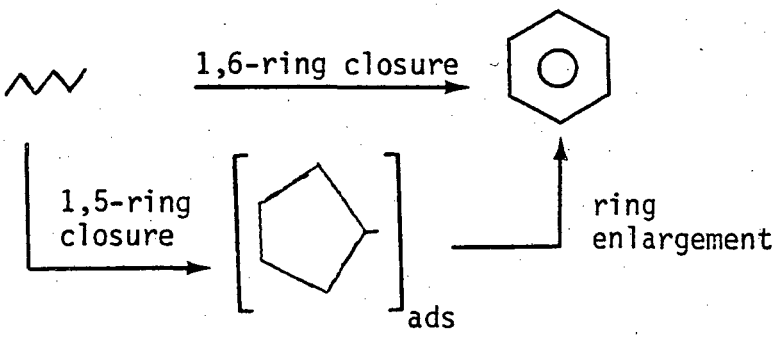

(3)

As ring enlargement activities are little or no larger than isomerization and aromatization rates (33), ring enlargement must usually occur during a single residence on the surface. Dautzenberg and Platteeuw (6,7) reported that benzene and methylcyclopentane are both initial products of n-hexane cyclization, whereas only methylcyclopentane is produced initially from 2-methylpentane. In this case aromatization appeared to result mostly from direct 1,6-ring closure, although 1,5-ring closure (leading to MCP) was also important. Sinfelt et al. (43) showed that methylcyclohexane, from direct 1,6-cyclization of n-heptane, is most probably an intermediate in the formation of toluene over Pt/Al_2O_3. The major aromatic products produced during dehydrocyclization of ten different octane and nonane isomers over Pt/Al_2O_3 (1 atm, 750 K) were also those expected for direct 1,6-ring

closure (44). Aromatization studies of ^{13}C-labelled n-heptane were recently reported by Gault and co-workers (41). Besides direct 1,6-ring closure, these workers identified a complex 3-step mechanism involving 1,5-ring closure, ring opening, and 1,6-ring closure all occurring during a single residence on the surface. This reaction pathway is consistent with earlier studies (45) of [1-^{14}C] n-heptane aromatization over monofunctional Pt/Al_2O_3 catalysts. Whereas direct 1,6-ring closure should yield 50 percent of the radioactivity in the methyl side chain, at 773 K only 40 percent of the toluene contained ^{14}C in the methyl group.

The results obtained in this work add notably to the large body of evidence which indicates that direct 1,6-ring closure is the primary reaction pathway for n-hexane aromatization on platinum. Aromatization was structure sensitive and favored by high temperatures and low hydrogen pressures. By contrast C_5-cyclization was structure insensitive and displayed highest selectivity at lower temperatures (<570 K) and higher hydrogen pressures (H_2/HC > 10). These differences in catalytic behavior appear to indicate that the reaction intermediates leading to aromatization have a lower hydrogen content than those leading to methylcyclopentane formation. With this in mind, it is likely that the structure sensitivity of n-hexane aromatization may originate in part from the different binding strengths of hydrogen on the surfaces with different atomic structure. It is well established that hydrogen is chemisorbed more strongly on (100) microfacets than (111) microfacets by about 3-5 kcal/mole (46,47). The

steady state concentration of surface hydrogen should therefore be higher on surfaces with (100) terraces. An increase in the concentration of surface hydrogen would be accompanied by a decrease in the concentration of reaction intermediates with very low hydrogen content (all other things being equal). As a result, it is natural to expect that the aromatization activity of (100) microfacets should be lower than that for (111) microfacets. Differences in aromatization rate constants that arise strictly from changes in surface structure may also contribute to the unique structure sensitivity of the aromatization reaction.

Hydrogenolysis Product Distributions. The positional selectivity of n-hexane hydrogenolysis displayed a marked dependence on platinum surface structure. The (100) and (13,1,1) platinum surfaces with high concentrations of (100) microfacets displayed a high specificity for scission of the internal c-c bonds with little accompanying terminal hydrogenolysis ($M_f \gtrsim 15$). By contrast, the (111) and (10,8,7) surfaces that were mostly composed of hexagonal (111) microfacets displayed a clear preference of hydrogenolysis of the central and terminal C-C bonds. In this case, the probability for scission of the C_2-C_3 bond was quite low. Average C-C bond rupture probabilities calculated for Pt(100) and Pt(111) from 4-12 runs at a total pressure of 220 Torr were

	$\underline{C_1-C_2}$	$\underline{C_2-C_3}$	$\underline{C_3-C_4}$	$\underline{C_4-C_5}$	$\underline{C_5-C_6}$
Pt(100)	0.08	0.20	0.44	0.20	0.08
Pt(111)	0.21	0.09	0.40	0.09	0.21

These probabilities differ from those reported previously for practical platinum catalysts where n-hexane hydrogenolysis was most often statistical (3,5,9), although in a few cases (12,14) a small preference was reported for internal scission (like Pt(100)). While Santacessaria (5) and Anderson (3) reported no changes in the distribution of n-hexane hydrogenolysis products produced over platinum catalysts when the average metal particle size was varied between 10 and 60Å or more, it is interesting to note that Yao et al. (48) observed a large variation in the distribution of n-pentane hydrogenolysis products produced over Rh/Al_2O_3 catalysts. Highly dispersed (probably raft-like (49)) rhodium particles displayed a high specificity for internal cleavage (like Pt(100)), whereas larger rhodium particles favored terminal C-C bond scission (like Pt(111)).

The differences in hydrogenolysis selectivity for single crystal surfaces with different atomic structure appear to arise directly from differences in the structure of the reaction intermediates which undergo C-C bond scission. A great volume of literature (20,21,27,31,33) suggests that α,γ-triadsorbed species are the most important class of intermediates for hydrogenolysis reactions of C_3 and larger alkane molecules. Perhaps the most convincing evidence in favor of these species was provided by Leclercq and co-workers (50) in

studies of sixteen different alkane hydrogenolysis reactions catalyzed over Pt/Al_2O_3. In this case, the reactivities of C-C bonds with different substitution were always well described by the intervention of 1,1,3- and 1,3,3-triadsorbed species, except when the 3 carbon was quarternary, in which case α,δ-adsorbed species also appeared to become important. The same workers presented evidence that hydrogenolysis was most favorable for C-C bonds α to a metal-carbon multiple bond. The latter prediction is consistent with recent extended Huckel calculations (51) which revealed that C-C bonds α to platinum-carbon multiple bonds in alkylidene ($Pt = CR_2$) and alkylidyne ($Pt \equiv CR$, $R = CH_3$) surface species are weakened relative to those α to platinum-carbon single bonds. These facts form a basis to interpret the hydrogenolysis selectivities displayed by the single crystal surfaces. Four unique possibilities exist for α,γ-triadsorption of n-hexane, namely 1,1,3-, 1,3,3-, 2,2,4-, and 2,4,4-triadsorbed species. A statistical distribution of these species would appear to favor internal scission, especially at the C_2-C_3 bond. In order to account for the distribution of products produced on Pt(100), it appears likely that 1,3,3- and 2,2,4-triadsorbed species may be formed preferentially on the (100) microfacets. For the (111) platinum surface, the 1,1,3- and 2,4,4-triadsorbed species would appear to be more important. The reasons why these preferences might exist are not clear. The suggestions are made here only as an analogy to previously accepted models for which there is no unequivocal proof. A similar agrument

was used to explain the distribution of n-pentane hydrogeolysis products produced over Rh/Al_2O_3 catalysts (48).

In addition to these α,γ-triadsorbed species, another possibility, which is clearly unique to the (111) surface, can be proposed to account for the higher selectivities for terminal cleavage on this surface. Dynamical LEED intensity analysis and high resolution ELS studies (52-54) have demonstrated that a common, stable surface species always results from the chemisorption of ethylene, propylene, and butenes on Pt(111) at 300-420 K. This species is the surface alkylidyne group, $Pt_3 \equiv C\text{-}R$ ($R = CH_3$, C_2H_5, C_3H_8), which occupies the 3-fold hollow sites that are unique to (111) microfacets. Formation of this surface species is accompanied by weakening of the α-C-C bond (51). If the isostructural hexylidyne species formed during n-hexane conversion on the (111) platinum surface, hydrogenolysis would obviously yield methane and pentane with very high selectivity.

Reaction Kinetics and Reaction Mechanism. The kinetic studies reported here for n-hexane reactions catalyzed over platinum single crystal surfaces are highly consistent with the 2-step reaction model originally proposed by Cimino et al. (55) and later applied by Sinfelt (31) and Maurel and co-workers (56) to hydrogenolysis reactions catalyzed over Group VIII metals, most notably platinum. The two most important features of the reaction kinetics were (1) apparent activation energies that decreased with increasing temperature and decreasing hydrogen pressure, and (2) the dependence of the reaction rates on hydrogen pressure which varied from slightly positive or

negative at lower temperatures (570 K) to first order at higher temperatures. These changes arise naturally if the reaction pathway involves the series of reaction steps (55,56)

$$H_2 \overset{K_H}{\rightleftharpoons} 2H(ads) \qquad 4.$$

$$n\text{-}C_6H_{14} \overset{\lambda}{\rightleftharpoons} n\text{-}C_6H_x(ads) + aH_2 \qquad 5.$$

$$n\text{-}C_6H_x(ads) + \begin{matrix} 2\delta H(ads) \\ \text{or } H_2 \end{matrix} \xrightarrow[\text{slow}]{k} \begin{matrix} \text{adsorbed fragments} \\ \text{or isomers} \\ H_2 \downarrow \text{ fast} \\ \text{products} \end{matrix} \qquad 6.$$

where $0 \leq \delta \leq 1$. In this reaction scheme dissociative chemisorption of hydrogen and hydrocarbon are assumed to be reversible and very rapid as compared to the rate of skeletal rearrangement. The rate determining step involves skeletal rearrangement or hydrogenolysis of intermediate $n\text{-}C_6H_x$ species which have lost 2a hydrogen atoms. This rearrangement is presumably accompanied by addition of 0-2 H(ads) or H_2 (55,56). All subsequent reaction steps are rapid. For any specific set of a and δ values, this reaction sequence leads to a rate equation (55,56),

$$R = k\lambda K_{H_2}^{\delta} P_{H_2}^{\delta} P_{HC} / (K_H^a P_{H_2}^a + \lambda P_{HC}) \qquad (2)$$

which indicates that the observed reaction rates involve a product of elementary rate coefficients and adsorption equilibrium constants.

In order to properly assess the validity of this reaction sequence several important facts need to be carefully considered:

(i) Deuterium exchange kinetics discussed in section 3.4 revealed that hydrogen and hydrocarbon chemisorption were indeed rapid and very reversible as compared to the rate of skeletal rearrangement. At 573 K, for example, complete deuterium exchange was about 100 times faster than skeletal rearrangement. However, this difference in rates decreased markedly with increasing temperature.

(ii) There is no logical reason to assume that a unique set of k, K, λ, a, and δ values is appropriate for each reaction pathway, viz., cyclization, isomerization, and hydrogenolysis. Physically it is more reasonable to expect that each pathway will have its own distribution of k, K, λ, a and δ values that may vary with surface structure. In this case, the concentrations of reaction intermediates with different hydrogen content are largely determined by thermodynamic considerations, and the identity of the most abundant surface intermediate will change markedly with reaction conditions. As a consequence, the reaction selectivity should also change drastically with reaction conditions as observed experimentally. Average values of a = 2-4 have been reported by Leclercq et al. (56) for a variety of alkane hydrogenolysis reactions catalyzed at 570-600 K and at atmospheric pressure over Pt/Al_2O_3 catalysts.

(iii) The appearance of hydrogen in the rate determining step (rxn 6) can arise as an artefact if hydrogen chemisorption or a subsequent hydrogen addition step becomes kinetically important. In this case, skeletal rearrangement could be unimolecular, although the intervention of hydrogen in prior to subsequent reaction steps would give rise to a positive order dependence on hydrogen pressure. The deuterium exchange kinetics discussed later clearly indicate that at high temperatures (>630 K), hydrocarbon chemisorption becomes largely irreversible, and hydrogen chemisorption becomes rate-limiting. In this case skeletal rearrangement appears to involve a series of effectively irreversible reaction steps. Phenomenologically, this situation ($\lambda P_{HC} >> K_H^a H_{H_2}^a$, $R \rightarrow k' P_{H_2}$) is still well described by Eq. (2), although the implicated reversibility is no longer valid. The notion that hydrogen chemisorption becomes rate limiting at high temperatures accounts for the fact the apparent activation energies for all reactions approached zero at high temperatures (>620 K).

(iv) The complete neglect of competition between adsorbed hydrogen and adsorbed hydrocarbons implicit in this model can be questioned on general grounds as noted by Kemball (57), Boudart (58), Frennet (59), and Martin (60). This competition appears to be important during ethane hydrogenolysis of nickel catalysts (60) where the order of the reaction with respect to hydrogen pressure is very negative (e.g., - 2). However, adsorption equilibrium constants reported by Maurel

et al. (56) clearly indicate that competition should be insignificant for larger hydrocarbon molecules such as n-hexane.

In view of these facts, it is clear that the two-step kinetic model can have value for describing the reaction kinetics, even though the exact form of the elementary step cannot be justified over a wide range of reaction conditions. The model appears to be most appropriate at lower reaction temperatures and intermediate hydrogen pressures where hydrogen adsorption is not rate-limiting. If this interpretation is accepted, it is interesting to consider what implications exist for the striking changes in reaction selectivity that were detected as a function of temperature and hydrogen pressure. Isomerization and C_5-cyclization were favored at lower temperatures and higher hydrogen pressures, whereas aromatization was preponderant at higher temperatures and lower hydrogen pressures. This is expected if the reaction intermediates leading to aromatization have a lower hydrogen content (higher a values) than those leading to C_5-cyclization. Paal and Teteryi (61) have shown that while hexadienes and hexatrienes aromatize with very high selectivity, C_5-cyclization of the same molecules is unfovorable even in the presence of excess hydrogen. In this case, aromatization clearly involved intermediates that were more extensively dehydrogenated than those required for C_5-cyclization. Hydrogenolysis of n-hexane on the platinum single crystal surfaces was favorable under all reaction conditions. This appears to indicate that the hydrogenolysis intermediates can tolerate a broader distribution of hydrogen content.

Deactivation Kinetics and Role of Adsorbed Carbonaceous Deposits. The platinum single crystal catalysts deactivated continuously during all of the n-hexane reaction studies. The deactivation rate displayed little dependence on platinum surface structure. Deactivation was accompanied by the deposition of about one or more monolayers of disordered, strongly bound carbonaceous deposit on the platinum surfaces that could be detected following the reactions by AES. Figure 3.25 shows Auger spectra that were recorded following n-hexane reactions on the (100) platinum surface at 573 and 673 K. The amount of carbon deposited increased with increasing temperature (Fig. 3.20) and decreasing hydrogen pressure. Deactivation rates correlated closely with the build-up of this deposit; i.e., deactivation rates increased with increasing temperature and decreasing hydrogen pressure. The deactivation kinetics could be described emperically by an exponential rate law, $R(t) = R(t = 0)\ \exp(-\alpha t^n)$, where the order parameter n decreased with increasing reaction temperature. In order to place these deactivation kinetics in context, three important properties of the carbon deposit that are discussed fully in Chapter 4 should now be considered: (i) the carbonaceous deposit is a non-graphitic, polymeric residue with an average hydrogen content of about one hydrogen atom per surface carbon atom, (ii) the carbonaceous deposit nucleates in the form of islands that are largely 2-dimensional at low temperatures (<570 K) but tend to become 3-dimensional at high temperatures (>630 K), and (iii) the general role of the carbon deposit is that of a non-selective poison; hydrocarbon catalysis takes place on a small

concentration of uncovered surface platinum sites that display normal platinum activity and selectivity.

With these facts in mind, a simplified but appropriate kinetic model for the deactivation process can be developed from the following series of reaction steps

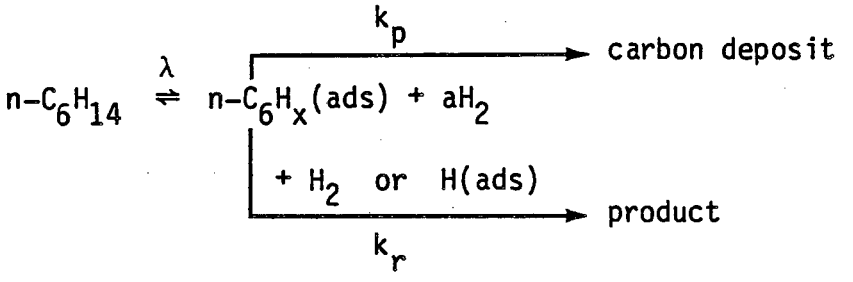

7.

where it is proposed that deactivation results from the pseudo-first order polymerization of adsorbed reactant molecules. According to this scheme dissociative hydrocarbon chemisorption is reversible (Section 3.4), and hydrocarbon conversion competes with deactivation. The net rate of skeletal rearrangement is of the form

$$R \simeq k_r P_{H_2} \theta_i \quad \text{or} \quad k_r \theta_i \theta_H \tag{3}$$

where θ_i is the surface coverage by adsorbed hydrocarbon, and θ_H is the surface coverage by hydrogen which is assumed to be small for simplicity (i.e., $\theta_H \simeq (K_H P_{H_2})^{1/2}$). Since the deactivation rate was slow compared with the individual adsorption-desorption and surface reaction steps, the steady state approximation can be applied to θ_i which yields

$$\theta_i = \frac{\lambda P_{HC}(1 - \theta_{HC})}{(\lambda \rho_{HC} + K_H^a p_{H_2}^a + k_r P_{H_2} / k_{-1} + k_p / k_{-1})} = \eta(1 - \theta_c) \qquad (4)$$

where $\lambda = k_1/k_{-1}$, and θ_c is the surface coverage by the deactivating carbon deposit. The rate of formation of this deposit is simply

$$\frac{d\theta_c}{dt} = k_p \theta_i = \eta k_p (1 - \theta_c) \qquad (5)$$

which integrates to

$$-\ln(1 - \theta_c) = \eta k_p t \qquad (6)$$

or

$$\theta_i(t) \approx (1 - \theta_c) = \exp(-\eta k_p t) \qquad (7)$$

The latter expression accounts for the first order deactivation that was observed at lower temperatures and predicts that the deactivation rates should increase with increasing temperature and decreasing hydrogen pressure as observed experimentally. The apparent activation energy for this process has 11-18 kcal/mole which is typical for polymerization reactions (62). Since dehydrogenation was always the fastest hydrocarbon conversion reaction, it is tempting to suggest that the nucleation and growth of the carbon deposit results from simple polymerization of chemisorbed hexenes.

At the lower reaction temperatures (<560 K), the carbon deposit assumed a 2-dimensional structure, and the deactivation was simply first order. Every molecule incorporated into the deposit was equally effective in blocking platinum surface sites that were required for skeletal rearrangement reactions. At higher temperatures the carbon deposit gradually converted into a 3-dimensional structure, and this conversion was accompanied by a continuous decrease in the apparent order for the deactivation reaction. It appears that this change in order can be correlated with a charge in morphology of the carbon deposit. Physically, the fractional order time dependence indicates that the molecules which were incorporated into the carbon deposit at high temperatures were not as effective in blocking platinum sites as at the lower temperatures. This is expected if polymerization proceeds at the surface but the deposit continuously rearranges (or decomposes) to restore a certain fraction of the platinum sites that were used for the polymerization process. In this case, the growth rate of the deposit could still be first order in chemisorbed hexane molecules, but an additional term would appear in equations in order to represent the shape of the deposit. This can be crudely represented by a "thickness function," $\tau(T) = g^{-1}T^{x}$, whose magnitude defines the "average thickness" of the deposit in terms of molecular layers. It follows that

$$\frac{d\theta_c}{dt} = \frac{\eta k_p}{\tau(T)} (1 - \theta_c) \qquad (8)$$

and

$$\theta_i(t) \approx (1-\theta_c) = \exp(-nk_p gT^{-x}t) \qquad (9)$$

Since gT^{-x} decreases with increasing temperature, the latter equation provides simple explanation for the experimental deactivation kinetics, $\theta_i(t) = \exp(-\alpha t^n)$, where n decreased with increasing temperature. From the concentrations of uncovered platinum sites determined by CO adsorption-desorption (Section 4.7) and the temperature dependence of the C_{273}/Pt_{237} AES peak-to-peak height ratio, the magnitudes of g and x were estimated to be about 1×10^{11} and 4, respectively.

Conclusions. The structure and temperature dependence of n-hexane skeletal rearrangement was investigated near atmospheric pressure over a series of platinum single crystal surfaces with well defined surface structure and composition. Aromatization of n-hexane to benzene displayed unique structure sensitivity in which the rates and selectivities for this important reforming reaction were maximized on platinum surfaces with high concentrations of contiguous (111) microfacets. The rates of parallel isomerization, C_5-cyclization, and hydrogenolysis reactions displayed little dependence on platinum surface structure. the distribution of hydrogenolysis products was influenced markedly by terrace structure. Platinum surfaces with (100) terraces favored internal C-C bond scission, whereas surfaces with (111) terraces displayed a higher selectivity for terminal hydrogenolysis.

Selectivities for n-hexane skeletal rearrangement varied markedly with temperature and hydrogen pressure and to a lesser extent with surface structure. Changes in selectivity with reaction conditions were related to a change in identity of the most abundant surface intermediate that results from a change in the surface concentration of chemisorbed hydrogen. Skeletal rearrangement was dominated by cyclic mechanisms involving both 1,5- and 1,6-ring closure. Polymerization of the adsorbed species competed with skeletal rearrangement and lead to the growth disordered carbonaceous deposits on the platinum surfaces. The primary role of these carbon deposits was that of a non-selective poison.

FIGURE CAPTIONS

Fig. 3.1. Product accumulation curves measured as a function of reaction time at 573 K for n-hexane conversion over Pt(100).

Fig. 3.2. Product accumulation curves measured as a function of reaction time at 573 K for n-hexane aromatization catalyzed over platinum single crystal surfaces.

Fig. 3.3. Product accumulation curves determined at several reaction temperatures for n-hexane aromatization catalyzed over the stepped (13,1,1) platinum surface.

Fig. 3.4. Product accumulation curves determined at several reaction temperatures for n-hexane hydrogenolysis and C_5-cyclization catalyzed over the flat (111) platinum surface.

Fig. 3.5. Arrhenius plots for n-hexane aromatization catalyzed over platinum single crystal surfaces.

Fig. 3.6. Arrhenius plot for n-hexane cyclization to methylcyclopentane catalyzed over platinum single crystal surfaces.

Fig. 3.7. Arrhenius plots for n-hexane hydrogenolysis catalyzed over platinum single crystal surfaces.

Fig. 3.8. Arrhenius plots for n-hexane isomerization to 2-methylpentane (lower frame) and 3-methylpentane (upper frame) catalyzed over platinum single crystal surfaces.

Fig. 3.9. Arrhenius plots for n-hexane reactions catalyzed over the stepped (13,1,1) platinum surface (H_2/HC = 10; P_{tot} = 220 Torr).

Fig. 3.10. Arrhenius plots for n-hexane reactions catalyzed over the flat (111) platinum surface (H_2/HC = 30; P_{tot} = 620 Torr).

Fig. 3.11. Arrhenius plots for n-hexane reactions catalyzed over the kinked (10,8,7) platinum surface (H_2/HC = 30, P_{tot} = 620 Torr).

Fig. 3.12. Order plots at 573-641 K for Pt(10,8,7) showing the dependence of n-hexane hydrogenolysis and aromatization rates on hydrogen pressure (P_{HC} = 20 Torr).

Fig. 3.13. Temperature dependence of the initial selectivities for n-hexane reactions catalyzed over Pt(111) (H_2/HC = 30, P_{tot} = 620 Torr): fractional selectivities for hydrogenolysis, isomerization (2MP + 3MP), and cyclization (MCP + Bz) are shown in the upper frame; kinetic selectivities for 2MP/3MP and Bz/MCP are shown in the lower frame.

Fig. 3.14. Temperature dependence of the initial kinetic selectivities for Bz/MCP (upper frame) and 2MP/3MP (lower frame) determined for n-hexane reactions catalyzed over platinum single crystal surfaces (H_2/HC = 10, P_{tot} = 220 Torr).

Fig. 3.15. Initial product distributions for n-hexane reactions catalyzed at 573 K over platinum single crystal surfaces (H_2/HC = 10, P_{tot} = 220 Torr).

Fig. 3.16. Initial product distributions for n-hexane reactions catalyzed at 673 K over platinum single crystal surfaces (H_2/HC = 30, P_{tot} = 620 Torr).

Fig. 3.17. Fission parameters determined as a function of reaction temperature for n-hexane hydrogenolysis catalyzed over platinum single crystal surfaces (H_2/HC = 10, P_{tot} = 220 Torr).

Fig. 3.18. Fission parameters determined as a function of reaction temperature for n-hexane hydrogenolysis catalyzed over Pt(111) showing the dependence of hydrogenolysis selectivity on hydrogen pressure (p_{HC} = 20 Torr).

Fig. 3.19. Product accumulation curves determined as a function of reaction time for n-hexane isomerization catalyzed over Pt(100) at 556 and 573 K. These curves illustrate the different deactivation behavior for the production of 2- and 3-methylpentanes.

Fig. 3.20. Temperature dependence of the C_{273}/Pt_{237} AES peak-to-peak height ratio measured following n-hexane reaction studies on platinum single crystal surfaces.

Fig. 3.21. Comparison between first order and half-order deactivation models for n-hexane hydrogenolysis and aromatization catalyzed on the kinked (10,8,7) platinum surface. Reaction rates measured as a function of reaction time, R(t), have been divided by initial rates, R_o, and plotted as a function of t (1st-order) or $t^{1/2}$ (1/2-order). The reaction temperatures were 553 K(●), 573 K (o), 623 K(▲), and 655 K(△).

Fig. 3.22. Arrhenius plot for n-hexane dehydrogenation catalyzed over platinum single crystal surfaces (H_2/HC = 10, P_{tot} = 220 Torr). The initial rates shown are lower limits to the absolute rates which could not be accurately determined due to thermodynamic constraints.

Fig. 3.23. Structure dependence of n-hexane C_5-cyclization and aromatization rates on platinum single crystal surfaces with different crystallographic orientation (at 573 K, H_2/HC = 10, P_{tot} = 220 Torr).

Fig. 3.24. Comparison of product distributions for n-hexane reactions catalyzed over Pt(111) and Pt/SiO_2 catalysts with different dispersion (5,12).

Fig. 3.25. Auger spectra recorded after n-hexane reaction studies catalyzed over Pt(100) at 573 and 673 K.

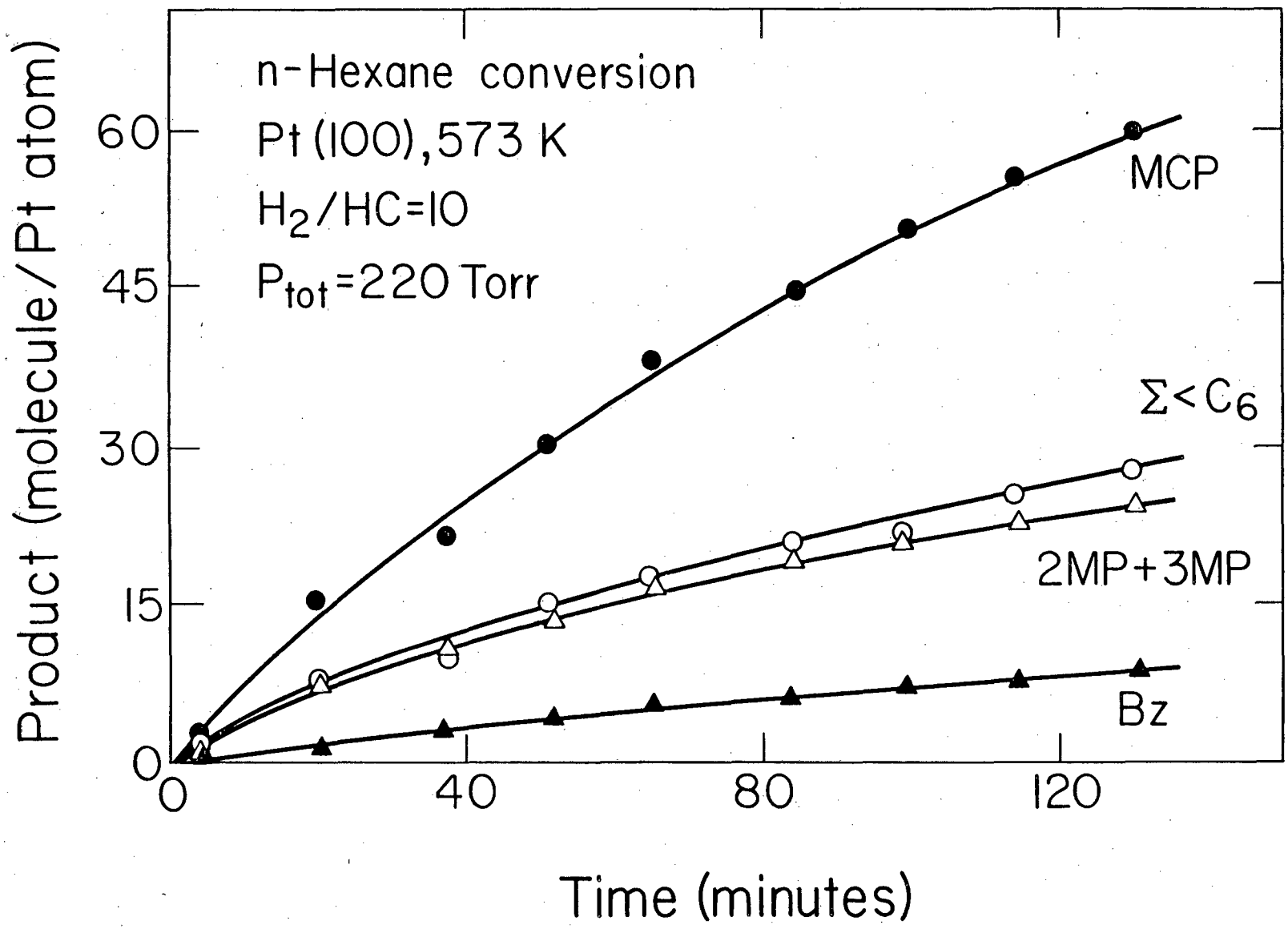

XBL 818-1094

Fig. 3.1

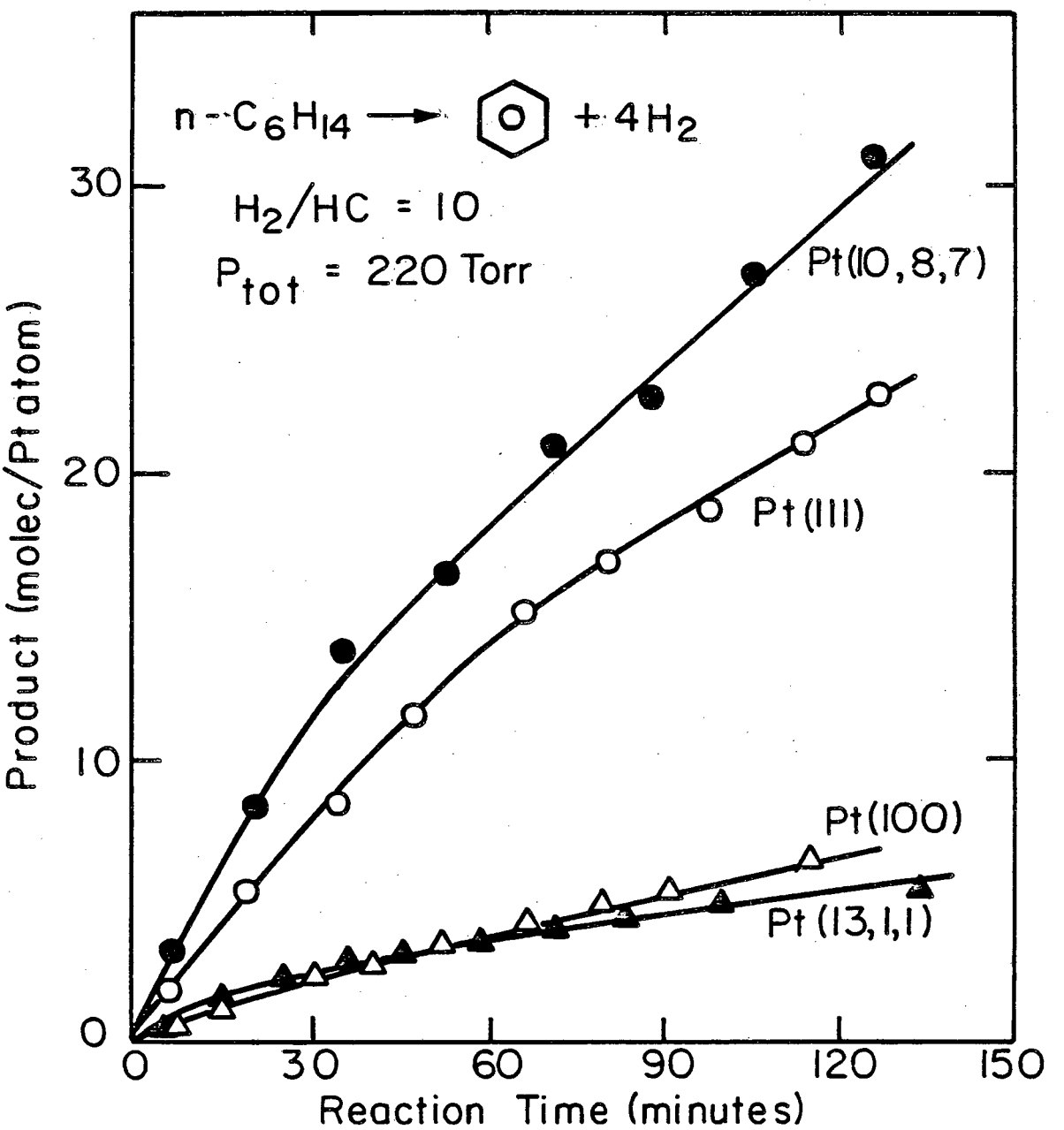

XBL 817-6138

Fig. 3.2

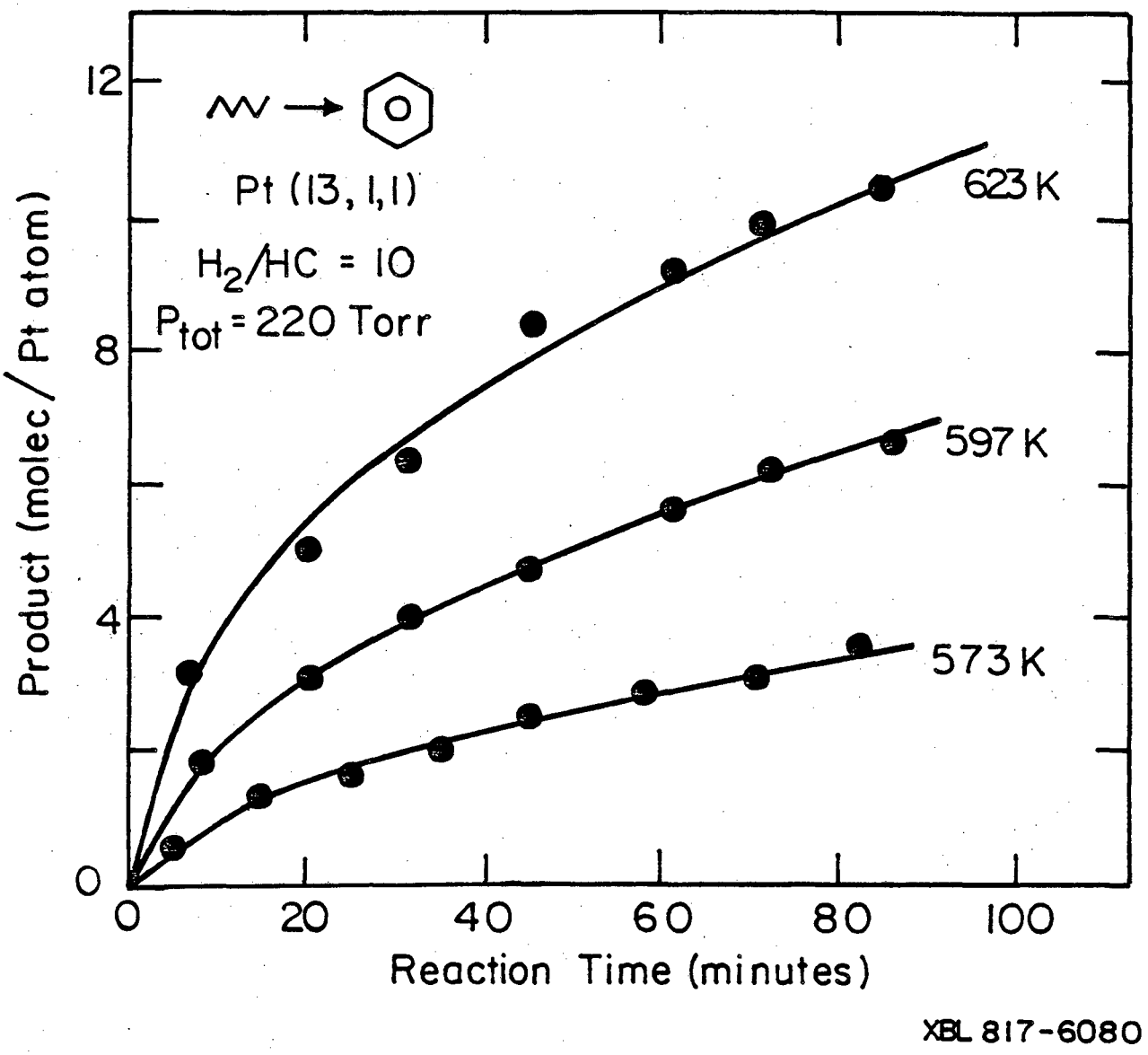
12
8
4
0
Product (molec / Pt atom)
Pt (13, 1, 1)
H_2/HC = 10
P_{tot} = 220 Torr
623 K
597 K
573 K
0
20
40
60
80
100
Reaction Time (minutes)
XBL 817-6080

Fig. 3.3

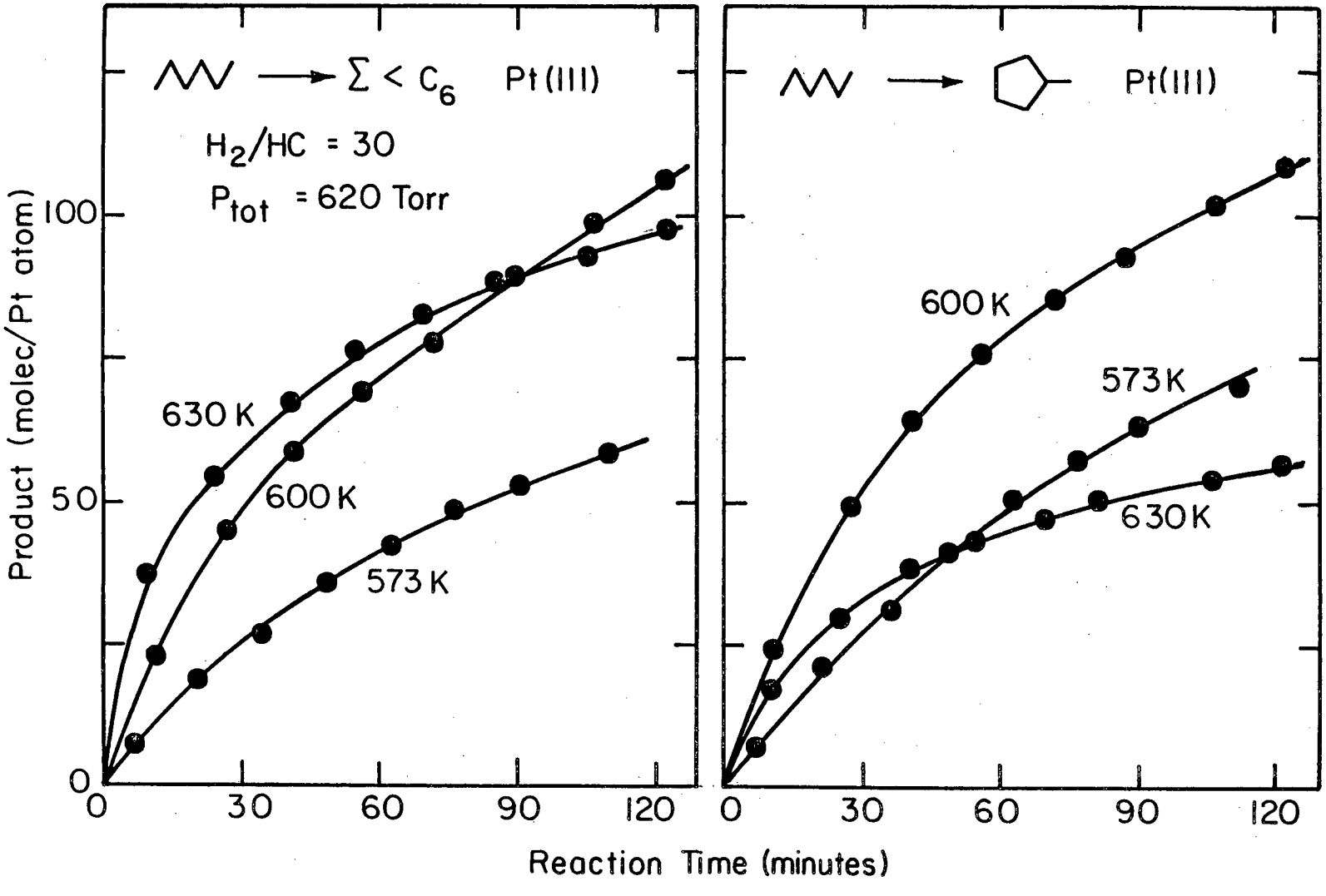

Fig. 3.4

XBL 817-6137

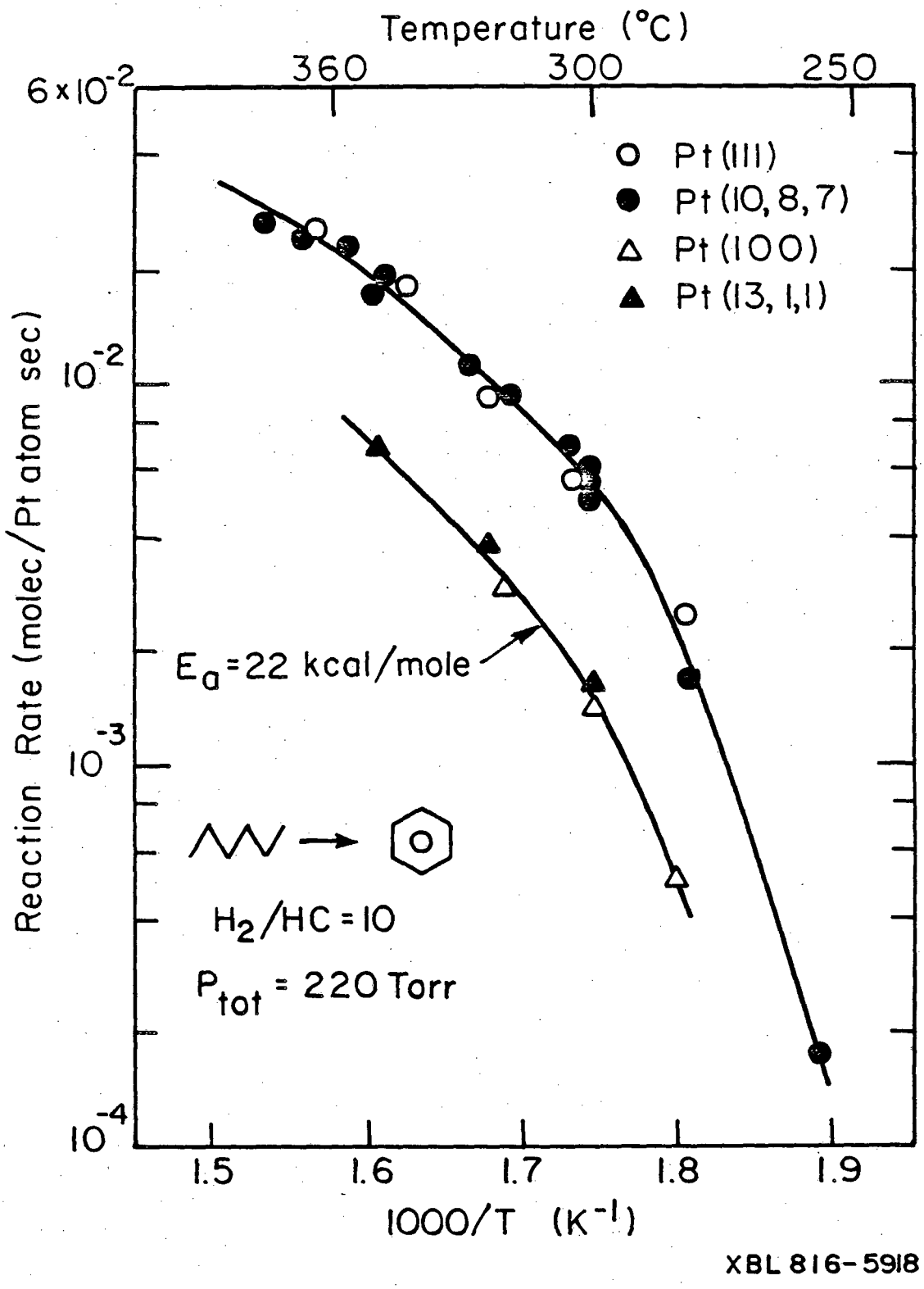
Temperature (°C)
360
300
250
6x10-2
10-2
10-3
10-4
Reaction Rate (molec/Pt atom sec)
Pt(111)
Pt(10,8,7)
Pt(100)
Pt(13,1,1)
Ea=22 kcal/mole
H2/HC=10
Ptot = 220 Torr
1.5
1.6
1.7
1.8
1.9
1000/T (K-1)
XBL 816-5918

Fig. 3.5

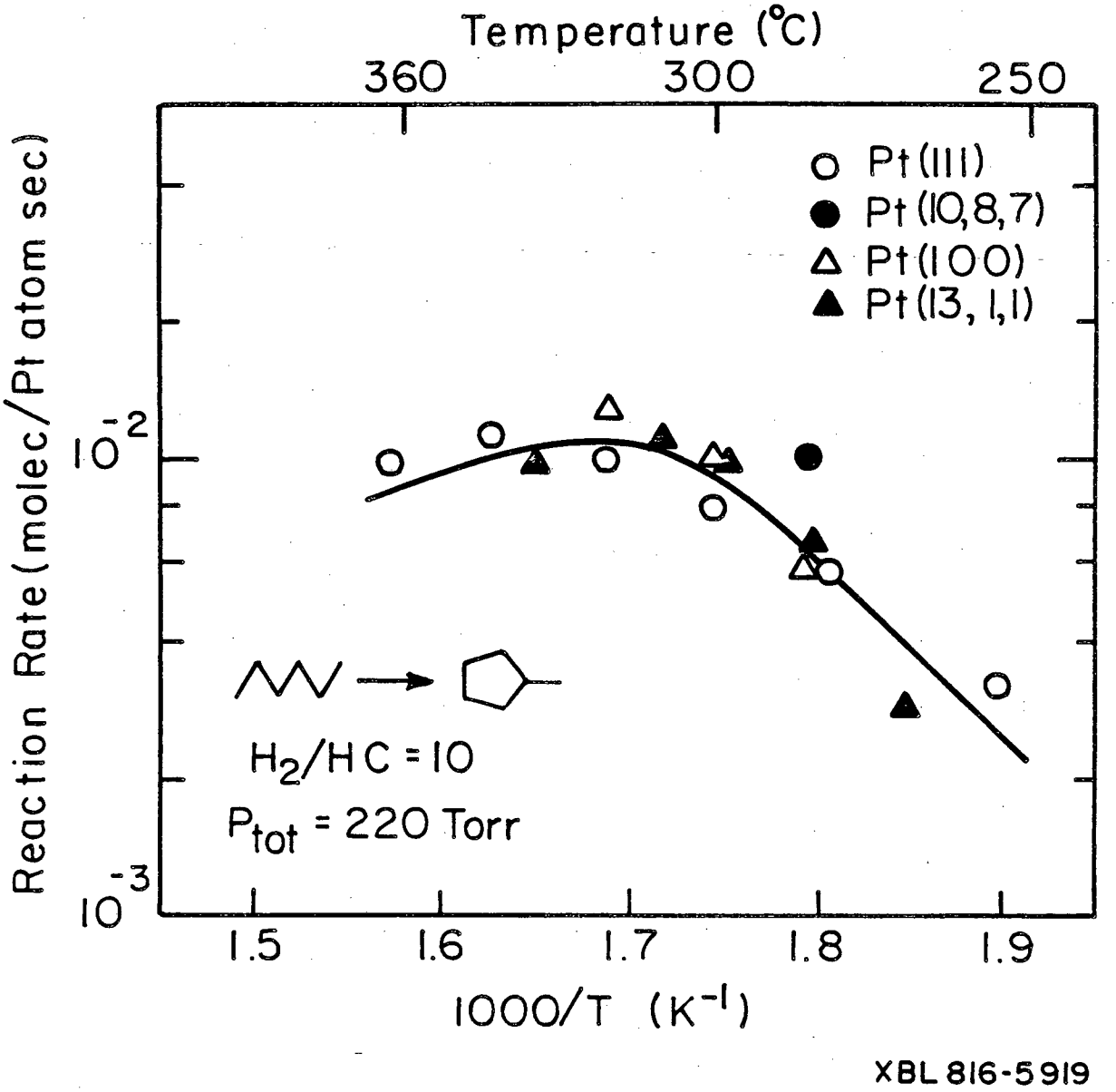
Temperature (°C)
360
300
250
Pt(111)
Pt(10,8,7)
Pt(100)
Pt(13,1,1)
Reaction Rate (molec/Pt atom sec)
10^{-2}
10^{-3}
$H_2/HC = 10$
$P_{tot} = 220$ Torr
1.5
1.6
1.7
1.8
1.9
1000/T (K^{-1})
XBL 816-5919

Fig. 3.6

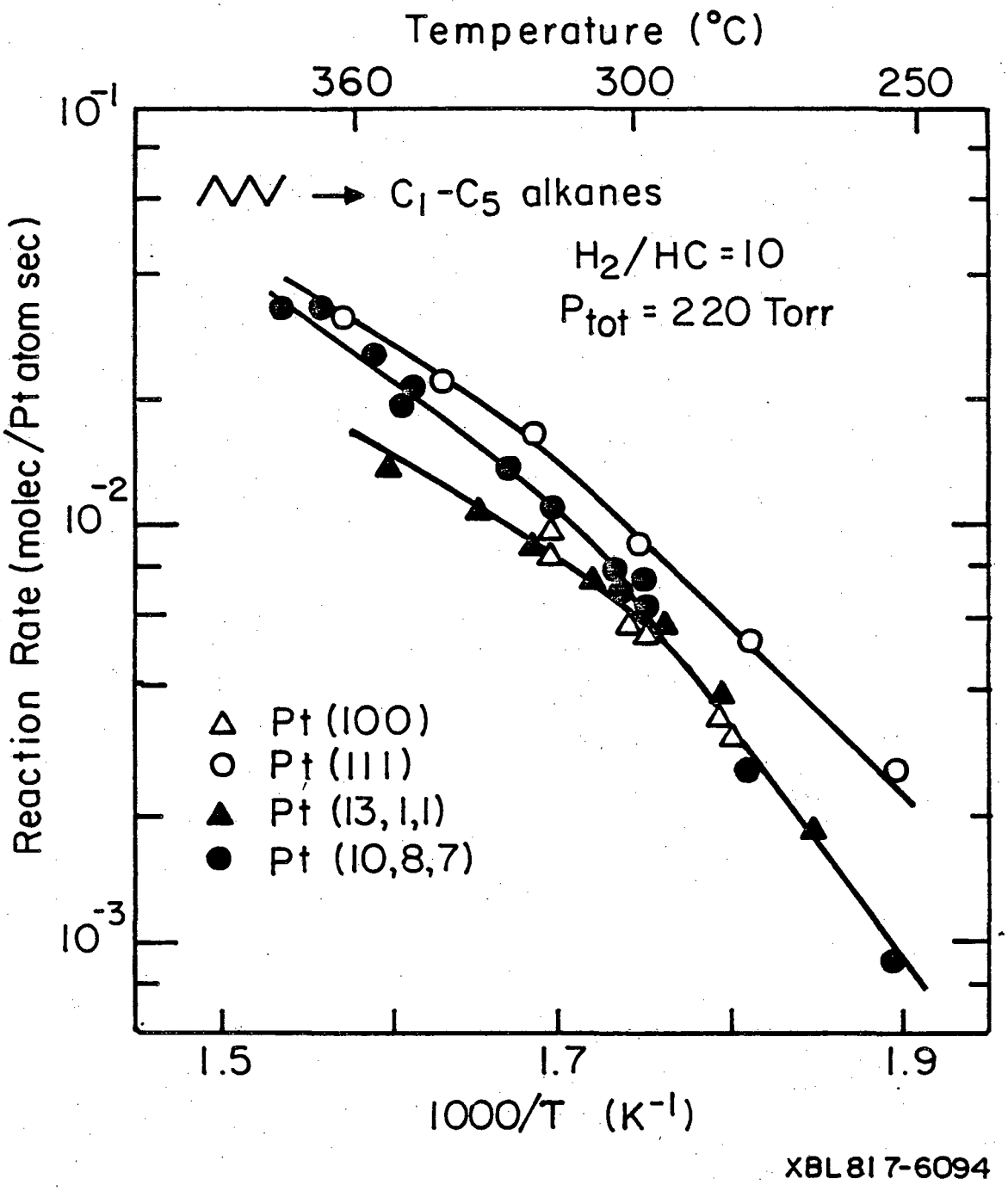
Temperature (°C)
360
300
250
10^{-1}
10^{-2}
10^{-3}
Reaction Rate (molec/Pt atom sec)
C_1-C_5 alkanes
$H_2/HC = 10$
P_{tot} = 220 Torr
Pt (100)
Pt (111)
Pt (13,1,1)
Pt (10,8,7)
1.5
1.7
1.9
1000/T (K^{-1})
XBL817-6094

Fig. 3.7

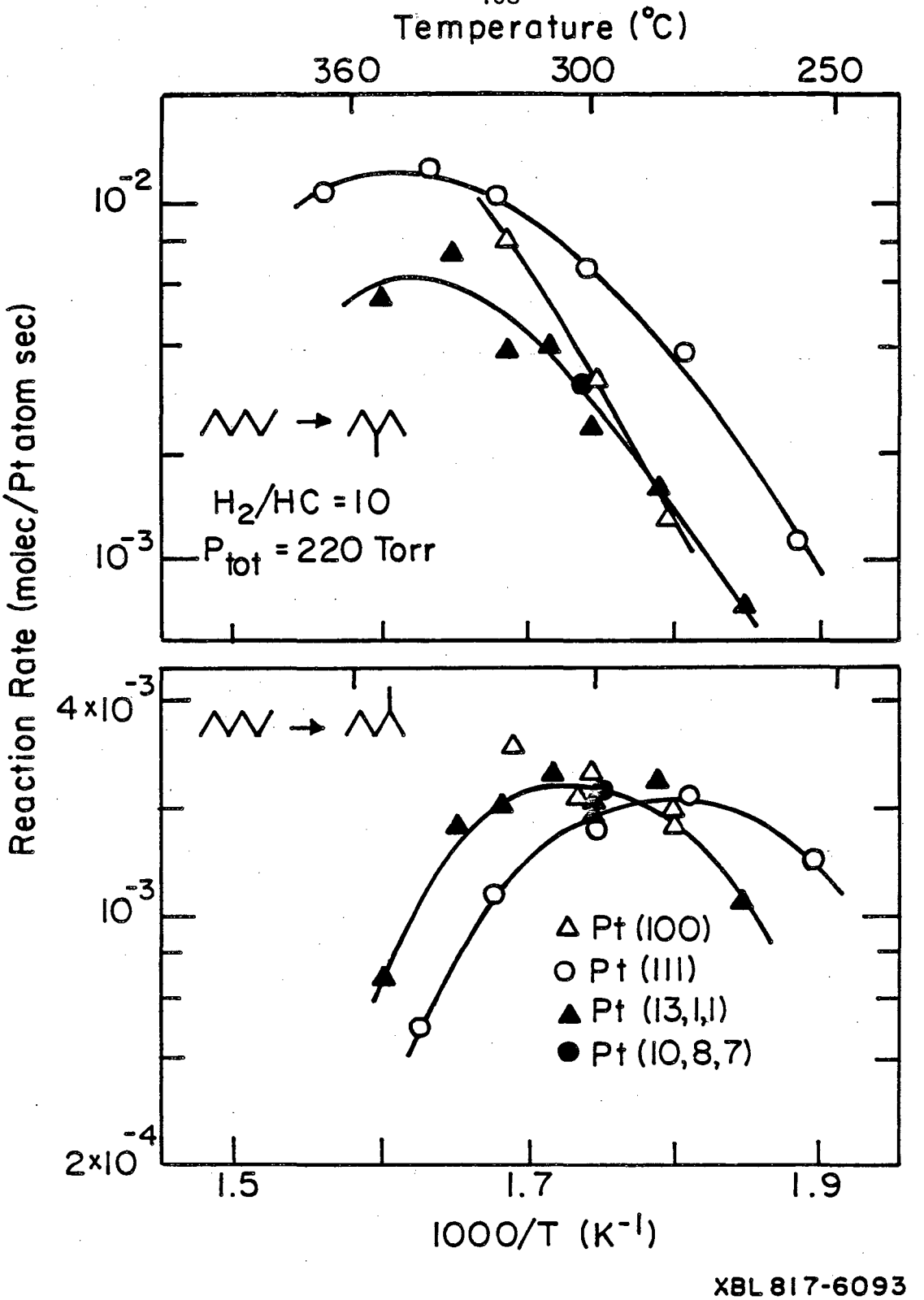
Temperature (°C)
360
300
250
Reaction Rate (molec/Pt atom sec)
10^-2
10^-3
H2/HC = 10
Ptot = 220 Torr
4x10^-3
10^-3
2x10^-4
Pt (100)
Pt (111)
Pt (13,1,1)
Pt (10,8,7)
1.5
1.7
1.9
1000/T (K^-1)
XBL 817-6093

Fig. 3.8

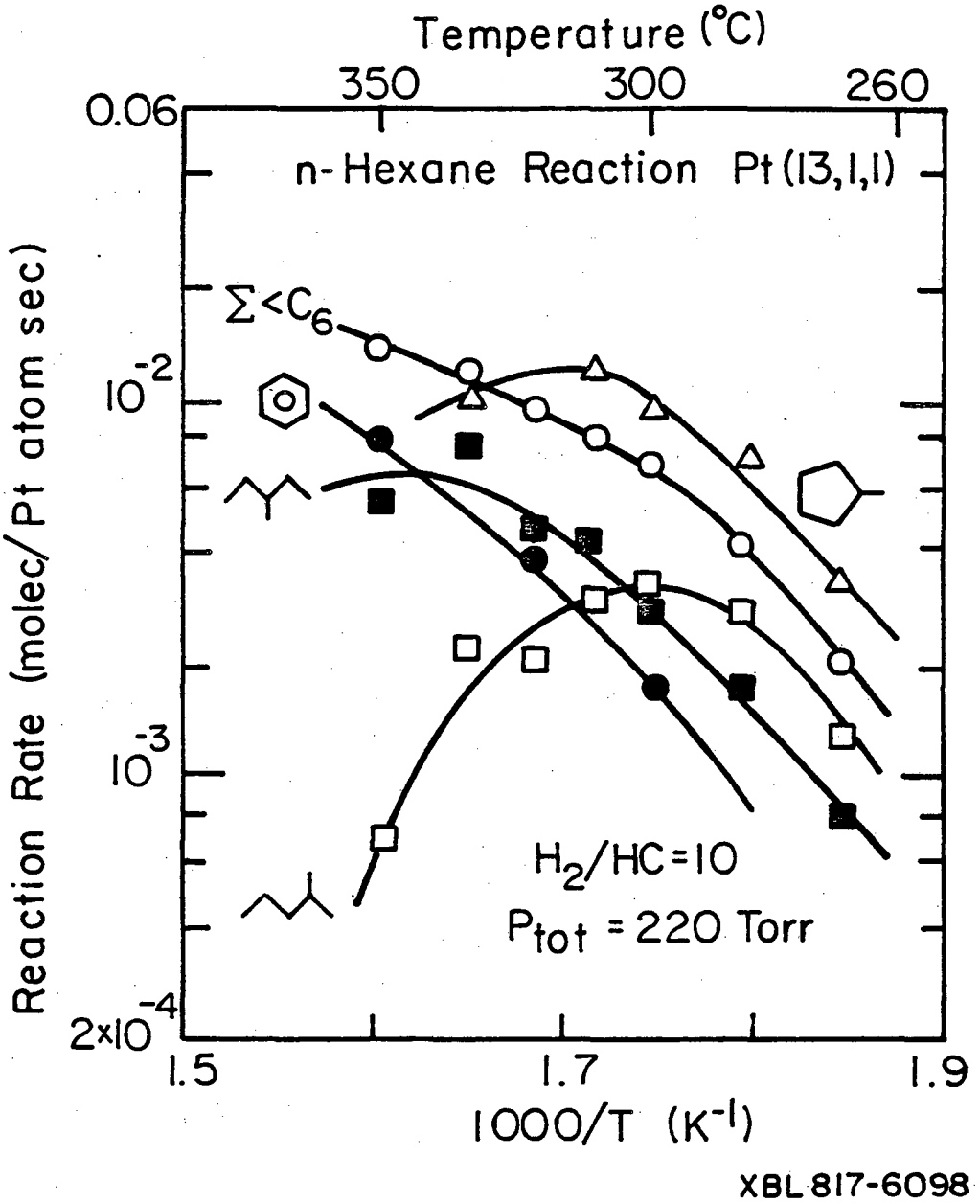
Temperature (°C)
350
300
260
0.06
n-Hexane Reaction Pt(13,1,1)
Σ<C6
10-2
10-3
2x10-4
Reaction Rate (molec/Pt atom sec)
H2/HC=10
Ptot = 220 Torr
1.5
1.7
1.9
1000/T (K-1)
XBL 817-6098

Fig. 3.9

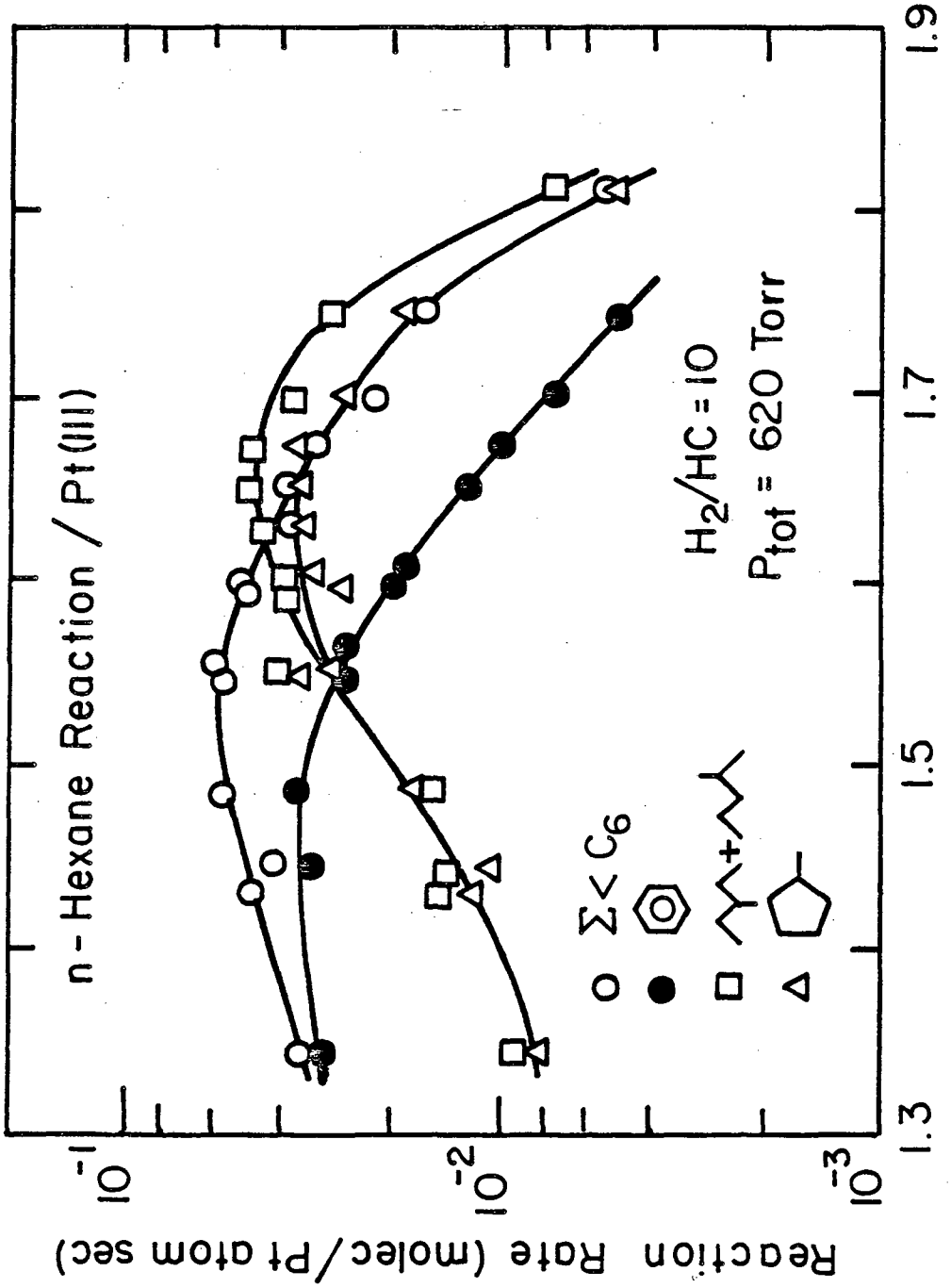

XBL 817-6097

Fig. 3.10

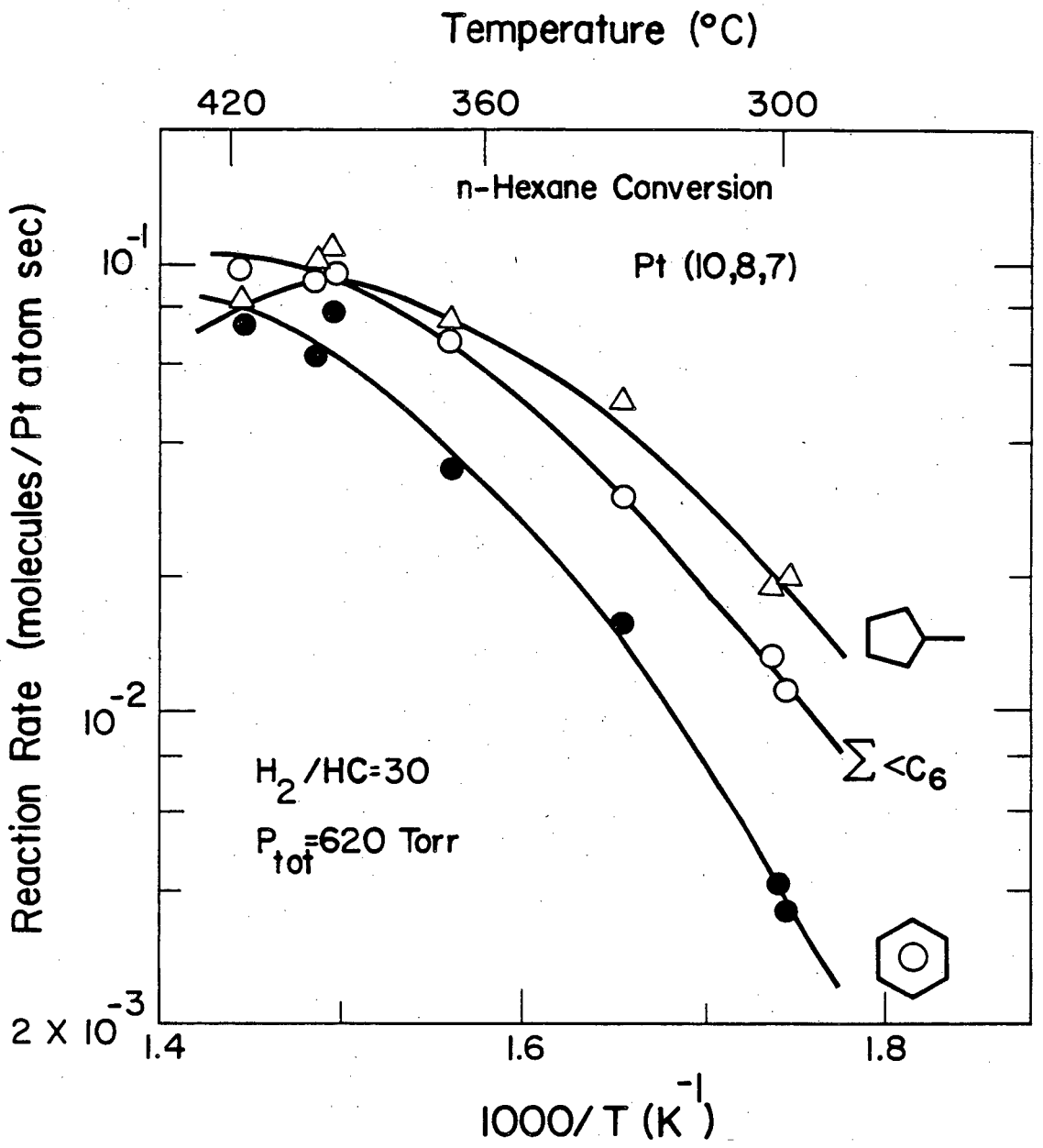

XBL 818-1099

Fig. 3.11

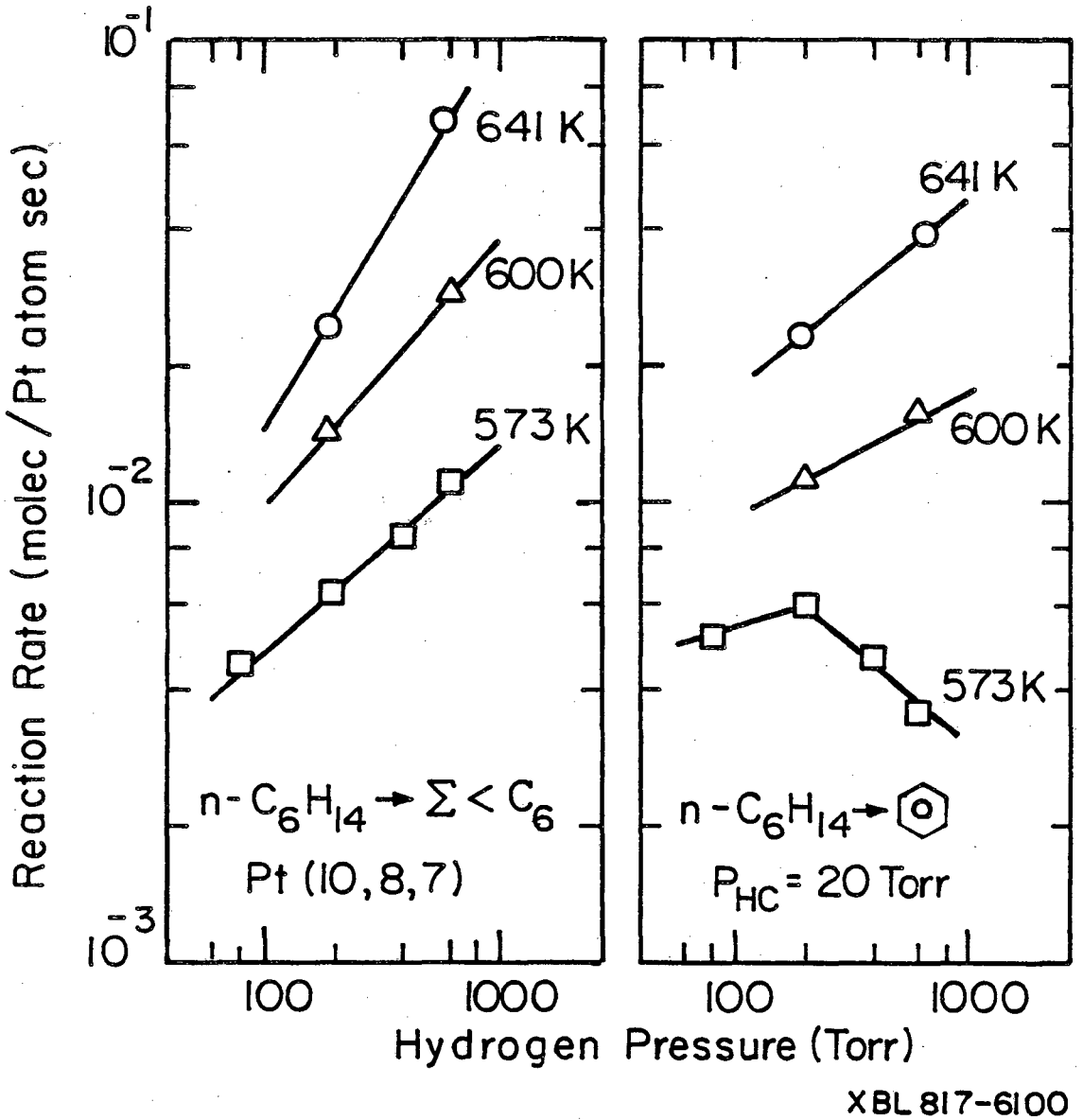
Reaction Rate (molec / Pt atom sec)
10^{-1}
10^{-2}
10^{-3}
641 K
600K
573 K
$n\text{-}C_6H_{14} \rightarrow \Sigma < C_6$
Pt (10,8,7)
641 K
600 K
573K
$n\text{-}C_6H_{14} \rightarrow$ ⬡
P_{HC} = 20 Torr
100
1000
100
1000
Hydrogen Pressure (Torr)
XBL 817-6100

Fig. 3.12

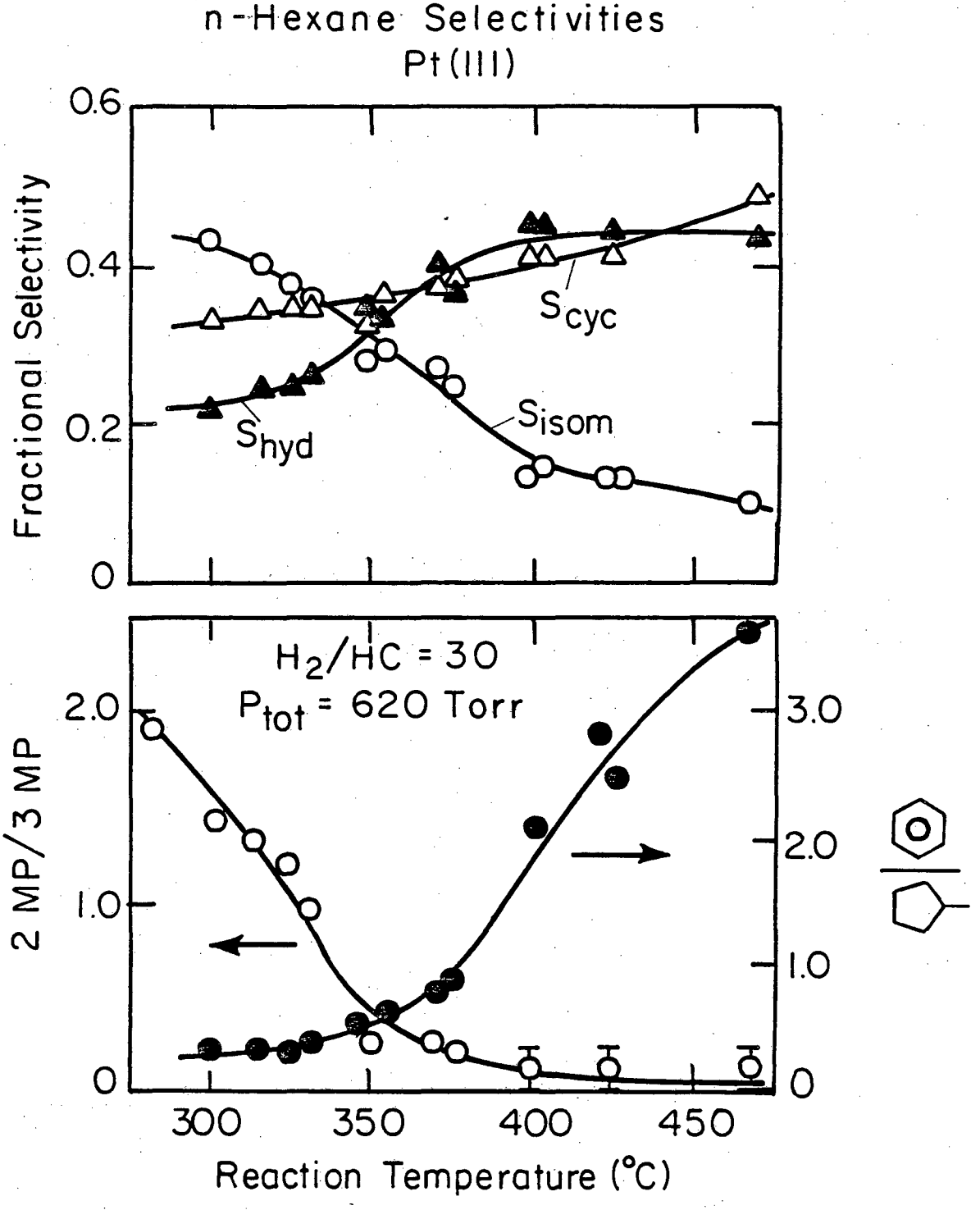
n-Hexane Selectivities
Pt(111)
Fractional Selectivity
0.6
0.4
0.2
0
S_{cyc}
S_{isom}
S_{hyd}
$H_2/HC = 30$
$P_{tot} = 620$ Torr
2 MP/3 MP
2.0
1.0
0
3.0
2.0
1.0
0
300
350
400
450
Reaction Temperature (°C)
XBL 816-5914

Fig. 3.13

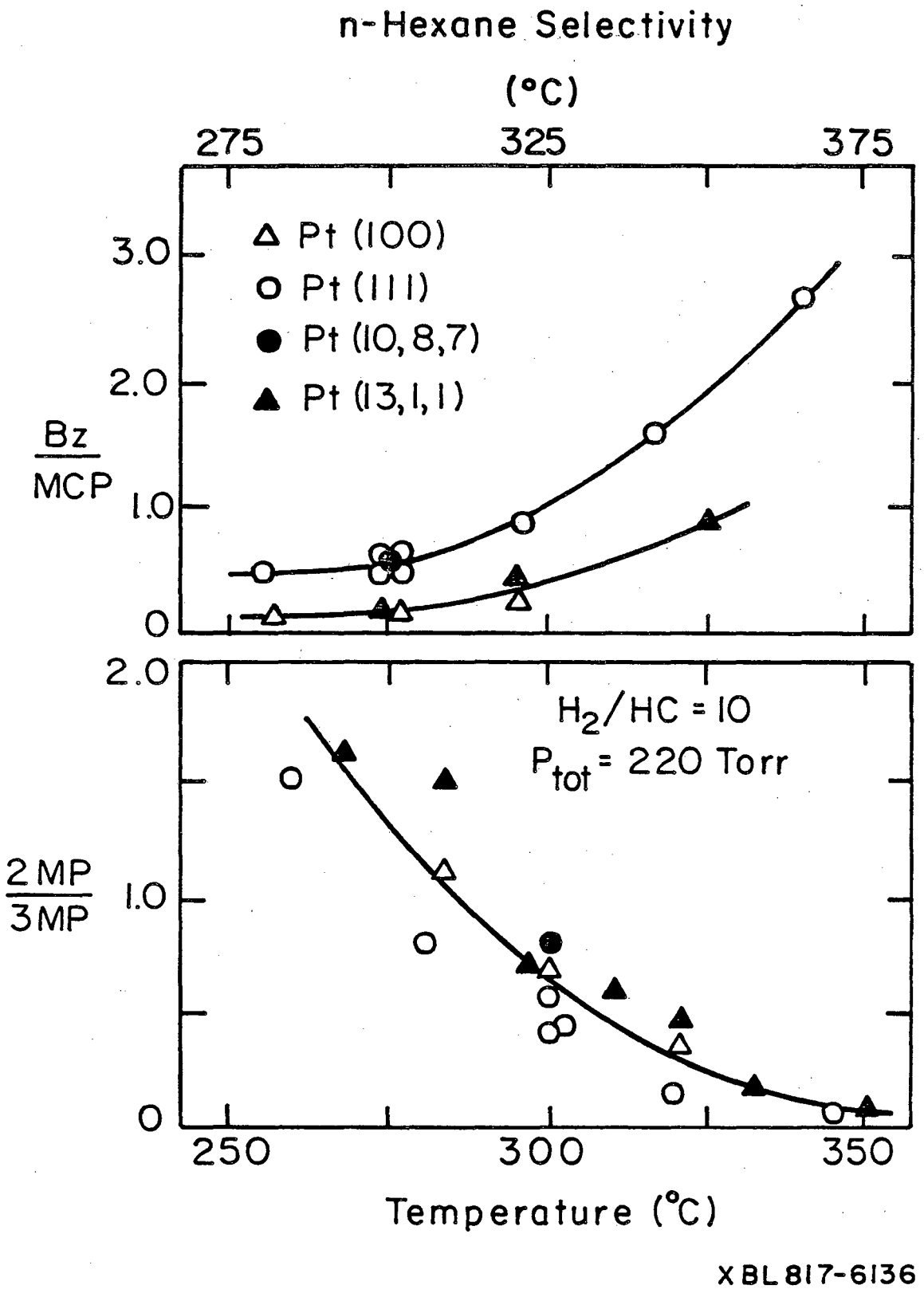
n-Hexane Selectivity
(°C)
275
325
375
Pt (100)
Pt (111)
Pt (10,8,7)
Pt (13,1,1)
3.0
2.0
1.0
0
Bz/MCP
H2/HC = 10
Ptot = 220 Torr
2MP/3MP
250
300
350
Temperature (°C)
XBL817-6136

Fig. 3.14

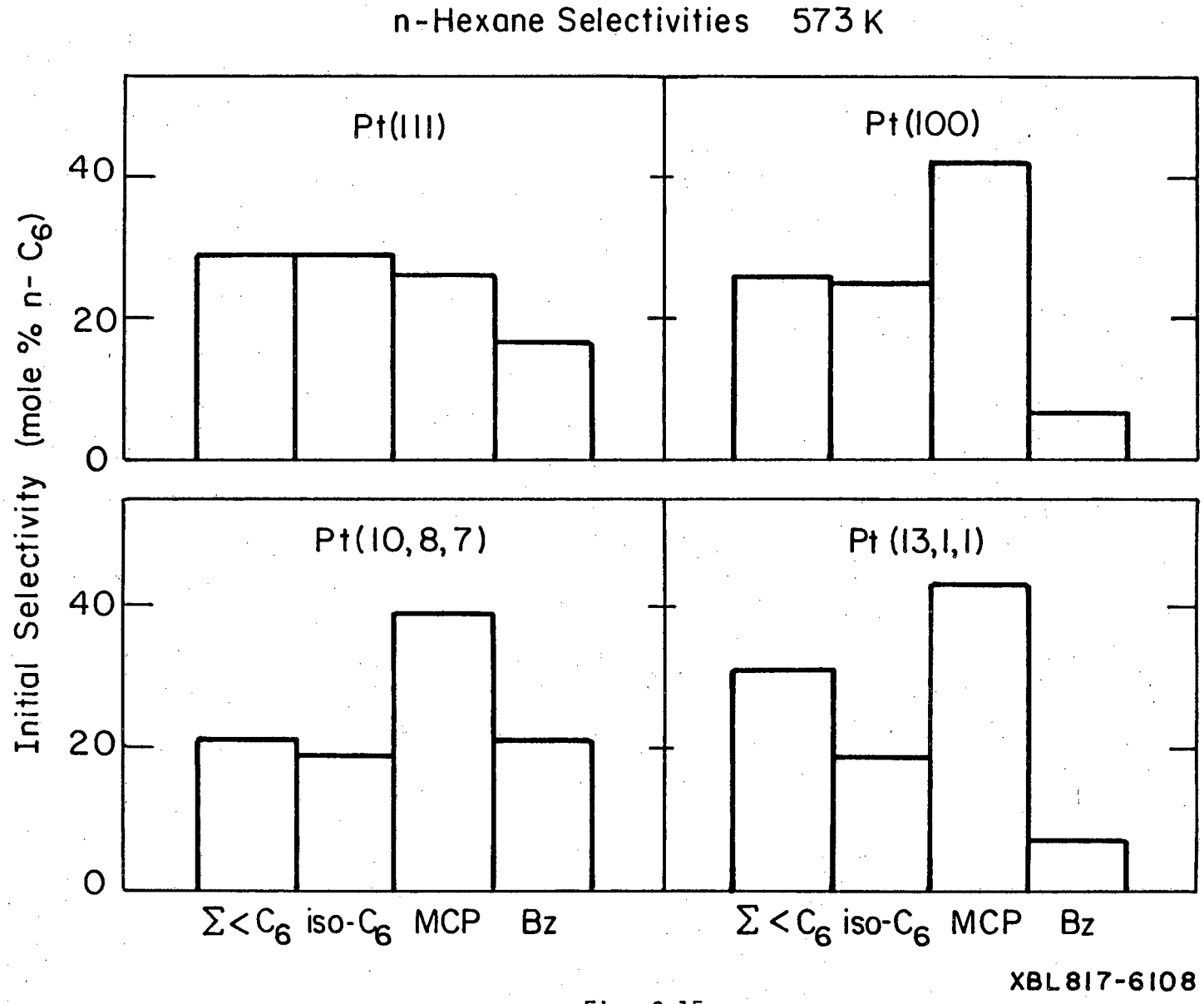
n-Hexane Selectivities 573 K
Pt(111)
Pt(100)
Pt(10,8,7)
Pt (13,1,1)
Initial Selectivity (mole % n- C6)
40
20
0
Σ<C6 iso-C6 MCP Bz
XBL817-6108

Fig. 3.15

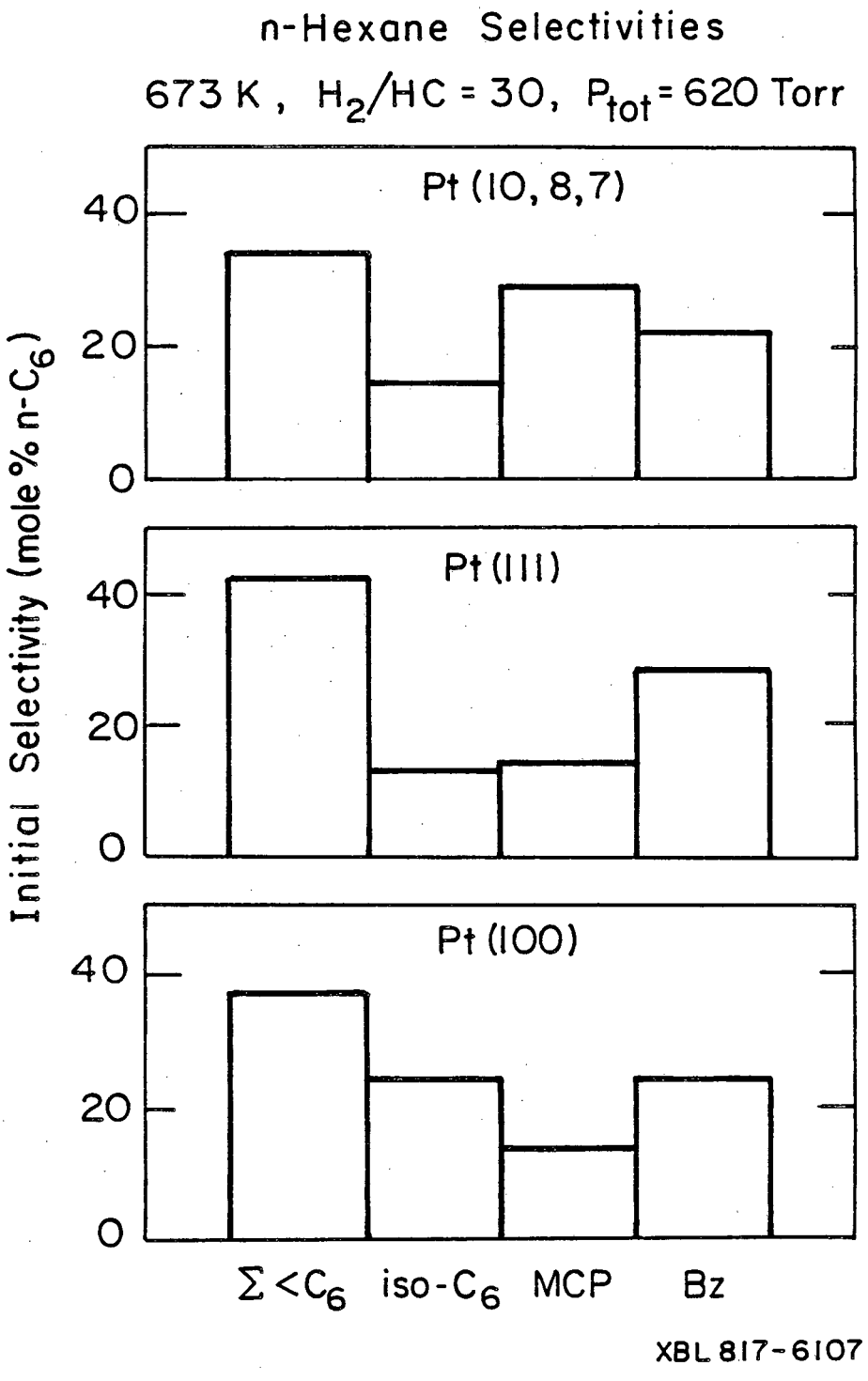
n-Hexane Selectivities
673 K, H_2/HC = 30, P_{tot} = 620 Torr
Pt (10, 8, 7)
Pt (111)
Pt (100)
Initial Selectivity (mole % n-C_6)
40
20
0
$\Sigma < C_6$
iso-C_6
MCP
Bz
XBL 817-6107

Fig. 3.16

Structure Sensitivity of n-Hexane Hydrogenolysis Selectivity

$H_2/HC = 10$, $P_{tot} = 220$ Torr

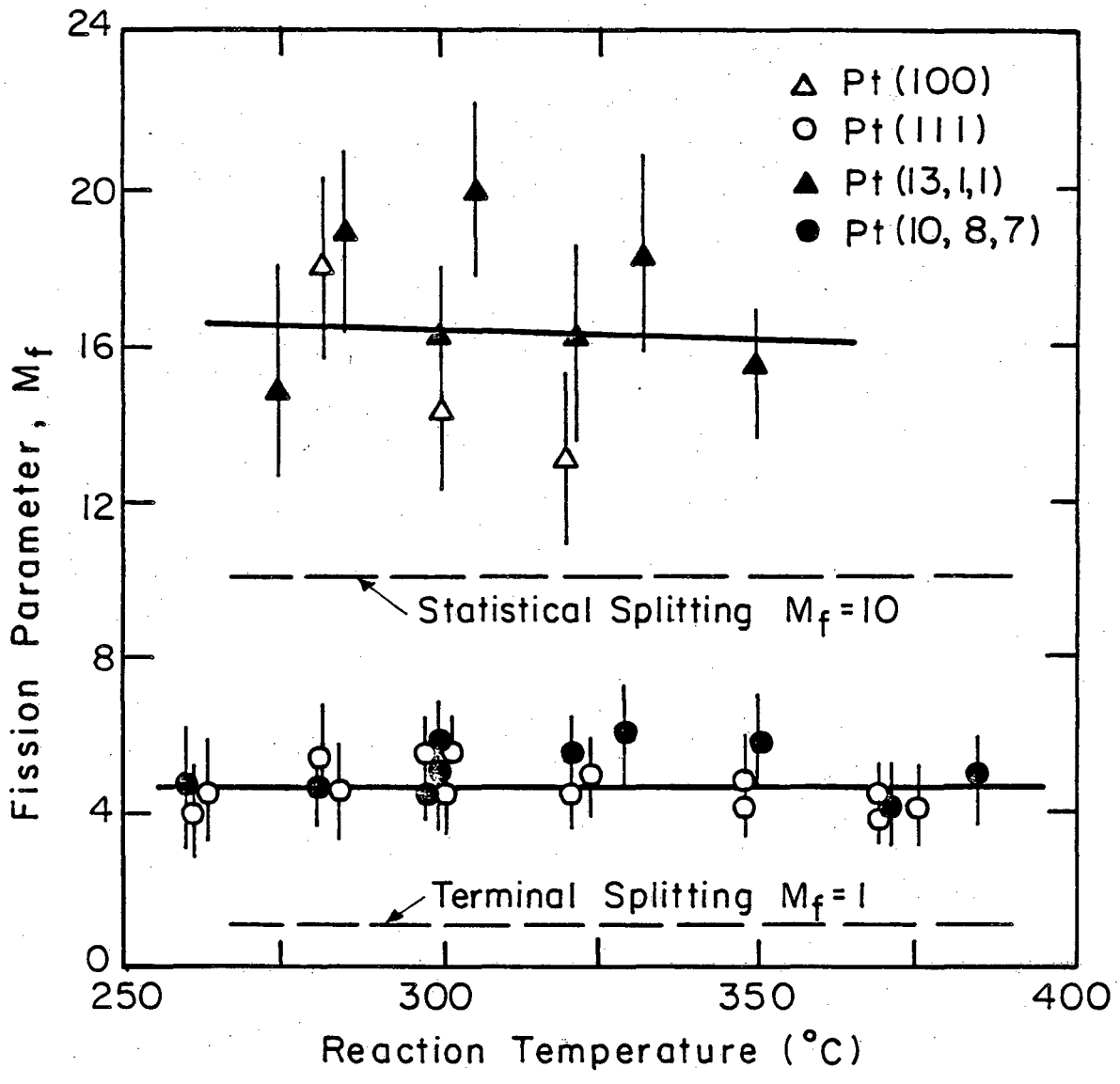

Fig. 3.17

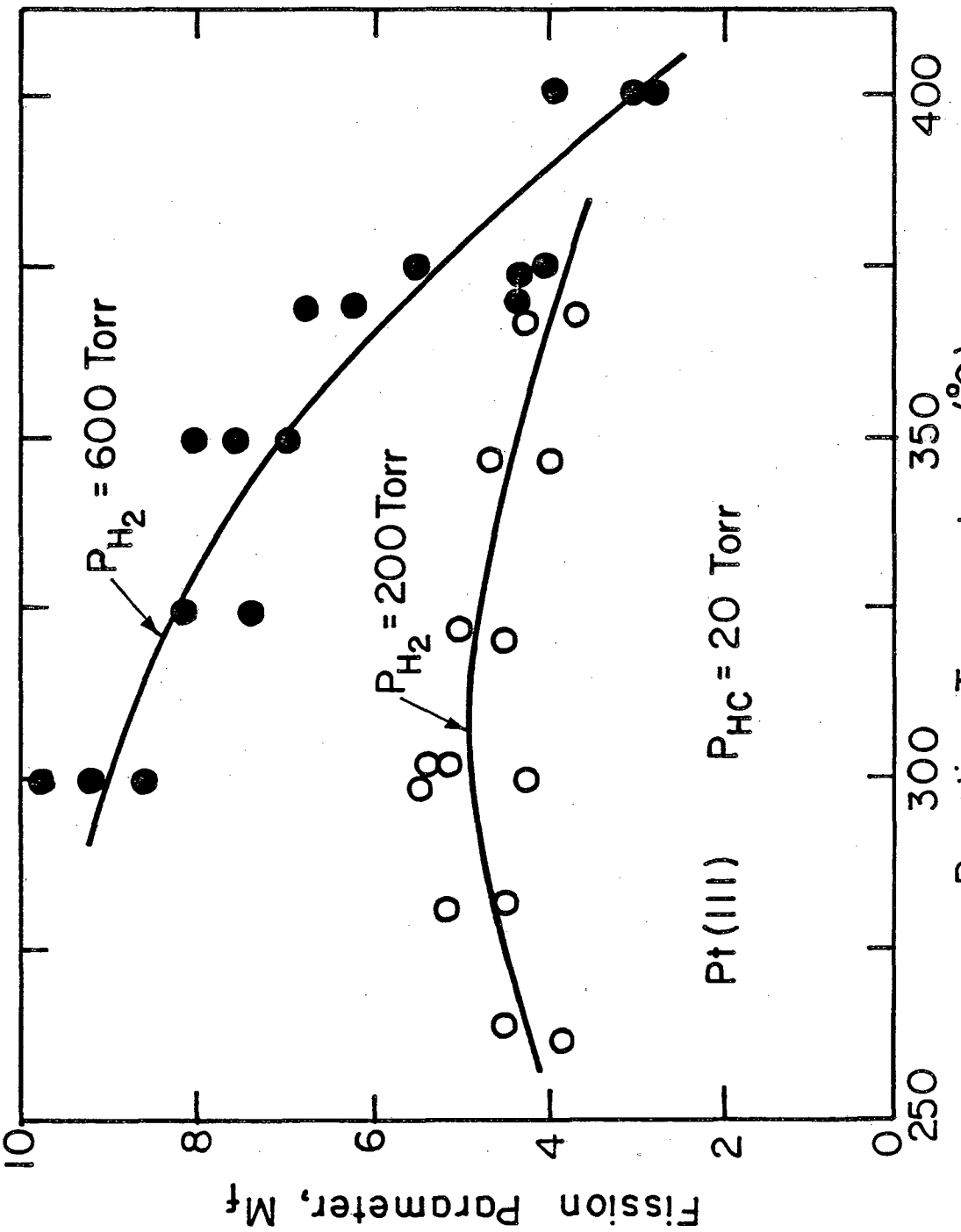

XBL817-6082

Fig. 3.18

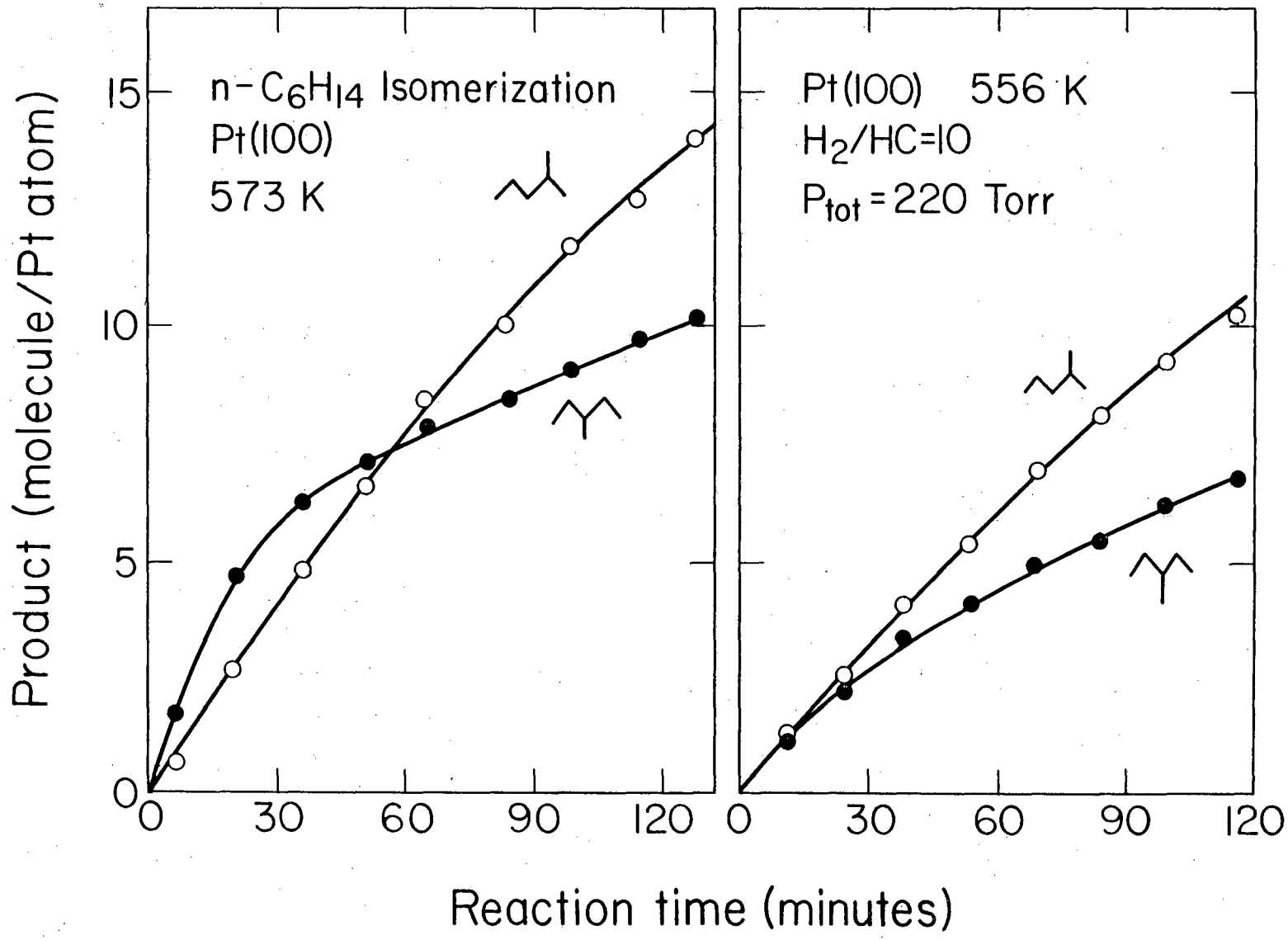

Fig. 3.19

XBL 818-1103

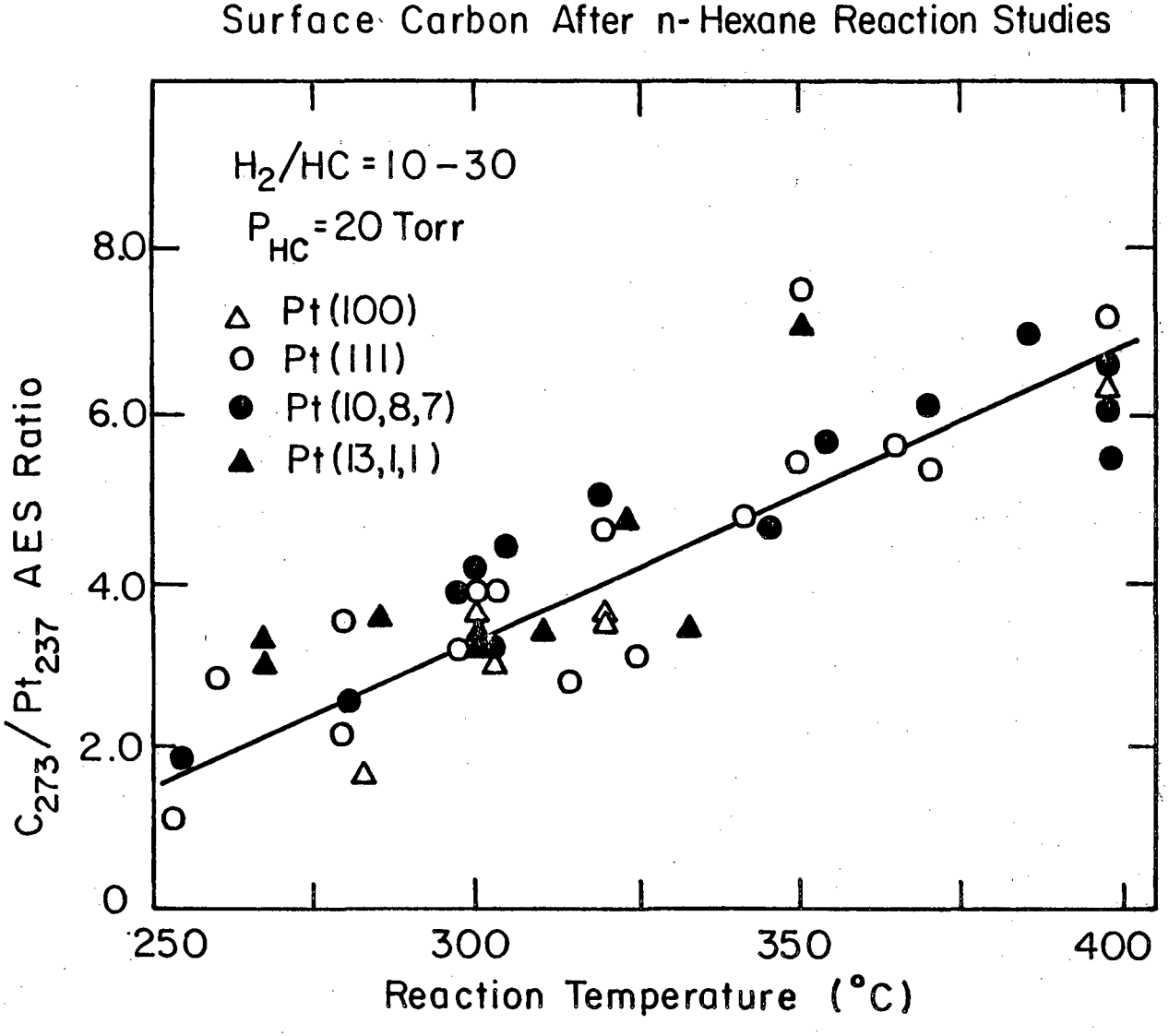

Fig. 3.20 XBL 817-6119

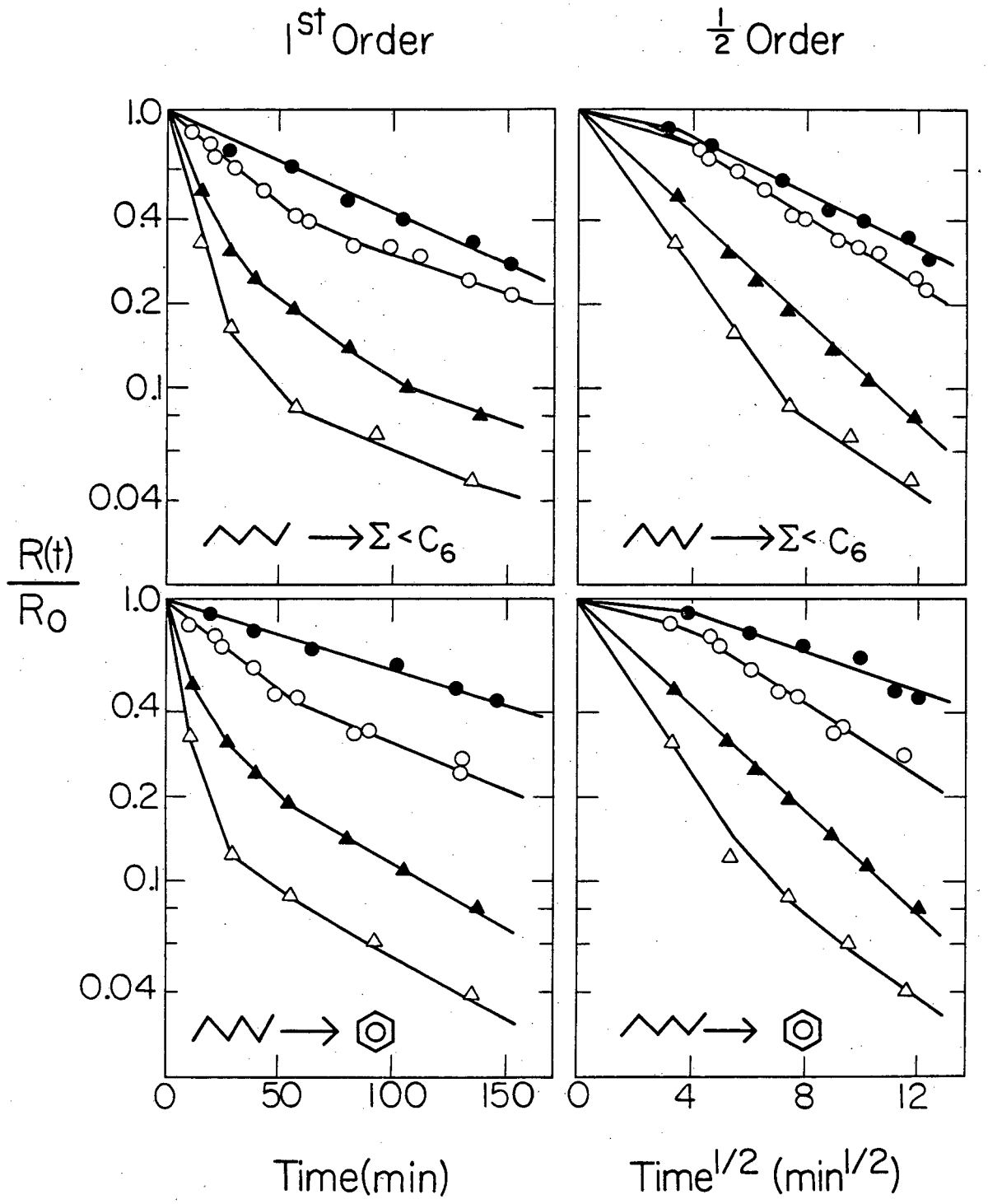
1st Order
1/2 Order
R(t)/R0
1.0
0.4
0.2
0.1
0.04
→Σ<C6
→Σ<C6
0
50
100
150
4
8
12
Time(min)
Time1/2 (min1/2)
XBL 818-1108

Fig. 3.21

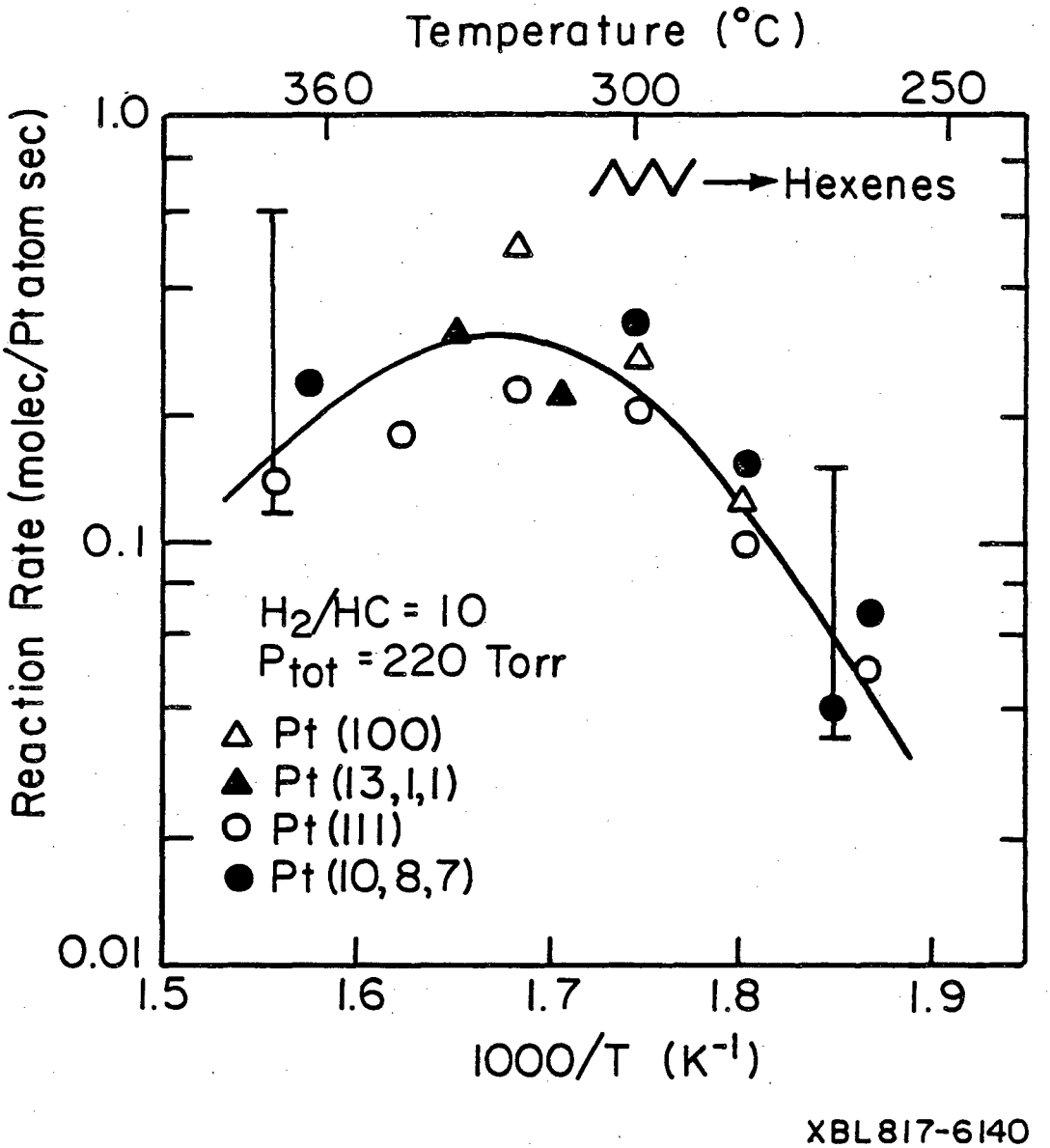
Temperature (°C)
360
300
250
1.0
0.1
0.01
Reaction Rate (molec/Pt atom sec)
Hexenes
H2/HC = 10
Ptot = 220 Torr
Pt (100)
Pt (13,1,1)
Pt (111)
Pt (10,8,7)
1.5
1.6
1.7
1.8
1.9
1000/T (K-1)
XBL817-6140

Fig. 3.22

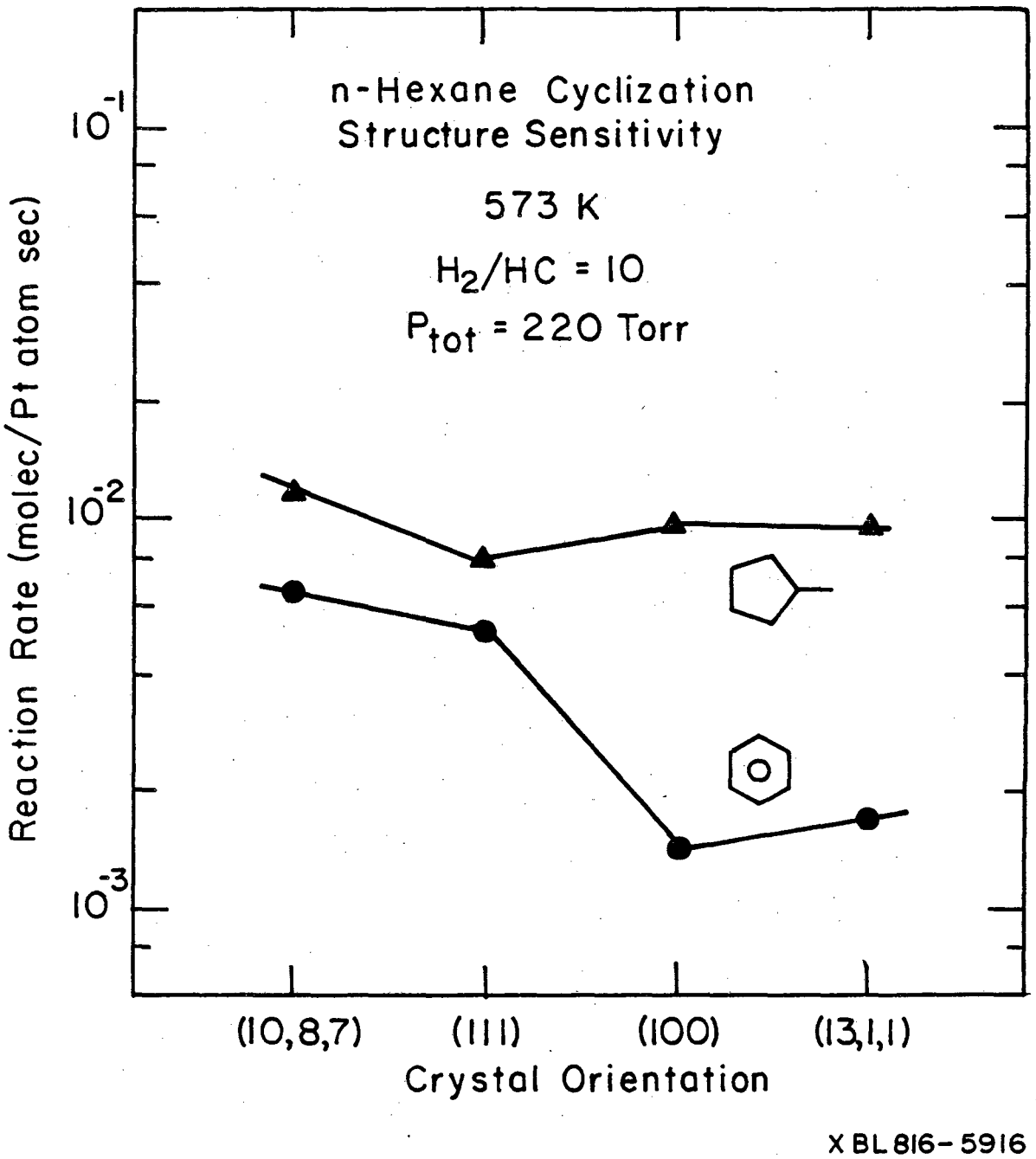
n-Hexane Cyclization
Structure Sensitivity
573 K
$H_2/HC = 10$
$P_{tot} = 220$ Torr
10^{-1}
10^{-2}
10^{-3}
Reaction Rate (molec/Pt atom sec)
(10,8,7)
(111)
(100)
(13,1,1)
Crystal Orientation
XBL816-5916

Fig. 3.23

Comparison between model and practical catalysts for n-hexane conversion at 300° C and 1 atm.

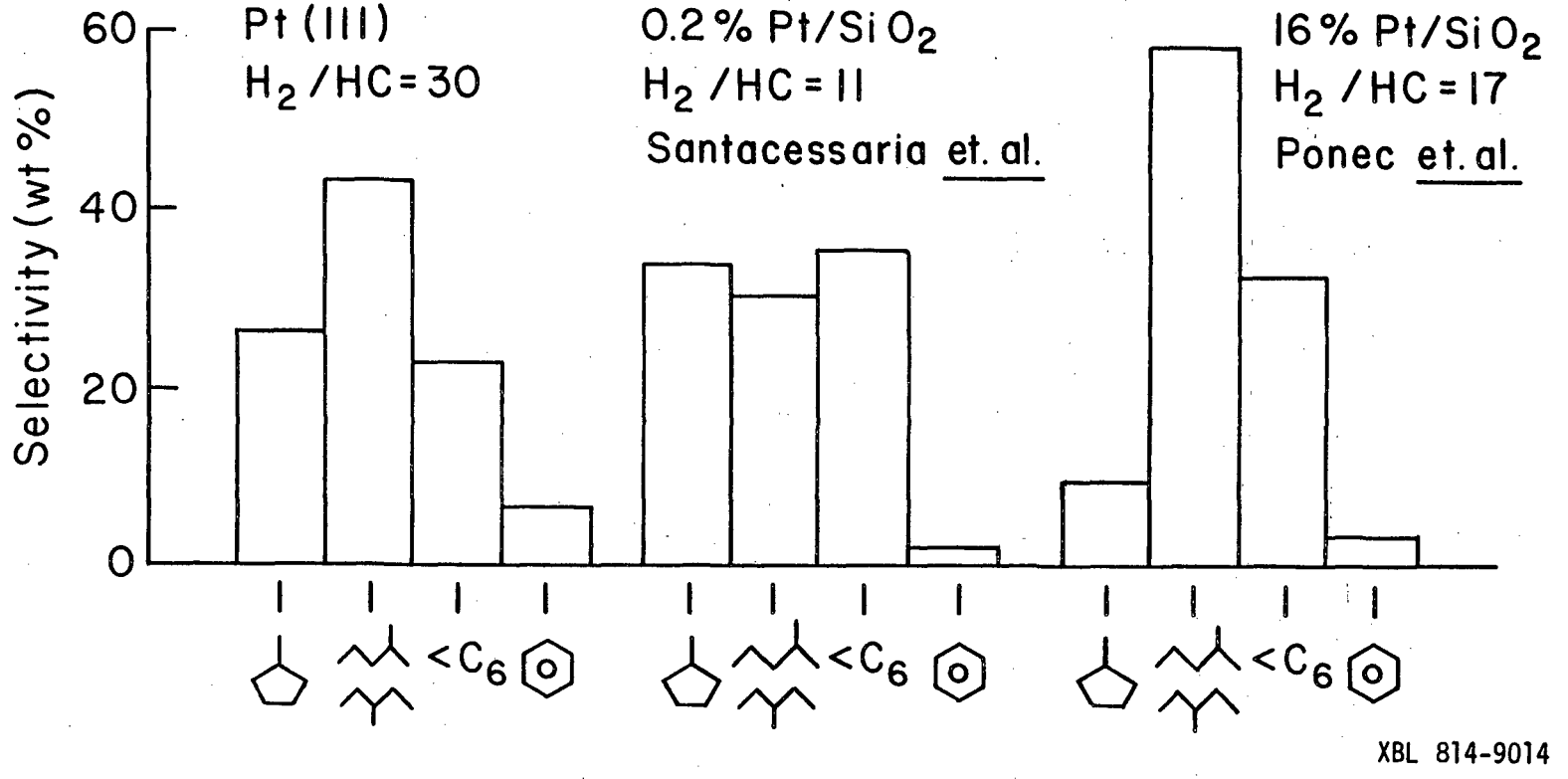

Fig. 3.24

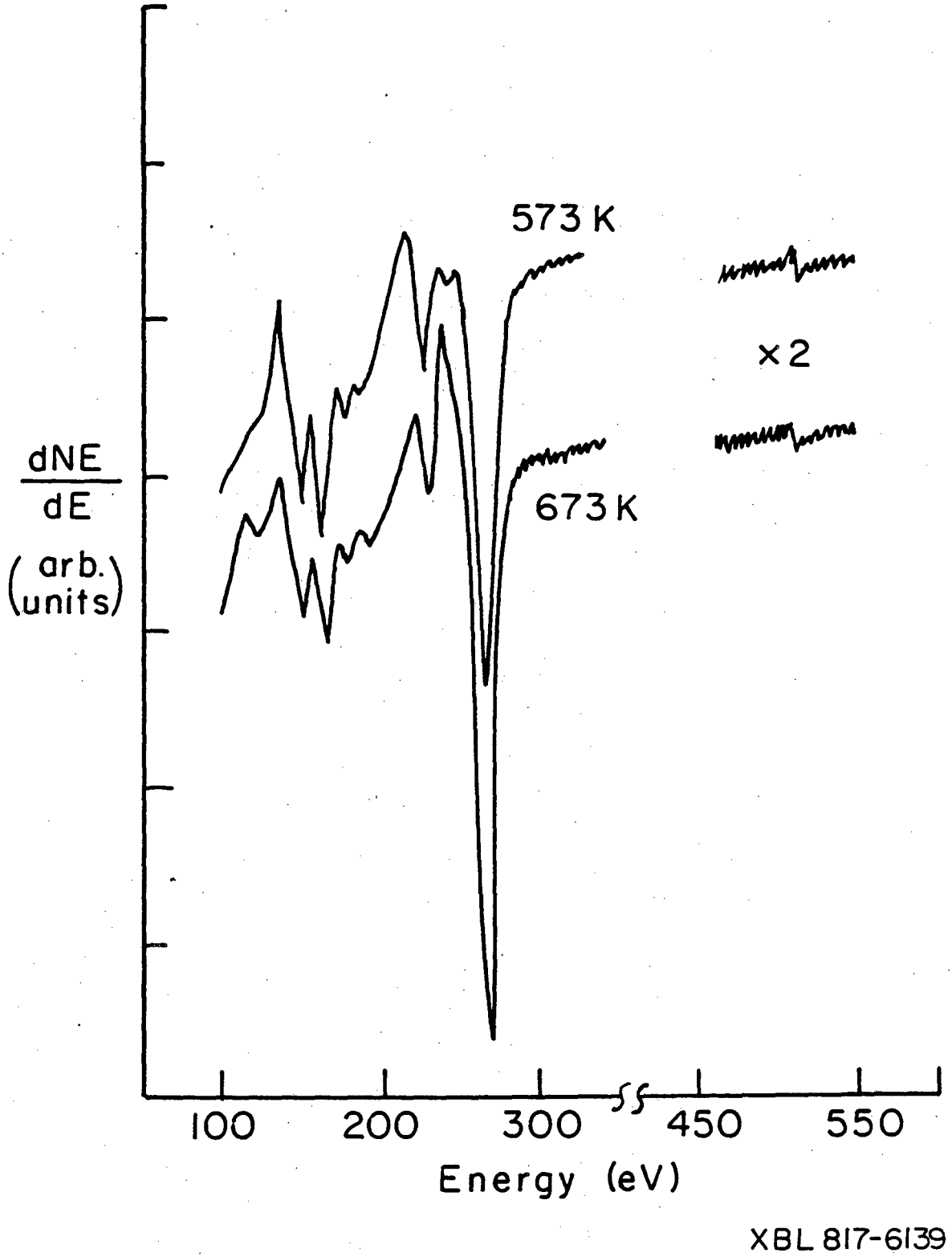
573 K
673 K
×2
dNE/dE (arb. units)
100
200
300
450
550
Energy (eV)
XBL 817-6139

Fig. 3.25

3.2. Structure and Temperature Dependence of n-Butane, Isobutane, and Neopentane Skeletal Rearrangement Catalyzed on Platinum Single Crystal Surfaces

3.2.1. Background

Bond-shift isomerization of C_4-alkanes is perhaps the simplest class of metal-catalyzed hydrocarbon skeletal rearrangement reactions. Among all Group VIII metals, platinum is a uniquely selective catalyst for these intrigueing, intramolecular (21) rearrangements (33). The extraordinary catalytic behavior of platinum has been attributed to several factors including the d-spacing of the metal (62) and the "orbital occupancy" of the almost-filled platinum d-bands which allows for easy promotion of d electrons into higher energy electronic states (63,64). A more complete understanding of this reaction chemistry at a predictive level will require detailed information about the structure sensitivity of the reaction pathway on an atomic scale that may serve as a basis for further theoretical analysis. Unfortunately, all previous investigations of metal-catalyzed isomerization reactions have been carried out using practical catalysts (i.e., films, powders, and supported catalysts) where the surface structure was heterogeneous and the surface composition was not known. To circumvent these difficulties surface analysis techniques have been developed in this laboratory (Chapter 2) which permit the kinetics of catalyzed reactions to be investigated on small area metal single crystal surfaces that possess well-defined atomic structure and surface composition. This section describes studies of n-butane, isobutane, and neopentane skeletal rearrangement reactions catalyzed on a series of initially

clean platinum single crystal surfaces with variable terrace, step, and kink structures. The studies were carried out near atmospheric pressure at temperatures between 540 and 640 K. We have observed that the flat (100) and stepped (13,1,1) platinum surfaces that contain high concentrations of contiguous (100) microfacets possess an exceptional ability to catalyze bond shift rearrangement in simple alkanes. The rates of competing hydrogenolysis reactions that involve C-C bond rupture displayed less dependence on surface structure, although the hydrogenolysis product distributions varied markedly with terrace structure.

3.2.2. Results

Isobutane Isomerization, Dehydrogenation, and Hydrogenolysis. The isomerization, dehydrogenation, and hydrogenolysis of isobutane were investigated over the flat (100) and (111), stepped (13,1,1), and kinked (10,8,7) platinum surfaces at temperatures between 540 and 640 K. Standard pressures used for these reactions were 20 Torr isobutane and 200 Torr hydrogen. Product accumulation curves determined as a function of time for isobutane isomerization and hydrogenolysis catalyzed at 573 K are compared for the four platinum surfaces in Fig. 3.26. The rate of reaction at any time is given by the slope of the product accumulation curve at that time. Initial reaction rates and fractional isomerization selectivities calculated from these data are summarized together with carbon coverages determined by AES following the reactions in Table 3.5. Hydrogenolysis and isomerization both displayed significant structure sensitivity.

Table 3.5. Initial reaction rates,, selectivities, and carbon coverages determined for isobutane reactions catalyzed at 573 K over Pt(100), Pt(111), Pt(13,1,1), and Pt(10,8,7) (a).

Catalyst	Initial Rates at 573 K (molec./Pt atom sec) (±20 percent)			Activation Energy (kcal/mole)		S_{isom} (b) (mole percent)	C/Pt (c) (±25 percent)
	Hydrog.	Isom.	Dehydrog.	Hydrog.	Isom.		
Pt(100)	0.0047	0.22	$\gtrsim$0.45	35	15	98	1.1
Pt(111)	0.0036	0.032	$\gtrsim$0.40	--	--	90	1.5
Pt(13,1,1)	0.0055	0.20	$\gtrsim$0.40	--	--	97	1.2
Pt(10,8,7)	0.014	0.060	$\gtrsim$0.90	16	13	81	1.4

(a) $H_2/HC = 10$, $P_{tot} = 220$ Torr.

(b) $S_{isom.} = R_{isom}/(R_{isom.} + R_{hydrog.})$.

(c) Carbon atoms per surface Pt atom.

Table 3.6. Summary of carbon coverages and deactivation-order parameters (a) for isobutane reactions catalyzed over Pt(10,8,7) and Pt(100) (b).

Pt(10,8,7)				Pt(100)			
T(K)	$n_{isom.}$ (±0.3)	$n_{hydrog.}$ (±0.3)	C/Pt (c) (±15 percent)	T(K)	$n_{isom.}$ (±0.3)	$n_{hydrog.}$ (±0.3)	C/Pt (c) (±25 percent)
543	1.0	1.0	0.8	561	1.0	1.0	
573	1.0	0.8	1.4	573	0.8	0.8	1.1
603	0.5	0.5	2.5	590	1.0	0.7	1.9
643	0.4	0.4	3.7	611	0.8	0.7	2.1

(a) The order parameter n is defined by $R_t = R_o \exp(-\alpha t^n)$.

(b) $H_2/HC = 10$, $P_{tot} = 220$ Torr.

(c) Carbon atoms per surface platinum atom.

Differences in initial rates between the least and most active crystal faces varied from a factor of four for hydrogenolysis to over a factor of six for isomerization. The order of activities for isomerization followed the sequence Pt(100) ≈ Pt(13,1,1) > Pt(10,8,7) > Pt(111), while the hydrogenolysis rates decreased in the order Pt(10,8,7) > Pt(13,1,1) ≈ Pt(100) ≈ Pt(111).

Auger analysis of the surface composition following these reaction studies revealed the build-up of a partial monolayer of strongly chemisorbed carbonaceous species (1.1-1.5 carbon atoms per surface platinum atom). No ordering in this layer could be detected by LEED. The slow but continuous deactivation that was observed for the hydrogenolysis and isomerization reactions over all four surfaces indicates that at least part of the carbon deposit was bound irreversibly as a deactivating residue. The rate of deactivation was similar for both reactions and appeared to be essentially independent of surface structure.

Isobutane underwent dehydrogenation as well as isomerization and hydrogenolysis under these reaction conditions. The dehydrogenation reaction produced equilibrium concentrations of isobutene within 15-30 min over all four platinum surfaces. Product accumulation curves for the dehydrogenation reaction catalyzed on the (10,8,7) platinum surface are shown at several reaction temperatures in Fig. 3.27. Since the dehydrogenation reaction was already close to equilibrium when the

first gas sample was injected into the gas chromatograph, initial dehydrogenation rates could not be determined accurately. As such the apparent dehydrogenation rates included in Table 3.5 represent a lower limit to the actual dehydrogenation rate. Despite these thermodynamic constraints, it is clear from Table 3.5 that the initial dehydrogenation rates were at least 2-6 times higher than the initial isomerization rates.

Arrhenius plots for isobutane isomerization and hydrogenolysis catalyzed on the (100) and (10,8,7) platinum surfaces are compared in the lower half of Fig. 3.28. Apparent activation energies estimated for reaction temperatures below about 600 K are summarized in Table 3.5. The temperature dependence of the isomerization and hydrogenolysis rates was markedly different on the two platinum surfaces. Isomerization activity on Pt(100) displayed a maximum at about 600 K and then decreased continuously with increasing temperature. The activation energy for hydrogenolysis was a substantial 35 ± 5 kcal/mole. The (10,8,7) platinum surface displayed lower activation energies (12-18 kcal/mole) for both reactions, and no rate maxima were detected as a function of temperature.

The kinetic selectivity for isomerization over hydrogenolysis is shown as a function of temperature for the (100) and (10,8,7) platinum surfaces in the upper half of Fig. 3.28. The isomerization selectivity was maximized at low temperatures and decreased drastically with increasing temperatures above about 580 K. Isomerization selectivity on the (100) surface displayed a maximum value of 57 at 561 K that was

about 14 times higher than that for Pt(10,8,7). At the highest temperatures studied (630 K), the rates of isomerization and hydrogenolysis tended to become equal on both surfaces.

Product accumulation curves for isobutane hydrogenolysis and isomerization catalyzed on the (10,8,7) platinum surface are compared at several temperatures in Fig. 3.29. The rate of deactivation increased with increasing reaction temperature. Increasing deactivation rates were accompanied by an increasing surface coverage by strongly bound carbonaceous species. Several different kinetic models were investigated to describe the deactivation kinetics that assumed that the deactivation was half, first, or second order with respect to time. Figure 3.30 compares data for isobutane hydrogenolysis catalyzed on Pt(10,8,7) at several temperatures using the half- and first-order deactivation schemes. At the lowest temperatures studied (540-560 K), the deactivation was well described by the first order model ($R_t = R_0 \exp(-\alpha t)$), whereas at higher temperatures the deactivation displayed a fractional order time dependence; i.e., $R_t = R_0 \exp(-\alpha t^n)$, $n < 1$. Best fit orders for the deactivation reaction where determined from order plots (not shown) of $\ln(\ln R_t - \ln R_0)$ versus $\ln t$. These values are summarized for isomerization and hydrogenolysis at several temperatures in Table 3.6 along with carbon coverages that were measured by AES following the reactions. It is clear that the order of the deactivation reaction decreased with increasing reaction temperature. The apparent activation energy for deactivation was estimated from the slopes of deactivation plots like those shown in

Fig. 3.30. Arrhenius plots for the deactivation rate constants, α, assuming first- and half-order deactivation are compared for hydrogenolysis over Pt(10,8,7) in Fig. 3.31. Carbon coverages determined by AES are also shown as a function of 1/T. The apparent activation energies for carbon deposition (~12 kcal/mole) and deactivation (10-21 kcal/mole) were equal within the experimental uncertainty.

Product distributions for isobutane hydrogenolysis catalyzed over the four platinum surfaces are summarized at several temperatures in Table 3.7. Fission parameters calculated from these distributions are shown as a function of temperature in Fig. 3.32. The (111) and (10,8,7) platinum surfaces that are mostly composed of hexagonal (111) microfacets displayed fission parameters smaller than one under all conditions. The (100) and (13,1,1) platinum surfaces that are mostly composed of square (100) microfacets always displayed fission parameters that were in the range 2-6. The (100) and (13,1,1) surfaces always produced more ethane and less methane and propane as compared to the (111) and (10,8,7) platinum surfaces. The enhanced ethane production rate appears to result from selective internal hydrogenolysis of an isomerization intermediate. Based on the low conversions of these experiments (<0.2 percent), the relative rates iso- and n-butane hydrogenolysis, and adsorption equilibrium constants reported by Maurel et al. (56) the possibility that secondary reactions of n-butane produced in isomerization contribute to these distributions can be ruled out.

Table 3.7. Product distributions for isobutane hydrogenolysis catalyzed over platinum single crystal surfaces (a)

Surface	T(K)	Hydrogenolysis Distribution (moles) C_1	C_2	C_3	Surface	T(K)	Hydrogenolysis Distribution (moles) C_1	C_2	C_3
Pt(100)	561	43	31	16	Pt(111)	573	55	11	34
	573	40	38	22	Pt(10,8,7)	543	65	6	29
	590	34	40	26		573	64	10	26
	611	40	36	24		603	71	7	22
	633	28	44	28		603	71	10	24
Pt(13,1,1)	573	30	48	22		643	67	10	23

(a) $H_2/HC = 10$ $P_{tpt} = 220$ Torr.

n-Butane Isomerization, Dehydrogenation, and Hydrogenolysis. The isomerization, dehydrogenation, and hydrogenolysis of n-butane were investigated on the (100), (111), and (13,1,1) platinum surfaces at 573-615 K with $H_2/HC = 10$ and $P_{tot} = 220$ Torr. Product accumulation curves determined as a function of time at 573 K are compared in Fig. 3.33 for the isomerization and hydrogenolysis reactions catalyzed on the initially clean platinum surfaces. Following 70-90 min reaction time at 573 K, the samples were heated to 615 K for an additional 40-60 min so that selectivities could be determined at a higher temperature. Initial turnover frequencies at 573 K, fractional isomerization selectivities at 573 and 615 K, and surface carbon coverages determined following the reactions at 615 K are summarized in Table 3.8. Isomerization of n-butane at 573 K displayed substantial structure sensitivity that was similar to that observed for isobutane isomerization. The (100) and (13,1,1) platinum surfaces exhibited isomerization activities that were at least three times higher than that for Pt(111); [Pt(13,1,1) $\approx$ Pt(100) > Pt(111)]. The hydrogenolysis and dehydrogenation reactions displayed very little structure sensitivity [Pt(13,1,1) $\approx$ Pt(100) $\approx$ Pt(111)]. The initial dehydrogenation rates reported in Table 3.8 represent lower limits to the absolute dehydrogenation rates which could not be measured directly because of thermodynamic constaints. The dehydrogenation reactions produced equilibrium concentrations of 1-, cis-2-, and trans-2-butenes within about 20 min over all three surfaces. The relative concentrations of

Table 3.8. Initial reaction rates, selectivities, and carbon coverages measured for n-butane reactions catalyzed over Pt(100), Pt(111), and Pt(13,1,1) (a).

	Initial Rates at 573K (molec/Pt atom sec)(±20%)			S_{isom}(mole %)		C/Pt (b)
Catalyst	Hydrog.	Isom.	Dehydrog.	573K	615K	at 615K
Pt(100)	0.0098	0.037	≳0.48	79	52	1.7
Pt(111)	0.0071	0.013	≳0.45	65	27	2.0
Pt(13,1,1)	0.0098	0.046	≳0.48	82	56	2.7

(a) $H_2/HC = 10$, $P_{tot} = 220$ Torr.

(b) Carbon atoms per surface platinum atom (±25 percent).

1-C_4H_8, cis-2-C_4H_8, and trans-2-C_4H_8 were 1:4.0-4.5:4.0-4.6 and 1:1.9-2.0:2.3-2.5 at 573 and 615 K, respectively. In spite of these thermodynamic effects, the initial dehydrogenation rates appeared to be at least ten times faster than hydrogenolysis and isomerization. Because the dehydrogenation reaction was influenced by thermodynamic effects, it was not considered in the calculation of isomerization selectivities. Fractional isomerization selectivities calculated on the basis of the hydrogenolysis and isomerization rates varied from 65 to 82 mole percent at 573 K and decreased markedly to 27-56 mole percent at 615 K.

Product distributions and fission parameters for n-butane hydrogenolysis are summarized in Table 3.9. At 573 K, the (111) surface exhibited a statistical hydrogenolysis distribution whereas the (100) and (13,1,1) platinum surfaces displayed much higher selectivities for scission of the internal C-C bond.

Neopentane Isomerization and Hydrogenolysis. The isomerization and hydrogenolysis of neopentane were investigated over the same platinum crystal surfaces under identical reaction conditions. Product accumulation curves determined as a function of reaction time at 573 K are compared for isomerization and hydrogenolysis in Fig. 3.34. Initial reaction rates, selectivities, and surface carbon and sulfur coverages measured after the reactions are tabulated in Table 3.10. In striking contrast to the C_4-alkane reactions, surface structure had very little influence on the initial rates and selectivities of the neopentane reactions. The fractional selectivity for isomerization was always in the range of 87-89 percent, and the difference in initial

Table 3.9. Product distributions and fission parameters for n-butane hydrogenolysis over platinum single crystal surfaces (a).

Catalyst	T(K)	Hydrogenolysis Distribution (moles) C_1	C_2	C_3	M_f
Pt(100)	573	23	58	19	5.9
	615	25	50	25	5.0
Pt(111)	573	40	30	30	2.2
	615	38	30	32	2.4
Pt(13,1,1)	573	33	49	28	3.5
	615	36	45	29	3.3

(a) $H_2/HC = 10$, $P_{tot} = 220$ Torr.

Table 3.10. Initial reaction rates, fractional isomerization selectivities, n-pentane to isopentane ratios, and surface carbon and sulfur coverages determined at 573 K for neopentane reactions catalyzed over platinum single crystal surfaces (a).

Catalyst	Initial Rates (molec/Pt atom sec) Isomerization	Hydrogenolysis	$S_{isom.}$ (mole percent)	$n\text{-}C_5/i\text{-}C_5$	C/Pt (b)	S/Pt (c)
Pt(100)	0.18	0.024	88	0.16	1.0	0.06
Pt(111)	0.11	0.015	87	0.03	1.9 (d)	0.04
Pt(13,1,1)	0.20	0.024	89	0.14	1.9 (d)	0.05
Pt(10,8,7)	0.20	0.026	88	0.02	1.0	0.06

(a) $H_2/HC = 10$, $P_{tot} = 220$ Torr.

(b) Carbon atoms per surface Pt atom (±20 percent).

(c) Sulfur atoms per surface Pt atom (±40 percent).

(d) At 615 K.

rates between the least active (111) and most active (10,8,7) platinum surfaces was less than a factor of two for both isomerization and hydrogenolysis. The selectivity in isomerization for n-pentane production was the only feature of the neopentane reaction chemistry that displayed notable structure sensitivity. While the (111) and (10,8,7) platinum surfaces yielded only 2-3 percent n-pentane in isomerization, the (100) and (13,1,1) surfaces produced 12-14 percent n-pentane. Thus, the (100) and (13,1,1) surfaces displayed a marked preference for two consecutive bond shift rearrangements during a single residence on the surface.

Arhenius plots for neopentane hydrogenolysis and isomerization catalyzed on the (10,8,7) platinum surface are compared in Fig. 3.35. For temperatures below about 600 K, both reaction pathways displayed normal Arrhenius behavior with activation energies in the range of 50-55 kcal/mole. At higher temperatures no further increase in initial rates was detected. Product accumulation curves are compared at several temperatures in Fig. 3.36 for isomerization and hydrogenolysis catalyzed on the (10,8,7) platinum surface. As with the n-hexane and C_4-alkane reactions, the rate of deactivation increased with increasing reaction temperature. Deactivation was accompanied by the deposition of about 1 monolayer of strongly chemisorbed carbonaceous species (Table 3.10).

Fission parameters and initial product distributions for neopentane hydrogenolysis are compared at several temperatures for the four platinum surfaces in Table 3.11. The (100) and (13,1,1) surfaces

Table 3.11. Initial product distributions and fission parameters for neopentane hydrogenolysis catalyzed on the (100), (111), (13,1,1), and (10,8,7) platinum single crystal surfaces (a).

Catalyst	Temp. (K)	Hydrogenolysis Distribution (moles) C 1	C 2	C 3	i-C 4	M f
Pt(100)	573	39	13	15	33	2.7
Pt(111)	573	49	5	4	42	1.3
	615	45	12	15	28	2.2
Pt(13,1,1)	573	40	11	13	36	2.5
	615	31	24	23	22	4.5
Pt(10,8,7)	543	58	4	11	27	1.0
	573	58	4	6	32	1.0
	604	51	7	16	26	1.6

(a) $H_2/HC = 10$, $P_{tot} = 220$ Torr.

exhibited a higher selectivity for multiple hydrogenolysis and/or internal splitting of isomerization intermediates, as these surfaces produced more ethane and propane and less methane as compared to the (111) and (10,8,7) platinum surfaces. As a result the fission parameters were largest for the (100) and (13,1,1) platinum surfaces.

3.2.3. Discussion.

Structure Sensitivities of Alkane Skeletal Rearrangement:

a) Isomerization. Significant differences in bond shift isomerization activity were detected for platinum single crystal surfaces with different atomic structure. Figure 3.37 summarizes initial rates as a function of crystallographic orientation for n-butane, isobutane, and neopentane isomerization catalyzed at 573 K. Isobutane and n-butane isomerization displayed maximum rates on the (100) and (13,1,1) platinum surfaces that were at least 3-5 times higher than the rates of the same reactions catalyzed over Pt(111) and Pt(10,8,7). High concentrations of (100) microfacets were required for high catalytic activity in butane isomerization. By contrast, neopentane isomerization activity displayed little dependence on platinum surface structure. This difference may be related to the fact that sulfur contamination was detected by AES only after the neopentane reaction studies. While the sulfur contamination was always small (3-6 percent of a monolayer, Section 2.6, Table 3.10), it could likely alter the structure sensitivity of this reaction pathway (Section 5.2). Since olefin intermediates could not form during neopentane reactions prior to skeletal rearrangement, different degrees of substitution for

the reacting hydrocarbons could also contribute to the different structure sensitivities for neopentane and butane isomerization. Olefin formation occurred readily during isobutane and n-butane reaction studies (Tables 3.5 and 3.8).

Results for n-hexane isomerization catalyzed over the same four platinum surfaces are also included in Fig. 3.37. The absence of structure sensitivity for this reaction was discussed in the previous section in terms of an isomerization mechanism that was dominated by C_5-cyclic intermediates. These intermediates were not possible during light alkane skeletal rearrangement.

The order of isomerization activities at 573 K for the different hydrocarbons followed the sequence neopentane $\gtrsim$ isobutane > n-butane > n-hexane. While this order varied slightly with surface structure, it tends to indicate that isomerization rates increase with increasing degree of substitution and decreasing molecular weight. Further studies using additional hydrocarbons would be worthwhile to confirm this correlation.

The structure sensitivities reported here for butane isomerization compare favorably with results reported by Anderson and Avery (21) for the same reactions catalyzed under similar conditions over oriented platinum films with (100) and (111) surface structure (T = 540-580 K, $H_2/HC = 12$, $P_{tot} = 48$ Torr). These workers observed higher isomerization activities on the oriented (100) films, and the differences in rates between (111) and (100) films were comparable to those described here for single crystal surfaces. Table 3.12 compares

catalytic activities and selectivities determined in this research at 573 K with those reported for oriented films and other types of platinum catalysts, e.g., unoriented films, powders, and Pt/SiO_2. the initially clean single crystal surfaces always displayed much higher catalytic activities than practical platinum catalysts.

The absence of significant structure sensitivity for neopentane isomerization appears to be in good agreement with results reported by Foger and Anderson (35) for neopentane reactions catalyzed at 530–600 K over Pt/SiO_2 catalysts (Table 3.12). While isomerization selectivity increased significantly in their studies when the average metal particle size was varied between 10 and 70Å, the isomerization rates changed by only a factor of two with no clear correlation with average metal particle size. Boudart and co-workers (34) have reported more significant variations in neopentane isomerization activity for a series of platinum catalysts with different supports and widely varying dispersion (Table 3.12). However, catalysts which experienced the same pretreatment usually displayed similar isomerization rates in good agreement with the results reported here.

Our results clearly indicate that the structure sensitivity of alkane isomerization depends markedly upon the structure of the reacting hydrocarbon. When structure sensitivity was detected, it originated primarily from the atomic structure of the (100) or (111) terraces. Steps and kinks that were present in high concentrations on the (13,1,1) and (10,8,7) platinum surfaces increased the isomerization rates only slightly as compared to the flat low index surfaces. The

structure sensitivity of isobutane isomerization diminished rapidly with increasing reaction temperature.

b) Hydrogenolysis. Hydrogenolysis activities determined at 573 K as a function of crystallographic orientation are shown for isobutane, n-butane, neopentane, and n-hexane in Fig. 3.38. In all cases but isobutane, the hydrogenolysis rates displayed little dependence on platinum surface structure. However, at 573 K, the kinked (10,8,7) surface was several times more active than the other platinum surfaces for isobutane hydrogenolysis. At lower temperatures, kink sites on the (10,8,7) surface appeared to be uniquely effective for this c-c bond breaking reaction. However, this difference in rates decreased sharply with increasing temperature (Fig. 3.28). Differences in hydrogenolysis rates for hydrocarbons with different structure were significantly smaller than those measured for the competing isomerization reactions.

The absence of significant structure sensitivity for the rates of alkane hydrogenolysis is somewhat surprising in view of results previously reported for isobutane (21), n-butane (21), and neopentane (34) reactions catalyzed over oriented films and supported platinum catalysts. The pioneering work of Anderson and Avery (21) indicated that platinum films with (100) orientation were considerably (2-15 times) more active than (111) platinum films for isobutane and n-butane hydrogenolysis (Table 3.12). Boudart and co-workers (34) noted similar, large changes in neopentane hydrogenolysis activity for a series of supported catalysts with widely varying dispersion. More

Table 3.12. Comparison between model and practical catalysts for light alkane skeletal rearrangement reactions.

Catalyst	H_2/HC	P_{tot}(Torr)	T(K)	Total Rate (a) (molec/Pt atom sec)	$S_{isom.}$(mole percent)	Ref.
Isobutane Reaction:						
Pt(100)	10	220	573	0.23	98	--
Pt(111)	10	220	573	0.036	90	--
Pt-film (100)	12	48	573	0.011	59	21
Pt-film (111)	12	48	573	1.3×10^{-3}	83	21
Pt-film	11.5	38	633	~0.03	73	65
Pt-powder	20	210	650	$\sim4\times10^{-4}$	73	66
n-Butane Reaction:						
Pt(100)	10	220	573	0.047	79	--
Pt(111)	10	220	573	0.020	65	--
Pt-film (100)	12	48	573	0.020	16	21
Pt-film (111)	12	48	593	9×10^{-3}	40	65
Pt-film	11.5	38	573	7×10^{-4}	22	66
Neopentane Reaction:						
Pt(100)	10	220	573	0.20	88	--
Pt(111)	10	220	573	0.13	87	--
Pt/SiO_2						
(d = 10Å)	20	760	573	~0.014	36	35
(d = 40Å)	20	760	573	~0.023	47	35
(d = 70Å)	20	760	573	~0.013	60	35
Pt/Al_2O_3 (D=0.73)	10	760	580	5×10^{-3}	60	34
Pt/SiO_2 (D=0.17)	10	760	580	0.017	23	34
Pt-powder ($D\sim10^{-2}$)	10	760	580	8×10^{-4}	90	34

(a) Isomerization plus hydrogenolysis.

recently, Foger and Anderson (35) reinvestigated neopentane hydrogenolysis catalyzed on a series of Pt/SiO_2 catalysts with average metal particle sizes varied etween 10 and 70Å. In this case, the hydrogenolysis rates displayed little dependence on catalyst dispersion (Table 3.12). The latter observation appears to compare most favorably with the results reported here for single crystal surfaces. However, all these comparisons should be considered cautiously since the surface compositions of the practical catalysts were not known and their catalytic activities were always lower than those measured for clean platinum. Surface impurities such as carbon and strongly bound subsurface oxygen always exert a profound influence on hydrogenolysis activity (Chapters 4 and 5).

Selectivity: The light alkane reaction studies have confirmed that platinum is an excellent dehydrogenation catalyst (28). Whenever dehydrogenation was possible (isobutane, n-butane, n-hexane) this reaction pathway was at least 3-50 times faster than the sum rate of all skeletal rearrangement reactions. Under our conditions (H_2/HC = 10, T = 540-630 K), hydrogenation-dehydrogenation equilibrium was established within minutes over all four platinum surfaces (Figs. 2.2 and 3.27).

At lower reaction temperatures ($\lesssim$570 K), the initially clean platinum single crystal surfaces displayed extraordinary selectivities for isomerization versus hydrogenolysis. These selectivities are compared in Table 3.12 with those reported previously for other types of platinum catalysts. The single crystal surfaces consistently displayed

higher isomerization selectivities than practical catalysts. A maximum isomerization selectivity of about 98 percent was observed for isobutane isomerization catalyzed over Pt(100) at 560 K. At 573 K, the isomerization selectivities decreased in the order isobutane $\gtrsim$ neopentane > n-butane. Selectivities for n-butane and isobutane isomerization decreased markedly with increasing temperature (Fig. 3.28), although with neopentane, the selectivity displayed little temperature dependence.

The drastic changes in butane isomerization selectivity with increasing temperature can best be explained if (1) a common surface intermediate exists for both reaction pathways, but the activation energy for hydrogenolysis is higher than that required for isomerization (as observed), or (2) hydrogenolysis and isomerization result from surface intermediates with different hydrogen content (composition); hydrogenolysis intermediates have lower hydrogen content and are favored at high temperatures. Both effects probably operate simultaneously. The fact that isobutane isomerization catalyzed on the (100) platinum surface displayed a maximum rate at about 590 K suggests strongly than expanation (2) is appropriate in this case. The same reasoning was used in the previous selection to interpret changes in n-hexane reaction selectivity as a function of reaction conditions.

The fractional selectivity for neopentane isomerization was always in the range 78-90 percent independent of platinum surface structure and the reaction temperature. These selectivities were generally much higher than those reported previously for other types of platinum

catalysts (Table 3.12). Foger and Anderson (35) noted that isomerization selectivity for Pt/SiO_2 catalysts increases with increasing average metal particle size. A limiting selectivity of about 90 percent was proposed for platinum surfaces that consist entirely of (111) microfacets. Our results certainly tend to confirm this suggestion. More importantly, we have clearly shown that high isomerization selectivity is not restricted to (111) surfaces. All initially clean platinum surfaces that contain high concentrations of contiguous (111) or (100) microfacets appear to display very high isomerization selectivity.

The selectivity for n-pentane production during neopentane reaction studies displayed a marked dependence on platinum surface structure. This unique reaction required two consecutive bond-shift rearrangements during a single residence on the platinum surface. It occurred readily only on the (100) and (13,1,1) platinum surfaces that contained high concentrations of (100) microfacets. In this case consecutive rearrangement accounted for about 15 percent of the total isomerization activity. Since the structure sensitivity of this reaction closely paralleled that for isobutane isomerization, it appears likely that isopentane intermediates are important in the reaction pathway leading to multiple rearrangement. Muller and Gault (42) have previously reported that consecutive rearrangements take place during isomerization reactions of dimethylbutanes catalyzed at 540–570 K over platinum films.

Hydrogenolysis Product Distributions. Significant differences in hydrogenolysis selectivity were detected for platinum single crystal surfaces with different atomic structure. Hydrogenolysis of n-butane at 573 K was mainly characterized by single C-C bond breaking events that were accompanied by 2-5 percent hydrocracking ($n\text{-}C_4 \rightarrow 4C_1$). Approximate C-C bond rupture probabilities were

	Pt(100)	Pt(111)	Pt(13,1,1)
$C_1\text{-}C_2$	0.20	0.34	0.26
$C_2\text{-}C_3$	0.60	0.33	0.48
$C_3\text{-}C_4$	0.20	0.33	0.26

The (111) platinum surface lead to statistical C-C bond breaking, whereas the (100) surface displayed a clear preference for scission of the internal c-c bond. The (13,1,1) surface with (111) steps and (100) terraces displayed intermediate behavior. Possible explanations for the different selectivities were proposed in the previous section in connection with studies of n-hexane hydrogenolysis catalyzed over the same platinum surfaces.

A more complicated series of reaction steps involving multiple c-c bond breaking events and skeletal rearrangement prior to hydrogenolysis was apparent during isobutane hydrogenolysis. The product distributions for Pt(111) and Pt(10,8,7) could be described by a series of successive demethylation processes where single c-c bond scission ($i\text{-}C_4 \rightarrow c_3 + c_1$) represented 65-80 percent of the total hydrogenolysis reaction. Similar product distributions were reported previously by

Dowie (65), Guczi (66), and Anderson (21) and co-workers for isobutane reactions catalyzed over platinum films. However, demethylation could only account for 45-55% of the hydrogenolysis products produced on the (100) and (13,1,1) platinum surfaces. In this case, ethane yields were always much too high to be represented by consecutive demethylation. Since conversions were always too low to allow for secondary reactions, a reasonable explanation for this unique selectivity appears to involve rearrangement to a surface intermediate with a structure like n-butane prior to hydrogenolysis, i.e.,

(1)

This process appears to be responsible for the unusually high fission parameters that were determined for isobutane hydrogenolysis catalyzed or the (100) and (13,1,1) platinum surfaces (Figure 3.29).

A similar analysis is applicable to neopentane hydrogenolysis. In this case demethylation represented 75-90 percent of the reaction over Pt(111) and Pt(10,8,7) but only 65-75 percent of the reaction over Pt(100) and Pt(13,1,1). Over the (100) and (13,1,1) platinum surfaces, ethane and propane were produced in yields that were again too high to be accounted for by consecutive demethylation. The formation of these hydrogenolysis products is expected only if skeletal isomerization precedes hydrogenolysis, i.e.,

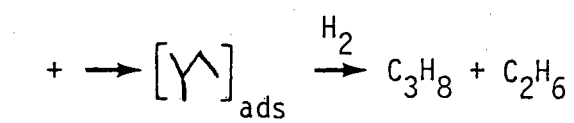

(2)

While the product distributions determined for neopentane hydrogenolysis on Pt(111) and Pt(10,8,7) compare closely with those reported previously for Pt-films and Pt/SiO_2(21,35), the product distributions for Pt(100) and Pt(13,1,1) appear to be unique to single crystal surfaces with high concentrations of (100) microfacets.

Nature of the Bond Shift Mechanism. A variety of one- and two-site mechanisms have been postulated (20-22, 34, 39, 67-69) for bond shift rearrangement of small alkanes on platinum (or palladium). With one notable exception (22), all the proposed single site mechanisms involved α,γ-adsorbed species that are heterogeneous analogs of platinacyclobutanes (70-74). The latter compounds have attracted much interest because of their ability to undergo a facile skeletal rearrangement (reaction 3),

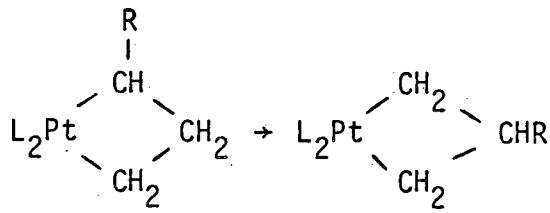

(3)

which appears to be very closely related to bond shift isomerization (71,73,74) (L = pyridine, R = methyl (73), phenyl (74)). Reaction pathways that were proposed for heterogeneous isomerization are summarized in scheme I with isobutane taken as an example. Each pathway has been reviewed critically elsewhere (20,26,27,75). The essential requirements of reactions 4, 6, and 7 are the transient existence of hydrocarbon intermediates with bridging methylene or methyl groups. Non rigorous calculations (20,76,77) suggest that these species are stabilized by multicenter bonds as in (I)

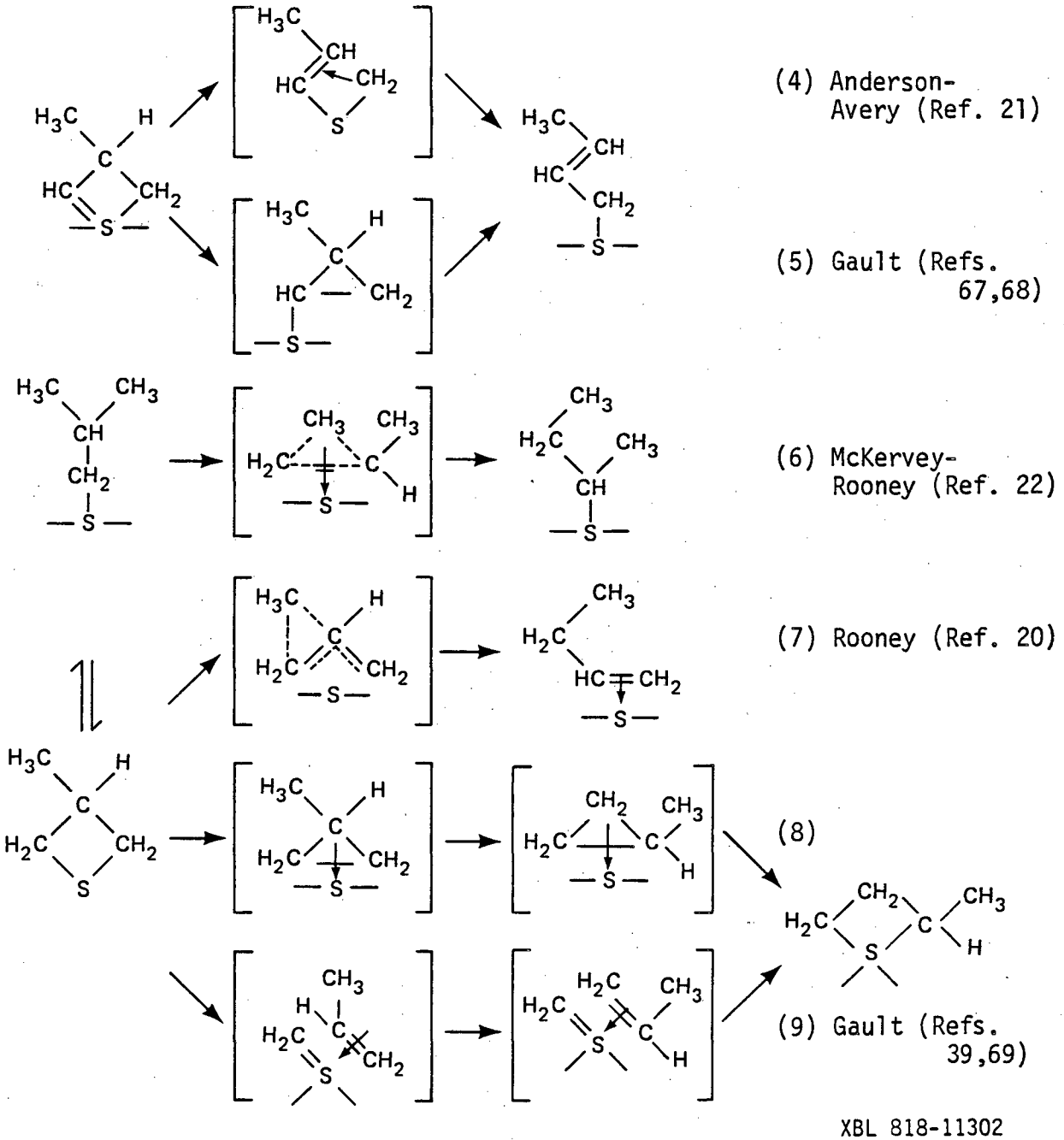

Scheme I. Possible mechanisms for isobutane isomerization catalyzed on platinum.

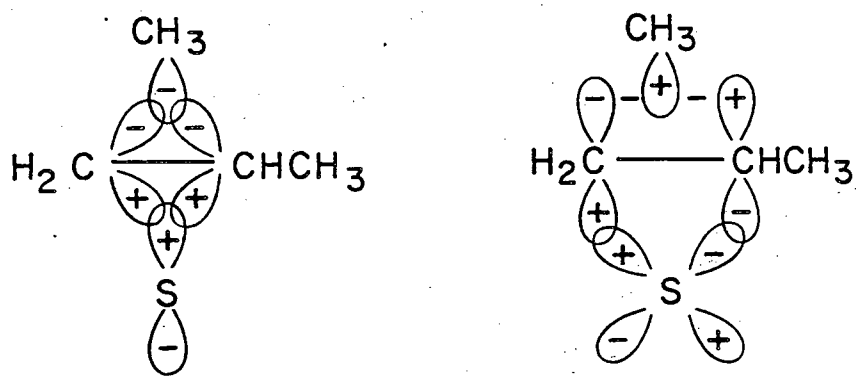

(I)

and partial charge transfer from the adsorbed species to the metal. Photoemission studies of energy level shifts (78) and work function changes (79,80) that accompany hydrocarbon chemisorption have shown that charge transfer does take place, that it is particularly marked in the case of platinum, and that it is reasonable in this case to think of surface intermediates with partial carbonium ion character. The Rooney mechanisms (reactions 6 and 7) that involve bridging methyl groups in transient olefin or π-allyl systems (20,22) appear to be closely related to the "concerted" mechanism proposed by Puddephatt and coworkers (73) in their studies of the homogeneous rearrangement. Reaction 8 involves formation of a discrete c_3-cyclic intermediate followed by edge-to-edge isomerization and ring opening (73). Reaction 9 requires interconversion to a carbene-olefin surface complex followed by rotation of the olefin and reformation of an isomeric surface species (39,69). The latter, metathesis-like (81)

rearrangement has been dismissed as improbable in both the homogeneous and heterogeneous reactions because (1) the homogeneous rearrangement is accompanied by complete retention of stereochemistry (71,73), (2) platinum is not known to catalyze metathesis (75,81), and (3) isomerization was accompanied by only little hydrogenolysis which would be expected in higher yields if complete c-c bond scission intervened.

The key question naturally arises whether the structure sensitivities reported here for iso- and n-butane isomerization can be related to any of the previously proposed reaction mechanisms. The answer appears to be yes. The (100) and (13,1,1) platinum surfaces have accessible d (and p) orbitals which emerge from the surfaces with appropriate angles and symmetries to form half-reaction states such as that depicted in (I). However, in the absence of extensive sp-d hybridization, the (111) surface and the terraces of the (10,8,7) surface do not possess such easily accessible orbitals. This is shown in Figure 3.39 which compares the directions of emergence of the t_{2g} and e_g orbitals from the (100) and (111) surfaces of an fcc metal (82). Only those orbitals which project out of the surface plane are indicated. In the bulk each of the 12 lobes of the atomic d-orbitals with t_{2g} symmetry overlaps with one lobe from a nearest neighbor atom that results in the formation of a collective t_{2g} band of d-electron energy states. The remaining 6 lobes for the d-orbitals with e_g symmetry are directed towards next-nearest atoms which produces a more localized band of e_g electronic states. Both bands are

split by intraatomic exchange (83), and the widths, positions, and occupancies of the d-bands have been considered explicitly elsewhere (84-87). The important points here are that (1) the same d-orbital symmetries are maintained at the surface, (2) the d-orbitals can be accurately regarded as localized, quasi-atomic like in character (88), and (3) neither d-band is completely filled, i.e., both types of d-orbitals are suitable for bonding with adsorbates. The (100) platinum surface has an e_g-orbital projecting normal to the surface and t_{2g}-orbitals that emerge at 45^o which are most suitable for the formation of intermediates such as (I). By contrast, the (111) platinum surface has no d (or p) orbitals which project either normal to the surface or in the direction of nearest neighbors. In this case, strong metal-hydrocarbon interaction appears to require σ-bonded surface species where a carbon atom becomes nested in the 3-fold hollow sites as observed for the stable ethylidyne surface species (Pt_3 C-CH_3) chemisorbed on Pt(111) (52,53). Stabilization of bridging species like (I) on Pt(111) appears to require a more complex bonding interaction involving a linear combination of t_{2g}-orbitals centered on two or more metal atoms.

The actual situation for the surface electronic structure under reaction conditions is undoubtedly far more complex than that suggested by this simplistic model which, at most, can help to guide one's thinking. Local crystal field effects at the surface determine the

occupations of the individual d-bands which generally differ from those for the bulk (64, 89). Recent ab initio calculations for nickel surfaces, for example, revealed that the surface d-bands are narrowed and more completely filled as compared to the bulk d-bands (64). Moreover, s-d hybridization appeared to become pronounced in the vicinity of the Fermi energy (64). Such hybridization could result in the production of new surface orbitals which are uniquely suited for catalysis of bond-shift rearrangement.

Deactivation Kinetics and Formation of Surface Carbon. The light alkane reaction rate studies were always accompanied by continuous deactivation. The deactivation rates displayed little dependence on surface structure and increased with increasing temperature. The deactivation kinetics for isobutane reactions catalyzed over Pt(100) and Pt(10,8,7) were correlated with the emperical rate expression $R_t = R_0 \exp(-\alpha t^n)$ where the order parameter n decreased from one at 550-570K to about 0.5 at 610-640K. A possible explanation for these deactivation kinetics was discussed in the preceding section in connection with n-hexane reaction studies on the same four platinum surfaces. The change in apparent order for the deactivation reaction was related to a change in the morphology of the carbonaceous deposit from 2-dimensional at low temperatures to 3-dimensional at high temperatures. The same conclusion appears to be applicable to the light alkane reaction studies. The only significant difference in deactivation behavior between the light alkane and n-hexane reaction studies was in the amount of carbon deposited. At any given temperature, less

carbon was deposited during light alkane reaction studies, although this difference became small at high temperatures.

FIGURE CAPTIONS

Fig. 3.26 Product accumulation curves determined as a function of reaction time at 573K for isobutane isomerization (left frame) and hydrogenolysis (right frame) catalyzed over platinum single crystal surfaces.

Fig. 3.27 Product accumulation curves determined at several temperatures (H_2/HC = 10, P_{tot} = 220 Torr) for isobutane dehydrogenation catalyzed over the kinked (10,8,7) platinum surface.

Fig. 3.28 Arrhenius plots (lower frame) and kinetic selectivities (upper frame) for isobutane isomerization and hydrogenolysis, catalyzed over the flat (100) and kinked (10,8,7) platinum surfaces.

Fig. 3.29 Product accumulation curves determined at several reaction temperatures for isobutane isomerization (left frame) and hydrogenolysis (right frame) catalyzed over Pt(10,8,7).

Fig. 3.30 Comparison between first-order and half-order deactivation models for isobutane hydrogenolysis catalyzed on the kinked (10,8,7) platinum surface. The reaction temperatures were 543K (○), 573K (●), 605K (△) and 643K (□).

Fig. 3.31 Arrhenius plots for the deactivation rate constants, α, determined for isobutane hydrogenolysis reactions catalyzed over Pt (10,8,7). A comparison is made between the first and half-order deactivation models, and the C_{273}/Pt_{237} AES peak-to-peak height ratio is also shown as a function of 1/T.

Fig. 3.39 Representations of the d-orbitals emerging from the (111) and (100) surfaces of an fcc metal (after Bond (82)). Darkened regions represent e_g orbitals that emerge at 36° and 90° with respect to the surface plane for Pt(111) and Pt(100), respectively. Cross-hatched regions correspond to t_{2g} orbitals that emerge at 54° and 45° with respect to the surface for Pt(111) and Pt(100), respectively. Not shown are in plane t_{2g} orbitals that are directed towards nearest neighbors and in plane e_g orbitals that are directed towards next-nearest neighbors (Pt(100)).

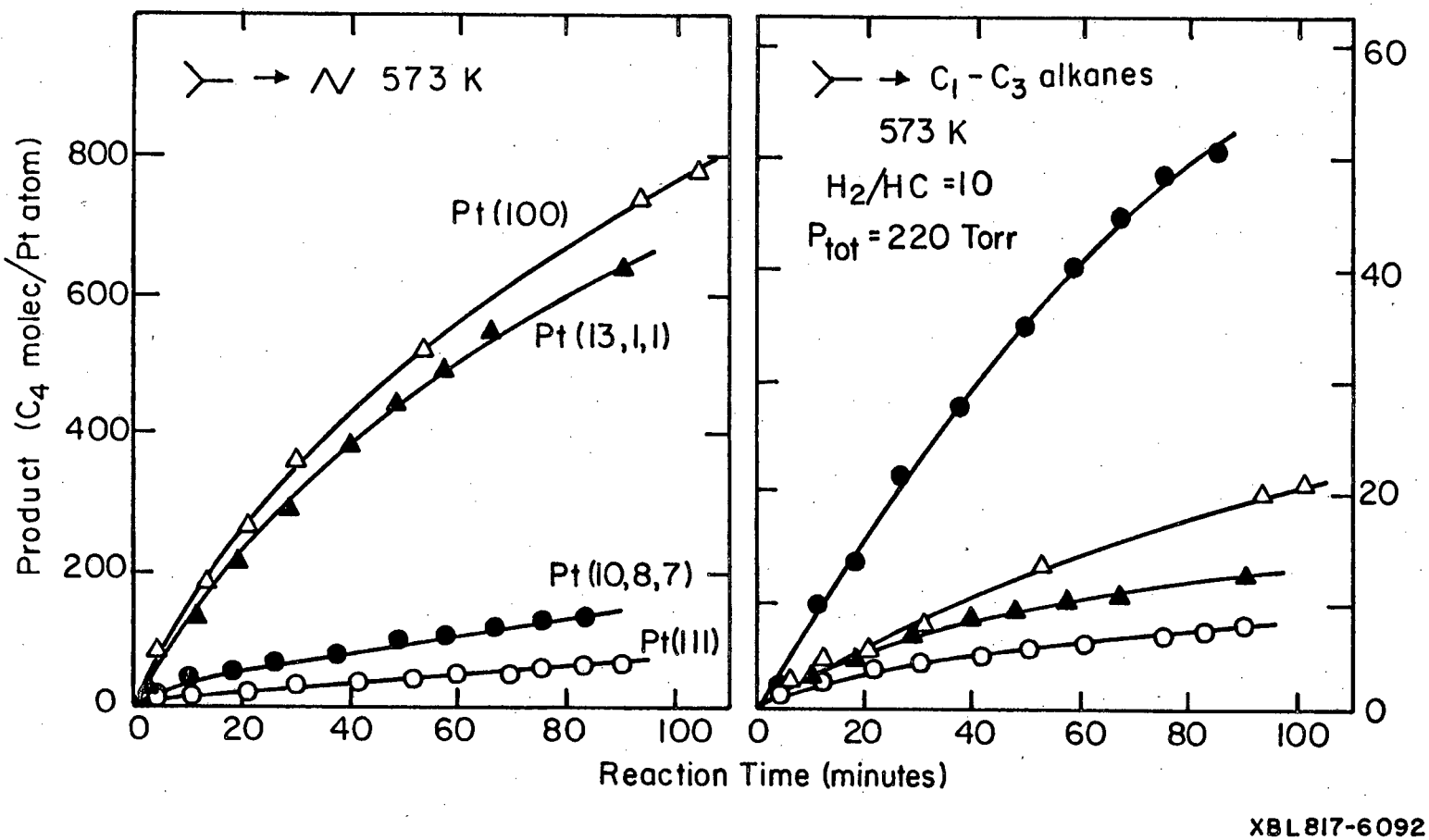
573 K
Pt(100)
Pt(13,1,1)
Pt(10,8,7)
Pt(111)
Product (C4 molec/Pt atom)
0
200
400
600
800
0
20
40
60
80
100
Reaction Time (minutes)
C1 - C3 alkanes
573 K
H2/HC =10
Ptot = 220 Torr
0
20
40
60
XBL817-6092

Fig. 3.26

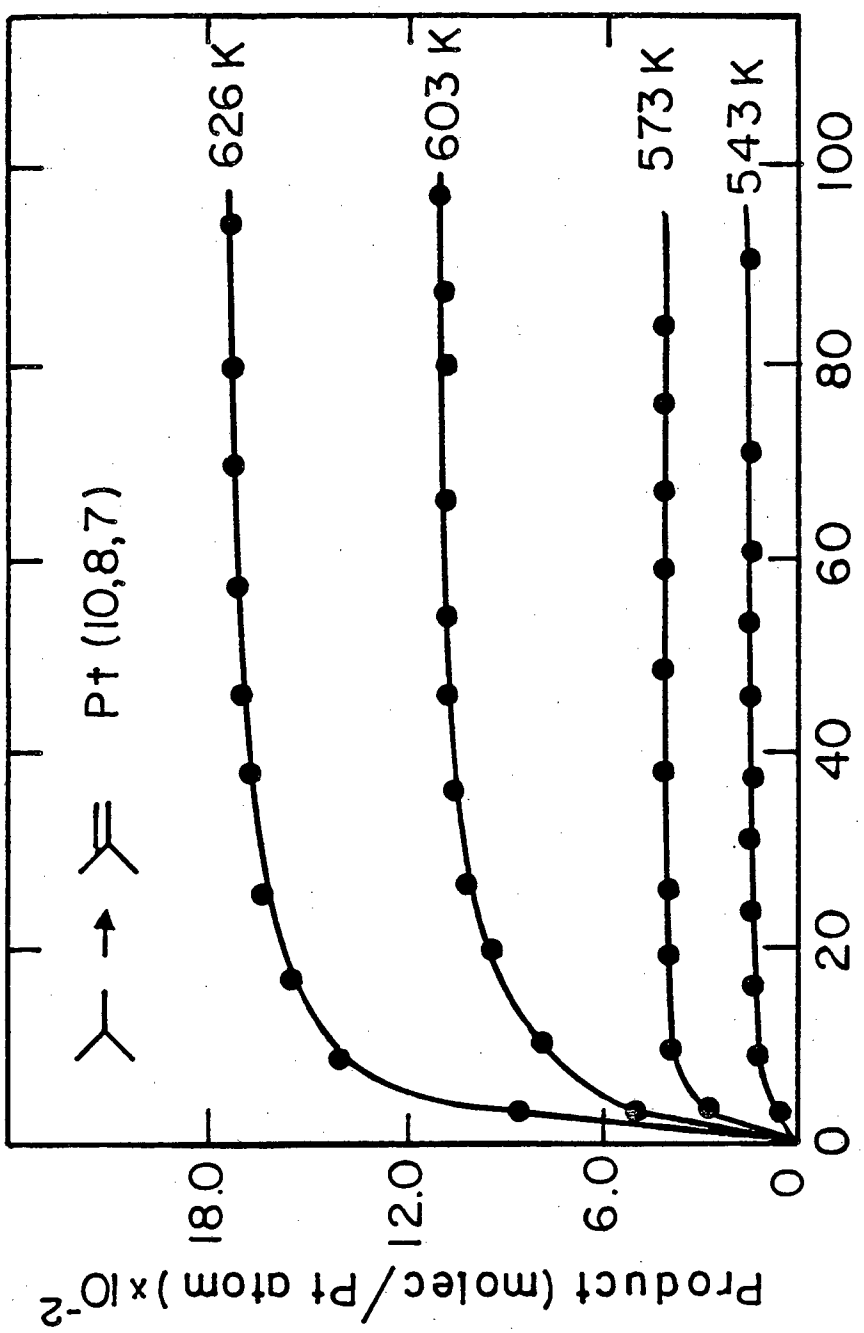

XBL 817-6114

Fig. 3.27

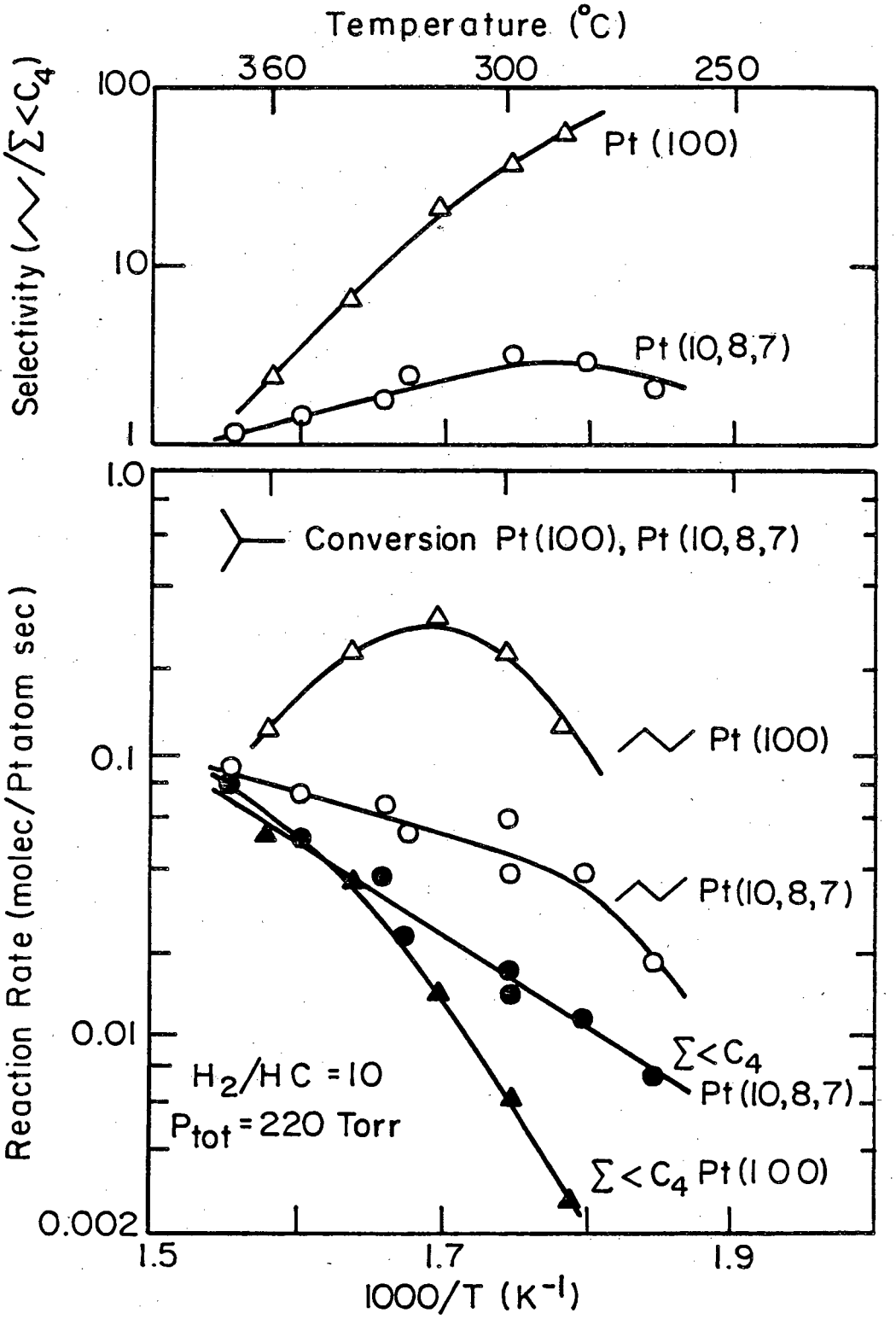
Temperature (°C)
360
300
250
100
10
1
Selectivity (∼/Σ<C4)
Pt (100)
Pt (10,8,7)
1.0
0.1
0.01
0.002
Reaction Rate (molec/Pt atom sec)
Conversion Pt(100), Pt (10,8,7)
Pt (100)
Pt(10,8,7)
Σ<C4
Pt (10,8,7)
Σ<C4 Pt (100)
H2/HC =10
Ptot = 220 Torr
1.5
1.7
1.9
1000/T (K-1)
XBL 817-6087

Fig. 3.28

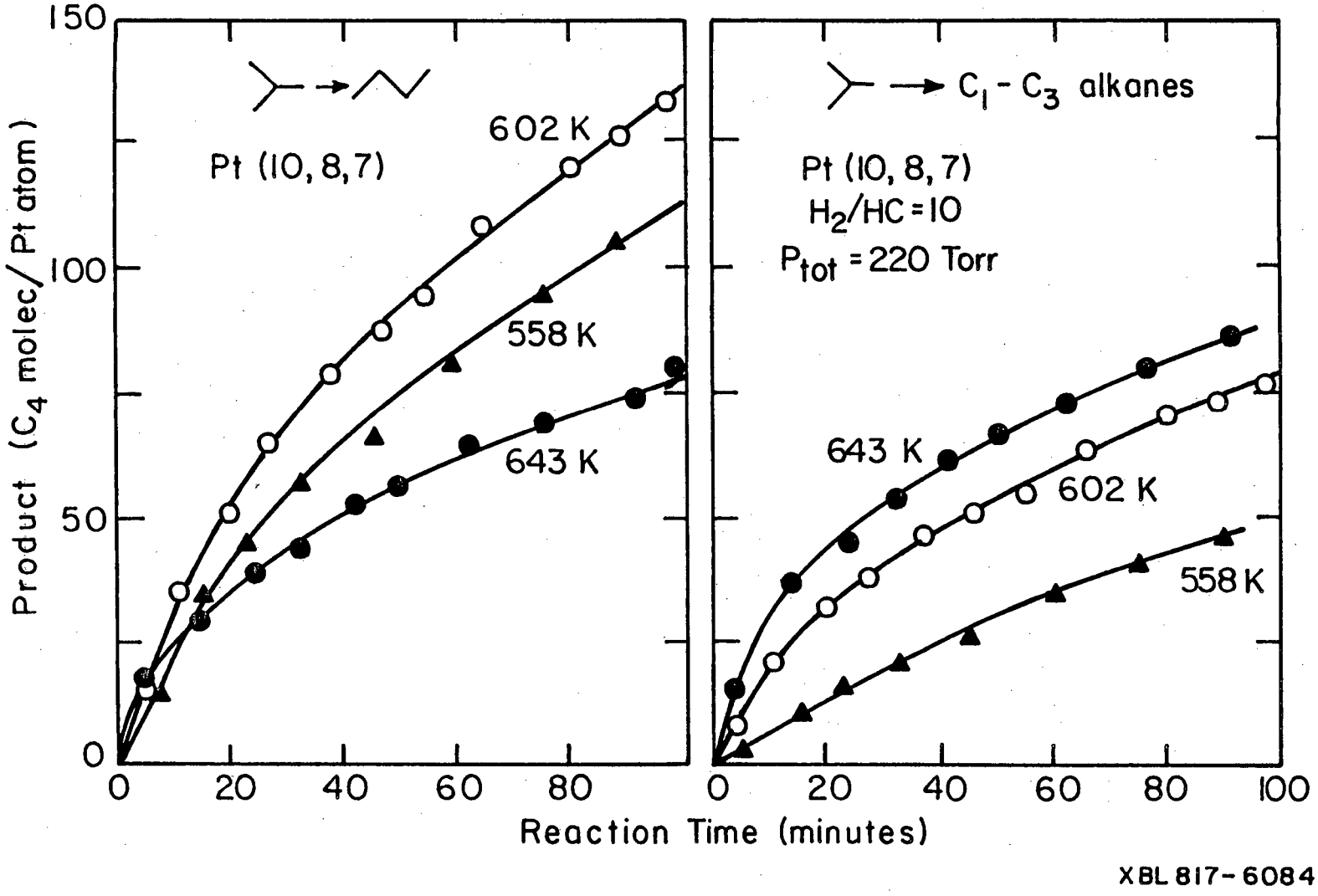
150
100
50
0
Product (C_4 molec/ Pt atom)
Pt (10, 8, 7)
602 K
558 K
643 K
$C_1 - C_3$ alkanes
Pt (10, 8, 7)
H_2/HC = 10
P_{tot} = 220 Torr
643 K
602 K
558 K
0
20
40
60
80
100
Reaction Time (minutes)
XBL 817-6084

Fig. 3.29

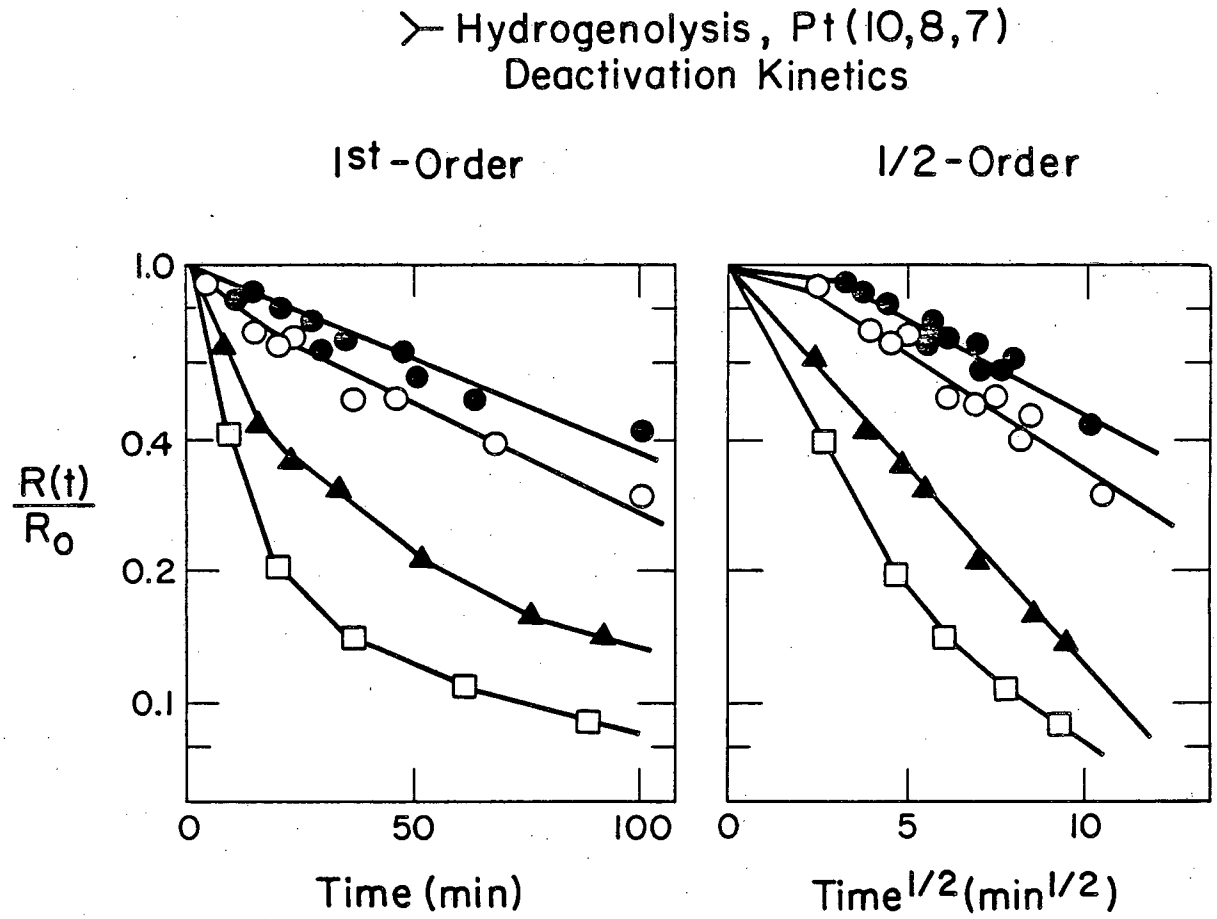

XBL 818-1093

Fig. 3.30

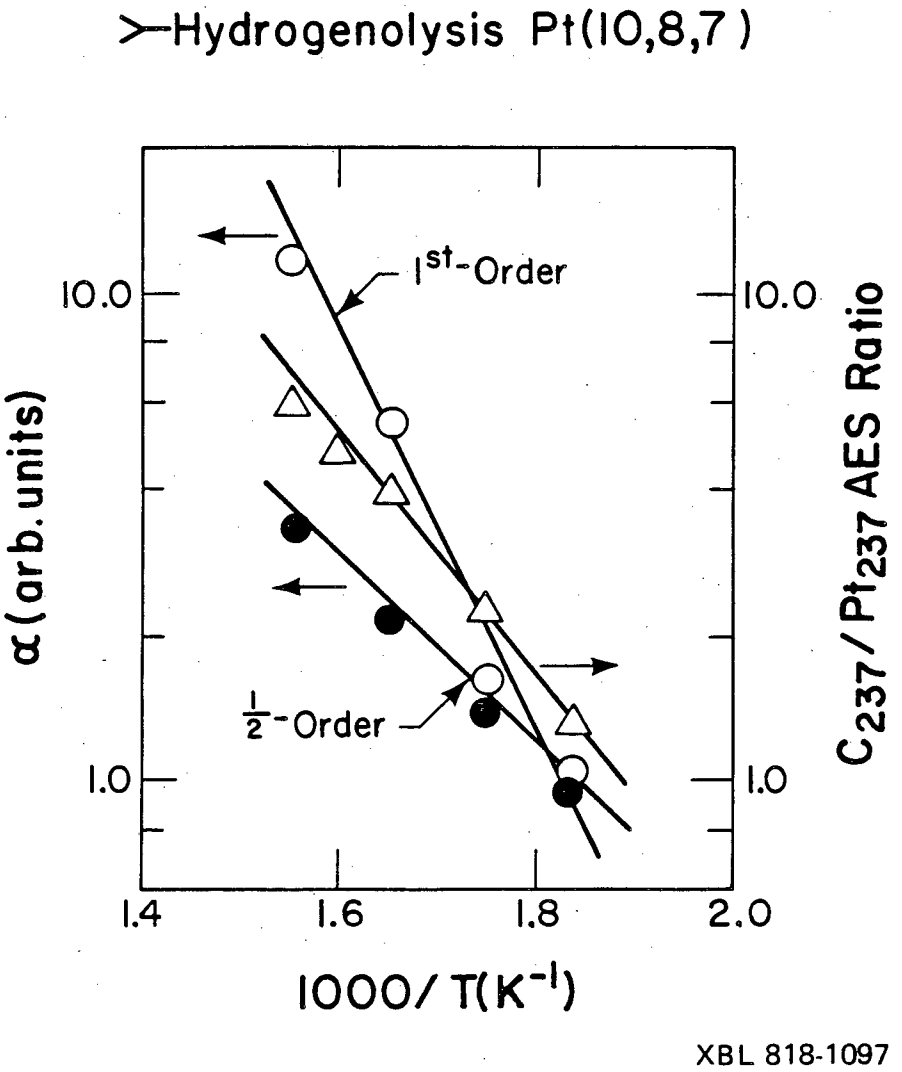
Hydrogenolysis Pt(10,8,7)
1st-Order
1/2-Order
10.0
1.0
α(arb.units)
C237/Pt237 AES Ratio
1.4
1.6
1.8
2.0
1000/T(K-1)
XBL 818-1097

Fig. 3.31

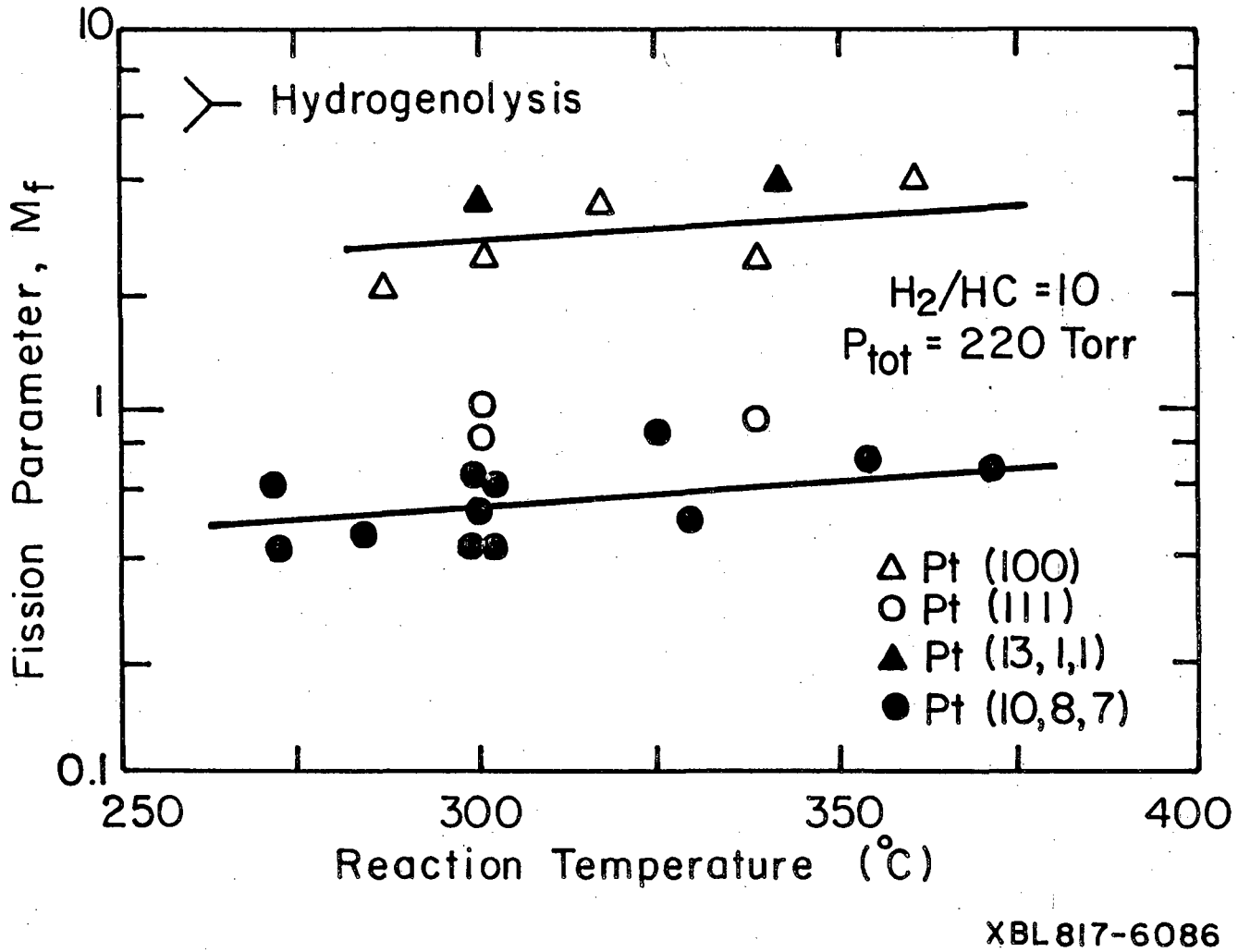
10
1
0.1
Hydrogenolysis
H_2/HC =10
P_{tot} = 220 Torr
Δ Pt (100)
o Pt (111)
▲ Pt (13,1,1)
● Pt (10,8,7)
Fission Parameter, M_f
250
300
350
400
Reaction Temperature (°C)
XBL817-6086

Fig. 3.32

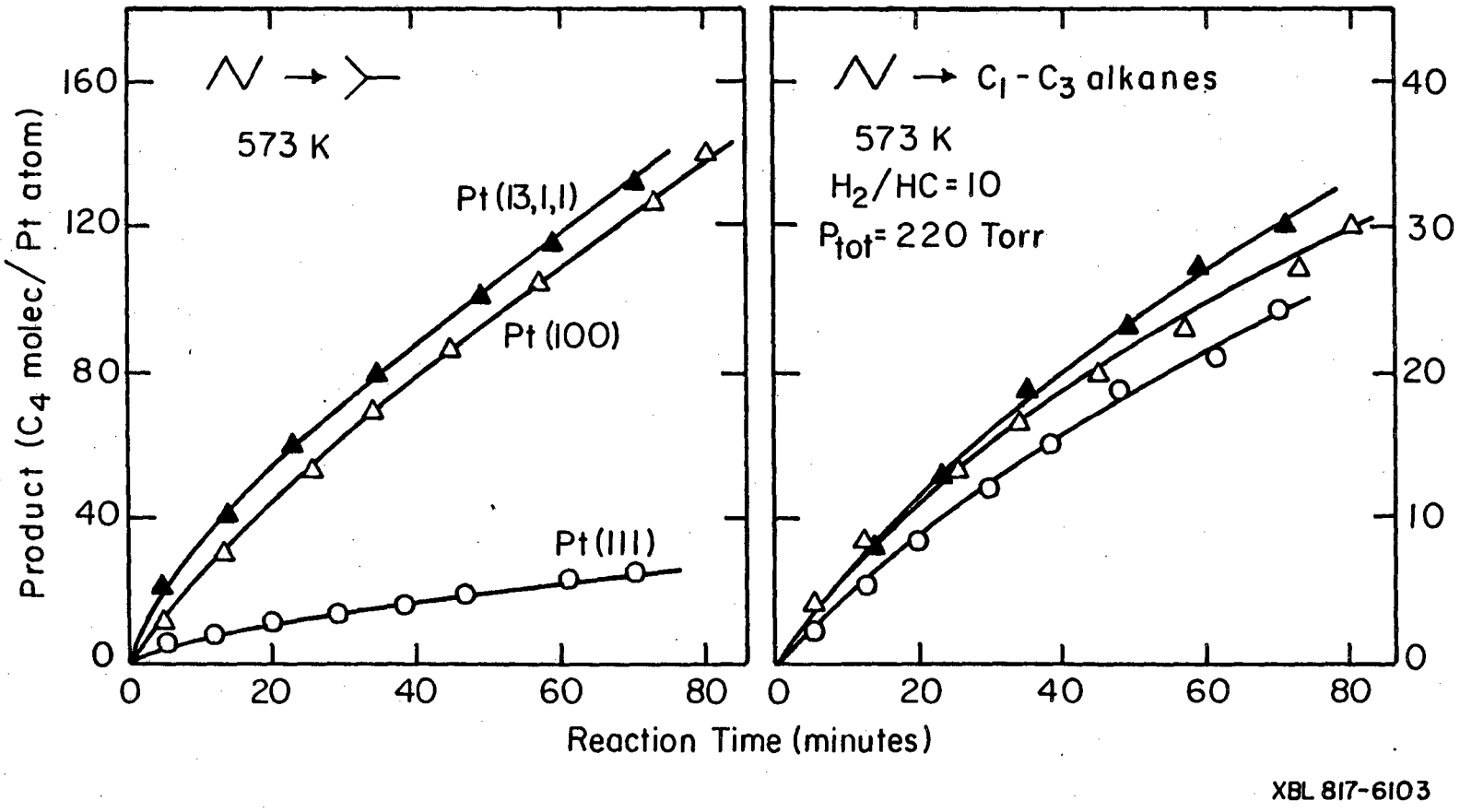

XBL 817-6103

Fig. 3.33

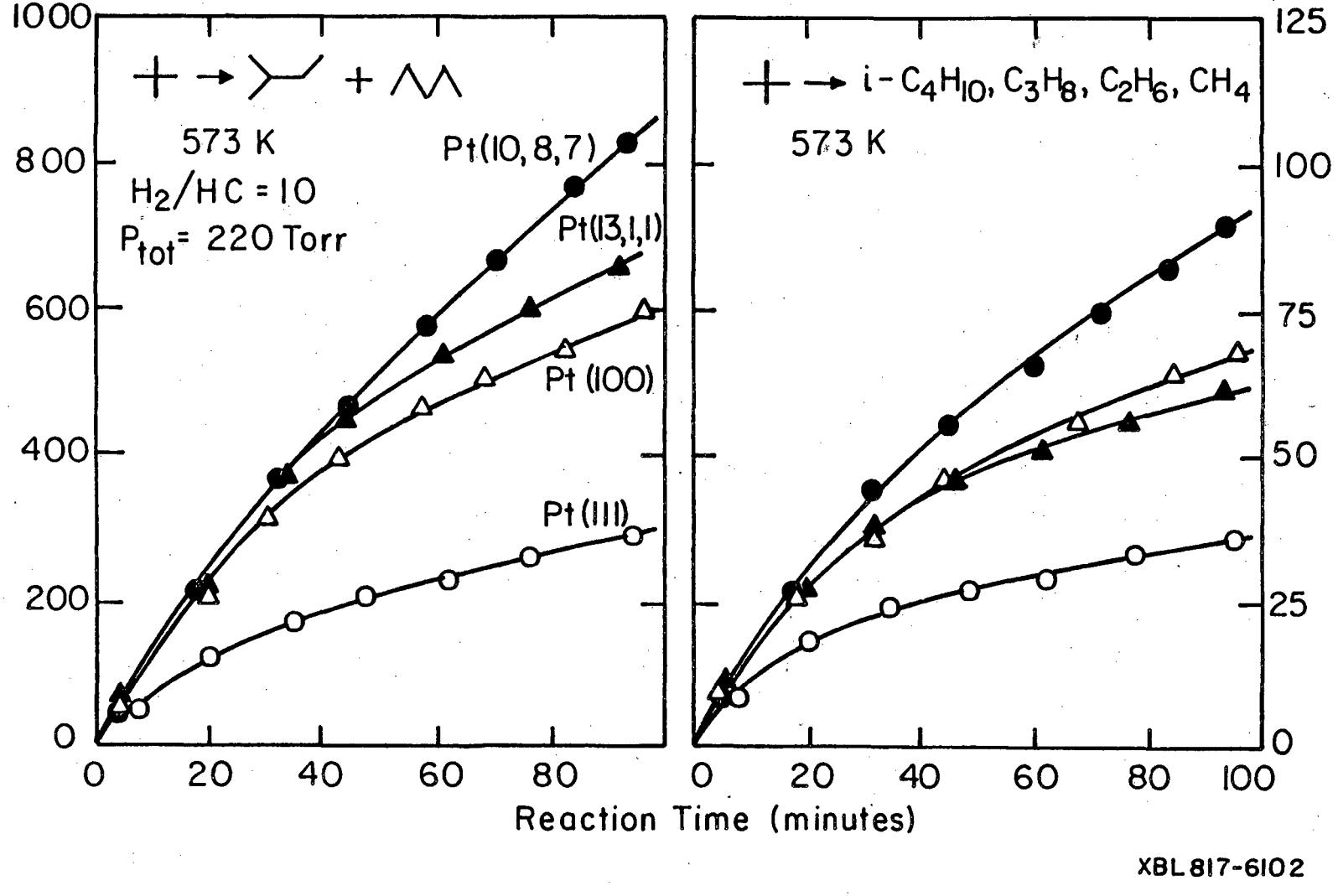
1000
800
600
400
200
0
573 K
H2/HC = 10
Ptot = 220 Torr
Pt(10,8,7)
Pt(13,1,1)
Pt (100)
Pt (111)
0
20
40
60
80
125
100
75
50
25
0
573 K
i - C4H10, C3H8, C2H6, CH4
0
20
40
60
80
100
Reaction Time (minutes)
XBL 817-6102

Fig. 3.34

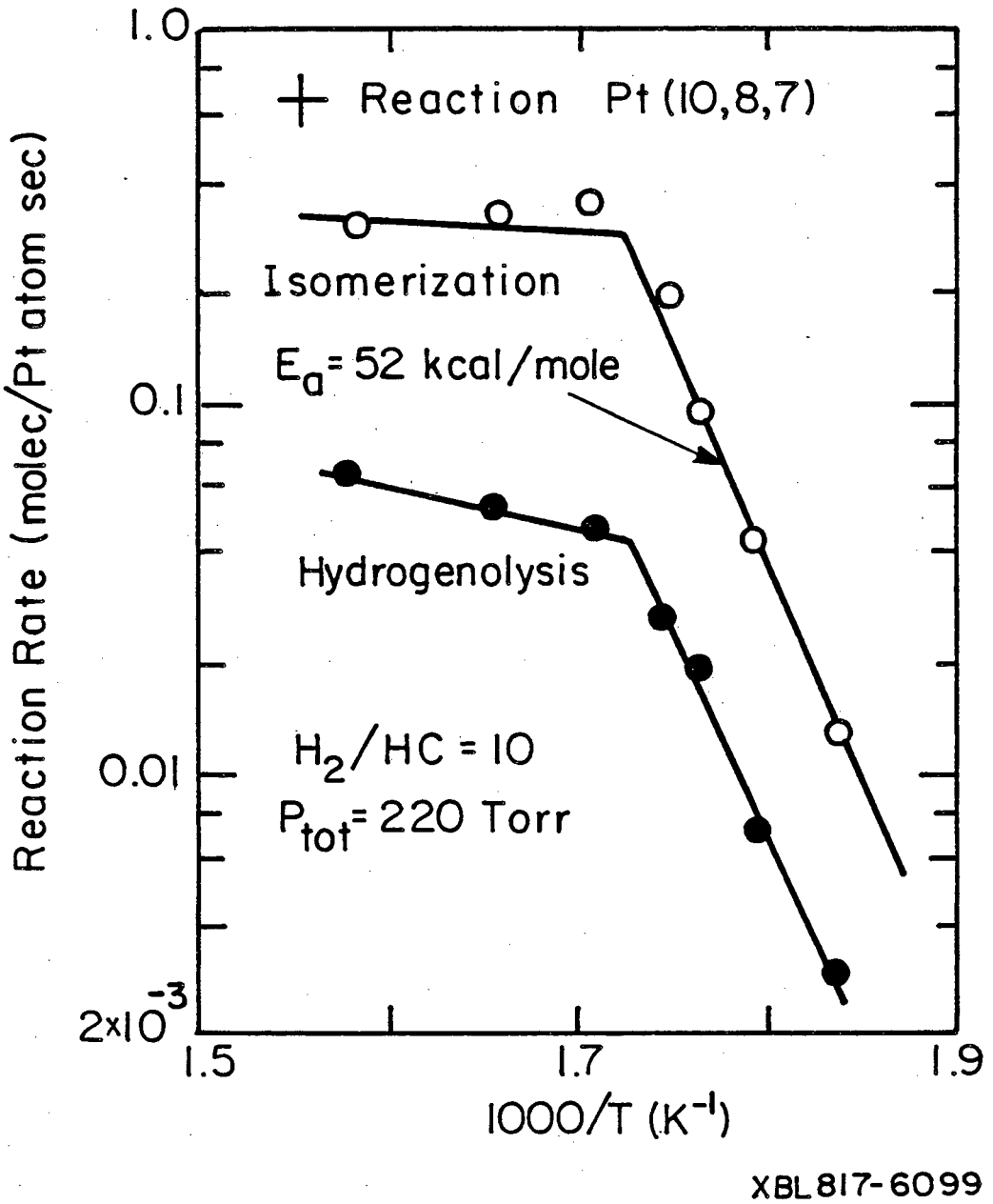
1.0
0.1
0.01
2x10^-3
Reaction Rate (molec/Pt atom sec)
Reaction Pt(10,8,7)
Isomerization
Ea = 52 kcal/mole
Hydrogenolysis
H2/HC = 10
Ptot = 220 Torr
1.5
1.7
1.9
1000/T (K^-1)
XBL817-6099

Fig. 3.35

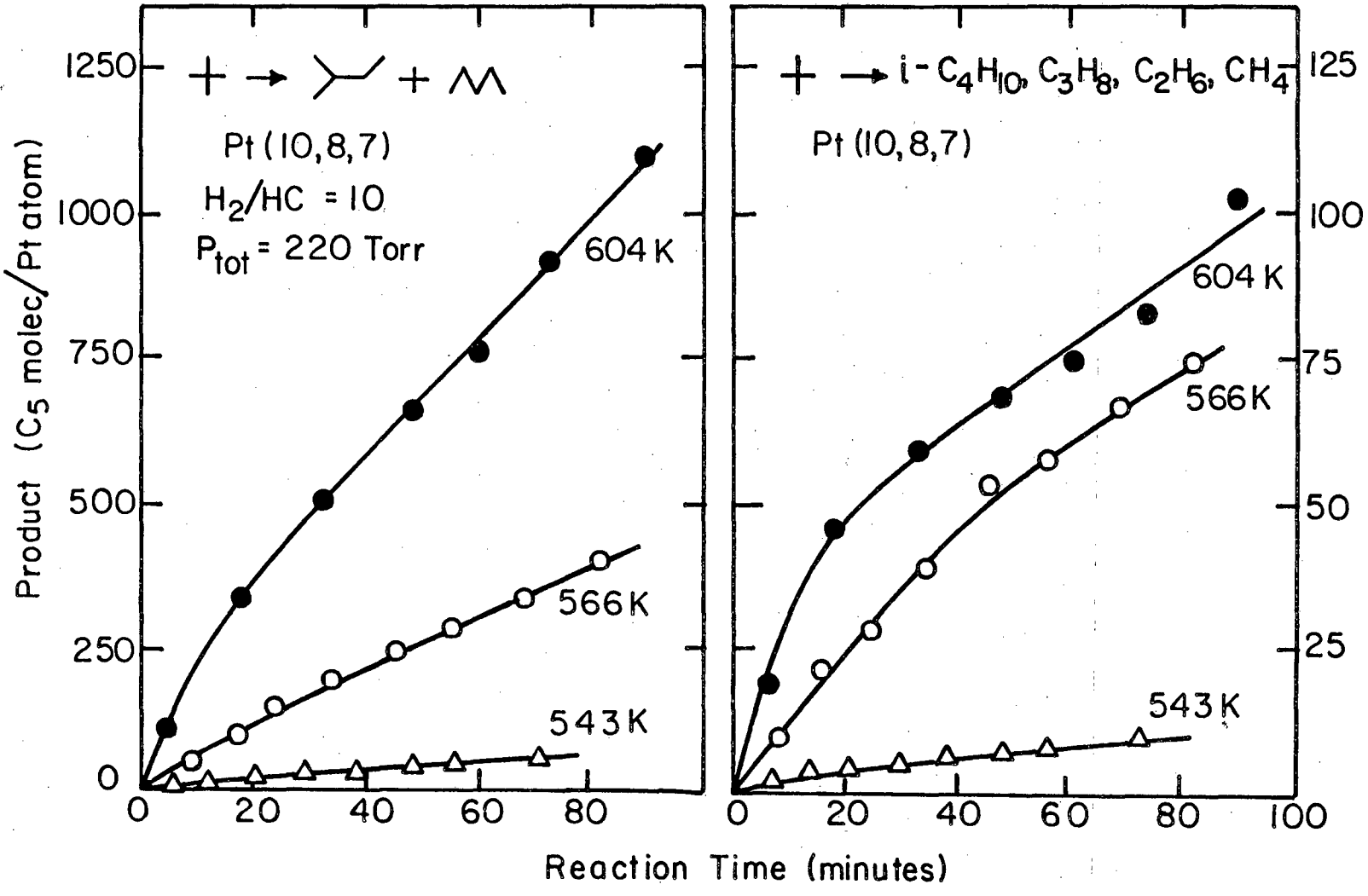
Product (C_5 molec/Pt atom)
1250
1000
750
500
250
0
+ → >—/ + /\/\
Pt (10,8,7)
H_2/HC = 10
P_{tot} = 220 Torr
604 K
566 K
543 K
0
20
40
60
80
+ → i-C_4H_{10}, C_3H_8, C_2H_6, CH_4
Pt (10,8,7)
125
100
75
50
25
604 K
566 K
543 K
0
20
40
60
80
100
Reaction Time (minutes)
XBL817-6089

Fig. 3.36

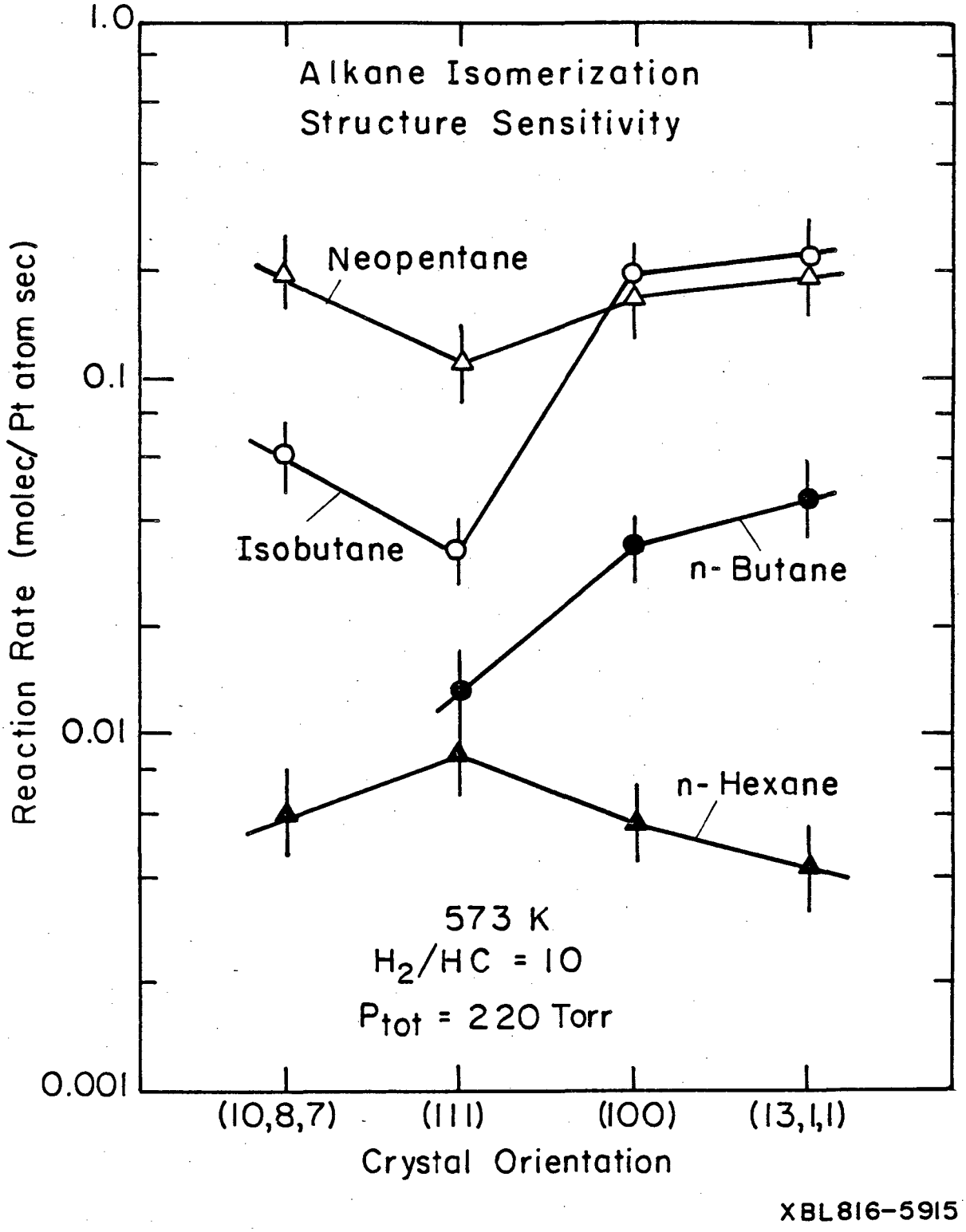
Alkane Isomerization
Structure Sensitivity
Neopentane
Isobutane
n-Butane
n-Hexane
573 K
H2/HC = 10
Ptot = 220 Torr
Reaction Rate (molec/Pt atom sec)
1.0
0.1
0.01
0.001
(10,8,7)
(111)
(100)
(13,1,1)
Crystal Orientation
XBL816-5915

Fig. 3.37

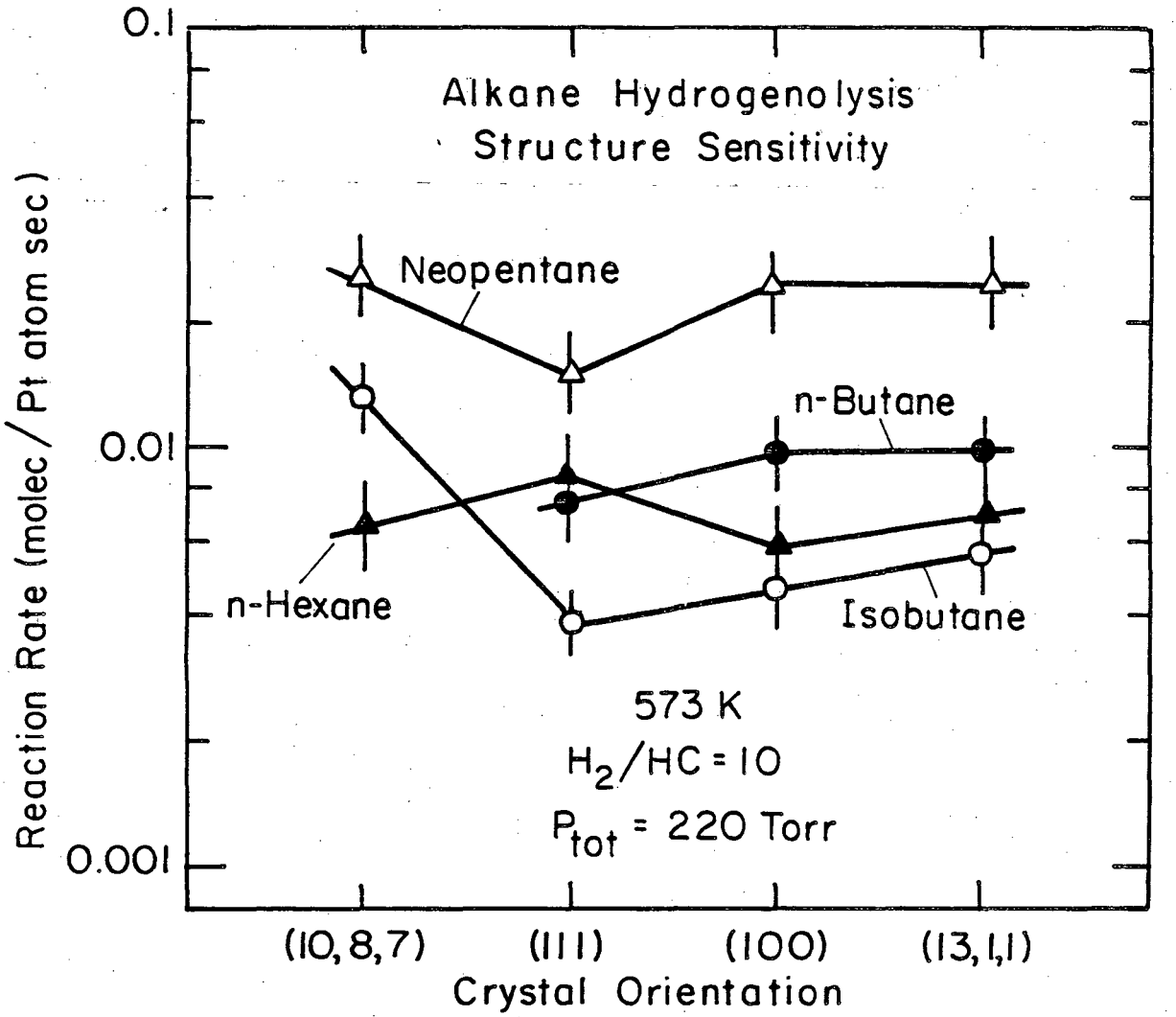
Alkane Hydrogenolysis
Structure Sensitivity
Neopentane
n-Butane
n-Hexane
Isobutane
573 K
H2/HC = 10
Ptot = 220 Torr
0.1
0.01
0.001
Reaction Rate (molec / Pt atom sec)
(10,8,7)
(111)
(100)
(13,1,1)
Crystal Orientation
XBL 816-5917

Fig. 3.38

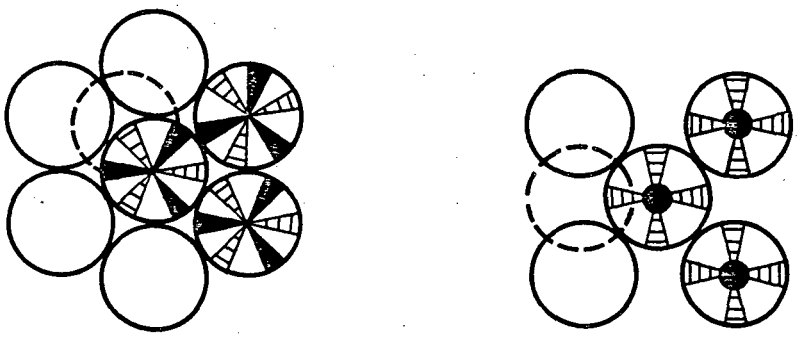

Pt (111)

Pt (100)

XBL 818-11303

Fig. 3.39

3.3 Correlation of Cyclohexene Reactions on Platinum Crystal Surfaces Over A 10-Order of Magnitude Pressure Range. Variations of Structure Sensitivity, Rates, and Reaction Probabilities

3.3.1 Background

The reactions of cyclohexene at low total pressures (10^{-8}-10^{-5} Torr) over platinum crystal surfaces have been investigated extensively (29,30). The hydrogenation and dehydrogenation reactions appear to be structure sensitive as indicated by the striking variations in catalytic behavior that are displayed by crystal surfaces of different atomic structure. At much higher pressures (10-10^{3} Torr) over silica supported platinum catalysts, Boudart and co-workers (90) have convincingly shown that cyclohexene hydrogenation is structure insensitive. The change of the reaction rate dependence on surface structure as the pressure is increased indicates that the reaction mechanism has changed. In order to explore how the reaction mechanism was altered, the catalyzed hydrogenation and dehydrogenation of cyclohexene was investigated over 10-orders of magnitude pressure range, from 10^{-8}-10^{2} Torr. Our catalyst was a stepped Pt(223) single crystal with a surface area of about 1 cm^{2}. The atomic surface structure of this sample consists of terraces of (111) orientation that are 5 atoms wide, separated by steps, one atom in height and of (100) orientation. The structure and composition of the surface was monitored by low energy electron diffraction (LEED) and Auger electron spectroscopy (AES) before and after the reaction studies, in situ, in the reaction chamber.

Our results indicate that at low reactant pressures the reaction occurs on an initially clean platinum surface and the kinetics are

characteristic of the uncovered metal. The catalyst deactivates rapidly however, due to the build-up of a monolayer of strongly bond carbonaceous species on the metal surface. At high reactant pressures ($\geq 10^{-1}$ Torr) platinum displays high, steady state catalytic activity in the presence of this carbonaceous overlayer which forms within seconds and usually persists in quasiequilibrium with gas phase hydrogen. It appears that while the hydrogenation and dehydrogenation of cyclohexene are structure sensitive on the clean platinum surface at low pressures these reactions may become structure insensitive in the presence of this carbonaceous deposit at high reactant pressures. This explains in part, the pressure dependence of the structure sensitivity of these reactions.

The turnover numbers increase by four to six orders of magnitude for the dehydrogenation and hydrogenation reactions, respectively, as the reactant pressure is increased from 10^{-8} to 10^{2} Torr. The reaction probabilities however, decrease by orders of magnitude with increasing pressure. Thus, the platinum surface becomes much less efficient to catalyze the surface reactions at high pressures.

3.3.2 Results and Discussion

The Build-up of the Carbonaceous Overlayer. Adsorption isotherms obtained at high and low pressures for cyclohexene chemisorption on the stepped (223) platinum surface are shown at several temperatures in Figure 3.40. The surface coverages were determined by AES

($C_{237}/Pt_{237} \simeq 2.8$ represents $\theta = 1$), and 1 Langmuir (L) corresponds to a gas exposure of 10^{-6} Torr sec (uncorrected for ion gauge sensitivity). Also shown are benzene and hydrogen thermal desorption spectra obtained after the low pressure exposures. While the surface coverage by adsorbed species increased little on going from 10^{-7} to 10 Torr, the surface coverage increased sharply with increasing temperature. As discussed in chapter 4, similar behavior was displayed by all types of hydrocarbons regardless of their structure, viz. ethylene, isobutane, neopentane, cyclohexene, n-hexane, n-heptane, and benzene. Following cyclohexene chemisorption at 300K, about 70-80 percent of the adsorbed species could be desorbed "reversibly" at ~370K in the molecular form as benzene. However, the bonding became much less reversible with increasing adsorption temperature. For adsorption temperatures above 400K, the bonding was effectively irreversible as the adsorbed layer then decomposed on further heating in vacuum with the evolution of hydrogen and only traces of benzene or other hydrocarbons. At higher adsorption temperatures the saturation coverage continued to increase, but the hydrogen content of the layer clearly diminished. After adsorption at temperatures higher than 650K, the adsorbed species no longer retained detectable amounts of hydrogen.

The temperature dependent cyclohexene bonding characteristics can be correlated with the catalytic behavior that was displayed during cyclohexene hydrogenation and dehydrogenation at both high and low reactant pressures. Product accumulation curves measured as a

function of reaction time for cyclohexene hydrogenation catalyzed over the (322) platinum surface are shown in Figure 3.41 for a total pressure of 77 Torr (H_2/HC = 10). At 300K, where cyclohexene chemisorbed reversibly, the product cyclohexane accumulated linearly as a function of time with no sign of deactivation. Continuous self-poisoning was observed at slightly higher temperatures corresponding to a gradual build-up of dissociatively absorbed species with multiple metal-organic bond multiplicity. Removal of these species by rehydrogenation appeared to occur slowly compared with the initial hydrogenation rate for clean platinum. At 450 K, a nearly complete monolayer of the strongly adsorbed species formed within minutes even in the presence of 70 Torr of hydrogen. Under these conditions, the rate of cyclohexane formation appeared to be partially controlled by the rate of intermolecular hydrogen transfer between the adsorbed species that covered the platinum surface. The rate of cyclohexane formation on the partially deactivated surface (2–4 molec/Pt atom sec at 425 K) corresponded closely with the initial rate of cyclohexene disproportionation in the complete absence of hydrogen, i.e.,

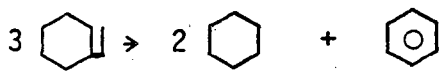

(1)

At 423 K with P_{Hc} = 10 Torr, for example, disproportionation displayed an initial turnover frequency of 3 molec/Pt atom sec and an activation energy of 17 ± 5 kcal/mole. The reaction produced 60 percent benezene and 40 percent cyclohexane. Product accumulation curves for the disproportionation reaction catalyzed at 438 K are shown in Figure 3.42.

Cyclohexane disproportionation is an excellent example of a hydrocarbon conversion reaction that must take place by intermolecular hydrogen transfer. The importance of this reaction pathway is reconsidered for other hydrocarbon molecules in Chapter 4.

In Figure 3.43 the rate of cyclohexane dehydrogenation at low reactant pressures ($\sim 10^{-6}$ Torr) is compared as a function of time with the build-up of the strongly bound carbonaceous surface species. The rate of deactivation at low reactant pressures correlated closely with the build-up of the carbonaceous deposit. The rapid self-poisoning demonstrates that the irreversibly adsorbed species were particularly effective in blocking sites that catalyze dehydrogenation. Reaction rates reported hereafter for low pressure reactions correspond to the maximum values that were obtained before the build-up of the carbon deposit. The catalytic activity observed at low pressures is clearly representative of the initially clean platinum surface. At high pressures, the initially clean platinum surface rapidly becomes covered by a monolayer of reversibly and irreversibly chemisorbed species. The catalytic behavior displayed during hydrogenation and dehydrogenation is given characteristic of an extensively precovered platninum surface.

In Figure 3.44 initial turnover frequencies measured for the hydrogenation reaction as a function of temperature over the stepped crystal surface are compared with those reported by Segal et al. (90) for dispersed platinum. The two sets of data agree well supporting the view (90) that the reaction at high pressures in structure insensitive.

The apparent activation energy for hydrogenation was 5.0 ± 0.5 kcal/mole on the stepped surface at 77 Torr.

The transition of the active platinum surface from being clean to continuously covered by the carbonaceous deposit was accompanied by a change from structure sensitive to structure insensitive catalytic behavior for the hydrogenation of cyclohexene. A change in mechanism is also indicated by the changing apparent activation energy for this reaction. It was less than 1 kcal/mole at low pressures while it was about 5 kcal/mole at high pressures. Similarly, the apparent activation energy for the dehydrogenation of cyclohexene was at least 8 kcal/mole at 77 Torr, while it was near zero at low pressures in the same temperature regime. A more pronounced increase in apparent activation energy with increasing pressure has also been observed during cyclohexane hydrogenolysis and dehydrogenation (28,30). The apparent activation energy for metal-catalyzed hydrocarbon reactions always appears to increase with increasing reactant pressures (33).

The Hydrogenation and Dehydrogenation Rate of Cyclohexene Over a Ten Order of Magnitude Pressure Range. Turnover frequencies and reaction probabilities determined at 425 K for the hydrogenation and dehydrogenation of cyclohexene in excess hydrogen are summarized in Figure 4.45. All the results were obtained using the stepped Pt(223) single crystal catalyst. The error bars at low pressures span the range of structure sensitivity for 2-6 different platinum crystal faces. Overall, the turnover numbers for hydrogenation and dehydrogenation varied by factors of 10^7 and 10^4, respectively, for a 10^9-fold increase in the cyclohexene

pressure. The fraction of reacting molecules that underwent dehydrogenation to benzene decreased from 94-100 percent at low pressure to just over 1 percent at a total pressure of 77 Torr. The dehydrogenation reaction probability - that is, the fraction of incident cyclohexene molecules that were convereted to benzene-declined markedly from ~0.05 at 10^{-7} Torr to less than 10^{-6} at 77 Torr. By contrast, the hydrogenation probability varied by only about two orders of magnitude (~10^{-3} - 10^{-5}) over the entire range of pressure, surprisingly exhibited a minimum at a total pressure of 10^{-2}-10^{-1} Torr and thereafter increased with increasing total pressure. In the pressure range of increasing reaction probability the hydrogenation rate was 1.3 order with respect to total pressure.

The enormous decline in the dehydrogenation probability with increasing pressure is mainly associated with the lengthy mean reaction time which was required for the dehydrogenation and desorption processes to occur. The 2-5 minute induction period observed before appreciable benzene desorption in our low pressure experiments (cf. Figure 3.43) indicates that the mean reaction time was on the order of 10 sec at 425°C and certainly no shorter than 10^{-1} sec. When the cyclohexene pressure was 10^{-7} Torr, the dehydrogenation probability was high (~0.05) because the time required for adsorption, surface reaction, and product transport away from the surface was short in comparison to the period between collisions of the reactant molecules with the surface (ca. 10^{-14} sec cm^2 at 10^{-7} Torr). At higher pressures the dehydrogenation efficiency decreased rapidly as the intercollision

period became much shorter than the mean reaction time. Under these conditions most of the surface sites where chemical reactions take place were continuously covered by adsorbed species. As a result, most of the incident hydrocarbon molecules scattered or desorbed from the surface before reactions could take place.

In order to assure that thermodynamic equilibrium considerations do not influence the kinetic data shown in Figure 3.45, the equilibrium constants and conversion concentrations of cyclohexene and benzene were calculated at low pressures ($\sim 10^{-7}$ Torr) and high pressures (77 Torr) at two temperature, 300 K and 425 K. These data are listed along with turnover frequencies in Table 3.13. It can be seen that at 425 K there was no thermodynamic boundary conditions that influenced the rates reported in Figure 3.45 with the possible exception of the low pressure hydrogenation reaction.

There could be another reason, in addition to the presence of the carbonaceous deposit, for the change of hydrogenation mechanism and reversal in selectivity at higher pressures. Reactive, weakly adsorbed hydrgeon (with heats of adsorption in the range of 8-10 kcal/mole) is identifiable on platinum only at pressures that exceed $\sim 10^{-1}$ Torr (91-94). At about this pressure the cyclohexene hydrogenation probability began to increase, and hydrogenation became the prevailing reaction pathway. While weakly adsorbed hydrogen hydrogenates benzene readily (92,95), studies by Basset et al. (92) indicate that strongly chemisorbed hydrogen ($-\Delta H_a \geq 15$ kcal/mole) does not add to benzene at all or at least not at an easily accessible rate. More general

Table 3.13. Equilibrium constants and turnover frequencies for cyclohexene reactions catalyzed at high and low pressure over Pt(223)

Reaction	T(K)	TN[a] low P	TN[a] high P	log[b]	C^a_{eq} low P	C^a_{eq} high P
Hydrogenation	300	$3\text{-}8\times10^{-6}$	2.8	13.08	99.9	99.9
	425	$3\text{-}8\times10^{-6}$	33	6.95	0.8	99.9
Dehydrogenation	300	2×10^{-4}	--	-3.96	99.9	0.2
	425	4×10^{-4}	0.4	0.65	99.9	99.7

a) Turnover frequencies (uncertainty ± 10 percent) and equilibrium conversions referred to initial pressures of 6×10^{-8} Torr C_6H_{10} and 6×10^{-7} Torr H_2 at low P; 7 Torr C_6H_{10} and 70 Torr H_2 at high P (1 Torr = 133 N m^{-2}).

b) Referred to ideal gas state at 1 atm (96).

considerations (33) suggest that at pressures of practical application this new type of weakly adsorbed hydrogen is responsible for most, perhaps all, metal-catalyzed hydrogenation reactions. Reversibly chemisorbed hydrogen must also be present under low pressure reaction conditions. However, the surface concentration, σ, at 10^{-6} Torr will be exceedingly small because its residence time, $\tau = \tau_o e^{-\Delta H_a/RT} = 10^{-8} - 10^{-5}$ sec, is short compared to the period between H_2 collisions with the surface ($1/F \cong 10^{-15}$ sec cm^2 at 10^{-6} Torr), so that $\sigma = F$ is less than $\sim 10^{10}$ cm^{-2}, i.e., less than 10^{-3} percent of a monolayer. At high pressures the steady state concentration of weakly adsorbed hydrogen will become appreciable as a result of the increased H_2 flux, and as a consequence, hydrogenation may become kinetically facile.

FIGURE CAPTIONS

3.40. Low and high pressure adsorption isotherms determined using AES for cyclohexene chemisorption on the stepped (322) platinum surface (upper frame). Benzene (lower left frame) and hydrogen (lower right frame) thermal desorption spectra obtained following the low pressure exposures at the indicated temperatures are also shown.

3.41. Product accumulation versus reaction time for cyclohexene hydrogenation over Pt(223) at several temperatures. Rapid sampling was facilitiated by the combined use of a mass spectrometer and gas chromatograph.

3.42. Product accumulation curves determined as a function of reaction time for cyclohexene disproportionation catalyzed at 438 K.

3.43. A comparison at 150°C of the cyclohexene dehydrogenation rate over Pt(223) at low pressures with the simultaneous build-up of the irreversibly chemisorbed carbonaceous overlayer. A C_{273}/Pt_{237} ratio of 2.8 corresponds to monolayer coverage.

3.44. Arrhenius plot for cyclohexene hydrogenation over Pt(223). For comparison the results of Segal, Madon, and Boudart (90) are included for P_{HC} = 13 Torr and P_{H_2} = 76 Torr.

3.45. Correlation of cyclohexene reaction rates and reaction probabilities over 10-orders of magnitude pressure range. The reactions were performed at 425 K over the stepped Pt(223) crystal surface with H_2/HC = 10.

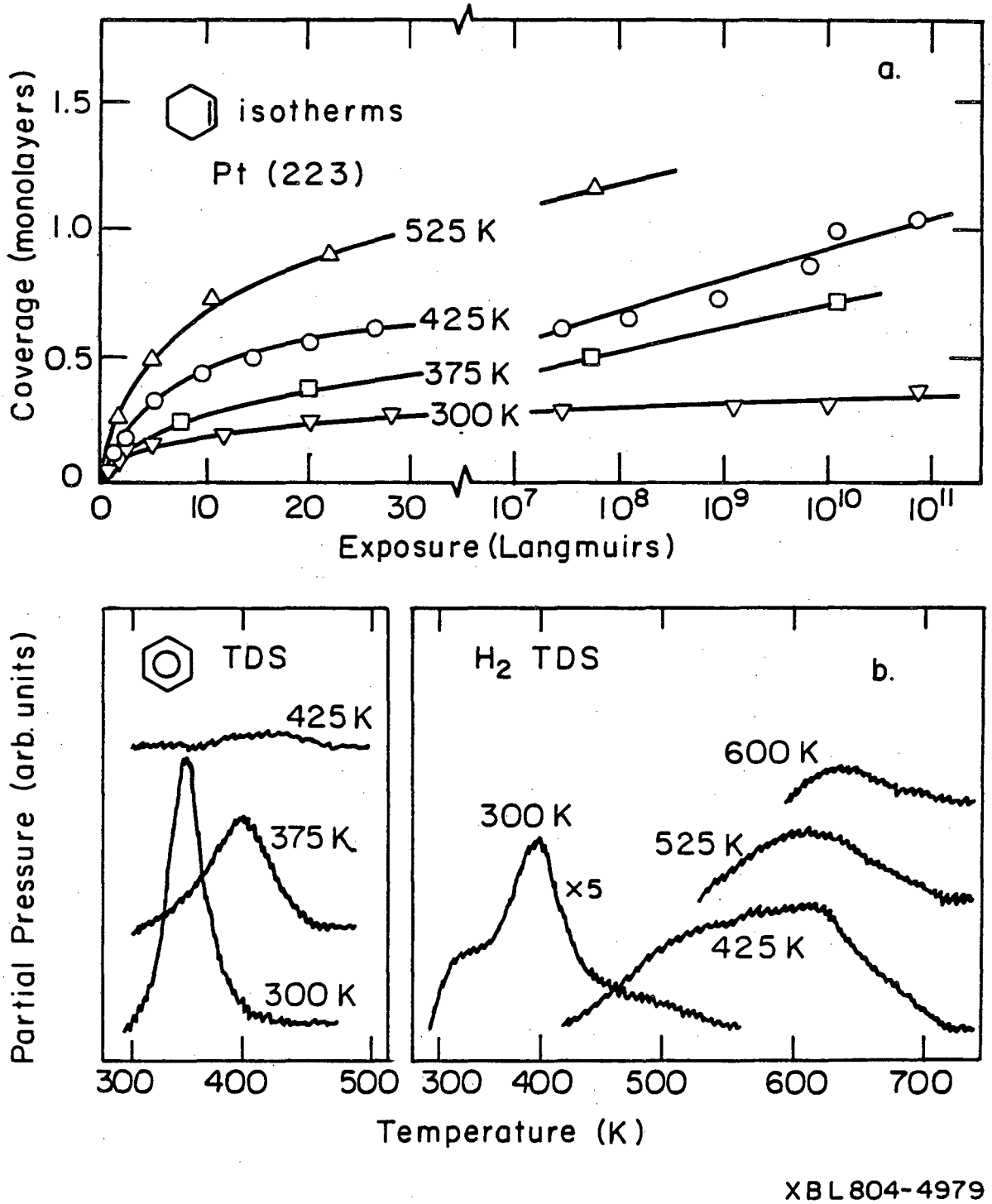
a.
isotherms
Pt (223)
525 K
425 K
375 K
300 K
Coverage (monolayers)
1.5
1.0
0.5
0
0
10
20
30
10^7
10^8
10^9
10^{10}
10^{11}
Exposure (Langmuirs)
TDS
425 K
375 K
300 K
H_2 TDS
b.
600 K
300 K
525 K
×5
425 K
Partial Pressure (arb. units)
300
400
500
300
400
500
600
700
Temperature (K)
XBL804-4979

Fig. 3.40

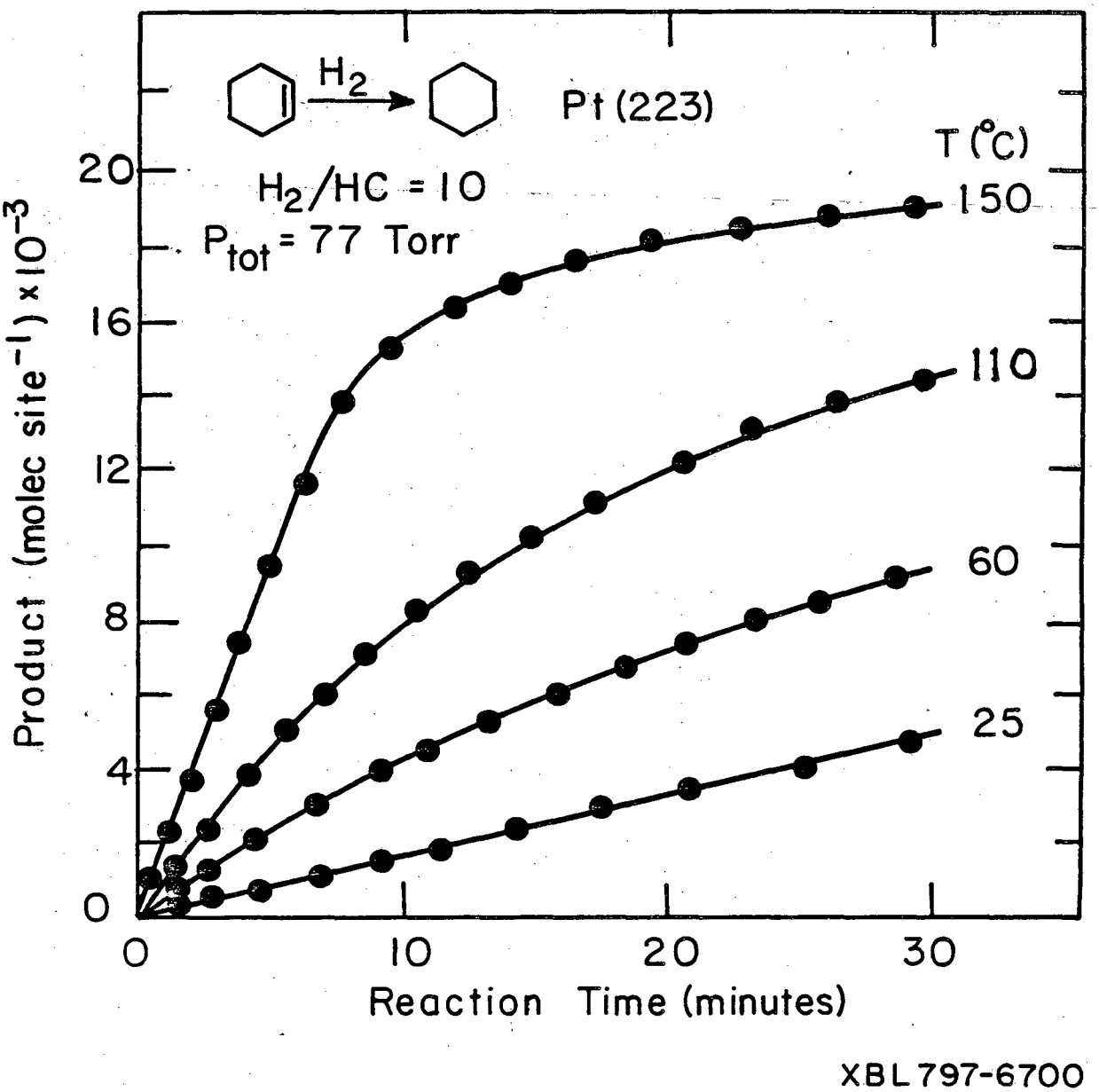
H2
Pt (223)
T (°C)
H2/HC = 10
Ptot = 77 Torr
150
110
60
25
Product (molec site-1) x10-3
0
4
8
12
16
20
0
10
20
30
Reaction Time (minutes)
XBL797-6700

Fig. 3.41

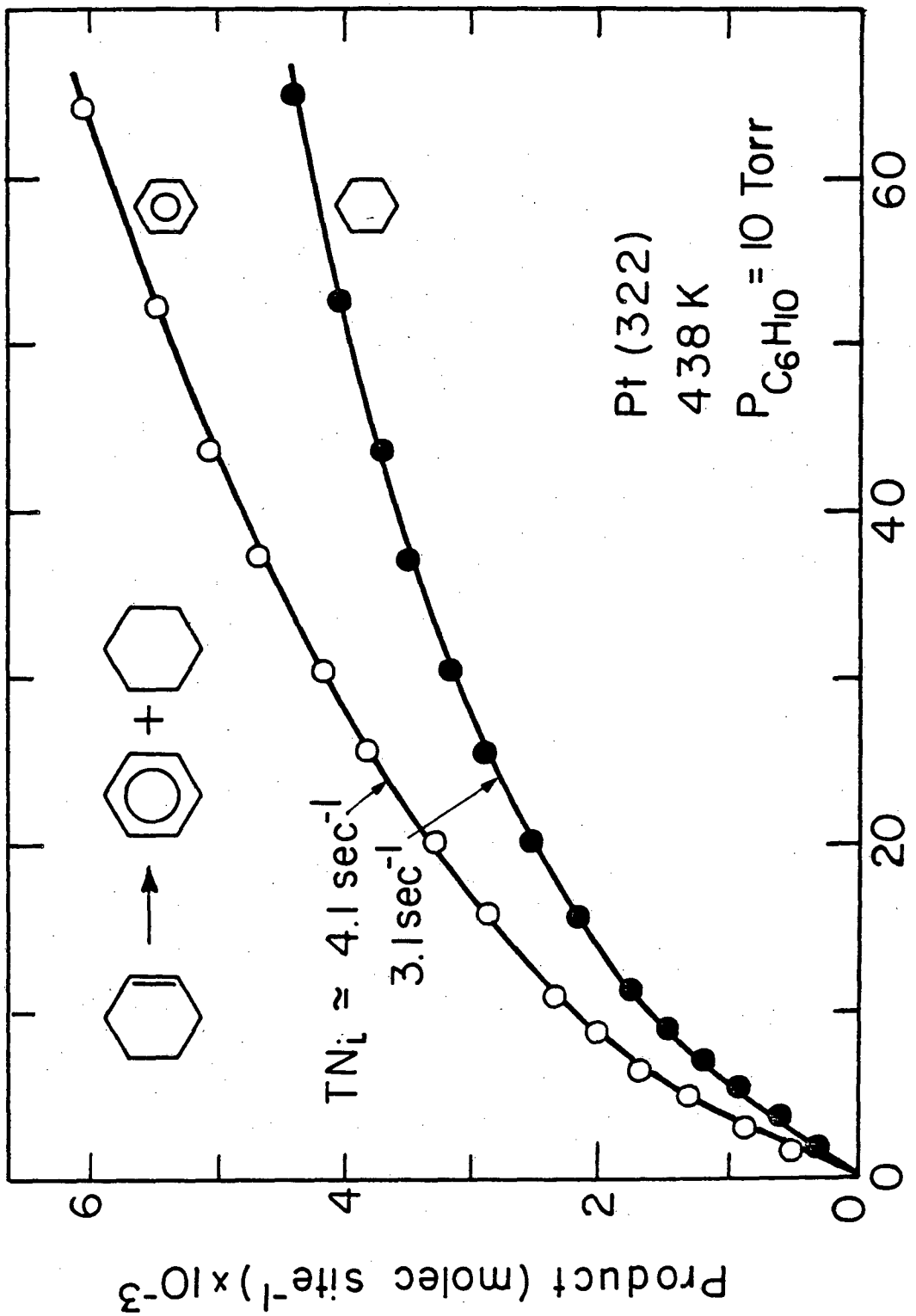

XBL 803-4865

Fig. 3.42

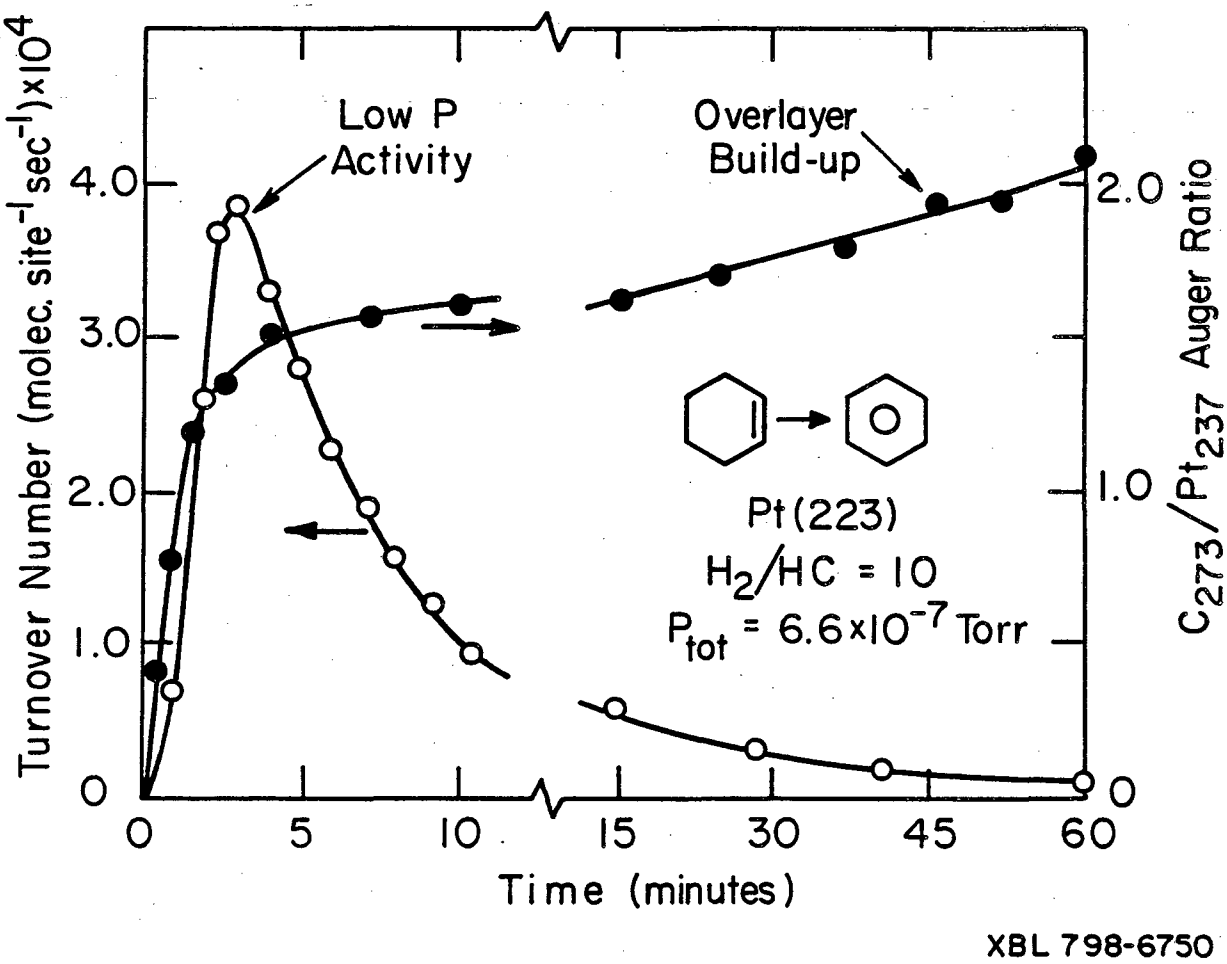
Turnover Number (molec. site^{-1}sec^{-1})x10^4
Low P
Activity
Overlayer
Build-up
4.0
3.0
2.0
1.0
0
2.0
1.0
0
C_{273}/Pt_{237} Auger Ratio
Pt(223)
H_2/HC = 10
P_{tot} = 6.6x10^{-7} Torr
0
5
10
15
30
45
60
Time (minutes)
XBL 798-6750

Fig. 3.43

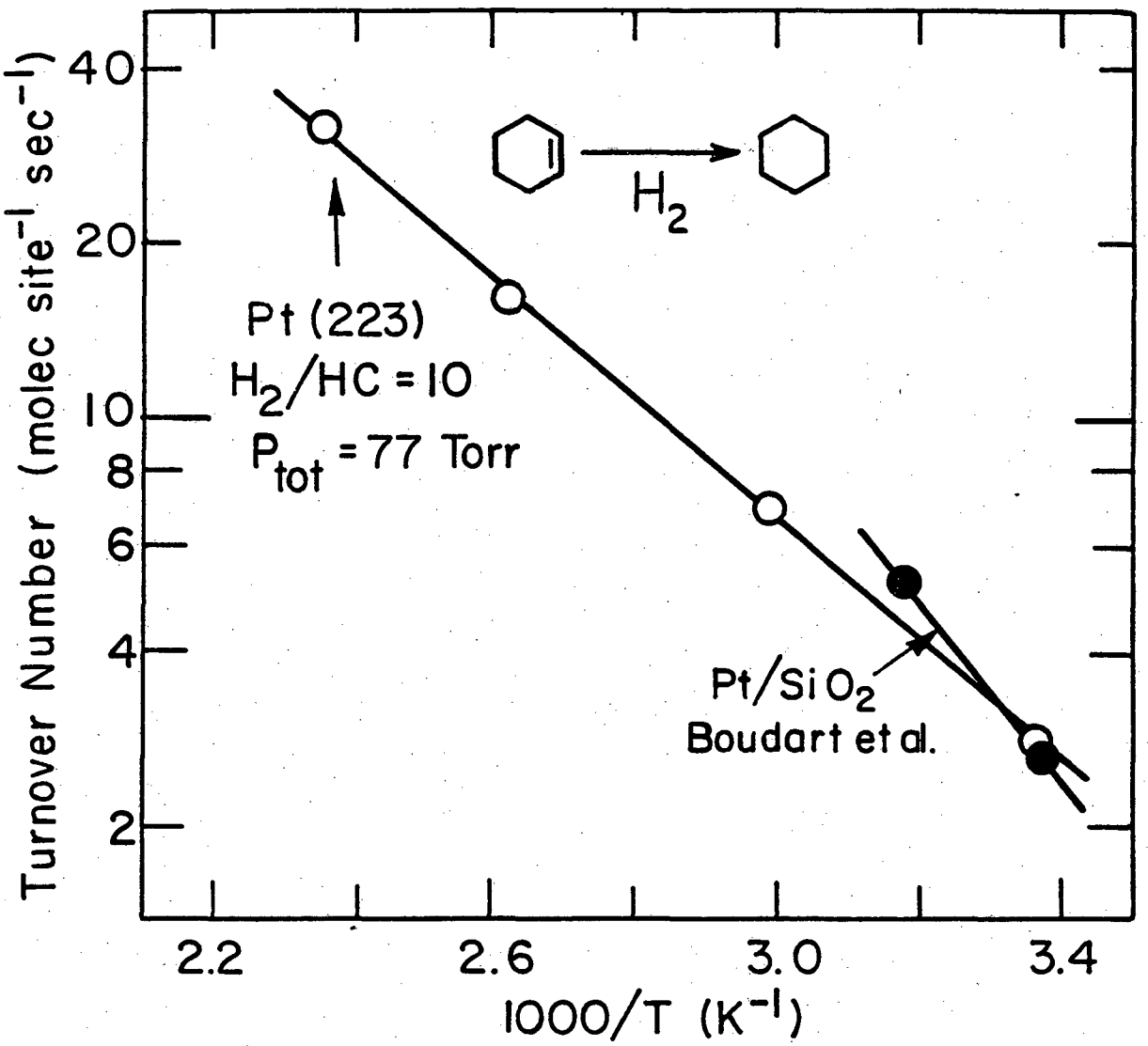
Turnover Number (molec site^{-1} sec^{-1})
40
20
10
8
6
4
2
2.2
2.6
3.0
3.4
1000/T (K^{-1})
H_2
Pt (223)
H_2/HC = 10
P_{tot} = 77 Torr
Pt/SiO_2
Boudart et al.
XBL797-6699

Fig. 3.44

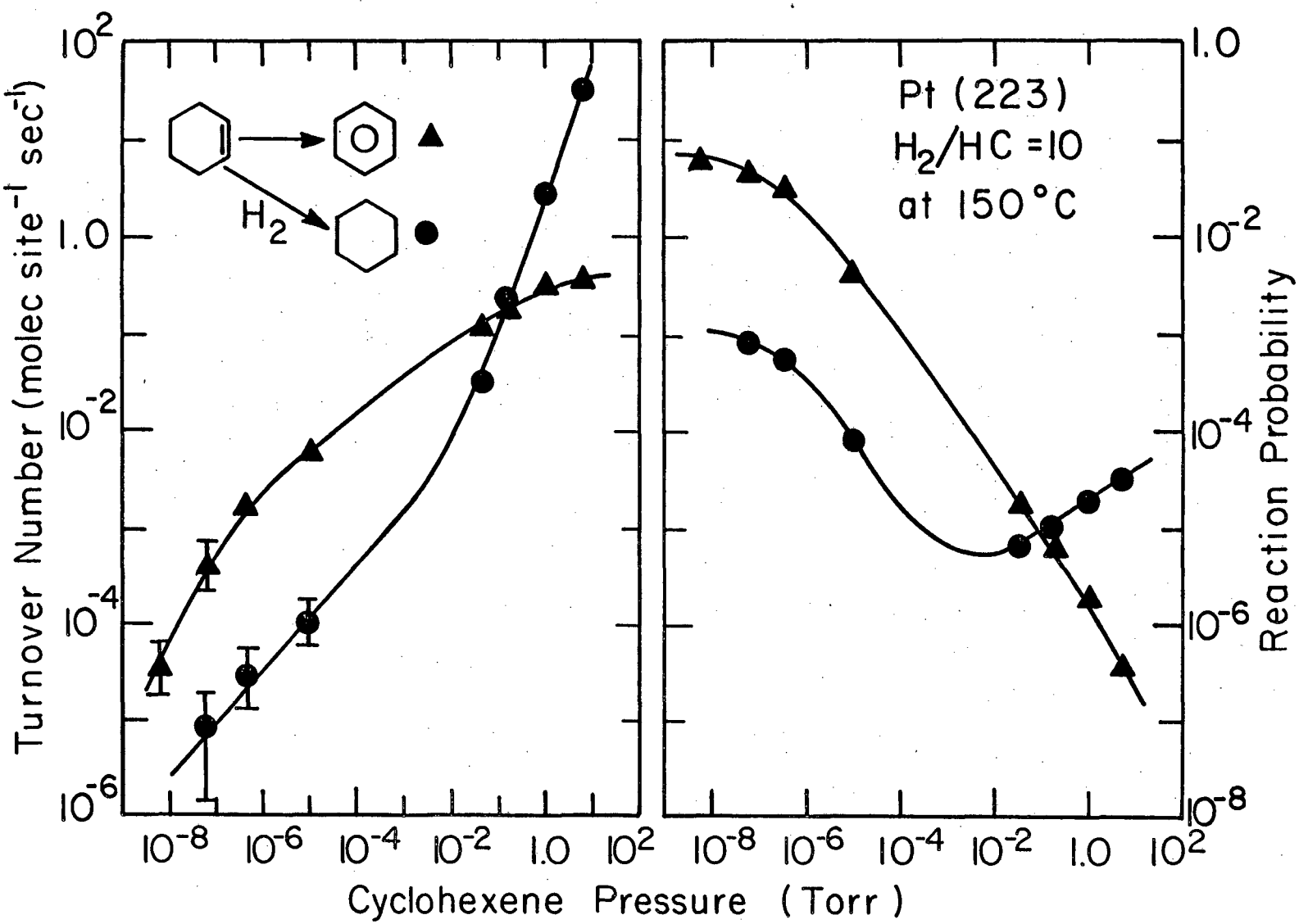

XBL 797-6698

Fig. 3.45

3.4 Deuterium Exchange Reactions of n-Hexane, n-Heptane, and Isobutane Catalyzed Over Platinum Single Crystal Surfaces

3.4.1 Background

Isotopic exchange reactions catalyzed over platinum between alkanes and deuterium gas have been investigated extensively in order to understand the energetics of C-H bond breaking processes which accompany dissociative hydrocarbon chemisorption on platinum. Exchange product distributions reported for propane (97), n-butane (65), pentanes (97), hexanes (97), and heptanes (97) revealed high selectivities for multiple exchange reactions in which several (often all) hydrogen atoms are replaced by deuterium during a single residence on the surface. Notable exceptions occurred only for molecules such as methane (98) and neopentane (99)) which contain only primary hydrogen atoms and often display maximum selectivities for exchange of a single hydrogen atom. While the multiplicity of deuterium exchange reactions can often reveal valuable information about the structure and composition of exchange reaction intermediates (75)), with few exceptions (65,100), the exchange reactions have been studied at temperatures that were lower than those rerquired for catalyzed hydrocarbon conversion reactions to occur at measurable rates, and the exchange kinetics were not investigated over a wide range of temperature and deuterium pressure.

The primary purpose of this section is to show that reaction rate studies carried out in deuterium at higher temperatures can be highly revealing if the kinetics of hydrocarbon conversion reactions are studied simultaneously with hydrocarbon-deuterium exchange. This section describes reaction kinetics and product distributions that were

measured for n-hexane, n-heptane, and isobutane deuterium exchange reactions catalyzed over the flat (111) and kinked (10,8,7) platinum single crystal surfaces. The studies were carried out near atmospheric pressure at temperatures between 500 and 650 K. Under these conditions hydrocarbon conversion to hydrogenolysis, isomerization, and cyclization products occurred simultaneously with deuterium exchange. Substantial inverse deuterium isotope effects that were detected for the hydrocarbon conversion reactions are reported in Section 3.5.

Several new features of the alkane-D_2 exchange reactions have been identified. Under our reaction conditions deuterium exchange appears to be structure-insensitive, and the kinetics appear to be controlled by the rate of dissociative deuterium chemisorption on the platinum surfaces that are always partially covered by strongly chemisorbed carbonaceous species. The exchange product distributions display little dependence on temperature, D_2-pressure, and surface composition. Under all conditions deuterium exchange occurs more rapidly than hydrocarbon conversion reactions.

3.4.2 Results

n-Hexane-D_2 Exchange Kinetics. Isotopic exchange reactions between n-hexane and deuterium gas were catalyzed over the flat (111) and kinked (10,8,7) crystal faces of platinum at temperatures between 508 and 658 K with total pressures ranging from 100 to 620 Torr. Total product accumulation curves measured as a function of reaction time for Pt(10,8,7) with $D_2/HC = 10$, and $P_{tot} = 220$ Torr are shown at several temperatures in Figure 3.46. There are two important features:

(1) the initial exchange rate was nearly constant over a wide range of temperature, and (2) self-poisoning caused by strongly chemisorbed carbonaceous species became increasingly pronounced with increasing temperature. The same catalytic behavior was observed for the flat (111) platinum surface. Initial exchange rates measured for both surfaces are compared as a function of temperature in Figure 3.47. Initial exchange activities were high with turnover frequencies in the range of 2-7 hexane molecules converted per surface platinum atom per second. Close agreement (±30 percent) was found for the initial rates determined over both surfaces. Also shown in Figure 3.47 are "steady state" exchange rates measured as a function of temperature after 2-1/2 to 3 hours of reaction. The exchange rates at the longer reaction times decreased markedly with increasing temperature because of the build-up of disordered carbon deposits on the platinum surface (as determined by AES). This is shown clearly in Figure 3.48 where the steady state rates are plotted as a function of $(1-\theta_{HC})$, the fraction of surface not covered by carbonaceous species. Surface coverages by carbonaceous species were estimated from Auger spectra recorded immediately after the reactions using a C_{273}/Pt_{237} peak-to-peak height ratio of 4.4 as one monolayer. This peak height ratio corresponds to 3.0 (±15 percent) carbon atoms per surface platinum atom (section 2.6). Steady state rates for both surfaces displayed a 1.6 ± 0.4 order dependence on the concentration of vacant platinum sites determined in this manner.

Exchange rates measured for the (10,8,7) platinum surface as a function of D_2 pressure with the temperature held constant at 573 K are shown in Figure 3.49. The initial exchange rate displayed a first-order (1.1 ± 0.3) dependence on deuterium pressure. The same reaction order for deuterium was obtained when the final rates at the end of the reactions were corrected for surface carbon coverage by dividing by the factor $(1-\theta_{HC})^{1.6}$.

n-Hexane-D_2 Exchange Selectivity. Initial product distributions for n-hexane-D_2 exchange were dominated by single exchange of one hydrogen atom ($C_6H_{13}D$) and complete exchange of all 14 hydrogen atoms (C_6D_{14}) under all reaction conditions. Multiple exchange processes always accounted for 70-85 percent of the total exchange reaction. Figure 3.50 shows initial isotopic distributions for Pt(10,8,7) that were determined at several different deuterium pressures with the temperature held constant at 573 K. Exchange product distributions determined as a function of reaction temperature for both platinum surfaces are summarized in Table 3.14. The kinetic selectivity for complete exchange over single exchange is shown as a function of temperature in the lower half of Figure 3.51. To compensate for isotopic dilution effects, complete exchange has been represented by the sum $d_{12} + d_{13} + d_{14}$. The kinetic selectivity for complete exchange displayed a maximum value of about 3 at temperatures between 550 and 590 K. The average number of deuterium atoms

Table 3.14 Initial product distributions for n-hexane-deuterium exchange catalyzed over Pt(111) and Pt(10,8,7) (a).

		Initial Distribution (Mole percent)													
Catalyst	T(K)	d_1	d_2	d_3	d_4	d_5	d_6	d_7	d_8	d_9	d_{10}	d_{11}	d_{12}	d_{13}	d_{14}
Pt(111)	533	27	2.8	2.1	1.6	1.8	1.9	1.8	1.4	1.5	2.8	2.8	3.1	14	33
	553	21	3.1	1.8	2.0	2.1	2.1	2.1	1.5	2.6	3.0	2.2	3.5	15	38
	573	20	4.2	2.7	2.3	2.3	2.5	2.1	0.7	1.0	1.9	3.2	4.4	15	37
	593	17	5.2	3.1	2.9	2.9	3.3	3.2	2.9	2.9	2.9	4.2	4.2	12	34
	638	17	6.2	3.6	3.5	3.6	3.7	3.7	3.5	3.5	3.5	4.1	4.3	11	29
Pt(10,8,7)	508	25	4.5	3.2	1.6	1.5	1.3	1.2	1.3	1.5	2.1	2.5	3.2	14	36
	533	23	3.8	2.7	1.7	1.6	1.6	1.3	1.3	1.6	1.6	2.1	2.6	14	41
	573	24	5.3	1.5	1.4	1.3	1.5	1.5	1.4	1.6	1.6	2.0	2.3	12	43
	593	17	8.1	6.0	2.9	3.1	2.9	3.1	2.9	2.9	2.9	3.2	3.5	10	29
	623	23	5.7	2.3	2.2	2.4	2.4	2.2	2.3	2.3	2.3	1.9	1.9	9	35
	658(b)	23	8.2	3.1	3.0	3.3	3.4	3.1	3.0	3.0	3.0	2.1	2.9	7	32
	573'(b)	14	3.4	3.0	2.5	2.5	2.6	3.0	3.4	3.5	3.5	3.8	4.2	10	39
	623'	22	4.8	2.8	2.3	2.2	2.2	2.2	2.4	2.9	2.9	3.2	4.0	8	38

a) $D_2/HC = 10$, $P_{tot} = 220$ Torr

b) Restart experiment over carbon covered platinum

incorporated, $\bar{M}$, displayed a similar dependence on reaction temperature as shown in the upper half of Figure 3.51. Exchange product distributions deterined in "restart" reactions carried out over platinum surfaces already covered with carbonaceous deposits from previous reaction sutdies were not significantly different from those measured for the initially clean platinum surfaces (Table 3.14).

Isobutane and n-Heptane-D_2 Exchange. Results for the exchange of isobutane and n-heptane with deuterium catalyzed over Pt(10,8,7) at 573-623 K are summarized in Table 3.15. The order of exchange reaction rates at 573 K followed the sequence isobutane > n-hexane $\geq$ n-heptane. Exchange product distributions for isobutane and n-heptane are compared in Table 3.16. Both reactions were characterized by mostly single or complete exchange with small contributions (1-5 percent) by all other possible multiple exchange products.

Composition of the Carbonaceous Deposits Thermal desorption studies were carried out following the deuterium exchange reactions in order to investigate the composition of the strongly chemisorbed hydrocarbon species which remained bonded on the platinum surfaces. Deuterium thermal desorption spectra recorded after n-hexane reaction studies over Pt(10.8,7) at 508 and 658 K are shown in Figure 3.52. The strongly adsorbed species that were deposited during the reactions contained mostly deuterium ($\geq$90 percent) with very small amounts of residual hydrogen. Sequential dehydrogenation and decomposition of the carbonaceous species took place in two or more steps with broad desorption peak maxima centered at 460 and 640 K.

Table 3.15 Reaction rates, average number of deuterium atoms incorporated, and surface carbon coverages measured for isobutane and n-heptane deuterium exchange catalyzed over Pt((10,8,7) (a).

Temperature (K)	Exchange Rates (molec/Pt atom sec). Initial	at 120 min.	$\bar{M}$	C_s/Pt (b) (±15%)
Isobutane				
573	27	11	8.0	0.7
n-heptane				
573	3.5	1.3	10.0	2.2
591	3.0	0.7	9.6	2.8
623	1.4	0.2	8.9	3.4

a) $D_2/HC = 10$, $P_{tot} = 220$ Torr

b) Carbon atoms per surface platinum atom.

Table 3.16 Product distributions for isobutane and n-heptane deuterium exchange catalyzed over Pt(10,8,7)[a]

		Initial Distribution (Mole)															
Reactant	T(K)	d_1	d_2	d_3	d_4	d_5	d_6	d_7	d_8	d_9	d_{10}	d_{11}	d_{12}	d_{13}	d_{14}	d_{15}	d_{16}
$i\text{-}C_4H_{10}$	573	12	2.2	1.5	3.4	1.2	3.3	0.7	1.0	22	53	--	--	--	--	--	--
$n\text{-}C_7H_{16}$	573	27	3.7	2.6	1.3	1.1	1.0	0.9	1.0	1.0	1.0	1.0	1.0	2.1	3.7	14	35
	623	21	9.6	3.5	2.6	2.7	2.8	2.4	3.0	2.6	2.4	2.4	2.6	2.6	2.6	11	26

$D_2/HC = 10$, $P_{tot} = 220$ Torr

Comparison Between Initial Reaction Rates for n-Hexane-D_2 Exchange and n-Hexane Conversion Reactions The total initial rate of n-hexane conversion to form hydrogenolysis, dehydrogenation, cyclization, and isomerization products, R_c is compared as a function of temperature with the overall n-hexane-deuterium exchange rate, R_x, for Pt(111) in Figure 3.53. The deuterium exchange rates have been corrected for the production of deuterated hexenes and thus refer exclusively to the production of deuterated hexanes (Section 2.8). It is clear that deuterium exchange occurred very rapidly compared with hydrocarbon conversion. For the total n-hexane conversion reaction (including dehydrogenation, R_d) the difference in initial rates, R_x/R_c, decreased from a factor of 20–30 at 530–550 K to about a factor of two at 640 K. Considering only the skeletal rearrangement reactions (isomerization, hydrogenolysis, and cyclization, $R_{sr} = R_c - R_d$), the difference in initial rates, R_x/R_{sr}, decreased from a factor of 400 at 530 K to about a factor of 10–15 at 640 K. Because all reaction products contained deuterium (Secton 2.8), the fractional selectivities for hydrocarbon conversion, $S_c = R_c/(R_c + R_x)$, and skeletal rearrangement, $S_{ss} = R_{sr}/(R_c + R_x)$, could be used to calculate the absolute probabilities that dissociatively chemisorbed molecules will undergo hydrocarbon conversion and skeletal rearrangement, respectively. These absolute reaction probabilities for dissociatively chemisorbed molecules (not to be confused with the kinetic reaction probability, $\gamma = (2\pi mkT)^{1/2}R_c/P$) are shown as a function of reaction temperature in Figure 3.54. The

probabilities for skeletal rearrangement and total conversion displayed magnitudes in the range 10^{-3} - 0.5 and both increased markedly with increasing reaction temperature.

3.4.3 Discussion

Structure Insensitivity of n-Hexane Deuterium Exchange. The flat (111) and kinked (10,8,7) platinum single crystal surfaces exhibited nearly identical catalytic behavior for isotopic exchange reactions between n-hexane and deuterium gas. Atomic steps and kinks which were present in high concentrations on the (10,8,7) surface did not produce notable changes in deactivation behavior, exchange product distributions, or exchange catalytic activity. Based on these results, n-hexane-D_2 exchange appears to be a good example of a structure insensitive reaction. Additional studies using (100) and (110) platinum single crystal surfaces would be worthwhile to further confirm this observation.

Deuterium Exchange Kinetics The kinetics of deuterium incorporation into both n-hexane and n-heptane catalyzed at 510-650 K displayed an apparent activation energy near zero (±5 kJ/mole). The rate of n-hexane-D_2 exchange exhibited a first order dependence on D_2 pressure (at 573 K) (Figure 3.49) and a positive 1.6 order dependence on the apparent concentration of uncovered platinum surface sites (Fig. 3.48). For Pt(10,8,7), the initial and steady state rates could both be expressed by a single rate expression,

$$R_x \simeq A(1-\theta_{HC})^{1.6}(D_2)^{1.1} \qquad (1)$$

where A, the apparent pseudo-first order pre-exponential factor, was on the order of 10^{-20} cm^3 Pt $atom^{-1}sec^{-1}$. These facts all support a reaction sequence in which the dissociative chemisorption of deuterium molecules at sites containing one or, more likely, two uncovered platinum atoms is rate controlling, e.g.

$$D_2 \rightarrow 2D(ads) \qquad (2)$$

This interpretation is supported by molecular beam reactive scattering studies which revealed that dissociative deuterium chemisorption and H_2-D_2 exchange occur over platinum with an activation energy very close to zero (101). Under our reaction conditions, there appears to exist only a small concentration of free sites located between adsorbed hydrocarbon species where deuterium is chemisorbed at low surface coverage.

Deuterium Exchange Product Distributions. Initial product distributions for n-hexane and n-heptane-deuterium exchange displayed little dependence on temperature, D_2 pressure, surface structure, and surface composition (Tables 3.14, 3.16, Figure 3.50). Simple replacement of a single hydrogen atom or complete exchange of all 14 or 16 hydrogen atoms prevailed under all reaction conditions. The selectivity for complete exchange over single exchange increased slowly with increasing temperature until a maximum selectivity was obtained at 560-600K. Similar behavior was reported by Long et al. (97) for n-hexane-D_2 exchange catalyzed at 340-470K over platinum films that

were prepared in ultra high vacuum. Under their reaction conditions (D_2/HC = 9.4, P_{tot} = 30 Torr) partial exchange reactions occurred preferentially in methylene groups. Product distributions dominated by complete exchange were also noted by Gault and Kemball for n-hexane-D_2 exchange catalyzed at 330-520 K over palladium and rhodium films (102).

The series of reaction steps shown below can be used to account for the observed pattern of n-hexane-D_2 exchange selectivity.

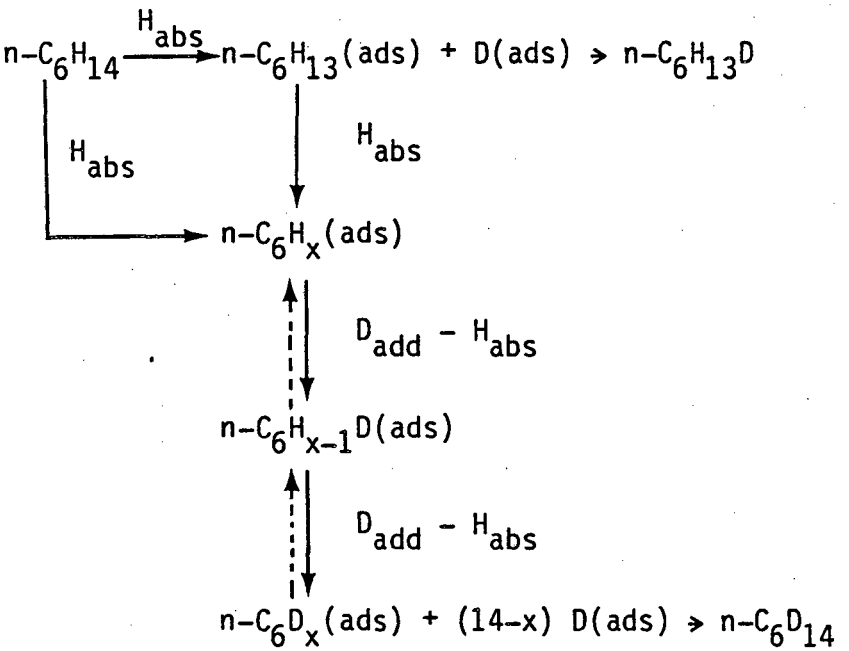

Dissociation of a single C-H bond produces surface alkyl species that yield n-$C_6H_{13}D$ upon deuterium addition. Further dissociation and rearrangment of the surface species yields strongly bonded intermediates which interconvert into C_6D_x species by a series of elementary deuterium addition and hydrogen abstraction processes.

These interconversion processes occur rapidly compared with the final deuterium addition step(s) that produce mostly n-C_6D_{14}. While the structures of the intermediate species involved in the interconversion pathway cannot be inferred directly from the exchange product distributions, it is notable that recent studies in our laboratory have shown that ethylidyne ($Pt_3 \equiv C - CH_3$) species are the most abundant surface intermediates involved in ethylene-deuterium exchange catalyzed over Pt(111) at 350-450 K (103). Similar alkylidyne and/or alkylidene surface species are expected to be important in the reaction pathway leading to multiple exchange in larger hydrocarbon molecules.

Reaction Times, Reaction Probabilities, and Role of Adsorbed Carbon Deposits. The results reported here clearly demonstrate that hydrocarbon-deuterium exchange reactions take place very rapidly compared with hydrocarbon skeletal rearrangement. For n-hexane reactions catalyzed over Pt(111) and Pt(10,8,7), the ratio of initial rates R_x/R_{sr} decreased drastically with increasing temperature from about 400 and 530 K to roughly 10 at 640 K. For isobutane, n-hexane, at n-heptane reactions catalyzed over Pt(10,8,7) at 573 K, the R_x/R_{sr} ratios varied between 290 (i-C_4H_{10}) and about 50 (n-C_7H_{16}). Because deuterium exchange occurred rapidly compared with all other competing chemical reactions, the overall rates of deuterium exchange can be used to determine minimum surface residence times that are required for dissociative chemisorption and rehydrogenation to occur. Under our reaction conditions, these residence times must be equal to or longer than the reaction times, $\tau = (R_x + R_c)^{-1}$, that were on the order of

10^{-1} sec. Because this time was very long compared with the period between surface collisions of gas phase hydrocarbon molecules ($\sim 10^{-21}$ sec cm^2), it is clear that the reaction probability of incident hydrocarbon molecules during a single collision with the platinum surface was very low and that most of the molecules simply desorbed or scattered from the surface without undergoing any chemical reaction. The kinetic reaction probability, calculated directly using the relation $\gamma = (2\pi mkT)^{1/2}(R_x + R_c)/P_{HC}$ was about 2×10^{-6}.

The strongly chemisorbed carbonaceous species which were deposited on the platinum surfaces during the deuterium exchange reactions were partially dehydrogenerated with an average deuterium (plus hydrogen) content of about one atom per surface carbon atom (Section 4.4). These species inhibited the dissociative chemisorption of deuterium molecules by site blockage and thereby decreased the rates of the alkane-deuterium exchange reactions. Uncovered platinum sites were required for the exchange reactions to occur at measurable rates. It therefore seems clear that the deuterium exchange reactions predominantly take place directly at the metal surface and not by means of hydrogen (or deuterium) transfer reactions with the strongly bound species. This conclusion is supported by carbon-14 radiotracer studies (Section 4.5) which have shown that hydrogen transfer is typically 5-10 times slower than direct hydrogenation using gas phase hydrogen.

FIGURE CAPTIONS

Figure 3.46. Total product accumulation curves measured as a function of reaction time for n-hexane-D_2 exchange catalyzed over the kinked (10,8,7) platinum surface.

Figure 3.47. Temperature dependence of the initial and steady state rates of n-hexane-D_2 exchange catalyzed over (111) and (10,8,7) platinum single crystal surfaces.

Figure 3.48. Correlation of steady state n-hexane-D_2 exchange rates with the fraction of surface not covered by strongly bound carbonaceous species. A C_{273}/Pt_{237} AES peak-to-peak height ratio of 4.4 was taken as one monolayer corresponding to 3.0 (±15 percent) carbon atoms per surface platinum atom (D_2/HC = 10, P_{tot} = 220 Torr).

Figure 3.49. Dependence of initial and steady state rates on deuterium pressure for n-hexane-D_2 exchange catalyzed over Pt(10,8,7).

Figure 3.50. Initial product distributions at several deuterium pressures for n-hexane-D_2 exchange catalyzed over Pt(10,8,7) at 573 K.

Figure 3.51. Average number of deuterium atoms incorporated (upper frame) and kinetic selectivities for complete exchange over single exchange (lower frame) determined for n-hexane-D_2 exchange reactions catalyzed at 500-650 K.

Figure 3.52. Deuterium thermal desorption spectra recorded after n-hexane-D_2 exchange reactions that were carried out over Pt(10,8,7) at 508 and 658 K. A linear heating rate of 74 ± 5 K sec^{-1} was used.

Figure 3.53. Comparison between initial reaction rates for n-hexane-D_2 exchange (R_x), n-hexane conversion (R_c), and n-hexane skeletal rearrangement (R_{sr}) reactions catalyzed over Pt(111).

Figure 3.54. Absolute reaction probabilities for n-hexane conversion and n-hexane skeletal rearrangement reactions catalyzed over Pt(111) in the presence of deuterium gas.

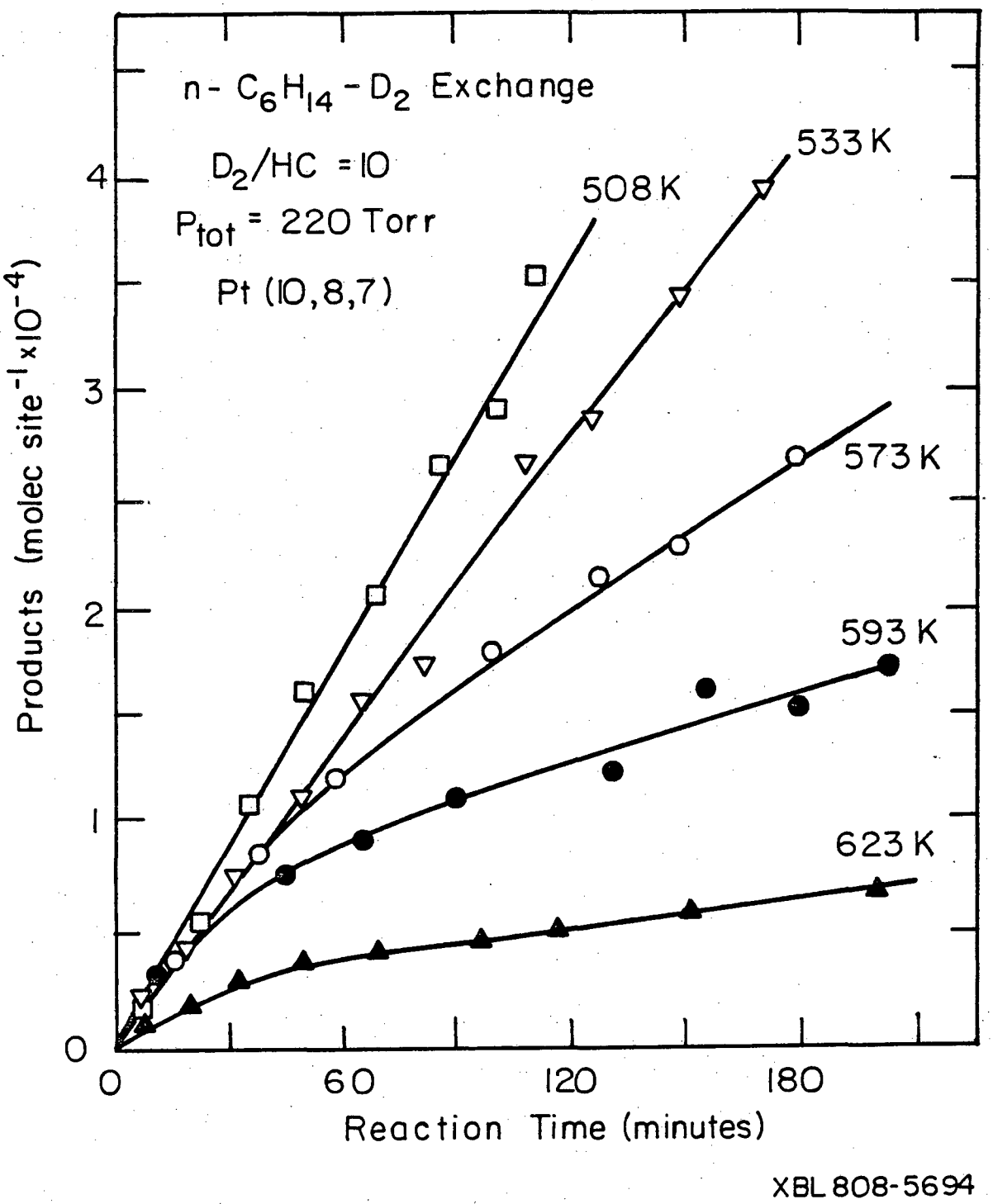
n- C6H14 - D2 Exchange
D2/HC = 10
Ptot = 220 Torr
Pt (10,8,7)
508 K
533 K
573 K
593 K
623 K
Products (molec site-1 x10-4)
Reaction Time (minutes)
0
1
2
3
4
0
60
120
180
XBL 808-5694

Fig. 3.46

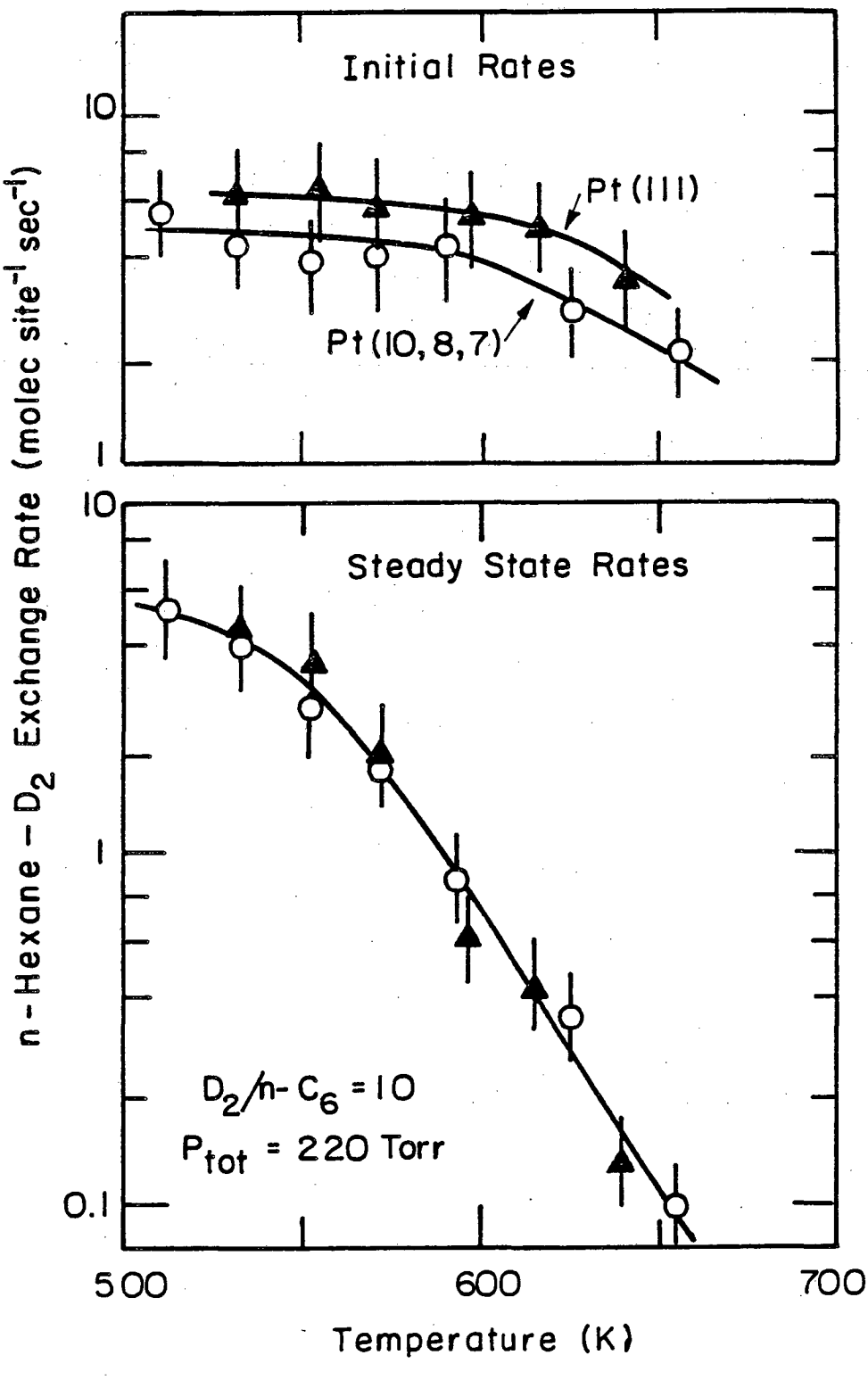
Initial Rates
10
1
Pt(111)
Pt(10,8,7)
10
Steady State Rates
1
0.1
n-Hexane - D_2 Exchange Rate (molec site^{-1} sec^{-1})
D_2/n-C_6 = 10
P_{tot} = 220 Torr
500
600
700
Temperature (K)
XBL 8010-6079

Fig. 3.47

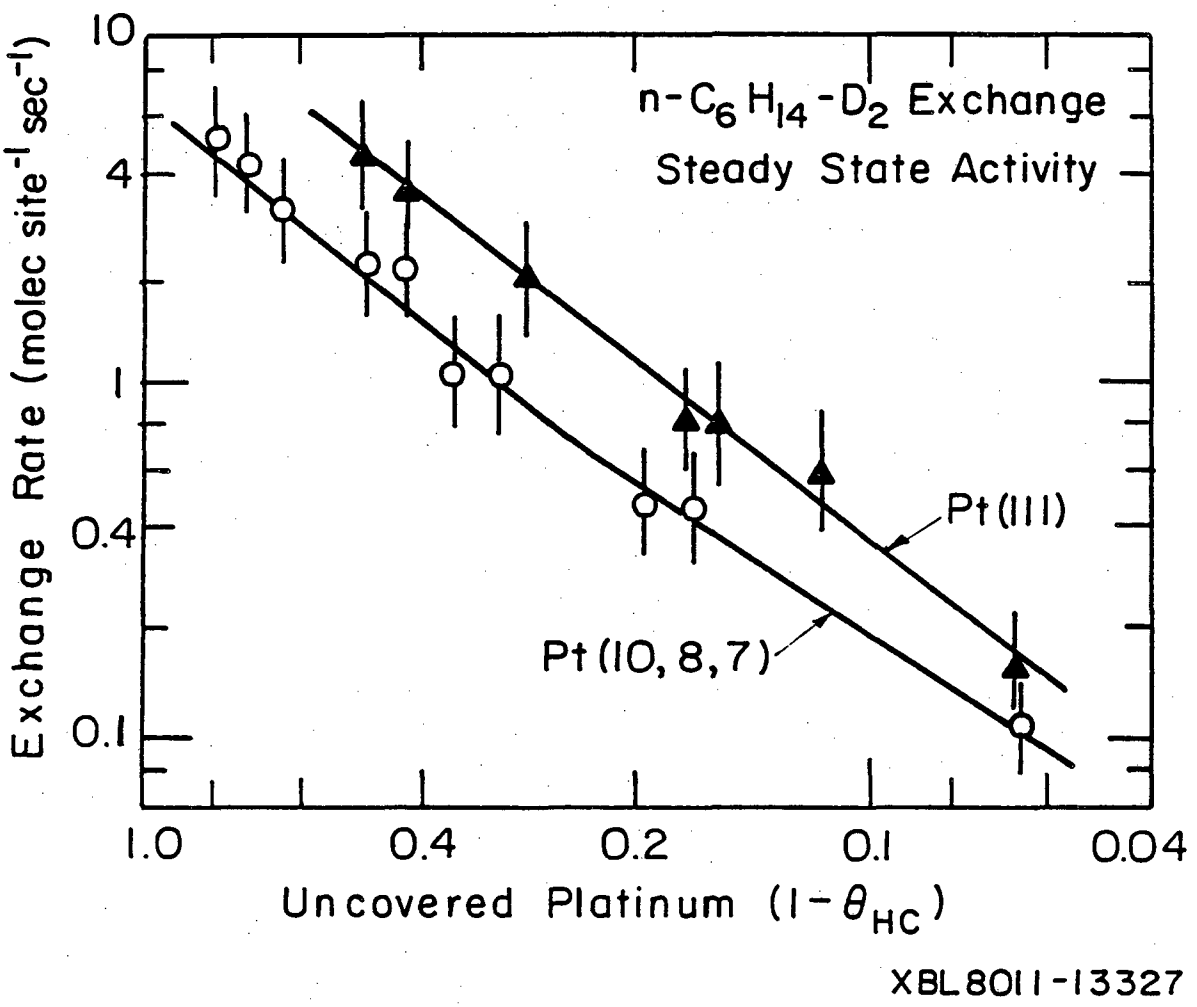
n-C6 H14 - D2 Exchange
Steady State Activity
Pt(111)
Pt(10, 8, 7)
Exchange Rate (molec site-1 sec-1)
10
4
1
0.4
0.1
1.0
0.4
0.2
0.1
0.04
Uncovered Platinum (1 - θHC)
XBL8011-13327

Fig. 3.48

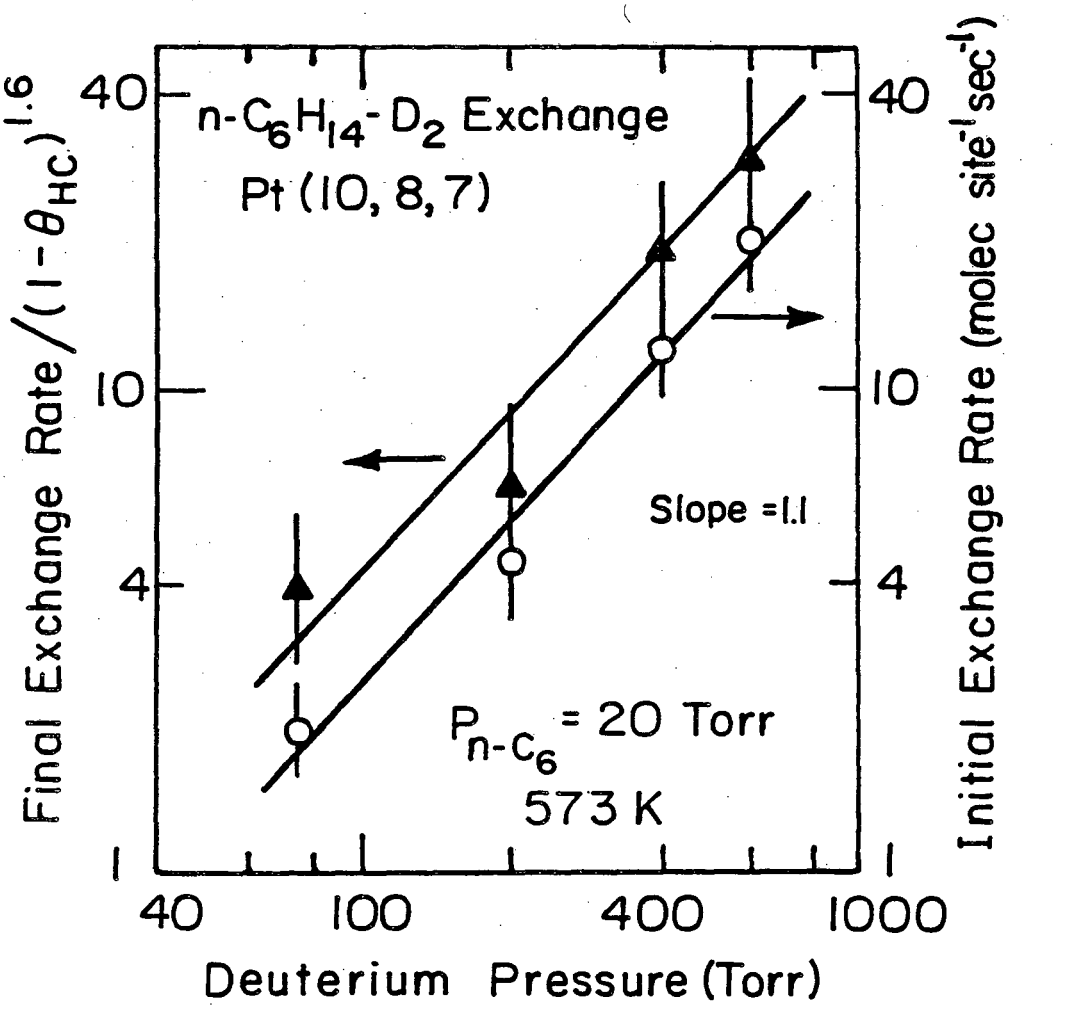
n-C6H14- D2 Exchange
Pt (10, 8, 7)
Slope =1.1
Pn-C6 = 20 Torr
573 K
Final Exchange Rate/(1-θHC)1.6
Initial Exchange Rate (molec site-1sec-1)
Deuterium Pressure (Torr)
40
10
4
1
40
100
400
1000
XBL 8011-13328

Fig. 3.49

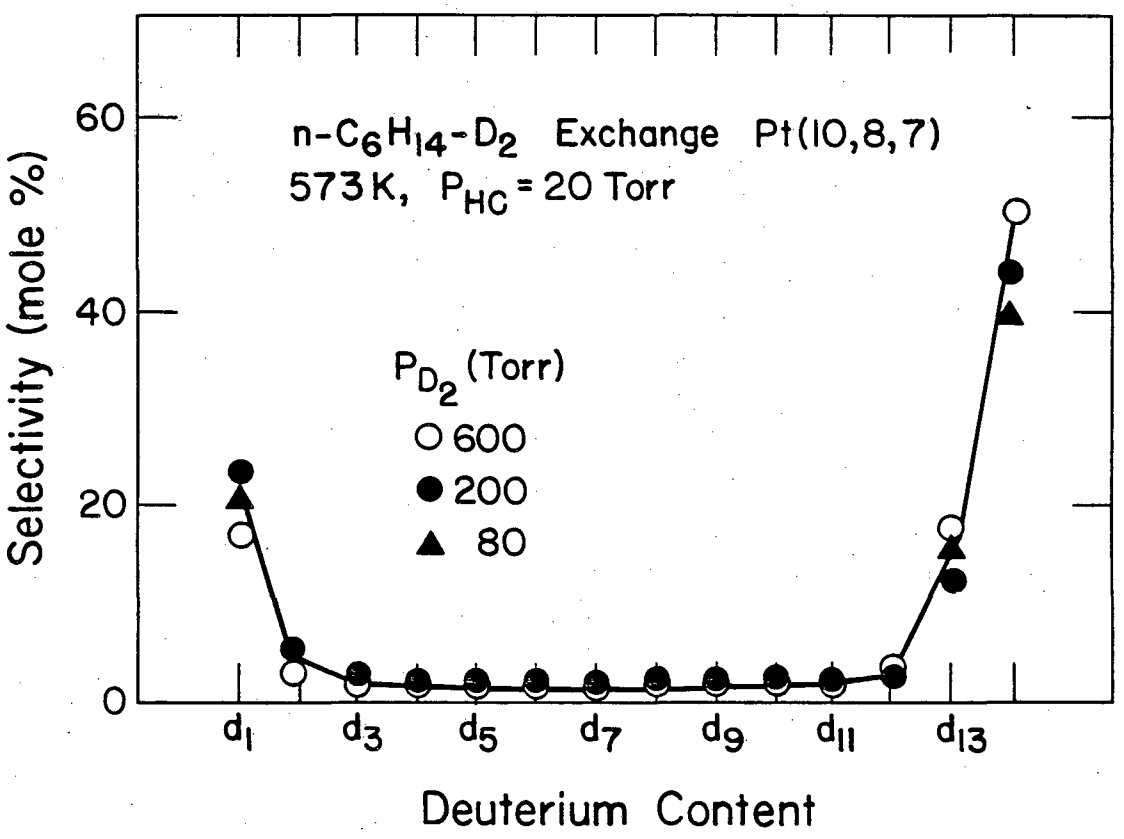

XBL 818-1101

Fig. 3.50

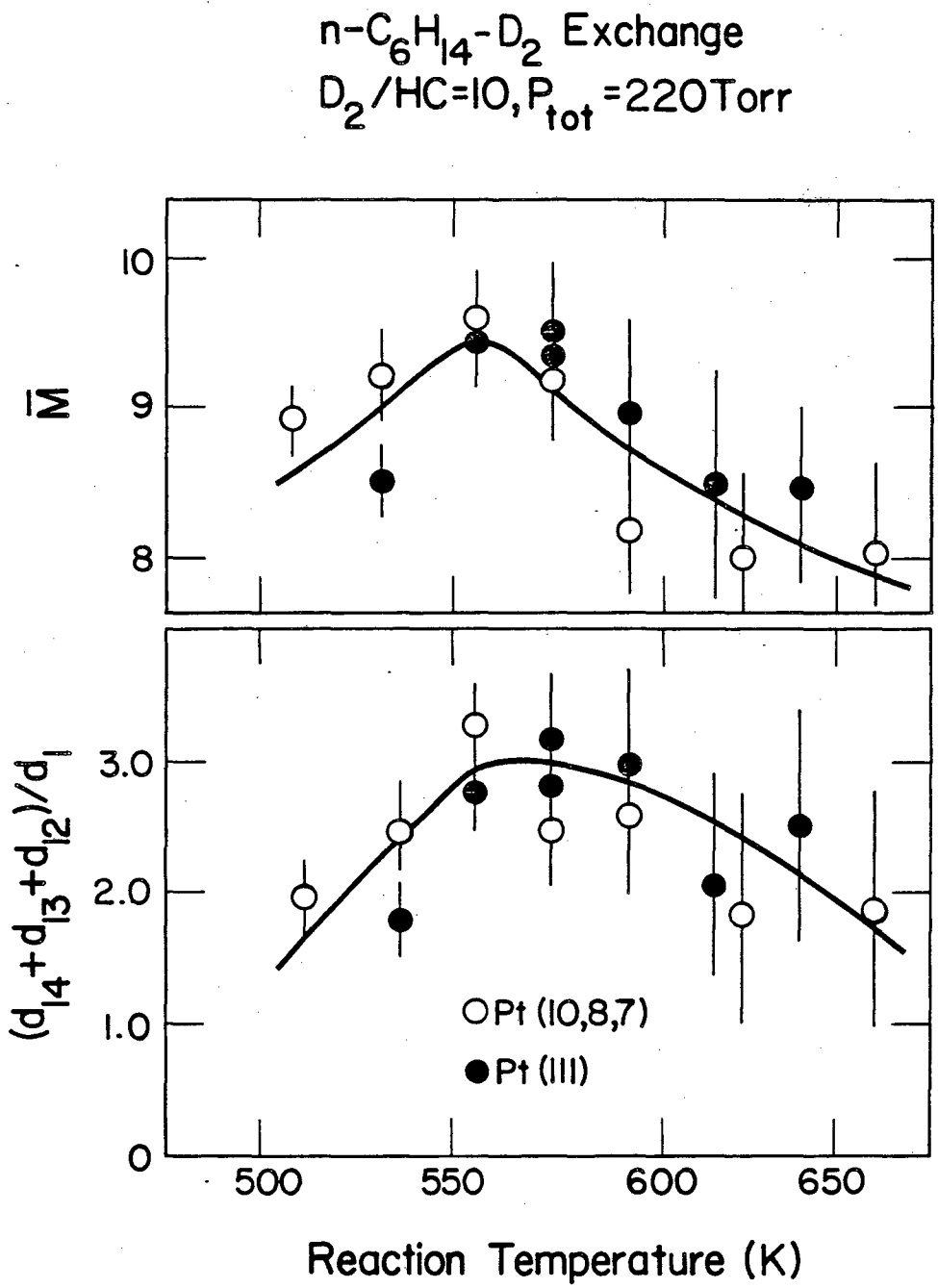
n-C6H14-D2 Exchange
D2/HC=10, Ptot=220Torr
M̄
10
9
8
(d14+d13+d12)/d11
3.0
2.0
1.0
0
500
550
600
650
Pt (10,8,7)
Pt (111)
Reaction Temperature (K)
XBL 818-1098

Fig. 3.51

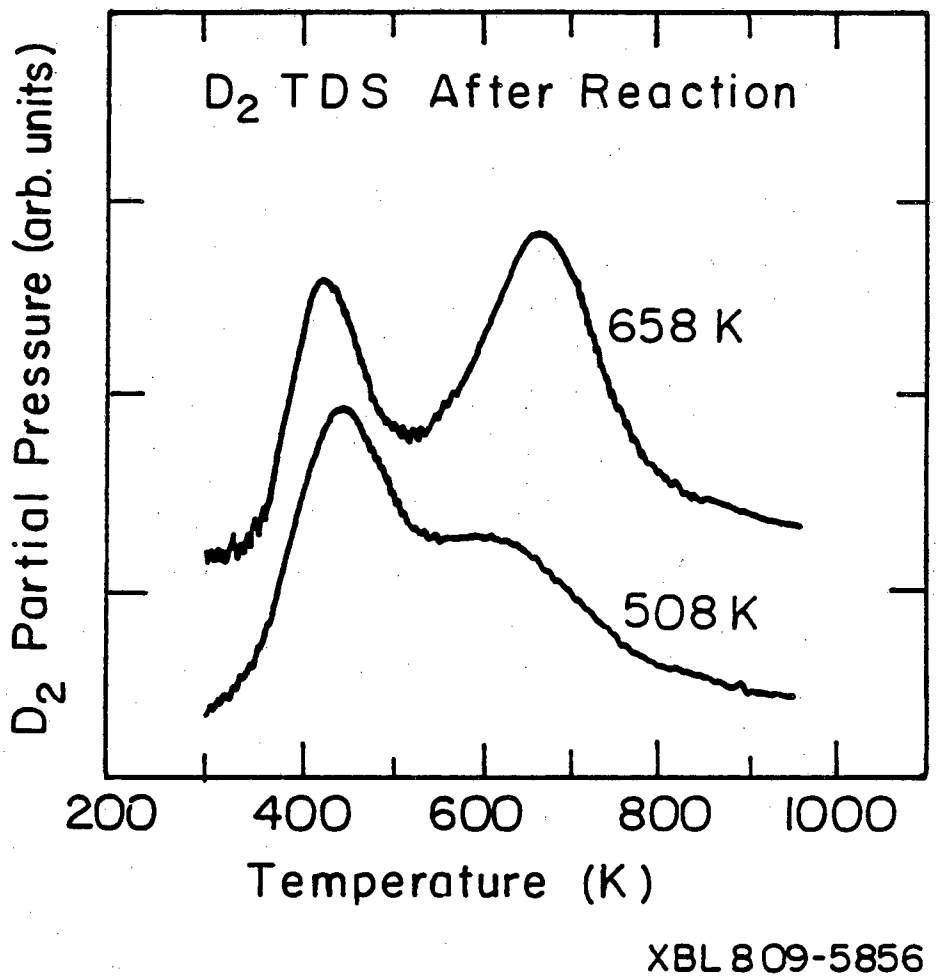
D2 TDS After Reaction
658 K
508 K
D2 Partial Pressure (arb. units)
200
400
600
800
1000
Temperature (K)
XBL 809-5856

Fig. 3.52

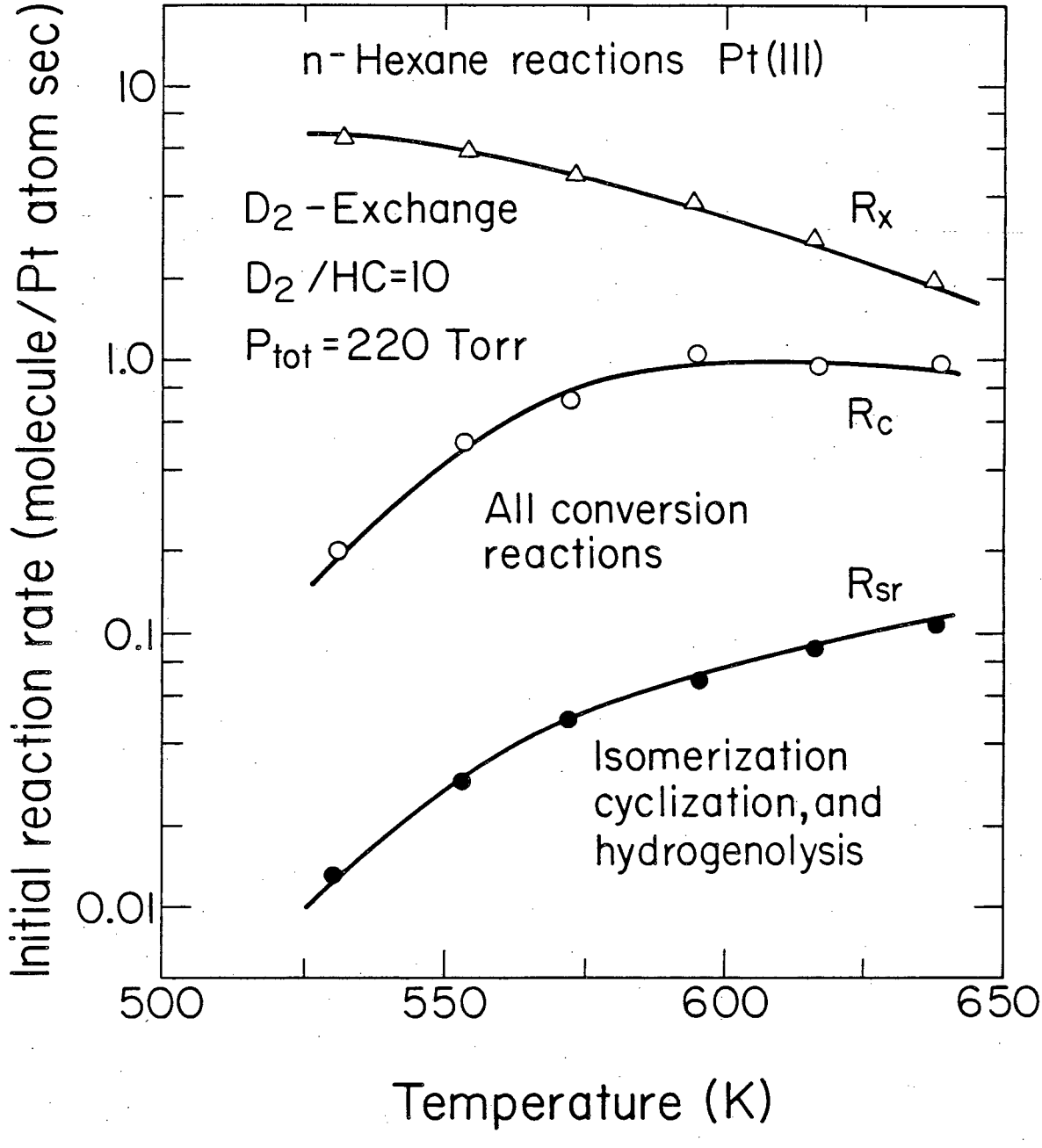
n-Hexane reactions Pt(111)
D2-Exchange
D2/HC=10
Ptot=220 Torr
Rx
Rc
All conversion reactions
Rsr
Isomerization cyclization, and hydrogenolysis
Initial reaction rate (molecule/Pt atom sec)
10
1.0
0.1
0.01
500
550
600
650
Temperature (K)
XBL 818-1095

Fig. 3.53

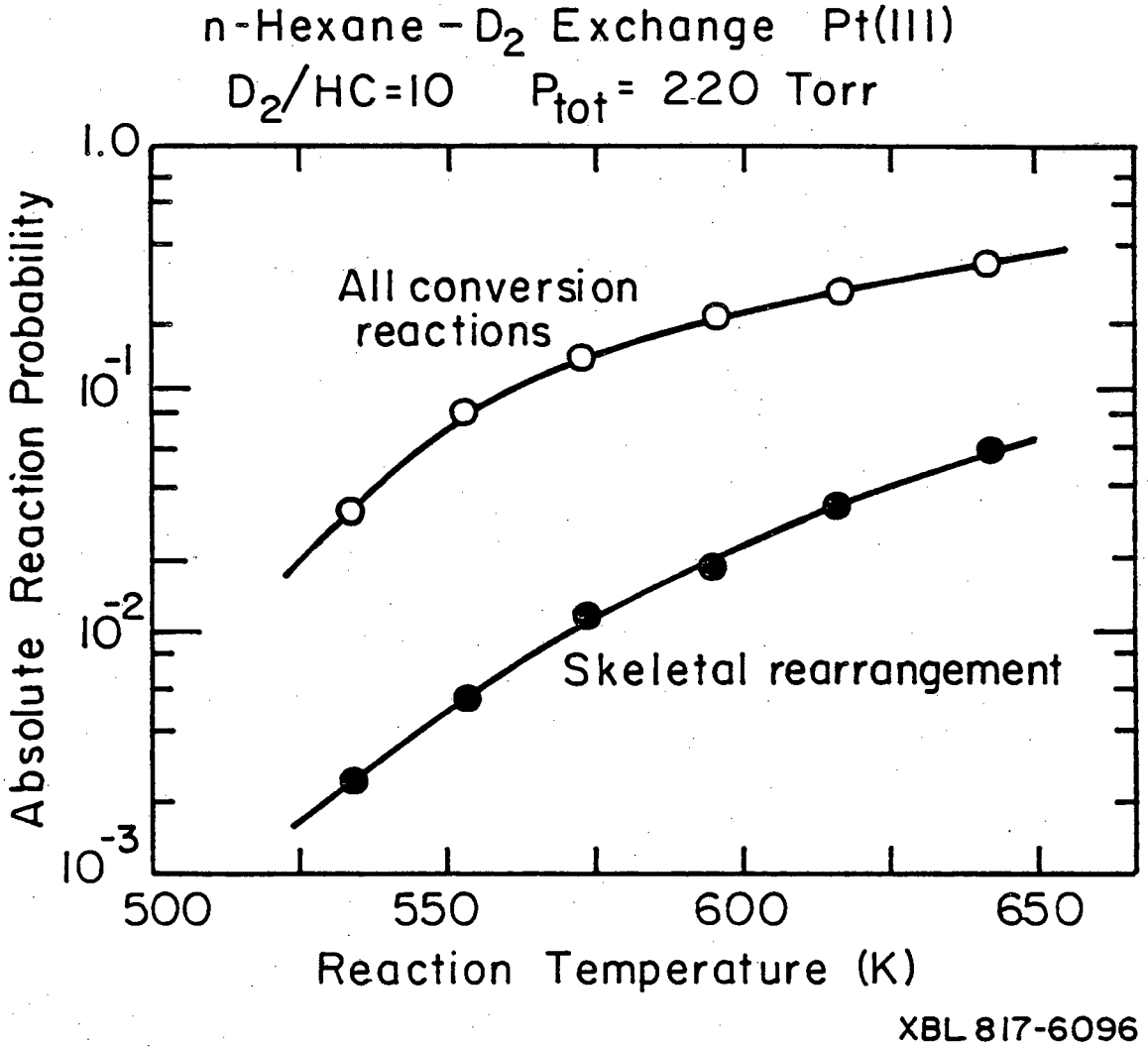
n-Hexane – D_2 Exchange Pt(111)
D_2/HC=10 P_{tot} = 220 Torr
Absolute Reaction Probability
1.0
10^{-1}
10^{-2}
10^{-3}
All conversion reactions
Skeletal rearrangement
500
550
600
650
Reaction Temperature (K)
XBL 817-6096

Fig. 3.54

3.5 Deuterium Isotope Effects for Hydrocarbon Reactions Catalyzed Over Platinum Single Crystal Surfaces

3.5.1. Background

Important information about the elementary steps of catalyzed surface reactions involving hydrogen containing molecules can often be derived from studies of deuterium isotope effects. As discussed by Ozaki (104), two major types of deuterium isotope effects can be distinguished, namely kinetic and thermodynamic isotope effects. A kinetic isotope on the rate of reaction arises when rate constants differ for reactions carried out in hydrogen and deuterium or with deuterated reactants. Because deuterium makes larger contributions to translational and rotational partition functions than hydrogen, and because X-D bonds (x = C,N,O, etc.) possess lower zero point energies than X-H bonds, rate constants for deuterium addition and X-D scission are generally smaller than rate constants for H addition and X-H scission, respectively ($k_H > k_D$). Alcohol dehydration (105) and olefin hydrogenation (106) are example reactions which display normal kinetic isotope effects with magnitudes in the range $R_H/R_D = 1.5 - 4.5$.

Thermodynamic isotope effects, by contrast originate from a change in the equilibrium surface concentration of a reaction intermediate. Because of the lower zero point energies for X-D bonds, reaction intermediates that contain deuterium are expected to display larger adsorption equilibrium constants and higher equilibrium surface concentrations than reaction intermediates which contain only hydrogen ($K_{XD} > K_{XH}$, $\theta_{XD} > \theta_{XH}$). Detailed interpretation of these effects can

be difficult because the thermodynamic isotope effect usually appears in combination with a kinetic isotope effect, i.e., $R_H/R_D \simeq k_H\theta_{XH}/k_D\theta_{XD}$ (107). However, inverse deuterium isotope effects with magnitudes R_D/R_H = 1.4-3.5 have been clearly established for several types of reactions including CO-hydrogenation (deuteration) over silica supported ruthernium (108) and ammonia (ND_3)-synthesis over unpromoted iron (109). For these reactions, the thermodynamic isotope effects appear to be larger than the kinetic isotope effects, and therefore, the reaction rates increase when the reactions are carried out in deuterium.

In the previous section, it was shown that n-hexane, n-heptane, and isobutane deuterium exchange reactions catalyzed near atmospheric pressure ever platinum single crystal surfaces take place very rapidly as compared with the initial rates of n-hexane conversion reactions to form hydrogenolysis, isomerization, dehydrogenation, and dehydrocyclization products. Provided that the reaction intermediates leading to hydrocarbon conversion in the presence of deuterium are partially deuterated, thermodynamic isotope effects should exist for the skeletal rearrangement reactions. Inverse deuterium isotope effects were in fact detected for a wide variety of reactions, and these isotope effects form the subject of this section.

It was discovered that the rates of alkane hydrogenolysis, isomerization, and cyclization reactions catalyzed in excess deuterium

at 500-650 K are about 1.4-3.0 times higher than the rates of the same reactions catalyzed in hydrogen under identical experimental conditions. The magnitude of these isotope effects depend little on platinum surface structure and appear to decrease slightly with increasing temperature. A change in selectivity results when parallel reactions display deuterium isotope effects with different magnitudes.

3.5.2 Results

Scope of the Isotope Effect. Initial reaction rates in deuterium and inverse deuterium isotope effects (R_D/R_H) measured for a variety of hydrocarbon reactions catalyzed at 573 K over the flat(111), stepped (13,1,1) and kinked (10,8,7) platinum surfaces are summarized in Table 3.17. Magnitudes of the deuterium isotope effects were determined graphically by comparing the initial slopes of product accumulation curves determined as a function of reaction time in the presence of hydrogen and in deuterium. Example product accumulation curves for n-hexane isomerization to 2-methylpentane and cyclization to methylcyclopentane over Pt(111) are shown in Figure 3.55. Hydrogenolysis reactions of isobutane, neopentane, n-hexane, cyclohexane, and n-heptane all displayed inverse isotope effects with magnitudes in the range R_D/R_H = 1.3-1.8. For isomerization reactions the isotope effects were in the range R_D/R_H = 1.2-3.3. Isomerization of n-hexane to 2-methylpentane displayed the largest isotope effect R_D/R_H = 3.0-3.3; n-hexane isomerization to 3-methylpentane displayed a smaller effect (R_D/R_H = 1.2-1.5) Isomerization and hydrogenolysis of neopentane and isobutane displayed isotope effects with equal magnitudes on all surfaces investigated. Cyclohexane dehydrogenation

Table 3.17. Initial reaction rates in deuterium and deuterium isotope effects measured for hydrocarbon reactions catalyzed at 573 K over the flat (111), stepped (13,1,1), and Kinked (10,8,7) platinum single crystal surfaces (a).

Reactant	Reaction	Initial Turnover Frequency (molec/Pt atom sec) (±15%)			Inverse Isotope Effect (R_D/R_H) (±30%)		
		Pt(111)	Pt(10,8,7)	Pt(13,1,1)	Pt(111)	Pt(10,8,7)	Pt(13,1,1)
Isobutane	Hydrogenolysis	0.0064	0.019	-----	1.8	1.4	-----
	Isomerization	0.053	0.075	-----	1.7	1.3	-----
Neopentane	Hydrogenolysis	-----	0.0047[b]	0.048	-----	1.7[b]	2.0
	Isomerization	-----	0.020[b]	0.40	-----	1.5[b]	2.0
Cyclohexane	Hydrogenolysis	0.005[c]	-----	-----	2.0[c]	-----	-----
	Dehydrogenation	9.6[c]	-----	-----	1.2[c]	-----	-----
n-Hexane	Hydrogenolysis	0.016	0.0089	0.013	1.8	1.4	1.9
	Isomerization	0.014	-----	0.0090	1.7	-----	2.1
	Cyclization	0.014	-----	0.018	1.7	-----	1.9
	Aromatization	0.0047	0.0042	-----	0.9	0.8	-----
n-Heptane	Hydrogenolysis	0.021[d]	-----	-----	1.6[d]	-----	-----
	Aromatization	0.0074[d]	-----	-----	0.8[d]	-----	-----

a) Reaction Conditions, $D_2/HC = 10$, $P_{tot} = 220$ Torr, 573 K

b) at 543 K

c) $D_2/HC = 6.7$, $P_{tot} = 115$ Torr

d) $D_2/HC = 32$, $P_{tot} = 495$ Torr

over Pt(111) exhibited a small inverse isotope effect ($R_D/R_H = 1.2$). Aromatization of n-hexane and n-heptane on the (111) and (10,8,7) platinum surfaces displayed unique behavior characterized by small kinetic isotope effects ($R_D/R_H \leq 1$).

Temperature Dependence of the Deuterium Isotope Effects. The temperature dependence of the deuterium isotope effects was investigated carefully for n-hexane reactions catalyzed over the flat(111) and kinked(10,8,7) platinum surfaces. Arrhenius plots for these reactions catalyzed in hydrogen and in deuterium are compared in Figures 3.56, 3.57, 3.58, and 3.59. The error bars represent estimated uncertainties that are based on the reproducibility (about ±15 percent) of the initial rate measurements. Hydrogenolysis and aromatization were the only reactions which displayed "normal" Arrhenius behavior over a wide range of temperature (ca. 520-650 K). Even for these reactions the apparent activation energies that were in the range 16-36 kcal/mole appeared to decrease with increasing reaction temperature. The other reactions (isomerization and C_5-cyclization) displayed rate maxima at 570-630 K that were discussed previously in Section 3.1. Inverse isotope effects observed for hydrogenolysis appeared to decrease in magnitude with increasing temperature. No significant isotope effect was detected for the aromatization reaction over either platinum surface. Figure 3.60 shows product accumulation curves for n-hexane aromatization catalyzed in deuterium at several temperatures on the (10,8,7) platinum surface. Reactions carried out in deuterium displayed deactivation behavior that was similar to that

for reactions carried out in hydrogen. The rate of deactivation increased with increasing reaction temperature.

Pressure Dependence of the Deuterium Isotope Effects. Initial reaction rates for n-hexane hydrogenolysis and aromatization catalyzed at 573K on the (10,8,7) platinum surface are shown as a function of hydrogen (or D_2) pressure in Figure 3.61. The inverse isotope effect for hydrogenolysis displayed a nearly constant magnitude for all total pressures between 100 and 620 Torr (i.e., R_D/R_H = 1.4-1.8). By contrast, the kinetic isotope effect for aromatization that was negligible at 100-220 Torr increased markedly with increasing H_2-D_2 pressures reaching a value $R_D/R_H \sim 3$ for total pressures of 620 Torr.

Isotope effects measured by Gillespie at several total pressures for cyclohexane dehydrogenation, ring opening, and hydrogenolysis catalyzed at 573 K on the (111) platinum surface are summarized in Table 3.18. These reactions displayed inverse isotope effects that decreased in magnitude with increasing pressure.

3.5.3 Discussion

Altered Selectivity for Reactions Catalyzed in Deuterium. Inverse isotope effects with magnitudes in the range R_D/R_H = 1.3-3.3) were detected for a variety of hydrogenolysis, isomerization, and C_s-cyclization reactions that were catalyzed over platinum single crystal surfaces in the presence of excess deuterium gas. Aromatization reactions displayed unique behavior characterized by a normal kinetic isotope effect $R_D/R_H < 1$. The magnitudes of all the isotope effects displayed little dependence on platinum surface structure. To the best

Table 3.18. Pressure dependence of the deuterium isotope effects measured for cyclohexane dehydrogenation, ring opening, and hydrogenolysis (a).

H_2-D_2 Pressure (Torr)	Inverse Isotope Effects (R_D/R_H) (±25%)		
	Dehydrogenation	Ring Opening	Hydrogenolysis
100	1.25	2.8	2.0
300	1.15	1.6	0.9
480	1.05	1.7	0.7

a) Pt(111) at 573 K, P_{HC} = 15 Torr

of our knowledge, deuterium isotope effects for metal catalyzed skeletal rearragnement reactions have not been considered previously.

Isotope effects measured for the hydrogenolysis and isomerization of isobutane and neopentane displayed equal magnitudes under all reaction conditions investigated. For these reactions, the selectivity was unaltered by the presence of deuterium. However, with n-hexane and n-heptane as reactants, parallel reactions usually displayed isotope effects with different magnitudes. In the presence of deuterium, the rate of formation of saturated hydrocarbon products was enhanced relative to the rate of formation of aromatics. As a result, the selectivities for these reactions were altered appreciably. This is shown clearly for n-hexane reactions catalyzed on the (10,8,7) platinum surface in Figure 3.62, where the kinetic selectivity for aromatization over hydrogenolysis in H_2 and D_2 is compared as a function of reaction temperature and hydrogen (D_2) pressure. The aromatization selectivity in deuterium was reduced over a wide range of reaction conditions. A similar effect was recently reported by Kellner and Bell (108) for Fischer-Tropsch reactions catalyzed over silica and alumina supported ruthenium. In this case the kinetic selectivity for C_3- and C_4-olefin synthesis over C_3- and C_4-alkane production was lowered when the reaction rate studies were carried out in deuterium. Whereas the rates of formation of alkane products displayed inverse isotope effects with magnitudes in the range R_D/R_H = 1.0-1.6, the isotope effects for olefin production were always very small, R_D/R_H - 1.0-1.2

Origin of the Inverse Isotope Effects. An idealized interpreation of the measured isotope effects can be developed by recalling that inverse isotope effects usually originate from a change in the equilibrium surface concentrations of one or more reaction intermediates. Differences in the vibrational frequencies of deuterated and hydrogenated species lead to the generalization (104) that equilibrium constants for addition of deuterium to an adsorbed species are larger than equilibrium constants for hydrogen addition ($K_D > K_H$). This conclusion appears to be correct at low temperatures where the largest portion of the isotope effect arises from zero point energy differences. However, this generalization is not strictly valid at high temperatures, since changes in the equilibrium constant due to isotopic substitution are also influenced by changes in the molecular masses that contribute to translational and rotational partition functions. As illustrated below, the mass effect considered alone leads to the prediction $K_H \geq K_D$.

Results presented in previous sections indicated that the kinetics of alkane skeletal rearrangement reactions catalyzed near atmospheric pressure over platinum single crystal surfaces can be reasonably described by the reaction sequence

$$H_2 \overset{K_H}{\rightleftharpoons} 2H\ (ads) \qquad (1)$$

$$C_nH_{2n+2} \overset{\lambda_H}{\rightleftharpoons} C_nH_x(ads) + aH_2 \qquad (2)$$

$$C_nH_x(ads) + 2\delta\ H(ads) \xrightarrow[\text{slow}]{k_H} C_nH_{x+2\delta}(ads) \xrightarrow{\text{isomer or fragments}} \quad (3)$$

$$C_nH_{x+2\delta}(ads) + H_2 \xrightarrow[\text{fast}]{} \text{products} \quad (4)$$

where $0 \leq \delta \leq 1$. In this scheme dissociative chemisorption of hydrogen and hydrocarbon are both assumed to be reversible and very rapid as compared to the rate of skeletal rearrangement. Adequate justification for this assumption was provided at lower reaction temperatures by the deuterium exchange kinetics discussed in the preceeding section. The rate determining step is believed to involve skeletal rearrangement (or hydrogenolysis) of an intermediate species which has lost 2a hydrogen atoms. Detailed kinetic studies by Maurel and coworkers have revealed that $\delta = 1$ and $a = 2$–4 for a wide variety of hydrogenolysis reactions catalyzed at atomspheric pressure over Pt/Al_2O_3 catalysts (56). All subsequent reaction steps are assumed to be rapid. Following reasoning used previously by Cimino et al. (55), Sinfelt (31), and Maurel (56). this reaction sequence leads to the rate expression

$$R_H = k_H K_H^{\delta} \lambda_H P_c P_{H_2}^{\delta} / (K_H^a P_{H_2}^a + \lambda P_c) \quad (1)$$

where k_H, K_H, and λ_H are the rate constant and equilibrium constants defined by reactions 1–3, and P_c and P_{H_2} are the partial pressures of hydrocarbon and hydrogen, respectively. The form of this rate expression indicates that apparent reaction rates involve a complex

products of elementary rate coefficients and adsorption equilibrium constants. The measured inverse isotope effects therefore appear to result from a combination of kinetic and thermodynamic isotope effects. A similar conclusion was reached by Kellner and Bell in studies of Fischer-Tropsch reactions catalyzed over supported ruthenium catalysts (108).

Using equation 1 the inverse isotope effect should have a magnitude given by

$$\frac{R_D}{R_H} = \frac{k_D K_D^{\delta} \lambda_D (K_H^a P_{H_2}^a + \lambda_H P_C)}{k_H K_H^{\delta} \lambda_H (K_D^a P_{D_2}^a + \lambda_D P_C)}, \qquad (2)$$

where k_D, K_D, and λ_D are the rate constant and adsorption equilibrium constants defined by the reactions

$$D_2 \overset{K_D}{\rightleftharpoons} 2D(ads) \qquad (5)$$

$$C_nH_{2n+2} + \beta D_2 \overset{\lambda_D}{\rightleftharpoons} C_nD_x(ads) + aD_2 + \beta H_2 \qquad (6)$$

$$C_nD_x(ads) + 2\delta D(ads) \xrightarrow{k_D} (C_nD_x + 2\delta(ads) \begin{matrix}\text{isomer or} \\ \text{fragments}\end{matrix} \qquad (7)$$

Reaction 6 assumes that complete exchange occurs in the intermediate C_nD_x species before skeletal rearrangement. This assumption is reasonably justified by the facts that (1) at lower temperatures (530-570 K) complete deuterium exchange was typically 100 times faster

than skeletal rearrangement, and (2) all reaction products appeared to be extensively deuterated (probably perdeuterated, Section 2.8). While it is highly unlikely that complete exchange prevails for every reacting molecule, application of this useful assumption permits a separation of the kinetic and thermodynamic isotope effects and a qualitative evaluation of their relative importance.

The factor K_D/K_H appearing in Eq. (2) can be evaluated directly using statistical considerations together with Pt-H (Pt-D) stretching frequencies recently reported by Ibach (110,111) and Primet et al. (112). These stretching frequencies are summarized in Table 3.19 for the two limiting cases of weak "reversible" and strong "irreversible" hydrogen chemisorption. These two types of chemisorbed hydrogen are distinguishable by their reactivities (91-94) and heats of adsorption (46,47,93,95). Reversibly adsorbed hydrogen displays a single stretching frequency of 2200 cm^{-1} (112) and can be reasonably modeled as a mobile 2-dimensional gas. In this case, it is easily derived that

$$\frac{K_D}{K_H} = \left(\frac{M_{H_2}}{M_{D_2}}\right)^{1/2} \exp\ [2(\nu_{H_2} - \nu_{D_2})\ h/2kT] \qquad (3)$$

where M_{H_2} and M_{D_2} are the molecular masses of H_2 and D_2 and the ν_i's are the vibrational frequencies defined in Table 3.19. This function predicts that K_D/K_H should increase slowly with increasing temperature from 0.54 to 0.64 for temperatures between 273 and 673 K. Strongly chemisorbed hydrogen, on the other hand, displays two

Table 3.19. Stretching frequencies for molecular and chemisorbed hydrogen and deuterium.

Species	Mode	Frequency (cm^{-1})	Ref.
H_2	$\nu_{A_1} = \nu_{H_2}$	4160	115
D_2	$\nu_{A_1} = \nu_{D_2}$	2990	115
Pt–H	$\nu_A = \nu_A^H$	550	110,111
("irreversible")	$\nu_E = \nu_E^H$	1230	
Pt–D	$\nu_A = \nu_A^D$	400	110,111
("irreversible")	$\nu_E = \nu_E^D$	900	
Pt–H	$\nu_A = \nu_{M-H}$	2120	112
("reversible")			
Pt–D	$\nu_A = \nu_{M-D}$	1585	112
("reversile")			

stretching frequencies (ν_A = 550 cm^{-1}, ν_E = 1230 cm^{-1}), one of which is doubly degenerate (110,111). In this case the hydrogen and deuterium adatoms are mostly immobile with 3 degrees of vibrational freedom. Accordingly, K_D/K_H can be estimated using

$$\frac{K_D}{K_H} = \left(\frac{M_{H_2}}{M_{D_2}}\right)^{5/2} \left(\frac{1-\exp(-h\nu_A^H/kT)}{1-\exp(-h\nu_A^D/leT)}\right)^2 \left(\frac{1-\exp(-h\nu_E^H/kT)}{1-\exp(-h\nu_E^D/kT)}\right)^4 \quad (4)$$

$$\times \exp\left\{[2(\nu_A^H+2\nu_A^H-\nu_A^D-2\nu_E^D) - (\nu_{H_2}-\nu_{D_2})]h/2kT\right\}$$

This function varies from 0.70 to 273 K to 0.58 at 673 K and displays a minimum of 0.55 at 473 K. It is therefore clear that $K_D/K_H \approx 0.6$ for both types of surface hydrogen under all reaction conditions appropriate to the work described here. It is interesting to note that for the strongly chemisorbed species, the exponential argument of Eq. (4) predicts that the heat of adsorption of D_2 on platinum should be about 0.7 kcal/mole higher than that for hydrogen. Little or not difference should exist in the case of the weaker reversible adsorption. The former prediction is in accord with the results of Gundry (113) and Wedler et al. (114) which indicate that deuterium is more strongly chemisorbed on nickel as compared to hydrogen by 0.6–1 kcal/mole.

The ratio of hydrocarbon adsorption equilibrium constants λ_D/λ_H defined by reactions 2 and 6 can be expressed by

$$\frac{\lambda_D}{\lambda_H} = \left(\frac{Q_{H_2}}{Q_{D_2}}\right)^{\beta-a} \frac{Q_{CD_x}}{Q_{CH_x}} \qquad (5)$$

where the Q_is are total partition functions for the reacting species. If it is assumed that the intermediate hydrocarbon species are immobile it follows that

$$\frac{\lambda_D}{\lambda_H} \geq \left(\frac{M_{H_2}}{M_{D_2}}\right)^{5/2(\beta-a)} \exp\left\{[(\nu_{D_2}-\nu_{H_2})(\beta-a)h-2(E^o_{CD_x}-E^o_{CH_x})]/2kT\right\} \qquad (6)$$

where vibrational partition functions for the intermediate $C_nH_x(C_nD_x)$ species have been neglected and $E^o_{CD_x}-E^o_{CH_x}$ represents the difference in zero point energies between deuterated and hydrogenated intermediates. According to Ozaki (104), this zero point energy difference corresponds to approximately 1.8 kcal/mole per C-H (C-D) bond. Table 3.20 summarizes λ_D/λ_H ratios calculated for several alkanes at 273 and 573 K using Eq. (6) with a varied between 1 and 4. At 273 K the calculations lead to the expected result that $\lambda_D/\lambda_H >> 1$, whereas 573 K, the conclusion arises that $\lambda_D/\lambda_H \approx 1$ independent of a and the reactant hydrocarbon. At the higher temperatures it appears that the zero point energy differences are always largely compensated by changes in moleculer mass. When vibrational partition functions for C_nH_x and C_nD_x are included, the λ_D/λ_H ratios will become larger, but no more than a factor of 2-4 at most. These partion fucntions cancel in the ratio $\lambda_D k_D/\lambda_H k_H$ which leads to the relation

($\delta = 1$)

Table 3.20 Temperature dependence of the hydrocarbon adsorption equilibrium constant ratios λ_D/λ_H calculated using Eq. 3.6.

Hydrocarbon	a	(β-a)	$E_{CH_x} - E_{CD_x}$ (kcal/mole)	λ_D/λ_H(lower limit) 298 K	573 K
i-C_4H_{10}	3	2	7.2	35	0.88
neo-C_5H_{12}	3	3	10.8	240	0.89
n-C_6H_{14}	1	6	21.6	5.5×10^4	0.79
"	2	5	18.0	9.2×10^3	0.83
"	3	4	14.4	1.5×10^3	0.86
"	4	3	10.8	240	0.89

a) $E_{CH_x} - E_{CD_x} = 1.8 \times$ (kcal/mole), ref. 104.

$$\frac{R_H K_D (K_H^a P_{H_2}^a + \lambda_H P_C)}{R_D K_H (K_D^a P_{D_2}^a + \lambda_D P_C)} = \left(\frac{Q_{D_2}}{Q_{H_2}}\right)^{\beta-a} \left(\frac{Q_{M-D}}{Q_{M-H}}\right)^2 \left(\frac{Q_{CH}^{\pm}}{Q_{CD}^{\pm}}\right) \exp[-(E_H^R - E_D^R)/kT] \qquad (7)$$

where $Q_{CH}^{\pm}$ and Q_{CD}^{+} are transition state partition functions and $(E_H^R - E_D^R)$ is the true difference in activation energy for reactions catalyzed in hydrogen and deuterium. From earlier considerations, it can be easily shown that at 573 K the left side of Eq. (7) has a magnitude in the range of 0.4–2 for all reasonable values of K, λ, and a. The right side can be expanded in terms of partition functions and evaluated indirectly assuming that the zero point energies for deuterated and hydrogenated transition state complexes lie between these for $C_nH_x(C_nD_x)$ and C_nH_{x+2} (C_nD_{x+2}). Using these upper and lower limits, Eq. (7) was evaluated at 573 K for several values of a. To account for the observed isotope effects it was found that

$$\prod_i \left(\frac{1-\exp(h\nu_i^{CD\pm}/kT)}{1-\exp(h\nu_i^{CH\pm}/kT)}\right) \quad \exp\left[-(E_H^R - E_D^R)/kT\right] \qquad (8)$$

must have a magnitude of order 0.1–1.0 where the $\nu_i^{CD\pm}$ and $\nu_i^{CH\pm}$ are normal modes for the transition state complexes. This relation can be satisifed only if $(E_H^R - E_D^R)$ lies in the range 2 ± 3 kcal/mole. This prediction is consistent with the experimental observation that the activation energy for n-hexane hydrogenolysis appeared to be slightly lowered in the presence of deuterium.

It has been assumed throughout this analysis that no competition exists between deuterium (H_2) and hydrocarbon for platinum surface sites. While this assumption appears to be reasonable for n-hexane (56), it may not be appropriate for lighter alkanes such as isobutane (58,59,60). According to the "landing site" models for hydrocarbon deuterium exchange (59) and ethane or propane hydrogenolysis (60,116), reaction rates are controlled by the rate of irreversible hydrocarbon chemisorption on surface sites that contain at least Z-adjacent metal atoms that are free from chemisorbed hydrogen. Rate expressions of the form

$$R = kP_c(1-\theta_H)^Z \qquad (9)$$

are predicted by these competitive models where $(1-\theta_H)^Z$ is the probability of having an ensemble of z-adjacent uncovered atoms. In this case, the deuterium isotope effects should have magnitudes given by

$$R_D/R_H \simeq k_D(1-\theta_D)^Z/k_H(1-\theta_H)^Z \qquad (10)$$

From previous considerations of K_H and K_D we expect that $\theta_D < \theta_H$. Since Z typically assumes values of 10-15 (50,60,115), it is clear that kinetic models which allow for competitive adsorption of the reactants also lead to the conclusion that inverse isotope effects should exist for hydrocarbon reactions catalyzed in the presence of deuterium gas.

Based on the assumptions involved, it is clear that the foregoing analyses provide little or no new information about the nature of the reaction mechanism. However, it is notable that the analysis certainly tends to confirm that the measured isotope effects are reasonable and that they are consistent with well established kinetic models for skeletal rearrangement (31,56,58,59). The important point is that the inverse isotope effects arise from a combination of kinetic and thermodynamic isotope effects. Both effects appear to be important under the conditions of the experiments.

FIGURE CAPTIONS

3.55. Comparison between product accumulation curves determined in hydrogen and deuterium for n-hexane isomerization and c_5-cyclization catalyzed over Pt(111) at 573 K.

3.56. Arrhenius plots for n-hexane hydrogenolysis catalyzed in hydrogen and deuterium over Pt(10,8,7).

3.57. Arrhenius plots for n-hexane aromatization catalyzed in hydrogen and deuterium over Pt(10,8,7).

3.58. Arrhenius plots for n-hexane hydrogenolysis and isomerization catalyzed over Pt(111).

3.59. Arrhenius plots for n-hexane aromatization, c_5-cyclization, and isomerization catalyzed over Pt(111).

3.60. Product accumulation curves determined as a function of reaction time for n-hexane aromatization catalyzed in deuterium over Pt(10,8,7).

3.61. Comparison between n-hexane hydrogenolysis and aromatization rates as a function of hydrogen (deuterium) pressure.

3.62. Initial kinetic selectivities for aromatization over hydrogenolysis determined for n-hexane reactions catalyzed in deuterium and hydrogen over Pt(10,8,7). The selectivities are shown as a function of reaction temperature (upper frame) and hydrogen (D_2) pressure (lower frame).

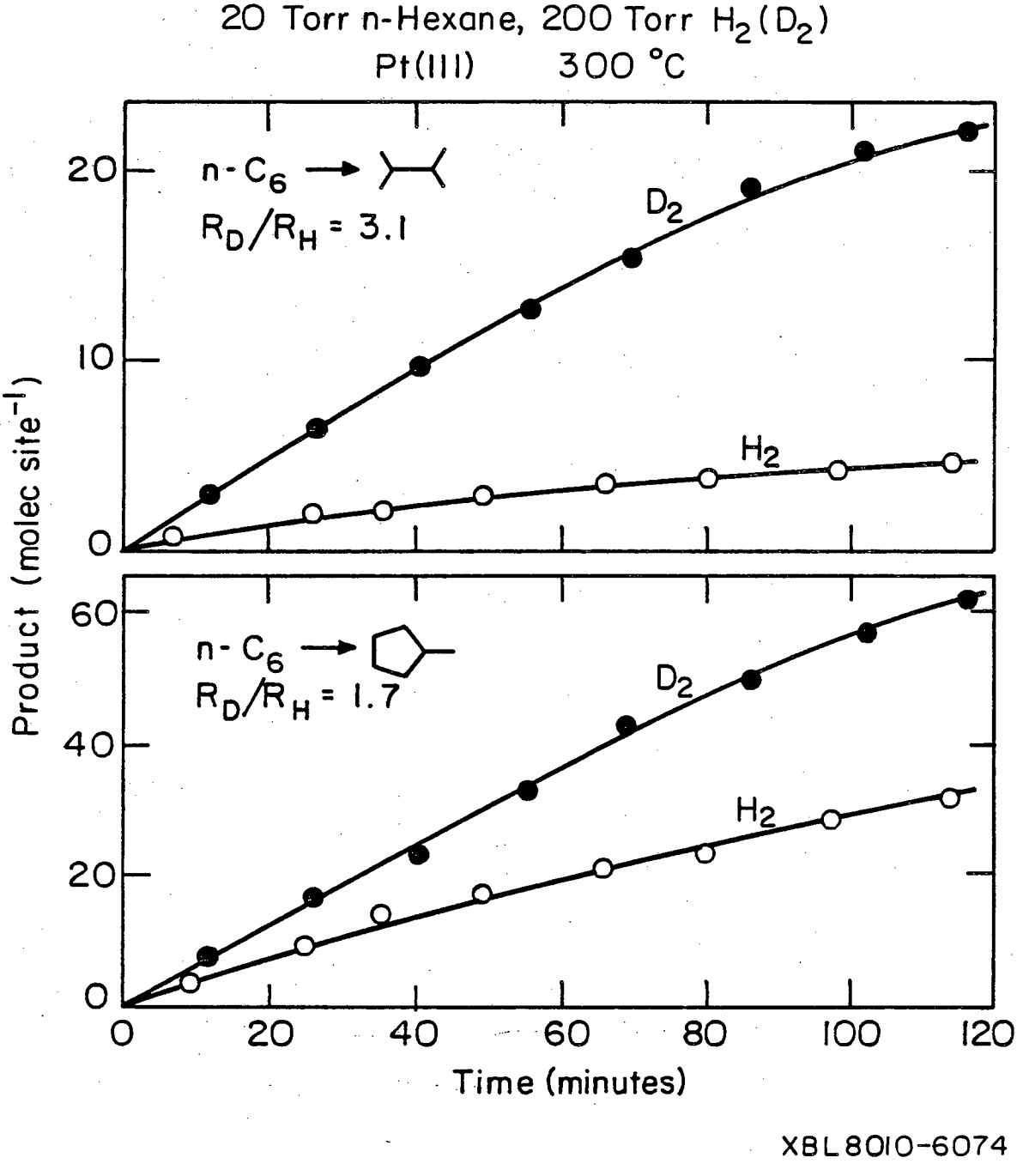

XBL8010-6074

Fig. 3.55

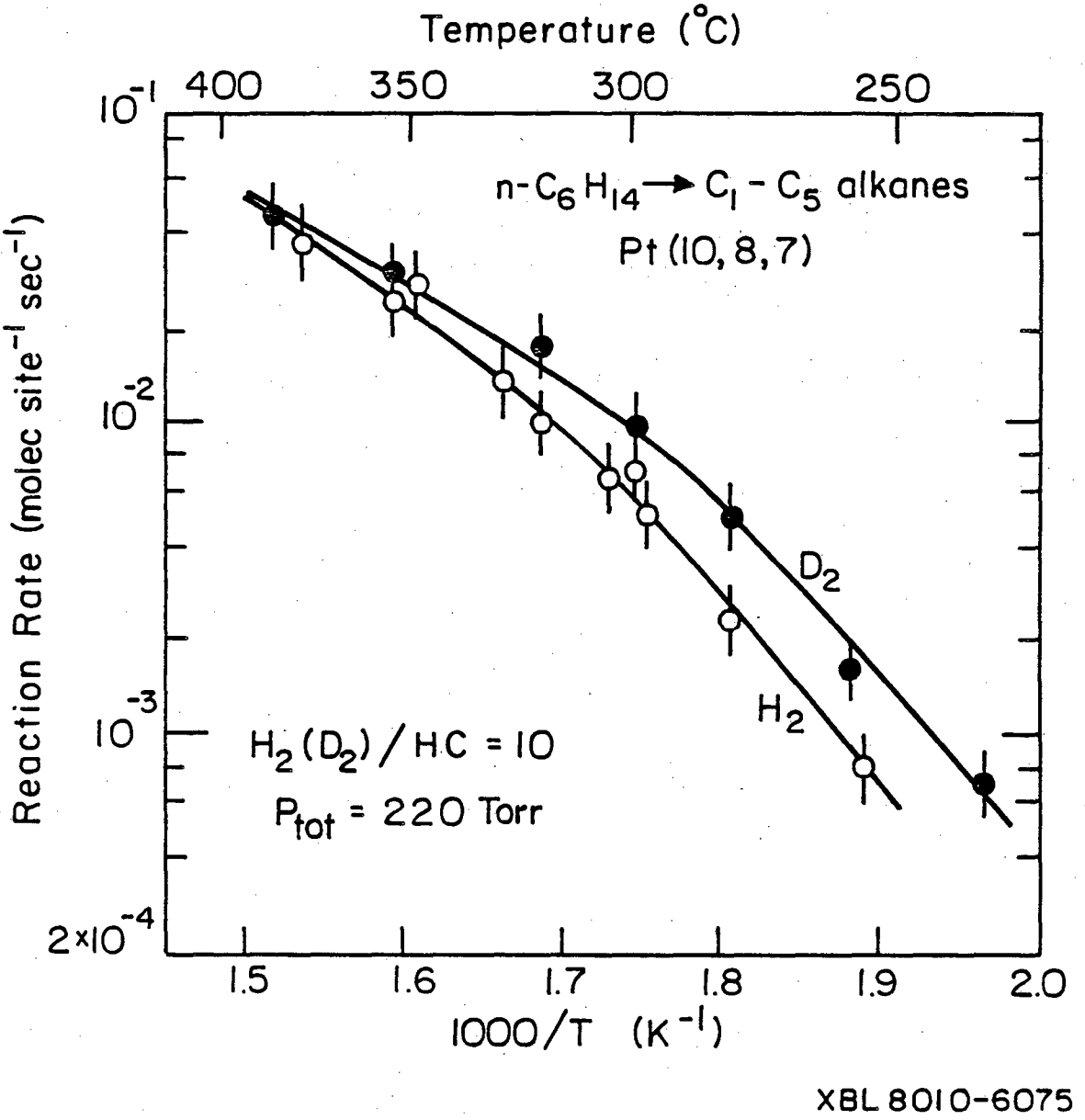
Temperature (°C)
400
350
300
250
10^{-1}
10^{-2}
10^{-3}
2×10^{-4}
Reaction Rate (molec site^{-1} sec^{-1})
n-C_6H_{14} → C_1 - C_5 alkanes
Pt (10, 8, 7)
D_2
H_2
H_2 (D_2) / HC = 10
P_{tot} = 220 Torr
1.5
1.6
1.7
1.8
1.9
2.0
1000/T (K^{-1})
XBL 8010-6075

Fig. 3.56

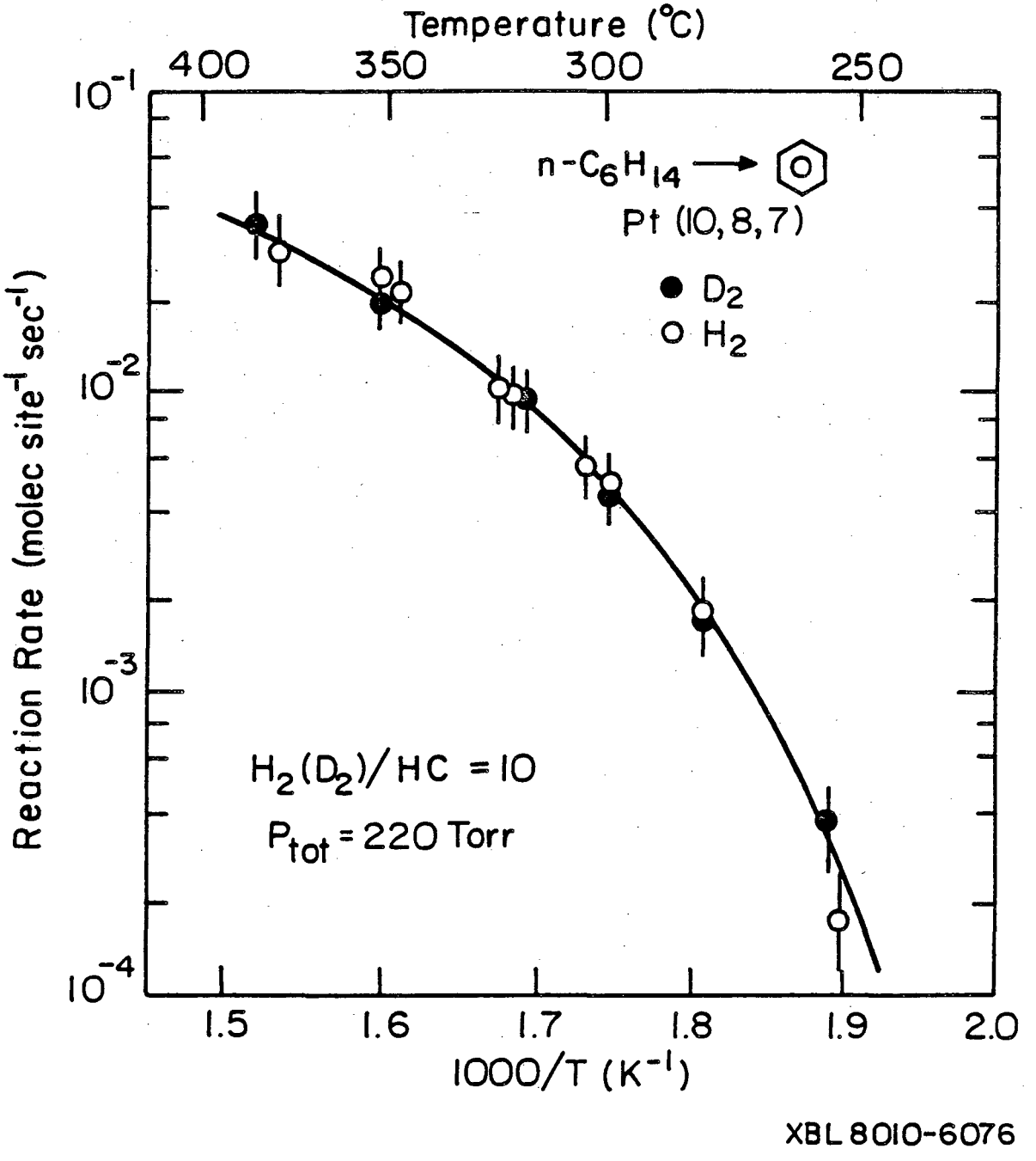
Temperature (°C)
400
350
300
250
10^{-1}
10^{-2}
10^{-3}
10^{-4}
Reaction Rate (molec site^{-1} sec^{-1})
n-C_6H_{14} → ⬡
Pt (10,8,7)
● D_2
○ H_2
$H_2(D_2)$/HC = 10
P_{tot} = 220 Torr
1.5
1.6
1.7
1.8
1.9
2.0
1000/T (K^{-1})
XBL 8010-6076

Fig. 3.57

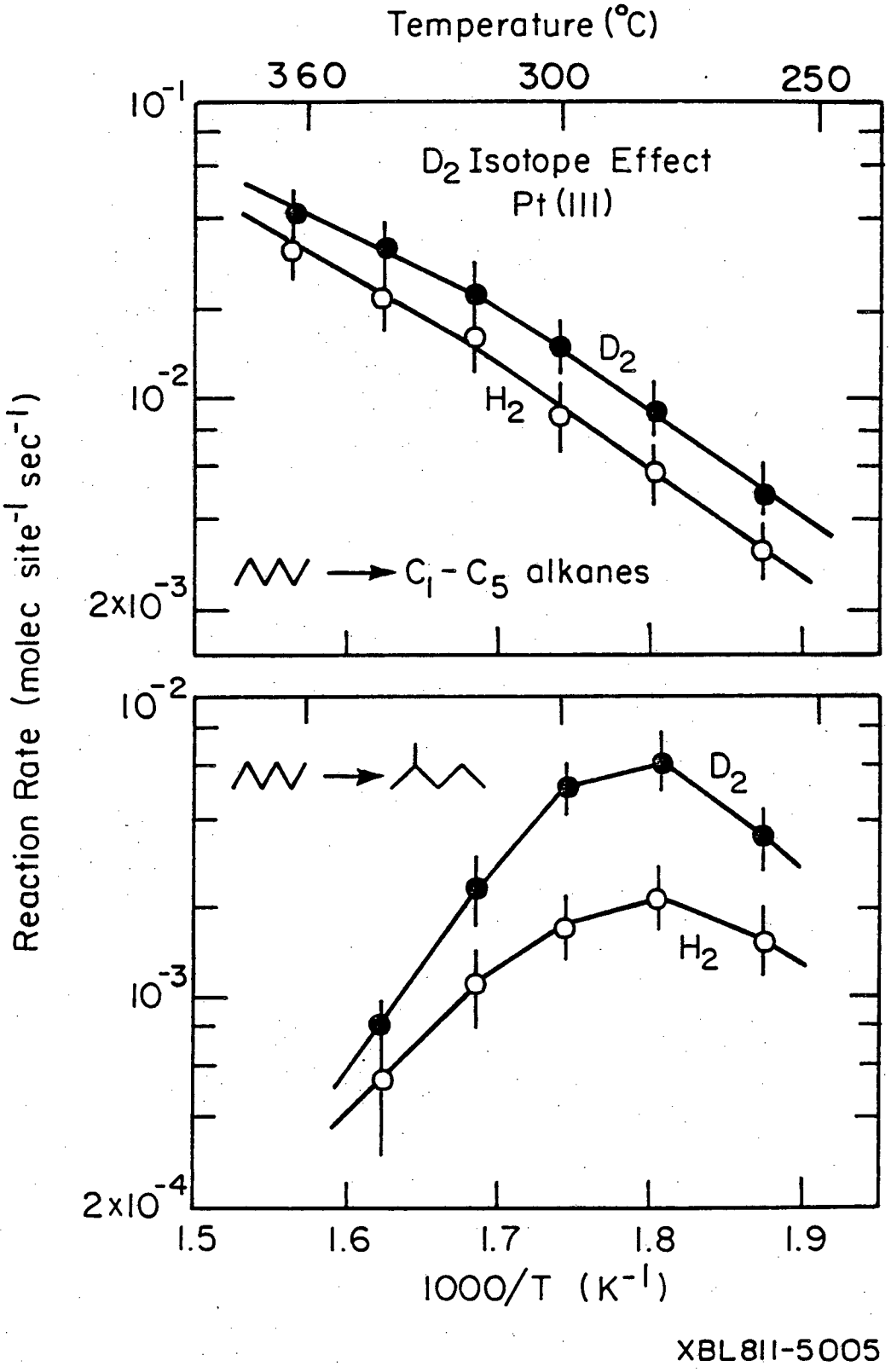
Temperature (°C)
360
300
250
10^{-1}
10^{-2}
2×10^{-3}
D_2 Isotope Effect
Pt(111)
D_2
H_2
$C_1 - C_5$ alkanes
10^{-2}
10^{-3}
2×10^{-4}
D_2
H_2
Reaction Rate (molec site^{-1} sec^{-1})
1.5
1.6
1.7
1.8
1.9
1000/T (K^{-1})
XBL811-5005

Fig. 3.58

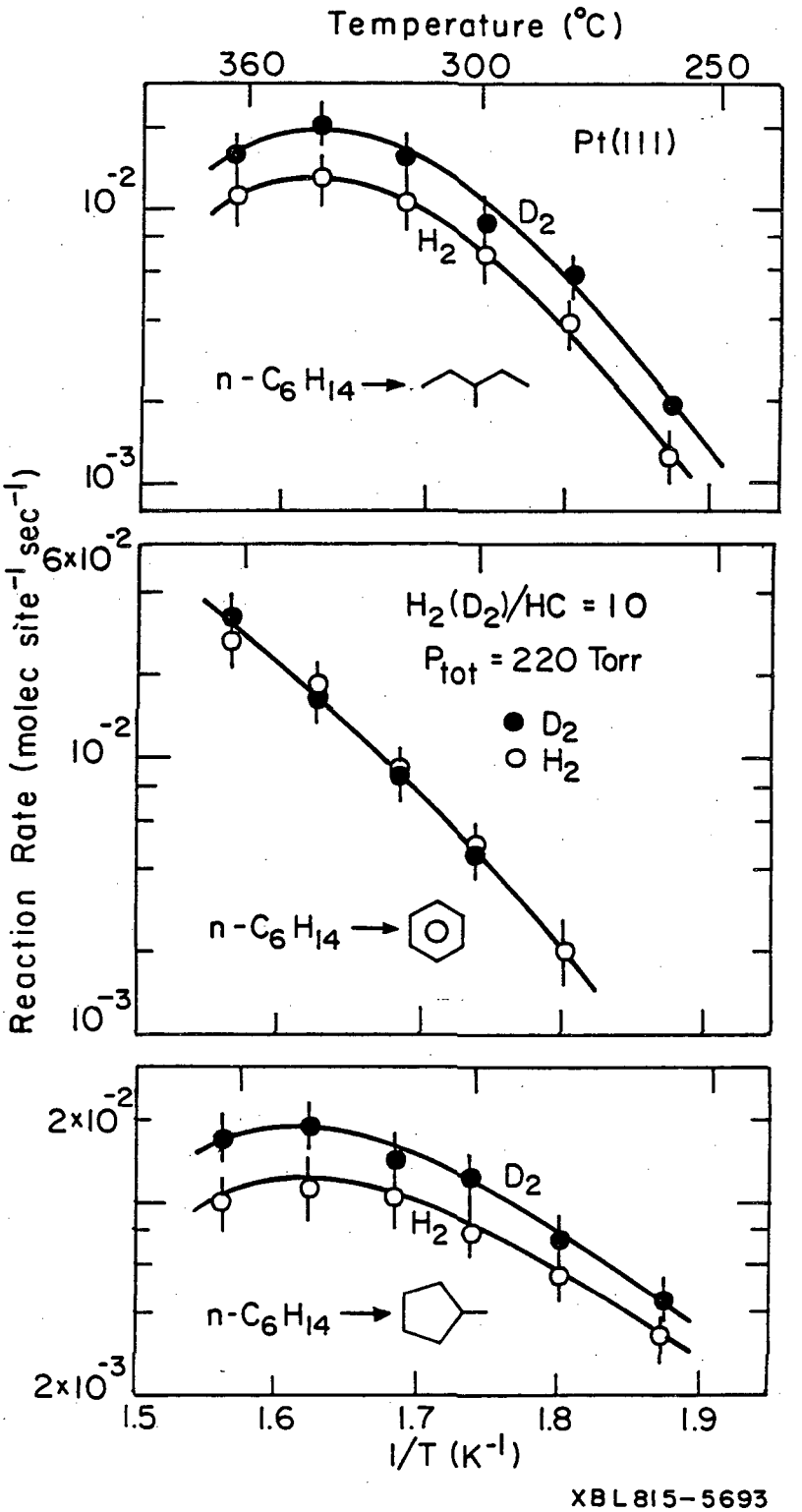
Temperature (°C)
360
300
250
Pt(111)
10^{-2}
10^{-3}
D_2
H_2
n - C_6H_{14} →
6×10^{-2}
10^{-2}
10^{-3}
$H_2(D_2)/HC = 10$
$P_{tot} = 220$ Torr
● D_2
○ H_2
n - C_6H_{14} →
2×10^{-2}
2×10^{-3}
D_2
H_2
n-C_6H_{14} →
Reaction Rate (molec site^{-1} sec^{-1})
1.5
1.6
1.7
1.8
1.9
1/T (K^{-1})
XBL815-5693

Fig. 3.59

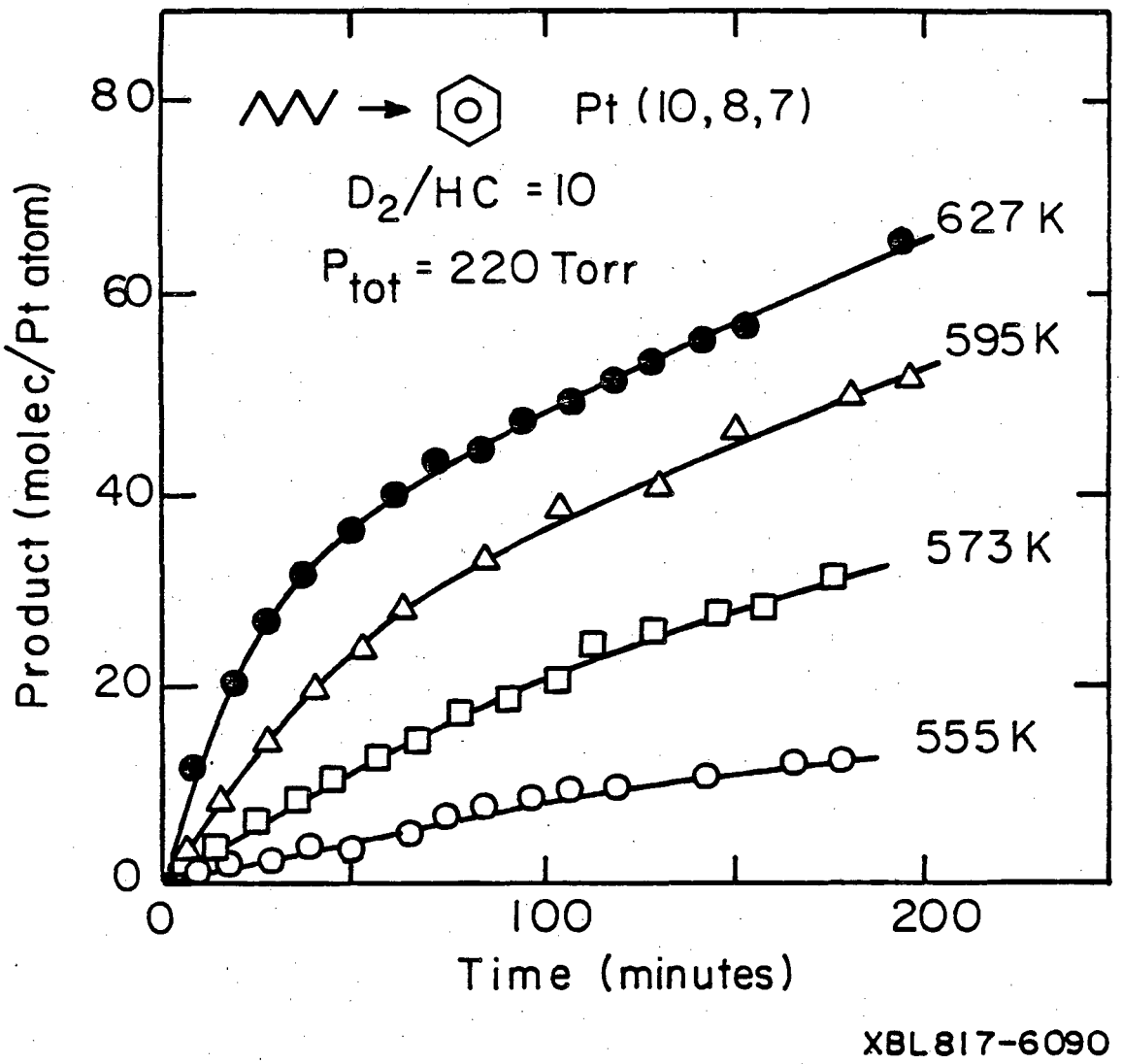
Pt (10,8,7)
D2/HC = 10
Ptot = 220 Torr
627 K
595 K
573 K
555 K
Product (molec/Pt atom)
Time (minutes)
0
20
40
60
80
0
100
200
XBL817-6090

Fig. 3.60

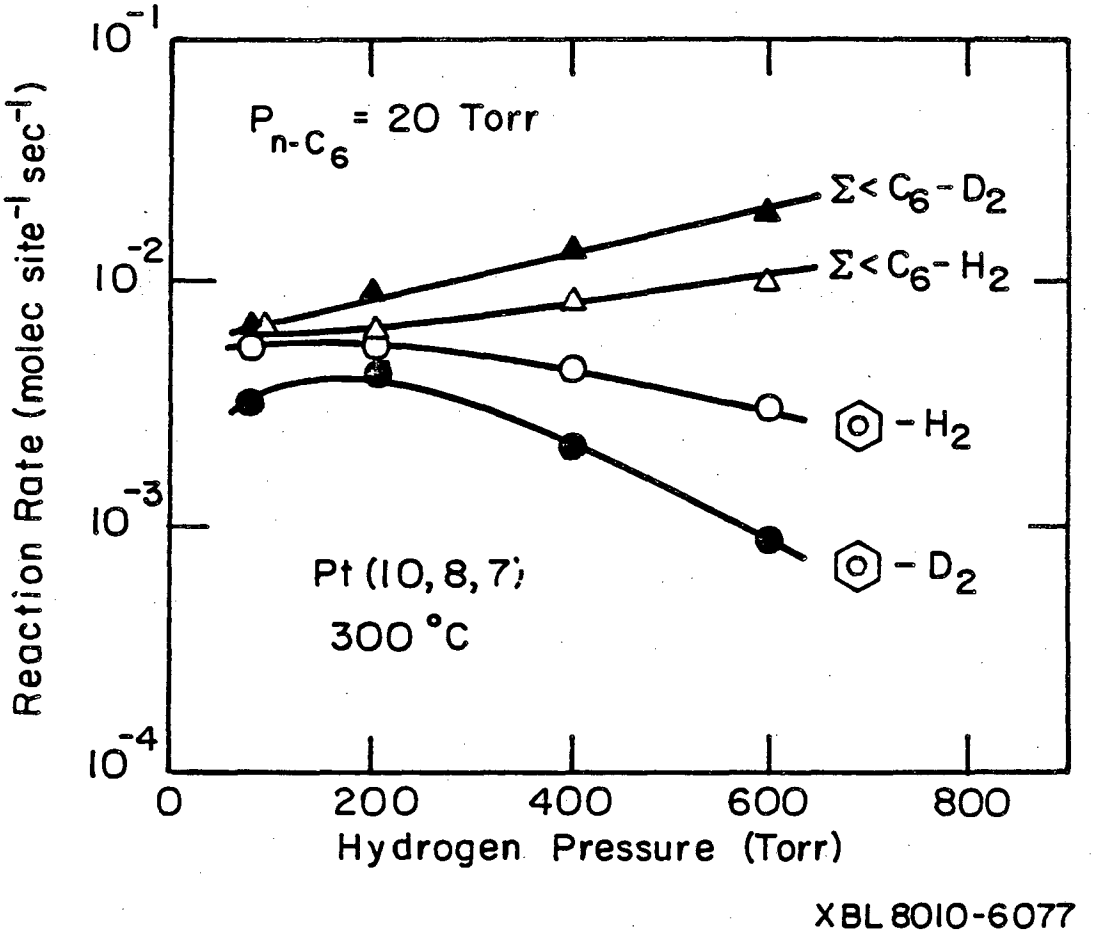
10^{-1}
10^{-2}
10^{-3}
10^{-4}
Reaction Rate (molec site^{-1} sec^{-1})
$P_{n\text{-}C_6}$ = 20 Torr
$\Sigma < C_6 - D_2$
$\Sigma < C_6 - H_2$
$- H_2$
$- D_2$
Pt (10, 8, 7)
300 °C
0
200
400
600
800
Hydrogen Pressure (Torr)
XBL 8010-6077

Fig. 3.61

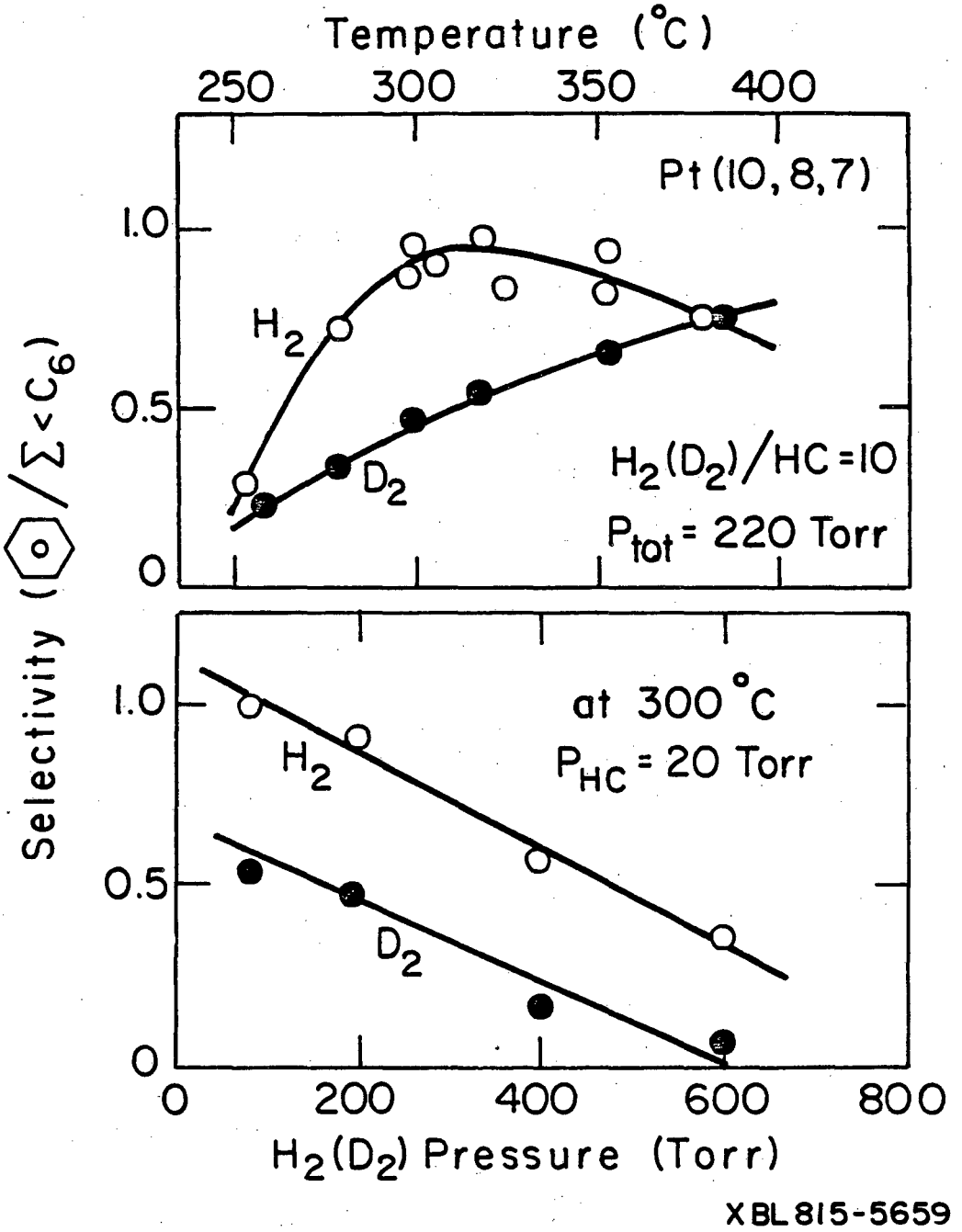
Temperature (°C)
250
300
350
400
Pt(10,8,7)
1.0
0.5
0
H2
D2
H2(D2)/HC=10
Ptot = 220 Torr
Selectivity (⬡/Σ<C6)
at 300°C
PHC = 20 Torr
0
200
400
600
800
H2(D2) Pressure (Torr)
XBL815-5659

Fig. 3.62

REFERENCES

1. E. Santacesaria, D. Gelosa, and S. Carra, J. Catal. 39, 403 (1975).
2. Z. Paal and P. Tetenyi, J. Catal. 29, 176 (1973).
3. J. R. Anderson and Y. Shimoyama, Proc. 5th Intern. Congr. Catal. (Miami, 1972), p. 695.
4. P. P. Lankhorst, H. C. DeJongste, and V. Ponec, in Catalyst Deactivation (B. Delmon and G. C. Froment, eds.) Elsevier, Amsterdam, 1980.
5. E. Santacessaria, D. Gelosa, S. Carra, and I. Adami, Ind. Eng. Chem. Prod. Res. Dev. 17, 68 (1978).
6. F. M. Dautzenberg and J. C. Platteeuw, J. Catal. 19, 41 (1970).
7. F. M. Dautzenberg and J. C. Platteeuw, J. Catal. 24, 264 (1972).
8. H. C. DeJongste, K. J. Kuijers, and V. Ponec, Proc. 6th Intern. Congr. Catal. (London, 1976), p. 915.
9. Z. Karpinski and T. Koscielski, J. Catal. 63, 313 (1980).
10. P. Biloen, J. N. Helle, H. Verbeek, F. M. Dautzenberg, and W. M. H. Sachtler, J. Catal. 63, 112 (1980).
11. F. M. Dautzenberg, J. N. Helle, P. Biloen, and W. M. H. Sachtler, J. Catal. 63, 119 (1980).
12. J. R. H. van Schaik, R. P. Dessing, and V. Ponec, J. Catal. 38, 273 (1975).
13. P. Biloen, F. M. Dautzenberg, and W. M. H. Sachtler, J. Catal. 50, 77 (1977).
14. A. D. Cinneide and F. G. Gault, J. Catal. 37, 311 (1975).

15. V. Ponec and W. M. H. Sachtler, Proc. 5th Intern. Congr. Catal. (Miami, 1972), p. 645.

16. T. J. Plunkett and J. K. A. Clarke, J. Catal. 35, 330 (1974).

17. J. K. A. Clarke, T. Manninger, and T. Baird, J. Catal. 54, 230 (1978).

18. Y. Barron, D. Coronet, G. Maire, and F. G. Gault, J. Catal. 2, 152 (1963).

19. C. Corolleur, D. Tamanova, and F. G. Gault, J. Catal. 24, 401 (1972) and references therein.

20. J. K. A. Clarke and J. J. Rooney, Adv. Catal. 25, 125 (1976).

21. J. R. Anderson and N. R. Avery, J. Catal. 5, 446 (1966).

22. M. A. McKervey, J. J. Rooney, and N. G. Samman, J. Catal. 30, 330 (1973).

23. V. Amir-Ebrahami, F. Garin, F. Weisang, and F. G. Gault, Nouv. J. Chemie 3, 529 (1979).

24. C. Corolleur, F. G. Gault, D. Juttard, G. Maire, and J. M. Muller, J. Catal. 7, 466 (1967).

25. G. Maire, C. Corolleur, D. Juttard, and F. G. Gault, J. Catal. 21, 250 (1971).

26. J. M. Dartigues, A. Chambellan, S. Corolleur, F. G. Gault, A. Renouprez, B. Moraweck, P. Bosch Giral, and G. Dalmai-Imelik, Nouv. J. Chemie 3, 591 (1979).

27. J. R. Anderson, Adv. Catal. 23, 1 (1973).

28. W. D. Gillespie, Ph. D. Thesis, University of California, Berkeley, 1980.

29. C. E. Smith (Hemminger), Ph. D. Thesis, University of California, Berkeley, 1978.

30. D. W. Blakely, Ph. D. Thesis, University of California, Berkeley, 1976.

31. J. H. Sinfelt, Adv. Catal. 23, 91 (1973).

32. G. A. Martin, J. Catal. 60, 452 (1979).

33. S. M. Davis and G. A. Somorjai, Hydrocarbon Conversion Over Metal Catalysts, in The Chemical Physics of Solid Surfaces and Heterogeneous Catalysis, Vol. 4, Elsevier, Amsterdam, 1981.

34. M. Boudart, A. W. Aldag, L. D. Ptak, and J. E. Benson, J. Catal. 11, 35 (1968).

35. K. Foger and J. R. Anderson, J. Catal. 54, 318 (1978).

36. D. R. Stull, E. F. Westrum, and G. C. Sinke, The Chemical Thermodynamics of Organic Compounds, Wiley, New York, 1969.

37. A. A. Balandin, Z. Physik. Chem. (Leipzig) B2, 289 (1929).

38. A. A. Balandin, Adv. Catal. 10, 96 (1958).

39. J. M. Muller and F. G. Gault, J. Catal. 24, 361 (1972).

40. F. Garin, S. Aeiyach, and G. Maire, J. Catal., in press.

41. V. Amir-Ebrahami, A. Choplin, P. Parayre, and F. G. Gault, Nouv. J. Chemie 4, 431 (1980).

42. J. M. Muller and F. G. Gault, Proc. 5th Intern. Congr. Catal. (Miami, 1972), p. 743.

43. J. H. Sinfelt, H. Hurwitz, and J. C. Rohrer, J. Catal. 1, 481 (1962).

44. B. H. Davis and P. B. Venuto, J. Catal. 15, 363 (1969).

45. B. H. Davis, J. Catal. 29, 398 (1973); 46, 348 (1977).

46. K. E. Lu and R. R. Rye, Surf. Sci. 45, 677 (1974).

47. K. Christmann and G. Ertl, Surf. Sci. 60, 211 (1976).

48. H. C. Yao, Y. F. Yu Yao, and K. Otto, J. Catal. 56, 21 (1979).

49. L. L. Murrell and D. J. C. Yates, J. Catal, 57, 41 (1979).

50. G. Leclercq, L. Leclercq, and R. Maurel, J. Catal. 50, 87 (1977).

51. C. Minot and G. A. Somorjai, to be published.

52. L. L. Kesmodel, L. H. Dubois and G. A. Somorjai, Chem. Phys. Lett. 56, 267 (1978).

53. L. L. Kesmodel, L. H. Dubois and G. A. Somorjai, J. Chem. Phys. 70, 2180 (1979).

54. R. J. Koestner, M. A. Van Hove, and G. A. Somorjai, Surf. Sci., in press.

55. A. Cimino, M. Boudart, and H. S. Taylor, J. Phys. Chem. 58, 796 (1954), and references therein.

56. G. Leclercq, L. Leclercq, and R. Maurel, J. Catal. 44, 68 (1976).

57. C. Kemball, Disc. Faraday Soc. 41, 190 (1966).

58. M. Boudart, AIChE J. 18, 465 (1972).

59. A. Frennet, G. Lienard, F. Crucq, and L. Delgols, J. Catal. 53, 150 (1978); 35, 18 (1974).

60. G. A. Martin, J. Catal. 60, 345 (1979).

61. Z. Paal and P. Tetenyi, J. Catal. 30, 350 (1973).

62. Z. Paal and P. Tetenyi, Nature 267, 234 (1977).

63. M. Boudart and L. Ptak, J. Catal. 16, 90 (1970).

64. J. Tersoff and L. M. Falicov, Phys. Rev. B, in press.

65. R. S. Dowie, D. A. Whan, and C. Kemball, Faraday Trans. 68, 2150 (1973).

66. L. Guczi, A. Sarkany, and P. Tetenyi, Faraday Trans. 70, 1971 (1974).

67. J. C. Prudhomme and F. G. Gault, Bull. Soc. Chim. France (1966), 827.

68. F. Garin and F. G. Gault, J. Amer. Chem. Soc. 97, 4466 (1975).

69. F. G. Gault, V. Amir-Ebrahami, F. Garin, F. Parayre, and F. Weisang, Bull. Soc. Chim. Belg. 88, 475 (1979).

70. P. Foley, R. DiCosimo, and G. M. Whitesides, J. Amer. Chem. Soc. 102, 6713 (1980).

71. C. P. Casey, D. M. Scheck, and A. J. Shusterman, J. Amer. Chem. Soc. 101, 4233 (1979).

72. T. H. Johnson and S. S. Cheng, J. Amer. Chem. Soc. 101, 5277 (1979).

73. R. J. Al-Essa, R. J. Puddephatt, P. J. Thompson, and C. F. H. Tipper, J. Amer. Chem. Soc. 102, 7546 (1980).

74. R. J. Al-Essa, R. J. Puddephatt, M. A. Quayser, and C. F. H. Tipper, J. Amer. Chem. Soc. 101, 364 (1979).

75. V. Ponec, Exchange and Reforming Reactions of Hydrocarbons on Metals and Alloys, in The Chemical Physics of Solid Surfaces and Heterogeneous Catalysis, Vol. IV, Elsevier, Amsterdam, 1981.

76. J. R. Anderson and N. R. Avery, J. Catal. 7, 315 (1967).

77. G. A. Olah, Chem. in Britain 8, 281 (1972).

78. J. E. Demuth and D. E. Eastman, Phys. Rev. Lett. 32, 1123 (1974).

79. J. L. Gland, Ph. D. thesis, University of California, Berkeley, 1973.

80. P. E. C. Franken and V. Ponec, Surf. Sci. 53, 341 (1975).

81. R. H. Grubbs, Prog. Inorg. Chem. 24, 1 (1978); N. Calderon, J. P. Lawrence and E. A. Ofstead, Adv. Organomet. Chem. 17, 449 (1979).

82. G. C. Bond, Faraday Disc 41, 200 (1966).

83. J. B. Goodenough, Magnetism and the Chemical Bond, Wiley, New York, 1963.

84. O. K. Anderson, Phys. Rev. B 2, 883 (1970).

85. K. A. Mills, R. F. Davis, S. D. Kevan, G. Thornton, and D. A. Shirley, Phys. Rev. B 22, 581 (1980).

86. M. M. Traum and N. V. Smith, Phys. Rev. B. 9, 1350 (1974); N. V. Smith, Phys. Rev. B 9, 1365 (1974); N. V. Smith, G. K. Wertheim, S. Hufner, and M. M. Traum, Phys. Rev. B 10, 3197 (1974).

87. M. C. Desjonqueres and F. Cyrot-Lackmann, Solid State Comm. 18, 1127 (1976); Y. W. Tsang and L. M. Falicov, J. Phys. C 9, 51 (1976).

88. S. G. Louie, Phys. Rev. Lett. 40, 1525 (1978); 42, 476 (1979).

89. P. H. Citrin and G. K. Wertheim, Phys. Rev. Lett. 41, 1425 (1978).

90. E. Segal, R. J. Madon, and M. Boudart, J. Catal. 52, 45 (1978).

91. M. Primet, J. M. Basset, M. V. Mathieu, and M. Prettre, J. Catal. 28, 368 (1973).

92. J. M. Basset, G. Dalmai-Imelik, M. Primet, and R. Mutin, J. Catal. 37, 22 (1975).

93. L. T. Dixon, R. Barth, R. J. Kokes, and J. W. Gryder, J. Catal. 37, 376 (1975).

94. J. D. Clewly, J. F. Lynch, and T. B. Flanagan, J. Catal. 36, 291 (1975).

95. P. C. Aben, J. C. Platteeuw, and B. Southamer, Proc. 4th Intern. Congr. Catal., Moscow, 1968, paper I-3.

96. D. R. Stull, E. F. Westrum and G. C. Sinke, The Chemical Thermodynamics of Organic Compounds, Wiley and Sons, Inc., New York, 1969.

97. M. A. Long, R. B. Moyes, P. B. Wells, and J. L. Garnett, J. Catal. 52, 206 (1978).

98. D. W. McKee and F. J. Norton, J. Catal. 3, 252 (1964).

99. C. Kemball, Faraday Trans. 50, 1344 (1954).

100. A. Sarkany, L. Guczi, and P. Tetenyi, J. Catal. 39, 181 (1975).

101. M. Salmeron, R. J. Gale, and G. A. Somorjai, J. Chem. Phys. 70, 2807 (1979) and references therein.

102. F. G. Gault and C. Kemball, Faraday Trans. 57, 1781 (1961).

103. M. Salmeron and G. A. Somorjai, J. Phys. Chem., in press.

104. A. Ozaki, Isotopic Studies of Heterogeneous Catalysis, Academic press, New York, 1977.

105. H. Knozinger and A. Scheglila, J. Catal. 17, 252 (1970).

106. Y. Inoue and I. Yasumori, J. Phys. Chem. 75, 880 (1971).

107. T. P. Wilson, J. Catal. 60, 167 (1979).

108. S. Kellner and A. T. Bell, J. Catal. 67, 000 (1981).

109. K. Aika and A. Ozaki, J. Catal. 14, 311 (1969); 19, 350 (1970).

110. A. M. Baro and H. Ibach, Surf. Sci. 92, 237 (1980).

111. A. M. Baro, H. D. Bruchman, and H. Ibach, Surf. Sci. 88, 384 (1979).

112. J. P. Candy, P. Fouilloux, and M. Primet, Surf. Sci. 72, 167 (1978).

113. P. M. Gundry, Proc. 2nd Intern. Congr. Catal., No. 51, 1083 (1960).

114. G. Wedler, F. J. Broker, G. Fisch, and G. Schroll, Z. Phys. Chem. N.F. 76, 212 (1971).

115. K. Nakamoto, Infrared Spectra of Inorganic and Coordination Compounds, Wiley, New York, 1970.

116. G. L. Dalmon and G. A. Martin, J. Catal. 66, 214 (1980).

CHAPTER 4. THE ROLE OF ADSORBED CARBON DEPOSITS IN HYDROCARBON CATALYSIS ON PLATINUM: STUDIES OF THE COMPOSITION AND REACTIVITY OF CHEMISORBED HYDROCARBONS AS A FUNCTION OF TEMPERATURE, PRESSURE, AND SURFACE STRUCTURE

4.1. Thermal Desorption Studies of Molecular Hydrocarbon Chemisorption on Platinum

4.1.1. Background

The energetics of hydrocarbon chemisorption on surfaces with different atomic structure is a very important consideration in hydrocarbon catalysis on metals. The surface residence times of adsorbed reactants, intermediates, and products are controlled by metal-organic bond energies that are closely related to heats of molecular and/or dissociative chemisorption. It has long been recognized that periodic trends in catalytic behavior for different metals may often be correlated with periodic variations in chemisorption bond energies (1). According to the Sabatier principle (2), maximum catalytic activity is expected when the bond energy is neither too strong nor too weak. Unfortunately, very little research has been carried out to investigate the energetics of molecular hydrocarbon chemisorption on well defined metal surfaces. Madey and Yates (3) used thermal desorption spectroscopy to determine desorption activation energies for ethane (~5 kcal/mole), cyclopropane (~8 kcal/mole), cyclohexane (~14 kcal/mole), and cyclooctane (~16 kcal/mole) chemisorbed at low temperatures on Ru(001). As long as molecular adsorption is non-activated these desorption activation energies can be equated with the enthalpies of molecular adsorption. The adsorption energies determined in this manner are only 3-8 kcal/mole in excess of molecular sublimation energies indicating that the gas-solid interaction potential is weak, at least in the case of molecular alkane adsorption.

In this section the adsorption energetics of simple alkanes, olefins, and benzene on platinum are briefly discussed in connection with thermal desorption studies. The low temperature alkane and olefin adsorption studies were mostly carried out by M. Salmeron using a special sample manipulator described elsewhere (4). As the first of several sections devoted to the temperature dependent bonding characteristics of hydrocarbons chemisorbed on platinum, the major goal here is to show that if the temperature is low enough (e.g., <150-250 K) alkanes and olefins always appear to chemisorb in a molecular form. Thermal desorption studies have provided energies of molecular adsorption which vary with molecular weight and degree of substitution and that are typically in the range of 10-20 kcal/mole.

4.1.2. Results and Discussion

Alkane Adsorption-Desorption. Thermal desorption spectra for n-butane and n-pentane chemisorbed at ~110 K on the (111) platinum surface are shown in Fig. 4.1. When chemisorbed at low coverages these molecules displayed single desorption peaks centered at 166 and 197 ± 3 K for n-C_4H_{10} and n-C_5H_{12}, respectively. Low temperature adsorption appeared to be completely reversible as desorption took place with no detectable decomposition. Chemisorption of n-hexane on Pt(111) at ~150 K produced a single desorption peak centered at 225 ± 10 K (5). In this case, molecular adsorption was not completely reversible as a part of the adsorbed species underwent dissociative chemisorption and decomposition upon heating to ~600 K.

The dependence of the alkane desorption peak temperatures and peak shapes on surface coverage were indicative of a simple first order desorption process. Table 4.1 summarizes the peak temperatures together with desorption activation energies calculated by the Edwards and Redhead methods discussed in Section 2.2. The adsorption energies ($\Delta H_{ads} = -E_d$) determined in this manner were small (10-14 kcal/mole) and consistent with a weak gas-solid interaction dominated by metal-hydrogen bonding. A clear tendency exists for these adsorption energies to increase with increasing molecular weight. These adsorption energies can be used to estimate mean surface residence times of adsorbed reactants and products which are involved in alkane conversion reactions catalyzed on platinum at higher temperatures. Mean residence times calculated for a reaction temperature of 573 K using $\tau = \tau_o \exp(E_d/RT)$ with $\tau_o = 10^{-13}$ sec and Redhead E_d values are included in Table 4.1. The surface residence times of the molecular alkane species (10^{-10} - 10^{-8} sec) under reaction conditions are clearly very short as compared to the minimum surface residence times for dissociatively adsorbed intermediates (~10^{-2} - 10^{-1} sec) that were discussed in connection with deuterium exchange reactions in Section 3.4.

Olefin Adsorption-Desorption. A similar series of low temperature adsorption-desorption experiments was carried out for ethylene, propylene, cis-2-butene, and trans-2-butene chemisorbed at ~120 K on the (111) platinum surface (4). Representative thermal desorption spectra for propylene and trans-2-butene are compared in Fig. 4.2.

Table 4.1. Desorption activation energies and mean surface residence times for alkanes chemisorbed on Pt(111).

Hydrocarbon	Desorption Peak Temperature (K)	Desorption Activation Energies (kcal/mole)		τ (a) (sec)
		Redhead	Edwards	
n-Butane	166	9.8	10 ± 2	5×10^{-10}
n-Pentane	197	11.7	11 ± 2	3×10^{-9}
n-Hexane	225	13.4		1×10^{-8}

a) Mean residence time at 573 K.

Temperatures of the desorption peak maxima, desorption activation energies, and mean surface residence times at 573 K are summarized for the four unsaturated hydrocarbons in Table 4.2. In contrast to alkanes, olefin chemisorption was largely irreversible. Only a small fraction of the adsorbed species desorbed in the molecular form; most underwent sequential dehydrogenation and decomposition upon heating to 600 K. Whereas alkane desorption temperatures increased regularly with increasing molecular weight, the temperatures required for molecular olefin desorption decreased slightly with increasing molecular weight. It appears that with increasing substitution the metal-olefin π-bonding interaction was weakened slightly by steric interactions with the methyl substituents. Similar behavior has been reported for metal-olefin coordination compounds (6). In all cases, the metal-olefin π-bonding interaction appeared to be stronger than the metal-hydrogen bonding displayed by chemisorbed alkanes.

Benzene Adsorption, Desorption, and Hydrogen Transfer. Thermal desorption spectra obtained for benzene chemisorbed at room temperature on the stepped (322) and kinked (654) platinum surfaces are shown in Fig. 4.3. Following saturation exposures of 5-15L, the initially clean (111), (322), and (654) platinum surfaces all displayed single desorption peaks centered at 370 ± 15 K that correspond to a desorption activation energy of 22 ± 5 kcal/mole. Benzene chemisorption was largely irreversible on all three surfaces, as only a small fraction ($\lesssim$5 percent, by ^{14}C-analysis) of the adsorbed species could be desorbed in the molecular form.

Table 4.2. Desorption activation energies and mean surface residence times for simple olefins chemisorbed on Pt(111).

Hydrocarbon	Desorption Peak Temperature (K)	Desorption Activation Energies (kcal/mole)		τ (a) (sec)
		Redhead	Edwards	
C_2H_4	285	17.1	14 ± 4	3×10^{-7}
C_3H_6	276	16.5	15 ± 3	2×10^{-7}
cis-2-C_4H_8	261	15.5	13 ± 3	7×10^{-8}
trans-2-C_4H_8	261	15.5	14 ± 3	7×10^{-8}

a) Mean residence time at 573 K.

A second desorption peak at 480 ± 20 K was detected when benzene was reexposed to the platinum surfaces that were precovered with partially dehydrogenated species which formed during the initial thermal desorption experiment. The intensity of this second desorption peak increased in consecutive experiments provided that the sample was not heated beyond 550 K. By contrast, the second desorption peak vanished when the samples were heated to high temperatures to desorb all residual hydrogen. For this reason, the second desorption peak appears to be associated with hydrogen transfer reactions between the different adsorbed species which exist on the platinum surface during the consecutive adsorption–desorption experiments, i.e.,

$$C_6H_6(ads) + {}^*C_6H_x(ads) \xrightarrow{\Delta} {}^*C_6H_x(ads) + C_6H_6(gas) \qquad (1)$$

Labelling experiments alternating $^{14}C_6H_6$ and C_6H_6 chemisorption would be valuable to confirm this phenomenon.

FIGURE CAPTIONS

Fig. 4.1. Thermal desorption spectra for n-butane (left frame) and n-pentane (right frame) chemisorbed on Pt(111) at about 110 K (3), (β = 12 K/sec).

Fig. 4.2. Thermal desorption spectra for trans-2-butene (left frame) and propylene (right frame) chemisorbed on Pt(111) at about 110 K (3), (β = 12 K/sec).

Fig. 4.3. Thermal desorption spectra for benzene chemisorbed at about 300 K on Pt(654) and Pt(322). Clean platinum surfaces are represented by the lower desorption curves. The remaining curves were obtained following consecutive adsorption experiments on the surfaces that were precovered with strongly bound carbonaceous species. The exposure sequence was 15,15,15, and 15L for Pt(654) and 0.8,5,8,10, and 15L for Pt(322).

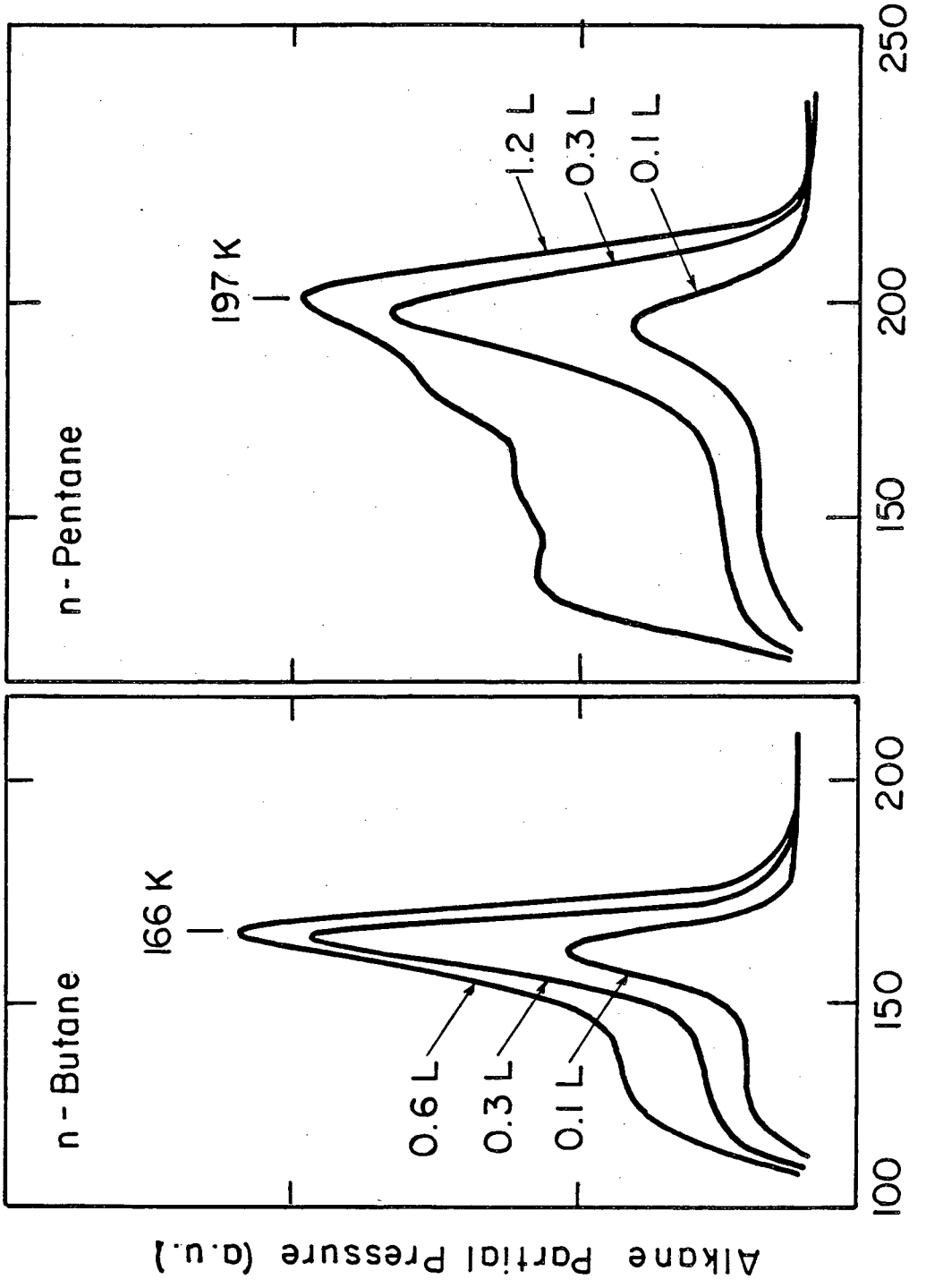

XBL 817-6112

Fig. 4.1

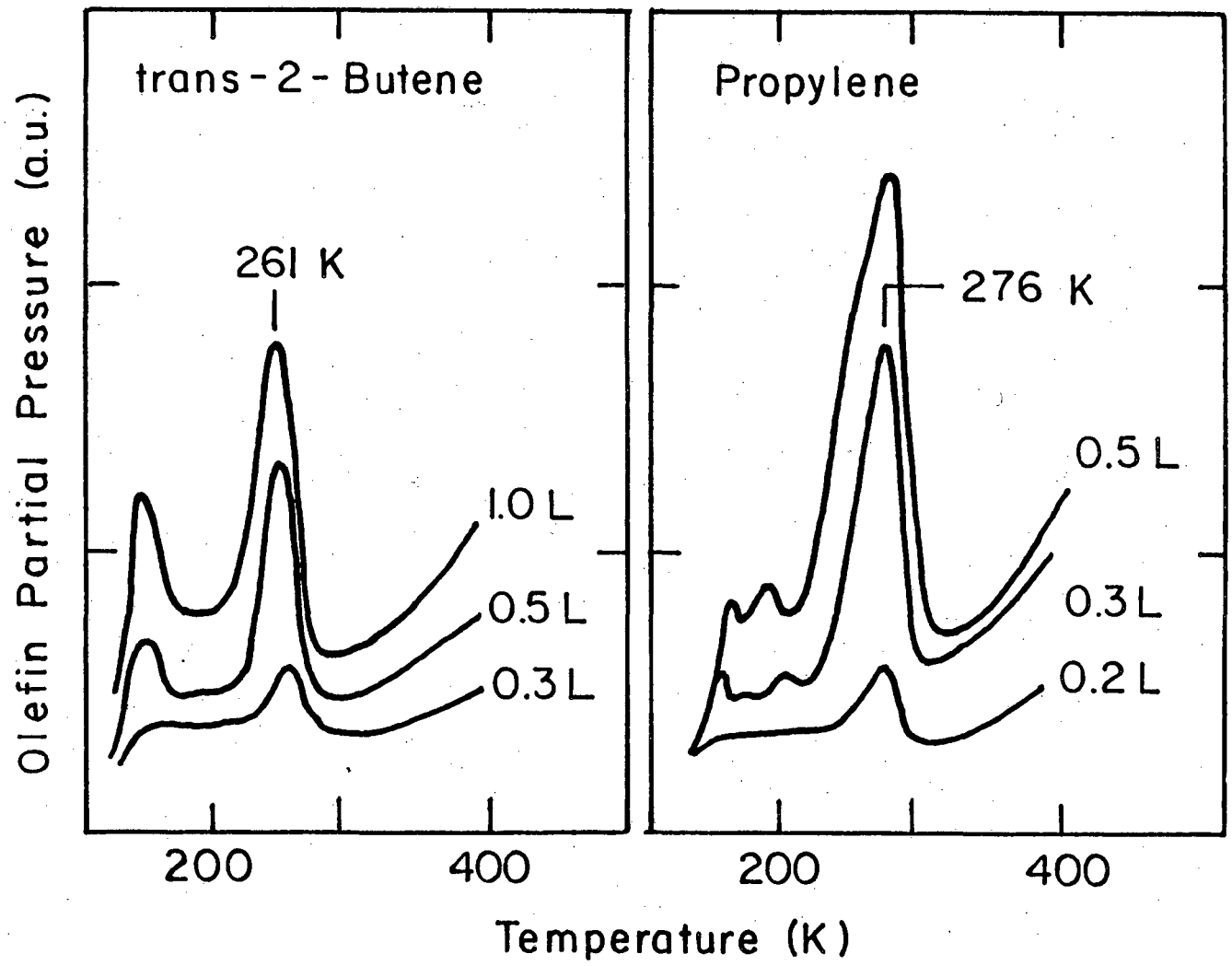

Fig. 4.2

XBL 817-6113

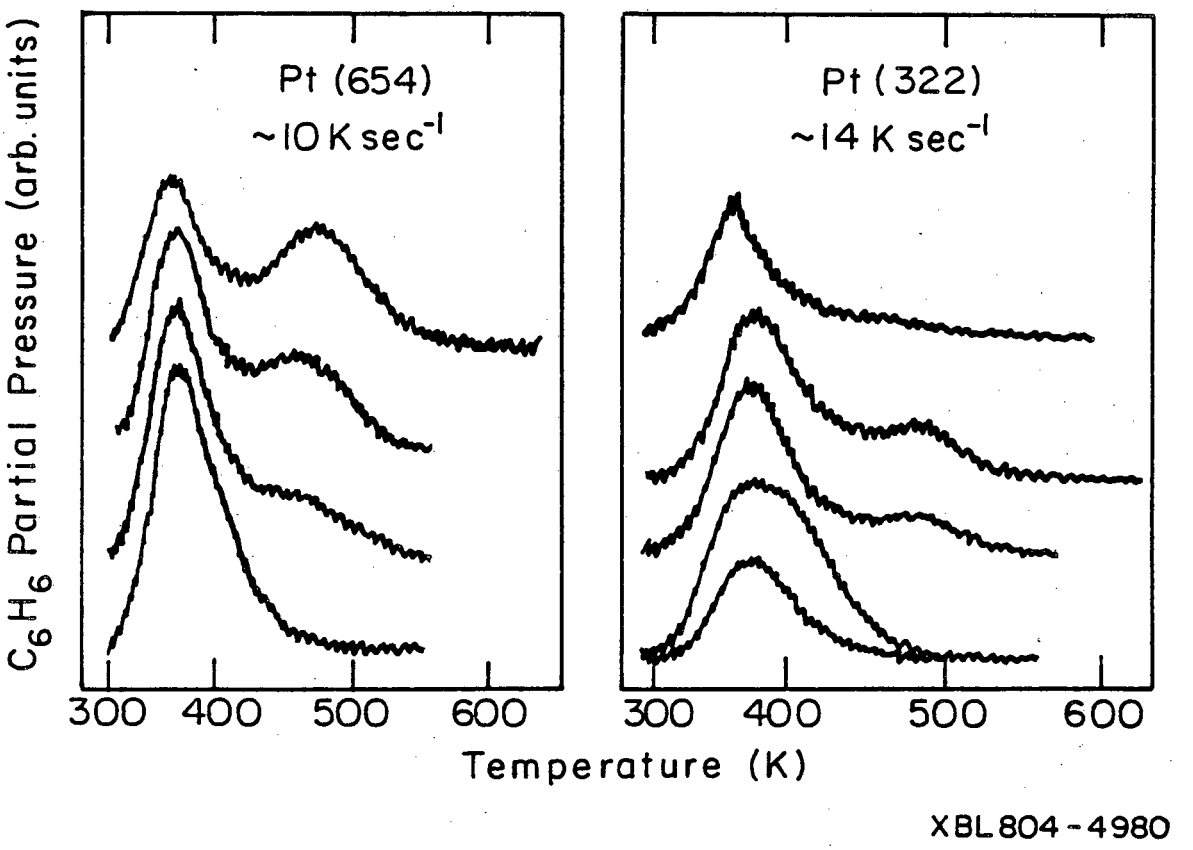
Pt (654)
~10 K sec^{-1}
Pt (322)
~14 K sec^{-1}
C_6H_6 Partial Pressure (arb. units)
300 400 500 600
300 400 500 600
Temperature (K)
XBL804-4980

Fig. 4.3

4.2. Thermal Desorption Studies of Hydrogen Chemisorption on Platinum

4.2.1. Background

The energetics of hydrogen chemisorption on platinum is especially important from the viewpoint of hydrocarbon catalysis. Reforming processes are nearly always carried out in the presence of excess hydrogen at pressures of 6-20 atm in order to suppress catalyst deactivation due to coke deposition. Because the partially dehydrogenated reaction intermediates exist in quasiequilibrium with surface and gas phase hydrogen, the hydrogen pressure can be conveniently varied to control the selectivity of skeletal rearrangement (Section 3.1).

Studies of hydrogen chemisorption on platinum single crystal surfaces using techniques such as cyclic voltametry (7), dynamic work function measurements (8), molecular beam reactive scattering (9), thermal desorption (8,10-13) and vibrational spectroscopy (14,15) have revealed the special importance of local atomic surface structure in controlling the adsorption energetics. Strongly chemisorbed states of surface hydrogen with heats of adsorption in the range of about 10-25 kcal/mole have been identified on the (111) (8-13) and (100) (10,13) platinum surfaces and also on a variety of stepped platinum crystal faces (11-13). These "strongly" adsorbed states correspond to hydrogen adatoms that occupy the 3- and 4-fold hollow sites which represent the absolute minimum of the gas-solid interaction potential (7,14,15). Four-fold sites provide a stronger interaction than 3-fold sites (7), and the interaction is altered further by the presence of surface irregularities on the platinum surfaces (11-13). Hydrogen

chemisorption on platinum at low temperatures (≲150 K) (13) or high hydrogen pressures (16,17) results in the appearance of new adsorbate binding states with reduced binding energy (~7-10 kcal/mole). The latter states have been collectively referred to as "weakly" or "reversibly" adsorbed hydrogen, and a small but growing body of evidence (18-20) indicates that this form of hydrogen is of decisive importance to catalysis. Infrared studies (16) suggest that these weakly bound surface species mostly occupy atop adsorption sites. The short surface residence times of the weakly adsorbed species preclude their investigation by the usual techniques of surface science except at very low temperatures.

This section summarizes results of hydrogen adsorption-desorption studies on several platinum single crystal surfaces with different atomic structure. The studies were carried out near room temperature and at low pressures. As such, only the more strongly bound states of surface hydrogen were investigated. As previously reported (8,12,13), surface irregularities on the platinum surfaces produced new adsorbate binding states with increased binding energy. Hydrogen coadsorption in the presence of "graphitic" surface carbon reduced both the initial sticking coefficient and saturation coverage for hydrogen chemisorption.

4.2.2. Results and Discussion

Thermal desorption spectra for hydrogen chemisorbed at about 305 K on the stepped (322) platinum surface are shown in Fig. 4.4. Figure 4.5 compares TDS results obtained under similar conditions for hydrogen chemisorbed on the flat (111), stepped (557), and kinked

(12,9,8) platinum surfaces. Spectra similar to those shown for Pt(12,9,8) were also obtained with the kinked (6,5,4) and (10,8,7) platinum surfaces (21). The flat (111) surface displayed a single desorption peak at about 330 K which corresponds to hydrogen atoms that occupy 3-fold hollow sites (11,14). In the limit of zero coverage, the heat of adsorption for this state is about 10-12 kcal/mole (11-13). The stepped (322) and (557) platinum surfaces displayed two desorption peaks centered at about 330 and 420 K. Collins and Spicer (12) attributed these states to hydrogen chemisorbed on the (111) terraces and (100) steps, respectively. The desorption temperature for the more strongly bound state is very close to that for hydrogen chemisorbed on unreconstructed Pt(100) (i.e., ~460 K) (13). The kinked surfaces all displayed a third desorption peak at about 470 K which is centered about 25 K higher than any state previously reported for hydrogen on platinum. This state appears to be associated with hydrogen chemisorption (perhaps intercalation) at sites adjacent to kink atoms as it was unique to and common among the kinked surfaces that were studied.

The saturation coverage for hydrogen adsorption under the experimental conditions used here (i.e., $T_{ads} \approx 300$ K) was always very low. The surface coverage was estimated from the desorption peak areas after calibrating the mass spectrometer sensitivity as described in Sections 2.2.4 and 2.6. Figure 4.6 shows hydrogen uptake results for the (10,8,7) platinum surface as a function of gas exposure at 310 ± 3 K. It can be seen that the saturation coverage represented roughly one hydrogen atom per ten surface platinum atoms. Also shown

in Fig. 4.6 are hydrogen uptake results obtained for Pt(10,8,7) when hydrogen was coadsorbed with strongly bound surface carbon. The carbon was deposited by preadsorbing n-hexane at 673 K. The strongly bound carbon reduced the saturation coverage and also appeared to reduce the sticking coefficient for dissociative hydrogen chemisorption.

FIGURE CAPTIONS

Fig. 4.4. Thermal desorption spectra for hydrogen chemisorbed on the stepped (322) platinum single crystal surface ($\beta \simeq 15$ k/sec).

Fig. 4.5. Thermal desorption spectra for hydrogen chemisorbed on the flat (111), stepped (557), and kinked (12,9,8) platinum single crystal surfaces. The lower curves have been taken from Ref. 12.

Fig. 4.6. Adsorption isotherms showing the different hydrogen adsorption properties of the initially clean and carbon covered (10,8,7) platinum single crystal surface.

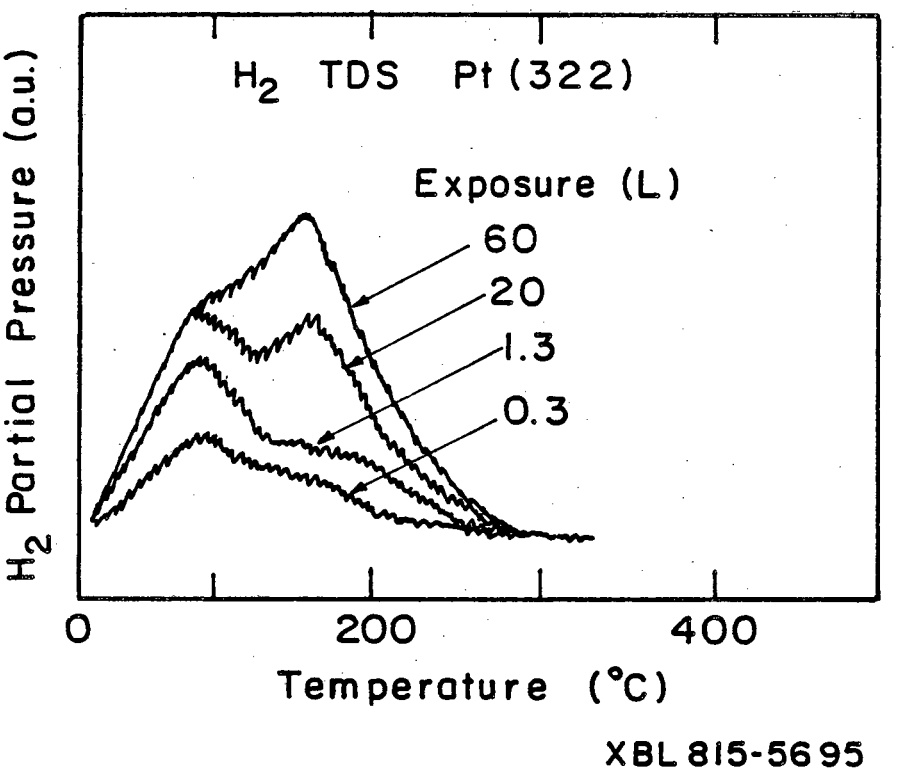
H2 TDS Pt(322)
Exposure (L)
60
20
1.3
0.3
H2 Partial Pressure (a.u.)
0
200
400
Temperature (°C)
XBL 815-5695

Fig. 4.4

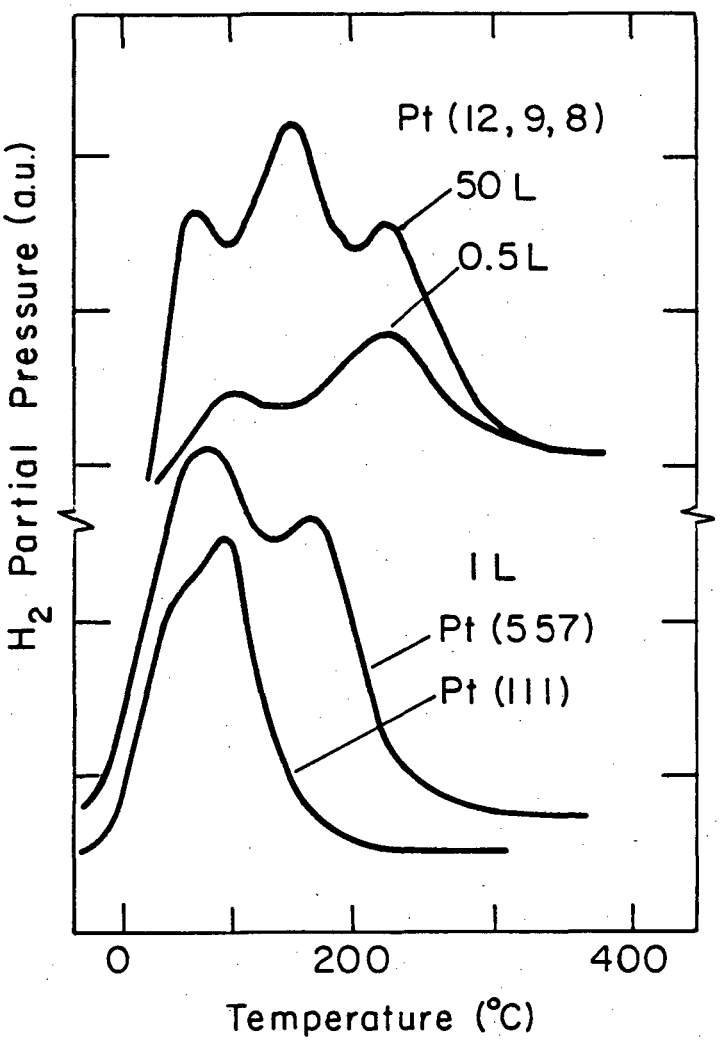
Pt (12, 9, 8)
50 L
0.5 L
1 L
Pt (557)
Pt (111)
H_2 Partial Pressure (a.u.)
0
200
400
Temperature (°C)
XBL 792-5816

Fig. 4.5

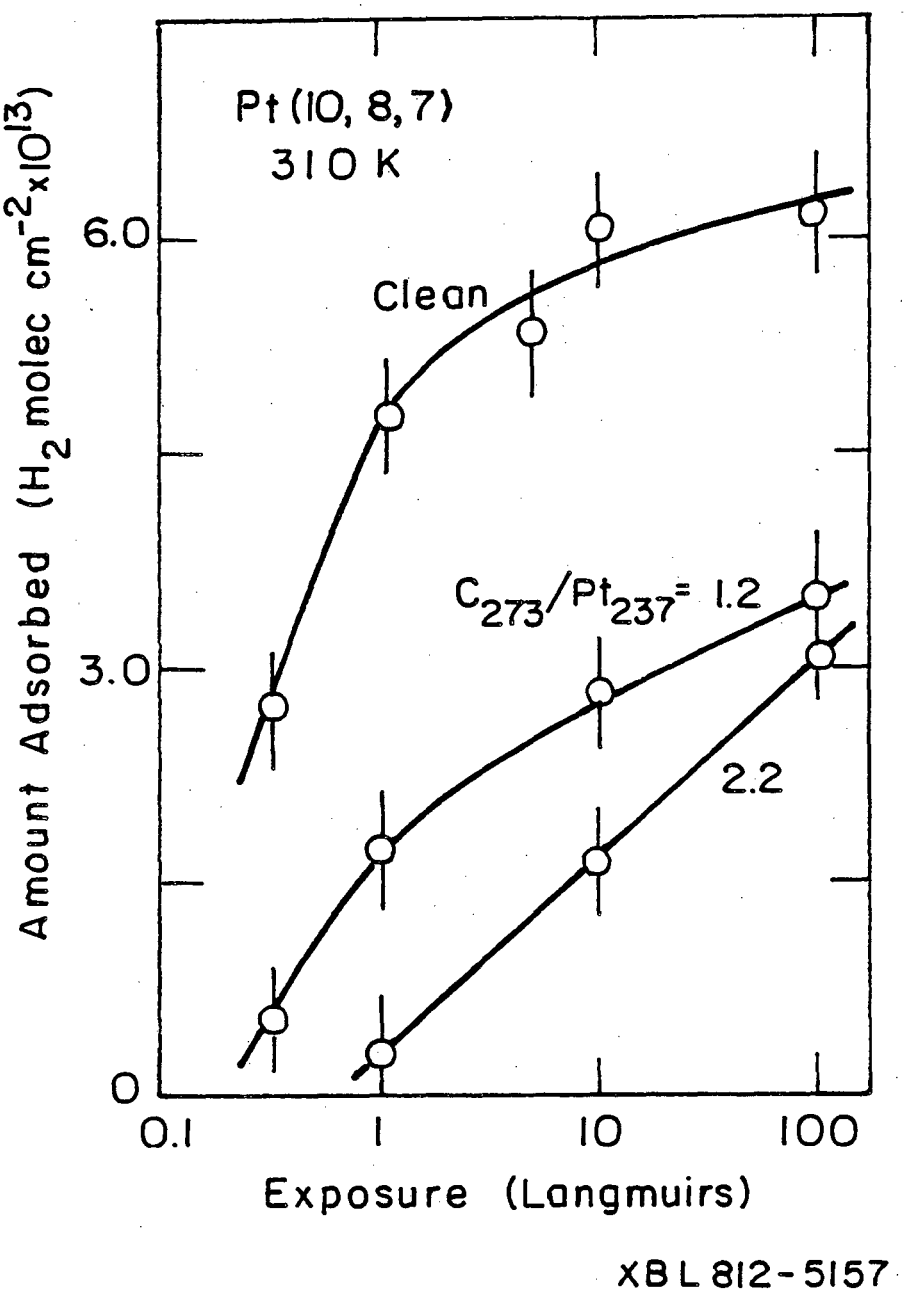
Pt (10, 8, 7)
310 K
Clean
C_{273}/Pt_{237}= 1.2
2.2
Amount Adsorbed (H_2 molec $cm^{-2} \times 10^{13}$)
6.0
3.0
0
0.1
1
10
100
Exposure (Langmuirs)
XBL 812-5157

Fig. 4.6

4.3. Thermal Desorption Studies of the Sequential Dehydrogenation of Hydrocarbons Chemisorbed on Platinum: Energetics of C-H Bond Breaking and Temperature Dependent Composition of the Adsorbed Species

4.3.1. Background.

Adsorption-desorption studies discussed in Section 3.1 provided heats of adsorption for molecular hydrocarbon species chemisorbed on platinum that were typically in the range of 10-20 kcal/mole. The metal-hydrocarbon interaction was not very strong, as unsaturated hydrocarbon molecules desorbed rapidly at 300-400 K, and the desorption temperatures for molecular alkanes were even lower. The chemistry of hydrocarbons chemisorbed on platinum at higher temperatures is dominated by dissociative chemisorption involving scission of one or more C-H bonds. An understanding of these elementary C-H bond breaking processes appears to be essential for establishing meaningful reaction pathways for catalyzed skeletal rearrangement. All the important hydrocarbon reforming reactions take place at high temperatures ($\geq$550 K) where C-H bond breaking occurs very easily.

Thermal desorption spectroscopy has been applied in this section to obtain detailed information about the energetics of the elementary C-H bond breaking processes. The evolution of hydrogen from chemisorbed hydrocarbons was monitored as a function of temperature to obtain a direct "fingerprint" of the reaction kinetics for sequential dehydrogenation (Section 2.2.3). Similar "temperature programmed reaction spectroscopy" techniques have been used widely by Madix and co-workers (22,23) in studies of formic acid and methanol decomposition reactions, although the technique has not been applied systematically

to investigate hydrocarbon interactions previously. In addition to the C-H bond breaking energetics, useful information has been obtained about the temperature dependent composition of the strongly adsorbed hydrocarbon species.

4.3.2. Results and Discussion

Thermal Desorption Studies of Sequential C-H Bond Breaking Processes. Hydrogen thermal desorption spectra representing the sequential dehydrogenation and decomposition of ethylene, propylene, and cis-2-butene chemisorbed at about 120 K on the (111) platinum surface are shown in Fig. 4.7 (courtesy of M. Salmeron). All three olefins displayed similar decomposition behavior characterized by three sets of desorption peaks denoted by the regions A, B, and C. The initial C-H bond breaking reaction (peak A) produced a sharp hydrogen desorption peak at 295 ± 5 K for all three olefins. This peak appeared at a temperature that was just 10-30 K higher than that required for molecular olefin desorption. A second dehydrogenation process (denoted by region B) occurred at temperatures of 383-497 ± 15 K. The desorption temperature for this C-H bond breaking process was highly sensitive to the structure of the original hydrocarbon. A final series of dehydrogenation reactions (denoted by region C) occurred at temperatures between 500 and 715 K. These desorption peaks appeared at similar temperatures for all three hydrocarbons and correspond to the complete dehydrogenation of the initially intact molecules.

Hydrogen thermal desorption spectra representing the sequential dehydrogenation and decomposition of benzene, ethylene, and n-hexane

chemisorbed on Pt(100), Pt(111), and Pt(10,8,7) at a series of increasing adsorption temperatures in the range 315-700 K are shown in Figs. 4.8-4.11. Under these conditions only the desorption peaks in regions B and C can be detected (these are the only ones for benzene (24)). These peaks occurred at similar temperatures for all hydrocarbons over all surfaces investigated. Temperatures corresponding to the desorption peak maxima are summarized together with the relative areas of the peaks for all the different hydrocarbons in Table 4.3.

Energetics of C-H Bond Breaking Processes. Activation energies for the C-H bond breaking processes that produced the different hydrogen desorption peaks were calculated using the methods described in Section 2.2. The assumption of first order reaction kinetics was justified by the fact that the desorption peak temperatures were invariant to changes in initial surface coverage. Table 4.4 summarizes activation energies for all the hydrocarbons investigated. The activation energies for dehydrogenation varied widely from about 18 kcal/mole for the desorption peaks in region A to 22-30 kcal/mole for the peaks in region B to 32-44 kcal/mole for the final, complete dehydrogenation steps that correspond to region C.

Temperature Dependent Composition of the Strongly Bound Surface Species. The hydrogen content of the metal-organic surface species (H/C), expressed as hydrogen atoms per surface carbon atom was determined as a function of adsorption temperature by measuring the total areas under hydrogen desorption peaks like those shown in Figs. 4.8 through 4.11 (Section 2.2.4). The temperature dependent

composition of the strongly adsorbed species resulting from benzene and n-hexane chemisorption on Pt(100), Pt(111), and Pt(10,8,7) is shown in Fig. 4.12. The hydrogen content of the surface species decreased with increasing adsorption temperature and approached zero at temperatures just higher than 670 K.

Nature of the C-H Bond Breaking Processes. The hydrogen thermal desorption spectra shown in Figs. 4.7-4.11 show clearly that the dehydrogenation of hydrocarbons chemisorbed on platinum always in a sequential manner. Each sequential dehydrogenation reaction produced a surface species that was stable from about room temperature to the temperature of the next higher C-H bond breaking process. Complete dehydrogenation occurred only after adsorption at temperatures that were higher than about 670 K.

Recent dynamical LEED intensity analysis (25,26) and high resolution ELS (27) studies of ethylene, propylene, and butenes chemisorbed on Pt(111) have revealed surface structures for the adsorbed species that can be used for an analysis of the hydrogen desorption peaks that were displayed in regions A, B, and C. Chemisorption of these unsaturated hydrocarbons at 300-400 K produces stable surface species with the alkylidyne surface structure, i.e.,

$$\left.\begin{array}{l} H_2C = CH_2 \\ H_2C = CHCH_3 \\ H_2C = CHCH_2CH_3 \end{array}\right\} \xrightarrow[300\text{-}400\ K]{Pt(111)} Pt_3 \equiv CR + \frac{1}{2} H_2 \qquad (1)$$

$$(R = CH_3, C_2H_5, C_3H_8)$$

Formation of these species requires scission of a single C-H bond corresponding to the sharp hydrogen desorption peak displayed in region A (at ~296 K). The activation energy for this process was about 18 kcal/mole independent of the structure of the initial hydrocarbon.

Further dehydrogenation of the alkylidyne surface species occurred in region B at temperatures between 380 and 500 K. These reactions yielded strongly bound metal-organic fragments with average composition "C_2H," "C_3H_2," and "C_4H_3." The activation energy for this rearrangement decreased from about 29 kcal/mole for ethylidyne to 22-25 kcal/mole for propylidyne and butylidyne. Vibrational spectroscopy studies (27,28) indicate that CH fragments are the most abundant surface species resulting from ethylidyne dehydrogenation on Pt(111). However, the appearance of several hydrogen desorption peaks in region C clearly suggests that more than one type of "CH" fragment must exist on the surface. These species appear to be of the type "C_2H," "C_3H," "C_nH" where the implicated polymerization has been demonstrated by radiotracer studies to be discussed in Section 4.5.

Ethylidyne dehydrogenation represents an important example of β-hydrogen abstraction from a multiple bonded surface species. Two hydrogens are lost in this process, i.e.,

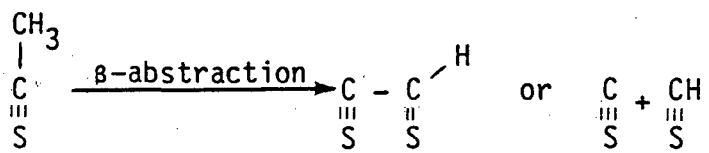

(2)

where S is a surface site composed of 1-3 platinum atoms. Similar rearrangements undoubtedly occur during the sequential dehydrogenation of propylidyne and butylidyne. Since in these cases the activation energies were lowered substantially relative to that for ethylidyne dehydrogenation, it appears very likely that γ-hydrogen abstraction may become favored over β-abstraction, i.e.,

$$S \equiv C - CH_2 - CH_3 \xrightarrow{\gamma\text{-abstraction}} \begin{matrix} & CH_2 & \\ / & & \backslash \\ C & & C \\ \| & & \| \\ S & & S \end{matrix} + \frac{3}{2} H_2 \qquad (3)$$

$$\text{or } 2\ S \equiv C_nH$$

Regardless of the exact structure of the resulting fragments (which is presently not known), it is clear that these species were exceedingly stable. Further dehydrogenation represented by the hydrogen desorption peaks in region C required activation energies in the range 34-44 kcal/mole. These high activation energies indicate that the remaining C-H bonds were not provided easy access to platinum surface sites. Careful vibrational spectroscopy studies are needed to clarify the structure and bonding of the stable fragments with low hydrogen content.

The sequential dehydrogenation of benzene and n-hexane chemisorbed on Pt(100), Pt(111), and Pt(10,8,7) appeared to occur by a similar series of reaction steps. With benzene, no dehydrogenation was detected until temperatures of about 420 K, and then rearrangement appeared to be accompanied by scission of three C-H bonds (on average).

The activation energy for this process (about 27 kcal/mole) was similar to that for alkylidyne decomposition and corresponds reasonably well with the resonance stabilization energy for the benzene molecule (36 kcal/mole (29)).

Rearrangement and sequential dehydrogenation of the adsorbed hydrocarbons must be accompanied by an increase in metal-organic bond multiplicity, polymerization of the adsorbed species, or (more likely) a combination of both these processes. As noted above, the average composition displayed by the adsorbed species at temperatures between 400 and 600 K was consistent with the formation of carbene ($M = CR_2$) and carbyne ($M \equiv CR$) type fragments on the surfaces. Polymerization becomes feasible only if these fragments have considerable mobility. Carbon-14 radiotracer studies presented in Section 4.5 have revealed that partial polymerization takes place readily at temperatures higher than about 470 K. The growth of graphitic carbon islands, that become detectable by LEED at temperatures higher than about 700 K, clearly involves extensive polymerization of the adsorbed species. It appears likely that sequential dehydrogenation at 450-700 K is generally accompanied by polymerization of the adsorbed species by a mechanism that involves the growth of graphitic carbon islands. Studies of the temperature dependent bonding characteristics of cyclohexene and benzene chemisorbed on Pt(100) using ultraviolet photoemission spectroscopy (UPS) (in collaboration with S. Ferrer) support this

conclusion. Figure 4.13 shows a series of UPS difference spectra obtained for cyclohexene chemisorbed on Pt(100) at 300-770 K. Identical spectra were obtained following benzene chemisorption on Pt(100) at 300 and 525 K. Following cyclohexene (benzene) chemisorption at 300 K the UPS difference spectra displayed peaks 8.5, 6.3, 4.4, and 2.3 eV below the Fermi energy which are indicative of an aromatic overlayer composed of benzene molecules (30,31) (8.5 eV = 3 $e_{1\mu}$ + $b_{2\mu}$ ($p\sigma$-orbitals); 6.3 eV = 3 e_{2g} + $1a_{2\mu}$ ($p\sigma$ + $p\pi$-orbitals); 4.4 eV = $1e_{1g}$ ($p\pi$-orbital); 2.3 eV = adsorbate induced change in d-band emission (31,32)). Since only the binding energy of the uppermost e_{2g} orbitals was increased relative to condensed benzene (31), chemical bonding appears to result mainly from the interaction of the doubly degenerate π-levels with surface d-orbitals. With increasing adsorption temperature the emission at 4.4 and 8.5 eV gradually diminished and was replaced by strong emission at 6.1 and 2.8 eV below E_f. The latter UPS peaks appear to be associated with graphitic surface carbon as indicated by the appearance of a "ring" LEED pattern indicative of rotationally ordered graphite (at 770 K). The continuous transition of the UPS spectra from aromatic to graphitic character at temperatures starting as low as 420 K certainly tends to suggest that sequential dehydrogenation is accompanied by the growth of graphitic carbon islands.

FIGURE CAPTIONS

Fig. 4.7. Hydrogen thermal desorption spectra illustrating the sequential dehydrogenation of ethylene, propylene, and cis-2-butene chemisorbed on Pt(111) at about 120 K (β = 12 K/sec).

Fig. 4.8. Hydrogen thermal desorption spectra illustrating the sequential dehydrogenation of benzene chemisorbed on Pt(10,8,7) at a series of temperatures in the range 340-680 K. The gas exposure was always about 36L and β = 69 K/sec.

Fig. 4.9. Hydrogen thermal desorption spectra representing the sequential dehydrogenation of benzene chemisorbed on Pt(100) at 340-500 K. The gas exposure was always about 36L and β = 98 K/sec.

Fig. 4.10. Hydrogen thermal desorption spectra representing the sequential dehydrogenation of n-hexane chemisorbed on Pt(10,8,7) at a series of temperatures in the range 325-700 K. The curves are displaced to the right with increasing adsorption temperature (T_{ads} = 330, 380, 440, 485, 520, 585, 625, 670, and 700 K; β = 69 K/sec).

Fig. 4.11. Hydrogen thermal desorption spectra representing the sequential dehydrogenation of ethylene chemisorbed on Pt(111) at 330-640 K (from left to right T_{ads} = 330, 370, 470, 505, 565, and 635 K; β = 88 K/sec).

Fig. 4.12. Temperature dependent (H/C) composition of the strongly bound surface species resulting from benzene and n-hexane chemisorption on Pt(100), Pt(111), and Pt(10,8,7).

Fig. 4.13. UPS difference spectra for cyclohexene chemisorbed on Pt(100) at 300-770 K.

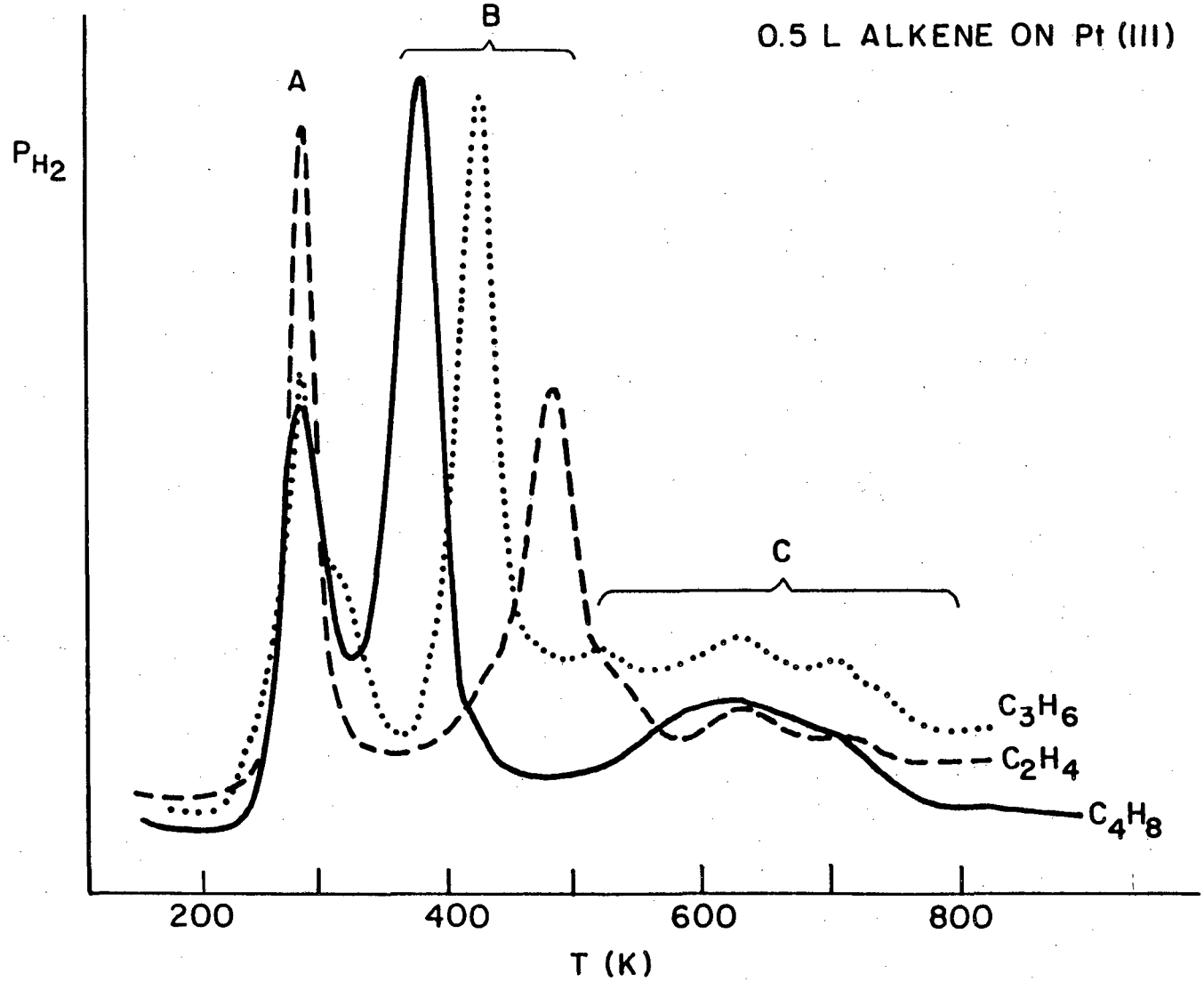

Fig. 4.7

XBL 814-5475

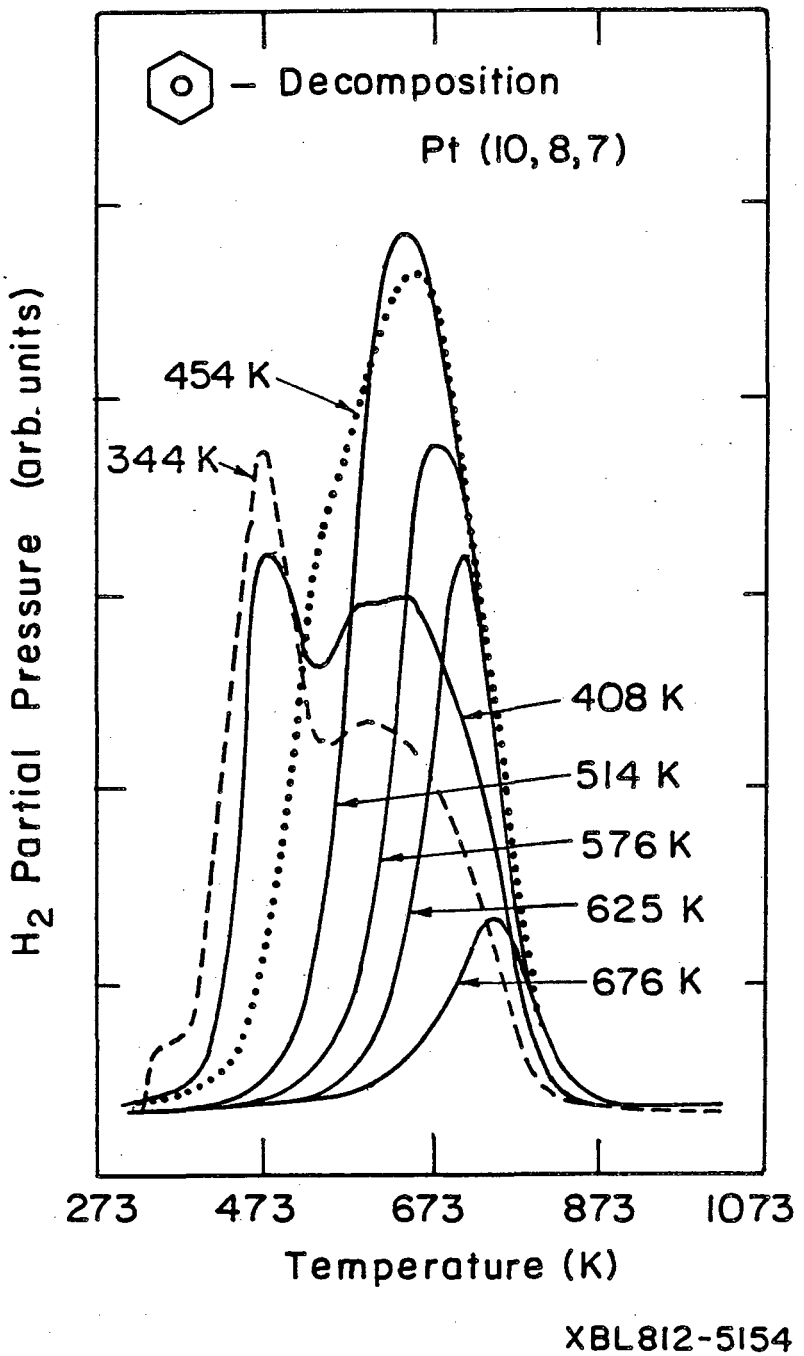
– Decomposition
Pt (10, 8, 7)
454 K
344 K
408 K
514 K
576 K
625 K
676 K
H2 Partial Pressure (arb. units)
273
473
673
873
1073
Temperature (K)
XBL812-5154

Fig. 4.8

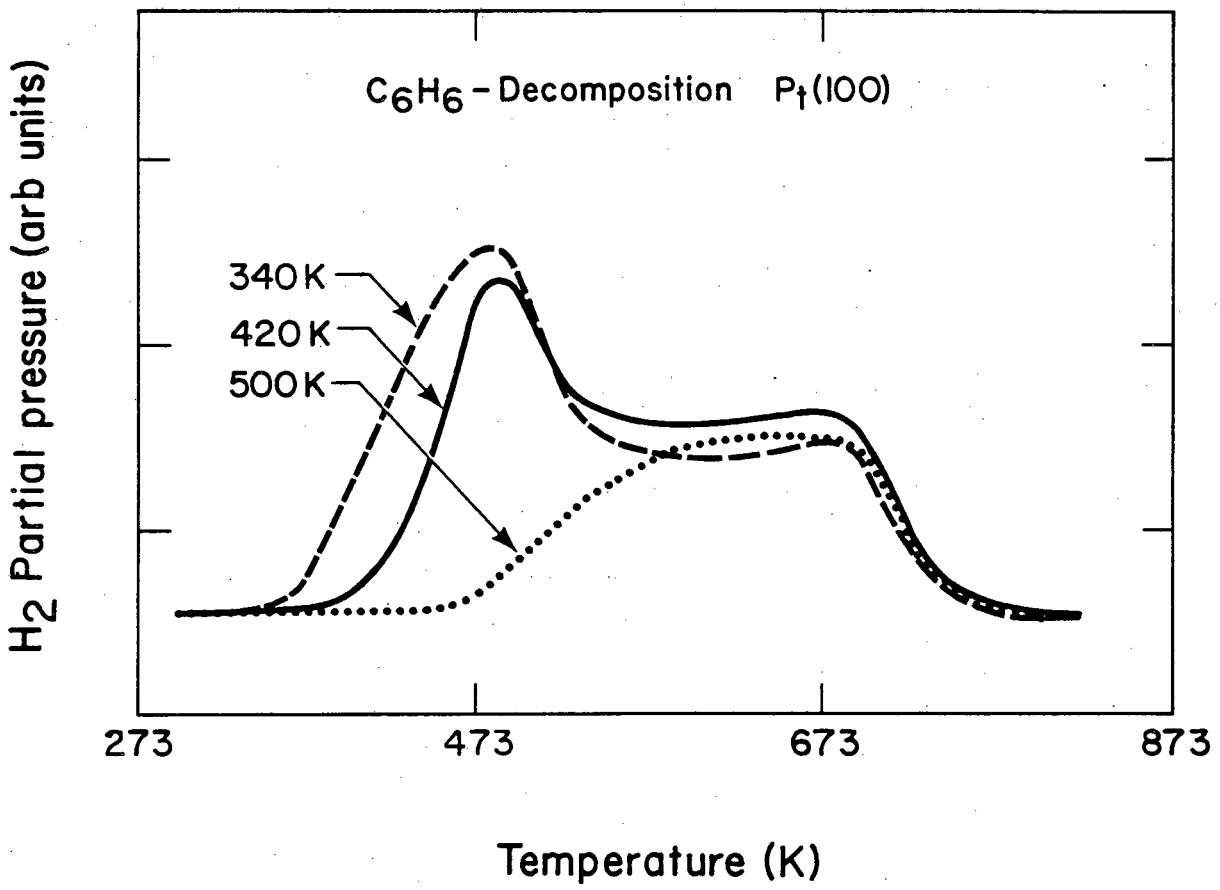

XBL 818-1100

Fig. 4.9

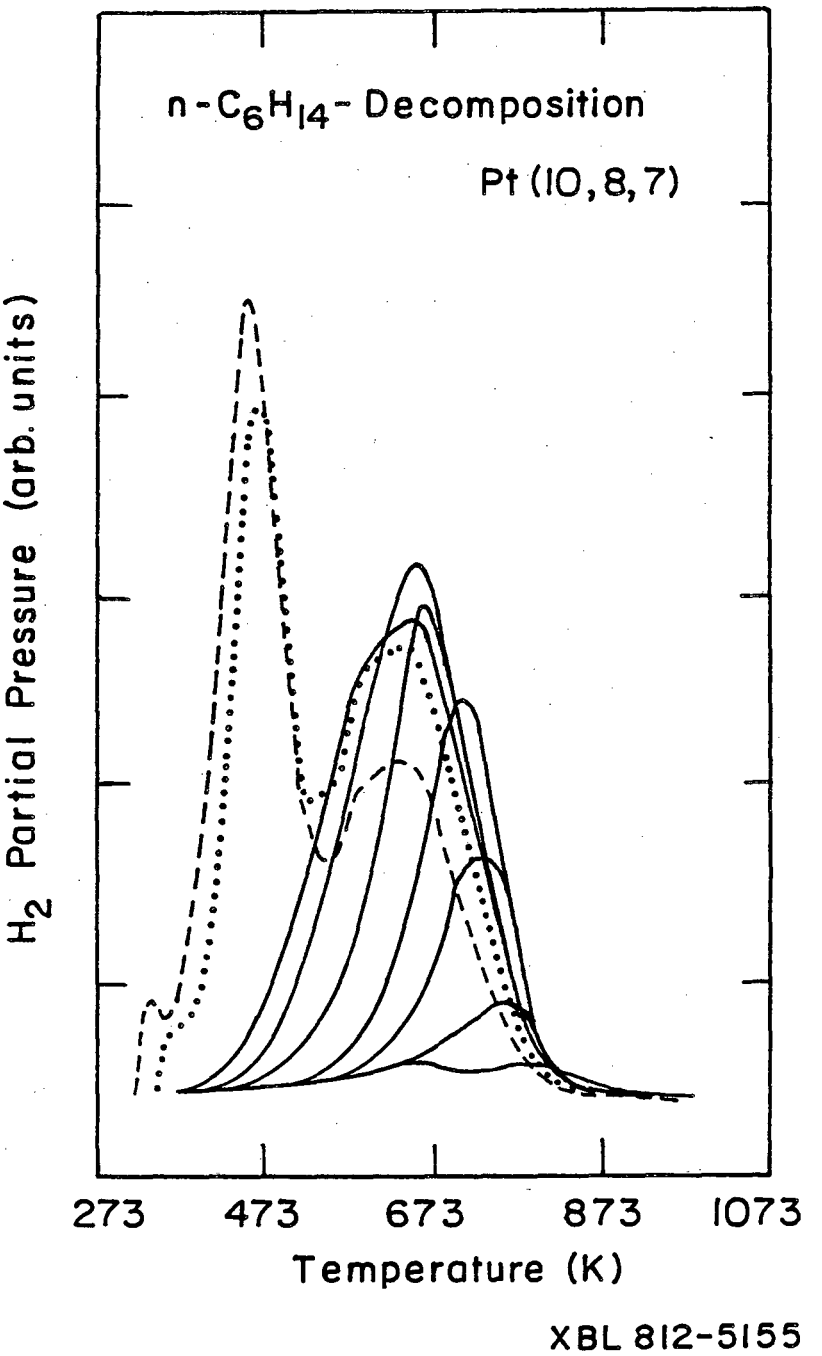
n-C6H14- Decomposition
Pt (10, 8, 7)
H2 Partial Pressure (arb. units)
273
473
673
873
1073
Temperature (K)
XBL 812-5155

Fig. 4.10

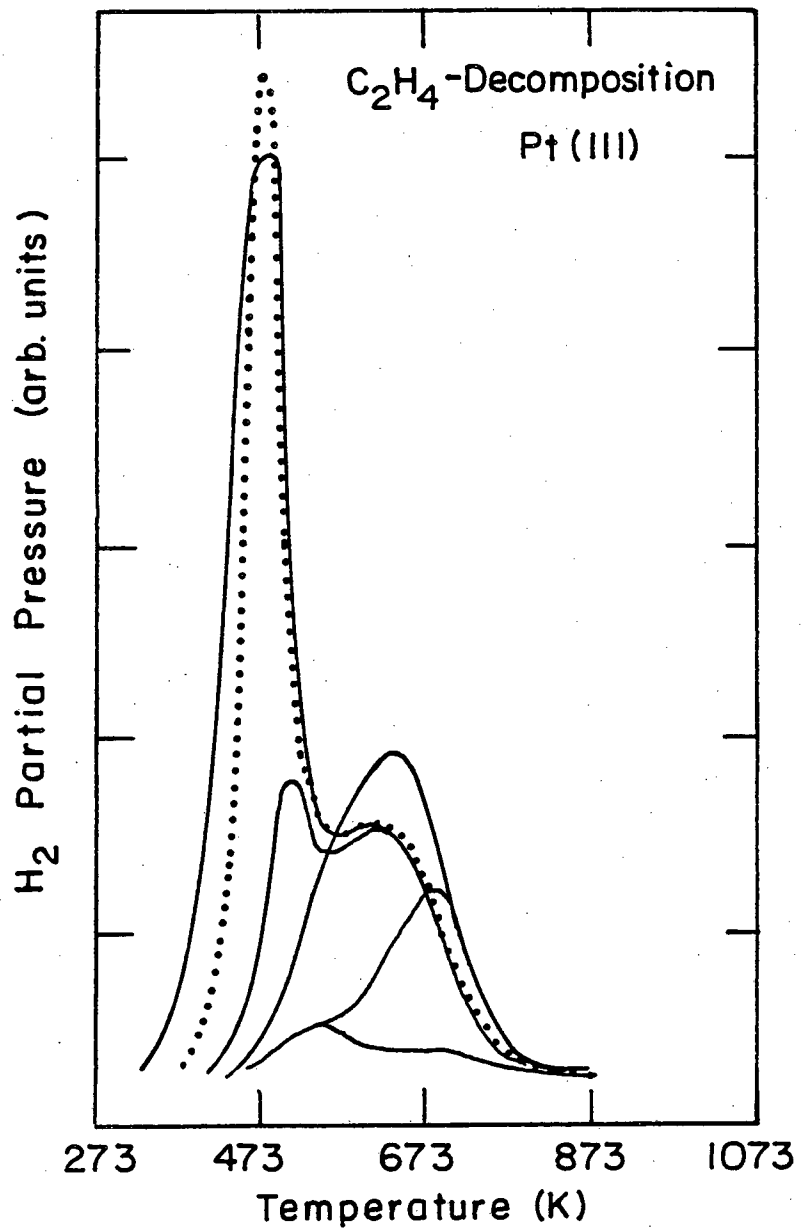
C_2H_4-Decomposition
Pt (111)
H_2 Partial Pressure (arb. units)
273
473
673
873
1073
Temperature (K)
XBL 812-5656

Fig. 4.11

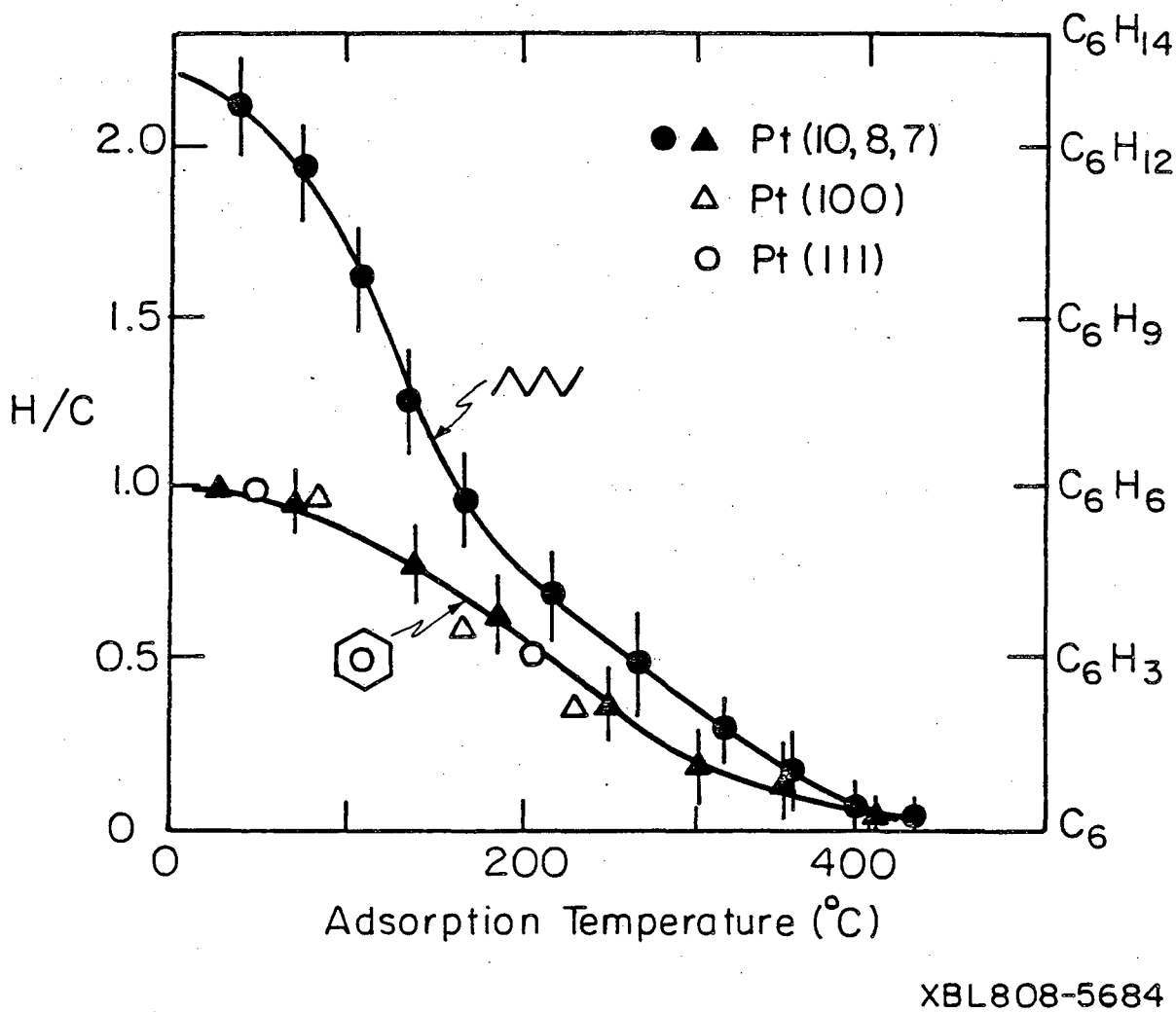
Hydrogen Content of the Adsorbed Layer
H/C
2.0
1.5
1.0
0.5
0
0
200
400
Adsorption Temperature (°C)
Pt (10, 8, 7)
Pt (100)
Pt (111)
C6H14
C6H12
C6H9
C6H6
C6H3
C6
XBL808-5684

Fig. 4.12

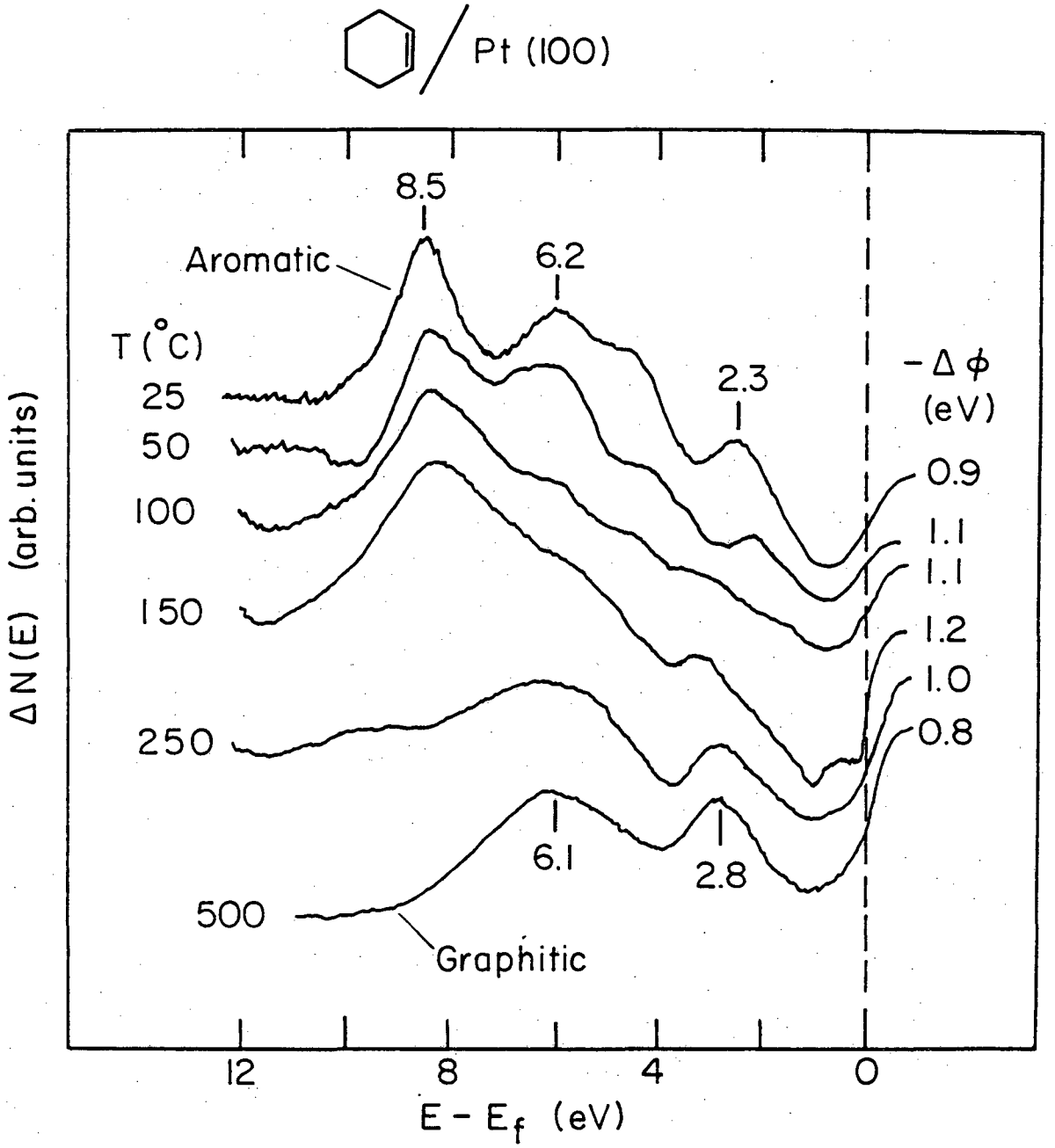
Pt (100)
8.5
Aromatic
6.2
2.3
T (°C)
25
50
100
150
250
500
6.1
2.8
Graphitic
-Δφ (eV)
0.9
1.1
1.1
1.2
1.0
0.8
ΔN(E) (arb. units)
12
8
4
0
E - Ef (eV)
XBL 811-5006

Fig. 4.13

4.4. Thermal Desorption Studies of the Composition Rehydrogenation, and Sequential Dehydrogenation of Hydrocarbon Overlayers Deposited During Reaction Rate Studies at Atmospheric Pressure

4.4.1. Background

Results presented in the preceeding section showed that "hydrogen storage" is always an important property of hydrocarbon species chemisorbed on platinum single crystal surfaces at temperatures between 300 and 680 K. Hydrogen thermal desorption studies provided activation energies for sequential dehydrogenation that varied from about 18 to 40 kcal/mole depending upon the hydrocarbon and adsorption temperature. The same thermal desorption studies provided important information about the temperature dependent composition of the strongly adsorbed species. A similar series of hydrogen thermal desorption studies was carried out following the reaction rate studies that were described in Chapter 3 in order to determine if the composition and dehydrogenation energetics were altered when the adsorbed species were deposited at high reactant pressures. While the dehydrogenation kinetics were not significantly different from those determined at low pressures, it was found that the hydrogen content of the adsorbed species was always much higher following the reaction studies at high reactant pressures. The same strongly adsorbed species that were responsible for catalyst deactivation displayed a surprisingly high capacity for hydrogen storage. These species typically retained 10-20 times more hydrogen than could be adsorbed on initially clean platinum surfaces. The

existence of this strongly bound hydrogen strongly supports the long advocated idea (33,34) that the carbon deposit responsible for catalyst deactivation is a non-graphitic polymeric residue.

4.4.2. Results and Discussion.

Hydrogen thermal desorption spectra recorded after n-hexane reaction studies that were carried out over Pt(111) and Pt(10,8,7) at 573-678 K are shown in Fig. 4.14. Also shown in the average (H/C) stoichiometry of the adsorbed layer as determined from the desorption peak areas and the total surface carbon coverage that was in the range 2-5 carbon atoms per surface platinum atom. To desorb all weakly and reversibly adsorbed species, the samples were cooled to near room temperature in the presence of 600 Torr of hydrogen before opening the isolation cell and recording the spectra in UHV. As such the spectra represent the sequential dehydrogenation and decomposition of the strongly adsorbed species that were deposited by the reaction mixture. This process took place in two or more steps with broad hydrogen desorption peaks centered at 440-460 K and 630-660 K. As discussed in the previous section, the first desorption peak corresponds to β-hydrogen abstraction and related rearrangement processes in aromatic, alkylidene, and alkylidyne surface species. The second desorption peak appears to represent the decomposition of CH fragments (28) and other CH_x groups in which the C-H bonds are not provided easy access to a metal site. The fraction of the total hydrogen which was retained in this chemical state increased with increasing reaction temperature in a manner which was roughly proportional to the total surface carbon

coverage. The area of the first desorption peak displayed little dependence or carbon coverage (reaction temperature).

Very similar hydrogen desorption spectra were obtained following the high pressure reactions of other hydrocarbon molecules including isobutane, n-butane, neopentane, cyclohexene, and n-heptane. Figure 4.15 compares TDS results for several molecules that were obtained following reaction studies catalyzed on the (10,8,7) platinum surface at 573 K (except cyclohexene-Pt(322)-425 K). Figure 4.16 summarizes hydrogen desorption spectra together with (H/C) ratios that were determined following a series of reactions on the (100) platinum surface. The (H/C) ratios and the shapes and positions of the hydrogen desorption peaks were always very similar independent of the platinum surface structure and the nature of the reacting hydrocarbon.

The (H/C) ratios shown in Figs. 4.14 and 4.16 clearly indicate that the carbonaceous deposits always store high concentrations of strongly bound hydrogen. For n-hexane reactions catalyzed over Pt(111) and Pt(10,8,7), the (H/C) ratios decreased slowly with increasing reaction temperature from about 1.6 at 573 K to about 1.0 at 678 K. Following alkane reaction studies on the (100) platinum surface at 573-615 K, the (H/C) ratios were always in the range 1.0-1.6. Under steady state reaction conditions at high hydrogen pressures and temperatures between 573 and 673 K these ratios are undoubtedly reduced, but it is very unlikely that they would approach zero. Under these conditions, the hydrogen which is retained by the carbon deposit can be made available to reacting molecules by means of hydrogen

transfer reactions. The importance of these processes are discussed further in the next section.

Deuterium exchange also occurred readily within these hydrogen containing carbonaceous deposits at both high and low reactant pressures. Deuterium thermal desorption spectra representing deuterium exchange in carbon deposits derived from n-hexane were shown in Fig. 3.52. Similar spectra were obtained following isobutane and neopentane reaction studies in the presence of deuterium. Salmeron has shown that ethylidyne species resulting from ethylene adsorption on Pt(111) at 300-450 K exchange deuterium readily even at D_2 pressures as low as 10^{-7} Torr (3). Vibrational ELS studies revealed that CH species also undergo facile deuterium exchange on (111) rhodium and platinum surfaces (27,28).

The amount of hydrogen which was stored by the carbonaceous deposit usually represented at least ten times more hydrogen than could be chemisorbed on initially clean platinum surfaces. This is shown in Fig. 4.17, which compares hydrogen thermal desorption spectra obtained for the stepped (322) platinum surface following (a) hydrogen chemisorption at ~300 K on the clean surface, (b) cyclohexene chemisorption at 425 K and low reactant pressures, and (c) a cyclohexene reaction study at 425 K, but at a total pressure of 77 Torr. The carbon coverages determined by AES following the low and high pressure cyclohexene reactions were identical with 15 percent (C/Pt ≈ 1.3). The amount of hydrogen stored by the adsorbed layer was clearly increased following the high pressure reactions.

Once desorbed, the strongly bound hydrogen could only be partially reintroduced by heating the carbon covered samples in 200-600 Torr of hydrogen at 423-573 K. As shown in Fig. 4.18 for cyclohexene and neopentane rehydrogenation experiments on the (322) platinum surface, the reintroduced hydrogen displayed a single desorption peak at 430-460 K. Very little if any of the hydrogen could be reintroduced into the higher energy binding states. Thus, the complete dehydrogenation and decomposition of the carbonaceous deposits was largely irreversible. This process was accompanied by major restructuring of the surface carbon which resulted in the formation of graphitic carbon islands and perhaps also amorphous carbon deposits. Poor quality "(9 x 9)-ring" diffraction patterns indicative of rotational disordered graphite were detected following experiments on the (322) platinum surface and several of the low pressure reaction studies discussed in Section 5.3. While LEED studies were not carried out for the other platinum surfaces, it appears likely from studies by Blakely (35) and Smith (36) that graphitic carbon was the dominant product of the overlayer decomposition reactions. This graphitic carbon displayed different hydrogen storage properties as compared to the carbonaceous overlayers that were deposited by the reaction mixtures. The single hydrogen desorption peak at about 450 K most probably arises from hydrogen which is incorporated into the peripheral edges (and/or defect sites) of the graphitic islands, i.e.,

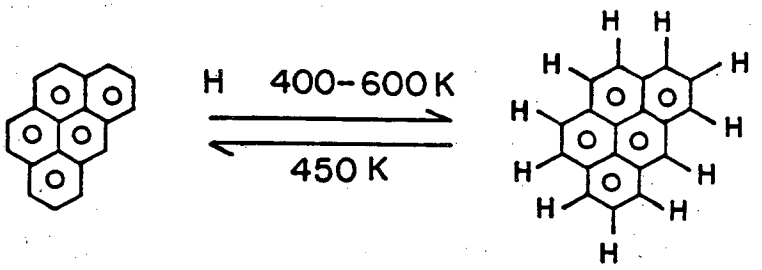

This desorption temperature was the same as that determined for the initial stages of benzene dehydrogenation (Section 4.3).

Regardless of the exact structure of the fully dehydrogenated carbon deposit, it appears clear that this was not the surface species responsible for the catalyst deactivation that was always observed during the high pressure reaction studies. The apparent hydrogen content of this deactivating residue was too high, (H/C) > 1. Polynuclear aromatics and related graphite precursors have hydrogen contents less than one hydrogen atom per surface carbon atom. Possible models for the structure of the deactivating residue are discussed further in Sections 4.7 and 4.8.

Finally, it should be noted that complete dehydrogenation of the carbonaceous deposit was accompanied by a small but distinct and irreversible change in line shape for the C_{273} Auger transition. This is shown in Fig. 4.19, where Auger spectra are compared before and after flashing the (111) sample to 770 K following an n-hexane reaction study at 623 K. While no chemical shift was detectable, the carbon Auger peak became appreciably sharper following dehydrogenation at high temperatures, and a distinct shoulder became apparent at

254–255 eV. After correcting for overlap with the Pt_{252} Auger peak, the latter lineshape appears to correlate closely with that for graphitic carbon deposited on nickel (37).

FIGURE CAPTIONS

Fig. 4.14. Hydrogen thermal desorption spectra (lower frame) recorded after n-hexane reaction studies that were carried out at 573-678 K over the flat (111) and kinked (10,8,7) platinum single crystal surfaces. The average hydrogen content of the carbonaceous deposits as determined from the total desorption peak areas is also shown as a function reaction temperature (upper frame) (β = 69-88 K/sec).

Fig. 4.15. Hydrogen thermal desorption spectra recorded after alkane reaction studies that were catalyzed over Pt(10,8,7) at 573 K (except cyclohexene, Pt(322), 425 K) (β = 69 K/sec).

Fig. 4.16. Hydrogen thermal desorption spectra recorded following a series of alkane reaction studies on the (100) platinum surface at 573 K (n-hexane, neopentane) and 615 K (isobutane, n-butane). The average hydrogen content of the carbonaceous overlayers is also shown.

Fig. 4.17. Comparison between hydrogen thermal desorption spectra for the clean Pt(322) platinum surface and Pt(322) following cyclohexene chemisorption at low (10^{-7} Torr) and high (7 Torr) reactant pressures.

Fig. 4.18. Hydrogen thermal desorption spectra recorded following cyclohexene (upper frame) and neopentane (lower frame) reaction studies on the (322) platinum surface. The solid TDS curves were obtained directly after the reactions. The dashed TDS curves were obtained after rehydrogenation experiments in which the carbon covered samples were heated in 200 Torr hydrogen at 420-560 K.

Fig. 4.19. Auger spectra for carbon deposits chemisorbed on platinum showing the change in lineshape for the 273 eV carbon Auger peak which accompanies complete dehydrogenation.

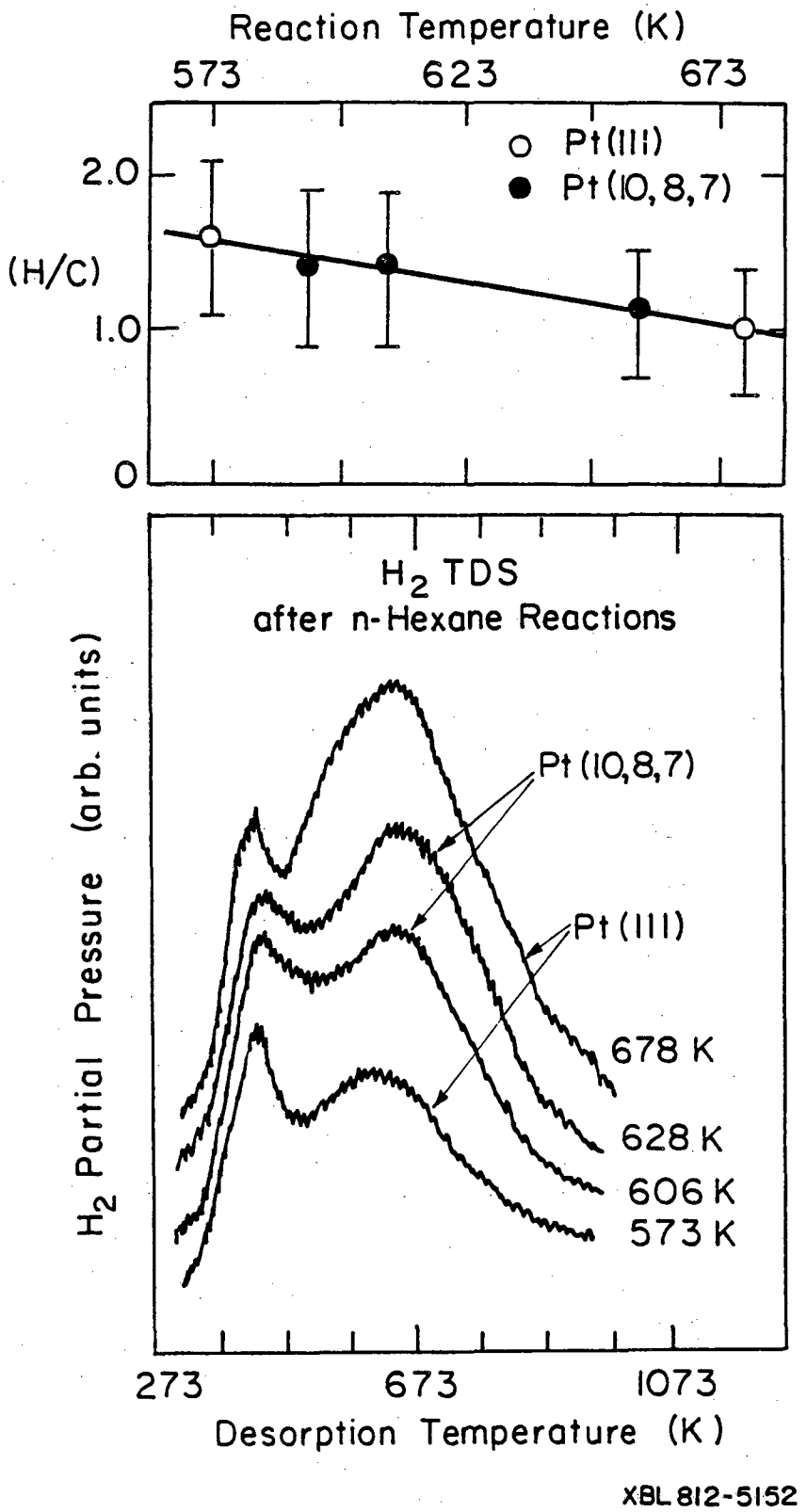
Reaction Temperature (K)
573
623
673
2.0
1.0
0
(H/C)
Pt(111)
Pt(10,8,7)
H2 TDS
after n-Hexane Reactions
H2 Partial Pressure (arb. units)
Pt(10,8,7)
Pt(111)
678 K
628 K
606 K
573 K
273
673
1073
Desorption Temperature (K)
XBL 812-5152

Fig. 4.14

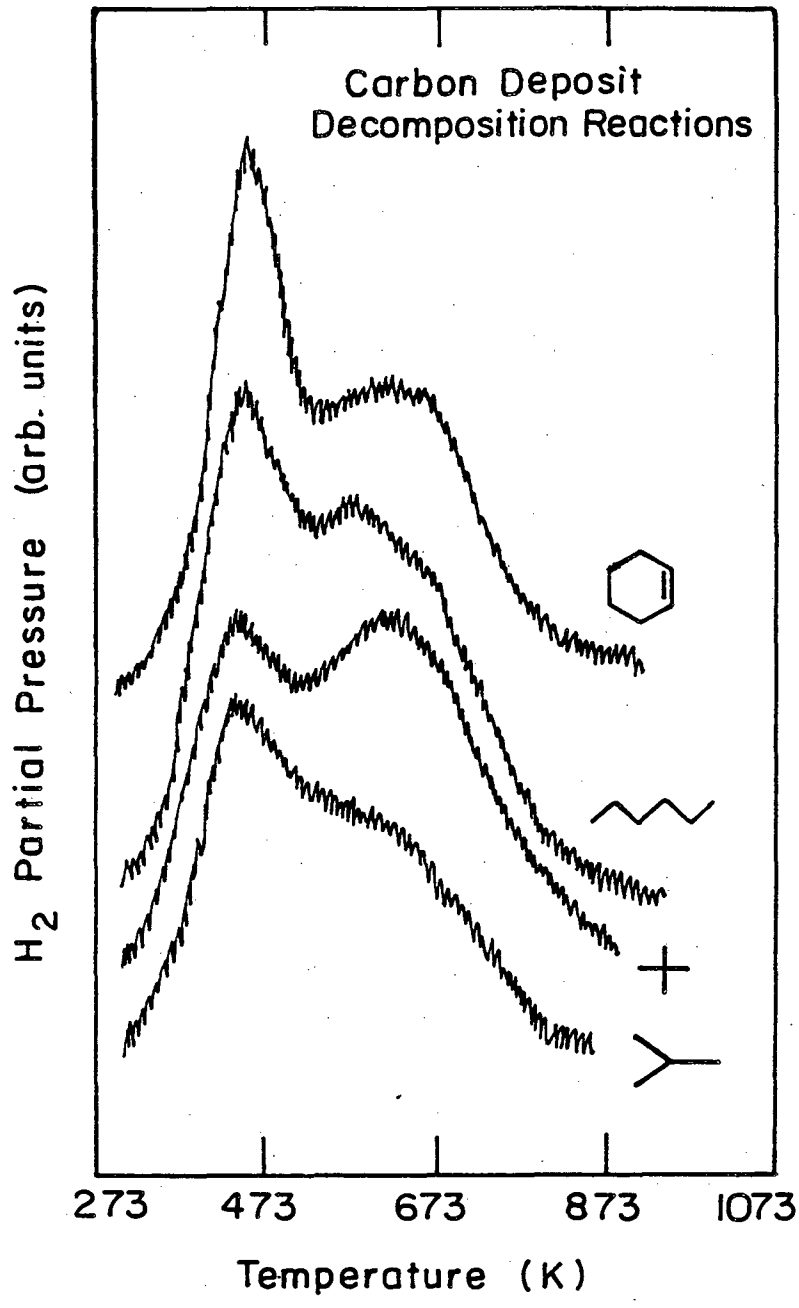
Carbon Deposit
Decomposition Reactions
H2 Partial Pressure (arb. units)
273
473
673
873
1073
Temperature (K)
XBL 812-5153

Fig. 4.15

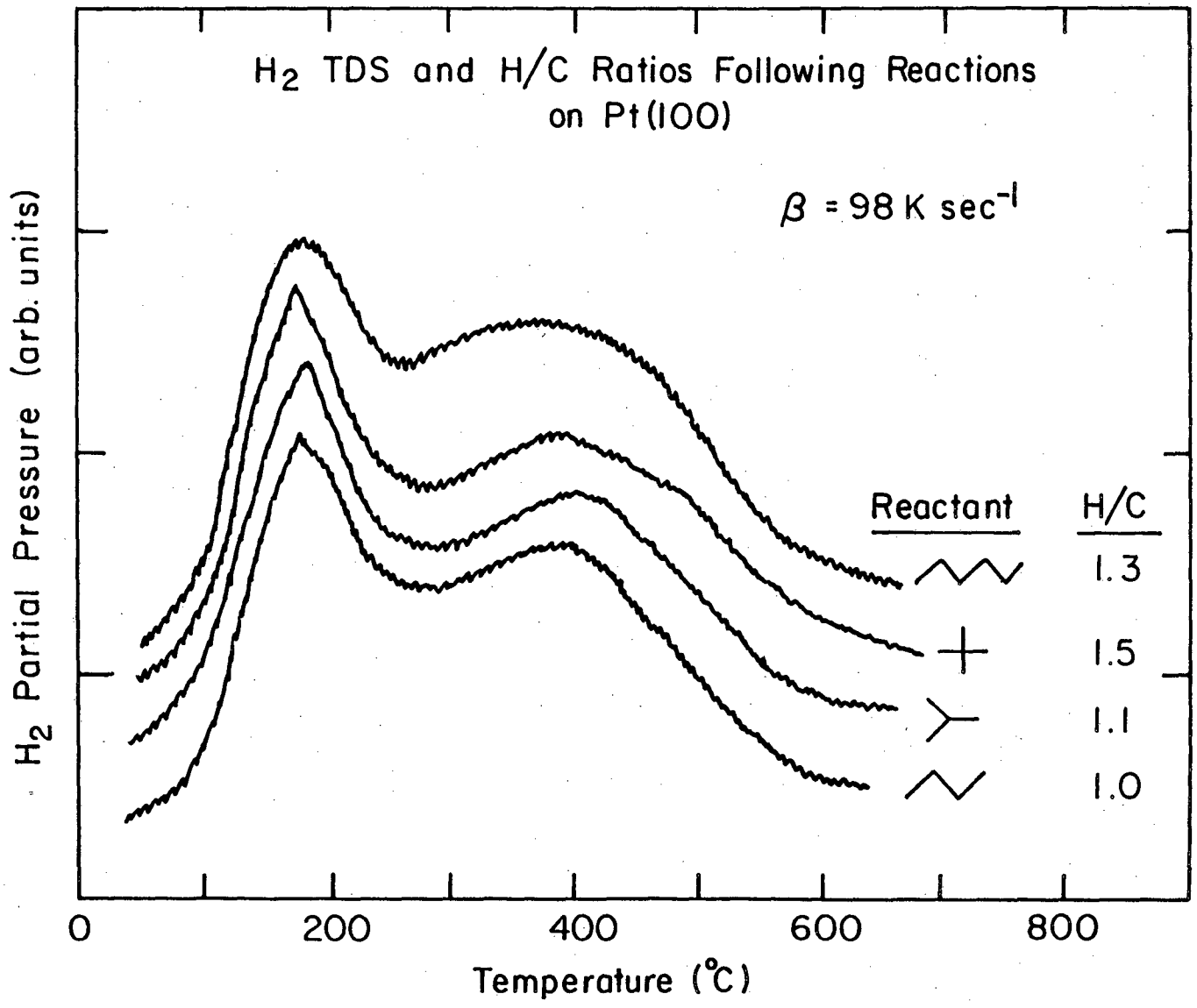

XBL817-6104

Fig. 4.16

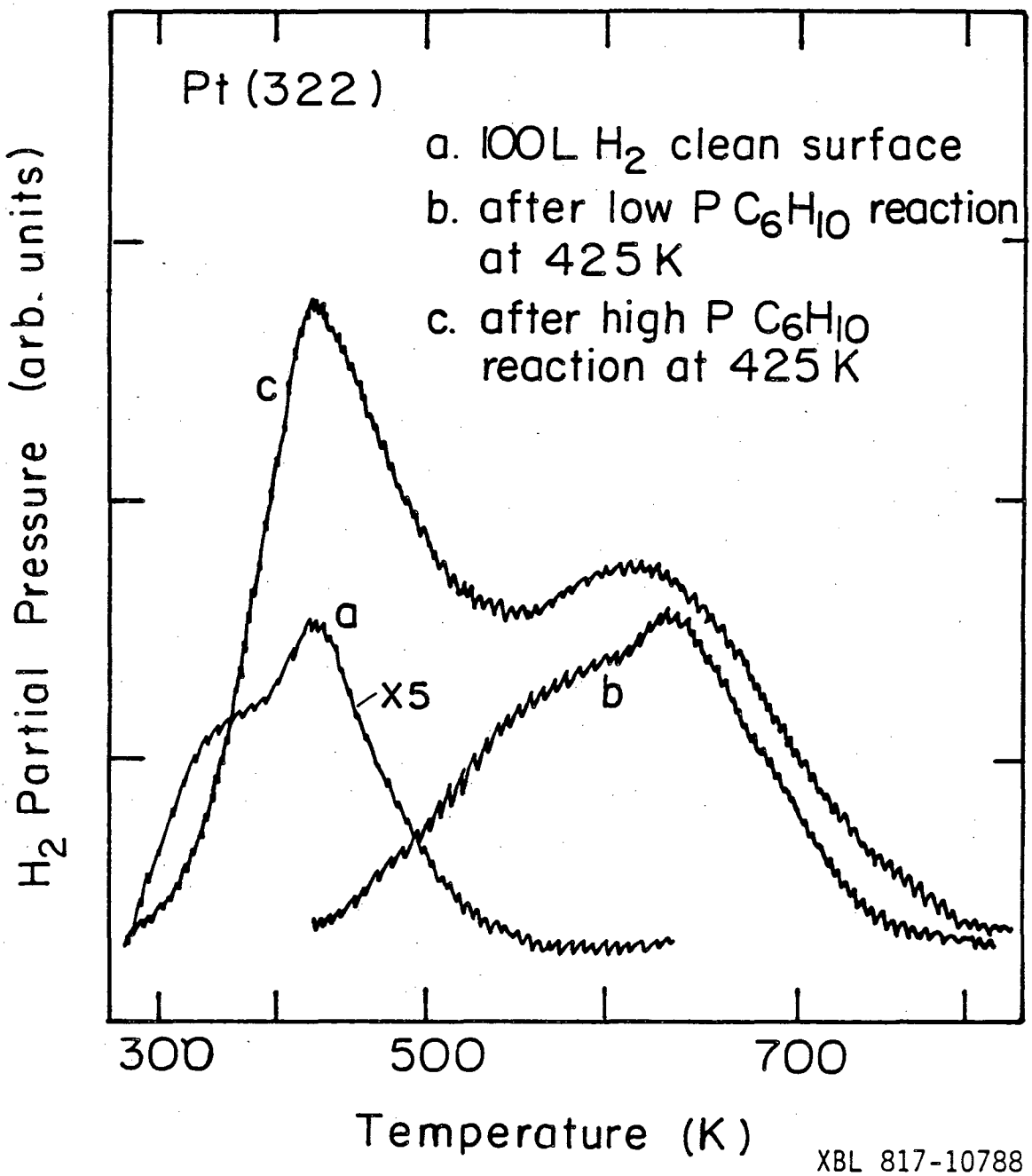
Pt (322)
a. 100L H_2 clean surface
b. after low P C_6H_{10} reaction at 425 K
c. after high P C_6H_{10} reaction at 425 K
c
a
X5
b
H_2 Partial Pressure (arb. units)
300
500
700
Temperature (K)
XBL 817-10788

Fig. 4.17

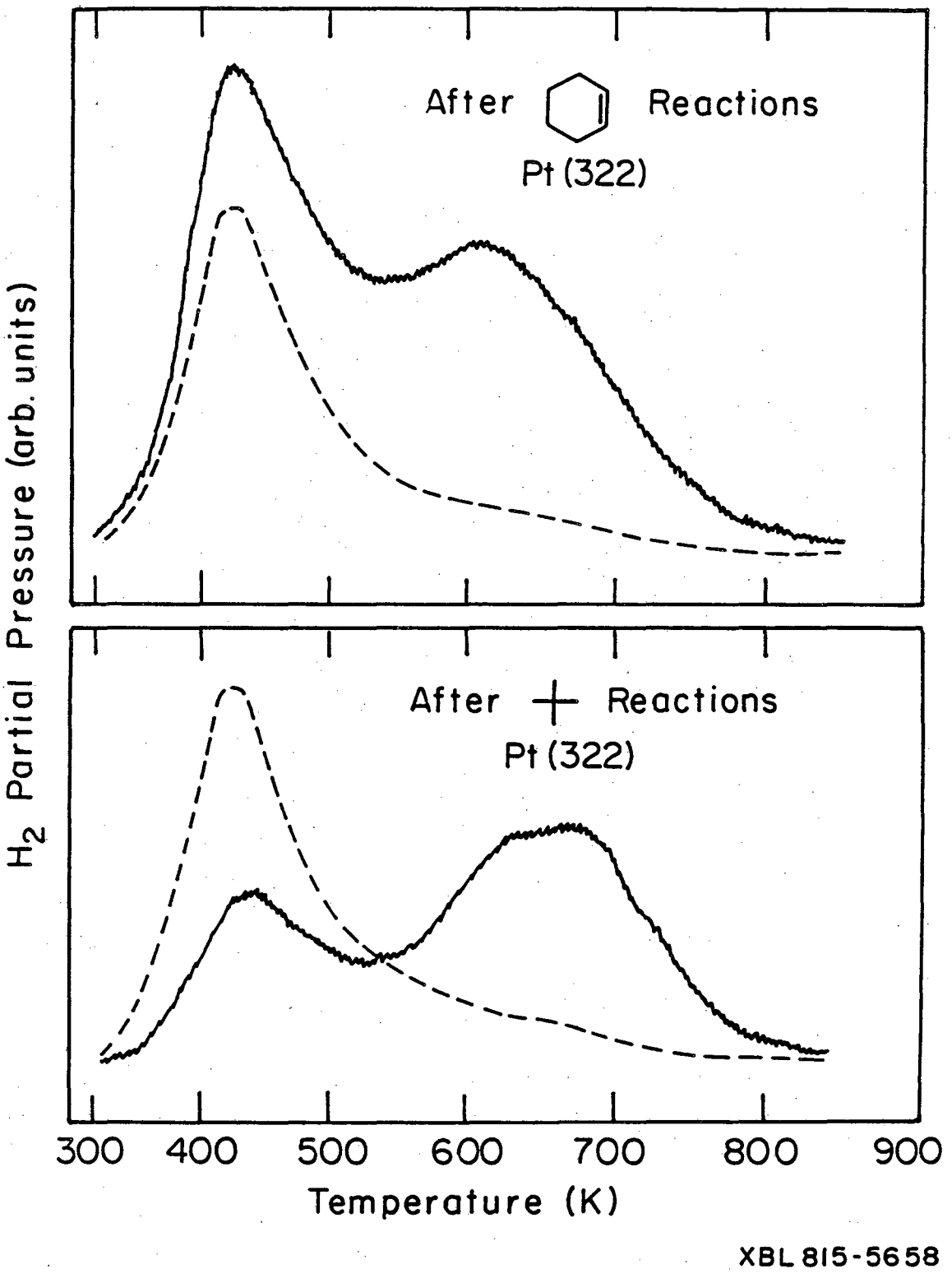
After Reactions
Pt (322)
After + Reactions
Pt (322)
H2 Partial Pressure (arb. units)
300
400
500
600
700
800
900
Temperature (K)
XBL 815-5658

Fig. 4.18

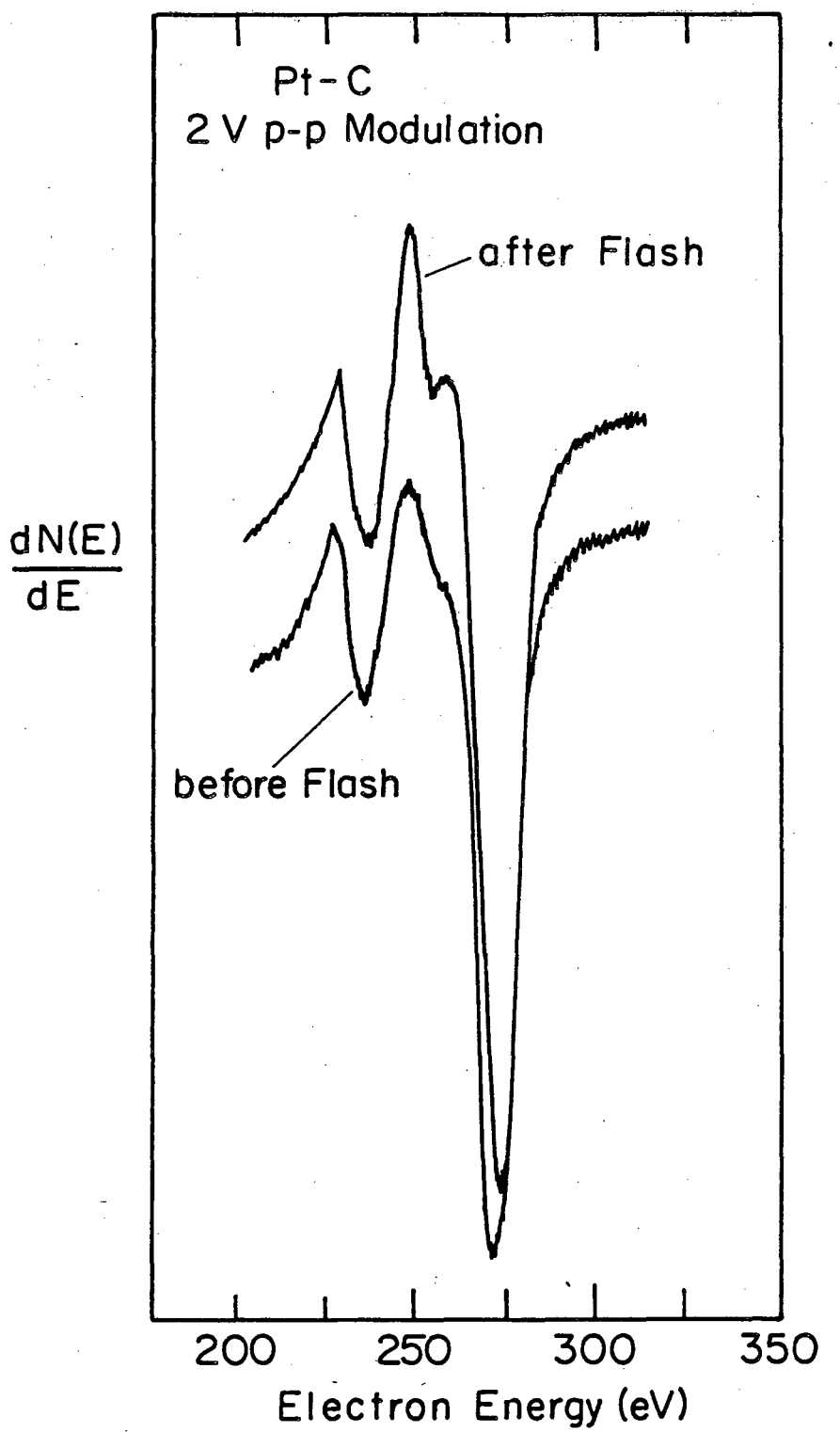
Pt-C
2 V p-p Modulation
after Flash
before Flash
dN(E)
dE
200
250
300
350
Electron Energy (eV)
XBL 815-5655

Fig. 4.19

4.5. Radiotracer Studies of ^{14}C-Ethylene and ^{14}C-Benzene Chemisorption, Rehydrogenation, and Hydrogen Transfer Reactions on Pt(111) and Pt(100)

4.5.1. Background

Radiotracer methods are among the most sensitive techniques for measuring very low concentrations of materials in a transient environment. They are of particular value when studying the residence time of an adsorbed monolayer in the presence of the same molecule in the gas phase as occurs in heterogeneous catalysis. Static radiotracer measurements yield the absolute adsorbate surface coverage on the catalyst, and dynamic experiments can also be carried out easily to determine the kinetics of important surface phenomena such as isothermal desorption, bulk dissolution, surface diffusion, and exchange or rehydrogenation reactions of these adsorbed species.

A distinction between the kinetics of intermolecular hydrogen transfer and direct rehydrogenation reaction steps is required to evaluate the nature of the participation of strongly bound carbonaceous species in hydrocarbon catalysis over platinum. Since the adsorbed species that form in these reactions are hydrocarbon fragments that may be derived from readily available compounds labelled with carbon-14, radiotracers can provide a direct method for determining the reaction pathway.

While the ^{14}C-radiotracer technique has been used by several groups to investigate the interactions of hydrocarbons with evaporated films and supported metal catalysts (38–41), the radiotracer technique has found only limited application in adsorption studies that are

carried out in ultra high vacuum using well defined surfaces. In studies of ^{14}CO chemisorption on nickel, Klier and his co-workers (42,43) described a thin window Geiger-Müller (GM) counter that could be used in vacuum systems at 10^{-10} Torr with a sensitivity sufficient to detect 10^{12} adsorbed molecules. A major difficulty in these studies was in mounting the detector in order to prevent the thin mica window from rupturing. In Section 2.3, an alternative method was described to detect ^{14}C-radiotracers which is simple, sensitive, rugged, and more versatile than the GM counter and is suitable for general surface studies. This section is devoted to a discussion of the results obtained when this technique was used to investigate the rehydrogenation and hydrogen transfer reactions of ^{14}C-ethylene and ^{14}C-benzene chemisorbed on the flat (111) and (100) platinum single crystal surfaces. Both molecules displayed increasing surface coverages, decreasing hydrogen content (Section 4.3), and decreasing reactivity with increasing adsorption temperature in the range 320-625 K. Reactivity studies carried out near atmospheric pressure revealed two distinct types of carbonaceous species on the platinum surfaces:

(1) an active form consisting of partially dehydrogenated hydrocarbon molecules (fragments) which readily undergo hydrogenation and hydrogen transfer reactions under mild conditions, and

(2) an inactive form that displays little reactivity over the entire range of temperature (320-675 K) and pressure (10^{-10} - 1 atm) investigated.

Removal of the active ^{14}C-carbonaceous species by hydrogen transfer reactions with unlabelled hydrocarbons, i.e.,

$$^{14}C_mH_x(ads) + {}^{12}C_nH_y(gas) \rightarrow {}^{14}C_mH_{x+z}(gas) + {}^{12}C_nH_{y-z}(ads) \qquad (1)$$

displayed reaction rates that were within about an order of magnitude to those measured for direct hydrogenation using gas phase hydrogen, viz.,

$$^{14}C_mH_x(ads) + \frac{z}{2} H_2 \rightarrow {}^{14}C_mH_{x+z}(gas) \qquad (2)$$

The proportion of the total surface carbon which existed in the active form decreased with increasing adsorption temperature.

4.5.2. Results and Discussion

^{14}C-Benzene Chemisorption on Pt(111) and Pt(100). Absolute surface concentrations determined from the rate of beta emission following the chemisorption of ^{14}C-benzene on Pt(111) are shown as a function of temperature and exposure in Fig. 4.20 (1 Langmuir = 10^{-6} Torr sec uncorrected for ion gauge sensitivity). The error bars represent estimated uncertainties for the measurements that are based on the accuracy of the detector efficiency calibration (±10 percent) and the specific radioactivity of the ^{14}C-benzene (16 ± 1 mc/mmole). Counting times ranged from 10 to 40 min and count rates for adsorbed species and background varied between 15–180 and 2–6 cpm, respectively. The level of background activity increased gradually during a series

of experiments but always decreased to a low value of 2-3 cpm after outgassing overnight.

The surface concentration by adsorbed species increased with increasing temperature and exposure. Complementary UPS (Section 4.4), TDS (section 4.3), LEED, and radiotracer studies revealed that irreversible, dissociative chemisorption occurred over most of this temperature range. No more than 5 percent of the adsorbed species could be desorbed in the molecular form following ^{14}C-benzene chemisorption at 298-330 K, and the adsorption was even less reversible at higher adsorption temperatures. Thermal desorption studies (Section 4.3) indicated that sequential dehydrogenation and decomposition occurred over the temperature range 420-680 K. Benzene chemisorbed on Pt(111) at 320-340 K displayed the $\begin{vmatrix} 4 & -2 \\ 0 & 5 \end{vmatrix}$ diffraction pattern shown in Fig. 4.21. As discussed by Stair (44), the pattern of triplet diffraction beams arises from 3 independent domains of the $\begin{vmatrix} 4 & -2 \\ 0 & 5 \end{vmatrix}$ overlayer structure. The rectangular unit mesh measures 10.8 by 13.2Å, and one benzene molecule per unit cell corresponds to a surface concentration of 7.5×10^{13} Bz/cm^2. This concentration corresponds closely with that determined directly from the radiotracer analysis ($8 \pm 1 \times 10^{13}$ Bz/cm^2). The maximum surface coverage achieved after ^{14}C-benzene chemisorption at 623 K corresponds to 2.0 carbon atoms per surface platinum atom. While no ordering could be detected at temperatures between 340 and 620 K it is notable that this maximum coverage approaches that expected for a close packed graphitic overlayer with C/Pt = 2.57.

The chemisorption of ^{14}C-benzene on evaporated platinum films was investigated by Tetenyi and Babernics (38). Figure 4.22 compares the adsorption behavior for the small area Pt(111) single crystal catalyst with that reported for the high area practical catalyst. In all cases the surface coverages measured for benzene on Pt(111) were much higher than those determined for benzene chemisorption on the platinum films. Since the films were not prepared in UHV, it is likely that surface impurities were present which would strongly suppress the chemisorption of benzene.

The adsorption behavior of ^{14}C-C_6H_6 on Pt(100) was very similar to that for ^{14}C-benzene on Pt(111). Surface coverages by adsorbed species increased with increasing temperature and exposure. The decomposition of benzene chemisorbed on Pt(100) was discussed in Section 4.3. LEED studies could not be carried out for this adsorption system.

^{14}C-Ethylene Chemisorption on Pt(111). Adsorption isotherms determined by radiotracer analysis for ^{14}C-ethylene chemisorption on Pt(111) at 333-573 K are shown in Fig. 4.23. For adsorption temperatures below 423 K the initial sticking coefficient S_0 and saturation coverage $c_s = 4 \times 10^{14} \pm 25$ percent molec/cm^2 were constant. At higher adsorption temperatures a slow adsorption process was apparent which continued for exposures $\gtrsim$20 L. The slow adsorption process was accompanied by extensive dehydrogenation and rearrangement of the adsorbed species (Section 4.3).

Ethylene adsorption on Pt(111) at 300–430 K leads to the formation of surface ethylidyne species which display a (2 x 2) overlayer structure (26,27). The atomic structure of this surface species as determined by dynamical LEED intensity analysis (26), high resolution ELS (27,28), and TDS (3,28) is shown in Fig. 4.24. The surface species occupies a 3-fold adsorption site with the c–c internuclear axis directed normal to the platinum surface with a c–c bond distance of 1.5Å. The α-carbon atom is bonded equivalently to 3-platinum atoms with a Pt–C bond length of 2.0Å. This exceedingly short platinum–carbon bond is indicative of metal-carbyne (M ≡ CR), carbene (M = CR_2), and vinylidene (M = C = CR_2) species that appear to display unique chemical activity in many types of skeletal rearrangement reactions. The saturation coverages and (H/C) ratios determined in this work over the temperature range 330–430 K are in excellent agreement with those predicted for the formation of the ethylidyne species in the expected (2 x 2) surface structure, i.e., (H/C) = 1.5, $C_s = 3.8 \times 10^{14}$ molec/cm^2. The radiotracer studies (Fig. 4.23) also show that this surface species forms according to first-order Langmuir adsorption kinetics

$$\frac{d\theta}{d\varepsilon} = \frac{S_o}{C_s(2\pi mkT)^{1/2}} (1 - \theta) \qquad (1)$$

where ε = Pt was the gas exposure, and S_o (the initial sticking coefficient) was constant at 0.9 ± 0.2 over the temperature range 330–420 K.

Rehydrogenation and Hydrogen Transfer Reactions of ^{14}C-Ethylene Chemisorbed on Pt(111). Time dependent studies of hydrocarbon residence times, rehydrogenation kinetics, and hydrogen transfer kinetics is a unique and important application for this radiotracer technique. Radiotracer decay curves representing the rehydrogenation of ethylidyne species chemisorbed on the (111) platinum surface are shown in Fig. 4.25. The ethylidyne species were prepared by chemisorbing ^{14}C-ethylene at 335-345 K and 10^{-7} Torr. The rehydrogenation reactions were carried out at 300-470 K in the presence of 1 atm of flowing hydrogen. The reactions were interrupted at intervals of 1-10 min so that the residual coverage $(\theta(t)/\theta(t = 0) = \theta/\theta_0 = cpm/cpm_0)$ by radioactive surface species could be determined as a function of the total reaction time. Two points are significant: (1) the ethylidyne species became highly reactive only at temperatures higher than about 340 K, and (2) the rehydrogenation reaction was not a simple first-order (or 2nd order) process. At 300 K only about 25 percent of the surface species were removed by rehydrogenation in 30 min reaction time. By contrast, at 370 K or higher temperatures, the same surface species underwent essentially complete rehydrogenation in just 2-5 min. From the initial slopes of the decay curves the activation energy for ethylidyne hydrogenation can be very roughly estimated as 5-10 kcal/mole. It is clear that ethylidyne species and related reaction intermediates with the alkylidyne surface structure (26) should be exceedingly reactive under typical alkane reaction conditions near 573 K.

Two possible explanations for the curvature displayed in the decay plots are the existence of multiple adsorption states and/or the deposition of background gases during the rehydrogenation experiments. Blank reactions carried out at 370-570 K revealed that low levels of background carbon contamination were gradually deposited during the rehydrogenation experiments (0.3-0.6 carbon atoms per platinum atom). This carbon could suppress the dissociative chemisorption of hydrogen molecules at longer reaction times and thereby decrease the rates of carbon-14 rehydrogenation.

A similar series of rehydrogenation reactions was carried out following the chemisorption of ^{14}C-ethylene on Pt(111) at 473 and 600 K. As discussed below, ethylene adsorption at these temperatures produced surface species with average composition "C_2H" (473 K) and "C" (600 K). Results of these reaction studies are shown in Fig. 4.26. Rehydrogenation of these more strongly adsorbed species at 370-640 K proceeded in at least two distinct stages. A very rapid initial stage ($R_h > 10^{-2}$ molec/Pt atom sec) which was complete within about 2 min was always followed by a very slow rehydrogenation reaction ($R_h \lesssim 10^{-5}$ molec/Pt atom sec) which continued for hours without reaching completion. The rapid initial reaction represents the hydrogenation of small C_1, C_2, CH, and C_2H fragments which appear to be present following ethylene chemisorption at 470-650 K (3,28). The very slow later stages of reaction appear to represent the gasification of graphitic-like surface species with very low hydrogen content. Similar catalytic behavior characterized by a two stage rehydrogenation

reaction was reported by Krebs and Bonzel (45) for the hydrogenation of surface carbon deposited on iron foils at 560 K.

These results show that for temperatures higher than about 470 K, ethylene chemisorption on Pt(111) is always partially irreversible. The proportion of the total surface carbon which existed in the inactive form increased with increasing adsorption temperature. In Fig. 4.27 the irreversibly adsorbed fraction is shown as a function of temperature along with the (H/C) stoichiometry of the adsorbed layer as determined from thermal desorption studies (Section 4.3). Irreversibly adsorbed fraction is defined as the proportion of preadsorbed ^{14}C-ethylene which could not be removed by rehydrogenation (40–80 min reaction time) at the same temperature at which the initial adsorption was carried out. The (H/C) ratio displayed a striking correlation with the adsorption reversibility. Sequential dehydrogenation of ethylidyne to "C_2H" like species at 450–470 K was accompanied by a marked decrease in reversibility from 95–100 percent to about 50–70 percent. The reversibility approached zero as the hydrogen content decreased further at higher adsorption temperatures.

The fact that the amount of inactive carbon deposited at 473 K was highly dependent upon the temperature of subsequent rehydrogenation reactions suggests strongly that the polymerization process responsible for the formation of the inactive carbon involves two independent pathways. Initial polymerization responsible for the overall shape of Fig. 4.27 appears to occur during adsorption. Further polymerization, which competes with direct hydrogenation, appears to occur during the

initial stages of the rehydrogenation reactions. Provided that the activation energy for polymerization is smaller than that for hydrogenation, the irreverisbly adsorbed fraction should decrease with increasing reaction temperature as observed experimentally.

The formation of inactive metal-organic surface species derived from ^{14}C-ethylene on alumina supported Ni (39), Pd (39), Rh (39,46), Ir (40) and Pt (39) catalysts was investigated by Thomson and Webb and co-workers. Inactive carbonaceous species were detected under all conditions of direct hydrogenation and hydrogen transfer with unlabelled ethylene and acetylene at 290-470 K. At 290 K, the irreversibly adsorbed fraction decreased in the sequence Pd (63 percent) > Ni (20 percent) > Ir (6-13 percent) > Pt (4-7 percent). The inactive fraction retained by the platinum catalyst increased to 40-60 percent at 470 K. These results appear to be in excellent agreement with those reported here for the small area (111) platinum single crystal surface.

The strongly adsorbed "C_2H" fragments resulting from ^{14}C-ethylene chemisorption on Pt(111) at 470 K could also be partially removed from the surface by intermolecular hydrogen transfer reactions with unlabelled hydrocarbons. Radiotracer decay curves illustrating hydrogen transfer between "C_2H" and n-hexane and cyclohexene at 523-573 K are shown in Fig. 4.28. A surprising feature of the hydrogen transfer reactions is the ease with which they occurred. Initial removal of the active ^{14}C-containing species by hydrogen transfer with 20 Torr of n-hexane or cyclohexene displayed initial reaction

rates (10^{-2} - 10^{-3} molec/Pt atom sec) that appeared to be within about an order of magnitude to those determined for direct hydrogenation in 1 atm of hydrogen. Hexenes and benzene were detected as byproducts of the hydrogen transfer reactions. Cyclohexene (a good hydrogen donor) underwent hydrogen transfer with "C_2H" more rapidly than n-hexane (a poor hydrogen donor). In the absence of hydrogen, the hydrogen transfer reactions were accompanied by the deposition of carbonaceous multilayers on the platinum surface (C_{273}/Pt_{237} = 5-8) that could be detected by AES.

Rehydrogenation and Hydrogen Transfer Reactions of ^{14}C-Benzene Chemisorbed on Pt(100) and Pt(111). Radiotracer decay curves representing the rehydrogenation and hydrogen transfer reactions of ^{14}C-benzene chemisorbed on Pt(100) and Pt(111) are shown in Figs. 4.29 to 4.31. The adsorbed species derived from ^{14}C-C_6H_6 chemisorption at 333 and 573 K displayed similar reactivities on both platinum surfaces, and these reactivities were much like those just described for ^{14}C-C_2H_4 chemisorbed on Pt(111). The weakly adsorbed species resulting from benzene chemisorption at 333 K underwent complete hydrogenation under mild conditions (T = 300-360 K, P_{H_2} = 1 atm) in a period of 10-25 min. By contrast, the more strongly adsorbed surface species produced by benzene chemisorption at 573 K could only be partially removed by 2 hr rehydrogenation even at temperatures as high as 673 K. In this case a rapid initial rehydrogenation process appeared to be followed by a very slow gasification reaction. The fraction of the total surface carbon which existed in the inactive

form increased with increasing adsorption temperature and decreasing reaction temperature. The strongly adsorbed species displayed significant reactivity in hydrogen transfer reactions with unlabelled benzene and n-hexane.

Significance of Hydrogen Transfer Reactions. The radiotracer studies clearly demonstrate that hydrogen transfer reactions take place between hydrocarbon species chemisorbed on the (111) platinum single crystal surface. These hydrogen transfer reactions displayed apparent reaction rates at 520-570 K which were typically 3-20 times slower than direct hydrogenation using gas phase hydrogen. Studies of cyclohexene hydrogenation and disproportionation catalyzed at 425 K over Pt(322) revealed that direct hydrogenation was ten times faster than hydrogen transfer (Section 3.3). Because the activation energy for disproportionation (~16 kcal/mole) was larger than that for direct hydrogenation (5-6 kcal/mole), the importance of the hydrogen transfer pathway is expected to increase with increasing reaction temperature. Overall, our results clearly suggest that many important types of hydrocarbon conversion reactions may be influenced by hydrogen transfer reactions between the adsorbed species that always cover the platinum surface. Under normal steady state reaction conditions at 540-700 K only a small concentration (1-20 percent) of uncovered platinum surface sites exists for dissociative chemisorption of hydrogen molecules. Under these conditions hydrogen transfer may become favored over direct hydrogenation since the latter process is strongly suppressed in the absence of uncovered platinum surface sites (Section 3.4).

The notion that hydrogen transfer reactions are important in reforming catalysis is not entirely new. Thomson and Webb (47) have argued that a generalized hydrogen transfer mechanism provides a "universal" explanation for the patterns of catalytic activity displayed by metal catalysts in olefin hydrogenation reactions. Gardner and Hansen (48) reached a similar conclusion in connection with studies of ethylene hydrogenation over tungsten catalysts. Unfortunately, the crucial experiments required to distinguish the kinetics of hydrogenation and hydrogen transfer were not reported in these studies. Our results certainly tend to confirm that hydrogen transfer reactions could be important, especially at higher reaction temperatures. Unfortunately, insufficient information now exists to determine exactly how important these processes may be.

Several reaction pathways for hydrogen transfer now have precedent in organometallic chemistry (49,50), and existing information indicates that the same pathways should be important in reactions on metal surfaces (51). A common feature of these pathways is the transient existence of metal-hydride intermediate. For hydrogen transfer on a metal surface these pathways can be represented by the reactions

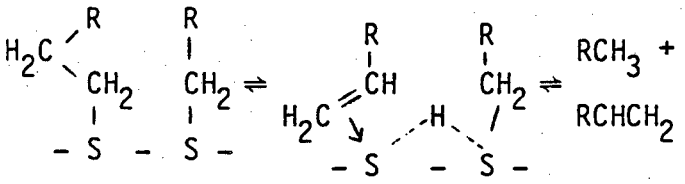

(3)

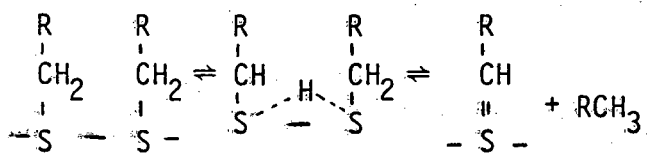

(4)

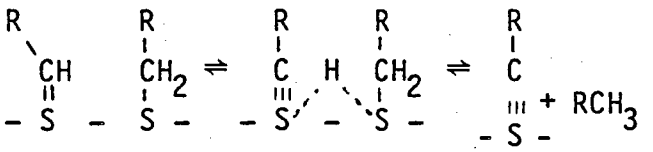

(5)

where S is a surface site composed of one or more platinum atoms. The first reaction encompases β-hydrogen abstraction and subsequent hydrogen transfer to produce an olefin and alkane. This pathway is consistent with the olefin production detected during hydrogen transfer on the (111) platinum surface. Coordination compounds of the type PtL_2R_2 where L = PEt_3 and R = ethyl (Et), cyclopropyl, cyclobutyl, and cyclopentyl undergo thermal decomposition by this pathway (49). The latter reactions involve α-hydrogen abstraction and alkane reductive elimination as observed for the rearrangement of $Ta(CH_2CMe_3)_2Cl_3$ and $TaCp(CH_2CMe_3)_2Br_2$ (50).

FIGURE CAPTIONS

Fig. 4.20. Adsorption "isobars" for ^{14}C-benzene chemisorption on Pt(111) at 315–620 K.

Fig. 4.21. LEED pattern and real space surface unit mesh for the $\begin{vmatrix} 4 & -2 \\ 0 & 5 \end{vmatrix}$ surface structure that is displayed by benzene chemisorbed on Pt(111) at 325 K. The diffraction pattern has been taken from Ref. 44; the same pattern but of poorer quality was observed in this research.

Fig. 4.22. Comparison between ^{14}C-benzene chemisorption on Pt(111) and Pt-films as reported by Tétényi and Babernics (38).

Fig. 4.23. Adsorption isotherms (left frame) for $^{14}C_2H_4$ chemisorbed on Pt(111) at 330–570 K. The adsorption behavior at 330–420 K is well described by a first-order Langmuir model (right frame).

Fig. 4.24. Atomic surface structure for ethylidyne species chemisorbed on Pt(111) (26).

Fig. 4.25. Radiotracer decay curves illustrating the rehydrogenation of ^{14}C-ethylidyne species chemisorbed on Pt(111).

Fig. 4.26. Radiotracer decay curves illustrating the partial rehydrogenation of ethylene decomposition products with average composition "C_2H" (left frame) and "C" (right frame). These species were prepared by chemisorbing ethylene on Pt(111) at 473 and 600 K.

Fig. 4.27. Composition and reactivity of ^{14}C-ethylene chemisorbed on Pt(111) at temperatures between 320 and 670 K; the irreversibly adsorbed fraction determined by radiotracer analysis displays an excellent correlation with the average hydrogen content (H/C), of the strongly adsorbed species.

Fig. 4.28. Radiotracer decay curves illustrating hydrogen transfer reactions between n-hexane (left frame) or cyclohexene (right frame) and "C_2H" surface species that were produced from ^{14}C-ethylene chemisorption on Pt(111) at 470 K.

Fig. 4.29. Radiotracer decay curves illustrating the rehydrogenation of ^{14}C-benzene chemisorbed on Pt(111). In the left frame ^{14}C-C_6H_6 was adsorbed at 333 K, and rehydrogenation was carried out in the presence of 1 atm H_2 at 348 K. In the right frame ^{14}C-benzene was chemisorbed at 573 K and rehydrogenation was carried out at the indicated temperatures.

Fig. 4.30. Radiotracer decay curves illustrating hydrogen transfer reactions between n-hexane or benzene with surface species that were derived from ^{14}C-benzene chemisorption on Pt(111) at 573 K.

Fig. 4.31. Radiotracer decay curves illustrating the rehydrogenation of ^{14}C-benzene chemisorbed on Pt(100).

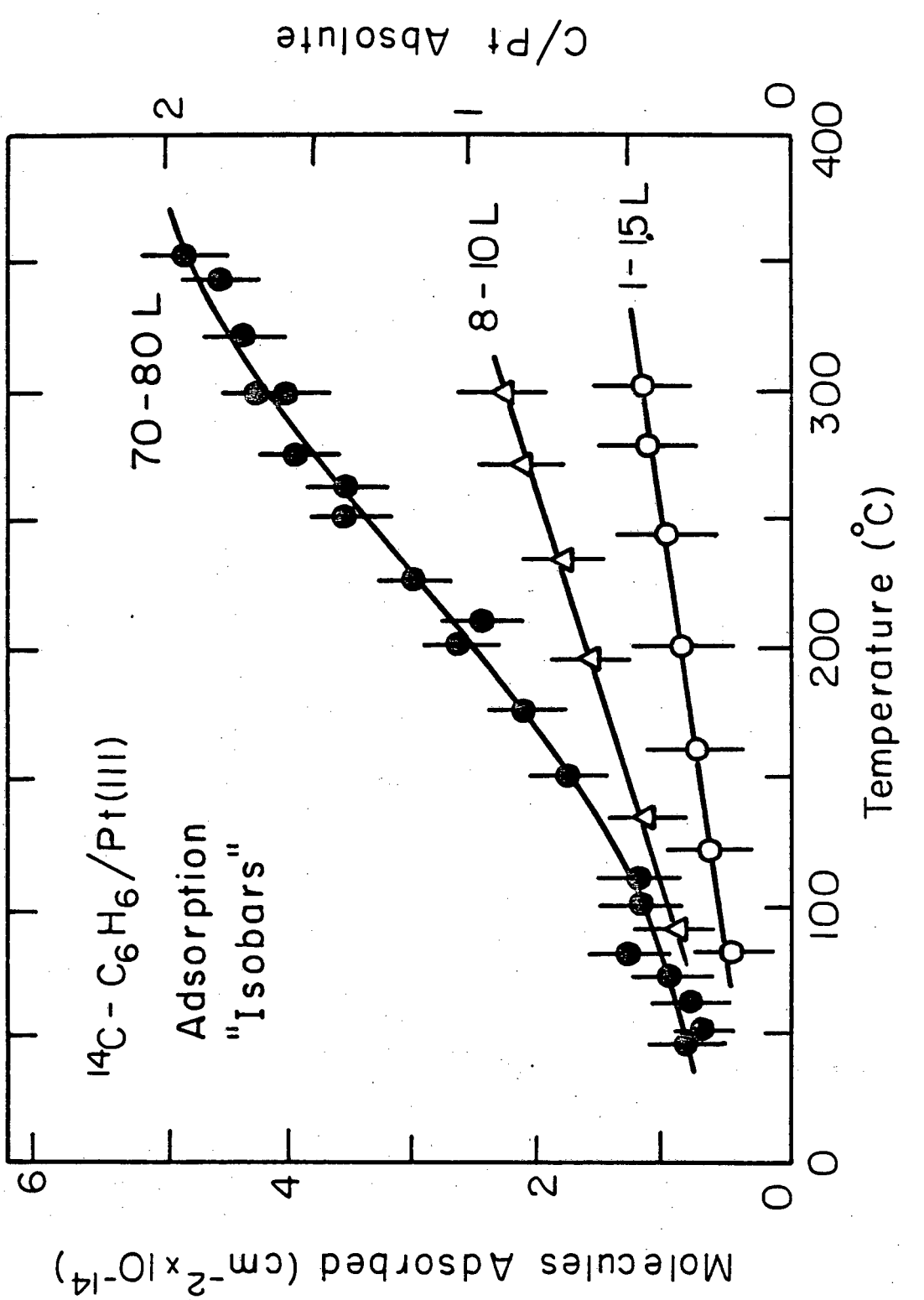

XBL808-5688

Fig. 4.20

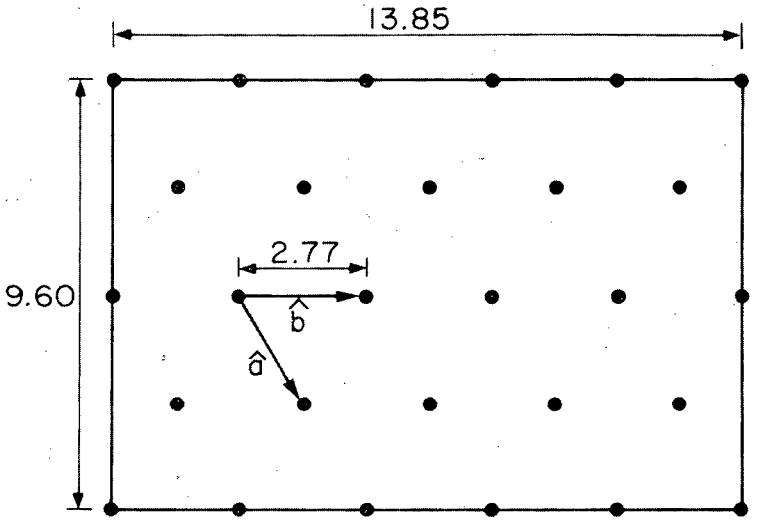

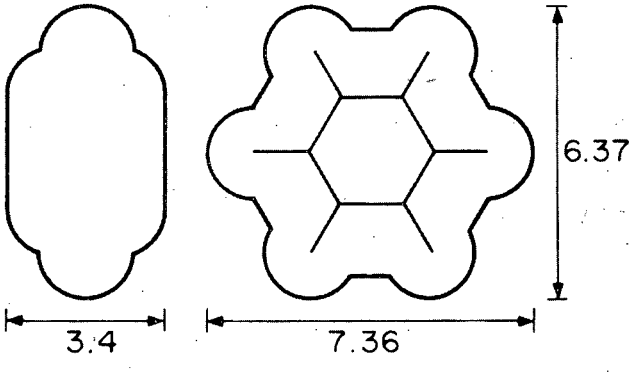

$$\text{Pt(III)} - \begin{vmatrix} 4\hat{a} & -2\hat{b} \\ 0 & 5\hat{b} \end{vmatrix} - \text{Benzene}$$

XBB 817-6804

Fig. 4.21

Comparison between Model and Practical Catalysts

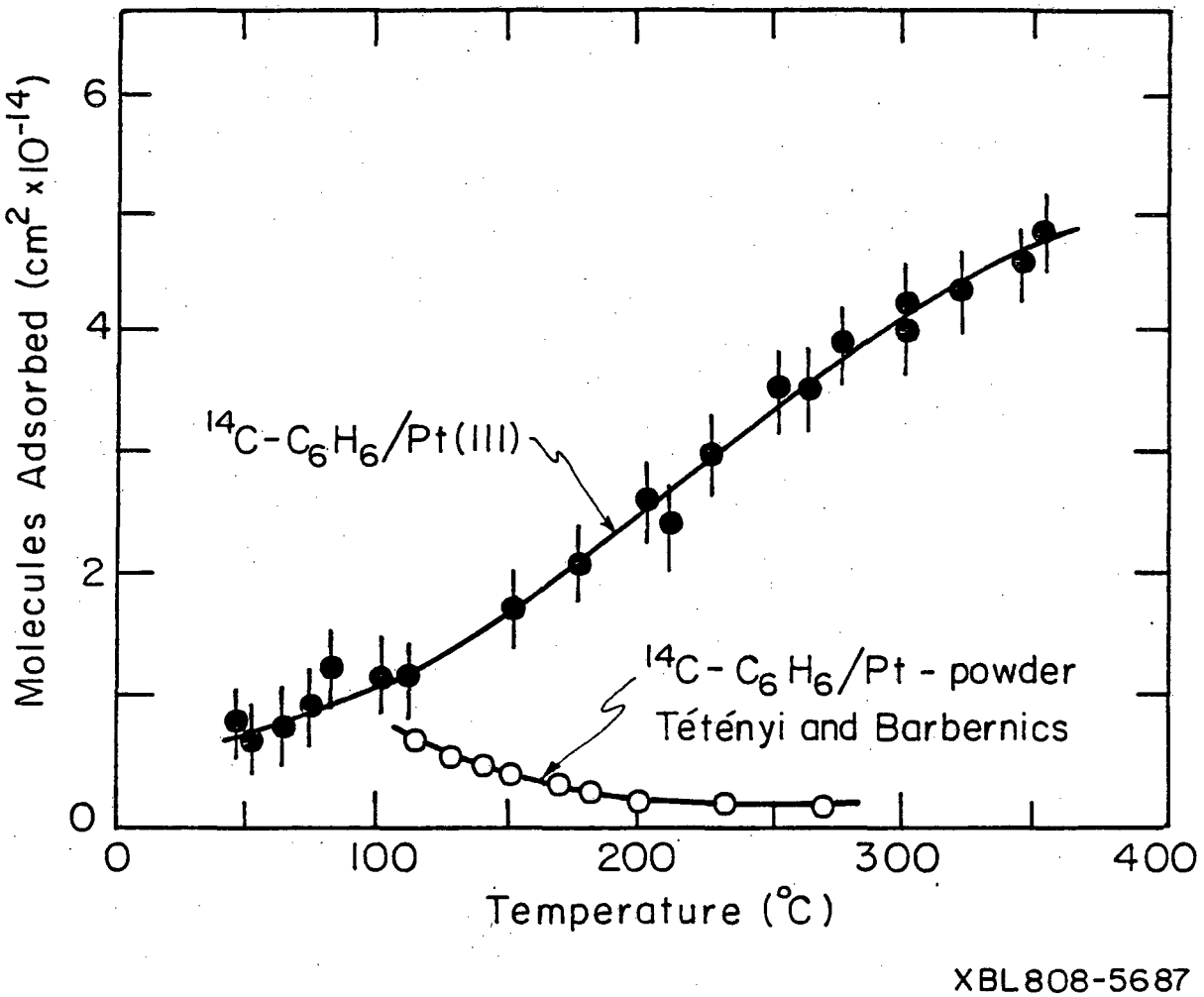

Fig. 4.22

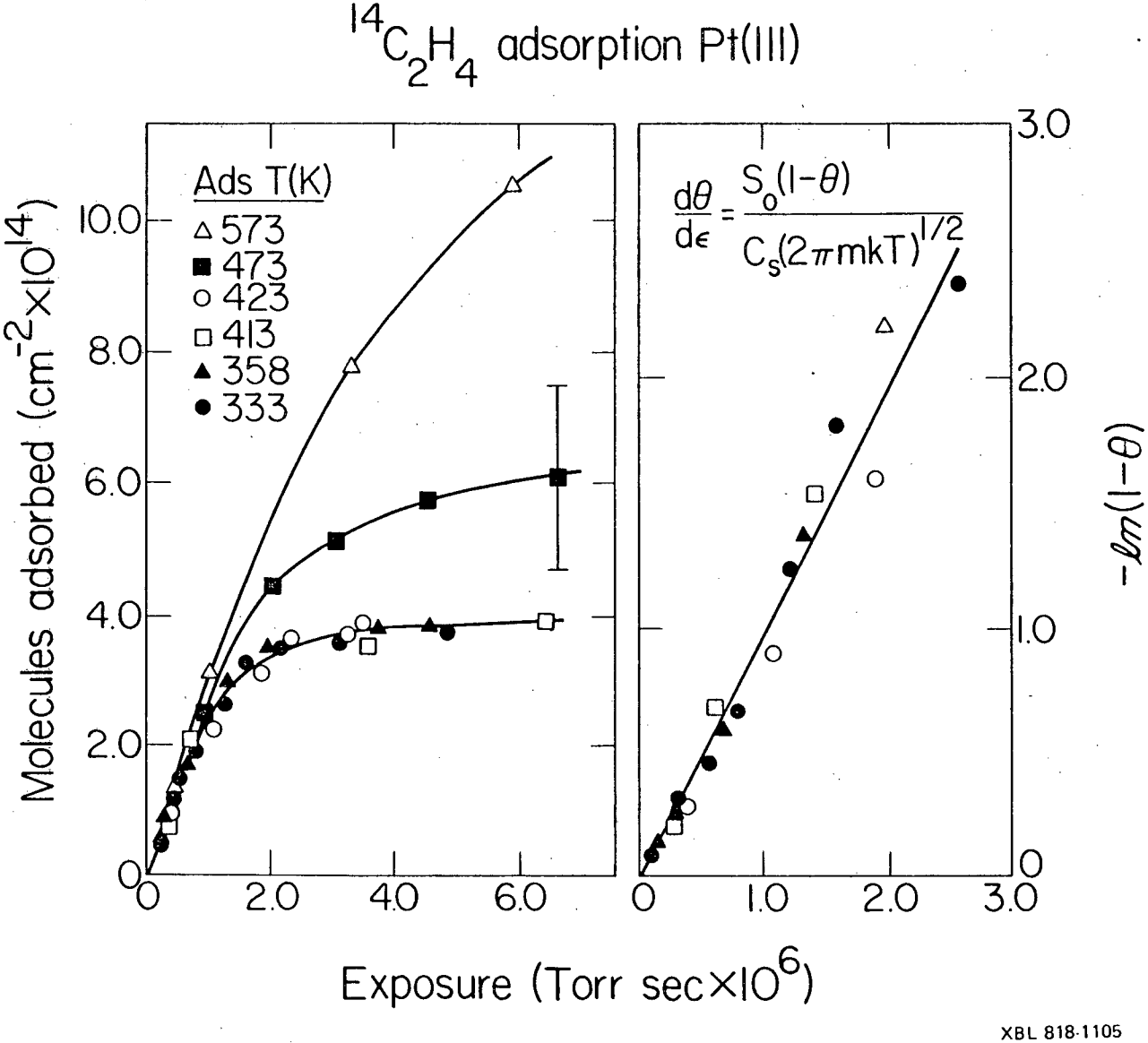

XBL 818-1105

Fig. 4.23

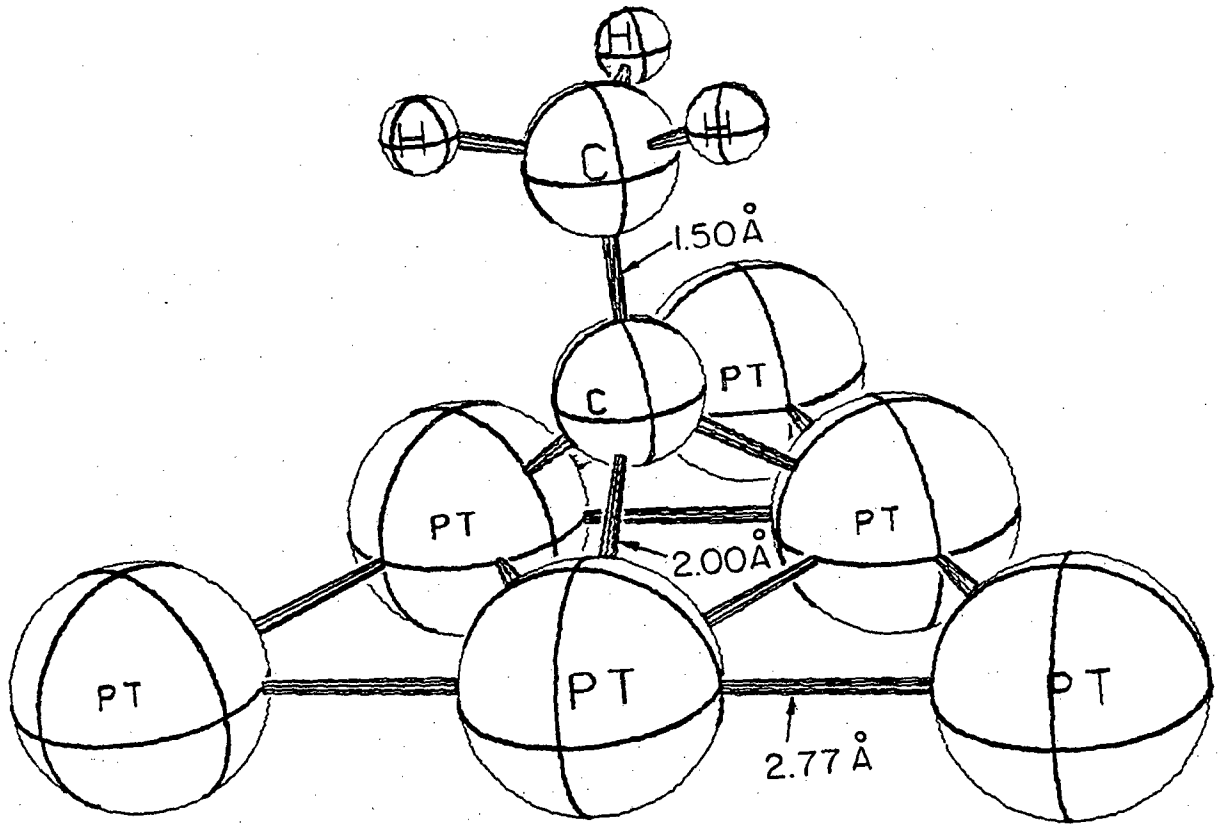

Pt (111) + ethylidyne

XBL794-6167

Fig. 4.24

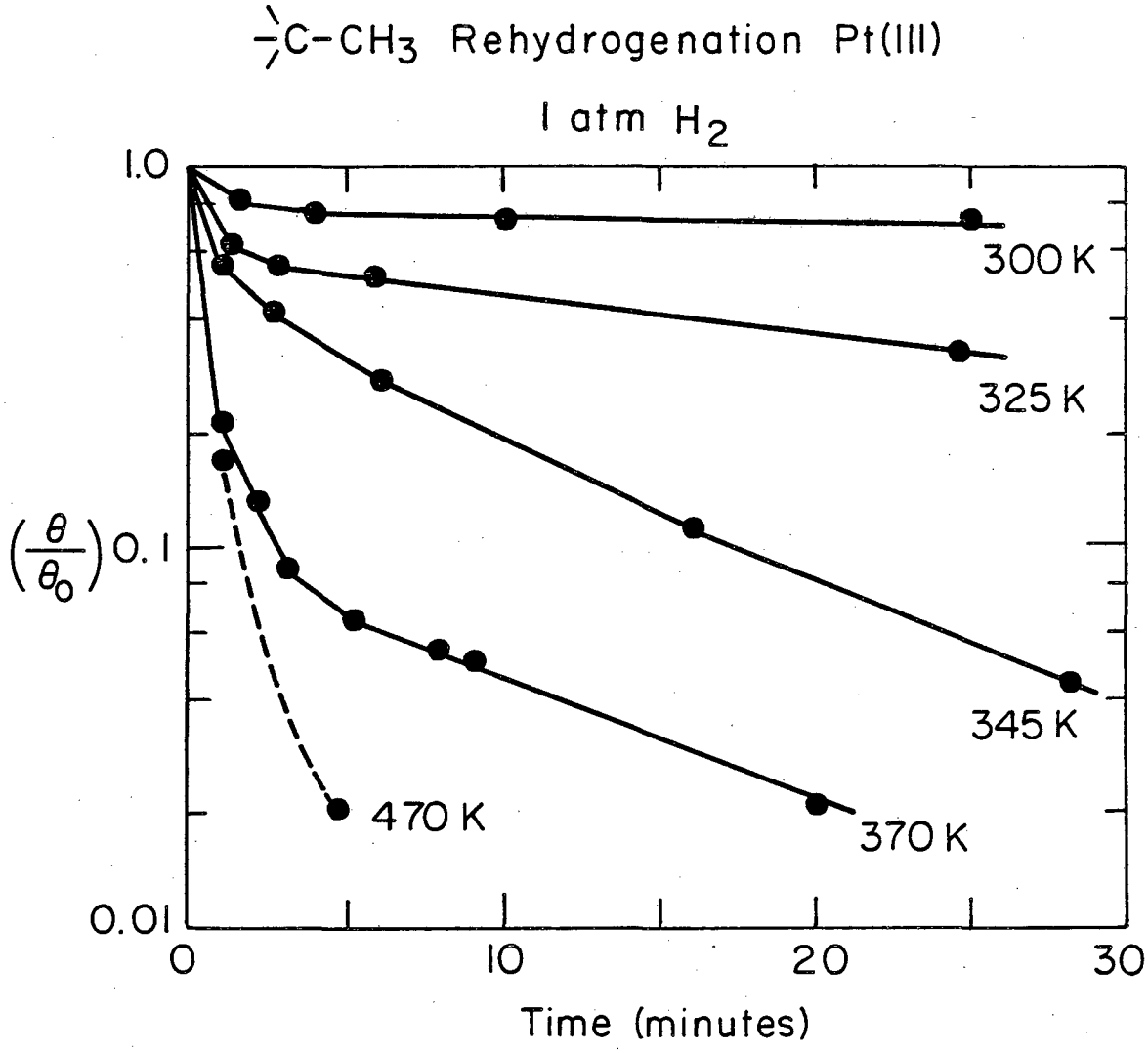
C-CH3 Rehydrogenation Pt(111)
1 atm H2
1.0
0.1
0.01
(θ/θ0)
300 K
325 K
345 K
370 K
470 K
0
10
20
30
Time (minutes)
XBL813-5385

Fig. 4.25

Rehydrogenation of Ethylene
Decomposition Products -Pt(111)

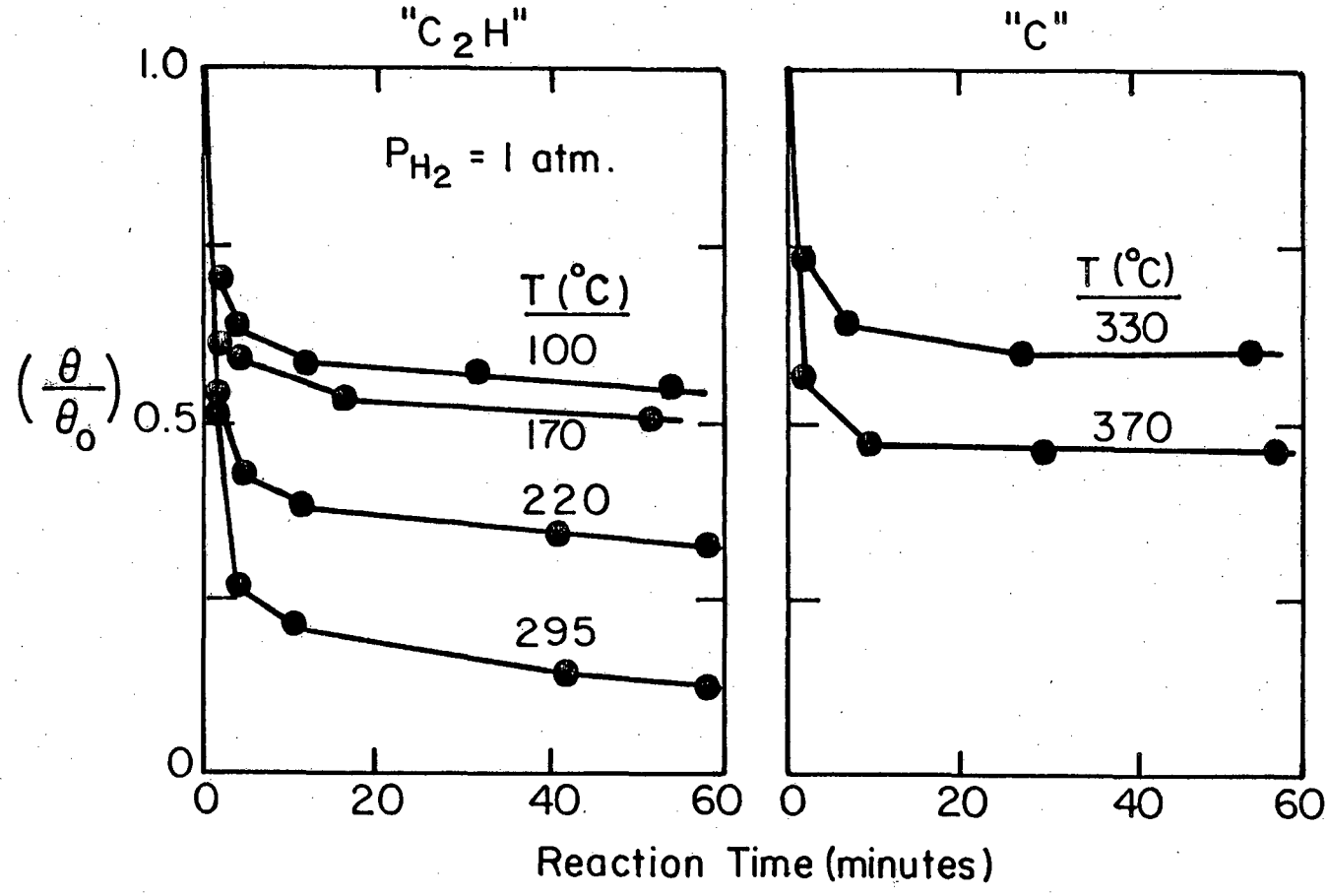

XBL 817-6083

Fig. 4.26

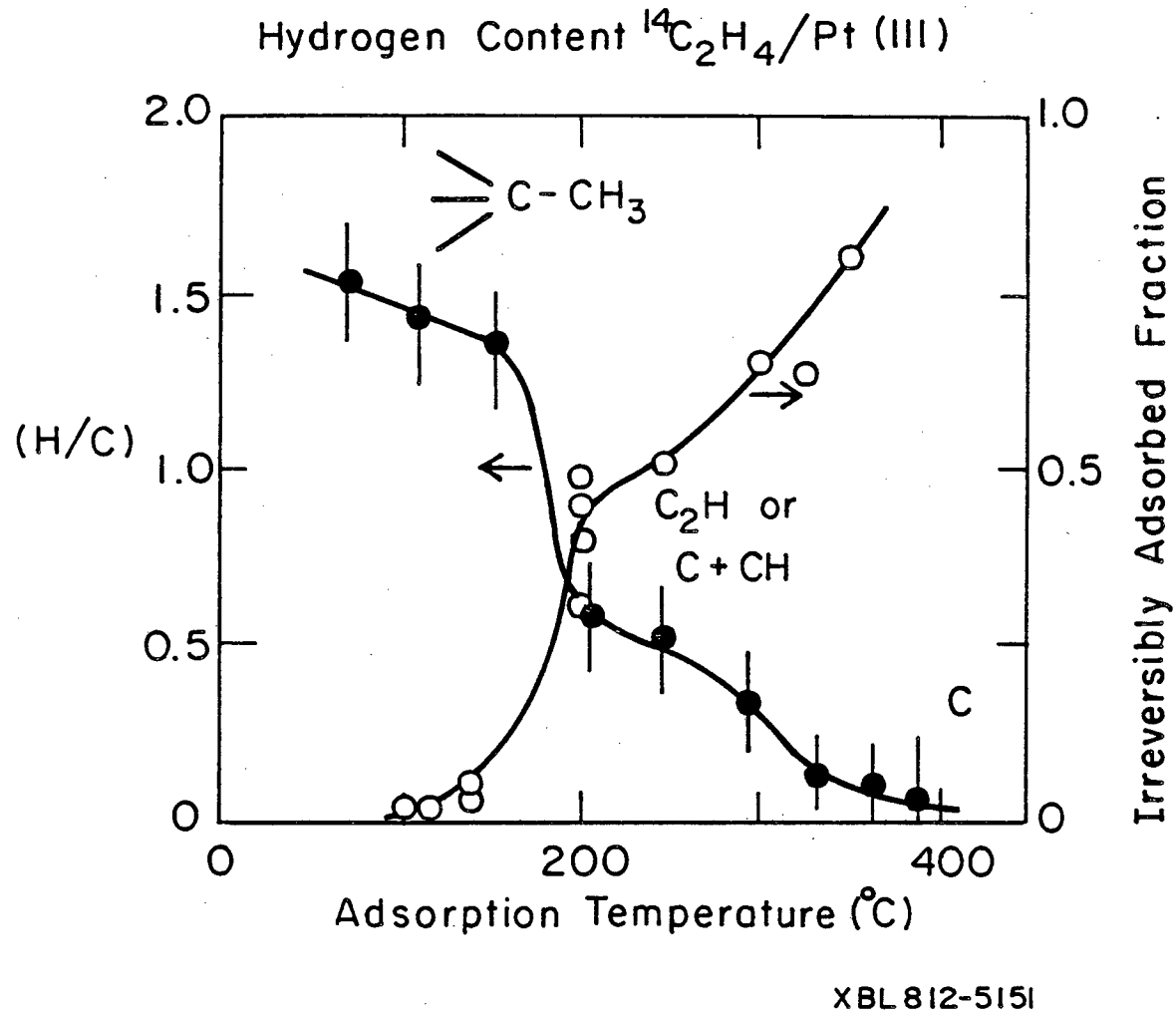
Hydrogen Content $^{14}C_2H_4$/Pt (111)
2.0
1.5
1.0
0.5
0
(H/C)
1.0
0.5
0
Irreversibly Adsorbed Fraction
C-CH3
C2H or
C+CH
C
0
200
400
Adsorption Temperature (°C)
XBL812-5151

Fig. 4.27

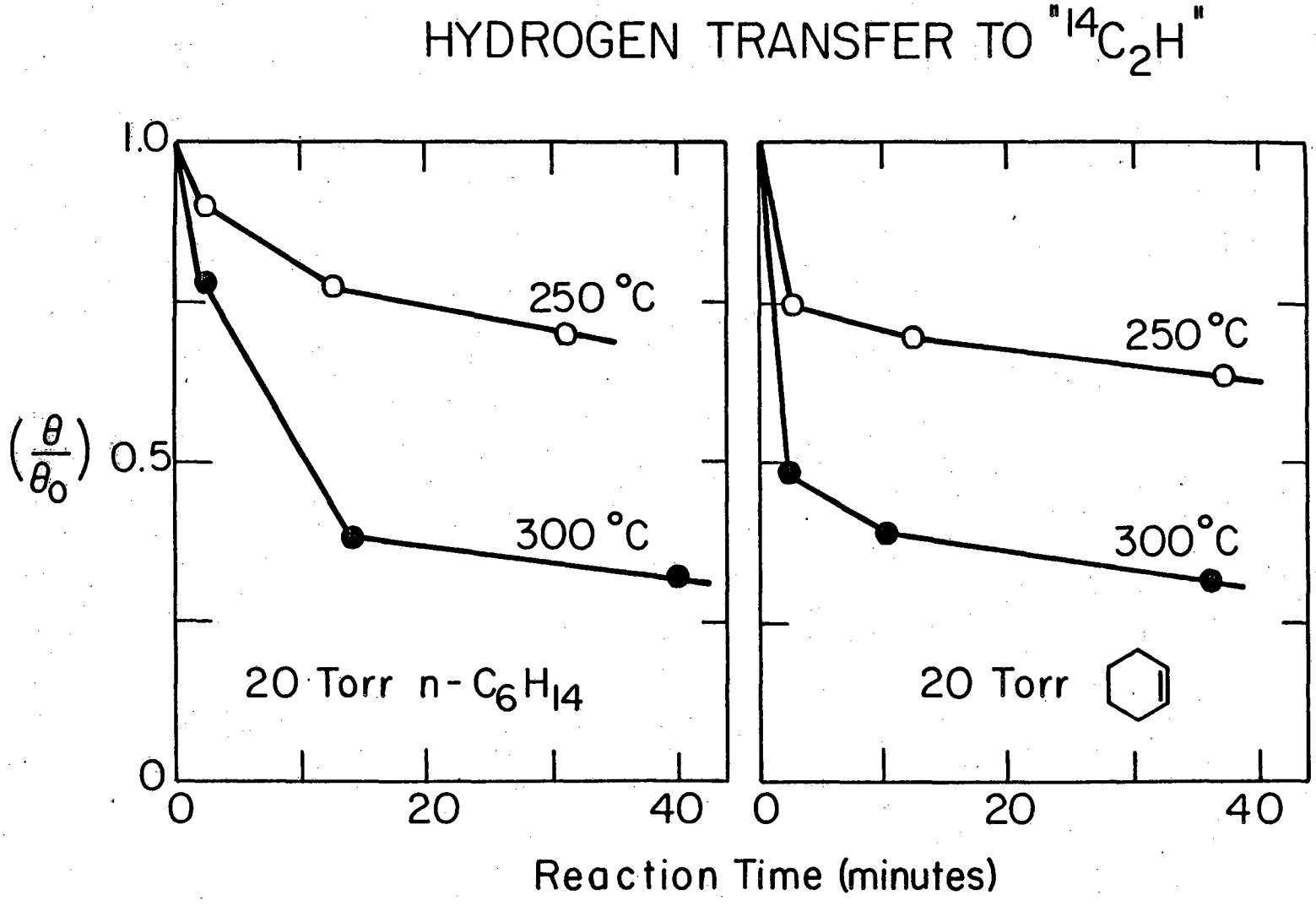

Fig. 4.28

XBL815-5660

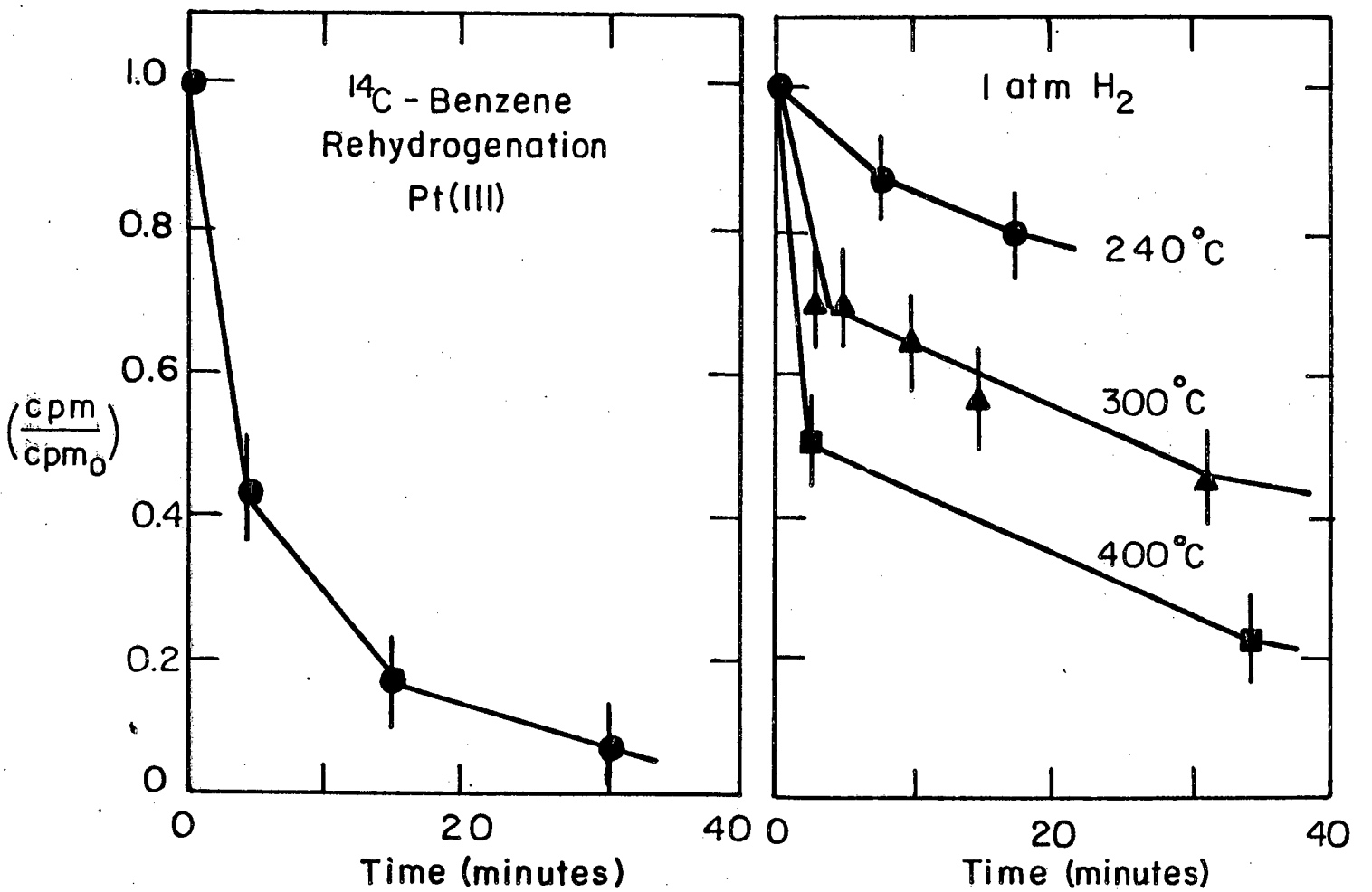

Fig. 4.29

XBL 808-5691A

Hydrogen Transfer from Unlabelled Hydrocarbons to ^{14}C-C_6H_6 Deposited on Pt(111) at 300 °C

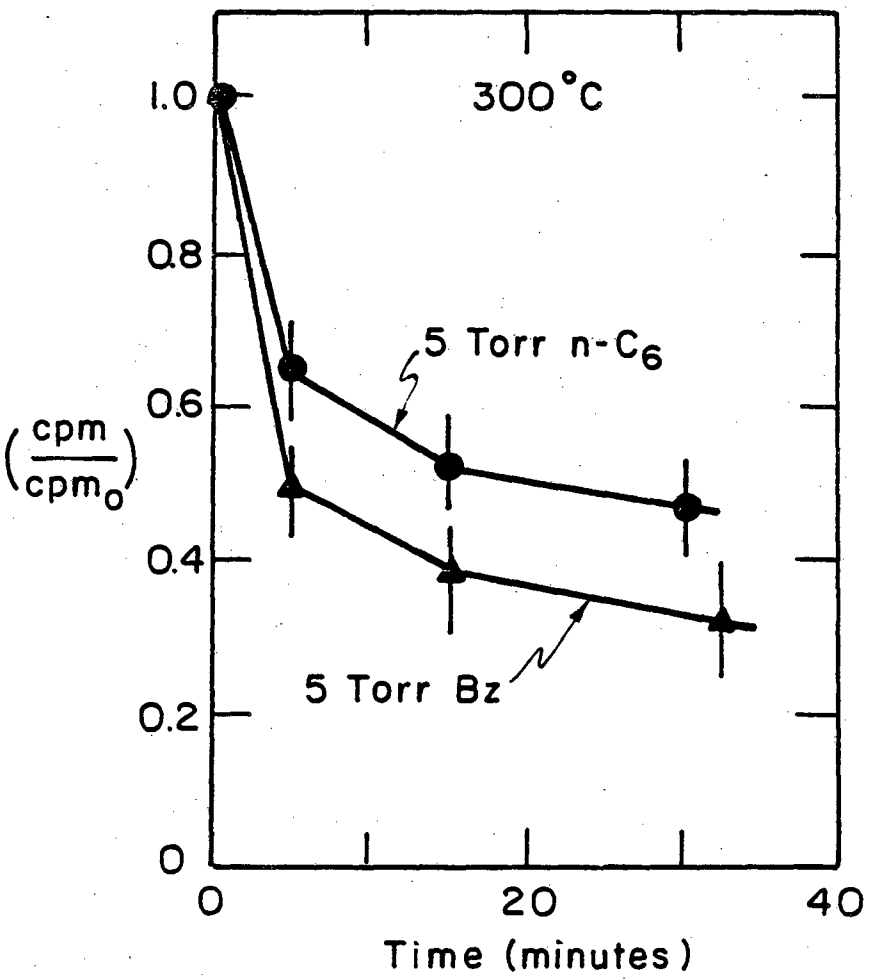

XBL 808-5690

Fig. 4.30

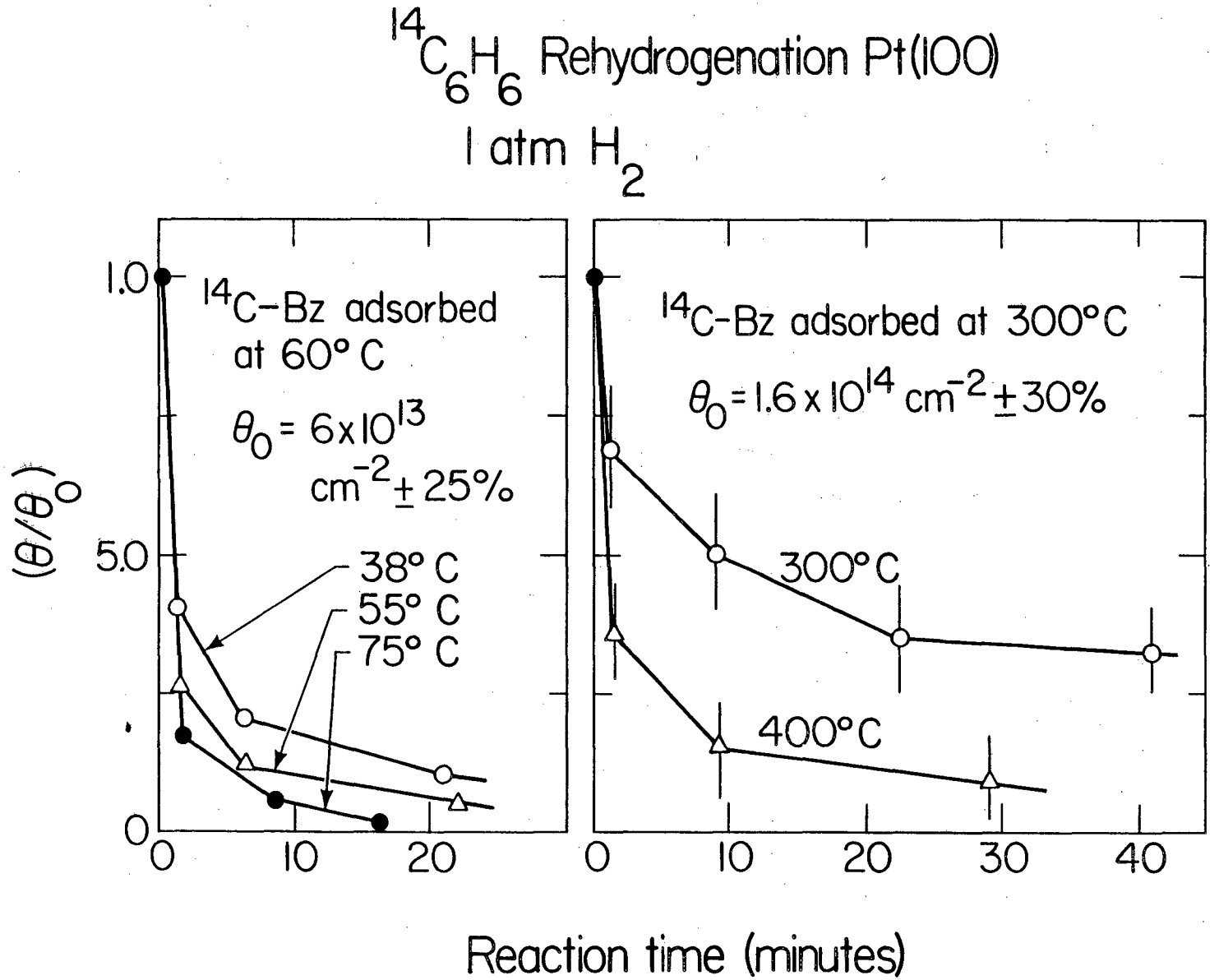

XBL 818-1102

Fig. 4 31

4.6. Catalytic Activity and Selectivity of Carbon Covered Platinum: Restart Reactions and Reaction Rate Studies Over Preadsorbed Overlayers Containing Carbon-14.

4.6.1. Background.

An extensive series of reaction rate studies was carried out to investigate how the catalytic activity and selectivity of platinum is altered by the presence of strongly adsorbed carbonaceous deposits. Two different types of experiments were carried out: (1) reaction rate studies over surfaces precovered with hydrocarbon overlayers, and (2) restart reaction studies. In the former experiments the initially clean platinum surfaces were pretreated with various hydrocarbons at low reactant pressures (~10^{-7} Torr) and temperatures between 473 and 673 K, the surface coverage by preadsorbed species was determined by AES (or radiotracer analysis), and then reaction studies were carried out near atmospheric pressure in the usual manner. Often the preadsorbed layer was labelled with carbon-14 so that its partial removal in subsequent reactions could be detected by radiotracer analysis. In the restart experiments, reaction rate studies were carried out for 90-180 min starting with an initially clean platinum surface, the reactions were stopped, Auger spectra were recorded for both crystal faces, and then the reactions were restarted using a fresh reaction mixture, often under exactly the same reaction conditions. These two types of experiments enabled the hydrogen content of the preadsorbed layers and the total surface carbon coverage to be varied independently.

The platinum surfaces that were covered with preadsorbed carbon deposits always displayed lower catalytic activities than initally

clean platinum surfaces. Only small changes in reaction selectivity were detected. During light alkane conversion reactions there was a tendency for isomerization activity to be suppressed more strongly than hydrogenolysis. During n-hexane reactions the selectivities for aromatization and hydrogenolysis were usually enhanced slightly relative to isomerization and c_5-cyclization. Since the changes in selectivity were always small, the general conclusion arises that surface carbon deposits function as non-selective poisons independent of their hydrogen content and the hydrocarbon from which it was formed.

4.6.2. Results and Discussion

Cyclohexene Hydrogenation and Dehydrogenation. Reaction studies on platinum surfaces covered with preadsorbed overlayers revealed that the strongly adsorbed carbonaceous species which form at low pressures and temperatures between 473 and 523 K act as non-selective poisons for simple hydrogenation and dehydrogenation reactions that can be catalyzed at low temperatures. This is shown in Fig. 4.32 for cyclohexene hydrogenation and dehydrogenation catalyzed at 300-425 K over the stepped (322) platinum surface. Ethylene, 1-butene, and benzene were preadsorbed at 473 K ($\theta < 0.5$) or 523 K ($\theta > 0.5$), the surface coverage by preadsorbed species was determined by AES ($\theta = 1$ corresponds to 2 carbon atoms per surface platinum atom ±25 percent), and then the cyclohexene reactions were carried out at a total pressure of 77 Torr (H_2/HC = 10). At 300 K, the preadsorbed species very effectively blocked the sites that were required for cyclohexene hydrogenation. The decline in activity with increasing overlayer coverage

corresponds to a $(1 - \theta)^2$ coverage dependence indicating that at least two platinum atoms were used in the rate determining step of this reaction. Based on the kinetic studies of Segal et al. (52), the rate determining step appears to be the dissociative chemisorption of hydrogen molecules on uncovered platinum surface sites.

At 425 K the dehydrogenation and hydrogenation reactions were both suppressed strongly by preadsorbed benzene but to a lesser extent by the preadsorbed light olefins. The light olefins appeared to rehydrogenate more readily than benzene thereby causing less deactivation with increasing overlayer coverage. The stronger inhibition by preadsorbed benzene is not too surprising in view of photoemission spectra like those shown in Fig. 4.12 and radiotracer studies (Section 4.5) which indicate that benzene may be partially graphetized following low pressure adsorption at 470–520 K.

Light Alkane Restart Reactions. Qualitative information about the rehydrogenation rates during alkane conversion reactions at higher temperatures can be determined in this manner by preadsorbing one type of hydrocarbon molecule and running a second reaction in the presence of the preadsorbed layer, or by running the reactions continuously changing the reactant hydrocarbon at periodic intervals. Restart experiments of the latter type reveal how hydrocarbon deposits derived from different molecules influence the activity and selectivity of hydrocarbon conversion reactions. Figure 4.33 compares product accumulation curves determined as a function of reaction time for isobutane isomerization catalyzed at 573 K over the stepped (13,1,1) platinum

surface that was initially clean (top curve) and initially precovered with carbon deposits from previous neopentane and n-hexane reactions (lower curves). The initially clean surface was the most active and selective catalyst for this reaction yielding about 97 percent n-butane and 3 percent hydrogenolysis products. Because part of the deactivation which occurred in the initial reactions was irreversible, the maximum level of activity that could be restored in the restart reactions was always several times less than that for the initially clean platinum surface. The greater deactivation which occurred after the n-hexane reaction correlated with an increased coverage by surface carbon. In Fig. 4.34 initial rates in isobutane and neopentane restart reactions have been divided by initial rates on clean platinum (R_r/R_c) and plotted as a function of the overlayer coverage. Table 4.5 summarizes reaction conditions and initial rates for the restart experiments. The catalytic activities for isomerization and hydrogenolysis on the (10,8,7) and (13,1,1) platinum surfaces both decreased markedly with increasing carbon coverage. Isomerization was generally suppressed more strongly than hydrogenolysis, particularly during isobutane reactions catalyzed over Pt(10,8,7).

n-Hexane Restart Reactions. A similar series of restart experiments was carried out for n-hexane reactions catalyzed over the (111) and (10,8,7) platinum surfaces. Reaction conditions and initial rates for several of the experiments are summarized in Table 4.6. Example product accumulation curves are shown in Fig. 4.35. The ratio of initial rates (R_r/R_c) is shown as a function of the preadsorbed

overlayer coverage for several sets of reaction conditions in Figs. 4.36 and 4.37. The error bars represent the spread in (R_r/R_c) values measured for parallel hydrogenolysis, isomerization, and cyclization reactions. Again it can be clearly seen that the catalytic activity for all reactions decreased with increasing carbon coverage. The deactivation displayed little dependence on platinum surface structure and the hydrocarbon from which the carbon deposit was formed. Many of the restart experiments were carried out following n-hexane reaction studies using identical experimental conditions. The (R_r/R_c) ratios for these experiments are shown as a function of reaction temperature in Fig. 4.38. It is apparent that the amount of deactivation which occurred in the initial reactions increased with increasing reaction temperature. This deactivation correlated to roughly first order with increasing surface carbon coverage. As indicated in Fig. 4.33 and 4.35, the catalytic activity measured in the restart reactions was usually more stable than that for initially clean platinum surfaces (Section 3.1).

A comparison between Fig. 4.34, 4.35 and 4.36 reveals that the n-hexane reactions generally displayed less deactivation at a given carbon coverage than the isobutane and neopentane reactions. The activity in light alkane restart reactions approached zero for "carbon coverages" greater than about two carbon atoms per surface platinum atom. By contrast, n-hexane continued to display appreciable activity at carbon coverages approaching four carbon atoms per surface platinum atom (equivalent--Section 2.6). The reasons for this difference are

not completely clear, but they are likely related to different site requirements for the light alkane and n-hexane reactions or differences in molecular residence times for the reacting species. The longer surface residence times for n-hexane (Section 4.1) may enable this molecule to diffuse more efficiently to uncovered platinum sites during a single residence on the surface.

It is clear that the working platinum catalyst can tolerate a substantial accumulation of surface carbon and still exhibit high activity and normal platinum selectivity for the more important reforming reactions of larger alkane molecules. This might be expected if the carbon deposit were to participate in the reforming reactions by hydrogen transfer or other indirect processes. In order for uncovered platinum sites to be totally responsible for the reaction chemistry, the carbon deposit must assume a 3-dimensional morphology which provides a small, steady-state concentration of uncovered platinum surface sites. Carbon monoxide adsorption studies reported in the next section indicate that uncovered platinum sites are indeed present during the restart reactions, and that these sites are responsible for the lowered catalytic activity that was displayed by the carbon covered surfaces. Supported platinum reforming catalysts that operate selectively for thousands of hours before requiring regeneration are known to accumulate high steady-state levels of "coke" deposits (as much as 5-10 percent by weight for 1 percent Pt/Al_2O_3 (53)). While it is known that much of this carbon is deposited on the support (53,54), our results clearly suggest that a part of this

"coke" deposit may also be present on the small platinum particles. The practical catalysts maintain an acceptable level of activity and selectivity only as long as a certain fraction of the platinum sites remain uncovered.

n-Hexane Reaction Studies on Surfaces Precovered with Overlayers Containing Carbon-14. Reaction rate studies carried over platinum surfaces precovered with hydrocarbon overlayers containing carbon-14 were also used to obtain information about the residence times and catalytic behavior of the metal-organic deposit. Figure 4.39 compares product accumulation curves determined as a function of reaction time at 573 and 623 K for n-hexane hydrogenolysis and cyclization catalyzed over the flat (111) platinum surface. Before these reactions were carried out the surface was precovered with about one monolayer of ^{14}C-benzene at the same temperature that was used for the subsequent reaction studies. The catalytic activity (TN_i = initial turnover frequency) and cyclization selectivity (S_i = fractional cyclization selectivity) increased with increasing reaction temperature as discussed in Section 3.1. The most important feature of these experiments, however, is the extent to which the preadsorbed overlayers are removed during the reactions by a combination of rehydrogenation and hydrogen transfer. This is indicated by cpm/cpm_0 which denotes the ^{14}C-count rate after 2 hr of reaction divided by the ^{14}C-count rate at the start of reaction. The ^{14}C-containing deposit that was produced at 573 K was largely removed (~75 percent) during n-hexane conversion at the same temperature. In contrast, at 623 K the radioactive

deposit was more securely bonded to the platinum surface and did not undergo appreciable rehydrogenation (<20 percent). Despite the continuous presence of this deposit, the n-hexane reactions took place with very appreciable rates and selectivities. Under these conditions, hydrocarbon conversion certainly occurred in the presence of the carbon deposit and perhaps in exchange with the ^{14}C-containing species. Table 4.7 summarizes initial rates and selectivities for other n-hexane reactions that were catalyzed over the (100) and (111) platinum surfaces following pretreatment with ^{14}C-ethylene and ^{14}C-benzene at 400-670 K. Reaction rates measured in the presence of the preadsorbed overlayers were always lower than initial rates determined for clean platinum surfaces. No significant changes in reaction selectivity were detected. The fraction of the preadsorbed ^{14}C-containing species which were irreversibly adsorbed is shown as a function of adsorption temperature in Fig. 4.40. As discussed in the preceeding section for ^{14}C-C_2H_4 rehydrogenation reactions, the irreverisbly adsorbed fraction increased with increasing adsorption temperature and decreasing reaction temperature. At any given pretreatment temperature, ethylene appeared to be adsorbed more irreversibly than benzene. The irreversibly adsorbed fraction displayed an inverse correlation with the hydrogen content of the preadsorbed species (Section 4.5).

Selectivity of Restart Reactions and Reaction Studies in the Presence of Preadsorbed Overlayers Containing Carbon-14. Only minor changes in reaction selectivity were detected for the carbon covered platinum surfaces independent of their surface structure, the reaction

Table. 4.7. Catalytic behavior of platinum in n-hexane reaction studies catalyzed over single crystal surfaces precovered with overlayers containing carbon-14.

Catalyst	Rxn T (K)	Preadsorbed Hydrocarbon (and T_{ads}(K))	R_c/R_{Pt} (a) (±0.1)	(θ/θ_o) (b) (±10 percent)	Initial Coverage (molec/cm^2 ± 30 percent)
Pt(100)	573 (c)	C_6H_6(573)	0.64	46	$4x10^{13}$
Pt(100)	573 (c)	C_6H_6(639)	0.66	84	$5x10^{13}$
Pt(100)	673	C_6H_6(639)	0.76	54	$5x10^{13}$
Pt(111)	573	C_2H_4(413)	0.92	2	$4x10^{14}$
Pt(111)	573	C_2H_4(523)	0.58	40	$4x10^{14}$
Pt(111)	573	C_2H_4(573)	0.36	65	$1x10^{15}$
Pt(111)	623	C_2H_4(523)	0.62	30	$5x10^{14}$
Pt(111)	623	C_2H_4(623)	0.45	82	$1.4x10^{15}$
Pt(111)	673	C_6H_6(673)	0.50	70	$6x10^{13}$

(a) Ratio of reaction rates for the preadsorbed overlayer experiments and clean platinum.

(b) Irreversibly adsorbed fraction of the preadsorbed overlayer.

(c) H_2/HC = 10, P_{tot} = 220 Torr; otherwise H_2/HC = 30, P_{tot} = 620 Torr.

temperature, the hydrocarbon from which the overlayer was derived, and the hydrogen content of the carbon deposit which was varied continuously between (H/C) = 0 and (H/C) = 1.5. These facts all seem to indicate that the general role of the carbon deposit is that of a non-selective poison. Uncovered platinum sites that were present in low concentrations in the restart experiments displayed normal activity and selectivity indicative of platinum catalysis.

During the n-hexane reaction studies on carbon covered Pt(111) and Pt(10,8,7), there was usually a tendency for aromatization and hydrogenolysis selectivities to be enhanced slightly relative to isomerization and c_5-cyclization. Example product distributions illustrating this effect are shown in Fig. 4.41 for n-hexane reactions catalyzed over Pt(111) at 600-670 K. The enhanced aromatization selectivity is highly desireable but not when it arises at the cost of catalytic activity with a concomitant increase in hydrogenolysis selectivity. Within isomerization, the kinetic selectivity for 2-methylpentane formation over 3-methylpentane production was always lowered on the carbon covered surfaces as compared to initially clean platinum. This change in isomerization selectivity would be expected from the results presented in Section 3.1.

Perhaps, the two most simple explanations that can be proposed to account for the slightly altered selectivity of the carbon covered

platinum surfaces are: (1) a change takes place in the size of the available sites where reactions take place, and/or (2) the concentration of surface hydrogen is reduced on the carbon covered surfaces. Of these possibilities only (2) is consistent with experimental facts. From studies of n-hexane reactions catalyzed over alloys (55-58), it has been clearly established that isomerization and c_5-cyclization can take place at surface sites consisting of isolated platinum atoms. By contrast, hydrogenolysis undoubtedly requires multiatomic platinum sites, and aromatization may as well (55,57). If carbon was uniformly deposited on the platinum surfaces, one would anticipate an increase in the concentration of monatomic sites relative to multiatomic sites, and this should be accompanied by an increase in isomerization and c_5-cyclization selectivity. Since the restart experiments always revealed exactly the opposite change in selectivity, proposal (1) appears to be largely unacceptable. This conclusion is consistent with the fact that carbon was deposited as non-uniform, polymeric islands (Section 4.7). Results discussed in Section 3.1 showed that with increasing temperature and decreasing hydrogen pressure, aromatization and hydrogenolysis selectivities increased at the expense of isomerization and c_5-cyclization. Within isomerization, the kinetic selectivity 2MP/3MP decreased with increasing temperature and decreasing hydrogen pressure. These changes in selectivity were related to a change in the identity of the most abundant surface intermediate that is caused by a decrease in the surface concentration of chemisorbed

hydrogen. Since exactly the same changes in reaction selectivity were observed during the restart experiments, proposal (2) appears to provide a simple and meaningful explanation for the slightly altered selectivity of carbon covered platinum. A possible reason why the surface concentration of hydrogen was reduced in the restart reactions was discussed in Section 4.2. The sticking coefficient of hydrogen appeared to be reduced on the carbon covered surfaces (e.g., $\theta_H \sim K_H^{1/2}$, $K_H \sim S_o$). Results obtained by Salmeron (3) also indicate that the binding energy of hydrogen is reduced by 2-3 kcal/mole when coadsorbed on platinum in the presence of hydrocarbons.

The increased aromatization selectivity that was detected for the carbon covered single crystal surfaces corresponds well with results reported by Hughes (59) for commercial Pt/Al_2O_3 and $Pt-Re/Al_2O_3$ catalysts. Supported catalysts that were pretreated with methyl- and dimethylcyclopentanes displayed a 2-10 percent increase in aromatization selectivity for reforming reactions of cyclopentanes and cyclohexanes. This change in selectivity was largest for the bimetallic catalysts. An increase in hydrogenolysis selectivity relative to isomerization and c_5-cyclization, like that observed in this research, was also reported by Karpinski (60) for n-hexane reactions catalyzed over Pt/SiO_2 catalysts that were deliberately deactivated at high temperatures. Paal et al. (61) reported the same effect for 3-methylpentane reactions catalyzed over platinum black. Ponec and co-workers (62) recently reported interesting results for n-hexane reactions catalyzed at 500-650 K on a series of Pt/SiO_2 catalysts

with average metal particle sizes varied between 20 and 80Å (H_2/HC = 16, P_{tot} = 1 atm). The catalytic behavior of freshly reduced catalysts was compared with that for the same catalysts following deliberate deactivation at 720 K. While little or no structure sensitivity was detected for the freshly reduced catalysts, significant structure sensitivity was observed for the catalysts which were modified by carbon deposition at high temperatures. Catalysts with high dispersion were much more resistant to deactivation than catalysts with low dispersion. These results appear to indicate that edge and corner atoms on dispersed crystallites are more resistant to coke deposition than atoms in close packed crystal faces. The Dutch workers also noted that cyclization selectivity was enhanced relative to isomerization on the deactivated catalysts.

A larger change in reaction selectivity was detected during isobutane and neopentane restart reactions catalyzed over Pt(10,8,7). In this case the kinetic selectivity for isomerization over hydrogenolysis clearly appeared to be lowered in the presence of surface carbon deposits. A smaller effect in the same direction was detected for the stepped (13,1,1) platinum surface. Since kink sites on the (10,8,7) surface were uniquely active for isobutane hydrogenolysis (Section 3.2), it appears likely that this change in selectivity may result from selective blocking of terrace sites by the carbon deposit. Results recently obtained by Zaera (63) from selective CO chemisorption studies confirm this interpretation. A similar change in selectivity was reported by Dowie et al. (64) for isobutane and n-butane restart

reactions catalyzed over platinum films at 630-680 K (H_2/HC = 11.5, $P_{tot} \approx 40$ Torr). However, at the lower temperatures (530-600 K) that correspond to this research, the opposite effect was detected in which isomerization selectivity was enhanced in the restart studies. Guczi and co-workers (64) noted a similar increase in isomerization selectivity for isobutane and n-butane restart reactions catalyzed over platinum black catalysts at 608 K (H_2/HC = 10, $P_{tot} \approx 200$ Torr). A direct comparison of these results with those determined for the single crystal catalysts may not be appropriate since isomerization selectivities for the film and powder catalysts were always much lower than those measured in this research.

Hydrogenation and Dehydrogenation at Higher Temperatures: Results presented earlier (Fig. 4.31) demonstrated that cyclohexene hydrogenation and dehydrogenation reactions catalyzed over Pt(322) at 300-423 K were suppressed strongly by preadsorbed carbon deposits. In order to investigate how hydrogenation and dehydrogenation activity was influenced at higher reaction temperatures, a couple of cyclohexene restart experiments were carried over the (111) platinum surface at 373-473 K. Results of these reactions are summarized in Table 4.8. While hydrogenation and dehydrogenation activity was lowered markedly on the carbon covered surfaces, the hydrogenation and dehydrogenation rates were still exceedingly high. These reactions were typically

Table 4.8. Reaction rates for cyclohexene restart experiments catalyzed over Pt(111) (a).

T(K)	Pretreatment	Reaction Rates (molec/Pt atom sec) Hydrogenation	Dehydrogenation	θ_i (b)
373	clean	>60 (c)	~0.18	0
373	n-hexane + H_2 623 K	0.5	~0.06	4.8
473	clean	>200 (c)	>18 (c)	0
473	n-hexane + H_2 623 K	>18 (c)	2.3	4.8

(a) $H_2/HC = 30$, $P_{tot} = 620$ Torr.

(b) Carbon atoms per surface Pt atom at the start of the restart experiment.

(c) The reactions were so fast that only lower limits could be established.

10^2-10^4 times faster than skeletal rearrangement restart reactions catalyzed at 573-673 K. The relative rates for hydrogenation, dehydrogenation, and skeletal rearrangement clearly indicate that platinum is a very effective hydrogenation-dehydrogenation catalyst even when the working catalyst surface is extensively covered by deactivating carbonaceous deposits. This is, of course, the source of synergism that is displayed by bi- and polyfunctional platinum reforming catalysts (66,67). In this case, olefins produced by the platinum component undergo secondary isomerization and cyclization reactions on the acid sites of the support (67). Platinum alone catalyzes the same skeletal rearrangement reactions but at a slow rate. Solid acids alone require very high temperatures to effect the initial dehydrogenation reactions that results in rapid coking (and cracking) (54,67). The combination of platinum with an acidic support allows both catalysts functions to operate with maximum efficiency.

FIGURE CAPTIONS

Fig. 4.32. Catalytic activity of the carbon covered (322) platinum surface for cyclohexene hydrogenation and dehydrogenation. Benzene, ethylene, and 1-butene were preadsorbed at 10^{-7} Torr and 475-525 K, the surface coverage by preadsorbed species was determined by AES, and then the cyclohexene reactions were carried out at 300 or 425 K.

Fig. 4.33. Product accumulation curves determined as a function of reaction time at 573 K for isobutane isomerization catalyzed over the clean (13,1,1) platinum surface and in restart reactions catalyzed over carbon covered Pt(13,1,1).

Fig. 4.34. Dependence of restart catalytic activity on surface carbon coverage for isobutane and neopentane restart reactions catalyzed over Pt(13,1,1) and Pt(10,8,7).

Fig. 4.35. Product accumulation curves for n-hexane restart reactions catalyzed over Pt(10,8,7): (A) at 573 K following isobutane reaction at 573 K; (B) at 623 K following n-hexane reaction at 623 K; and (c) at 573 K following isobutane reaction at 603 K.

Fig. 4.36. Dependence of restart catalytic activity on surface carbon coverage for n-hexane restart reactions catalyzed over Pt(111) and Pt(10,8,7) (H_2/HC = 10, P_{tot} = 220 Torr).

Fig. 4.37. Dependence of restart catalytic activity on surface carbon coverage for n-hexane restart reactions catalyzed over Pt(111) (H_2/HC = 30, P_{tot} = 620 Torr). A few of the data at 573 K represent reaction studies catalyzed over preadsorbed overlayers containing carbon-14.

Fig. 4.38. Dependence of restart catalytic activity on reaction temperature for n-hexane restart reactions catalyzed over Pt(111) and Pt(10,8,7). The initial and restart reactions were carried out using identical experimental conditions.

Fig. 4.39. Product accumulation curves determined as a function of reaction time at 573 and 623 K for n-hexane cyclization and hydrogenolysis catalyzed over Pt(111). Before the reactions were carried out the surface was precovered with about one monolayer of ^{14}C-benzene (70 L exposure) at the same temperature as used for subsequent reaction studies (TN_i = initial turnover frequency; S_c = fractional cyclization selectivity, cpm/cpm_o = irreversibly adsorbed fraction of ^{14}C).

Fig. 4.40. Dependence of the irreversibly adsorbed fraction on adsorption temperature for n-hexane reaction studies catalyzed on platinum surfaces with preadsorbed overlayers containing carbon-14.

Fig. 4.41. Comparison between product distributions for n-hexane reactions catalyzed at 600-670 K over the initially clean (111) platinum surface and in restart reactions catalyzed over carbon covered Pt(111).

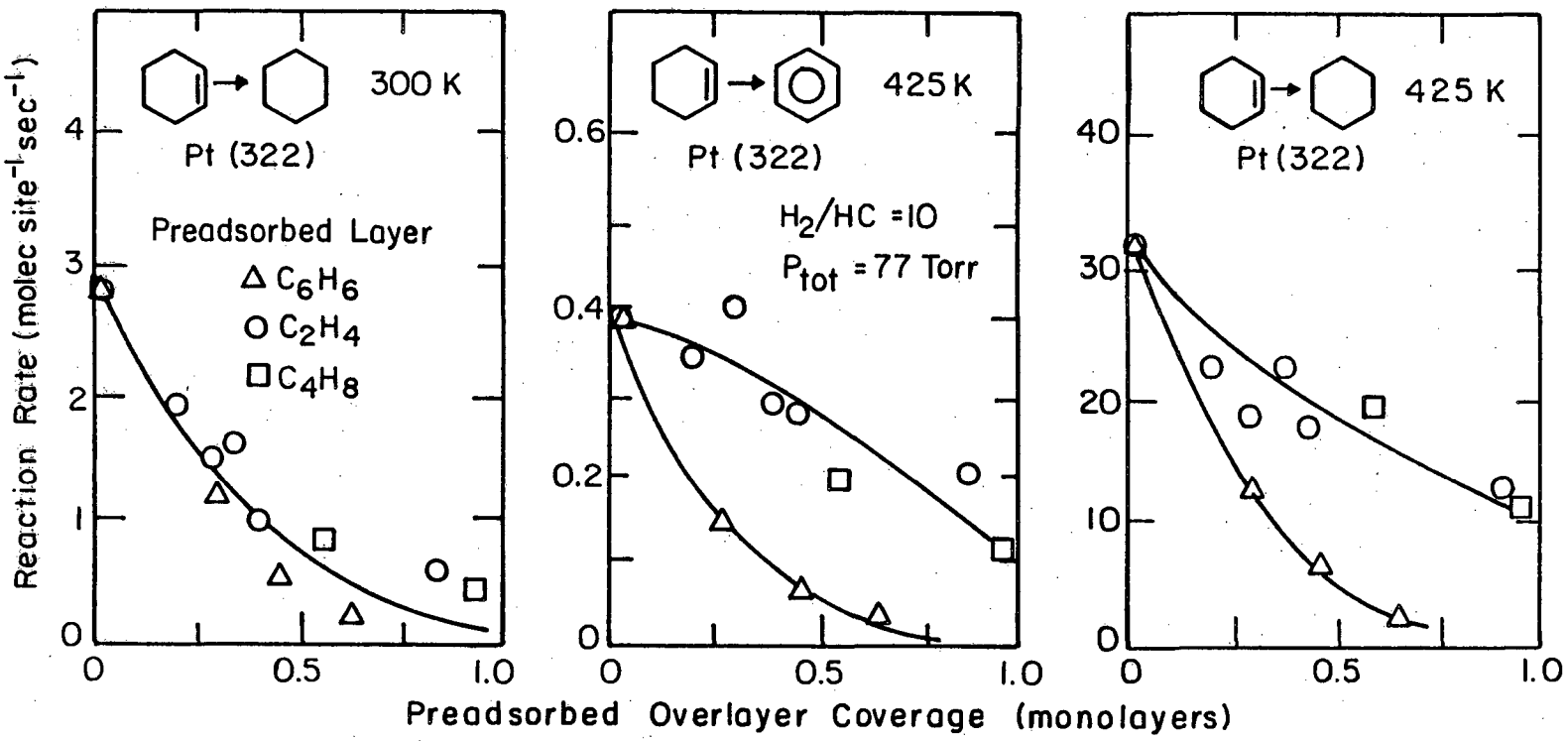

XBL 812-5156

Fig. 4.32

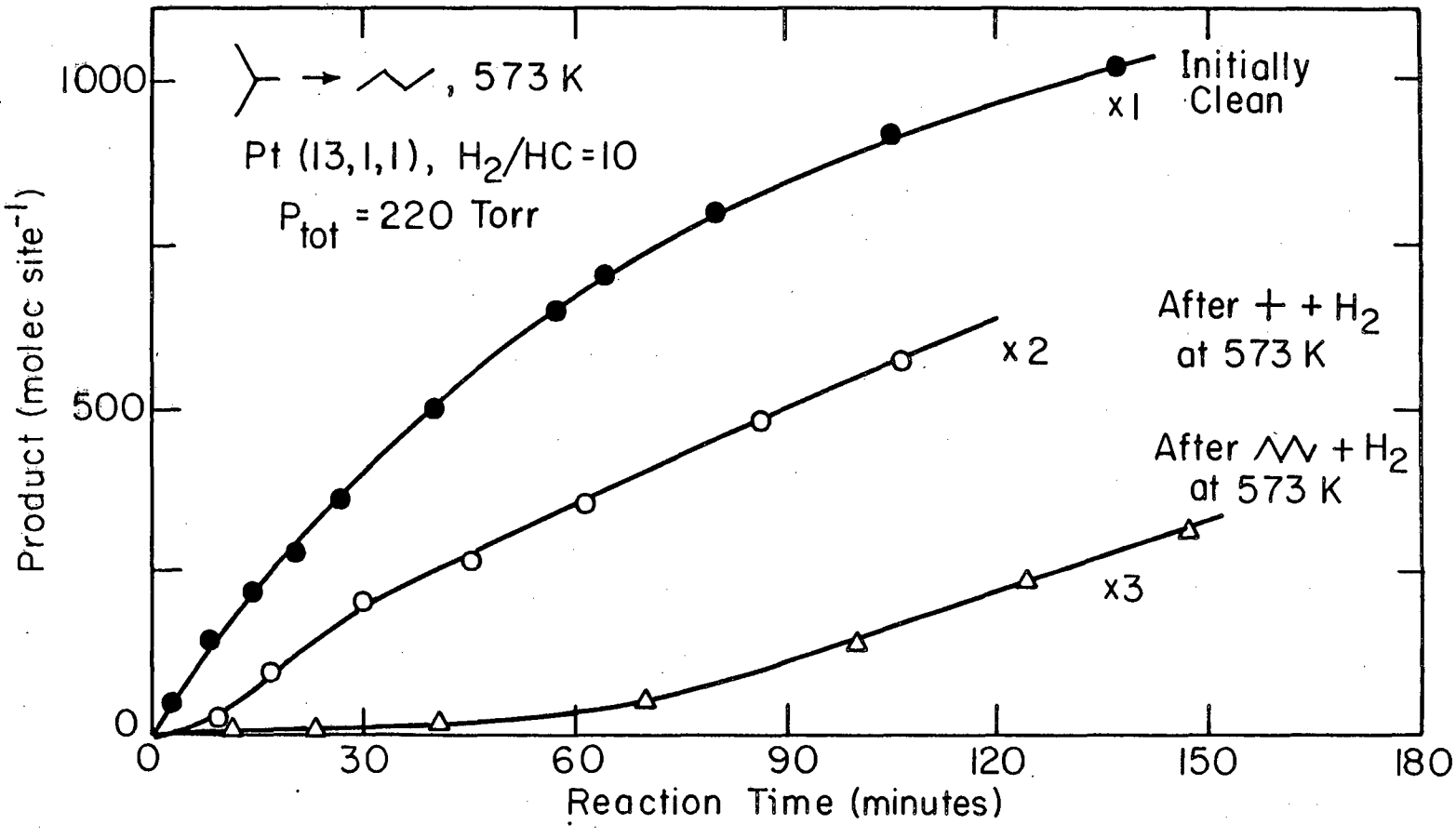

XBL805-5216

Fig. 4.33

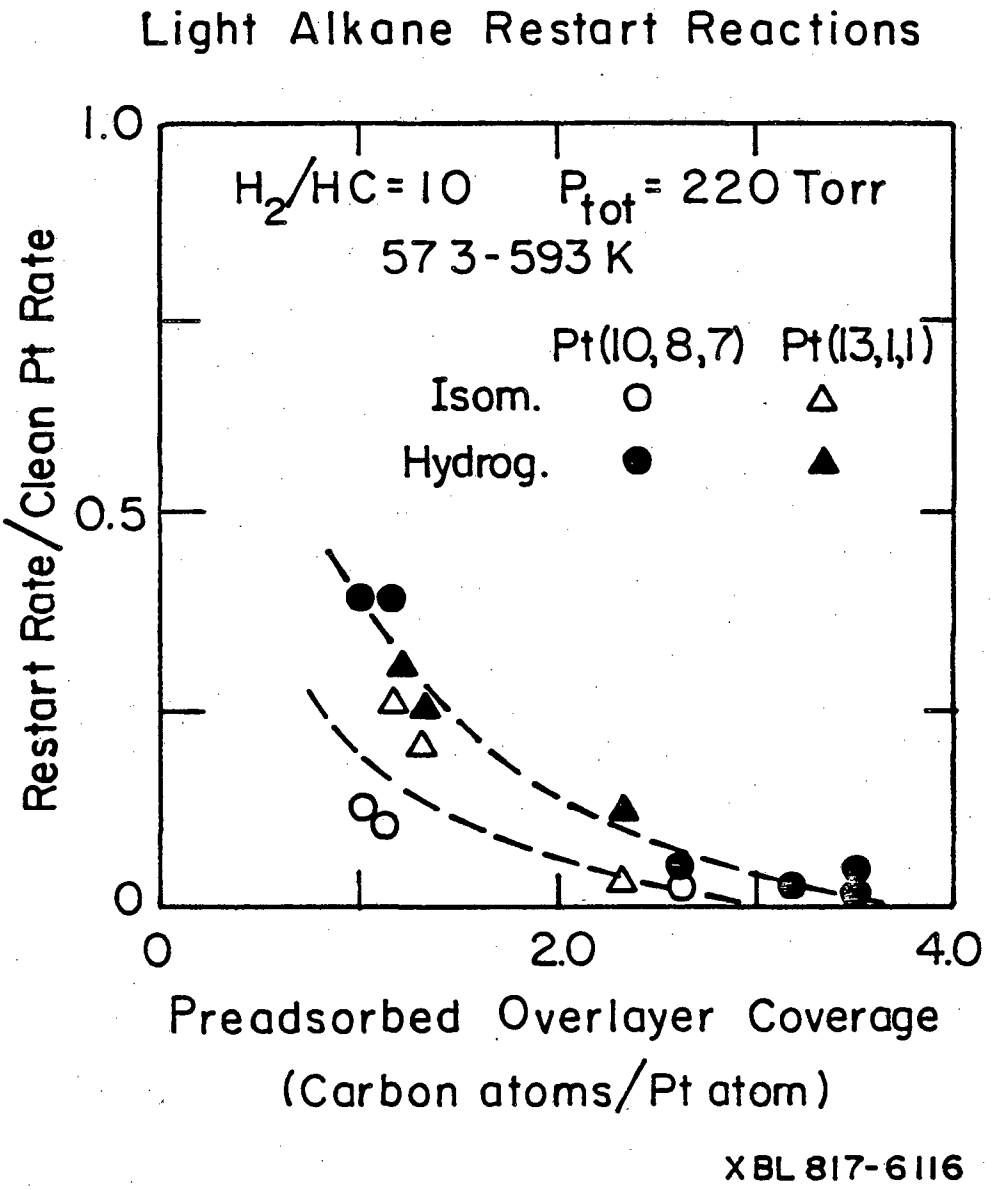
Light Alkane Restart Reactions
1.0
0.5
0
$H_2/HC = 10$ $P_{tot} = 220$ Torr
573-593 K
Pt(10,8,7) Pt(13,1,1)
Isom. O △
Hydrog. ● ▲
Restart Rate/Clean Pt Rate
0
2.0
4.0
Preadsorbed Overlayer Coverage
(Carbon atoms/Pt atom)
XBL 817-6116

Fig. 4.34

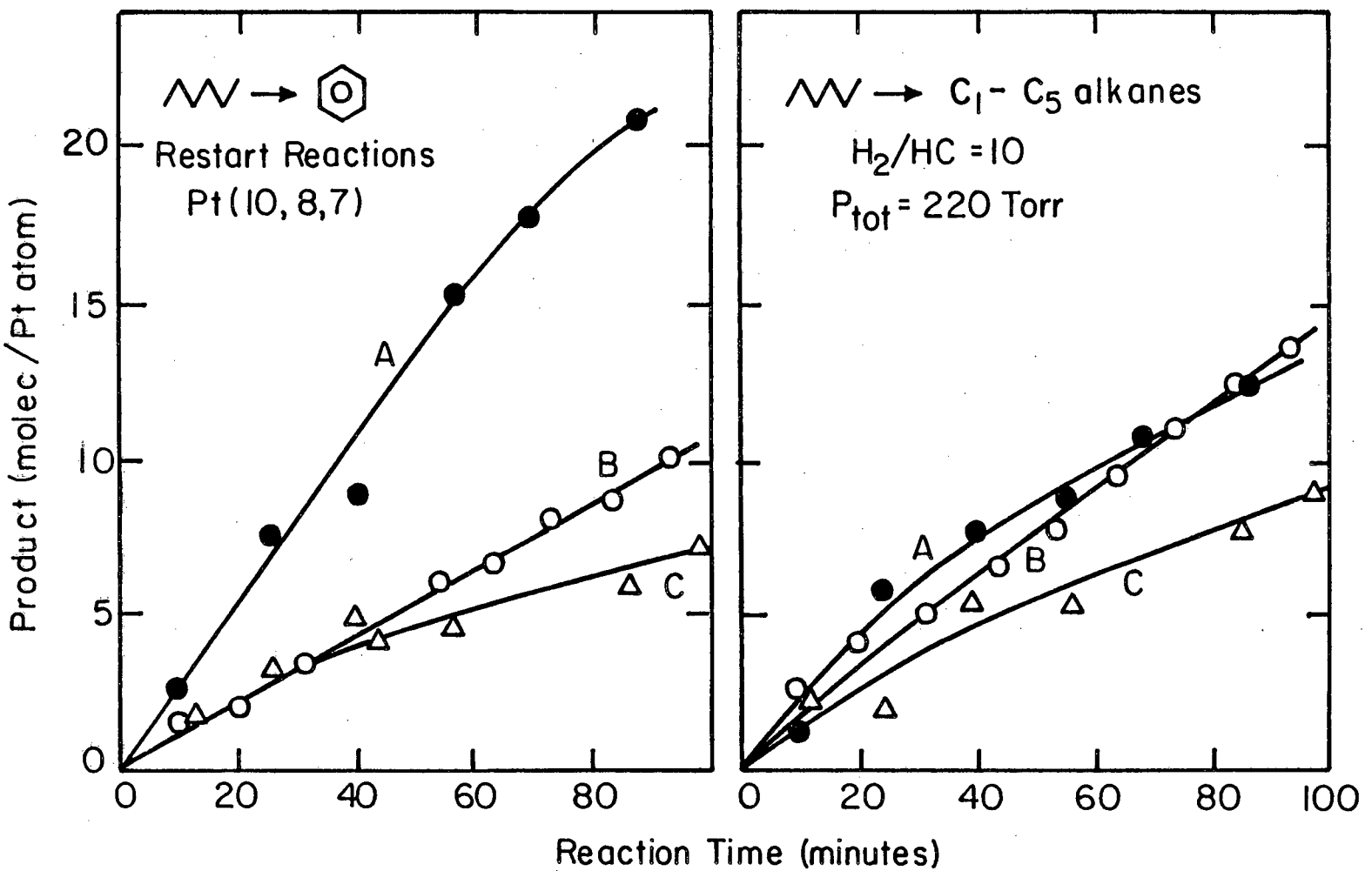

XBL 817-6091

Fig. 4.35

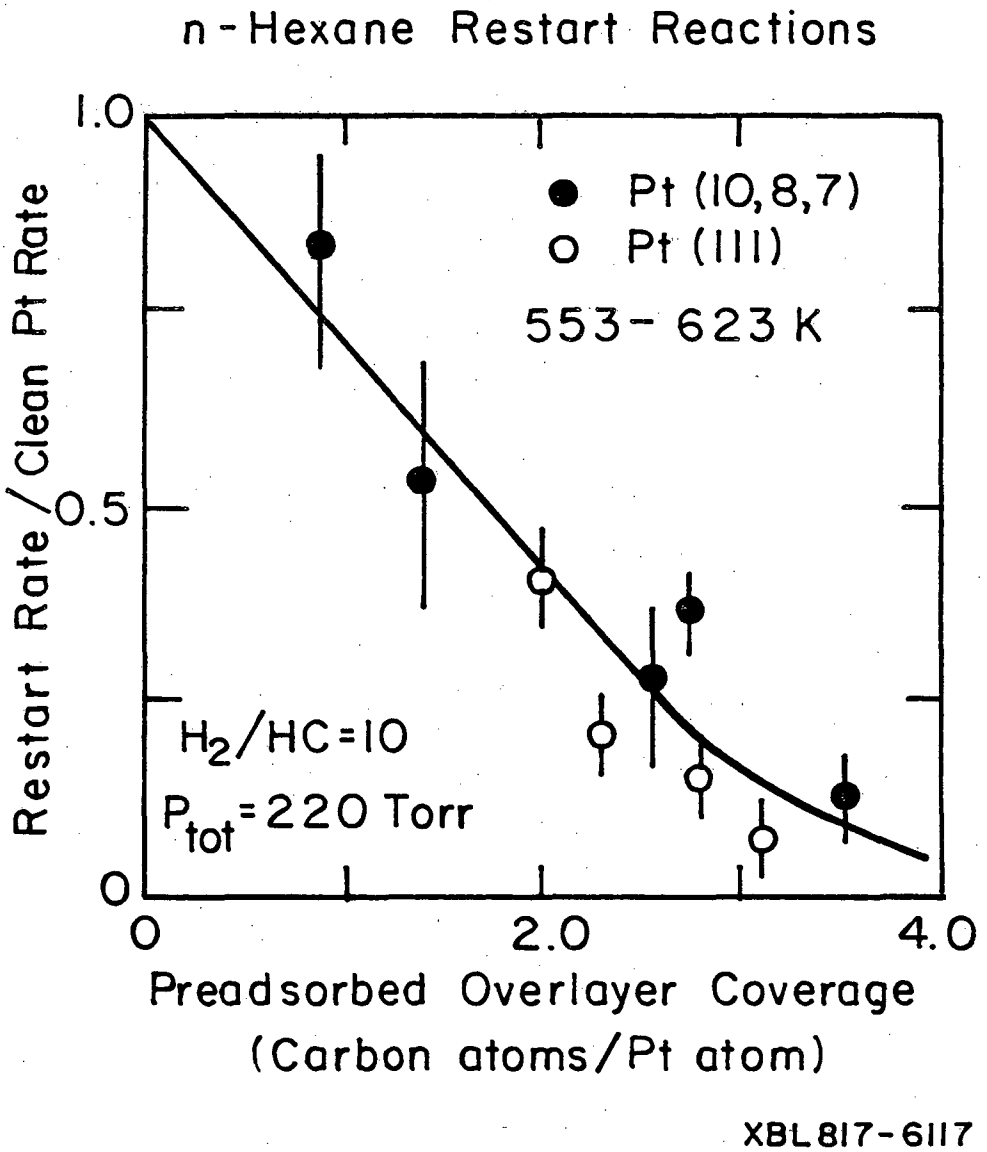
n-Hexane Restart Reactions
1.0
0.5
0
Restart Rate / Clean Pt Rate
Pt (10,8,7)
Pt (111)
553-623 K
H2/HC=10
Ptot=220 Torr
0
2.0
4.0
Preadsorbed Overlayer Coverage
(Carbon atoms/Pt atom)
XBL817-6117

Fig. 4.36

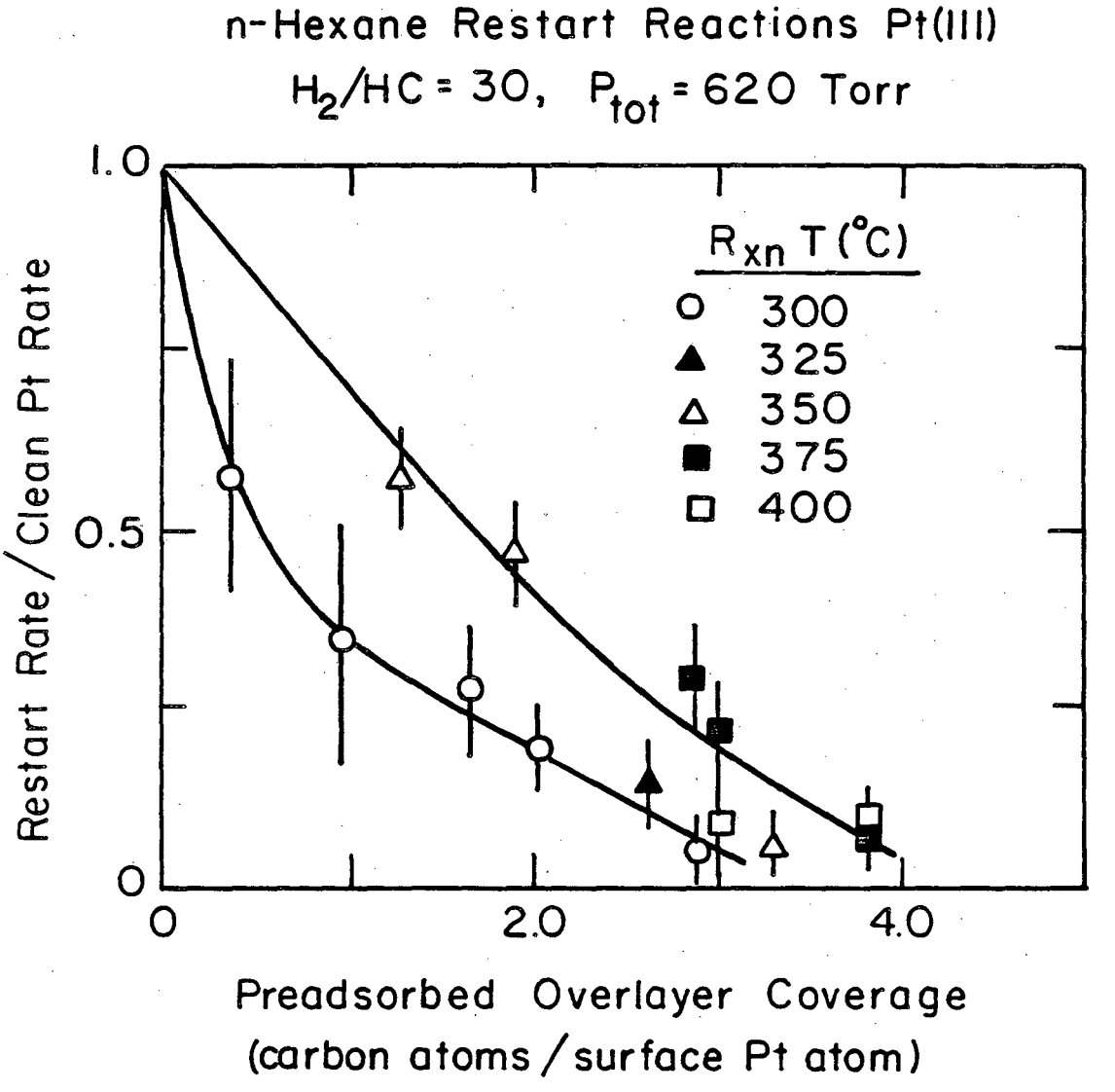
n-Hexane Restart Reactions Pt(111)
$H_2/HC = 30$, $P_{tot} = 620$ Torr
Restart Rate / Clean Pt Rate
1.0
0.5
0
0
2.0
4.0
R_{xn} T (°C)
300
325
350
375
400
Preadsorbed Overlayer Coverage
(carbon atoms / surface Pt atom)
XBL 816-5920

Fig. 4.37

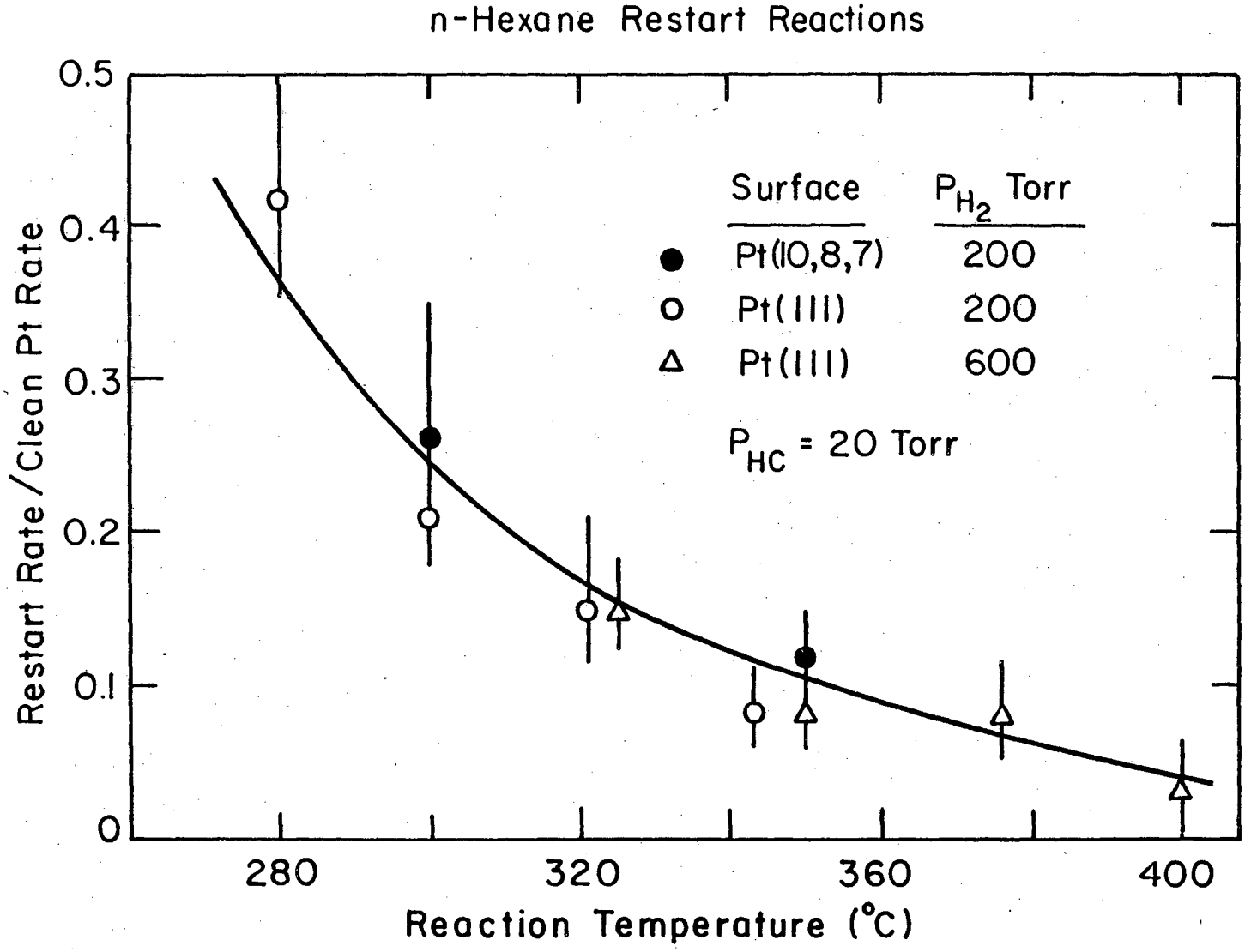

XBL 817-6118

Fig. 4.38

n-Hexane Conversion over Preadsorbed ^{14}C-C_6H_6 Layers

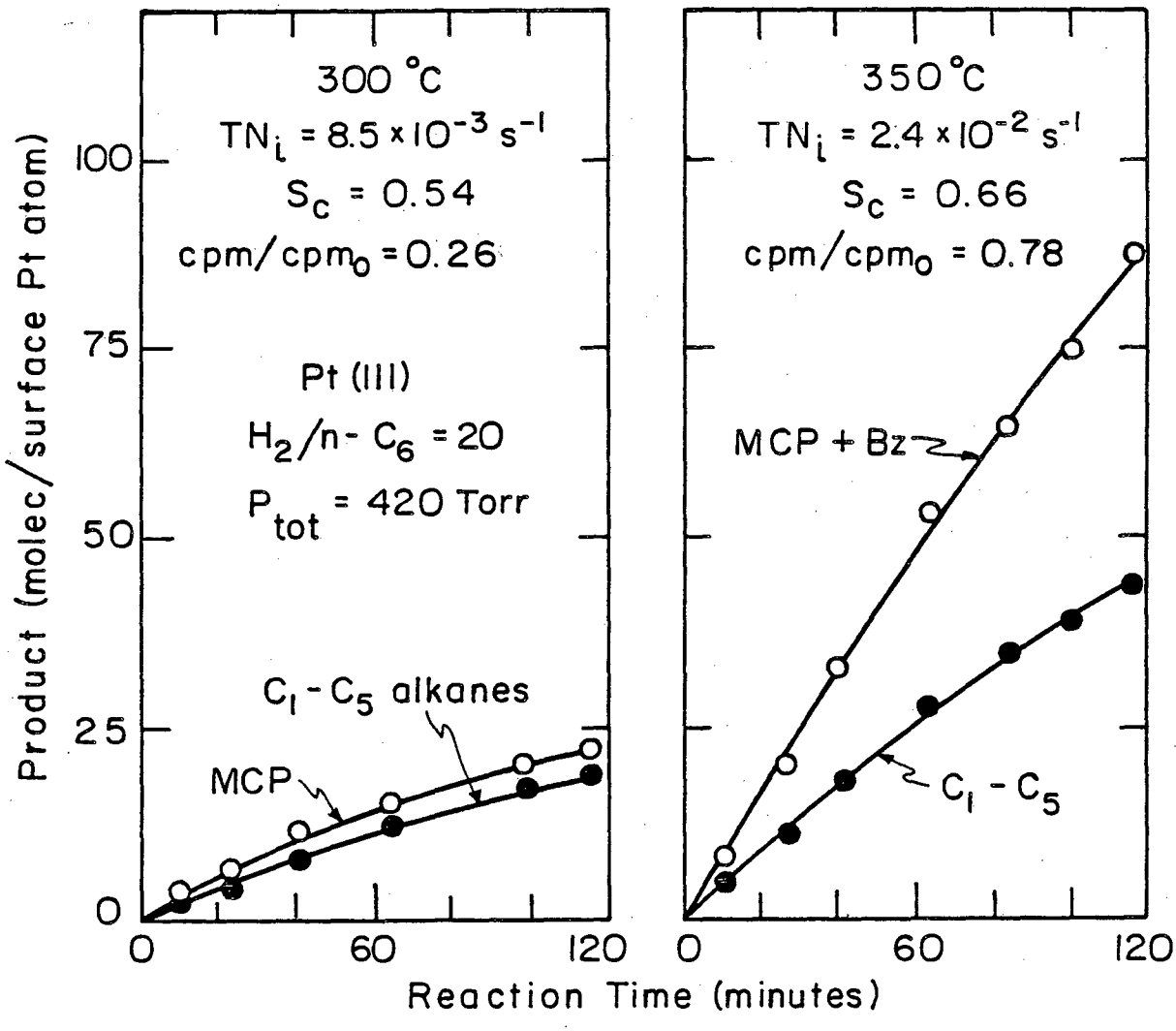

Fig. 4.39

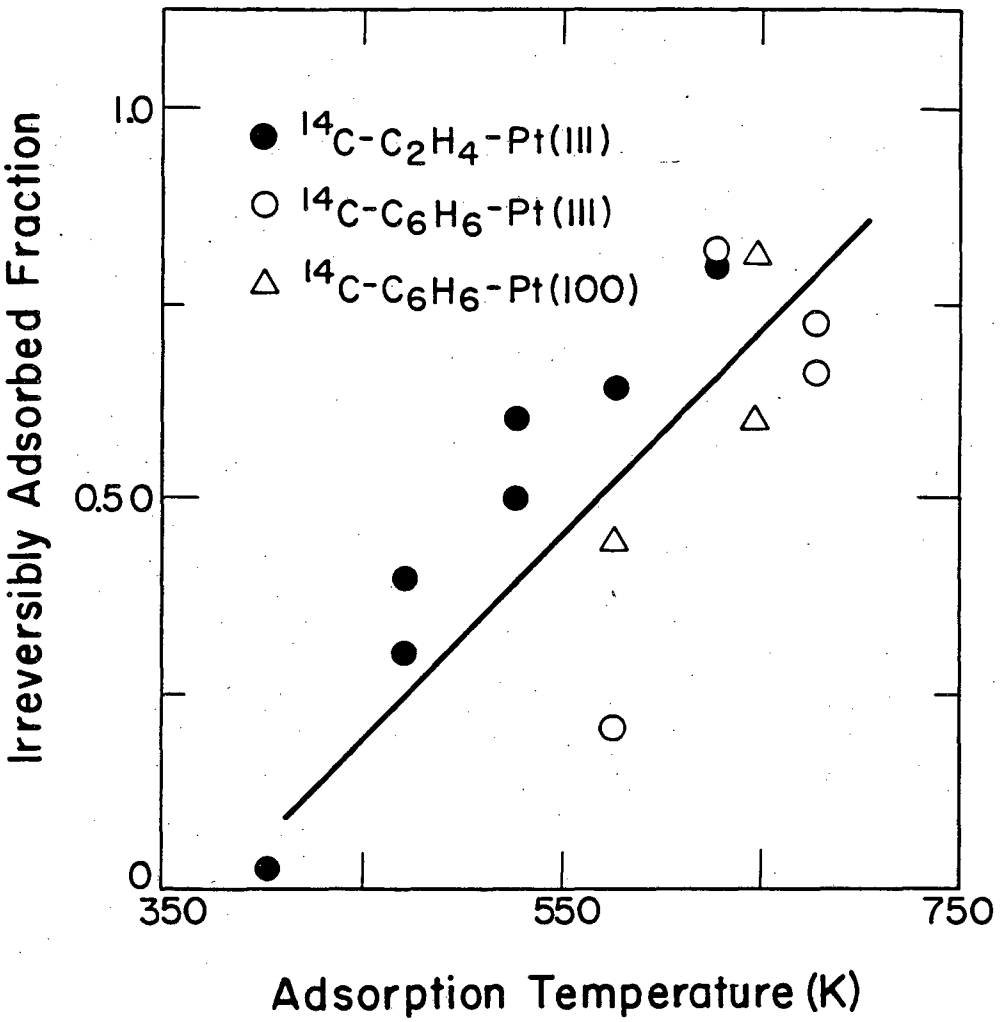

XBL 818-1096

Fig. 4.40

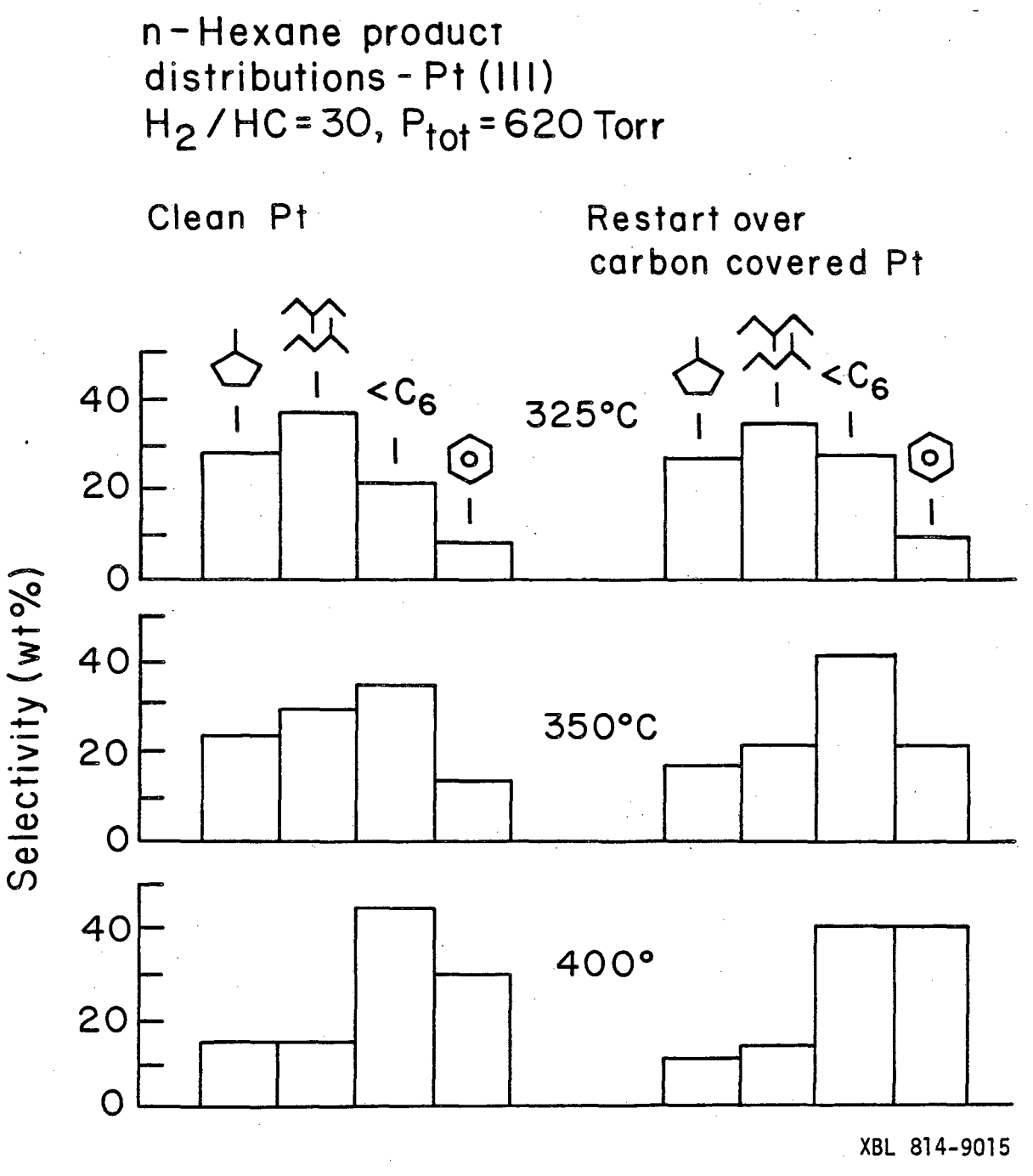
n-Hexane product
distributions - Pt (111)
H_2 / HC = 30, P_{tot} = 620 Torr
Clean Pt
Restart over
carbon covered Pt
<C6
325°C
350°C
400°
Selectivity (wt%)
40
20
0
XBL 814-9015

Fig. 4.41

4.7. Morphology of the Carbon Deposit: Titration of Uncovered Platinum Surface Sites by CO Chemisorption Following n-Hexane Reaction Studies

4.7.1. Background

The chemisorption of carbon monoxide on platinum single crystal surfaces has been investigated extensively using a variety of surface analysis techniques ranging from LEED (68), TDS (69,70), UPS (70), and dynamic work function measurements (70) to HRELS (71,72), reflection infrared spectroscopy (69), and modulated molecular beam scattering (73). These studies have provided a rather complete picture of the gas-solid interaction including surface structures, adsorption energetics, and repulsive lateral interactions. Carbon monoxide adsorption on the flat (111) platinum surface leads initially to a $(\sqrt{3} \times \sqrt{3})$-R30° surface structure which transforms upon further exposure to a c(4x2) structure and eventually compresses into a close packed overlayer of carbon monoxide molecules (68). Vibrational spectroscopy studies have revealed that the adsorbed molecules occupy only "atop" sites (ν_{CO} = 2080 cm^{-1}) at low coverages, whereas at saturation both atop and "bridge" sites (ν_{CO} = 1870 cm^{-1}) are occupied in roughly equal proportions (71,71). Because of repulsive interactions between the adsorbed species the desorption activation energy decreases from about 28 kcal/mole at low coverages to about 23 kcal/mole near saturation. Similar results were reported for the flat (100) and various stepped platinum surfaces (69,35).

The adsorption of CO on supported platinum catalysts has also been investigated in some detail (74), with emphasis focused on the

stoichiometry of adsorption; i.e., how many CO molecules are adsorbed per metal atom. The selective chemisorption of carbon monoxide is one of the most reliable experimental methods available for determining the exposed area of supported metal catalysts (75). The dispersion of supported platinum catalysts is sometimes determined in this manner (74) by assuming that one CO molecule is adsorbed per surface platinum atom. The major goal of this section is to show that the same selective CO adsorption technique can be used to titrate exposed (uncovered) platinum sites on single crystal surfaces. This technique was used to determine the concentration of uncovered platinum surface sites which remained following n-hexane reaction studies that were catalyzed at 540-700 K over the (100), (111), and (13,1,1) platinum single crystal surfaces.

Results presented in the previous sections of this chapter provided important information about the composition and reactivity of strongly bound carbon deposits that are always presented during hydrocarbon catalysis over platinum single crystal surfaces. The results strongly suggested that the carbon deposit is an unreactive polymeric residue whose primary role is that of a non-selective poison. According to this picture, a small concentration of uncovered platinum surface sites should always exist under steady state reaction conditions. These sites would be responsible for most (if not all) of the catalytic activity that is displayed by the carbon covered surfaces. In order to further confirm that this model is correct, information was required concerning the structure and morphology of the carbon deposit. Since

the carbon deposits were always disordered, low energy electron diffraction was clearly useless for this purpose. It was expected that if uncovered sites do exist on the carbon covered platinum surfaces, these sites should be detectable by selective chemisorption of hydrogen, CO, or other simple gases. As noted earlier, CO adsorption was indeed detected on the carbon covered surfaces, and the adsorption behavior was completely consistent with the model suggested above. Thermal desorption studies revealed that uncovered sites were always present at concentrations of 2–25 percent, even when the apparent coverage by the carbon deposit was equivalent to several layers of graphitic carbon. These results very clearly indicate that the carbon deposit assumes a 3-dimensional structure.

4.7.2. Results and Discussion

Carbon monoxide adsorption and thermal desorption studies were carried out for the clean (100), (111), and (13,1,1) platinum surfaces, the same surfaces after pretreatment with n-hexane at low pressures and 673–773 K, and the same surfaces following n-hexane reaction studies that were catalyzed near atmospheric pressure at temperatures between 540 and 700 K. Figures 4.42 and 4.43 compare CO thermal desorption spectra obtained under these conditions for the flat (111) and stepped (13,1,1) platinum surfaces. Spectra for Pt(100) were essentially identical to those shown for Pt(13,1,1). All the adsorptions were carried out at 300–310 K, and 36 L represented saturation exposure.

The clean (111) platinum surface displayed a single CO desorption peak centered at 440–490 K. Due to repulsive interactions, the temperature of the desorption peak maximum shifted to lower temperatures with increasing CO coverage. The clean Pt(13,1,1) surface exhibited a series of overlapping desorption peaks, the most prominent of which displayed a desorption peak maximum at about 565 K (560 K–Pt(100)). The position of this peak was not altered with increasing CO coverage.

The CO desorption spectra that were recorded following the n–hexane reaction rate studies always displayed very similar peak shapes and desorption peak temperatures to those determined for the initially clean platinum surfaces. However, the desorption peak areas were reduced markedly indicating that only a small concentration of uncovered sites remained after the high pressure reactions. It can be seen that the desorption peak areas decreased with increasing surface carbon coverage which is represented by the C_{273}/Pt_{237} AES peak–to–peak height ratio.

A distinctly lower desorption temperature was detected when CO was chemisorbed on the platinum surfaces that were pretreated with n–hexane at 10^{-7} Torr and temperatures between 673 and 773 K. The new desorption peak maxima appeared at about 430 and 490 K for Pt(111) and Pt(13,1,1), respectively. The graphitic–like surface carbon produced under these conditions reduced both the binding energy and the saturation coverage of the CO molecules.

Activation energies for CO desorption were estimated from the temperatures of the desorption peak maxima using Eq. (2.9) (which assumes first-order desorption kinetics with $\nu_1 = 10^{13}$ sec^{-1}). Figure 4.44 compares desorption activation energies as a function of CO coverage for the clean and graphite covered (111) and (13,1,1) platinum surfaces. The activation energies for CO desorption from the clean Pt(111) surface decreased from about 27 kcal/mole at zero coverage to roughly 24 kcal/mole at saturation. Activation energies for the (100) and (13,1,1) platinum surfaces varied between 29 and 31 kcal/mole ($E_d^{(100)} \approx E_d^{(13,1,1)} > E_d^{(111)}$). All the CO desorption activation energies appeared to be lowered by 3-4 kcal/mole when CO was coadsorbed in the presence of graphitic surface carbon.

The concentration of uncovered surface platinum sites which remained after the high pressure n-hexane reaction studies was estimated by comparing the CO desorption peak areas measured following the reactions with those determined for the clean platinum surfaces. In Fig. 4.45 the CO uptake determined following reaction rate studies has been divided by the saturation CO uptake for clean platinum surfaces, and the ratio $(\theta/\theta_o)_{CO}$ has been plotted as a function of the total surface carbon deposited by the reaction mixture. For comparison, CO uptake results for the graphite covered (111) and (13,1,1) platinum surfaces are also shown as a function of surface carbon coverage. Two points are of paramount importance: (1) at any given carbon coverage as determined by AES, much more CO was adsorbed following the high pressure reaction studies than on the graphite covered surfaces, and

(2) the shape of the CO uptake curve determined following the reaction studies displayed a striking resemblence to the restart catalytic activity curves discussed in Section 4.6 (e.g., Figs. 4.36 and 4.37). The formation of 3-dimensional carbonaceous islands during the high pressure reactions affords a very simple explanation for the first observation. It is not at all surprising that at elevated temperatures and pressures polymerization of the adsorbed species competes with skeletal rearrangement and leads to the growth of 3-D carbon islands with a hydrogen content in the range (H/C) = 1.0-1.6. The implications of this point are discussed further below. The great similarity of the CO uptake and restart catalytic activity curves as a function of surface carbon coverage provides rather decisive proof that uncovered platinum atoms are the active sites for all types of catalyzed hydrocarbon conversion reactions. This conclusion is entirely consistent with the fact that little or no change in reaction selectivity was detected in the restart reactions. Uncovered platinum sites that are present in low concentrations do not appear to be affected either structurally or electronically by the presence of the carbon deposit. These sites maintain their normal, unique level of high activity and extraordinary selectivity even at very high coverages that exceed 3-4 carbon atoms per surface platinum atom.

In the upper frame of Fig. 4.46, the concentration of uncovered platinum sites determined by CO adsorption-desorption is shown as a function of reaction temperature. As expected from the deactivation

analysis presented in Chapter 3 and the restart reactions discussed in Section 4.6, the concentration of vacant sites decreased with increasing reaction temperature. The scatter apparent in these data mainly arises from differences in reaction times (60–130 min) and hydrogen pressure ($P^{(111)}$ = 600 Torr, $P^{(100)} = P^{(13,1,1)}$ = 200 Torr).

If uncovered platinum sites are the exclusive source of catalytic activity for n-hexane reforming reactions, one would expect that a linear (or higher order) correlation should exist between reaction rates and the concentration of uncovered surface sites. An attempt to establish such a correlation is shown in the lower frame of Fig. 4.46. Final rates determined at the end of the n-hexane reaction studies were divided by initial rates in the same reactions and plotted as a function of the fractional concentration of uncovered sites. All the data fall into a broad envelope corresponding to a fractional (0.6–0.9) order dependence of the final rates on vacant sites. This dependence would be naturally expected if (1) hydrogen transfer reactions between the carbon deposit and reactant molecules contribute to the overall catalytic activity, (2) the concentration of uncovered sites determined by CO adsorption is underestimated, or (3) the initial rates are underestimated because a certain amount of carbon is deposited instantly as the reactions commence. Background catalytic activity could also contribute to the deviation from first-order behavior. Which of these effects is most important cannot be readily determined from the existing data. Considering the uncertainty involved in the

determination of reaction rates and uncovered sites, the deviation from first order behavior cannot be considered very significant.

The CO adsorption studies clearly suggest that the growth of 3-dimensional carbonaceous islands takes place during hydrocarbon catalysis over platinum single crystal surfaces. The average thickness of these islands can be roughly estimated using a homogeneous attenuation model for AES peak intensities (Section 2.2) together with the concentration of uncovered platinum sites that was determined by CO thermal desorption. According to this model the average overlayer thickness is given by

$$Z = \lambda_s \left\{ \ln(1 - (\theta/\theta_o)_{CO}) - \ln(I_s/I_s^o - (\theta/\theta_o)_{CO}) \right\} \qquad (1)$$

where λ_s is the attenuation length for the substrate Auger electrons, I_s is the substrate Auger peak intensity, and I_s^o is the AES peak intensity for the initially clean surface. Evaluation of Eq. (1) for the 237 eV platinum Auger transition with λ_s = 7Å yielded values of the average overlayer thickness which increased with increasing reaction temperature from about 5-7Å at 550 K to 10-14Å at 670-700 K. These figures should not be taken too seriously as it is not known if the carbon deposit assumes a uniform thickness. However, the implication that the average thickness increases with increasing temperature is highly notable. The deactivation kinetics discussed in Chapter 3

were well described by the rate equation $R(t) = R(t=0)\ \exp(-\alpha t^n)$ where n decreased from about one at 540-560 K to 0.3-0.5 at 620-670 K. This change in order for the deactivation reaction with increasing temperature is naturally expected if the structure of the carbon deposit changed from two dimensional at low temperatures to three dimensional at high temperatures. The existing experimental data certainly tend to indicate that this change takes place.

The shapes and positions of the CO desorption peaks obtained following the n-hexane reactions also provide important information about the structure of the uncovered platinum sites. At very high carbon coverages the temperature of the CO desorption peak maximum for Pt(111) was about 570 K, whereas at lower carbon coverages the desorption peak maximum was shifted to about 540 K. This shift largely results from repulsive interactions between the adsorbed CO molecules (69). The fact that the CO desorption temperature at high carbon coverages ($C_{273}/Pt_{237} \gtrsim 5$) was very similar to that determined for the clean Pt(111) surface in the limit of zero CO coverage (~485 K) strongly suggests that the uncovered sites are mostly isolated, i.e., only 1-10 adjacent atoms. By contrast, the CO desorption temperature at lower carbon coverages ($C_{273}/Pt_{237} = 1\text{-}3$) was close to that measured for clean platinum at saturation CO coverage (~540 K). In this case it appears that the uncovered platinum sites exist in the form of patches which contain enough metal atoms for the lateral interactions to become important. Dipole coupling calculations by Crossley and King (69) suggest that this is possible only if the un-

covered patches contain at least 10–20 contiguous platinum atoms. This apparent change in the size of the available sites with increasing temperature (carbon coverage) may contribute to the small changes in reaction selectivity that were often detected in the restart experiments.

Finally, it must be noted that the CO adsorption results are inconsistent with the idea that carbon may be dissolved into the near surface region. Extensive dissolution of surface carbon during the high pressure reactions would likely result in major restructuring within the topmost surface layer. Such restructuring would cause the appearance of new adsorbate binding states as observed for CO adsorption on oxidized Pt(111) and Pt(110) (76,77) and sulphidized Pt(110) (78) and Fe(100) (79). No evidence for any such states was ever detected. In addition, the hydrogen TDS results clearly revealed that the carbon deposit is extensively hydrogenated with at least one hydrogen atom per surface carbon atom. It is difficult to imagine a process in which CH_x fragments could be stabilized in the subsurface region. While the possibility that a part of the carbon is dissolved in the near surface region cannot be conclusively ruled out, the experimental evidence certainly tends to demonstrate that most of the carbon deposit is formed on the external surface.

FIGURE CAPTIONS

Fig. 4.42. Comparison between CO thermal desorption spectra for the clean (111) platinum surface (left frame), Pt(111) following n-hexane reaction rate studies (middle frame); and Pt(111) following the preadsorption of n-hexane at 673 K (right frame). The adsorption temperature was 310-315 K and $\beta \simeq$ 90 K/sec.

Fig. 4.43. Comparison between CO thermal desorption spectra for the clean (13,1,1) platinum surface (left frame), Pt(13,1,1) following n-hexane reaction rate studies (middle frame), and Pt(13,1,1) following the preadsorption of n-hexane at about 670 K (right frame). The adsorption temperature was 310-315 K and $\beta \simeq 80$ K/sec.

Fig. 4.44. Activation energies for CO desorption as a function of the fractional CO coverage on the (13,1,1) and (111) platinum surfaces. The activation energies were calculated using the Redhead method (Section 2.2.3) assuming $\nu_1 = 10^{13}$ sec^{-1}.

Fig. 4.45. Fractional concentrations of uncovered platinum surface sites determined by CO adsorption-desorption as a function of surface carbon coverage on the (100), (111), and (13,1,1) platinum surfaces. A comparison is made between the CO uptake determined following n-hexane reaction studies and CO uptake determined when CO was coadsorbed with "graphitic" surface carbon.

Fig. 4.46. Fractional concentrations of uncovered platinum surface sites determined by CO adsorption-desorption following n-hexane reaction studies on the (100), (111), and (13,1,1) platinum surfaces are shown as a function of reaction temperature (upper frame). Final rates estimated at the end of the n-hexane reaction studies have been divided by initial rates on clean platinum and plotted as a function of the fractional concentration of uncovered sites (lower frame).

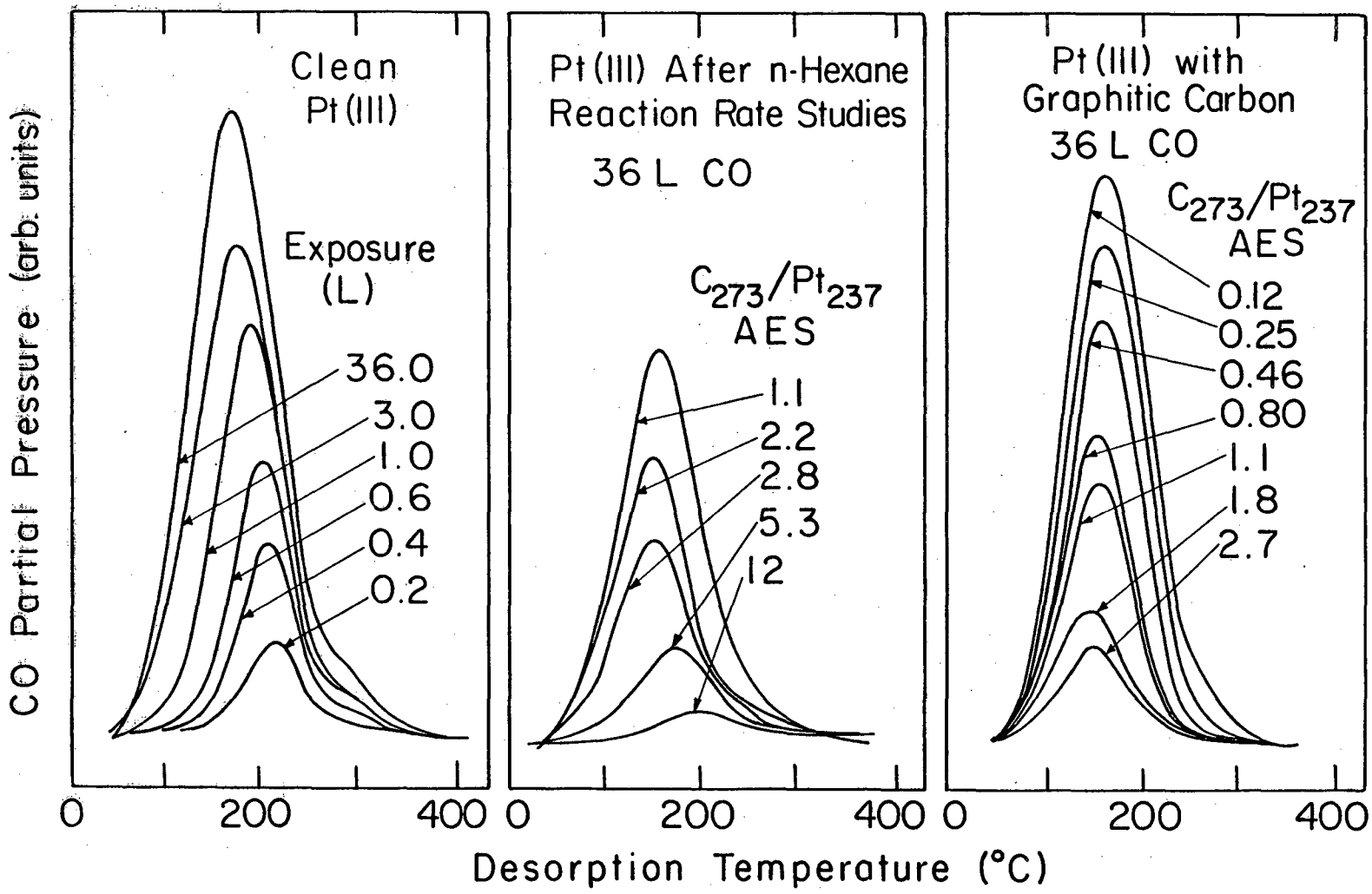

XBL 815-5661

Fig. 4.42

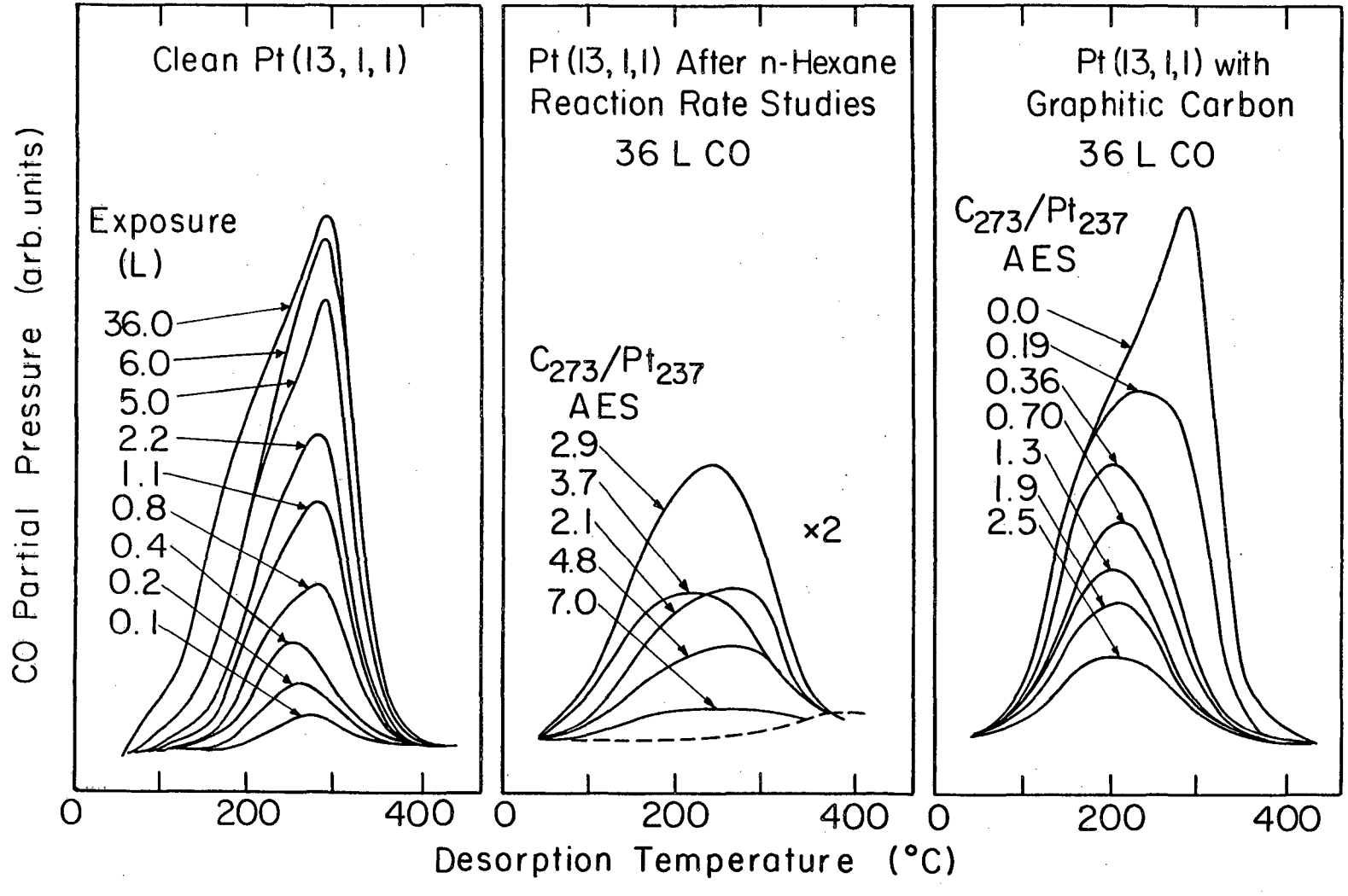

Fig. 4.43

X BL 815-5662

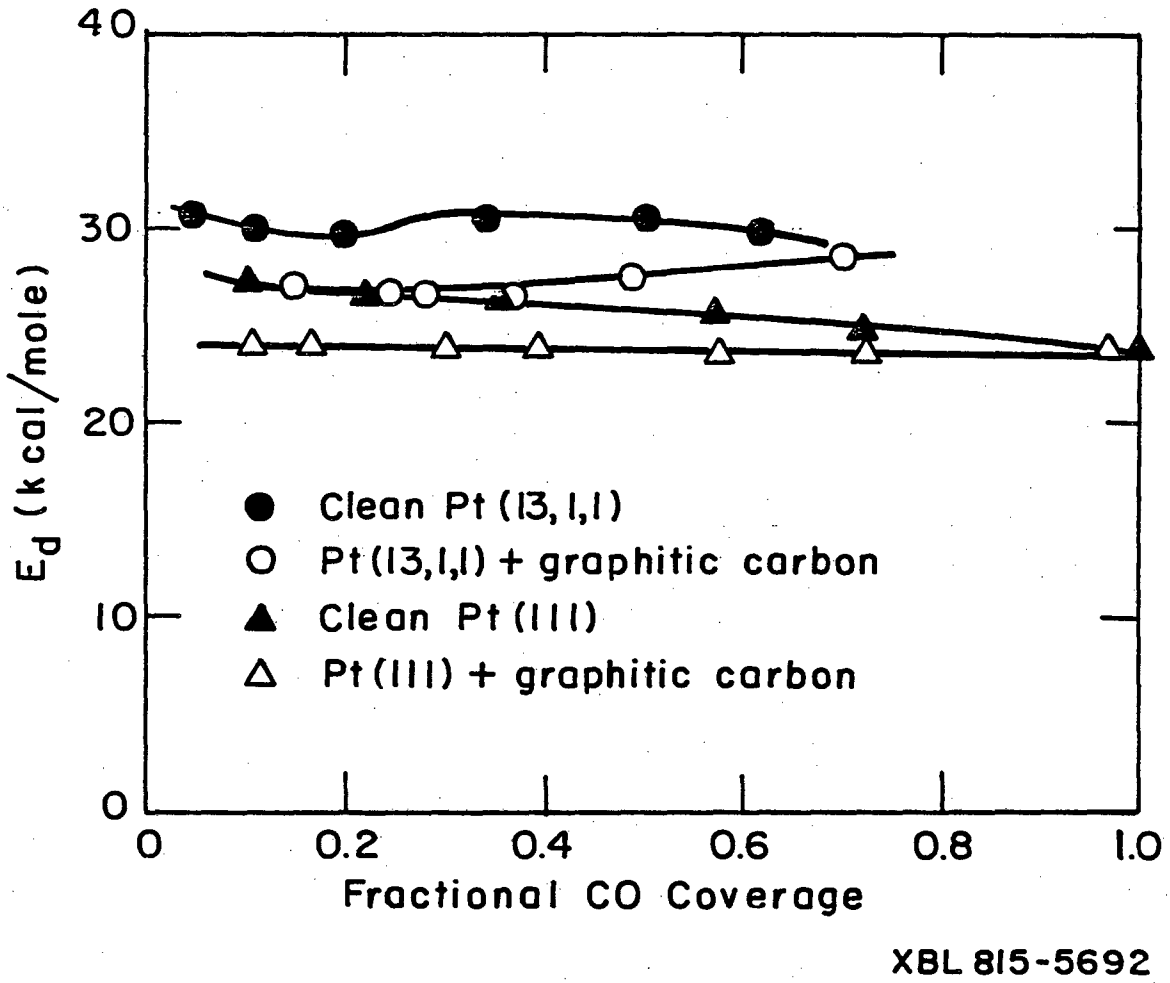
40
30
20
10
0
E_d (kcal/mole)
0
0.2
0.4
0.6
0.8
1.0
Fractional CO Coverage
Clean Pt (13, 1, 1)
Pt (13, 1, 1) + graphitic carbon
Clean Pt (111)
Pt (111) + graphitic carbon
XBL 815-5692

Fig. 4.44

CO Chemisorption on Carbon Covered Pt(111), Pt(100) and Pt(13, 1,1)

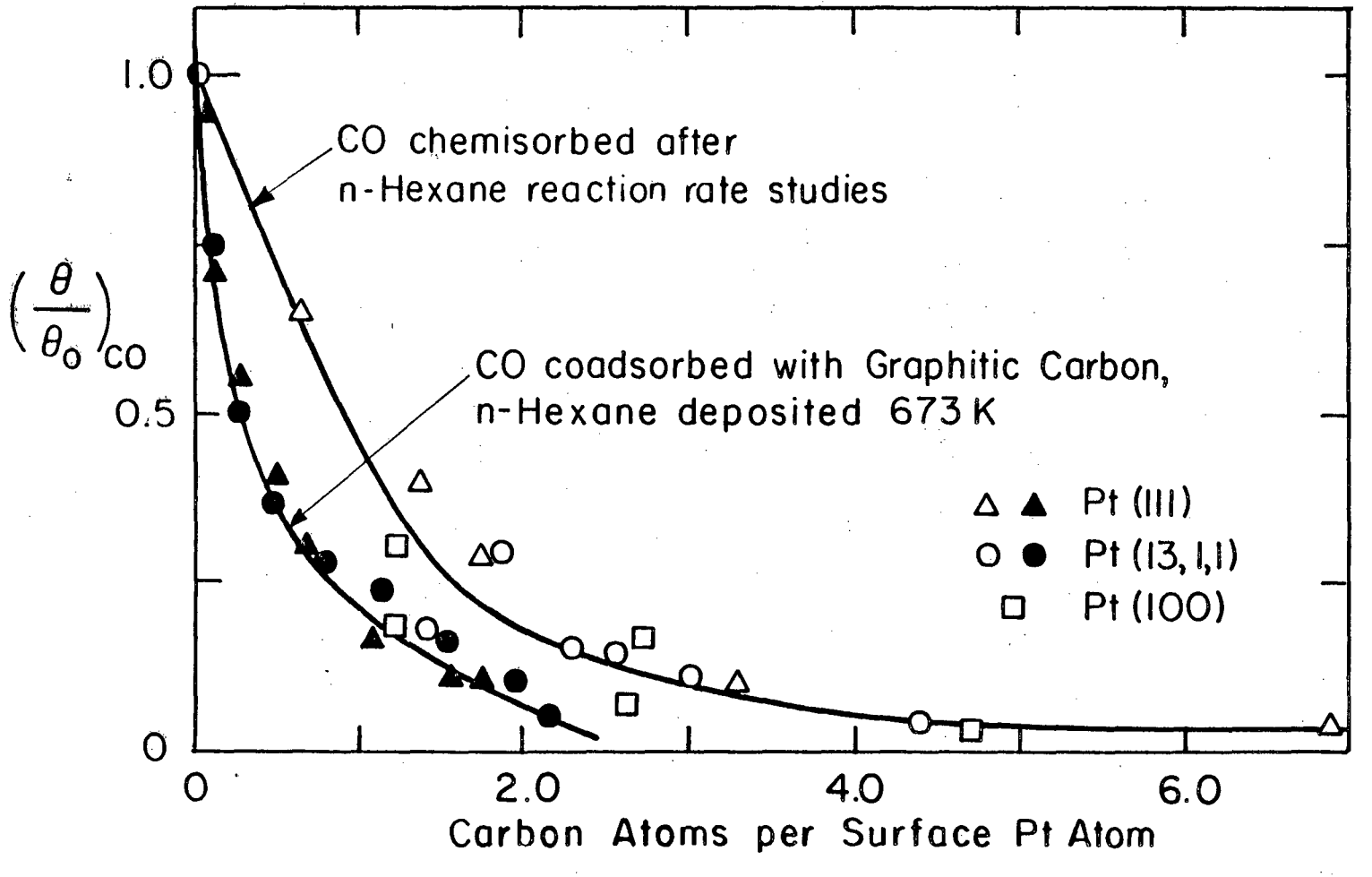

Fig. 4.45

XBL 816-5851

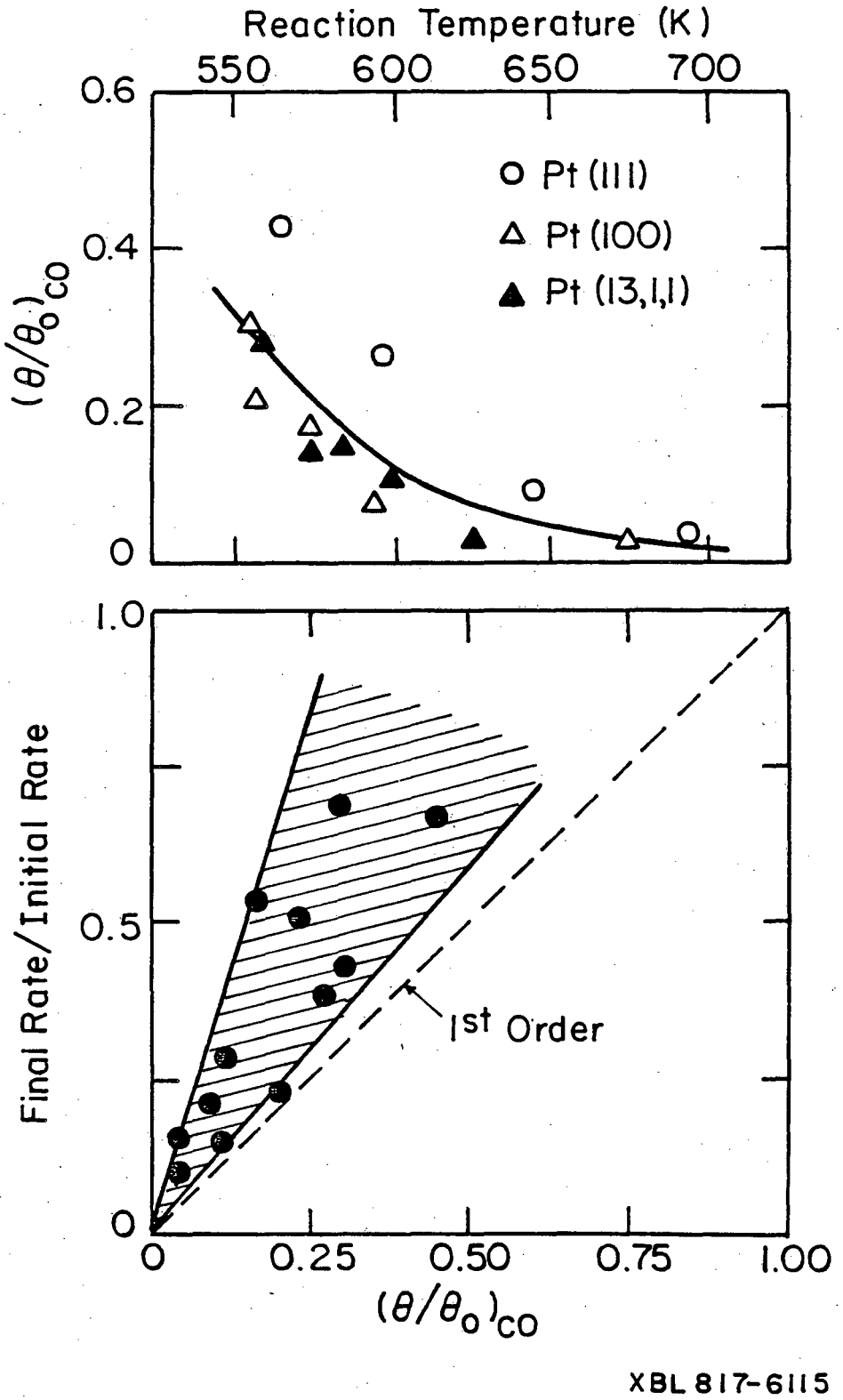
Reaction Temperature (K)
550
600
650
700
0.6
0.4
0.2
0
$(\theta/\theta_0)_{CO}$
Pt (111)
Pt (100)
Pt (13,1,1)
1.0
0.5
0
Final Rate/Initial Rate
1st Order
0
0.25
0.50
0.75
1.00
$(\theta/\theta_0)_{CO}$
XBL 817-6115

Fig. 4.46

4.8. Model for the Role of Adsorbed Carbon Deposits in Hydrocarbon Catalysis over Platinum

The ultimate goal of this research was to provide a detailed conclusion regarding the role of strongly adsorbed hydrocarbon deposits in hydrocarbon catalysis over platinum. In Chapter 3 emphasis was focused on the reaction dynamics and structure sensitivities (site-requirements) of catalyzed hydrocarbon skeletal rearrangement reactions. Average surface residence times under reaction conditions required for hydrogenation-dehydrogenation (10^{-2}-1 sec) and skeletal rearrangement (1-10^{3} sec) were established. In this chapter special attention was devoted to the temperature dependent bonding characteristics of chemisorbed hydrocarbons, the effects of surface carbon deposits on catalytic activity and selectivity, and several pertinent properties of the carbon deposit, most notably its composition, reactivity, and morphology. These properties were investigated using new applications for a variety of long-established surface analysis methods. The new techniques revealed that almost any type of experiment which is possible using practical catalysts can be carried out better using small area single crystal catalysts. The purpose of this section is to summarize the major conclusions of the combined surface science and catalysis studies. The same conclusions should be more-or-less applicable in other areas of catalysis that involve carbon containing molecules (e.g., Fischer-Tropsch synthesis and hydrotreating).

Temperature Dependent Catalytic Behavior of Hydrocarbons Chemisorbed on Platinum. The reaction chemistry of hydrocarbons chemisorbed on platinum is characterized by three distinguishable temperature regimes in which the bond strength, bond-multiplicity, and catalytic behavior of the metal-organic layer are distinctly different;

(1) Low temperatures ($\leq$300 K)
Reversible hydrocarbon chemisorption
Clean metal catalysis at high hydrogen pressures

(2) High temperatures ($\gtrsim$750 K)
Multilayer carbon build-up
Poisoning by graphitic coke

(3) Medium temperatures (~350-700 K)
Reversible (1 atm) or irreversible (10^{-7} Torr) adsorption with sequential bond breaking, skeletal rearrangement and intermolecular hydrogen transfer.
Catalysis by active C_xH_y fragments at high hydrogen pressures (~1 atm)

Provided that the temperature is low enough ($\lesssim$300 K), hydrocarbons chemisorb molecularly, or at least more-or-less reversibly, on any platinum surface. Alkanes are dissociatively adsorbed to a very small extent. Thermal desorption studies provided adsorption energies for simple alkanes, olefins, and benzene that varied from about 10 to 20 kcal/mole. In the presence of 1 atm of hydrogen these weakly adsorbed species readily undergo hydrogen addition and deuterium exchange processes which continuously regenerates the clean metal active sites that are responsible for these reactions. At the other extreme, if the temperature is higher than about 750 K (700 K, 10^{-7} Torr; $\gtrsim$800 K 1 atm) all hydrocarbons adsorb dissociatively and irreversibly leading to the growth of graphitic carbon islands that eventually

condense into continuous overlayers that poison all catalytic activity. In the more interesting intermediate temperature range of about 350–700 K, the adsorbed species rapidly undergo sequential C–H bond breaking, skeletal rearrangements, and hydrogen transfer processes that produce catalytically active C_xH_y fragments that constitute the catalytically active surface. Over this temperature range, hydrogenation, dehydrogenation, and deuterium exchange all occur at rates that are typically $10–10^3$ times faster than skeletal rearrangement. Under these conditions, (1) uncovered metal sites remain available for hydrogen and hydrocarbon chemisorption, and (2) dissociatively adsorbed reaction intermediates exist in quasiequilibrium with gas phase hydrogen. The uncovered platinum sites are responsible for the unique selectivity of platinum catalysis. The existence of these sites also accounts for the structure sensitivities that are often displayed during alkane skeletal rearrangement. Aromatization activity and selectivity was maximized on flat, stepped, and kinked platinum surfaces with (111) terraces. The low coordination number step and kink atoms were particularly effective for catalyzing n-heptane aromatization (80). By contrast, the less important bond shift isomerization reactions of butanes occurred preferentially on platinum surfaces with (100) terraces. The specific reaction chemistry that is displayed by each type of site appears to depend strongly on both the local stereochemistry and electronic properties of that site. For certain reactions such as aromatization and bond-shift isomerization, the reaction

selectivity can be predictably tailored by controlling the terrace structure and the concentrations of steps and kinks.

Nature of the Working Catalyst Surface Composition. A model for the working surface composition of platinum reforming catalysts that emerges from this research is shown in Fig. 4.47. Auger electron spectroscopy revealed that during steady state hydrocarbon conversion, platinum surfaces always become covered with about one or more monolayers of strongly bound carbonaceous deposit. In the absence of other chemical additives, the formation of this carbon deposit must be considered as a fundamental feature of the catalytic chemistry. The carbon deposit resulted from the activated nucleation and growth ($E_a \approx$ 10–20 kcal/mole) of unreactive polymeric islands with an average hydrogen content of about 1.0–1.5 hydrogen atoms per surface carbon atom. The structure of this deposit varied from two-dimensional at low temperatures ($\lesssim$570 K) to three-dimensional at high temperatures ($\gtrsim$600 K). Catalyst deactivation kinetics together with radiotracer and restart reaction kinetics demonstrated that the primary role of this carbon deposit was that of a non-selective poison, i.e., the deposit simply blocks platinum surface sites from incident reactant molecules. Perhaps the most important chemical property of the carbon deposit was its dynamic ability to exchange hydrogen with reacting surface species. Existing evidence suggests that this property may alter the selectivity of skeletal rearrangement at high reaction temperatures ($\gtrsim$600 K).

Carbon monoxide adsorption-desorption studies revealed that a small concentration of uncovered platinum surface sites (ca 2-25 percent) always persists in the presence of this carbon deposit. The uncovered sites appear to exist in the form of patches or ensembles that contain several contiguous surface atoms. The concentration of these sites decreases with increasing reaction temperature. The existence of these exposed, multiatomic sites is essential to rationalize the high selectivities for hydrogenolysis and aromatization that are displayed by carbon covered platinum.

Another important feature of the catalyzed hydrocarbon reactions was the long surface residence times of the dissociatively chemisorbed intermediates which were on the order of seconds. Within this residence time the adsorbed species can diffuse over long distances (e.g., 10^{-8}-10^{-3} cm) and visit many different types of surface sites. All sites that are contained in an uncovered patch can therefore become available for sequential bond breaking and skeletal rearrangement. It may even be possible for the adsorbed species to visit adjacent ensembles by diffusing over or through the strongly bound carbonaceous deposit. Creative experiments are required to further investigate the mobility of the adsorbed species.

The chemical composition of the carbonaceous deposit was intermediate between that expected for polyacetylene (H/C = 1.0) and polyethylacetylene (H/C = 1.5), or related surface species such as (I) and (II).

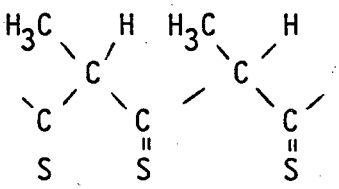

(H/C = 4/3)

(I)

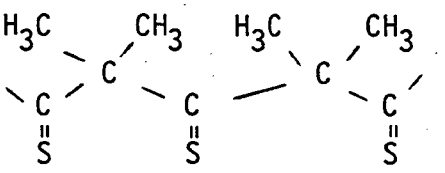

(H/C = 1.5)

(II)

The actual structure of the deposit appears to be heterogeneous and cannot be determined from the existing data. However, a polymeric residue is clearly required to account for the low reactivity and high hydrogen content of this surface species. Paal and Tetenyi (81) previously proposed that an organic layer consisting of polyolefins is responsible for catalyst deactivation during skeletal rearrangement of hexadienes and hexatrienes over platinum black.

Implications for Alloy Catalysis and Hydrocarbon Catalysis by Other Group VIII Metals. Very few, if any, commercial reforming processes continue to use catalysts that are based exclusively on platinum as the metal component. Instead, bifunctional catalysts consisting of bimetallic alloys dispersed on acidic supports that are selectively poisoned with sulfur and alkali metal ions (to inhibit hydrogenolysis) have become the state-of-the-art petroleum reforming catalysts. As compared to platinum alone, the bimetallic alloys such as Pt-Re, Pt-Au, Ir-Au, and Pd-Au offer superior activity, selectivity, and poison resistance (82). The improved poison resistance of the Group VIII-Group IB alloys can be easily understood in the context of the present research. Since Group IB metals do not form strong bonds with hydrocarbon adsorbates, the formation of carbonaceous deposits with high

metal-organic bond multiplicity cannot take place. Polymerization of the adsorbed species that is required for the formation of carbonaceous deposits still can and probably does occur at exposed Group VIII metal sites. However, since these sites are isolated and mostly surrounded by a matrix of inactive sites, any process that leads to rehydrogenation at the active sites will be accompanied by permanent removal of the carbonaceous deposit. In this case, the larger hydrocarbon molecules can easily desorb or "spill-over" onto the acid sites of the support where hydrocracking takes place. With platinum alone, the carbon deposit can readily form multiple bonds with several adjacent metal atoms. The probability that rehydrogenation will take place simultaneously at multiple sites is vanishingly small. As such, the nucleation and growth of carbonaceous deposits on pure platinum is effectively irreversible.

It is natural to ask if the same type of stable, strongly bound polymeric residues will be present during hydrocarbon catalysis over other Group VIII metals. While insufficient information now exists for a general conclusion, it appears likely that polymeric carbon deposits may be unique to platinum and perhaps also nickel or palladium catalysts. The reason for suggesting this is shown clearly in Fig. 4.48 where a comparison is made between rhenium and all the metals of Group VIII for several alkane hydrogenolysis reactions (83). The periodic pattern of reactivity displayed for these reactions does not depend appreciably on the alkane, surface structure, or catalyst type. Within the 4d and 5d series, maximum activity is always observed with

rutherium and osmium catalysts, i.e., in the first subgroup of Group VIII. From ruthenium to palladium, and osmium to platinum, the hydrogenolysis activity decreases by 6-9 orders of magnitude. In the first transition series, cobalt and nickel both exhibit comparably high activity. The very low hydrogenolysis activity of platinum catalysts may account in part for the high stability of the carbonaceous deposit, since, once formed, the polymeric residue has only a small probability for undergoing C-C bond breaking processes that would lead to its continuous decomposition and removal. By contrast, with active hydrogenolysis metals such as ruthenium, rhodium, osmium, and iridium, it appears likely that continuous hydrogenolysis and decomposition reactions may preclude the formation of polymeric carbonaceous deposits. This proposal could be easily tested by reaction rate studies over single crystal surfaces of other Group VIII metals.

FIGURE CAPTIONS

Fig. 4.47. Model for the working surface composition of platinum reforming catalysts.

Fig. 4.48. Periodic variation in the catalytic activity of metal catalysts for alkane hydrogenolysis reactions catalyzed near atmospheric pressure (83).

MODEL FOR THE WORKING PLATINUM CATALYST

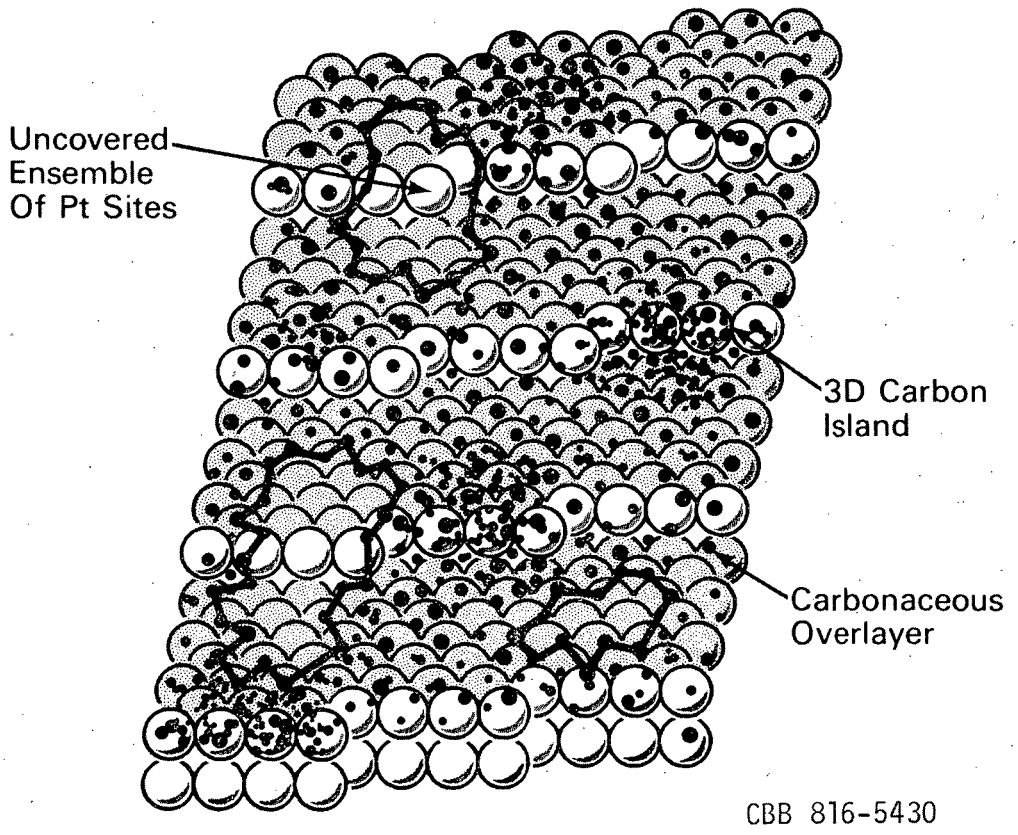

Fig. 4.47

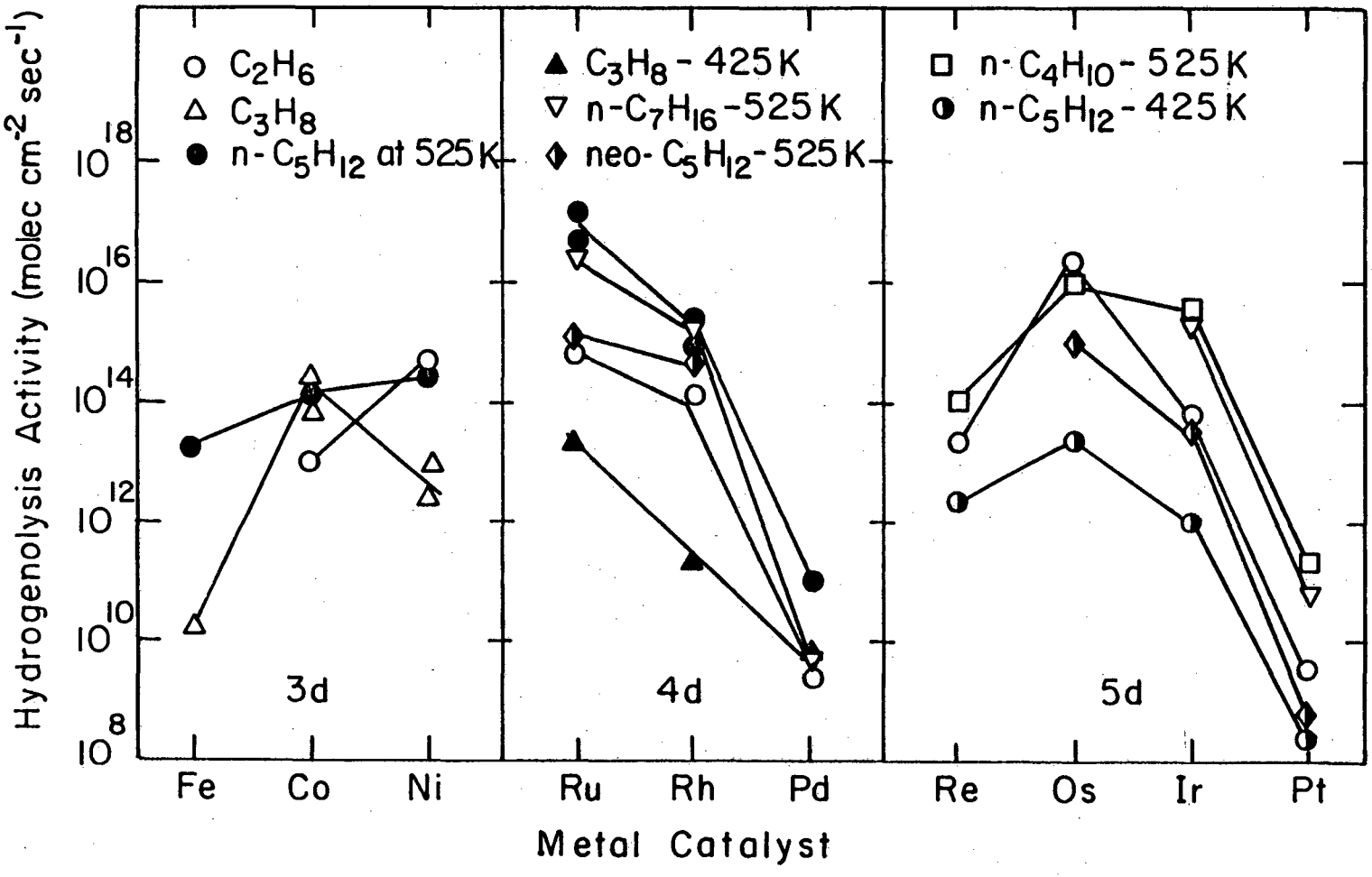

XBL803-4868

Fig. 4.48

REFERENCES

1. See, for example, W. M. H. Sachtler, Discovery 26, 16 (1965).
2. P. Sabatier, Ber. Deutsche Chem. Ges. 44, 2001 (1911).
3. T. E. Madey and J. T. Yates, Jr., Surf. Sci. 76, 397 (1978).
4. M. Salmeron and G. A. Somorjai, J. Phys. Chem., in press.
5. L. Firment, Ph. D. Thesis, University of California, Berkeley, 1977.
6. M. L. H. Green, "The Transition Elements," in Organometallic Compounds, Vol. 2, Chapman and Hall, London, 1977, p. 21; F. R. Hepner, K. N. Trueblood, and H. J. Lucas, J. Amer. Chem. Soc. 74, 1333 (1952) and references therein.
7. P. N. Ross, Jr., J. Electrochem. Soc. 126, 67 (1979); 126, 78 (1979).
8. K. Christmann and G. Ertl, Surf. Sci. 60, 365 (1976).
9. M. Salmeron, R. J. Gale, and G. A. Somorjai, J. Chem. Phys. 70, 2807 (1979) and references therein.
10. K. E. Lu and R. R. Rye, Surf, Sci. 45, 677 (1974); J. Vac. Sci. Technol. 12, 334 (1975).
11. K. Christmann, G. Ertl, and T. Pignet, Surf. Sci. 54, 365 (1976).
12. D. M. Collins and W. E. Spicer, Surf. Sci. 69, 85 (1977).
13. R. W. McCabe and L. D. Schmidt, Proc. 7th Intern. Vacuum Congr. and 3rd Intern Conf. Solid Surfaces, Vienna, 1977, p. 1201.
14. A. M. Baro and H. Ibach, Surf. Sci. 92, 237 (1980).
15. A. M. Baro, H. D. Bruchman, and H. Ibach, Surf. Sci. 88, 384 (1979).

16. J. P. Candy, P. Fouilloux, and M. Primet, Surf. Sci. 72, 167 (1978).

17. M. Primet, J. M. Basset, M. V. Mathieu, and M. Prettre, J. Catal. 28, 368 (1973).

18. S. M. Davis and G. A. Somorjai, J. Catal. 65, 78 (1980).

19. P. C. Aben, J. C. Platteeuw, and B. Southamer, Proc. 4th Intern. Congr. Catal., Moscow, 1968, paper I-3.

20. J. M. Basset, G. Dalmai Imelik, M. Primet, and R. Mutin, J. Catal. 37, 22 (1975).

21. S. M. Davis and G. A. Somorjai, Surf. Sci. 91, 73 (1980).

22. R. J. Madix, Adv. Catalysis 29, 1 (1980).

23. R. J. Madix, CRC Crit. Rev. Solid State and Mats. Sci. 7, 143 (1978).

24. M. C. Tsai and E. L. Muetterties, private communication.

25. R. J. Koestner, M. A. Van Hove, and G. A. Somorjai, Surf. Sci., in press.

26. L. L. Kesmodel, L. H. Dubois, and G. A. Somorjai, J. Chem. Phys. 70, 2180 (1979).

27. L. Dubois, Ph. D. Thesis, University of California, Berkeley, 1980.

28. A. M. Baro and H. Ibach, J. Chem. Phys. 74, 4194 (1981).

29. G. Herzberg, Electronic Spectra of Polyatomic Molecules, D. Van Nostrand, Princeton, NJ, 1966.

30. T. E. Fischer, S. R. Kelemen, and H. P. Bonzel, Surf. Sci. 64, 157 (1977).

31. J. E. Demuth and D. E. Eastman, Phys. Rev. Lett. 32, 1123 (1974).

32. T. A. Carlson and C. P. Anderson, Chem. Phys. Lett. 10, 561 (1971).

33. B. J. Cooper and D. L. Trimm, in Catalyst Deactivation (B. Delmon and G. F. Froment, eds.), Elsevier, Amsterdam, 1980.

34. D. L. Trimm, Catal. Rev. 16, 155 (1977), and references therein.

35. D. W. Blakely, Ph. D. Thesis, University of California, Berkeley, 1976.

36. C. E. Smith, Ph. D. Thesis, University of California, Berkeley, 1978.

37. M. A. Smith, S. Sinharoy, and L. L. Leverson, J. Vac. Sci. Technol. 16, 462 (1979).

38. P. Tetenyi and L. Babernics, J. Catal. 8, 215 (1967).

39. G. F. Taylor, J. J. Thomson, and G. Webb, J. Catal. 12, 191 (1968).

40. S. V. Norval, S. J. Thomson, and G. Webb, Appl. Surf. Sci. 4, 51 (1980).

41. B. H. Davis, J. Catal. 29, 398 (1973); 46, 348 (1977).

42. K. Klier, Rev. Sci. Instr. 40, 1525 (1969).

43. K. Klier, A. C. Zettlemoyer, and H. Leidheiser, J. Chem. Phys. 52, 589 (1970).

44. P. C. Stair and G. A. Somorjai, J. Chem. Phys. 67, 4361 (1977).

45. H. J. Krebs and H. P. Bonzel, Surf. Sci. 99, 570 (1980).

46. J. U. Reid, S. J. Thomson, and G. Webb, J. Catal. 30, 372 (1973).

47. S. J. Thomson and G. Webb, J. C. S. Chem. Comm. 526 (1976).

48. N. C. Gardner and R. S. Hansen, J. Phys. Chem. 74, 3298 (1970).

49. T. J. McCarthy, R. G. Nuzzo, and G. M. Whitesides, J. Amer. Chem. Soc. 103, 3396 (1981).

50. R. R. Schrock, Acc. Chem. Res. 12, 98 (1979).

51. E. L. Muetterties, T. N. Rhodin, E. Band, C. Brucker, and W. R. Pretzer, Chem. Rev. 79, 91 (1979).

52. E. Segal, R. J. Madon, and M. Boudart, J. Catal. 52, 45 (1978).

53. D. W. Blakely, private communication.

54. H. Heinemann, private communication.

55. J. W. A. Sachtler and G. A. Somorjai, to be published.

56. J. R. H. Van Schaik, R. P. Dessing, and V. Ponec, J. Catal. 38, 273 (1975).

57. A. O'Cinneide and F. G. Gault, J. Catal. 37, 311 (1975).

58. V. Ponec and W. M. H. Sachtler, Proc. 5th Intern. Congr. Catal. (Miami-1972), p. 645.

59. T. Hughes, private communication.

60. Z. Karpinski and T. Koscielski, J. Catal. 63, 313 (1980).

61. Z. Paal, M. Dobrovolszky, and P. Tetenyi, J. Catal. 46, 65 (1977).

62. P. P. Lankhorst, H. C. DeJongste, and V. Ponec, in Catalyst Deactivation (B. Delmon and G. F. Froment, eds.) Elsevier, Amsterdam, 1980.

63. F. Zaera and G. A. Somorjai, to be published.

64. R. S. Dowie, D. A. Whan, and C. Kemball, Faraday Trans. 68, 2150 (1973).

65. L. Guczi, A. Sarkany and P. Tetenyi, Faraday Trans. 70, 1971 (1974).

66. B. C. Gates, J. R. Katzer, and G. C. A. Schuit, Chemistry of Catalytic Processes, McGraw-Hill, New York, 1979; P. B. Weisz, Adv. Catal. 13, 137 (1962).

67. F. C. Ciapetta and D. N. Wallace, Catal. Rev. 5, 67 (1972); G. A. Mills, H. Heinemann, T. H. Milliken, and K. G. Oblad, Ind. Eng. Chem. 45, 135 (1953).

68. G. Ertl, M. Neumann, and K. M. Streit, Surf. Sci. 64, 393 (1977).

69. A. Crossley and D. A. King, Surf. Sci. 95, 131 (1980).

70. P. R. Norton, J. W. Goodale, and E. B. Selkirk, Surf. Sci. 83, 189 (1979).

71. H. Hopster and H. Ibach, Surf. Sci. 77, 109 (1978).

72. N. R. Avery, J. Chem. Phys. 74, 4202 (1981).

73. T. H. Lin and G. A. Somorjai, Surf. Sci. 107, 573 (1981); C. T. Campbell, G. Ertl, H. Kuipers, and J. Segner, Surf. Sci. 107, 220 (1981).

74. T. R. Hughes, R. J. Houston, and R. P. Sieg, Ind. Eng. Chem. Proc. Design and Develop. 1, 96 (1962).

75. S. J. Gregg and K. S. W. Sing, Adsorption Surface Area and Porosity, Academic Press, New York, 1967, Chapter 6; J. H. Sinfelt and D. J. C. Yates, J. Catal. 10, 362 (1968); M. A. Vannice, J. Catal. 37, 449 (1975); R. B. Anderson, Experimental Methods in Catalytic Research, Vols. 1-3, Academic Press, New York, 1968-76.

76. R. W. McCabe and L. D. Schmidt, Surf. Sci. 65, 189 (1977).

77. R. W. McCabe and L. D. Schmidt, Surf. Sci. 60, 85 (1976).

78. H. P. Bonzel and R. Ku, J. Chem. Phys. 58, 4617 (1973).

79. J. Benziger and R. J. Madix, Surf. Sci. 94, 119 (1980).

80. W. D. Gillespie, Ph. D. Thesis, University of California, Berkeley, 1980.

81. Z. Paal and P. Tetenyi, J. Catal. 30, 350 (1973).

82. W. M. H. Sachtler and R. A. Van Santen, Adv. Catal. 26, 69 (1977).

83. S. M. Davis and G. A. Somorjai, Hydrocarbon Conversion Over Metal Catalysts in The Chemical Physics of Solid Surfaces and Heterogeneous Catalysis, Elsevier, Amsterdam, 1981.

CHAPTER 5. THE ROLE OF OTHER CHEMICAL ADDITIVES IN HYDROCARBON CATALYSIS OVER PLATINUM

5.1. Effect of Calcium and Oxygen Impurities on Hydrocarbon Reactions Catalyzed Over Pt(13,1,1)

5.1.1. Background

Main group metal oxides are frequently employed as promoters in the preparation of dispersed metal practical catalysts. Potassium oxide, for example, is often used to stabilize iron ammonia synthesis and Fischer-Tropsch catalysts (1,2). A German patent has reported enhanced cyclization selectivity over Na_2O promoted platinum catalysts (3). While the role of these catalyst additives is presently not well understood, it is very clear that under certain conditions metal-metal oxide electronic interactions that render the metal electron deficient or compound formation reactions can take place that result in large changes in catalytic activity and selectivity.

It is very easy to prepare new platinum single crystal surfaces that are free of contaminants other than calcium plus oxygen impurities. These impurities segregate in the near surface region during the initial stages of cleaning and annealing as complex surface compounds that may cover a significant fraction of the surface. The structure and composition of these compounds was investigated extensively by Maire and co-workers (4) using a variety of platinum single crystal surfaces; viz., Pt(100), Pt(111), Pt(S)-[5(100) x (111)], and Pt(S)-[6(111) x (100)]. In all cases, excellent agreement was obtained when a comparison was carried out between the unit meshes derived from LEED patterns of the contaminated platinum crystals with

that of the tetragonal compound $CaPt_2O_4$ (a = 5.78Å, c = 5.60Å) (5). Accordingly, these workers concluded that the "bronze-like" mixed metal oxide is formed in the near surface region of the platinum crystals. A closely related compound with hexagonal symmetry $CaO{\cdot}PtO_2$ (a = 9.33Å, c = 11.24Å) has been reported by McDaniel (6). Scanning Auger microscopy studies by Ross (7) and LEED studies by Salmeron (8), on the other hand, suggest that much of contamination is present in the simple form of CaO islands. Regardless of the exact structure and morphology of the calcium-oxygen impurity, it was suspected that its presence could alter the catalytic behavior of platinum in hydrocarbon catalysis. Such changes might be related to the strong metal support interactions that are often displayed by practical catalysts (9). To test this hypothesis several alkane conversion reactions were studied over the stepped (13,1,1) platinum surface that was initially contaminated by calcium plus strongly bound surface oxygen. This section describes the Striking changes in catalytic selectivity that resulted under these conditions.

5.1.2. Results and Discussion

The catalytic conversion of isobutane, neopentane, and n-hexane on the stepped (13,1,1) platinum surface was investigated at 573 K and at a total pressure of 220 Torr (H_2/HC = 10). Before the reaction rate studies were carried out, the "new" single crystal was heated for several hours at 1070 K in 3 x 10^{-7} Torr of oxygen. Figure 5.1 shows an Auger spectrum recorded after the high temperature oxygen pretreatment. Only platinum, calcium, and oxygen were detectable with

$Pt_{237}/Ca_{295}/O_{510}$ AES peak-to-peak heights in the ratio 1:1.6:2.7. Both crystal faces displayed the same peak height ratios (±8 percent), and the relative peak heights were unaltered by further heating in oxygen at 1073 K or vacuum at 1220 K. Based on published sensitivity factors for Pt, Ca (10), and CaO (11), the measured peak height ratios correspond to approximate atomic ratios Pt:Ca:O of 1:0.15:0.35 (±30 percent). These figures assume isotropic distribution of Pt, Ca^{+2}, and O_2^- within the sampled depth of the Auger spectrum and are thought to represent a lower limit of the calcium-oxide surface concentration. These peak height ratios represent the initial composition of the contaminated surface in all reaction rate studies. The single crystal was later cleaned by etching in aqua regia and argon ion sputtering for about 20 hours which removed all residual traces of calcium and oxygen.

Initial reaction rates (TN = turnover number) and product distributions at 573 K for isobutane, neopentane, and n-hexane reactions catalyzed on the clean and contaminated surface are compared in Fig. 5.2. The contaminated surface displayed catalytic activities that were 2-6 times lower than that of the initially clean (13,1,1) surface. More significant are the dramatic changes in selectivity which resulted on the contaminated surface that are mainly reflected by a marked increase in the relative rate of hydrogenolysis during all three reactions. Hydrogenolysis product distributions dominated by 75-95 percent methane indicate that a complete degradation reaction ($M_f << 1$) was highly favorable on the contaminated surface. In comparison, the clean

platinum surface displayed nearly statistical hydrogenolysis product distributions (Section 3.1). While isobutane and neopentane isomerization proceeded very selectively over the clean (13,1,1) platinum surface (85-97 percent), these reactions were efficiently poisoned in the presence of the calcium-oxide impurity. With n-hexane as the reactant, both cyclization and isomerization were retarded strongly on the contaminated surface.

Product accumulation curves obtained as a function of reaction time for neopentane isomerization and hydrogenolysis catalyzed on the contaminated (13,1,1) platinum surface are compared in Fig. 5.3. Hydrogenolysis displayed less deactivation as a function of time than isomerization or cyclization during the conversion of all three reactants. During the isobutane reaction the hydrogenolysis rate actually increased slightly with time. No significant differences in the build-up of strongly adsorbed carbon deposits was detected between the clean and contaminated platinum surface. Figure 5.1 shows an Auger spectrum obtained after the n-hexane reaction. Except for slight attenuation of the Ca_{295} peak by the C_{273} peak, the composition of the near surface region appeared to be stable and unaltered under the reaction conditions.

Insufficient information presently exists to offer a complete explanation for the unique chemistry that is displayed by platinum in the presence of the calcium-oxide impurity. The changes in selectivity observed for the n-hexane reaction are similar to those reported by Gillespie (12) for n-heptane hydrogenolysis and aromatization catalyzed

over oxidized platinum single crystal surfaces in the absence of calcium. In both cases it appears likely that a Pt-oxide electronic interaction takes place which renders the surface platinum atoms electron deficient with a band structure more like iridium or osmium. These metals are much more active in hydrogenolysis and less selective in isomerization and cyclization as compared to platinum (13). Since hydrogenolysis is an unwanted reaction, it is clear from these studies that calcium oxide would be an undesirable additive in platinum reforming catalysts. These results also indicate that considerable care must be taken in the preparation of "clean" platinum surfaces for catalytic studies. It is likely that even small amounts of calcium contamination may cause considerable changes in catalytic behavior.

FIGURE CAPTIONS

Fig. 5.1. Auger spectra recorded before and after reaction on the Pt(13,1,1) surface that was contaminated with a steady state level of calcium plus strongly bound oxygen impurities.

Fig. 5.2. Comparison of reaction rates (TN = turnover frequency) and product distributions for isobutane neopentane and n-hexane reactions catalyzed on the clean Pt(13,1,1) surface and the Pt(13,1,1) surface when it was contaminated by calcium oxide impurities (T = 573 K, H_2/HC = 10, P_{tot} = 220 Torr).

Fig. 5.3. Product accumulation curves measured as a function of reaction time for neopentane isomerization and hydrogenolysis catalyzed over Pt(13,1,1) contaminated by calcium oxide impurities.

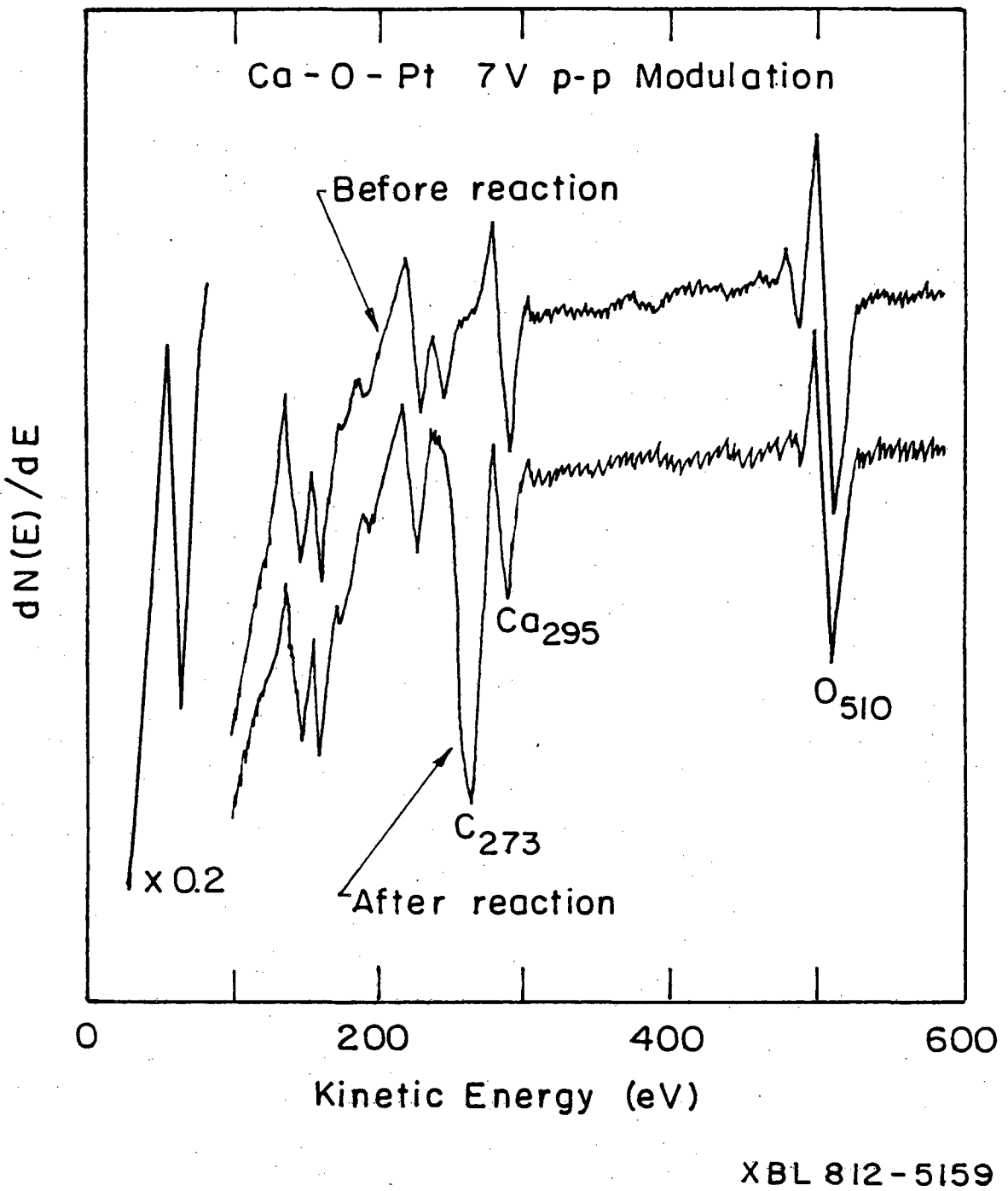
Ca - O - Pt 7V p-p Modulation
Before reaction
dN(E)/dE
Ca295
O510
C273
x 0.2
After reaction
0
200
400
600
Kinetic Energy (eV)
XBL 812-5159

Fig. 5.1

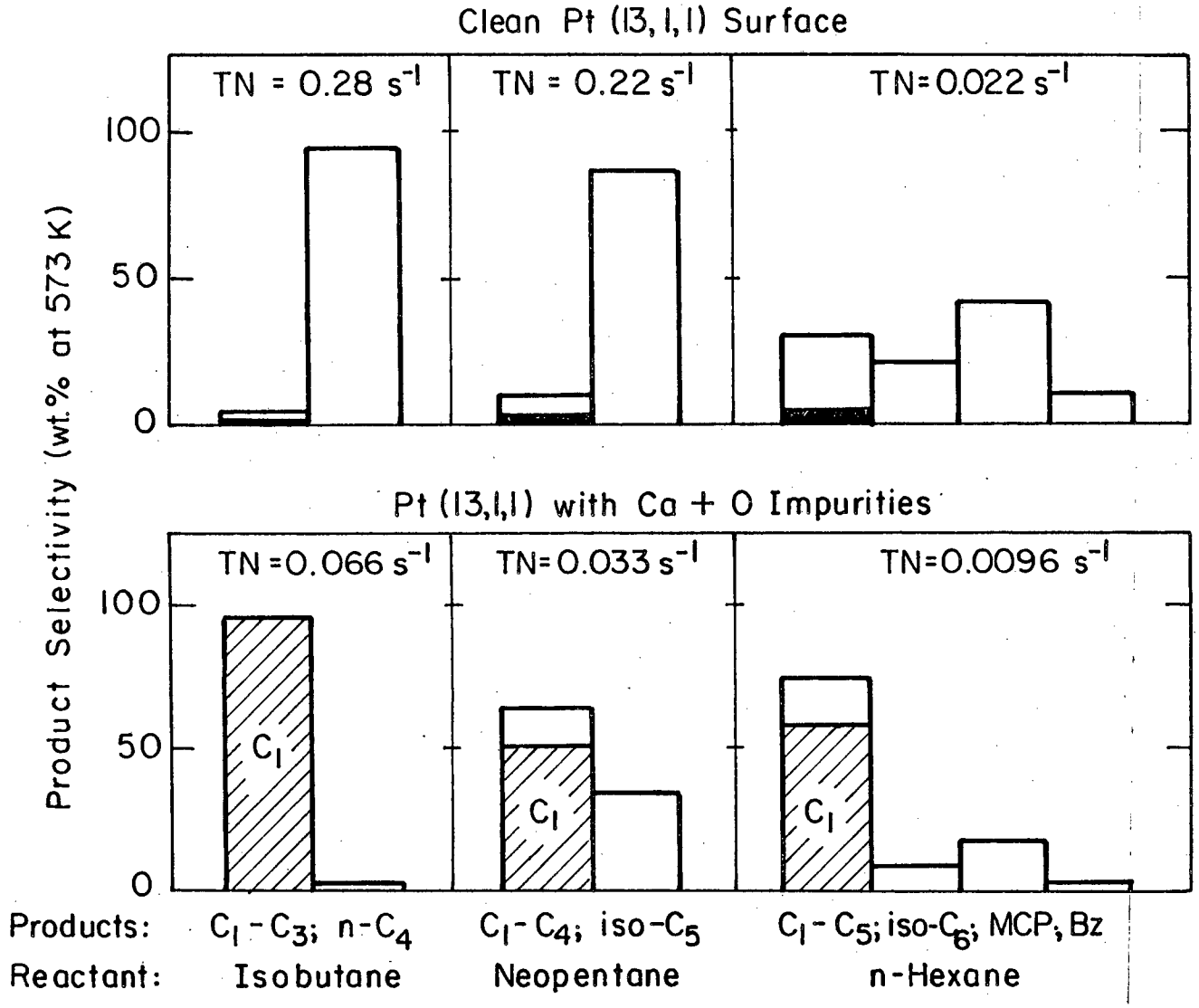

Fig. 5.2

XBL 817-6105

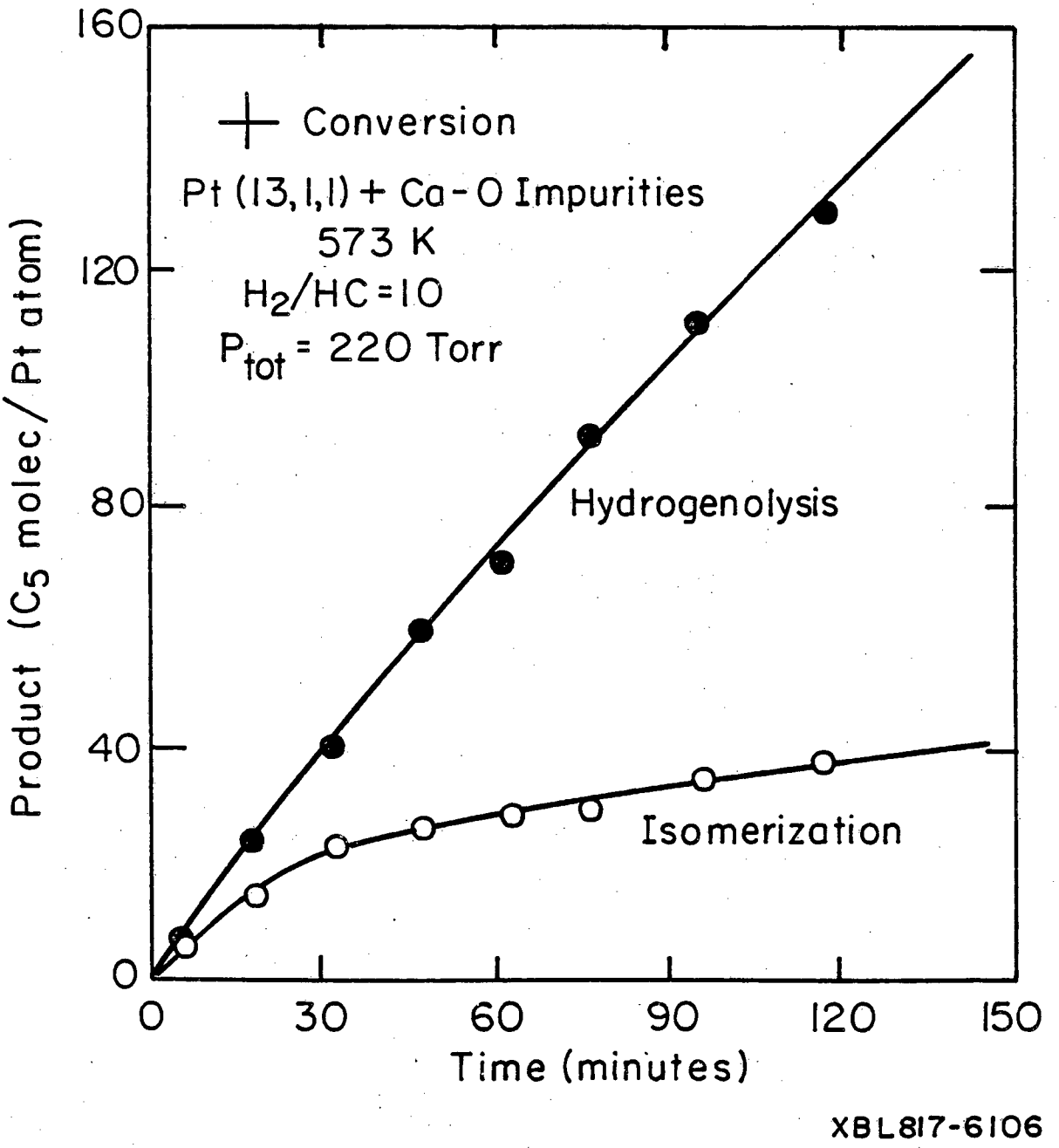
160
120
80
40
0
Product (C_5 molec / Pt atom)
Conversion
Pt (13,1,1) + Ca-O Impurities
573 K
H_2/HC = 10
P_{tot} = 220 Torr
Hydrogenolysis
Isomerization
0
30
60
90
120
150
Time (minutes)
XBL817-6106

Fig. 5.3

5.2. Effect of Sulfur and Thiophene Pretreatment on n-Hexane Reactions Catalyzed on Pt(111)

5.2.1. Background

Sulfur is an essential chemical additive in virtually all commercial reforming catalysts. Bi- and multimetallic catalysts of the Pt-Re and Pt-Ir families, in particular, must be sulfided to obtain acceptable selectivities during reforming of parrafinic petroleum feedstocks (14). The main effects of presulfidization are to lower hydrogenolysis activity relative to isomerization and cyclization and to reduce the rate of coke formation. In these respects, sulfur is the classic example of a selective poison. Sulfidization of reforming catalysts is usually carried out by pretreatment with H_2S/H_2 mixtures (50-500 ppm H_2S) at about 770 K followed by hydrogen reduction for several hours at the same temperature (14). The final reduction cycle is thought to remove ("strip") much of the originally present sulfur resulting in finished catalysts with low surface sulfur concentrations (14,15). In the Pt-Re case, the final catalysts have been formulated Pt-ReS_x (15), where it was suggested that the surface sulfur is uniquely and selectively associated with rhenium atoms. An all-or-nothing conclusion of this nature is difficult to justify in view of the known thermodynamic stability of a wide variety of bulk and surface transition metal sulfides (16-18). Surface science experiments are clearly warranted (indeed, desperately needed) to clarify the role of sulfur in all types of platinum based reforming catalysts. For this reason a limited series of n-hexane reactions was carried out over a Pt(111) single crystal surface that was deliberately pretreated

with sulfur. This section describes the interesting results that were obtained which will hopefully provide an impetus for further research in this area.

5.2.2. Results and Discussion

Two different forms of sulfur pretreatment were investigated. in the first case, surface sulfur was deposited by heating the (111) single crystal sample at 1070-1170 K in a $H_2^-O_2$ ambient (10^{-8} - 10^{-7} Torr) that contained a sulfur impurity of unknown concentration. This pretreatment produced a surface free of contaminants other than sulfur. In the second case, thiophene (C_4H_4S) was preadsorbed at low pressures and 573 K. Surface sulfur concentrations were estimated from Auger spectra recorded directly after the pretreatments as described in Section 2.5. Figure 5.4 compares Auger spectra recorded directly before and after reaction on the thiophene pretreated surface.

The n-hexane reaction rate studies were carried out at two different sets of conditions: (1) 573 K, H_2/HC = 10, P_{tot} = 220 Torr; and (2) 613 K, H_2/HC = 30, P_{tot} = 620 Torr. Table 5.1 summarizes initial rates and selectivities for reactions carried out over the clean and sulfur pretreated surface. Only three reactions, hydrogenolysis, isomerization, and C_s-cyclization, have been considered because irregularities in the gas chromatograph column did not permit complete separation of benzene at the time these experiments were carried out. In the lower half of Fig. 5.5, initial reaction rates on the sulfur pretreated surface, R_s, have been divided by initial rates on clean platinum, R_c, and plotted as a function of the corrected

Table 5.1. Initial reaction rates and fractional selectivities for n-hexane reactions catalyzed over sulfur pretreated Pt(111).

Rxn. T (K)	$\frac{S_{152} + Pt_{150}}{Pt_{237}}$ (a)	(S/Pt) (b)	Turnover Numbers (±20 percent) (molec/Pt atom sec^{-1}) Hydrog.	Isom.	Cyc.	Selectivities (±10 percent) (mole percent) Hydrog.	Isom.	Cyc.
573 (c)	1.2	0	0.0087	0.0087	0.0078	35	35	30
573 (c)	5.7	0.09	0.0025	0.0033	0.0036	27	35	38
613 (d)	1.2	0	0.037	0.039	0.034	34	35	31
613 (d)	2.6	0.03	0.024	0.031	0.024	30	39	30
613 (d,e)	6.6	0.11	0.008	0.014	0.013	23	40	37

(a) AES ratio.
(b) Sulfur atoms per surface Pt atom (±50 percent)
(c) $H_2/HC = 10$, $P_{tot} = 220$ Torr.
(d) $H_2/HC = 30$, $P_{tot} = 620$ Torr.
(e) Thiophene pretreated.

S_{152}/Pt_{237} AES peak-to-peak height ratio. It is clear that the catalytic activity for all reactions decreased with increasing sulfur coverage. Both forms of sulfur (atomic and heterocyclic) produced similar deactivation behavior. Hydrogenolysis was poisoned strongly, whereas isomerization and cyclization were suppressed to a lesser extent. As a result, the selectivity of the n-hexane reaction changed significantly with increasing sulfur coverage. This is emphasized in the upper half of Fig. 5.5 where initial product distributions for the clean and thiophene pretreated (111) platinum surface are compared at 613 K. The selectivity for isomerization and cyclization was clearly enhanced on the sulfur pretreated surface. Similar changes in selectivity have been noted by Biloen et al. (15) for n-hexane reactions catalyzed over sulfided platinum on silica catalysts.

No significant changes in carbon build-up, poisoning behavior, or hydrogenolysis product distributions were detected on the sulfur pretreated Pt(111) surface. These observations are in slight contrast to results reported for practical catalysts (14,19) where sulfidization enhanced long term catalysts stability and shifted the hydrogenolysis product distributions in favor of internal bond splitting reactions. It is notable that the stability of the preadsorbed sulfur species under reaction conditions did depend upon the form of sulfur pretreatment. Whereas atomic sulfur appeared to be completely stable under reaction conditions, thiophene was partially removed during reaction because of rehydrogenation of the hydrocarbon skeleton (cf. Fig. 5.4).

The changes in selectivity observed for the sulfur pretreated (111) platinum surface can be easily interpreted in terms of a simple ensemble effect. Much experimental evidence indicates that hydrogenolysis reactions require multiatomic (3-15) metal sites (13,20), whereas isomerization and C_5-cyclization reactions can apparently proceed readily at sites consisting of a single platinum atom (13,21). On the sulfur pretreated surface the concentration of monatomic sites is enhanced relative to that for multiatomic platinum sites. As a result, the selectivity for methylpentane and methylcyclopentane formation increases. Electronic effects might also contribute to these changes in selectivity, but at present, there is no evidence to indicate that such electronic effects are operative. Regardless of the exact origin of the altered selectivity, the results presented in this section demonstrate that the chemical additive, sulfur, can exert a desireable selective poisoning effect on hydrocarbon reactions catalyzed over platinum.

FIGURE CAPTIONS

Fig. 5.4. Auger spectra recorded before and after n-hexane reaction rate studies on the Pt(111) surface that was pretreated with thiophene at 573 K.

Fig. 5.5. Catalytic behavior of sulfur pretreated Pt(111) for n-hexane isomerization, cyclization, and hydrogenolysis. In the lower frame reaction rates on the sulfur pretreated surface have been divided by reaction rates on clean platinum and plotted as a function of the corrected S_{152}/Pt_{237} AES peak height ratio. In the upper frame product distributions are compared at 613 K for the clean and thiophene pretreated surface.

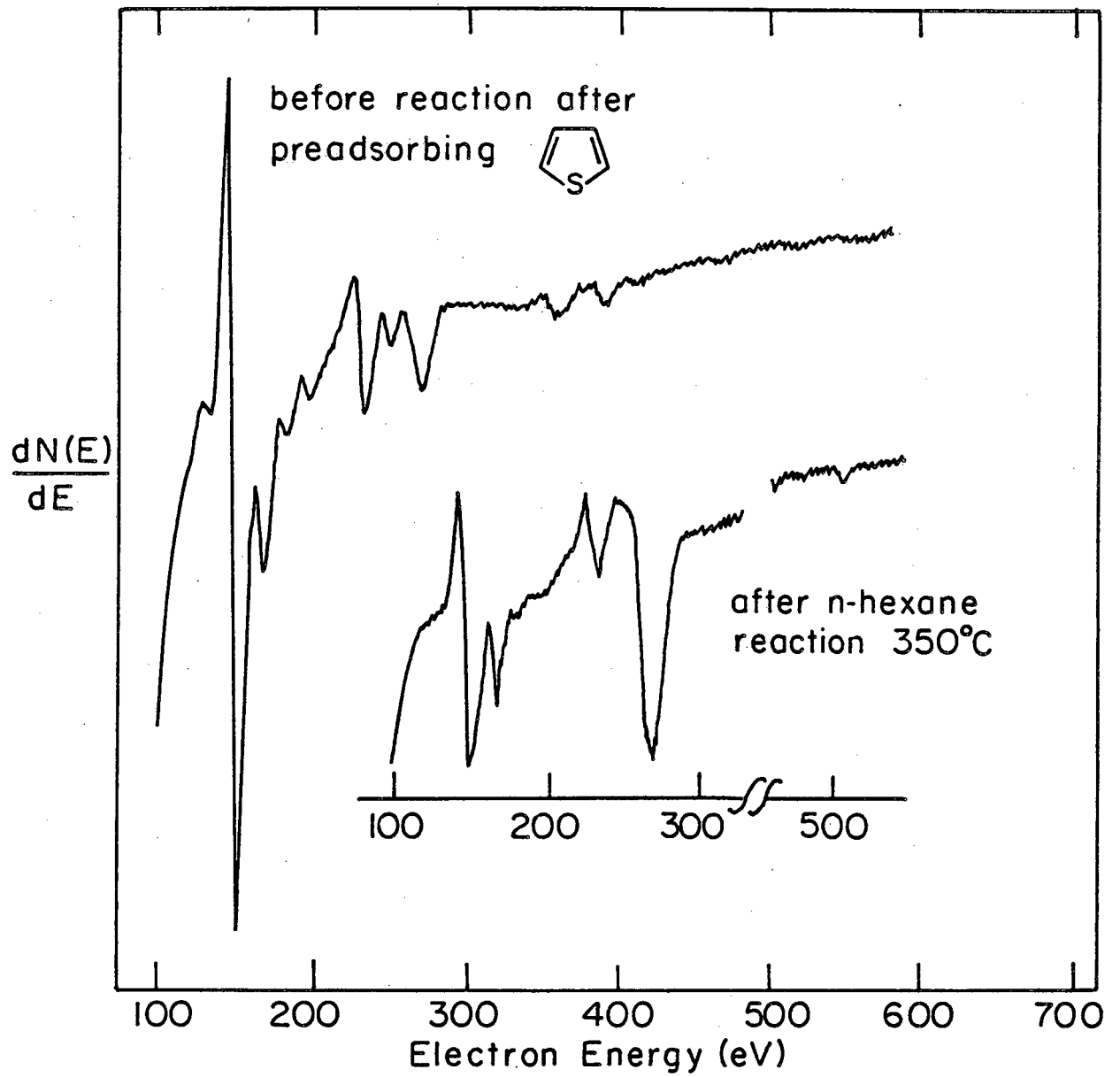
before reaction after
preadsorbing
S
dN(E)
dE
after n-hexane
reaction 350°C
100
200
300
500
100
200
300
400
500
600
700
Electron Energy (eV)
XBL 815-5656

Fig. 5.4

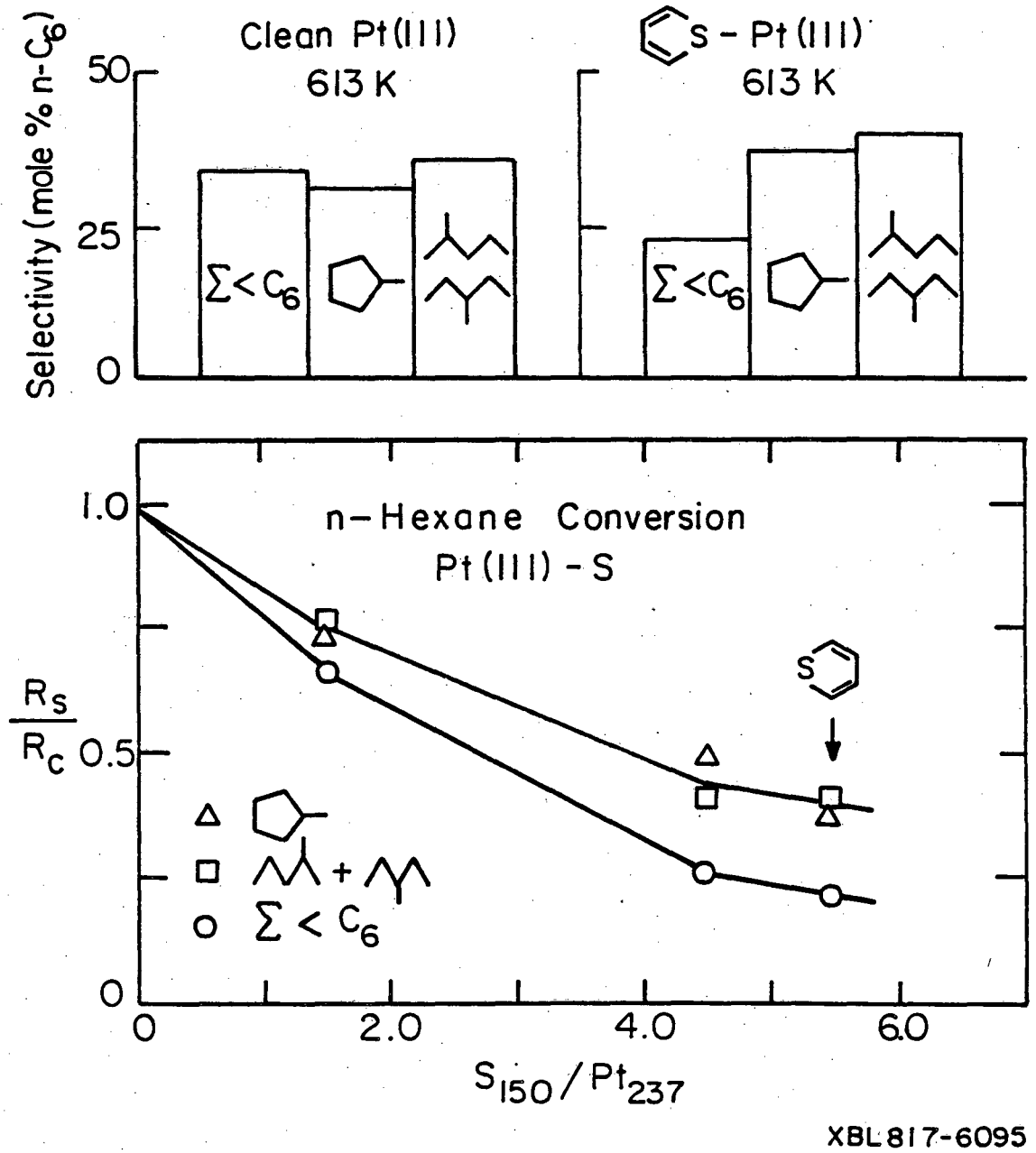
Clean Pt(111)
613 K
S - Pt(111)
613 K
Selectivity (mole % n-C6)
50
25
0
Σ<C6
Σ<C6
n-Hexane Conversion
Pt(111) - S
1.0
0.5
0
Rs/Rc
S
Σ<C6
0
2.0
4.0
6.0
S150/Pt237
XBL817-6095

Fig. 5.5

5.3. Low Pressure Studies of the Effect of Strongly Bound Surface Oxygen on Hydrocarbon Reactions Catalyzed by Platinum Single Crystal Surfaces with Variable Kink Concentrations

5.3.1. Background

The existence of strongly bound states of surface and subsurface oxygen is now well documented for most of the Group VIII transition metals, viz., Ni (22,23), Ru (24,25), Pd (26), Rh (27-31), Ir (32,33), and Pt (34-37). The oxide-like surface compounds form irreversibly, usually at elevated temperatures, and display chemical properties distinctly different from oxygen chemisorbed at ambient or lower temperatures. Ordered (Ni, Pd, Rh, Ir), epitaxially ordered (Ni, sometimes Pd, Pt, and Rh), or disordered (Ru, Rh, Ir) oxide structures have been detected by low energy electron diffraction depending upon the pretreatment conditions, the tendency for oxygen bulk dissolution, and thus, the near surface region oxygen: metal stoichiometry. As compared to the corresponding bulk oxides, the surface oxides display extraordinary thermal stabilities with decomposition temperatures typically 200-500 K higher than those for the bulk oxides. The enhanced stability of the metastable surface oxides appears to be controlled by the slow kinetics of oxygen diffusion, recombination, and reequilibration within the solid near surface region (38).

While all but a few studies have focused exclusively on structural characterization of the unique surface oxides, it is expected that these compounds will have marked influence on the catalytic behavior of transition metals. Virtually all commercial reforming catalysts experience air calcination or other forms of oxygen pretreatment at

temperatures where stable surface oxides form readily. An important question, therefore, concerns what effect strongly bound oxygen has on the catalytic activity, selectivity, and stability of Group VIII metals. Previous investigations of the effect of oxygen on the catalytic behavior of the flat Pt(111), stepped Pt(557), and kinked Pt(10,8,7) crystal faces (12,34) revealed that the strongly bound oxygen imparts unique chemical activity to the high kink concentration surface; much enhanced dehydrogenation and hydrogenation rates during low pressure studies (34), and significantly enhanced hydrogenolysis rates during high pressure studies (12). The combination of kink sites with strongly bound oxygen appears to be the decisive factor controlling the rate and selectivity of platinum in a variety of reactions. Therefore, more detailed investigation of the catalytic behavior of other kinked platinum surfaces in the presence of strongly bound oxygen is warranted.

This section reports results of oxygen chemisorption and low pressure hydrocarbon catalysis studies for a series of platinum crystal surfaces with variable kink concentrations. It is shown that oxygen adsorbs at 1070 K to form an ordered, near surface, oxide layer which activates the C-H bond breaking ability of the kinked platinum surfaces. The oxygen pretreated kinked surfaces also display an increased resistance to self-poisoning that appears to result from the increased strength of hydrogen binding at surface irregularities.

5.3.2. Results

LEED Studies of the Oxidation of Kinked Pt Surfaces. Idealized atomic surface structures and LEED patterns for the kinked platinum single crystal surfaces used in these studies are shown in Fig. 5.6. Upon pretreatment in 2-10 x 10^{-7} Torr of oxygen at 1070 K, ordered oxygen structures were initially detected for Pt(654), Pt(10,8,7), and Pt(12,9,8) when the O_{510}/Pt_{237} AES peak-to-peak height ratio was 0.2-0.25. As shown in Fig. 5.7a for Pt(12,9,8) the predominant pattern was due to a $(\sqrt{3} \times \sqrt{3})$-R30°-O structure on the (111) terraces. On Pt(10,8,7) the diffraction spots from the oxygen surface structure were once streaked along the same direction as the diffraction spots due to the substrate, indicating that the oxygen layer was coherent over several terraces. On Pt(10,8,7) and Pt(12,9,8) with $0.25 \lesssim O_{510}/Pt_{237} \lesssim 0.4$, a (2 x 2)-O structure of lower intensity sometimes coexisted with the $(\sqrt{3} \times \sqrt{3})$-R30° oxygen structure. Only the $(\sqrt{3} \times \sqrt{3})$-R30° structure was observed at $O_{510}/Pt_{237} = 0.5$. This oxide "monolayer" has at least one oxygen atom from every three Pt surface atoms or about 5 x 10^{14} O atoms cm^{-2}. No ordered structures were detected for the oxygen pretreated (321) platinum surface.

The growth of ordered multilayers was detected for Pt(12,9,8) and Pt(654) following extensive oxygen exposures at 1073 K ($\gtrsim 10^3$ L). Oxide growth was accompanied by increased background intensity and gradual attenuation of the substrate diffraction features. The $(\sqrt{3} \times \sqrt{3})$-R30° structure observed for Pt(654) with $O_{510}/Pt_{237} = 1.2$ and 5-8 percent "compressed" $(\sqrt{3} \times \sqrt{3})$-R30° diffraction pattern

(expanded structure) which emerged for Pt(12,9,8) with O_{510}/Pt_{237} = 1.0-1.8 are shown in Figs. 5.7b and 5.7c, respectively. The latter pattern was also accompanied by very weak (1 x 4) diffraction features.

Thermal Desorption Studies of the Strongly Bound Surface Oxygen. The results of oxygen thermal desorption from Pt(12,9,8), Pt(10,8,7), and Pt(654) are shown in Fig. 5.8. The crystals were exposed to O_2 at 1070 K, cooled to ~320 K to obtain an Auger spectrum, and thereafter flashed to ~1450 K. The O_{510}/Pt_{237} AES peak ratio following a TDS run was $\leq$0.05 independent of the step orientation and initial oxygen coverage. The spectra for Pt(10,8,7) and Pt(654) were obtained with crystal mounted 0.5 cm strands of 15 mil Pt wire. Heating rates were consequently non-linear and decreased from ~45 to $\leq$15 $Ksec^{-1}$ over the illustrated range of temperature. For Pt(12,9,8) the crystal was specially mounted on Ta strips and carefully shielded by gold foils to expose only a crystal face in close line of sight to the mass spectrometer ionizer. In this configuration the heating rate was nearly constant at 15 $\pm$ 4 $Ksec^{-1}$.

Two adsorption states, or site dependent manifolds therefore, appear to exist for strongly bound oxygen on each surface. The state with the lower desorption temperature (~1050 K) tended to populate first. The coverage dependence of the desorption peak shapes and temperatures for this state on Pt(12,9,8) were indicative of 2nd order desorption kinetics from a strongly chemisorbed phase. Desorption activation energies for this state (estimated from deconvoluted spectra using Edwards expansion for 2nd order desorption kinetics)

decreased from 60 ± 10 kcal/mole at low coverage to 45 ± 10 kcal/mole near saturation. The second state with the higher desorption temperature (~1220 K) began to populate before the first state reached saturation and, thereafter, continued to grow on further O_2 exposure at 1070 K. This state appears to be due to a second phase of strongly bound oxygen that is located below the topmost surface layer. Order plots (not shown) of ln R_d as a function of ln θ for the second state at 1220 and 1270 K indicated that the desorption order for the second phase was one. Similar desorption temperatures (1070–1270 K) and kinetic behavior have been reported for subsurface oxygen on Pd(111) (26,39) and on oxide phase on Ir(110) (32).

Reaction Rate Studies on the Kinked Pt Surfaces: Cyclohexene Dehydrogenation. The dehydrogenation of cyclohexene to benzene was studied as a function of temperature on the clean surfaces and as a function of the O_{510}/Pt_{237} pph ratio at 427 K. Standard pressures utilized for these experiments were 6×10^{-8} Torr C_6H_{10} and 1×10^{-6} Torr H_2.

The temperature dependence of the maximum dehydrogenation rate is shown in Fig. 5.9. The turnover number, Tn_m (benzene molecules formed per surface Pt atom per sec) consistently exhibited a maximum at about 370 K, and the apparent activation energy below the temperature of this maximum was small. The surfaces with 5-atom terraces behaved similarly, exhibiting the same small activation energy of Ea ~3–4 kcal $mole^{-1}$ for $T \lesssim 380$ K. The reaction required essentially no activation energy on the (321) crystal plane.

The effect of surface preoxidation on cyclohexene dehydrogenation activity is shown in Fig. 5.10. Oxidation enhanced the initial rate of the reaction on all four kinked platinum surfaces. The extent of enhancement depended on the terrace width and kink concentration. For a constant terrace width, the maximum enhancement in the rate of dehydrogenation varied from 60 percent to almost 3-fold and shifted to higher oxygen concentrations with increasing kink concentration. As indicated in Fig. 5.9, half a "monolayer" ($\gtrsim 2.5 \times 10^{14}$ O atoms cm^{-2} of strongly bound oxygen increased the dehydrogenation activity of Pt(654) at all temperatures.

As illustrated in Fig. 5.11, TNm refers to the maximum in the time dependent reactivity, TN(t), that was observed 3–15 min after starting the reaction. This reaction, as well as the others investigated, self-poisoned over a period of 0.5–10 hr, depending on the pressure, surface structure, temperature and to some extent the oxygen concentration. In all cases self-poisoning was accompanied by deposition of 60–90 percent of a monolayer of a disordered partially dehydrogenated carbonaceous overlayer ($C_{237}/Pt_{237} \sim 3.2$ represents monolayer coverage).

By flashing the crystals in vacuum and on stream to 150°C or higher temperatures following 100–200 min of reaction, we determined that self-poisoning was slower and largely reversible when the reaction temperature was below 390 K. Self-poisoning was irreversible and comparatively fast on all the surfaces above 410 K. At 427 K, a rapid initial decline in activity, complete within half an hour, was followed

by a low level, steady state, benzene production rate which persisted for several hours before diminishing to the background level. As indicated in Fig. 5.11a, kinked Pt(654) irreversibly poisoned slower than stepped Pt(557) which deactivated slower than low index Pt(111) [Pt(654) < Pt(557) < Pt(111)]. The kinked surfaces deactivated at similar rates for a given reactant pressure, temperature and oxygen coverage. As shown in Fig. 5.11c, surfaces oxidized to submonolayer coverages usually deactivated slightly slower than clean surfaces, and both consistently self-poisoned slower than platinum surfaces covered with oxide multilayers ($O_{510}/Pt_{237} \gtrsim 0.5$).

Cyclohexene Hydrogenation. Cyclohexene underwent hydrogenation as well as dehydrogenation under the conditions of these experiments. Initial turnover numbers for cyclohexane production as a function of oxygen concentration are shown in Fig. 5.12. Only the clean surfaces with (210) step orientation, viz., Pt(321) and Pt(654), displayed measurable activity at 427 K. Hydrogenation required no activation energy ($E_a \lesssim 1$ kcal/mole) on these surfaces and accounted for less than 5 percent of the total cyclohexene conversion. All the surfaces produced cyclohexane at detectable rates following oxygen pretreatment. Similar low-level hydrogenation activity was reported by Smith (40) for stepped Pt(557) after preoxidation in an earlier study. As discussed in detail in that work, the hydrogenation reaction was a transient associated with the initially clean, oxidized platinum

surfaces. The hydrogenation rate decayed rapidly to zero over a period of about 1-2 min. Cyclohexene continued to undergo dehydrogenation after the hydrogenation reaction had completely self-poisoned.

Cyclohexane Dehydrogenation. The dehydrogenation of cyclohexane to benzene was also investigated on the clean and oxidized surfaces. Results obtained at 427 K with 2×10^{-6} Torr C_6H_{12} and 1×10^{-5} Torr H_2 are illustrated in Fig. 5.13. The shapes of the curves were generally similar to those for cyclohexene dehydrogenation, but the reaction probabilities were about two orders of magnitude smaller. With the terrace width held constant, the maximum activity shifted to higher oxygen concentrations with increasing kink concentration. At $O_{510}/Pt_{237} \sim 0.2$, the Pt(10,8,7) crystal face exhibited 3-fold activity enhancement over the clean platinum surface. Cyclohexene was sometimes produced as a minor dehydrogenation product ($TN_m \lesssim 2 \times 10^{-5}$ mole site^{-1}sec^{-1}) after 2 to 4 hr on stream. Results for a series of reactions with varying pressures are summarized in Table 5.2. As indicated, the initial rate was approximately 1st order in hydrocarbon and fractional positive order in H_2 pressures. The parameter $t_{1/2}$ was the time required for the activity to drop on one-half its maximum value. This parameter indicates that self-poisoning and carbonaceous overlayer buildup rates were inverse order in H_2 pressure and consistently slower than during cyclohexene dehydrogenation, even when the cyclohexane pressure was 25 times greater.

Table 5.2. Variations in poisoning behavior and cyclohexane dehydrogenation activity with reactant pressure at 427 K.

Surface	P_{H_2} (Torr)	P_{HC} (Torr)	TN_m [a] (molec site^{-1}sec^{-1})x10^5	$t_{1/2}$ [b]/(hr)
Pt(10,8,7)	5×10^{-6}	5×10^{-7}	0.7	4
	1×10^{-5}	2×10^{-6}	2.1	0.6
	1×10^{-4}	1×10^{-5}	6.5	0.2
Pt(654)	1×10^{-5}	5×10^{-7}	0.7	5
	2×10^{-6}	2×10^{-6}	0.8	0.4
	6×10^{-6}	2×10^{-6}	1.7	0.5
	1×10^{-5}	2×10^{-6}	2.4	0.6
	4×10^{-5}	2×10^{-6}	3.0	0.8
	1×10^{-4}	1×10^{-5}	8.5	0.2

(a) ±15 percent.

(b) Time required for the rate to decrease to one half of its maximum value; i.e., $TN(t_{1/2}) = 1/2\ TN_m$.

5.3.3. Discussion

Nature of the Surface Platinum Oxide. A $(\sqrt{3} \times \sqrt{3})$-R30° surface structure was observed for the oxidized kinked platinum surfaces at "monolayer coverage" independent of the substrate step orientation. Neither the $(\sqrt{3} \times \sqrt{3})$-R30° structure for Pt(111) vicinal surfaces, nor the (2 x 2) structure observed by Smith (40) for Pt(111), correspond to epitaxial growth of PtO, Pt_3O_4, or PtO_2. Epitaxial growth of PtO was reported for Pt(110) at about 1070 K (36). The appearance of the bulk-oxide coincidence mesh was preceeded in the coverage range spanning this study by the formation of a simpler c(2 x 2) transient oxide structure. Both ordered layers on Pt(110) decomposed at about 1250 K in reasonable agreement with the TDS results presented here. Unique oxygen bonding states which exist in the near surface region stabilize the surface platinum oxide at temperatures far in excess of those required for thermal desorption of chemisorbed oxygen (~725 K) and thermal decomposition of bulk platinum oxides (725-870 K) (41). More recent studies by Salmeron (38) revealed the formation of compressed $(\sqrt{3} \times \sqrt{3})$-R30° diffraction patterns for Pt(111) and Pt(332) following extensive oxygen treatment at 1070 K ($O_{510}/Pt_{237} \gtrsim 1$). These diffraction patterns are analogous to that shown for Pt(12,9,8) in Fig. 5.7c. Salmeron's analysis of this diffraction pattern revealed excellent agreement with the (0001) plane of α-PtO_2 (a = 5.37Å). Ion scattering studies by Niehus and Comsa (42) have shown that the strongly bound oxygen is entirely located below the topmost layer of platinum atoms, at least in the case of Pt(111). This conclusion is supported by the

facts that: (1) high temperature oxygen pretreatment causes a 1 eV decrease in the platinum work function (43); and (2) the strongly bound oxygen displayed no reactivity with CO or H_2 at temperatures up to 1000 K. Thus it appears that oxygen adsorption and dissolution at high temperatures leads to the formation of a complex subsurface platinum oxide. At high oxygen concentrations the structure of this surface compound resembles PtO_2.

Reactivity of Oxygen Pretreated Platinum. The dehydrogenation activity of the kinked platinum surfaces with 5-atom terraces was enhanced by low concentrations of strongly bound subsurface oxygen. The maximum in activity shifted to higher oxygen concentrations with increasing kink concentration. The maxima appeared at about the same coverage as the initial onset of ordering in the oxide layer and, also, at about the same coverage where the second oxygen adsorption state began to populate. The activity decreased sharply at higher concentrations corresponding to a large buildup of subsurface oxygen. The reactivity of all the surfaces dropped and attained the same low values at coverages we have associated with an oxide monolayer, i.e., $O_{510}/Pt_{237} \sim 0.5$.

The terrace width was also important in determining the catalytic activity. The reactivity of Pt(321) and its poisoning behavior changed little with oxygen pretreatment. This is probably due to a steric effect since the Pt(321) terraces (ca. 5Å) are barely wide enough to accommodate π-bonded cyclohexene or benzene molecules (Van der Waals radii (7.2-7.6Å).

Significant enhancements in catalytic activity due to surface oxidation were detected only for the kinked platinum surfaces that also had wider terraces (5 atoms wide or ~14Å) of (111) orientation. A factor of two or more enhancement in reactivity was obtained by the combined presence of oxygen and kink sites on the surfaces. As noted earlier, surface oxygen was not notably effective in activating the C-H bond breaking activity of the low index (111) and stepped (557) platinum surfaces (34). The resistance of the (111) and (557) platinum surfaces to self-poisoning was also unchanged by surface oxygen (40). In contrast, on the kinked Pt(654), Pt(10,8,7) and Pt(12,9,8) crystal faces strongly bound oxygen inhibited deactivation, especially at lower temperatures and thus stabilized sites that would otherwise poison rapidly. Strongly bound oxygen promoted both the activity and stability of the kinked surfaces with 5 atom wide terraces.

The presence of strongly bound oxygen also altered the selectivities of the kinked platinum crystal surfaces for cyclohexene hydrogenation and dehydrogenation. The kinetic selectivity for hydrogenation over dehydrogenation ($TN_{\bigcirc}/TN_{\bigcirc}$) was maximized at low oxygen concentrations corresponding to the maximum hydrogenation activity; i.e., at O_{510}/Pt_{237} = 0.0, 0.20, 0.12, and 0.25 for Pt(321), (654), (10,8,7), and (12,9,8), respectively. In general, the hydrogenation reaction appeared to be insignificant as compared to dehydrogenation since the dehydrogenation reaction was always 10-100 times faster.

A change in the electronic structure of the platinum surface through oxidation provides the most viable explanation for the enhanced reactivity of the oxidized kinked platinum surfaces. Such changes could affect the binding strength of hydrogen and hydrocarbon reactants, intermediates, or products, thereby producing different rates and selectivities for hydrocarbon conversion reactions. McCabe and Schmidt reported that strongly bound oxygen created new binding states for H_2 and CO with increased binding energy on Pt(110) and Pt(111) surfaces (44,45). These authors proposed two additional mechanisms which could account for the different chemistry of the oxygen pretreated platinum; namely surface restructuring during oxidation or compound formation between oxygen and hydrogen or other gases. While surface restructuring certainly occurs over many oxygen treated platinum crystal faces (46), no restructuring could be detected for any of the kinked surfaces used in these studies. Since the strongly bound oxygen is predominantly located below the surface, one can reasonably argue that compound formation is probably not the primary mechanism for the enhanced reactivity.

It should be emphasized that the low pressure hydrocarbon reactions described here are not strictly catalytic because the integrated turnover frequencies were generally less than one product molecule per surface Pt atom. Nevertheless, there are notable similarities between our results and results obtained near atmospheric pressure using supported platinum catalysts. Poltorak et al. (47,48) reported that highly dispersed catalysts displayed enhanced activity

for cyclohexene hydrogenation following oxidation at 670 K. The activity of catalysts with low dispersions ($\bar{d} \gtrsim 50$Å) was not altered appreciably. These results are consistent with those reported here assuming that the highly dispersed particles have high concentrations of edge and kink sites. On the other hand, there are also significant differences between the results of high and low pressure studies as would be expected from the discussion of previous sections. Using the same (10,8,7) platinum crystal near atmospheric pressure, Gillespie found only a small oxygen effect for cyclohexane dehydrogenation to benzene at catalyzed 573 K. A much larger oxygen effect was observed for cyclohexane hydrogenolysis to light alkane fragments in which the hydrogenolysis rate increased with increasing oxygen concentration. The different nature of the oxygen effect at high and low pressures most probably arises from large differences in the steady state surface concentrations of chemisorbed hydrogen and hydrocarbon species.

Clean Surface Reactivity. Among the clean surfaces at 425 K, Pt(321) (20 percent kinks) was distinctly more active for cyclohexane dehydrogenation and cyclohexene hydrogenation, but generally less active for cyclohexene dehydrogenation. The order of activities of the clean surfaces for cyclohexane dehydrogenation, (321) > (654) ~ (10,8,7) ~ (12,9.8) > 557) ~ (111), correlates to some extent with kink concentration. Nonetheless, the difference in reactivity between the least and most active planes was only about a factor of two. These low pressure results agree with results for dispersed catalysts at high pressures (49) that indicate that cyclohexane dehydrogenation is

essentially structure insensitive. At atmospheric pressure and 573 K, Gillespie (12) found that the kinked (10,8,7) platinum surface was about four times more active than Pt(111) for cyclohexane dehydrogenation.

From the viewpoint of structure sensitivity, the most striking result of this study is that both clean surfaces with (210) step orientation [Pt(321) and Pt(654)] exhibited measurable hydrogenation activity at 423 K. Moreover, the hydrogenation activity was proportional to the density of monatomic (210) steps. The (12,9,8), (10,8,7), (557) and (111) crystal faces produced quantifiable amounts of cyclohexane only after the surfaces were preoxidized. It is interesting that Cunningham and Gwathmey (50) found a Ni(321) crystal to be at least a factor of two more active for ethylene hydrogenation than Ni(100), Ni(110) or Ni(111) in the first reactivity study using oriented crystal catalysts. More experiments at higher pressures should be carried out to establish if sites associated with (210) steps are especially active for olefin hydrogenation.

Poison Resistance of Kinked Pt Surfaces. The cyclohexene dehydrogenation activity increased rapidly between 300 and 370 K. Thermal desorption studies (Section 3.2) indicated that the benzene desorption rate becomes appreciable in this temperature range. The surfaces reversibly poisoned and saturated with benzene, or a precursor, when the reaction was carried out below the benzene desorption temperature of about 390 K. At higher temperatures the rates decreased and the kinetics were dominated by rapid irreversible self-poisoning.

At 427 K the deactivation rate was comparable to the benzene production rate. Irreversible poisoning was facilitated by a rapidly decreasing concentration of chemisorbed hydrogen with increasing temperatures. The residence time for the reacting species decreased more rapidly than the mean time necessary for benzene production as the steady state hydrogen coverage diminished with increasing reaction temperature. Hydrogen was chemisorbed more strongly on the kinked surfaces and, consequently, kinked surfaces irreversibly poisoned more slowly than stepped Pt(557) or Pt(111). The poisoning behavior and structure sensitivity of cyclohexene dehydrogenation at low pressures correlates with the strength of the metal-hydrogen chemisorption bond. Surface hydrogen appears to be an important additive inhibiting irreversible carbon buildup during low pressure hydrocarbon dehydrogenation.

Conclusions. Low concentrations of strongly bound surface oxygen enhance the C-H bond breaking of kinked Pt crystal surfaces and alter the product distribution during hydrocarbon hydrogenation and dehydrogenation. A combination of high surface kink concentration and the presence of strongly bound oxygen are needed to obtain this effect.

Chemisorbed hydrogen, bound strongly at surface kinks, also plays an important role in inhibiting irreversible self-poisoning reactions and concomitant buildup of carbonaceous deposits.

Similar phenomena, due to surface additives, are expected to be important for supported Pt catalysts were stable surface oxides could form during oxygen pretreatments or by chemical interactions between the metal particles and the oxide support. Hydrogen prevents self-poisoning of kinked Pt surfaces.

FIGURE CAPTIONS

Fig. 5.6. Idealized atomic surface structures and LEED patterns for the platinum surfaces studied.

Fig. 5.7. LEED patterns for ordered ($\sqrt{3}$ x $\sqrt{3}$)-R30° oxygen layers: (A) Pt(12,9,8), 45 V O_{510}/Pt_{237} = 0.38; (B) Pt(654), 105 V, O_{510}/Pt_{237} = 1.18; (C) Pt(12,9.8), 56 V O_{510}/Pt_{237} = 1.3.

Fig. 5.8. Thermal desorption of O_2 from Pt(10,8,7), Pt(654) and Pt(12,9,8); 1 L = 10^{-6} Torr sec.

Fig. 5.9. Temperature dependence of cyclohexene dehydrogenation to benzene with P_{HC} = 6 x 10^{-8} Torr and P_{H_2} = 1 x 10^{-6} Torr.

Fig. 5.10. Maximum turnover numbers at 150°C for the dehydrogenation of cyclohexene to benzene as a function of oxygen coverage.

Fig. 5.11. Time dependent poisoning behavior during cyclohexene dehydrogenation to benzene at constant pressure (6 x 10^{-8} Torr CH and 1 x 10^{-6} Torr H_2) (a) effect of surface structure; (b) effect of temperature; (c) effect of surface oxygen.

Fig. 5.12. Maximum turnover numbers at 150°C for the hydrogenation of cyclohexene to cyclohexane as a function of oxygen coverage.

Fig. 5.13. Maximum turnover numbers at 150°C for the dehydrogenation of cyclohexane to benzene as a function of oxygen coverage.

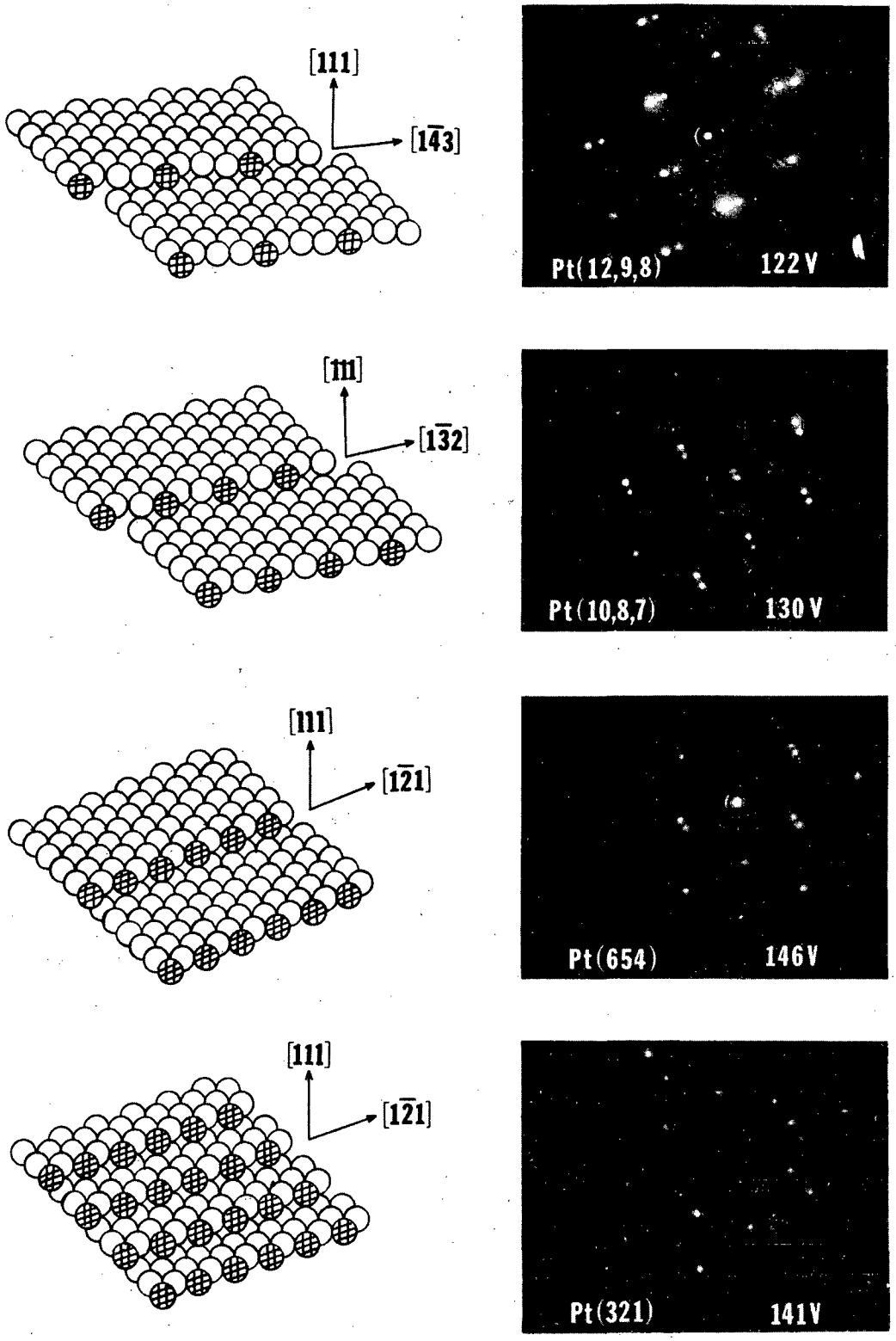

XBB 793-2960

Fig. 5.6

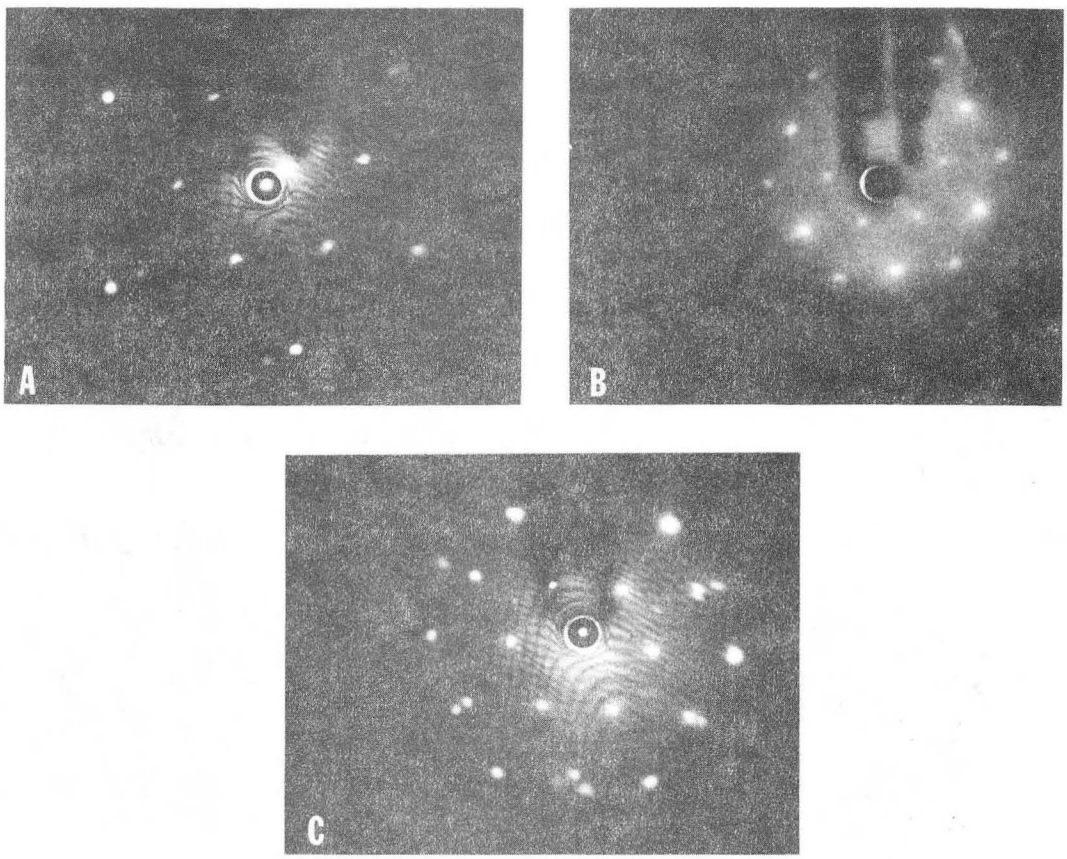

XBB 795-6638

Fig. 5.7

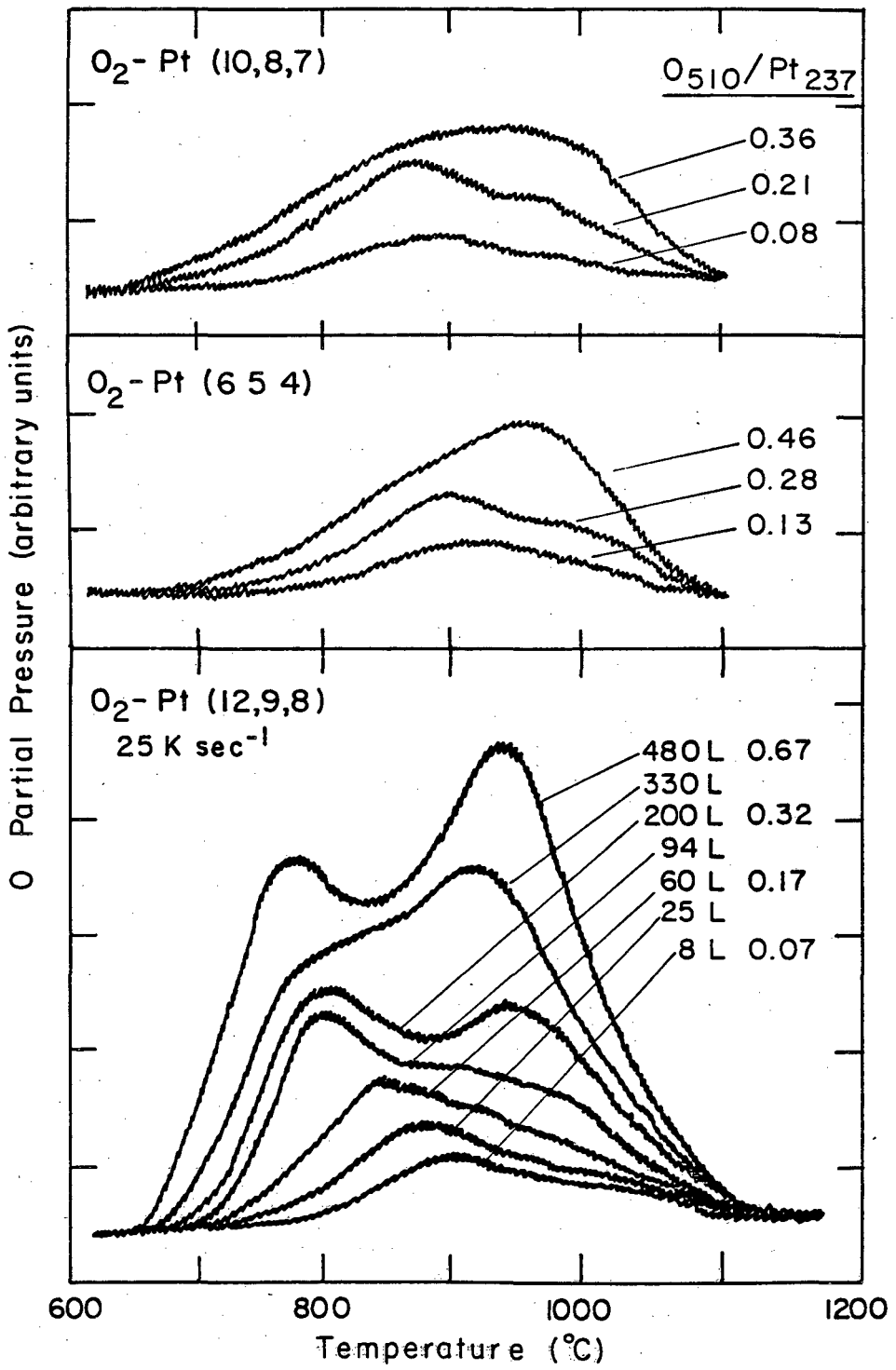
O2 - Pt (10,8,7)
O510/Pt237
0.36
0.21
0.08
O2 - Pt (6 5 4)
0.46
0.28
0.13
O2 - Pt (12,9,8)
25 K sec-1
480 L 0.67
330 L
200 L 0.32
94 L
60 L 0.17
25 L
8 L 0.07
O Partial Pressure (arbitrary units)
600
800
1000
1200
Temperature (°C)
XBL 794-6178

Fig. 5.8

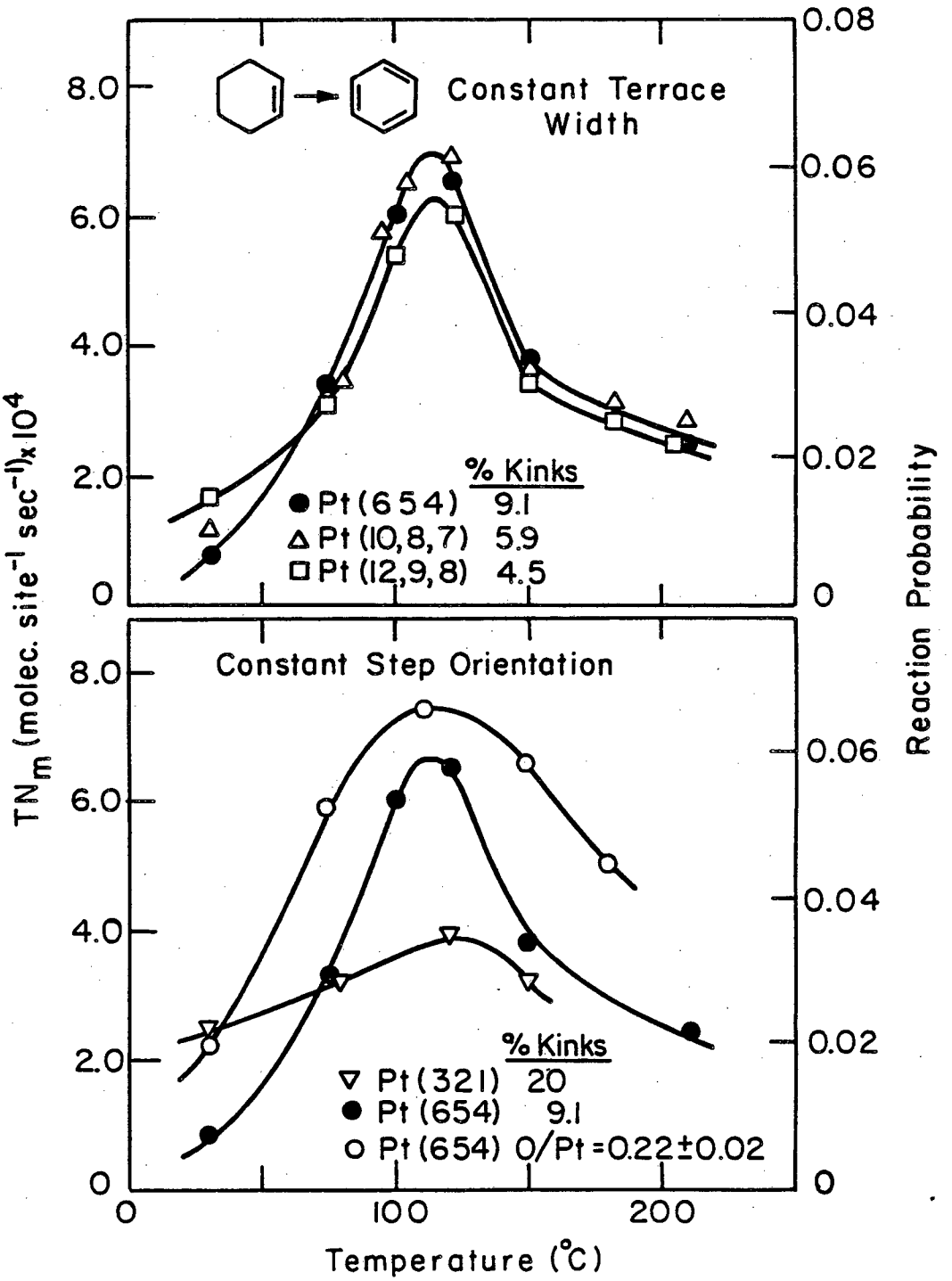

XBL792-5821

Fig. 5.9

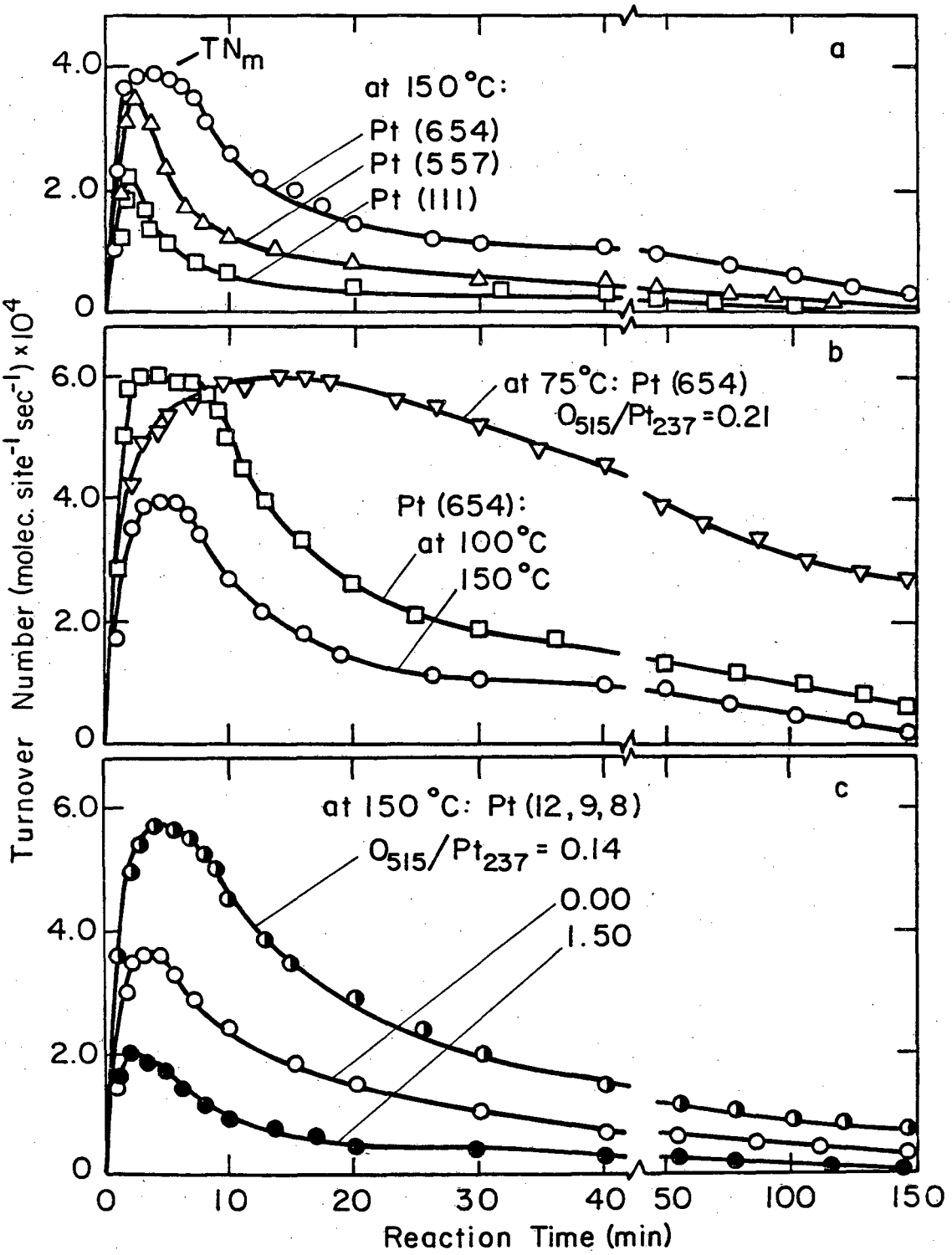
TNm
a
at 150°C:
Pt (654)
Pt (557)
Pt (111)
b
at 75°C: Pt (654)
O515/Pt237 =0.21
Pt (654):
at 100°C
150°C
c
at 150°C: Pt (12,9,8)
O515/Pt237 = 0.14
0.00
1.50
Turnover Number (molec. site-1 sec-1) x10^4
Reaction Time (min)
XBL 794-6179

Fig. 5.10

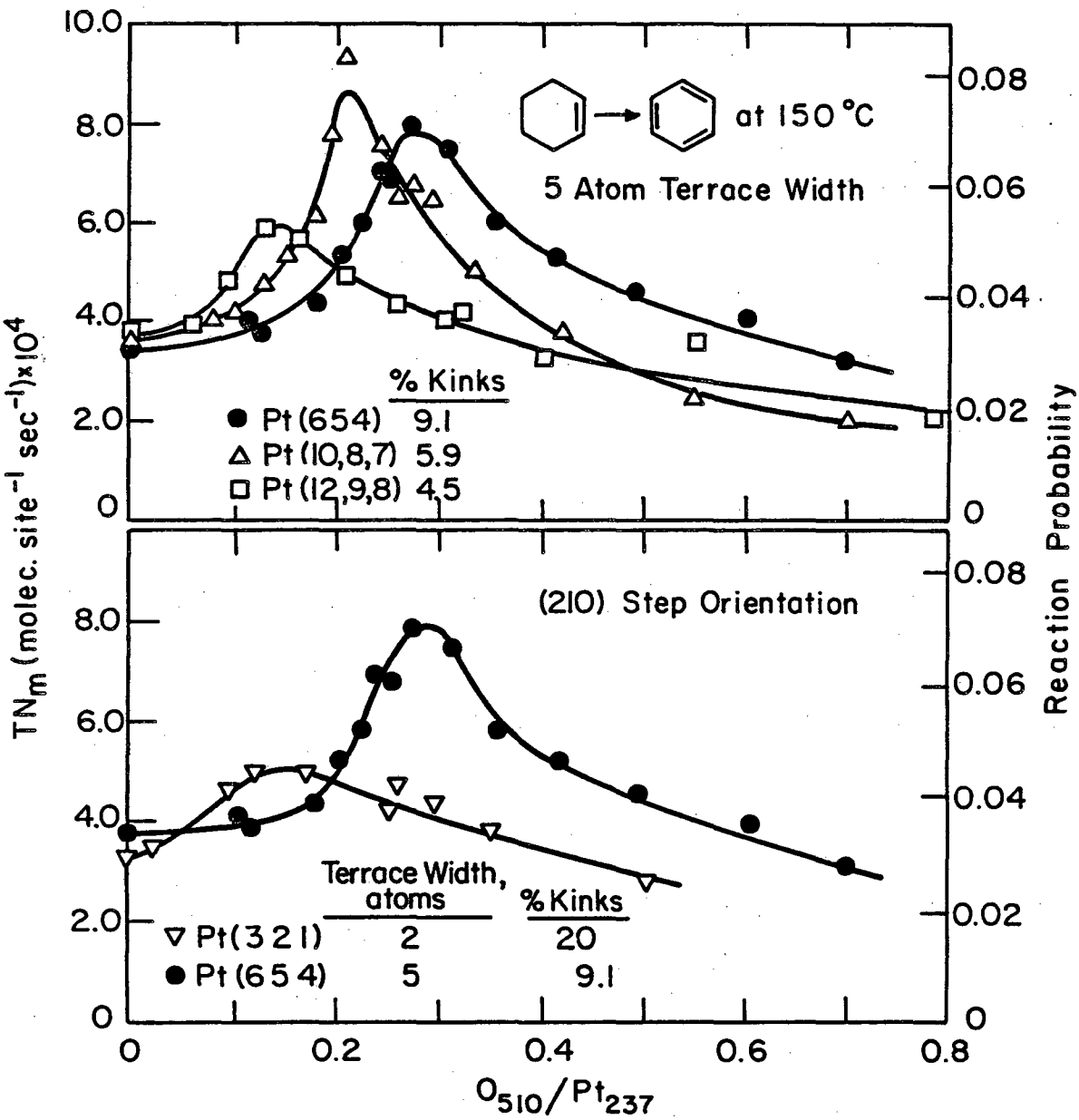
10.0
8.0
6.0
4.0
2.0
0
0.08
0.06
0.04
0.02
0
at 150 °C
5 Atom Terrace Width
% Kinks
● Pt(654) 9.1
△ Pt(10,8,7) 5.9
□ Pt(12,9,8) 4.5
(210) Step Orientation
Terrace Width, atoms
% Kinks
▽ Pt(321) 2 20
● Pt(654) 5 9.1
0
0.2
0.4
0.6
0.8
TN_m (molec. site^{-1} sec^{-1})x10^4
Reaction Probability
O_{510}/Pt_{237}
XBL792-5824

Fig. 5.11

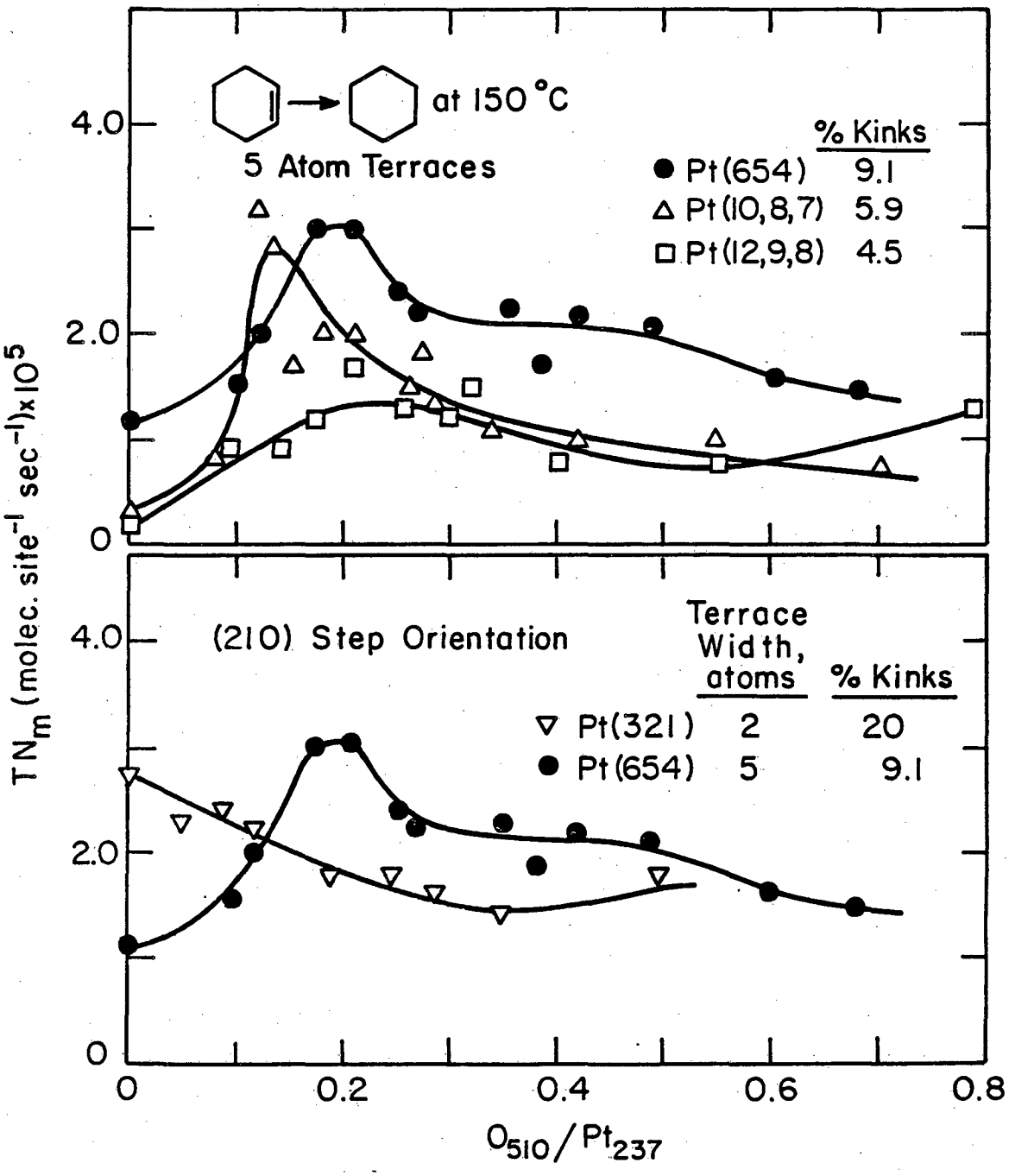
at 150 °C
5 Atom Terraces
% Kinks
Pt(654) 9.1
Pt(10,8,7) 5.9
Pt(12,9,8) 4.5
(210) Step Orientation
Terrace Width, atoms
% Kinks
Pt(321) 2 20
Pt(654) 5 9.1
TN_m (molec. site^-1 sec^-1) x 10^5
O_510/Pt_237
0
2.0
4.0
0.2
0.4
0.6
0.8
XBL792-5823

Fig. 5.12

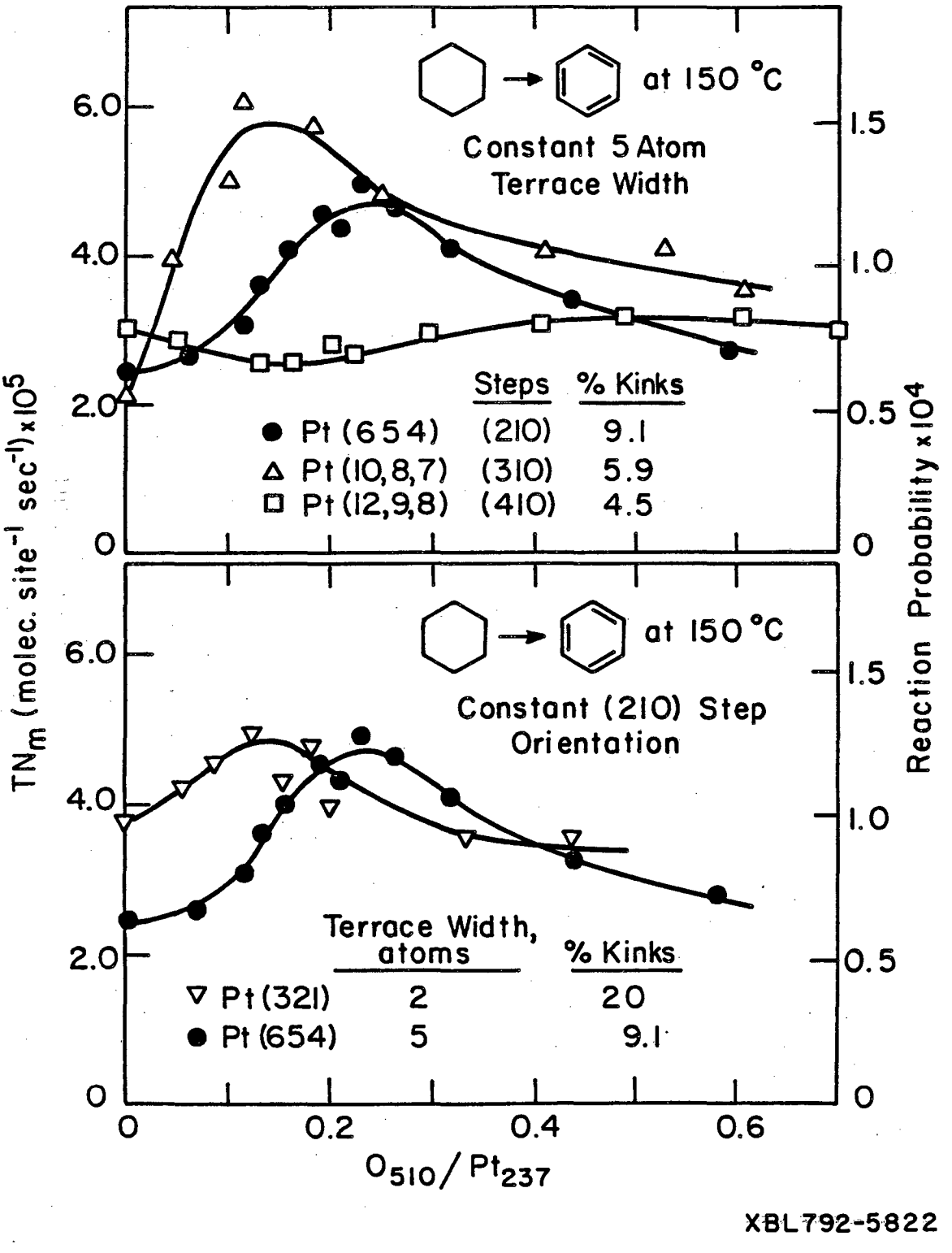
at 150 °C
Constant 5 Atom Terrace Width
Steps % Kinks
Pt (6 5 4) (210) 9.1
Pt (10,8,7) (310) 5.9
Pt (12,9,8) (410) 4.5
at 150 °C
Constant (210) Step Orientation
Terrace Width, atoms
% Kinks
Pt (321) 2 20
Pt (654) 5 9.1
TNm (molec. site-1 sec-1) x 10^5
Reaction Probability x 10^4
O510/Pt237
XBL792-5822

Fig. 5.13

REFERENCES

1. P. H. Emmett, in The Physical Basis for Heterogeneous Catalysis, ed. E. Drauglis and R. I. Jafee, Plenum, N. Y., 1975.
2. H. H. Storch, Adv. Catal. 1, 115 (1948).
G. A. Somorjai, Surf. Sci. 89, 496 (1979).
3. J. M. McCarroll, Surf. Sci. 53, 297 (1975) and references therein.
4. G. Lindauer, P. Legare , and G. Maire, Proc. 3rd Europ. Conf. Surf. Sci., Cannes, 1980.
5. D. Cahen, J. A. Ibers, and R. D. Shannon, Inorg. Chem. 11, 2311 (1972).
6. C. L. McDaniel, J. Amer. Cer. Soc. 55, 426 (1972).
7. P. N. Ross, private communication.
8. M. Salmerón, private communication.
9. S. J. Tauster and S. C. Fung, J. Catal. 55, 29 (1978).
10. Physical Electronics Auger Manual.
11. A. Shih, C. Hor, and G. A. Haas, Appl. Surf. Sci. 2, 112 (1979).
12. W. D. Gillespie, Ph. D. Thesis, University of California, Berkeley, 1980.
13. S. M. Davis and G. A. Somorjai, Hydrocarbon Conversion Over Metal Catalysts, in The Chemical Physics of Solid Surfaces and Heterogeneous Catalysis, D. A. King and D. P. Woodruff, eds., Elsevier, 1981.
14. W. C. Baird and C. H. Mauldin, private communication.
15. P. Biloen, J. N. Helle, H. Verbeek, F. M. Dautzenberg, and W. M. H. Sachtler, J. Catal. 63, 112 (1980).

16. J. Oudar, Catal. Rev. 22, 171 (1980).

17. K. C. Mills, Thermodynamic Data for Inorganic Sulfides, Selenides, and Tellurides, Butterworths, London, 1974.

18. T. A. Pecoraro and R. R. Chianelli, J. Catal. 67, 430 (1981).

19. S. Sivasanker and A. V. Ramaswamy, J. Catal. 37, 533 (1975).

20. J. K. A. Clarke and J. J. Rooney, Adv.. Catal. 25, 125 (1976) and references therein; M. Boudart, Proc. 6th Int. Congr. Catal., London, 1976, paper 1; G. A. Martin, J. Catal. 60, 345 (1979).

21. J. R. Anderson and Y. Shimoyama, Proc. 5th Int. Congr. Catal., Miami, 1972, p. 695; V. Amir-Ebrahami, F. Garin, F. Weisang, and F. G. Gault, Nouv. J. Chim. 3, 529 (1979) and references therein.

22. P. R. Norton, R. L. Tapping, and J. W. Goodale, Surf. Sci. 65, 13 (1977).

23. P. H. Holloway and J. B. Hudson, Surf. Sci. 43, 123 (1974).

24. R. Klein and A. Shih, Surf. Sci. 69, 403 (1977).

25. P. D. Reed, C. M. Comrie, and R. M. Lambert, Surf. Sci. 64, 603 (1977).

26. H. Conrad, G. Ertl, J. Kuppers and E. E. Latta, Surf. Sci. 65, 245 (1977).

27. P. A. Thiel, J. T. Yates, and W. H. Weinberg, Surf. Sci. 82, 22 (1979).

28. D. G. Castner, B. A. Sexton, and G. A. Somorjai, Surf. Sci. 71, 519 (1978).

29. C. W. Tucker, Jr., J. Appl. Phys. 37, 4147 (1966).

30. C. W. Tucker, Jr., J. Appl. Phys. 38, 2696 (1967).

31. D. G. Castner and G. A. Somorjai, Appl. Surf. Sci. 6, 29 (1980).

32. J. L. Taylor, D. E. Ibbetson, and W. H. Weinberg, Surf. Sci. 79, 349 (1979).

33. V. P. Ivanov, G. K. Boreskov, V. I. Savchenko, W. F. Egelhoff, Jr., and W. H. Weinberg, Surf. Sci. 61, 207 (1976).

34. C. E. Smith, J. P. Biberian and G. A. Somorjai, J. Catal. 57, 426 (1979).

35. M. Salmerón and G. A. Somorjai, Surf. Sci. 91, 373 (1980).

36. R. Ducros and R. P. Merrill, Surf. Sci. 55, 227 (1976).

37. J. L. Gland and V. N. Korchak, Surf. Sci. 75, 733 (1978).

38. M. Salmerón, L. Brewer, and G. A. Somorjai, submitted for publication.

39. D. L. Weisman, M. L. Shek, and W. E. Spicer, undisclosed preprint.

40. C. E. Smith, Ph. D. Thesis, University of California, Berkeley, 1978.

41. J. C. Chaston, Platinum Metals Rev. 8, 50 (1964).

42. H. Niehus and G. Comsa, Surf. Sci. 93, L147 (1980).

43. D. R. Monroe, V. Lampton, and R. P. Merrill, J. Vac. Sci. Technol. 14, 44 (1977).

44. R. W. McCabe and L. D. Schmidt, Surf. Sci. 60, 85 (1976).

45. R. W. McCabe and L. D. Schmidt, Surf. Sci. 65, 189 (1977).

46. D. W. Blakely, Ph. D. Thesis, University of California, Berkeley, 1976.

47. O. M. Poltorak and U. S. Boronin, Russ. J. Phys. Chem. 40, 1436 (1966).

48. A. M. Mitrafanova, V. S. Boronin, and O. M. Poltorak, Russ. J. Phys. Chem. 46, 32 (1972).

49. R. W. Maatman, P. Mahaffy, P. Hoekstra, and C. Addink, J. Catal. 23, 105 (1973).

50. R. E. Cunningham and A. T. Gwathmey, Adv. Catal. 9, 25 (1957).

This report was done with support from the Department of Energy. Any conclusions or opinions expressed in this report represent solely those of the author(s) and not necessarily those of The Regents of the University of California, the Lawrence Berkeley Laboratory or the Department of Energy.

Reference to a company or product name does not imply approval or recommendation of the product by the University of California or the U.S. Department of Energy to the exclusion of others that may be suitable.

TECHNICAL INFORMATION DEPARTMENT
LAWRENCE BERKELEY LABORATORY
UNIVERSITY OF CALIFORNIA
BERKELEY, CALIFORNIA 94720